



Hybrid Optimization Algorithm for Resource Allocation in LTE-Based D2D Communication

Amel Austine* and R. Suji Pramila

Department of Computer Science and Engineering, Noorul Islam Centre for Higher Education,
Kumaracoil, Tamilnadu, India

*Corresponding Author: Amel Austine. Email: amelaustine@gmail.com

Received: 13 May 2022; Accepted: 16 December 2022

Abstract: In a cellular network, direct Device-to-Device (D2D) communication enhances Quality of Service (QoS) in terms of coverage, throughput and amount of power consumed. Since the D2D pairs involve cellular resources for communication, the chances of interference are high. D2D communications demand minimum interference along with maximum throughput and sum rate which can be achieved by employing optimal resources and efficient power allocation procedures. In this research, a hybrid optimization model called Genetic Algorithm-Adaptive Bat Optimization (GA-ABO) algorithm is proposed for efficient resource allocation in a cellular network with D2D communication. Simulation analysis demonstrates that the proposed model involves reduced interference with maximum sum rate and throughput. The performance of the proposed model is compared with the existing Ant Colony Optimization-based resource exchange and GAME (ACO-GAME) theory models, Trader-assisted Resource EXchange mechanism-Radio Access Network (TREX-RAN) and De-centralized Radio Access Network (TREX-DRAN), and greedy CYcle-Complete preferences (CYC) models. The proposed model offers a maximum sum rate of 83 kB/s, which is much better than the existing techniques.

Keywords: Device-to-Device communication; Genetic Algorithm (GA); Adaptive Bat Optimization (ABO) algorithm; resource exchange

1 Introduction

Demand for data-oriented applications increases every day, which increases the data requirements. High-definition videos, virtual applications, etc., involve large volumes of data. To meet the data requirements, cellular service providers have introduced new technologies. However, owing to several applications and connections, the service providers face issues related to security, link and interference management, and resource allocation. The main advantage of 5G is its support for D2D communication that aids in managing traffic offloading [1,2]. Communication between devices does



This work is licensed under a Creative Commons Attribution 4.0 International License, which permits unrestricted use, distribution, and reproduction in any medium, provided the original work is properly cited.

not involve a Base Station (BS). This D2D communication will be helpful even during a disaster. The network that supports D2D communication is categorized into in-band and out-band networks. The categorization is performed based on the dedicated frequency band. In case the communication is underlaid or overlaid, it is an in-band D2D. If communication involves an unlicensed frequency band, it is an out-band D2D network. Out-band involves zero interference and offers high capacity but lags in performance due to different types of interfaces. A simple illustration of the D2D and cellular links is depicted in Fig. 1.

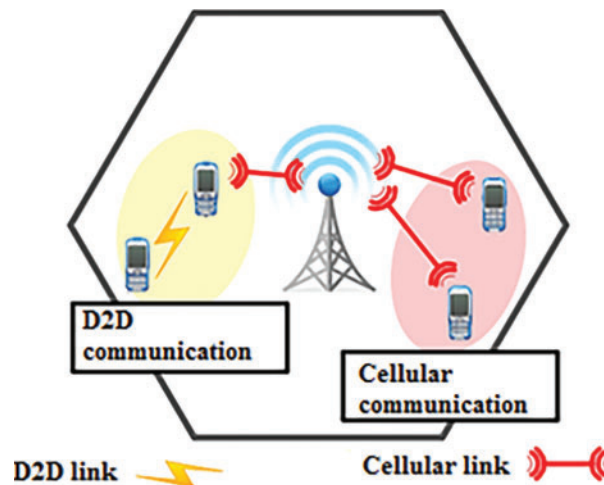


Figure 1: Illustration of D2D and cellular link

The significant aspects which impact the D2D performance are broadly analyzed for identifying the research objective. Network architecture, standardization procedures, methods of identifying and selecting neighbors, resource allocation with power control, network spectral efficiency, coverage probability, relaying and security are taken into consideration (Fig. 2).

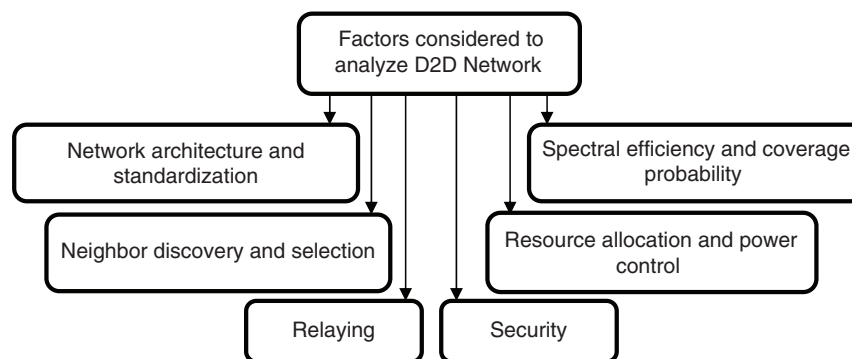


Figure 2: Major factors in D2D network

Different modes of communication of D2D are considered. To support mmWave D2D proximity services, the architecture is modified to manage operations like discovering, establishing and maintaining links. Based on Long-Term Evolution (LTE) internetworking, the mmWave D2D networks cover a wide range of transmissions. Another important aspect of this network is identifying neighbors and choosing the most appropriate one for communication. This crucial process initially discovers all

the neighbors and selects one based on the best link. Network-centric and device-centric schemes are popular approaches followed in D2D for neighbor discovery. In the case of network-centric approaches, the network is responsible for identifying the neighbor devices. In the case of device-centric neighbor discovery, the devices are accountable. In a denser environment, network-centric schemes perform better than device-centric ones. To reduce communication overhead as well as power consumption, neighbors should be rapidly discovered.

Once neighboring devices are discovered, and the best one is chosen for communication, resources are allocated and power control is effectively done. Since users in a D2D network use the same resources as cellular users, there are high chances for interference. Interference causes energy degradation and affects system efficiency. Hence, appropriate interference management schemes are required. Interference in D2D may be based on network and frequency. When it is based on frequency, it is subdivided into uplink and downlink interferences. In the case of network-based interference, it is divided into homogeneous interference and heterogeneous interference. Cancellation, avoidance and coordination are the major interference management factors. Interference is evaded by preventing cellular users from transmitting data in the D2D user range. In case of interference co-ordination, D2D and cellular user requirements are analyzed, and optimal resources are allocated without any interference. To support interference cancellation, successive and full duplex-based methods can be implemented. Only in-band D2D networks demand interference management schemes.

Traffic reduction at the BS and improved spectral efficiency with increased coverage probability are the other features of D2D. Poisson cluster process, stochastic geometry and probability theory are widely utilized to analyze the spectral efficiency and coverage probability [3]. Coverage probability in a D2D network is improved using D2D relays, which deliver connections to out-of-range users and establish routes over blockages in the network. Relaying schemes like decode and forward, amplify and forward, and demodulate and forward are used in D2D transmissions. To choose optimal relays, fuzzy logic and optimization algorithms are employed [4]. Finally, security is the primary factor that enables other factors to be reliable and effective. As the overall process involves direct communication among users, data transmission is reliable if appropriate resource allocation methods are employed [5,6,7]. So, resource allocation is the primary factor to be considered before establishing D2D links. It is essential to ensure resource availability and utilization during communication. So in this research work, a hybrid optimization algorithm is presented for optimal resource allocation. The contributions are presented to emphasize the significant works carried out in this research.

- A hybrid optimization algorithm for resource allocation in LTE-based D2D communication using the Genetic Algorithm-Adaptive Bat Optimization (GA-ABO) algorithm is proposed.
- A simulation analysis of the proposed hybrid optimization model is presented with a detailed discussion.
- A detailed analysis of the proposed and traditional resource allocation models is presented, and a comparative analysis is carried out to validate the better performances.

The remaining sections are organized as follows. A literature survey is presented in Section 2 which discusses the features of existing research works in D2D. The proposed hybrid optimization model is presented in Section 3. Section 4 presents the simulation analysis and results, whereas Section 5 summarizes the research work.

2 Related Works

An extensive survey of existing D2D approaches is performed based on methodology and features. The primary aim of D2D communication is to reutilize the resources in cellular communication. It helps in improving spectrum management and avoids delay while servicing users. Resource allocation procedure in D2D is the foremost challenge regarding throughput and interference. The D2D resource allocation model presented in [8] throws light on game-theoretic and other mathematical models designed for resource allocation. A similar game theory-based content-sharing model that improves overall performance is presented in [9]. The presented approach ensures the scheme's robustness, enabling it to obtain better decisions, offering improved QoS. The Gale-Shapley resource allocation algorithm is presented and evaluated in terms of optimality, convergence, complexity and stability. The presented approach improves overall efficiency and minimizes losses compared to traditional approaches.

The dynamic resource block sharing model presented in [10] highlights the interference mitigation challenges in D2D communication. As resource allocation is crucial while connecting multiple BSs, a game theory-based dynamic resource blocking model that maximizes resource utilization and allocates optimal resource block to the user with improved throughput is essential. The radio resource allocation technique presented in [11] allocates resource blocks based on sector or region to each D2D user. The adaptive allocation procedure calculates the resource requirements of each application and allocates resources based on the priority factor. Reduced complexity and improved performance are the observed features of the presented model. Though the game theory is widely adopted in resource sharing in D2D communication, it is essential to maintain QoS by improving the sum rate. The resources are to be appropriately reused without any collisions or overlap. A cooperative game theory presented in [12] efficiently manages overlapping and improves the sum rate and system utility. The presented approach improves communication by stabilizing the links and reducing the resource overlap in contrast to traditional systems.

The channel allocation problem in D2D communication reported in [13] focuses on improving the network utility by splitting the allocation process into channel sharing and selection. The presented game theory-based approach incorporates a coalition scheme and interference graph to solve the issues. The presented approach reduces computation complexity and attains high throughput in contrast to the existing state-of-art techniques. The multi-agent hierarchical learning algorithm presented in [14] allocates resources based on Stackelberg's game theory. By considering the social and physical factors, the non-overlapping contents are chosen, and diverse QoS requirements are satisfied. The method improves network throughput and increases the content hit rate in contrast to other methods.

The D2D model presented in [15] introduces a new sharing paradigm that allows the user equipment to share resources without cellular user equipment. The presented pure D2D model supports IoT applications and improves the quality of links in the network. Ensuring signal quality and efficient resource sharing are the predominant features of the presented approach. Resource-sharing in [16] incorporates Lagrangian Dual Optimization that improves the performance of IoT networks. Channel selection technique is included in the resource-sharing procedure that allows multiple users to share channels between D2D users. The dual optimization model defines the D2D user's optimal power and balances the sum rate and transmission power. Thus, the presented approach improves resource utilization and overall QoS of communication.

The joint optimization model presented in [17] improves channel assignment and offers security to cellular users. By analyzing the downlink resource allocation issues along with single and multi-channel

D2D communications, it is seen that the presented joint optimization model performs better than other optimization approaches. The D2D model presented in [18] offers better interference management by using graph theory and coloring procedure. The challenges in interference management are overcome by investigating power allocation and performing resource block assignment by using graph theory. Graph coloring is employed for resource sharing to reduce computational complexity and address joint optimization problems. The optimal power and resource allocation analysis reported in [19] discusses the interference issues seen in underlying D2D communication. Instead of a single resource block assignment, the sum rate is improved by assigning multiple resource blocks from different cellular users, which reduces the power factors.

Full-duplex D2D resource allocation scheme presented in [20] employs the Khun-Munkers algorithm and a poly block-based algorithm for dealing with power allocation and channel assignment. Link interference and channel assignment flexibilities are expressed as non-convex optimization problems. A poly block-based algorithm resolves power allocation problems, and channel assignment issues are resolved using the Khun-Munkers algorithm. Initially, the presented approach assigns channel, allocates power to enhance QoS, and reduces interference seen among D2D links.

Admission control and resource allocation procedures for D2D communication are presented in [21]. Optimal solution is obtained using a greedy algorithm [22]. The best set of D2D links is determined in the admission control procedure to enhance QoS, and the resource allocation procedure supports D2D and cellular communication to maintain long-term QoS. The presented algorithm decouples power and channel allocation and minimizes energy consumption in contrast to the existing techniques. A cooperative relaying procedure for supporting D2D communication is presented in [23]. It employs a branch and cut algorithm to perform optimized linear resource allocation. A distributed greedy algorithm is presented to handle large-scale networks and obtain optimal solutions in D2D resource management.

The spectrum efficiency and capacity of 5G mobile networks are improved using D2D links. However, mm-wave resource allocation and interference management are complex processes. To overcome this, a heuristic algorithm that considers dynamic propagation conditions and provides optimal solutions to improve spectrum efficiency is presented in [24]. The presented approach improves the overall performance and reduces the computation complexity through its optimal solution. A joint resource allocation procedure reported in [25] utilizes the orthogonality of D2D links and transmission model uniqueness to obtain a 3-dimensional power model channel for supporting D2D communication. The presented approach introduces a cooperative mode that supports efficient resource allocation, and a sub-optimal scheme that reduces the time complexity in contrast to the existing methodologies.

To enhance the sum rate, a weighted bipartite matching algorithm is proposed in [26]. It classifies resource sharing into three types: one-to-one, one-to-many and many-to-many. The presented approach allocates optimal resources to users based on their requirements which avoids interference and improves system capacity offering improved throughput in contrast to other algorithms.

From the literature review carried out, it is observed that interference management and resource sharing are the main goals to be addressed and are solved by using game theory. The optimization problems are solved using statistical and probability models, and nature-inspired optimization algorithms are not employed in any of the research. By considering this, a hybrid optimization algorithm is presented in this paper to improve the sum rate and throughput in D2D communication.

3 Proposed Work

This section presents the proposed hybrid optimization for efficient resource allocation in a cellular network supporting D2D communication. A hybrid optimization model called Genetic Algorithm-Adaptive Bat Optimization (GA-ABO) algorithm is proposed to enhance the performance of D2D communication. In the proposed optimization algorithm, the system model is initially defined followed by detailed steps for resource allocation. Consider a single-cell dynamic system for analysis that has BS at the center. Users in the cell (ℓ) is expressed as a set $\mathcal{L} = \{1, 2, \dots, \ell\}$. D2D pairs are denoted as ' k ', and expressed as $\mathcal{K} = \{1, 2, \dots, k\}$. The D2D pair in the system is equipped with a transmitter and receiver. The cellular user position and D2D pairs are updated in every time slot to indicate their dynamic characteristics. The links to the cellular users are provided as an orthogonal uplink resource, and D2D users utilize the resource not more than once per link. Similarly, cellular links can be assigned to a D2D link. Fig. 3 depicts the complete system model used in the proposed work.

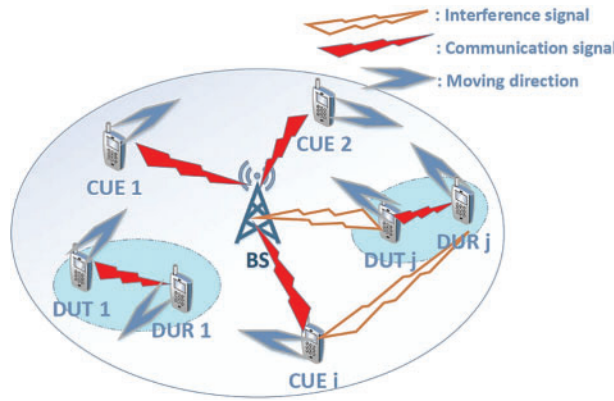


Figure 3: System model

As resources are reused, interference management in D2D communication is considered as a significant factor which introduces interference between cellular and D2D pairs. If a D2D pair utilizes the cellular user resource, then the Signal to Interference and Noise Ratio (SINR) for cellular and D2D pairs is expressed as shown in Eqs. (1) and (2), respectively.

$$\text{SINR}_{i,j,t}^c = \frac{p_{i,j,t}^c h_{i,\mathcal{B},t}}{\sigma^2 + p_{i,j,t}^d h_{j,\mathcal{B},t}} \quad (1)$$

$$\text{SINR}_{i,j,t}^d = \frac{p_{i,j,t}^d h_{j,t}}{\sigma^2 + p_{i,j,t}^c h_{i,j,t}} \quad (2)$$

where ' j ' represents the D2D pair which utilizes the cellular user resource ' i ', and ' t ' represents the time slot. The transmission powers of cellular user are represented as ' $p_{i,j,t}^c$ ' and D2D transmitter transmission power is represented as ' $p_{i,j,t}^d$ '. The channel gain between the cellular user and the BS is represented as ' $h_{i,\mathcal{B},t}$ ', which indicates the interfering channel gain from the D2D transmitter to the BS. The noise power is represented as ' σ^2 '. The data rate of the cellular link and D2D link is expressed as,

$$r_{i,j,t}^c = \log_2 (1 + \text{SINR}_{i,j,t}^c) \quad (3)$$

$$r_{i,j,t}^d = \log_2 (1 + \text{SINR}_{i,j,t}^d) \quad (4)$$

The data rate for cellular users when there is no interference in the D2D links is obtained based on the maximum power.

$$r_{i,t}^c = \log_2 \left(1 + \frac{\mathcal{P}_{\max}^c h_{i,\mathcal{B},t}}{\sigma^2} \right) \quad (5)$$

where, the maximum transmit power is represented as ' \mathcal{P}_{\max}^c '. The sum rate at the receiver end is formulated for all used subcarriers.

$$\varphi_j = \sum_{r \in R} w_r \log_2 \left(1 + \frac{\mathcal{P}_{\max}^c h_{i,\mathcal{B},t}}{\sigma^2 + p_{i,j,t}^c h_{i,j,t} + p_{i,j,t}^c h_{i,\mathcal{B},t}} \right) \quad (6)$$

Throughput maximization and sum rate enhancement are the objectives with minimum QoS target for cellular users.

$$\max \min \sum_{r \in R} w_r \log_2 \left(1 + \frac{\mathcal{P}_{\max}^c h_{i,\mathcal{B},t}}{\sigma^2 + p_{i,j,t}^c h_{i,j,t} + p_{i,j,t}^c h_{i,\mathcal{B},t}} \right) \quad (7)$$

GA and ABO algorithms are incorporated in the proposed work for efficient resource allocation. GA is an iterative optimization procedure that is derived based on biological metaphors to obtain a new solution in the search space. It encodes the solution, which is similar to a data structure. A set of random solutions are initialized. By using a fitness function, the performance of every individual is evaluated. In every iteration, better solutions are chosen for the next generation, and new solutions are obtained by combining the parents by crossover or modifying the solutions through mutation. These solutions replace weaker solutions so that progressive development toward a better solution is possible. The main advantage of GA is the elimination of weaker candidates and the improvement of optimal solutions. In the conventional GA, the length of the chromosomes is fixed based on the number of D2D transmitters. But in the case of proposed approach, every chromosome handles a dynamic subcarrier. The collection of chromosomes is termed as individuals, and the chromosomes denote subcarriers. An orthogonal resource allocation procedure is employed for cellular users, wherein the number of users and subcarriers are equal.

Evaluation of fitness function in GA is essential as it defines how close the obtained solution is to the optimal solution. The fitness value minimizes the data rate for the D2D transmitter. The fitness function is formulated as follows

$$\text{if } (r_m \geq \tau_m) \text{ then } f(x) = \max \min \varphi_j \quad (8)$$

$$\text{Else } f(x) = 0$$

where ' τ_m ' represents the pre-defined threshold. In every iteration, the individual characteristics are estimated using the fitness function, and the bests are selected for the next generation. Various schemes are employed in GA for determining the best solution. Random selection identifies the best individuals for the next generation, truncation-based selection selects the individuals based on fitness function, and route wheel selection selects the individuals based on a probability function. In the proposed work, the truncation-based selection is employed, which selects the best solution based on the fitness function. Crossover and mutation operators are used in GA to produce the next generation. The crossover operator modifies the distribution scheme and produces the next generation without altering the fitness function, whereas in the case of the mutation operator, random mutation is performed by altering the genes. Binary mutation modifies every bit in the chromosome to obtain a new generation.

ABO algorithm is used in enhancing the genetic model's optimal solution. The ABO model optimizes ' $\kappa_{ij,t}^{\mathcal{C}}$ ', ' $\kappa_{ij,t}^{\mathcal{D}}$ ' and ' φ_j '. BO is a nature-inspired optimization procedure that is derived using bats' echolocation behaviors. The network parameters of BO are represented as a matrix function, and the optimal solution for every instance is updated. Each bat has a different velocity function (v_j^k), and their location is represented as ' x_j^k '. For each iteration, the frequency ' f_j^k ' and loudness ' A_j^k ' are used to maximize the D2D pairs sum rate. Based on the nearest solution, loudness and frequency are modified. The optimal solution is controlled by position, so that each bat updates the location based on the global optimal location ($best_i$) and random location (R_{nd}) for each iteration. The bat's position is mathematically formulated based on the global and random locations and is expressed as follows.

$$x_{i+1}^k = w_i \times x_i^k + f_{1i} \times (R_{nd} - x_i^k) + f_{2i} \times (xbest_i - x_i^k) \quad (9)$$

$$R_{nd} = 2 \times rnd \times x_j^k \quad (10)$$

$$f_{1i} = 1 - e^{-|f_i - best_i|} \quad (11)$$

$$f_{2i} = 1 - f_{1i} \quad (12)$$

where, random numbers are in the range [0,1], and inertia weight is represented as ' w_i '. The updated frequency functions are represented as ' f_{1i} ' and ' f_{2i} '. The average position of all bats is represented as ' \bar{f}_i '. The convergence function of the optimization model is formulated as,

$$w_j = w_{min} + (w_{max} - w_{min}) \times rnd + \sigma \times \left(\frac{1}{2} \times rndn + \frac{1}{2} \times prand \right) \quad (13)$$

where, normal and Poisson distributed random functions are represented as ' $rndn$ ' and ' $prand$ '. The maximum and minimum inertia weights are represented as ' w_{max} ' and ' w_{min} ', respectively. From the current solution, the new solution is obtained using the random walk.

$$x_{new} = xbest_j + \varepsilon \bar{A}_j \quad (14)$$

where, ' ε ' is a random number whose range is $[-1,1]$. The average loudness of bats is represented as ' \bar{A}_j ' which is given as ' A_j^k '. The loudness and emission pulse of bats are updated as follows to obtain the optimum solution, which minimizes the interference and maximizes throughput and sum rate.

$$A_j^k \leftarrow \alpha A_{j-1}^k \quad (15)$$

$$r_j^k \leftarrow r_0^k (1 - e^{-\varphi_j}) \quad (16)$$

where, ' α ' is constant, and at the end of iterations, the optimal solution is obtained based on the best position. The pseudocode for the proposed hybrid optimization algorithm is presented as follows.

Algorithm 1: Pseudocode for hybrid GA-ABO algorithm for resource allocation in D2D communication

Generate random population

For (i = 1 to population size) do

 Obtain the fitness value of each individual

 Select parent individual for next generation

 Apply crossover to obtain new children

 Apply mutation operations

 Calculate the fitness function of each child

(Continued)

Algorithm 1: Continued

```

Select the best for next generation
For (i = 1 to number of bats) do
  For (each bat i) do
    Calculate the global and random locations using  $x_{i+1}^k$  and  $R_{nd}$ 
    Obtain the convergence function  $w_j$ 
    Update the position of bats  $A_j^k = \alpha A_{j-1}^k$ 
    Calculate the new solution  $x_{new}$ 
  End for
End for
End

```

4 Results and Discussion

Hybrid optimization algorithm for D2D network resource allocation is evaluated through simulation analysis performed using Network simulator NS-3. [Table 1](#) shows the simulation parameters used in the proposed model experimentation. For better validation, existing algorithms like ACO-GAME, T-REX-RAN, T-REX-DRAN and greedy CYC are considered for comparative analysis.

Table 1: Simulation parameters

Parameter	Value
Number of cellular users	40
Number of D2D pairs	40
Channel bandwidth	10 Mhz
Network size	1000 m \times 1000 m
Maximum transmission powers	23 dBm
Base station coverage range	500 m
D2D transmitter's coverage range	10–50 m
Mutation rate	0.04
Population size	50
Crossover rate	0.3
Total iterations	500
Noise power density	−110 dBm/Hz

[Fig. 4](#) depicts the network topology of the proposed model. The size of the network is taken as 1000 m \times 1000 m, while the channel bandwidth is considered to be 10 MHz. The minimum bandwidth for 5G standard is taken as 5 Mhz, whereas the optimum is 40 MHz. Owing to simulation constraints, the bandwidth is chosen as 10 MHz. The termination criteria for proposed and existing models are selected for 500 iterations, and algorithms are allowed to execute for 40 independent runs. The interference level is measured, and an average value is considered for comparative analysis based on D2D pairs.

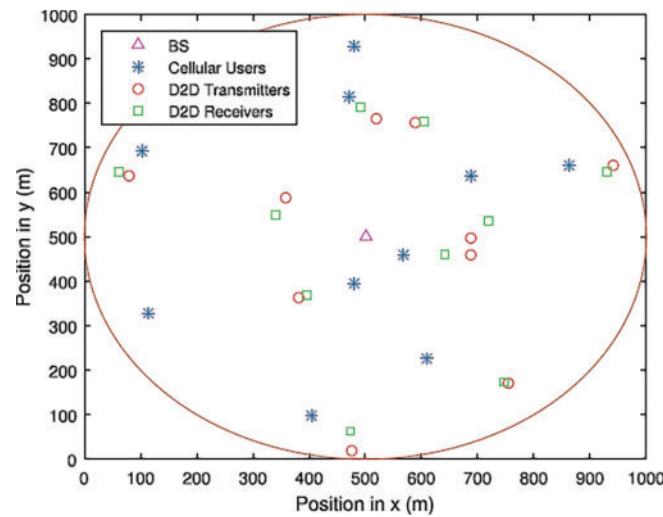


Figure 4: Network topology with cellular users and D2D pairs

Fig. 5 shows the average interference vs. D2D pairs in the cell. It is observed that the proposed hybrid optimization algorithm offers better performance in contrast to other models. The algorithm offers optimal solution, and enhances network performance by minimizing the average interference level in contrast to other methods.

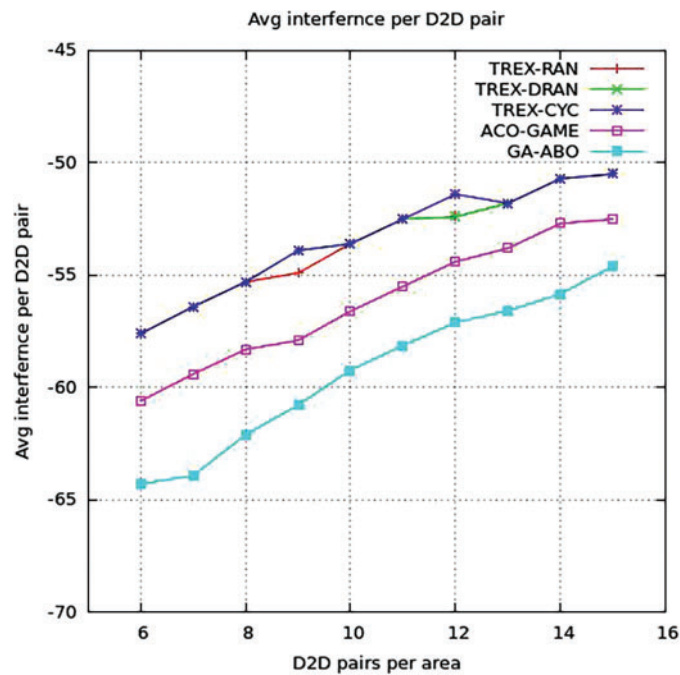


Figure 5: Analysis of average interference

Similarly, the average interference is analyzed based on the total number of resource blocks. The total Resource Block Groups (RBGs) are dynamically varied, and the interference of D2D pairs is measured (Fig. 6). From the results, it is observed that the proposed hybrid optimization model

exhibits minimum interference as resource blocks are gradually increased. Initially, interference is increased owing to reuse of limited resource blocks. But, when number of resource blocks increases, the interference reduces. The proposed resource allocation procedure ensures that interference is maintained at a proper level without interfering with cellular user services. TREX-RAN, TREX-DRAN and TREX-CYC do not offer better performance due to improper resource allocation procedures.

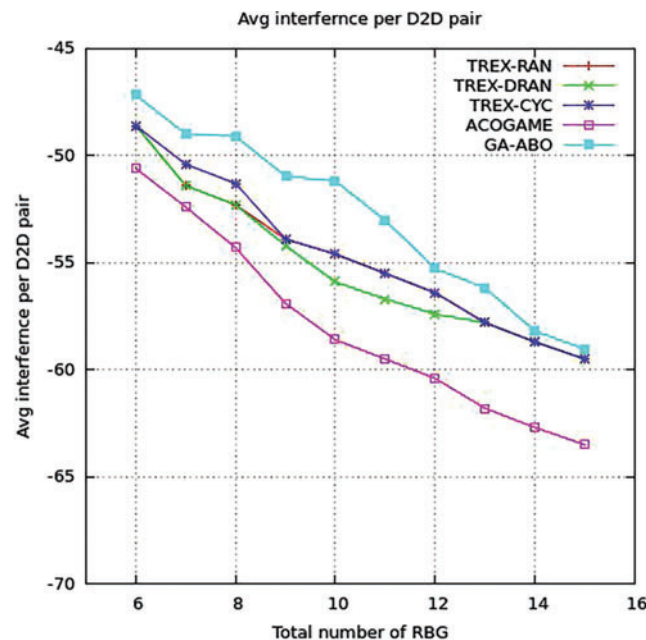


Figure 6: Average interference per resource block groups

In addition to average interference, the sum rate of the proposed model and existing models are compared and analyzed based on the total number of users and D2D pairs. Fig. 7 depicts the comparative analysis of the sum rate against the total number of users. The sum rates of TREX models do not converge in a better way. So for experimental analysis, ACO-GAME based resource exchange and conventional ACO-GAME models are considered for analysis. It is observed that the proposed hybrid optimization model exhibits a maximum sum rate throughout the process. Gradually, the user count is increased, and the performance is measured. It is evident from Fig. 7 that the maximum sum rate attained by the proposed model is 83 kB/s which is 5% greater than the ACO-GAME model and 14% greater than the conventional ACO model.

Similarly, the sum rate for the proposed model and existing models are compared and analyzed for D2D pairs. Fig. 8 depicts the comparative analysis of the sum rate concerning D2D pairs. The pairs are gradually increased, and the performance is measured. It is observed that the proposed model exhibits a maximum sum rate in contrast to ACO-based models. The improved performance is due to the optimal selection of resources and power, which improves the resource exchange and overall QoS of D2D communication.

From the simulation analysis, it is evident that the hybrid optimization algorithm offers improved resource allocation. The results demonstrate better performance of the proposed model in terms of maximum sum rate and minimum interference. The model can be used in real-time LTE applications.

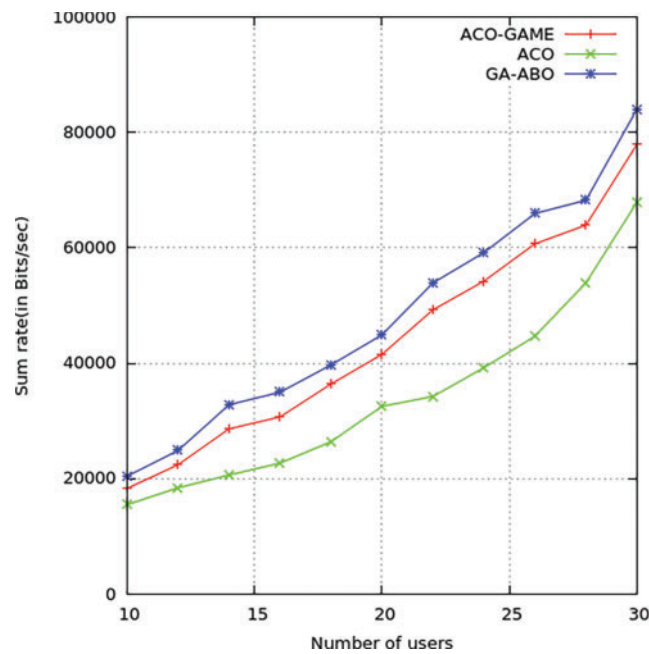


Figure 7: Sum rate per total number of users

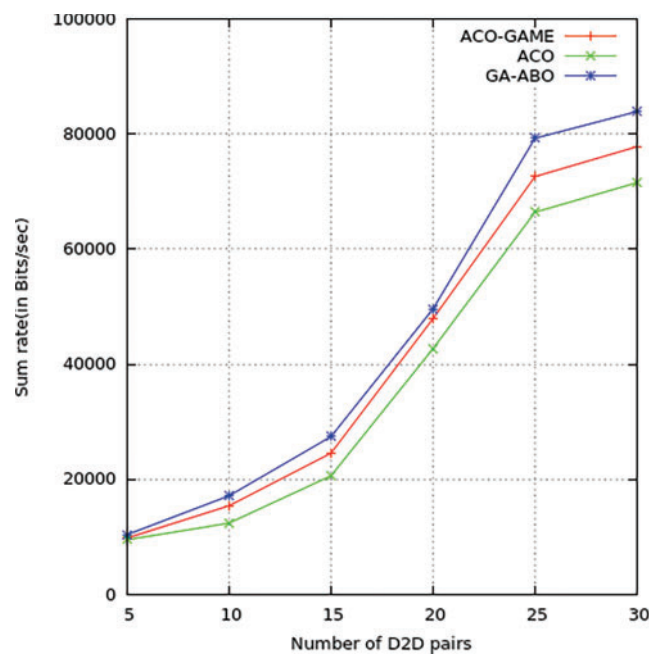


Figure 8: Sum rate per D2D pairs

5 Conclusions

A hybrid optimization model D2D communication is presented in this research work using the Genetic Algorithm-Adaptive Bat Optimization (GA-ABO) algorithm. Resource exchange mechanism plays a dominant role in ensuring the consistency of D2D pairs in D2D communication, as cellular

user's resources are used for direct communication. The existing approaches presented for D2D communication focus on resource allocation through a simple statistical process. However, the performance is improved by incorporating optimization algorithms into the resource allocation process. Based on this, the proposed hybrid optimization algorithm improves the sum rate and throughput, and minimizes the interference level. The results obtained through simulation analysis of the proposed model are compared with existing models based on average interference, throughput and sum rate. For a maximum sum rate of 94 kB/s, the proposed model exhibits better performance than the existing approaches. Further, it is planned to extend this research by incorporating deep learning techniques for better performance.

Funding Statement: The authors received no specific funding for this study.

Conflicts of Interest: The authors declare that they have no conflicts of interest to report regarding the present study.

References

- [1] W. Sun, G. Z. Dai, X. R. Zhang, X. Z. He, X. Chen *et al.*, "TBE-Net: A three-branch embedding network with part-aware ability and feature complementary learning for vehicle re-identification," *IEEE Transactions on Intelligent Transportation Systems*, vol. 23, no. 9, pp. 14557–14569, 2022.
- [2] W. Sun, L. Dai, X. R. Zhang, P. S. Chang, X. Z. He *et al.*, "RSOD: Real-time small object detection algorithm in UAV-based traffic monitoring," *Applied Intelligence*, vol. 52, no. 8, pp. 8448–8463, 2022.
- [3] X. Cai, X. Mo, J. Chen and J. Xu, "D2D-enabled data sharing for distributed machine learning at wireless network edge," *IEEE Wireless Communications Letters*, vol. 9, no. 9, pp. 1457–1461, 2020.
- [4] S. Kim, "D2D enabled cellular network spectrum allocation scheme based on the cooperative bargaining solution," *IEEE Access*, vol. 8, pp. 53710–53719, 2020.
- [5] H. Sun and R. Grishman, "Lexicalized dependency paths based supervised learning for relation extraction," *Computer Systems Science and Engineering*, vol. 43, no. 3, pp. 861–870, 2022.
- [6] A. Sultana, L. Zhao and X. Fernando, "Efficient resource allocation in device-to-device communication using cognitive radio technology," *IEEE Transactions on Vehicular Technology*, vol. 66, no. 11, pp. 10024–10034, 2017.
- [7] H. Xu, W. Xu, Z. Yang, Y. Pan, J. Shi *et al.*, "Energy-efficient resource allocation in D2D underlaid cellular uplinks," *IEEE Communications Letters*, vol. 21, no. 3, pp. 560–563, 2017.
- [8] R. Rathi and N. Gupta, "Game-theoretic and non-game theoretic resource allocation approaches for D2D communication," *Ain Shams Engineering Journal*, vol. 12, no. 2, pp. 2385–2393, 2021.
- [9] X. Shi, D. Wu, C. Yue, C. Wan, X. Guan *et al.*, "Resource allocation for covert communication in D2D content sharing: A matching game approach," *IEEE Access*, vol. 7, pp. 72835–72849, 2019.
- [10] P. Kumar Barik, A. Shukla, R. Datta and C. Singhal, "A resource sharing scheme for intercell D2D communication in cellular networks: A repeated game theoretic approach," *IEEE Transactions on Vehicular Technology*, vol. 69, no. 7, pp. 7806–7820, 2020.
- [11] P. Gandotra, R. Kumar Jha and S. Jain, "Sector-based radio resource allocation (SBRRA) algorithm for better quality of service and experience in device-to-device (D2D) communication," *IEEE Transactions on Vehicular Technology*, vol. 67, no. 7, pp. 5750–5765, 2018.
- [12] J. Hu, W. Heng, Y. Zhu, G. Wang, X. Li *et al.*, "Overlapping coalition formation games for joint interference management and resource allocation in D2D communications," *IEEE Access*, vol. 6, pp. 6341–6349, 2018.
- [13] Y. Liu, Y. Wang, R. Sun and Z. Miao, "Distributed resource allocation for D2D-assisted small cell networks with heterogeneous spectrum," *IEEE Access*, vol. 7, pp. 83900–83914, 2019.

- [14] J. Wang, Y. Sun, B. Wang, B. Wang, A. Wang *et al.*, “Resource allocation for D2D video multicast using multi-leader multi-follower stackelberg game with personalized incentives,” *IEEE Access*, vol. 7, pp. 117019–117028, 2019.
- [15] W. -K. Lai, Y. -C. Wang, H. -C. Lin and J. -W. Li, “Efficient resource allocation and power control for LTE-A D2D communication with pure D2D model,” *IEEE Transactions on Vehicular Technology*, vol. 69, no. 3, pp. 3202–3216, 2020.
- [16] P. Khuntia and R. Hazra, “An efficient channel and power allocation scheme for D2D enabled cellular communication system: An IoT application,” *IEEE Sensors Journal*, vol. 21, no. 22, pp. 25340–25351, 2021.
- [17] J. Wang, Y. Huang, S. Jin, R. Schober, X. You *et al.*, “Resource management for device-to-device communication: A physical layer security perspective,” *IEEE Journal on Selected Areas in Communications*, vol. 36, no. 4, pp. 946–960, 2018.
- [18] T. Yang, R. Zhang, X. Cheng and L. Yang, “Graph coloring based resource sharing (GCRS) scheme for D2D communications underlaying full-duplex cellular networks,” *IEEE Transactions on Vehicular Technology*, vol. 66, no. 8, pp. 7506–7517, 2017.
- [19] R. AliHemmati, B. Liang, M. Dong, G. Boudreau, S. H. Seyedmehdi *et al.*, “Power allocation for underlay device-to-device communication over multiple channels,” *IEEE Transactions on Signal and Information Processing over Networks*, vol. 4, no. 3, pp. 467–480, 2018.
- [20] H. Chour, E. A. Jorswieck, F. Bader, Y. Nasser, O. Bazzi *et al.*, “Global optimal resource allocation for efficient FD-D2D enabled cellular network,” *IEEE Access*, vol. 7, pp. 59690–59707, 2019.
- [21] S. Cicalò and V. Tralli, “QoS-aware admission control and resource allocation for D2D communications underlaying cellular networks,” *IEEE Transactions on Wireless Communications*, vol. 17, no. 8, pp. 5256–5269, 2018.
- [22] H. Meshgi, D. Zhao and R. Zheng, “Optimal resource allocation in multicast device-to-device communications underlaying LTE networks,” *IEEE Transactions on Vehicular Technology*, vol. 66, no. 9, pp. 8357–8371, 2017.
- [23] X. Xiao, M. Ahmed, X. Chen, Y. Zhao, Y. Li *et al.*, “Accelerating content delivery via efficient resource allocation for network coding aided D2D communications,” *IEEE Access*, vol. 7, pp. 115783–115796, 2019.
- [24] Y. Chen, B. Ai, Y. Niu, R. He, Z. Zhong *et al.*, “Resource allocation for device-to-device communications in multi-cell multi-band heterogeneous cellular networks,” *IEEE Transactions on Vehicular Technology*, vol. 68, no. 5, pp. 4760–4773, 2019.
- [25] R. Zhang, C. Qi, Y. Li, Y. Ruan, C. -X. Wang *et al.*, “Towards energy-efficient underlaid device-to-device communications: A joint resource management approach,” *IEEE Access*, vol. 7, pp. 31385–31396, 2019.
- [26] F. Hussain, M. Y. Hassan, M. S. Hossen and S. Choudhury, “System capacity maximization with efficient resource allocation algorithms in D2D communication,” *IEEE Access*, vol. 6, pp. 32409–32424, 2018.



De-noising and Demosaicking of Bayer image using deep convolutional attention residual learning

S.P. Predeep Kumar¹ · K. John Peter² · C. Sahaya Kingsly²

Received: 29 June 2022 / Revised: 22 September 2022 / Accepted: 2 January 2023 /

Published online: 26 January 2023

© The Author(s), under exclusive licence to Springer Science+Business Media, LLC, part of Springer Nature 2023

Abstract

Nowadays, the resolution of image sensors in digital cameras is increased by minimizing the size of pixel sensors. As the size is reduced, the pixel sensor receives low light energy and becomes sensitive to thermal noise. The Color Filter Array (CFA) has a significant effect with the presence of noise, and the missing data is required to be reconstructed from the noisy data. This paper proposed a deep convolutional neural network with Honey Badger Algorithm (DCNN-HBA) for Bayer image de-noising. The deep CNN model is easily adopted and flexible for any CFA design with spatially varying color and exposures. After de-noising, attention-based deep residual learning (A-DRL) is applied to de-mosaicking the noise-free Bayer image. The channel attention is involved in which the network considers more relevant information and features. The proposed algorithm improves the quality of the image after reconstruction. The performance of the proposed work is evaluated with the performance metrics such as Peak Signal to Noise Ratio (PSNR), Color Peak Signal to Noise Ratio (CPSNR), Structural Similarity (SSIM), and Mean Structural Similarity (MSSIM) and compared with the traditional de-mosaicking approaches. By using our proposed work, the performance of PSNR, SSIM, CPSNR and MSSIM is improved by 43.23 dB, 0.997, 43.30 dB and 0.9975, respectively.

Key words Color Filter Array interpolation · De-noising · De-mosaicking · Deep convolutional neural network · Honey Badger Algorithm · Deep residual learning

✉ S.P. Predeep Kumar
sppredeep@gmail.com

K. John Peter
kjohnpeter@gmail.com

C. Sahaya Kingsly
kingsly2k7@gmail.com

¹ Department of Computer Science and Engineering, Viswajyothi College of Engineering and Technology, Muvattupuzha, Ernakulam, India

² Department of Computer Science and Engineering, Mangalam College of Engineering, Ettumanoor, Kottayam, India

1 Introduction

The key stages in the Digital Imaging (DI) pipeline are de-mosaicking and de-noising, representing three different color values for each pixel from a specific noise estimation [7, 20]. Nowadays, digital cameras have received huge attention because most people prefer to take photographs with digital cameras rather than film cameras. Once the digital image or photograph is recorded, considerable processing is needed to deliver a viewable or suitable image to the user [16]. Some image processing procedures involved are compression, white balance adjustment, sensor non-uniformities and non-linearities, etc. However, the most significant segment of this image processing chain is called demosaicking or CFA Interpolation [11].

Demosaicking is a procedure for evaluating the missing color values for every pixel in an original image. Demosaicking effectively reconstructs the high-quality, full-resolution color images recorded using the digital camera [29, 30]. In general, the computer color image requires three color samples, namely R (red), G (green), and B (blue), at each pixel location. Since the 3-chip color camera is expensive, most cameras use a single sensor covered with CFA. However, most digital cameras utilize single or monochromatic imaging sensors to minimize costs. CFA permits single color to be calculated at each pixel, and the most popular Bayer CFA extracts more green information than red or blue information. It is necessary to perform de-noising because the demosaicking process is complicated due to noise. The filtering based approaches are commonly used to suppress the noise present in the image [19]. Some artifacts caused by demosaicking are moire, zippering around edges, and checkboard patterns.

Demosaicking aims to transform a sequence of light intensity interpretations into color images, whereas de-noising intends to minimize the noise generated from the sensor [14, 15, 23, 26]. Some of the noisy sources of sensor data are photon shot noise, electronic noise (readout, variance in amplifier gains and thermal noise etc.). Modern imaging systems often follow the Pre-processing step to eradicate the most severe sensor defects such as pixel gains, variations in column and dead pixels, etc. De-noising is performed after demosaicking because once the image is demosaicked, the noise's statistical properties can be changed dramatically [8, 18]. Recently, Deep learning (DL) has gained huge success, mainly in the fields of image processing and computer vision (CV) [1, 2, 6]. Many DL-based demosaicking methods have been used recently, focusing on accuracy with negligible computation cost. Optimization approaches are included to improve the performance of deep learning-based approaches [21].

However, the DL-based techniques minimize the model parameters and effectively extract the features of the mosaic image. Moreover, the de-noising process aims to enhance the demosaicked image quality, which can be well-suited for modern computing applications.

In our work, A-DRL is used in the proposed demosaicking, which solves the problem of recovering missing information. In addition, color and other light properties, such as polarization and exposures present in the CFA, are resolved. DCNN-HBA de-noising is applied without degrading high frequency contents such as texture or image details. The proposed de-noising and demosaicking work use a deep learning network with the activation function of ReLU, which resolves the problem of gradient exploding or vanishing. The contribution of the proposed work is described as follows.

- In this paper, DCNN is proposed in which mapping from noisy HIS to the de-noised one is learned directly. In addition, the hyperparameters are optimized with the HBA algorithm, which reduces the network loss.
- After de-noising, A-DRL is applied for generating demosaicked images. The spatial, spectral information is jointly utilized, and the multi-scale features are fused with the adaptation of the convolutional layer with varying size reception fields.
- A residual learning network uses shortcut connections to extract the multilevel information for efficient noise removal. It regulates the flow of information from feature representation to the final output of residual for minimizing feature vanishes issues and degradation.
- The channel attention technique focuses on more discriminative features or information. The capacity of discriminative learning is improved, making us aware of relevant information and features.

The outline of the paper is as follows. Section 2 denotes the related work of demosaicking. The proposed methodology is described in section 3. Experimental results and discussion is presented in section 4. Section 5 discusses significant aspects of our work and concludes.

A list of symbols used is given in Table 1.

2 Related works

The works related to the proposed demosaicking are described as follows.

Wang et al. [27] presented the high-quality compact image demosaicking based on Neural Network (NN) for edge-computing device applications. Here, the UNet++ algorithm was modelled for obtaining a compact demosaicking structure. The Gaussian smoothing (GS) layers were adopted instead of down-sampling operations. The densely connected (DC) blocks were used to extract the features of the mosaic image by considering the correlation among the feature maps. Each block adopts separable depth-wise convolutions to minimize the number of model parameters. The receptive fields were expanded using the Gaussian smoothing (GS) layer without eliminating the image information and downsampling image size. The running speed of the network was improved by 42%. The accuracy of the demosaicked images was 83.53%, with mean Average Precision (mAP) (75.44%). The limitation identified was that the image features were difficult to analyze multiple scale images features.

Kokkinos and Stamatiou et al. [13] developed the procedure of deep image demosaicking using cascaded Convolutional Residual De-noising (CRD) networks. The DL based CRD system has obtained images of high quality for de-noising and demosaicking issues. The model performed well when the network was trained with smaller datasets and generated superior outcomes compared to the baseline architectures. The demosaic scenario was evaluated using the datasets such as VDP, Kodak, McMaster and Moire. Extensive experiments have proven that the CRD network has outperformed existing noise-free and noisy data methods. The de-noising process was completed with the Residual Denoising Network (ResDNet), and demosaicking was done with the Majorization-Minimization (MM) framework. The major drawbacks were the occurrence of image restoration problems.

Syu et al. [22] introduced the demosaicking process with DNN. Here, dual CNN models were developed to learn the mapping among mosaic and original images representing whole information. Here, the Bayer CFA was utilized for demosaicking with CNN. The Demosaicking CNN (DMCNN) was used to explore features automatically and has optimized

Table 1 List of Symbols

Symbols	Explanation
$M_{i,j}$	Mosaic image
I_g	Green channel
I_r	Red channel
I_b	Blue channel
y	Output vector
z	signal
n	filter
g	Number of elements
k	Representation of each feature
N	Total number of feature
$f(\cdot)$	Nonlinear activation function
W_k	Convolutional filter
p, q	Representation of element
$Z_{k,i,j}$	Output of pooling layer
$x_{k,p,q}$	Input elements for pooling operation
$R_{i,j}$	Pooling elements
σ	Softmax function
\vec{a}	Input vector
$e^{(\cdot)}$	Exponential function
M	Number of classes
A_i	Initial value of HBA
VC_i	Upper bound values
MC_i	Lower bound values
s	Search space boundary
D	Constant value
U	Total number of iterations
t	Current iteration
β	Density factor
A^{new}	Updated value of HBA
A_i, A_b	Optimal solution of HBA
γ	Constant number, down sampling ratio
G	Parameter
r_3, r_4, r_5 and r_6	Random number
y_b	prey
J	Smell intensity
T	
d_i	distance
H_i	Input feature map
H_{i-1}	Output feature map
Y_i	Residual component
X_{CA}	Learned calibration of weight
Y_i	Residual component
δ	ReLU function
X_1, X_2, X_3, X_4	Weight set
GAP	Global average pooling
$l(\Theta)$	Loss function
Θ_1, Θ_2	First and second stage parameter
G	channel
μ	Gaussian noise
I_μ	Corrupted image
I_μ	De-noised mosaic image
R	Maximum fluctuation
MSE	Mean square error
H	Height of the image
W	Width of the image
$\ \cdot \ $	Norm vector
$I()$	RGB color value for pixel

the data-driven pattern. The end-to-end learning was exploited using Very Deep DMCNN (DMCNN-VD) for processing demosaicking. The pattern layer was introduced and embedded into the demosaicking model for the CFA pattern joint optimization. The dual CNN models effectively and flexibly accomplished joint demosaicking and de-noising. The performance was evaluated on diverse patterns with PSNR on three color models. With the Kodak dataset and Bayer pattern, the DMCNN-VD approach obtained higher values as R (43.28), G (46.10), and B (41.99). It is difficult to deal with high dynamic range (DR) due to varied ranges, affecting the training process.

Kim et al. [12] developed the inter-channel weighted Nonlocal Means Least Square (NLMLS) approach for noisy Bayer CFA de-noising. The noisy CFA patterns were de-noised with the polynomial model's 2D (2 dimensional) approximation. The conventional 2D approximation can be affected by the edge discontinuities. Evaluating NLM weights reconstructs the pixel value with updated weights in order to find improved 2D filters. The integration of inter-channel information with polynomial approximation was used to identify the noisy image's NL weights. The dataset used for experiments was McMaster. The noise levels varied with $\sigma = 7.65$ obtained higher SSIM (0.9886) and $\sigma = 12.75$ acquired a higher value as 0.9868. The drawback was that the proposed approach was only tested with Bayer patterns, causing complexities when tested with other CFA patterns.

Guo et al. [5] developed the Green channel based joint De-noising and Demosaicking for processing with burst real-world images. The green channel has a higher priority than the other two due to its better quality and double the sampling rate. With the Green Channel Prior Network (GCP-Net), the features were extracted, which can be further used to guide both the feature upsampling and extraction of the entire image. The offset was measured from GCP to minimize noise's effect and balance the shift among the frames. The experimentation was conducted on real work as well as synthetic datasets. The drawbacks of the GCP-Net were higher visual artifacts were generated, and difficult to eliminate the image noise.

In the existing work of de-noising, deep learning, NN, Residual Network (Resnet), NLMLS and GCP-Net are used for demosaicking the original input image. The multi-scale image features are difficult to analyze in dense block based feature extraction. CRD based de-noising uses majorization and minimization approaches, and it has the issue of image restoration occurrences. The dual CNN model has an optimized data-driven pattern which has the issue of dynamic range variations. The interchannel NLMLS are affected by edge discontinuities of the CFA pattern. Green channel based joint DD has better quality and double sampling rate. The image noises are difficult to reduce due to the effect of visual artifacts. The existing approaches are not feasible for producing more relevant parts of spectral information. In the proposed work, more discriminative spatial information is obtained for efficient demosaicking in which both multi-scale spatial and spectral feature information is extracted. The information flow is regulated with skipped connection to resolve vanish gradient or degradation issues. In addition to that, the learning process is controlled with optimal hyperparameters with the HBO algorithm.

3 Proposed methodology for de-noising and DEMOSAICKING

The image data contains various spectral and spatial information used in many applications. These images are noisy and need to be reconstructed for better processing. In this work, the Bayer image is considered for de-noising and demosaicking. The DCNN with HBA

optimization algorithm is used for de-noising the Bayer images, which are demosaicked with A-DRL. Initially, the Bayer image formation is described for our proposed approach. There are several images required to be trained in the proposed model. In order to develop the proposed system model, it is impossible to get the image directly from the camera and train the model. These images are obtained by downsampling the RGB images.

The overall architecture of proposed de-noising and demosaicking is shown in Fig. 1. Initially, the input from the Kodak dataset is given as input, and the input images are de-noised with DCNN and HBA optimization. The hyperparameter optimization can be accomplished with the HBA algorithm. After de-noising, the de-noised images are demosaicked with A-DRL to obtain the final output.

The mosaic images are obtained using the green, red and blue channels and are described as follows.

$$M_{i,j} = \begin{cases} I_g(i \bmod 2) = 0 \text{ and } (j \bmod 2) = 0 \\ I_g(i \bmod 2) = 1 \text{ and } (j \bmod 2) = 1 \\ I_r(i \bmod 2) = 0 \text{ and } (j \bmod 2) = 1 \\ I_b(i \bmod 2) = 1 \text{ and } (j \bmod 2) = 0 \end{cases} \quad (1)$$

From the sequence of GRGB, the mosaic image M with the Bayer pattern is obtained.

a. De-noising with DCNN-HBA

The hardware or sensor introduces noises in real mosaic images during capturing. For de-noising, the Bayer images DCNN-HBA are used to obtain accurate noise estimation for noise removal. The performance of de-noising can be enhanced with several convolutional layers, batch normalization and a ReLU. In order to deal with real Bayer images, the discriminative learning technique with HBA optimization is used. The computational cost of de-noising is reduced with the spatial activation function. The DCNN is trained on images corrupted by known Gaussian noise. The residual of the image is produced by convoluting the images with deep CNN. The residual is compared with the added noise to compute during the learning procedure. The noise obtained from the trained network is subtracted from the noisy image, producing a noise-free image. The DCNN is used to de-noise the mosaic image as it does not affect the originality of the mosaic image. DCNN is trained to greyscale mosaic images, giving better results than normal greyscale images. The proposed DCNN architecture is shown in Fig. 2.

The proposed de-noising architecture consists of input, convolutional, pooling, and fully connected and output layers. Each convolution layer used is convolved based on the kernel size. In order to represent the feature maps, the pooling operation is applied after each convolution. The rectified linear unit is used as an activation function. The fully connected

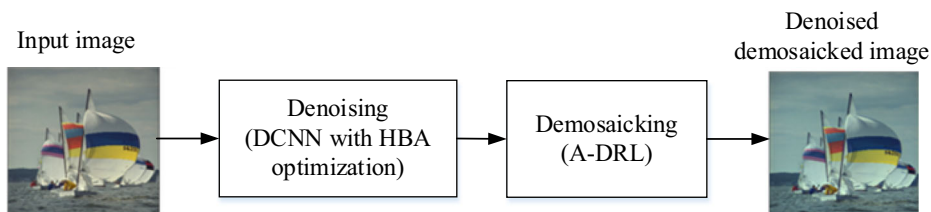


Fig. 1 The overall process flow for the proposed de-noising and demosaicking

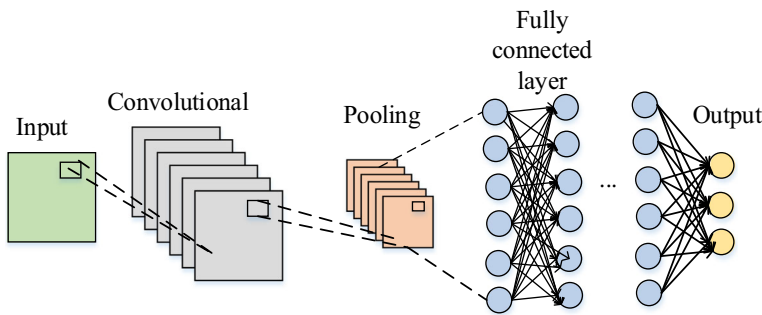


Fig. 2 The Deep CNN Architecture for proposed de-noising

layer has more output neurons than the final layer. The convolution operation is involved in the following equation.

$$y_n = \sum_{k=0}^{N-1} z_k g_{n-k} \quad (2)$$

Where, z represents the signal, n represents the filter and g represents the number of elements. The output vector used is represented as y . The convolutional layer act as a feature extractor as it learns the representation of features from the input images. The neurons of each convolutional layer are arranged into feature maps. In the feature map, each neuron of the receptive field is connected to the adjacent neurons of the previous layer with trainable weights. The convolved results are passed through the nonlinear activation function to compute the new feature maps. In the feature map, all neurons have the same weight within the same convolutional layer. The features are extracted from each location, and the k^{th} feature map z_k can be computed as

$$z_k = f(W_k * y) \quad (3)$$

Where, W_k represents the convolutional filter of k^{th} feature map and y represents the input image. The multiplication sign denotes the 2D convolutional operation utilized to compute the inner product at each layer of the input image. $f(\cdot)$ denotes the nonlinear activation function.

In the feature map, the spatial resolution is reduced with the pooling layer, and spatial invariance is attained. The maximum value is propagated with the pooling layer within the receptive field. In each receptive field, the largest element is chosen by the pooling as represented as

$$Z_{k_{i,j}} = \max_{(p,q) \in R_{i,j}} x_{k_{p,q}} \quad (4)$$

Where, (p, q) represents the location, $Z_{k_{i,j}}$ represents the k^{th} feature map output based on the pooling operation, $x_{k_{p,q}}$ represents the elements and $R_{i,j}$ represents the pooling elements. In the fully connected layer, the softmax activation function is used. The softmax function is represented as follows.

$$\sigma(\vec{a})_i = \frac{e^{x_i}}{\sum_{j=1}^M e^{x_j}} \quad (5)$$

Where, σ represents the softmax, \vec{a} denotes the input vector, e^{x_i} represents the exponential function for the input vector, M denotes the number of classes in the multi-class classifier, e^{x_j} represents the exponential function for the output vector.

In order to accelerate the training process, batch normalization is added to the hidden layer. The network loss is minimized with HBA optimization.

i) *HBA based parameter optimization for Deep CNN*

The hyper-parameters used in the DCNN are optimized with the HBA global optimization based on the honey badger's behaviour to catch its prey. This process is accomplished with the stages of digging and Honey. The prey is estimated in the digging stage based on the smell of honey badger. In the honey stage, the beehive is determined by following the honey bird with the honey badger.

The initial value of HBA is assigned as follows.

$$A_i = M_i C_i + s_1 * (VC_i - MC_i), i = 1, 2, \dots, M \quad (6)$$

Where, the upper bound values are represented as VC and the lower bound values are represented as MC , the search space boundary s_1 is represented as a random number in the range of $s_1 \in [0, 1]$. By using the density factors, the exploration and exploitation are balanced. It is defined as,

$$\beta = D * \exp^{(-t/U)} \quad (7)$$

Where, the constant value is represented as $D > 1$, the total number of iterations is represented as U and the current iteration is represented as t . The solution in the next step is updated with the digging stage. It is accomplished with the cardioid movement, which is represented as,

$$A^{new} = A_c + G * \gamma * J * A_b + G * \beta * e^i * s_3 * [\cos(2\pi r_4) * [1 - \cos(2\pi r_5)]] \quad (8)$$

Where, A^{new} denotes the updated value of A_i , A_b denotes the optimal solution obtained, γ represents the constant number and G represents the parameter, and the random numbers are denoted as r_3, r_4, r_5 and r_6 . The parameter value G is obtained using the following equation.

$$G = \begin{cases} 1, & \text{If } (r_6 \leq 0.5), \\ -1, & \text{Else.} \end{cases} \quad (9)$$

For the prey y_b , the smell intensity is denoted as J , which denotes the distance between y_i and y_b . It is described as follows.

$$J_i = r_2 * \frac{T}{4\pi d_i^2} \quad (10)$$

$$T = (A^i - A^{i+1})^2, d_i = A_b - A_i \quad (11)$$

Using the honey stage operator, the solution is updated. This process is accomplished with the following equation.

$$A^{new} = A_b + G * r_7 * \beta * d_i \quad (12)$$

The step-by-step procedure of the HBA algorithm is described as follows. Algorithm 1: Procedure of HBA.

```

Input: The number of solutions  $M$  and the number of iterations  $U$ .
For the solution  $A$ , set the initial value
 $t = t + 1$ 
while  $t \leq U$  do
  Compute the objective value for  $A_i, i = 1, 2, \dots, M$ .
  Determine optimal solution  $A_b$ 
  Modify the parameter  $D$ 
  for  $i = 1 : M$  do
    If ( $rand < 0.5$ ) then
      Update  $A_i$  with equation (8) to (11)
    Else
      update  $A_i$  with equation (12)
    end if
  end for
   $t = t + 1$ 
End while
Return  $A_b$ 

```

b. Demosaicking with A-DRL

A-DRL is introduced to attain the trade-off between degrading network performance and increasing the network depth. It utilizes several stack layers' input to attain the current layer's input. It resolves the issue of exploding gradient or vanishing. While varying the dimensionality of the input causes information loss. It can be resolved by enlarging the receptive field in which the filter size and depth are increased. However, increasing the depth causes network performance degradation, and increasing the filter size induces the number of parameters and the computational cost to increase. The proposed architecture of A-DRL based demosaicking is shown in Fig. 3. Different kind of complicated features is extracted with various residual learning based architecture. The

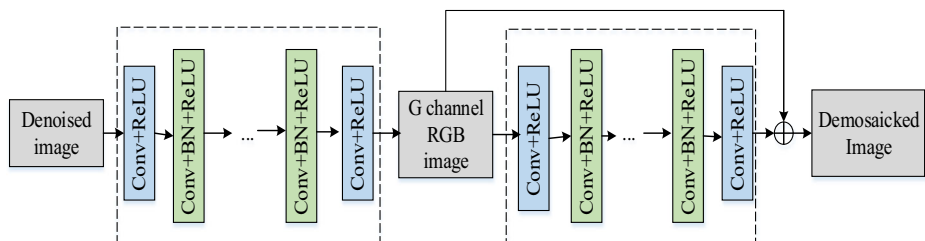


Fig. 3 Architecture of Bayer image Demosaicking with A-DRL

demosaieking performance can be improved by increasing the width of the network. The proposed network contains two layers, namely Conv+ReLU and Conv+BN + ReLU. Where Conv, ReLU and BN represent the convolutional, rectified linear unit and batch normalization. The information obtained from the receptive field has more information with the help of the dilation factor. The concatenate operation adds residual blocks used in the channel.

i) *Residual block*

If the number of layers in the network is high, the information extracted from the initial layer may be lost. Due to the slow training process, the gradient vanishing problem affects the deeper network. The feature map is directly passed to the later layers to solve this issue. Hence, it improves the process flow and contributes to the back propagation of gradients, accelerating the training process.

ii) *Channel Attention Block*

For high-frequency extraction, convolutional layers give more attention to facilitating demosaieking. The features are adaptively modulated with a channel attention block. The structure of the channel attention block (CAB) is shown in Fig. 3. The output of i^{th} block is represented as,

$$H_i = H_{i-1} + X_{CA} * Y_i \quad (13)$$

Where, the input and output feature map is represented as H_i and H_{i-1} . The two-stacked convolution layer is involved with the filter size 3×3 , which produces the residual component Y_i . It is represented as

$$Y_i = X_2 * \delta(X_1 * H_{i-1}) \quad (14)$$

Where, the weight set is denoted as X_1 and X_2 and δ denotes the ReLU function. The learned calibration of weight is represented as X_{CA} in which the global average pooling on Y_i is accomplished. After convolutional and ReLU, the channel number is down-sampled with the ratio γ . Using the convolutional layer with the sigmoid function increases the number of channels to the original size.

$$X_{CA} = \text{Sigmoid}(X_4 * \delta(X_3 * \text{GAP}(Y_i))) \quad (15)$$

Where, the weight set is represented as X_3 and X_4 and the global average pooling operation is denoted as GAP .

iii) *Residual Learning and loss function*

For the training set $\{z_i, y_i\}_{i=1}^M$, the initially demosaiicked image of i^{th} input is represented as z_i , and the ground truth image is represented as y_i . The loss function used to learn the network parameter is described as follows.

$$l(\Theta) = \frac{1}{2M} \sum_{i=1}^M \left(\left\| F(z_i, G; \Theta_1) - y_{i,G} \right\|^2 + \left\| F(z_i; \Theta_1, \Theta_2) - y_i \right\|^2 \right) \quad (16)$$

Where, M represents the batch pairs, and the first and second stage parameters are denoted as Θ_1 and Θ_2 , $z_{i,G}$ represents the G channel of i^{th} demosaicked image and $y_{i,G}$ is the G channel of the ground truth image.

Using the residual learning strategy, the noise μ is determined and eliminated from the corrupted image I_μ . The de-noised mosaic image is computed as

$$I_m = I_\mu - \mu \quad (17)$$

Where, I_μ represents the corrupted image and μ represents the Gaussian noise. The residual space considered is smoother and easier for demosaicking the Bayer image. Using DCNN-HBA and A-DRL, the network learns the features automatically for target applications by learning through data. The input is added with learned residual information since the residual learning converges faster to construct the final solution by learning residual information. Moreover, the artifacts of the images tend to be more coherent, making residual information easier to learn.

4 Experimental results and analysis

a. Implementation platform and dataset description

The proposed approach is implemented with PYTHON software. It was executed with the system configuration of Intel(R) Core(TM)2 Duo CPU E8400 @ 3.00GHz 2.99 GHz processor, 195 GB storage, 8 GB RAM, and Windows 10 Pro operating system. The proposed Bayer image de-noising and demosaicking is implemented with Kodak 24 dataset. It contains 24 uncompressed images of PNG true color captured with a film camera. The size of each image is 768×512 pixels, released for unrestricted research usage by Kodak Corporation. Initially, the image from the Kodak dataset is converted into a mosaic image.

b. Experimental results

The proposed A-DRL is modelled with 17 layers with a filter size of 64×64 . There are 15 hidden layers used with batch size 128. The kernel size is chosen as 3×3 , and the depth of each kernel is 3 because the image is RGB. The rectified linear unit is used as the activation function with the alpha value of 0.01. In DCNN, the weight parameters are optimized with HBA with a learning rate of 0.001, batch size 4, and epoch 100. These parameters are defined based on previous research in which each parameter is varied to find the optimal set of values for de-noising and demosaicking. Based on the previous observation, the parameters for DCNN, A-DRL and HBO is assigned. It is given that pre-training the DRL minimizes the training time due to the initialization of joint de-noising and demosaicking images. All weights are initialized based on [10]. The learning procedure has been accomplished with the initial learning rate 10^{-2} . The network parameters are updated based on the proposed algorithm, and each iteration's sum is considered. While increasing the number of iterations, each parameter's value varies.

The architecture of the proposed DCNN model is described in Table 2. It consists of 9 layers, including 3 fully connected layers, 3 pooling layers and 3 convolutional layers. Each convolutional layer is convolved with kernel sizes 3, 4 and 4; after convolution, max pooling is

Table 2 Summary of proposed DCNN model

Layer	Type	Number of nodes	Kernel size	Stride
1	Conv.	258×5	3	1
2	Pooling	129×5	2	2
3	Conv.	126×10	4	1
4	Pooling	63×10	2	2
5	Conv.	60×20	4	1
6	Pooling	30×20	2	2
7	FC	30	—	—
8	FC	20	—	—
9	FC	5	—	—

applied to reduce the feature map size. The kernel size is assigned to 1 and 2. The activation function used is rectified linear unit for layers 1, 3, 5, 7, and 8. The fully connected layer contains 30, 20 and 5 neurons at each layer. In addition, the softmax function is used at the output layer. The sample size, learning rate, regularization and momentum parameters are assigned to $10, 3 \times 10^{-3}, 0.2$, and 0.7 .

The performance of the proposed work is evaluated with the performance metrics such as PSNR, CPSNR, SSIM and MSSIM. The PSNR measures the quality between original and reconstructed images. In between two images, the PSNR is computed as,

$$PSNR = 10 \log_{10} \left(\frac{R^2}{MSE} \right) \quad (18)$$

Where, R represents the maximum fluctuation and MSE represents the mean square error between two images. The MSE is computed based on the row and column of each image pixel.

The color PSNR is used to compute the intensity variation between separate channels of original and demosaicked images. The CPSNR between the ground truth and the demosaicked image is computed as

$$CPSNR = 10 \times \log_{10} \left(\frac{255^2}{CMSE} \right) \quad (19)$$

The CMSE is computed as

$$CMSE = \frac{\sum_{C \in \{R, G, B\}} \sum_i^H \sum_j^W \|I_o^C(i, j) - I_d^C(i, j)\|_2^2}{3 \times H \times W} \quad (20)$$

Where, H represents the height of the image, W represents the width of the image, $\|\cdot\|_2$ represents the l_2 norm of the vector, $I_o^C(i, j)$ and $I_d^C(i, j)$ represents the R, G, and B color value for i, j pixel. From a perceptual point of view, the image quality is further evaluated with SSIM. In the human visual system, SSIM is one of the supporting performance evaluation metrics, which provides the similarity yield between the original and demosaicked images. Instead of pixel intensity variation, SSIM considered the degradation caused by the structure of the demosaicked image. It considers three kinds of similarity: contrast similarity, luminance similarity and structure similarity. In addition to the SSIM measure, MSSIM is computed separately based on each color channel.

The comparison of the original image from the dataset and the demosaicked image is shown in Fig. 4. In Fig. 4, the initial and demosaicked images are differentiated with the effect of the proposed demosaicking algorithm.

Figure 5 presents the PSNR result of the proposed approach for all images from the Kodak dataset. The green colour channel has a higher PSNR value than the three-colour channel. The CPSNR is computed separately for each color channel of the demosaicked Kodak image dataset. While comparing with the three color channels, the CPSNR of the green color channel is higher than other color channels such as red and blue. The blue color channel has attained the lowest CPSNR among all color channels. Considering the 24 images from the Kodak dataset, there is a slight deviation between images in terms of CPSNR. The proposed CPSNR ranges between 40 dB to 50 dB for all images.

Table 3, the PSNR of the proposed approach is compared with the existing techniques such as Adaptive Heterogeneity Direction (AHD), Alternative Projection (AP), Bilinear Interpolation (BIL), Residual Interpolation (RI), Weighted Edge (WE), and Improved Posterior Decision (IPD) [9]. In Table 3, the proposed approach has a PSNR greater than 44 dB. But in the case of existing approaches, it ranges from 25 dB to 43 dB. When considering the variation of each image, it is high for the existing approaches and lowers for the proposed approach in the range of 3 dB.

Figure 6 shows the comparison result of PSNR with other demosaicking approaches. The PSNR values achieved with the existing approaches such as Deep High Textured Network-Deep Smooth Textured Network (DHTN-DSTN) with optimization [10], Flexible Image Optimization (FlexISP), DeepJoint and Alternating Direction Method of Multipliers (ADMM) are 32.94 dB, 31.17 dB, 32.01 dB, and 32.63 dB. For the proposed approach, the PSNR value is 43.23 dB. The higher value of PSNR indicates the efficiency of the demosaicking procedure. Compared with the existing approaches, the performance of the proposed approach is high. The existing approaches are in the range of up to 37 dB. The range of PSNR lies between 30 dB to 37 dB for Flex ISP, DeepJoint, ADMM and (DHTN&DSTN) + Opt. Flex ISP and ADMM have the lowest performance considering the existing demosaicking approaches.

In Fig. 7, the PSNR result is compared for three color channels. The results are separately evaluated for the R, G, and B color channels. The results are compared with Learned



Fig. 4 The image from the Kodak dataset (left side) and the final de-noised and demosaicked image (right side)

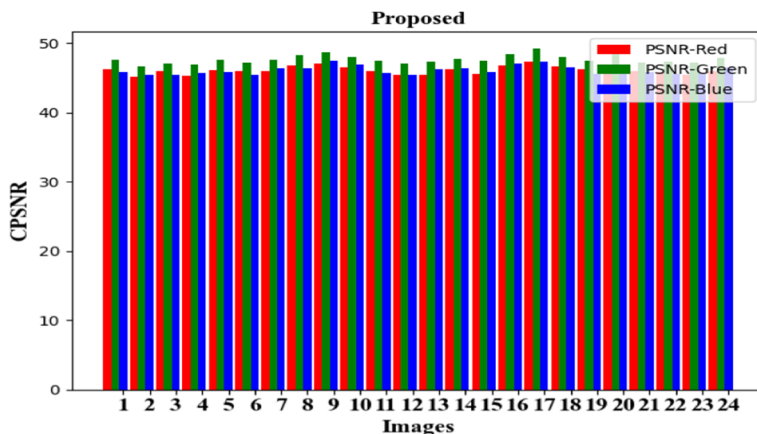


Fig. 5 PSNR (dB) value of 24 images from Kodak dataset for different color channels of the output image

Simultaneous Sparse Coding (LSSC), Directional Difference Regression (DDR), Fused Regression (FR) and Iterative Residual Interpolation- Progressive Collaborative Representation (IRI-PCR) techniques. Compared with the three color channels, the PSNR of the red channel is low, and a higher PSNR is achieved for the green color channel. In the red color channel, the PSNR obtained for the proposed method, LSSC, DDR, FR, and IRI-PCR [17] is 43.42 dB, 40.53 dB, 37.08 dB, 40.15 dB and 40.02 dB. In the green color channel, the PSNR obtained for the proposed method, LSSC, DDR, FR and IRI-PCR, is 43.25 dB, 44.31 dB, 43.88 dB,

Table 3 Comparison table for proposed PSNR (dB) comparison with AHD, AP, BIL, RI, WE, and IPD approaches

Image No	AHD(dB)	AP(dB)	BIL(dB)	RI(dB)	WE(dB)	IPD(dB)	Proposed(dB)
1	35.12365	37.82559	26.34246	33.28362	38.66908	33.80081	44.67638
2	39.14441	39.57975	33.14758	38.60495	39.53599	40.81597	44.96106
3	41.15674	41.21406	34.51965	37.86927	40.84143	42.2465	44.93012
4	38.67537	40.1833	33.68422	39.21196	39.37491	41.34468	45.55014
5	35.39069	37.40025	26.67253	34.81466	36.10685	39.52928	45.19389
6	37.57617	38.54925	27.81229	33.87583	39.39936	34.08699	45.57246
7	4.051,801	41.83905	33.52544	38.58664	40.89483	42.19047	46.24991
8	33.74326	35.07306	23.54213	32.67506	41.90167	42.58102	46.71093
9	41.05238	41.8027	32.38597	38.67506	41.90167	42.58102	46.01864
10	40.50117	41.91221	32.43697	39.90842	41.95163	38.73789	45.38616
11	37.47875	39.24883	29.14545	35.84941	39.54117	40.04738	45.08246
12	41.65404	42.64677	33.49666	37.59205	42.56146	37.39145	45.31668
13	31.31608	34.2403	23.87083	30.92762	35.9223	36.36908	45.76487
14	35.22152	35.49806	29.21216	34.30985	33.92549	36.33077	45.38243
15	37.93509	39.37607	33.04679	37.80148	38.97836	40.25264	46.39559
16	41.96713	41.96713	31.31421	36.94948	42.64641	36.38566	47.13999
17	39.25633	41.08726	32.03806	38.71668	41.75534	38.86249	45.96258
18	34.67103	36.99468	28.06782	34.79721	37.03895	38.925	47.13999
19	38.28772	39.46088	27.92443	36.52326	40.35815	36.2505	45.96258
20	39.04057	40.41298	31.62433	38.13648	40.7109	37.99864	46.52933
21	36.29068	37.36113	30.36722	35.83545	37.77811	39.71259	45.08885
22	36.29068	37.361133	30.36722	35.83545	37.77811	39.54055	45.22531
23	41.63791	41.86702	35.11318	39.3922	40.98141	42.82304	45.13111
24	32.97968	34.1665	26.75876	32.78057	35.03707	36.25295	45.87023

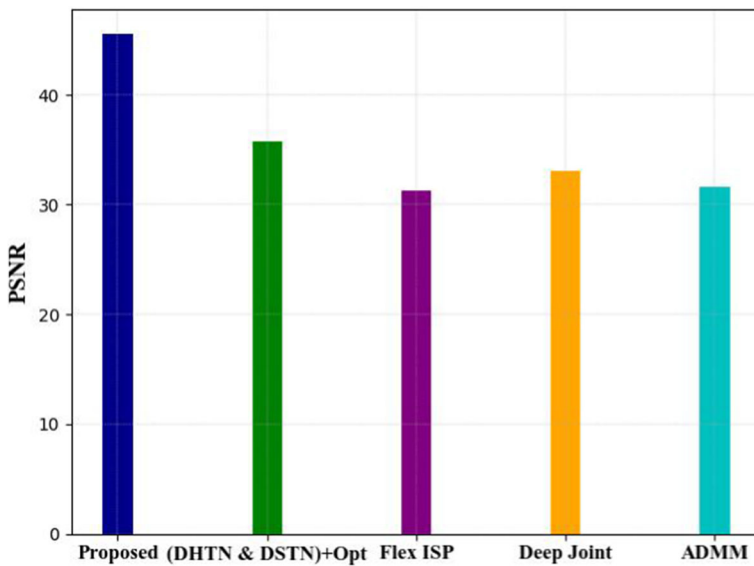


Fig. 6 PSNR (dB) comparison of the proposed approach with (DHTN&DSTN) + Opt, DeepJoint and ADMM approaches

43.81 dB and 43.52 dB. In the blue color channel, the PSNR obtained for the proposed method, LSSC, DDR, FR and IRI-PCR, is 43.26 dB, 40.64 dB, 40.35 dB, 40.30 dB and 39.78 dB. The green channel PSNR value is higher compared with the blue and red color channels.

The CPSNR comparison for different approaches is shown in Fig. 8. The color PSNR is computed by taking the average value of three color channels such as green, blue and red. The color PSNR values are nearly the same for all approaches. The CPSNR values obtained for the

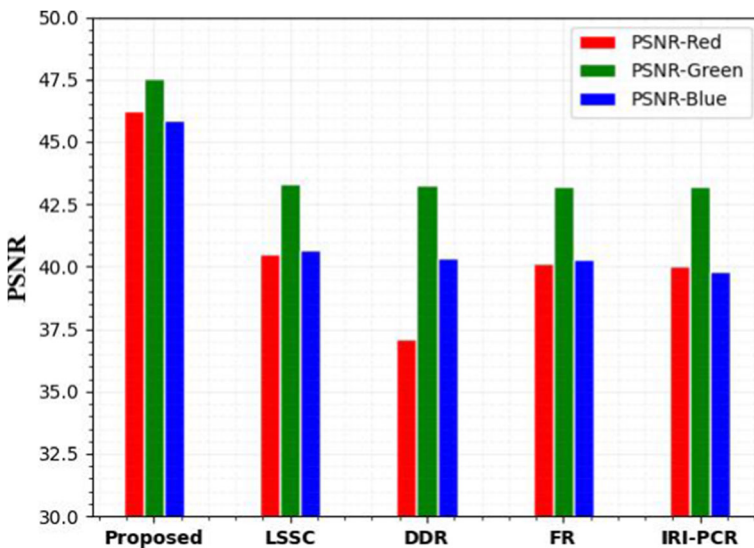


Fig. 7 PSNR (dB) comparison of proposed R G B color channels with LSSC, DDR, FR and IRI-PCR approaches

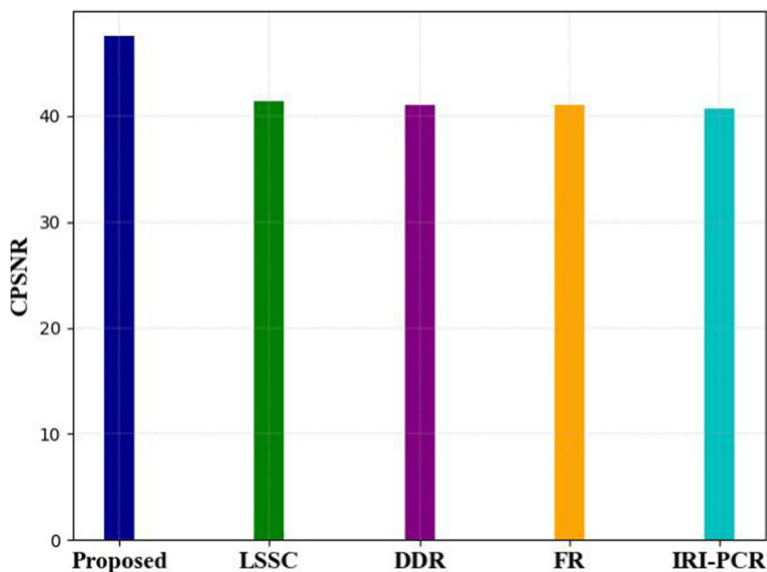


Fig. 8 CPSNR (dB) comparison of the proposed approach with LSSC, DDR, DDR, FR and IRI-PCR approaches

proposed method, LSSC, DDR, FR and IRI-PCR, are 43.30 dB, 41.44 dB, 41.06 dB, 41.03 dB and 40.74 dB. Compared with the existing approaches, the highest CPSNR is attained with the proposed demosaicking approach. The LSSC, DDR, FR and IRI-PCR are providing the lowest performance, which is in the range of 40 dB. Increasing the CPSNR represents the highest level of performance, and a low CPSNR value denotes low demosaicking performance.

The SSIM value is computed for the proposed approach and compared with the existing demosaicking approaches, as shown in Fig. 9. For all approaches, the SSIM value is above 98,

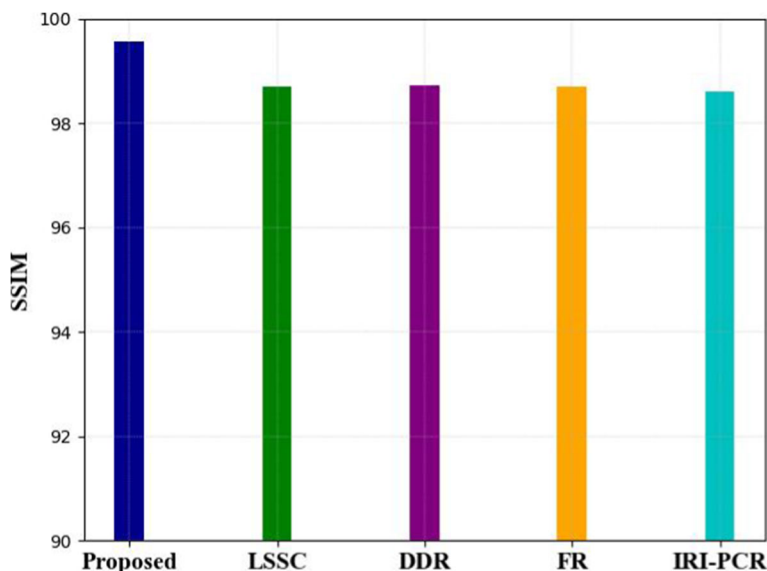


Fig. 9 Comparison of proposed SSIM with LSSC, DDR, FR and IRI-PCR approaches

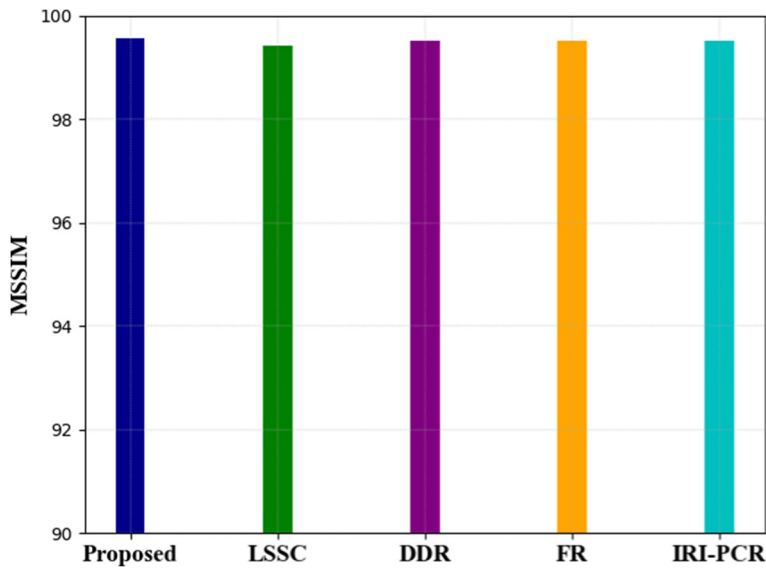


Fig. 10 Comparison of proposed MSSIM with LSSC, DDR, FR and IRI-PCR approaches

and for the proposed approach, it reaches nearly 100. The optimal result for SSIM is obtained for the proposed approach. The SSIM value obtained with the proposed method, LSSC, DDR, FR and IRI-PCR, are 0.997, 0.986, 0.987, 0.987 and 0.985. The SSIM result of the proposed approach is higher than the other existing approaches. The lower most performance is obtained with the existing FR based approach, DDR and IRI-PCR. The lower SSIM indicates lower demosaicking performance, and the higher SSIM indicates better demosaicking performance.

Figure 10 shows the MSSIM comparison of the proposed approach with other existing approaches. While evaluating the SSIM performance, all approaches are nearly at the optimal position. But, the performance of the proposed approach is higher than the other existing approaches. The MSSIM values obtained with the proposed method, LSSC, DDR, FR and IRI-PCR are 0.9975, 0.9972, 0.9968, 0.9967 and 0.9968. When compared with the existing approaches, better performance is attained with the proposed algorithm. The existing approaches have the lowest performance compared to the proposed demosaicking algorithm. In Table 4, the PSNR and SSIM of the proposed approach are compared with the existing approaches such as IDP, DHTN-DSTN, PCR, Generative Adversarial Model (GAN),

Table 4 Comparing the performance of PSNR, CPSNR, SSIM and MSSIM with state-of-the-art approaches

Techniques	PSNR	SSIM
DHTN-DSTN [10]	32.94	0.821
IPD [9]	42.58	0.989
PCR [17]	40.75	0.9859
GAN [28]	42.64	0.9894
FS-Net [4]	26.96	0.850
RCL [3]	39.01	0.9658
CNN [24]	36.33	0.9487
Proposed	43.23	0.997

Table 5 Comparison of network complexity and size

Techniques	Complexity	Parameters
FS-Net [4]	2.76	546 k
DnCNN [25]	1.40	1.11 M
BRDNet [25]	2.78	1.11 M
Proposed	1.10	540 k

Frequency Selection Network (FS-Net), CNN, and Residual contrastive Learning (RCL). The parameters such as PSNR and SSIM are used to evaluate the accuracy of the proposed model.

Compared with the performance of PSNR, CPSNR, SSIM and MSSIM, a better result is obtained with the proposed demosaicking approach, which shows the efficiency of the proposed approach. It is noted that increasing the number of layers reduces the residuals, and almost black images are produced. Extra residuals are created by reducing the number of layers in the network. The proposed algorithm is effective for images of high dimensional range with varying color and spatial exposure.

In order to make a perfect comparison, the same test procedures and conditions are performed for all demosaicking models. The proposed approach has obtained a higher trade-off between the quality of demosaicked images and processing complexity. The computational complexity of the proposed approach is compared with the existing approaches and is given in Table 5.

In addition, it can also be estimated with the number of add operations and the number of parameters used to evaluate the memory requirement of network weight. The network complexity and the size of the network are compared with existing methods. While using the least amount of parameters, the network complexity is high since it uses the same network for varying amounts of iterations. For the proposed approach, the size and complexity of the network are low to achieve better image quality. The computational complexity has been analyzed by considering the data size $n \times p \times q$. Initially, CNN has used for de-noising the image, it involves deep learning with convolution and pooling operations. Hence the computational complexity is set with the ranking s for de-noising. The total complexity of de-noising is estimated as $O(npqs + (n + p + q)s^4 + s^6)$. In addition, the optimization algorithm is used with A-DRL, which has the complexity of $O(npq \log(mpq))$. By considering the problem of demosaicking, the complexity of spatial and spectral dimensions of the image is $O(6npq)$. By considering the entire proposed de-noising and demosaicking with the computational complexity per iteration is $(npq + (n + p + q)s^4 + s^6 + npq \log(npq) + 6npq)$.

5 Conclusion

This paper proposed the Bayer image de-noising and demosaicking with DCNN-HBA and A-DRN. Initially, the CFA pattern's Bayer image is used to construct noisy mosaic images. After getting the Bayer image, the proposed work is implemented to remove the noise and reconstruct the original image. For de-noising, DCNN-HBA is used in which the quality of the image is increased. Attention-based DRL reconstructs the image with reduced loss. The attention mechanism is added in DRL, which retains more relevant information required for demosaicking. The attention approach and HBA algorithms were used to resolve the vanishing or gradient issue. Each pixel's missing information and visual artifacts are inferred to

reconstruct full-quality color images. The proposed demosaicking approach A-DRL is compared with the existing approaches, showing the reduction of more visual artifacts. The higher PSNR, CPSNR, SSIM and MSSIM value indicates the better perceptual quality of demosaicked images. Future work of this research focuses on enhancing the network capacity for removing more complex noise with the preservation of better image quality in real world environment.

Authors contributions All authors have equal contributions to this work.

Funding No funding is provided for the preparation of the manuscript.

Availability of data and materials No data Availability.

Declarations

Conflict of interest Authors S.P. Predeep Kumar, K. John Peter, C. Sahaya Kingsly declare that they have no conflict of interest.

Ethical approval This article does not contain any studies with human participants or animals performed by any authors.

Consent to participate All the authors involved have agreed to participate in this submitted article.

Consent to publish All the authors involved in this manuscript give full consent for publication of this submitted article.

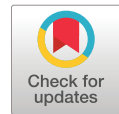
References

1. Arbuji A, Jagtap S, Agrawal A, Dalpe R, Sawant P Deep Joint Denoising and Demosaicking Using Convolutional Neural Network
2. Buades A, Duran J (2018) Joint de-noising and demosaicking of raw video sequences. In 2018 25th IEEE international conference on image processing (ICIP) IEEE 2172–2176
3. Dong N, Maggioni M, Yang Y, Pérez-Pellitero E, Leonardis A and McDonagh S (n.d.) Residual Contrastive Learning for Image Reconstruction: Learning Transferable Representations from Noisy Images
4. Elgendy OA, Gnanasambandam A, Chan SH, Ma J (2021) Low-light demosaicking and de-noising for small pixels using learned frequency selection. IEEE Transact Comput Imag 7:137–150
5. Guo S, Liang Z, Zhang L (2021) Joint de-noising and demosaicking with green channel prior for real-world burst images. IEEE Trans Imag Proc 30:6930–6942
6. Janjušević N, Khalilian-Gourtani A, Wang Y (2021) CDLNet: noise-adaptive convolutional dictionary learning network for blind Denoising and Demosaicing. arXiv preprint arXiv:2112.00913
7. Jayachandran S (2017) Digital imaging in dentistry: a review. Contemporary Clin Dentis 8(2):193–194
8. Jin Q, Facciolo G, Morel JM (2020) A review of an old dilemma: Demosaicking first, or de-noising first? In proceedings of the IEEE/CVF conference on computer vision and pattern recognition workshops 514–515.
9. John Peter K, Prabhu S (2017) Demosaicking on color filter array images using improved posterior decision approach. Int J Print Packag Allied Sci 5(1):729–739
10. Khadidos AO, Khadidos AO, Khan FQ, Tsaramirsis G, Ahmad A (2021) Bayer image demosaicking and de-noising based on specialized networks using deep learning. Multimed Syst, Springer 27(4):807–819
11. Kiku D, Monno Y, Tanaka M, Okutomi M (2016) Beyond color difference: residual interpolation for color image demosaicking. IEEE Trans Imag Proc 25(3):1288–1300
12. Kim Y, Ryu H, Lee S, Lee YJ (2020) Joint Demosaicking and Denoising based on Interchannel nonlocal mean weighted moving least squares method. Sensors 20(17):4697

13. Kokkinos F, Lefkimmiatis S (2018) Deep image demosaicking using a cascade of convolutional residual de-noising networks. In proceedings of the European conference on computer vision (ECCV) 303–319
14. Ma K, Gharbi M, Adams A, Kamil S, Li TM, Barnes C, Ragan-Kelley J (2022) Searching for fast Demosaicking algorithms. *ACM Transac Graph (TOG)* 41:1–18
15. Mihoubi S, Lapray PJ, Bigué L (2018) Survey of demosaicking methods for polarization filter array images. *Sensors* 18(11):3688
16. Morrison AO, Gardner JM (2015) Microscopic image photography techniques of the past, present, and future. *Archives Pathol Lab Med* 139(12):1558–1564
17. Ni Z, Ma KK, Zeng H, Zhong B (2020) Color image demosaicing using progressive collaborative representation. *IEEE Trans Imag Proc* 29:4952–4964
18. Park SH, Kim HS, Lancel S, Parmar M, Wandell BA (2009) A case for de-noising before demosaicking color filter array data. In 2009 Conference record of the forty-third Asilomar conference on signals, Systems and Computers, IEEE 860–864
19. Qiao Z, Wen X, Zhou X, Qin F, Liu S, Gao B, Liu W, Chi D, Liu Z (2023) Adaptive iterative guided filtering for suppressing background noise in ptychographical imaging. *Optics LasEngin, Elsevier* 160: 107233
20. Rafi Nazari M (2017) De-noising and demosaicking of color images. PhD diss., Université d'Ottawa/University of Ottawa
21. Rostami M, Berahmand K, Nasiri E, Forouzandeh S (2021) Review of swarm intelligence-based feature selection methods. *Engineering Applications of Artificial Intelligence, Elsevier*, 100: 104210
22. Syu NS, Chen YS, Chuang YY (2018) Learning deep convolutional networks for demosaicing. *arXiv preprint arXiv:1802.03769*
23. Tan DS, Chen WY, Hua KL (2018) DeepDemosaicking: adaptive image demosaicking via multiple deep fully convolutional networks. *IEEE Trans Imag Proc* 27(5):2408–2419
24. Tan H, Xiao H, Liu Y, Zhang M (2022) Two-stage CNN model for joint Demosaicing and Denoising of burst Bayer images. *Computational intelligence and neuroscience*, [hindawi.com](https://www.hindawi.com), 2022
25. Tian C, Xu Y, Zuo W (2020) Image de-noising using deep CNN with batch renormalization. *Neural Netw, Elsevier* 121:461–473
26. Wang Y, Cao R, Guan Y, Liu T, Yu Z (2021) A deep survey in the applications of demosaicking. In 2021 3rd international academic exchange conference on science and technology innovation (IAECST), IEEE 596–602.
27. Wang S, Zhao M, Dou R, Yu S, Liu L, Wu N (2021) A compact high-quality image Demosaicking neural network for edge-computing devices. *Sensors* 21(9):3265
28. Wu F, Huang T, Dong W, Shi G, Zheng Z, Li X (2021) Toward blind joint demosaicing and de-noising of raw color filter array data. *Neurocomput Elsevier* 453:369–382
29. Ye W, Ma KK (2015) Color image demosaicing using iterative residual interpolation. *IEEE Trans Imag Proc* 24(12):5879–5891
30. Zhang C, Li Y, Wang J, Hao P (2016) Universal demosaicking of color filter arrays. *IEEE Trans Imag Proc* 25(11):5173–5186

Publisher's note Springer Nature remains neutral with regard to jurisdictional claims in published maps and institutional affiliations.

Springer Nature or its licensor (e.g. a society or other partner) holds exclusive rights to this article under a publishing agreement with the author(s) or other rightsholder(s); author self-archiving of the accepted manuscript version of this article is solely governed by the terms of such publishing agreement and applicable law.



Evolutionary Algorithm Based Feature Subset Selection for Students Academic Performance Analysis

Ierin Babu^{1,*}, R. MathuSoothana² and S. Kumar²

¹Department of Computer Science and Engineering, Noorul Islam Centre for Higher Education, Kanyakumari, 629180, India

²Department of Information Technology, Noorul Islam Centre for Higher Education, Kanyakumari, 629180, India

*Corresponding Author: Ierin Babu. Email: ierinbabu84@gmail.com

Received: 27 June 2022; Accepted: 23 November 2022

Abstract: Educational Data Mining (EDM) is an emergent discipline that concentrates on the design of self-learning and adaptive approaches. Higher education institutions have started to utilize analytical tools to improve students' grades and retention. Prediction of students' performance is a difficult process owing to the massive quantity of educational data. Therefore, Artificial Intelligence (AI) techniques can be used for educational data mining in a big data environment. At the same time, in EDM, the feature selection process becomes necessary in creation of feature subsets. Since the feature selection performance affects the predictive performance of any model, it is important to elaborately investigate the outcome of students' performance model related to the feature selection techniques. With this motivation, this paper presents a new Metaheuristic Optimization-based Feature Subset Selection with an Optimal Deep Learning model (MOFSS-ODL) for predicting students' performance. In addition, the proposed model uses an isolation forest-based outlier detection approach to eliminate the existence of outliers. Besides, the Chaotic Monarch Butterfly Optimization Algorithm (CBOA) is used for the selection of highly related features with low complexity and high performance. Then, a sailfish optimizer with stacked sparse autoencoder (SFO-SSAE) approach is utilized for the classification of educational data. The MOFSS-ODL model is tested against a benchmark student's performance data set from the UCI repository. A wide-ranging simulation analysis portrayed the improved predictive performance of the MOFSS-ODL technique over recent approaches in terms of different measures. Compared to other methods, experimental results prove that the proposed (MOFSS-ODL) classification model does a great job of predicting students' academic progress, with an accuracy of 96.49%.

Keywords: Students' performance analysis; educational data mining; feature selection; deep learning; metaheuristics; outlier detection



This work is licensed under a Creative Commons Attribution 4.0 International License, which permits unrestricted use, distribution, and reproduction in any medium, provided the original work is properly cited.

1 Introduction

Recently, different kinds of learning management systems (LMSs) have been effectively adopted by higher education institutions and universities, collecting large amounts of educational data and recording various student learning features [1]. Educational Data Mining (EDM) is a rapidly expanding scientific field that provides the potential to analyze these information and harness useful knowledge from it. Eventually, a plethora of prediction algorithms have been efficiently used in an educational context to resolve a great number of challenges [2]. But, creating prediction methods in the field of EDM by using TL models has been poorly studied until now. Thus, the most important question in current research is whether a prediction algorithm trained on a previous course would perform well on a novel one [3]. observes that a course (a) is populated with distinct instructors and students, (b) may have features that could not be transmitted (for example, a feature determined on specific learning resources that is inaccessible on other courses) and (c) would change over time in different ways, despite being structurally and contextually distinct. Additionally, the difficulty in course design and the LMS have a great influence on the course progress at the time of semester. Hence, there might be a problem where the transfer learning (TL) method might not reflect the anticipated result, which shows some uncertainty regarding the prediction accuracy of the recently established learning algorithm [4].

Prediction and students' performance analysis are the two extensively discussed areas of research in educational systems [5]. Despite their disparate goals, the outcomes of performance analysis have a significant impact on predictive research. The analysis of student progress during their studies offers university management data regarding the possibilities of success for all the students. Conventionally, this analysis can be made by the lecturers who utilize their communication with students in classroom activities and mid-term assessments to take timely action and find those "at risk" of dropping out [6]. In the current scheme of higher education, the communication time between students and lecturers is continuously decreasing and finding endangered students has become even more challenging. This is because of the increasing number of students and access to online learning resources for students [7]. More precise predictions of student's success could be achieved by the current systems of machine learning and data mining analysis.

The prediction of learner performance can be accomplished with the help of several data mining approaches. For example, the machine learning (ML) methods as stated in research works of [8] 2020. The data mining systems are categorised as (a) ML algorithms (like neural networks, symbolic learning, swarm optimization), (b) statistical approaches (namely cluster analysis, regression analysis, discriminant analysis) and (c) artificial intelligence techniques (for example, fuzzy logic, genetic algorithms, neural computation). In this regard, the present study aims at examining the capacity of artificial neural networks (ANN) to forecast team's performance. Generally, ANN is a subdivision of Artificial Intelligence (AI), which includes the application of Deep Learning (DL) and Machine Learning (ML). The ANN theory was stimulated by the human brain and especially by the biological neural networks. It contains synapsis node for perceptrons and artificial neurons.

The synopsis is found in neural connections and the biological brain is used for learning and memory. The connection strength, i.e., the synaptic weights corresponding to the memorized data, can be changed at the time of the learning method. An array of neurons composes an ANN layer [9]. Usually, all the neurons receive signals (the weighted amount of their inputs), next process them and employ an activation function for signaling neurons related. A simple ANN framework includes output, input, and hidden layers. In contrast, a Deep Neural Network (DNN) method consists of (a) the output layer, (b) the input layer and (c) more than two hidden layers (Denses). The basic functions for training and activating the DNNs are the loss function (feed-forward loop), the optimizer (back-propagation loop) and the activation function [10].

This paper designs a novel metaheuristic optimization-based feature subset selection with an optimal deep learning model (MOFSS-ODL) to predict students' performance. The proposed MOFSS-ODL technique uses an isolation forest (IF) based outlier detection approach to eliminate the existence of outliers. Moreover, the Chaotic Monarch Butterfly Optimization Algorithm (CBOA) is applied to choose highly related features with low complexity and high performance. Furthermore, a sailfish optimizer with stacked sparse autoencoder (SFO-SSAE) approach is employed to classify the educational data. To validate the enhanced predictive outcome of the MOFSS-ODL technique, a series of simulations were carried out against a benchmark students' performance data set from the UCI repository and the results are inspected under several dimensions.

2 Related Works

This section offers a comprehensive review of existing students' performance analysis prediction models. In Akour et al. [11], an effort has been made to examine the efficacy of utilizing the DL method more precisely to forecast students' achievements, which could assist in forecasting when the student can complete their degree or not. The simulation result shows that the presented method outperforms the current approach in terms of predictive performance. In Harvey et al. [12], a prediction method is examined and developed in this work for analysing a K-12 education data set. The LR, DT and NB methods are among the two classifications used in the development of these prediction methods. The NB method gives the most accurate predictions for high school students' SAT and Math scores.

Orji et al. [13] carried out prior research on determining methods of improving student engagement in online learning techniques via data-driven intervention. Student engagement in this work can be described by objective information (activity log of a certain UG course in a TELS). Activity logs are unbiased data and a reflection of students' actual learning behaviour (uncontrolled). In this work, the logs of student learning activities from TELS are mined, which employed UG courses, to explore variances among student's learning behaviours as they are related to their engagement levels and academic performance (evaluated based on last grade point on a course). Supervised (RF) and unsupervised (Clustering) ML methods are applied in examining the relationships.

Xu et al. [14] designed a new ML technique to predict students' performance in degree programs, i.e., one capable of addressing these major problems. The presented model consists of 2 key characteristics. Initially, a bilayer framework including a cascade of ensemble predictors and multiple base predictors was proposed to make predictions according to the student's evolving performance state. Next, a data-driven technique based on probabilistic matrix factorization and latent factor model is presented for discovering the course significance, i.e., significant enough to construct an effective base predictor.

Hamoud et al. [15] present method-based DT models and recommend the best method-based performances. This method makes use of the three created categories (REPTree, J48 Random Tree and the questionnaire filled out by the student). The study includes sixty questions that cover the subject, such as social activity, health, academic achievement, and relationships and how this affects student efficiency. A total of 161 questionnaires were collected. This approach was developed using the Weka 3.8 tool [16] investigated data logged by a TEL scheme called Digital Electronics Education and Design Suite (DEEDS) using a machine learning technique. The ANN, SVM, LR, NB and DT classifiers are included in the ML method. When entering input data, the DEEDS approach allows students to perform digital design problems with varying levels of complexity. Reshma et al. [17] use a deep ANN on a set of hand-crafted features extracted from the virtual learning environment clickstream data to forecast at-risk students and provide a measure for earlier intervention in this situation. The results show that the provided strategy performs better in categorization.

Waheed et al. [18] developed a comprehensive study of limitations, hardware resources and performance. This study can be implemented by using Collaboratory to accelerate the DL method for CB and another GPU-centric application. The selected test-case is a parallel tree-based combinatorial search and 2 CV applications: object segmentation or localization and object classification or detection. The hardware under the accelerated running time is related to a conventional workstation and strong Linux servers armed with twenty physical cores. Cyril et al. [19] proposed a new end-to-end DL technique and suggested a DPCNN method for predicting students' performances. This paper also presents multitasking learning methods and forecast the performance of students from different majors in an unified architecture.

3 The Proposed Model

In this study, an effective MOFSS-ODL technique was designed to predict students' performance. The proposed MOFSS-ODL technique encompasses IF-based outlier detection, CBOA-based feature selection, SSAE-based classification, and SFO-based parameter optimization. Fig. 1 illustrates the overall working process of the proposed MOFSS-ODL technique.

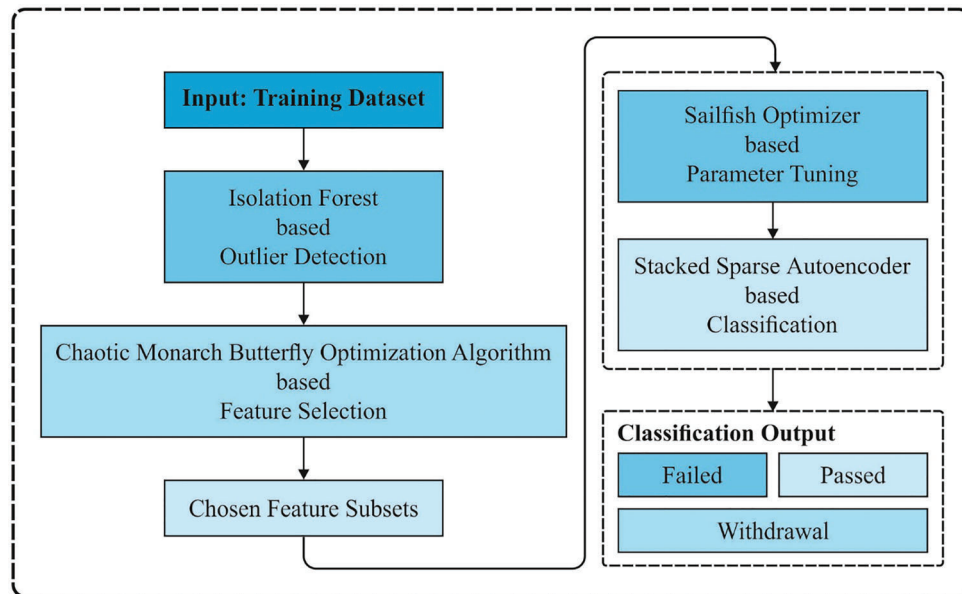


Figure 1: Overall process of MOFSS-ODL technique

3.1 Isolation Forest Based Outlier Detection

At the primary stage, the IF technique is applied to eradicate the presence of outliers in educational data. The IF is an unsupervised algorithm employed in collective-based models to separate the anomalies by evaluating the isolation scores for each data point. The IF has a similar idea of utilising the tree algorithm as the RF model. It processes data points to recurrent random splits that are based on feature selection [20]. The major benefit of the IF technique is how, it processes information. Rather than processing each data point, it employs a DT mode for isolating the outliers, which decreases the processing and execution time and the respective memory requirements. The IF method functions by splitting the algorithm into various segments, which are needed for the subsampling size. The IF estimation starts with specific data points. Next, based on the selected value, it sets a range between the minimum and maximum values to define the outlier scores for all the data points in the tree. The score can be measured by setting a path length for isolating the outliers.

3.2 CBOA Based Feature Selection Technique

During the feature selection process, the CBOA is utilized to choose an optimal subset of features from the educational data; the concept of the BOA method is established in [21]. In BOA, each monarch butterfly is idealized and situated in Mexico (Land 2), southern Canada (Land 1), and the northern US. Next, the position of the monarch butterfly is upgraded in two ways, such as through butterfly adjusting and migration operators. Initially, the offspring are produced (a position upgrade) via the migration operators. Next, the position of another monarch butterfly is upgraded using the butterfly adjusting operators. Furthermore, both operators could be performed concurrently. Thus, the BOA method is appropriate for similar processing and has a good balance of diversification and strengthening. The BOA method includes two significant operators, which are listed below.

In migration operator, the aim is to upgrade the migration of monarch butterflies among Land1 and Land2. NP is the overall amount of monarch butterflies and $NP1 = \text{ceil}(p \times NP)$ and $NP2 = NP - NP1$ are the number of monarch butterflies in Land1 and Land2, respectively, whereas p represents the migration rate of monarch butterfly with $p = 5/12$ in BOA, $\text{ceil}(x)$ rounds x to the near integer better than or equivalent to x , the sub-population of Land1 is represented as Sub-population1 and the sub-population of Land2 is represented as Sub-population2. Next, the migration operators are denoted by

$$x_{t,k}^{t+1} = \begin{cases} x_{r_1,k}^t & r > pr \leq p, \\ x_{r_2,k}^t & \end{cases} \quad (1)$$

In which $x_{i,k}^{t+1}$ represent the k th component of x_i in generation $t + 1$; likewise, $x_{r_1,k}^t$ signifies the k th component of χ_{r_1} in generation t and $x_{r_2,k}^t$ indicates the k th component of χ_{r_2} in generation t ; the present generation value is t , r_1 & r_2 Monarch butterflies are arbitrarily chosen from Sub-population1 and Sub-population2, respectively. Now, r is estimated by $r = \text{rand} \times \text{peri}$, in which peri denotes the migration period, i.e., equivalent to 1. 2 in BOA and rand indicates an arbitrary value in the range of zero and one [22]. Fig. 2 illustrates the flowchart of BOA.

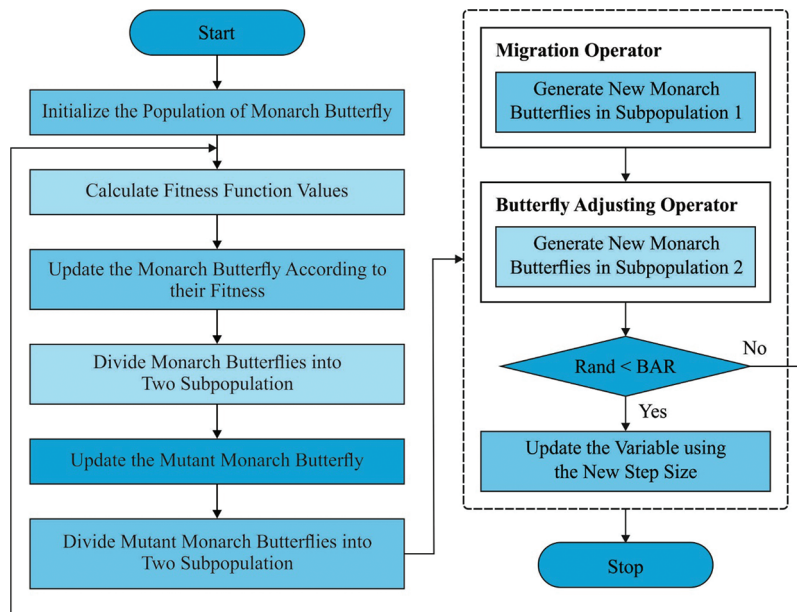


Figure 2: Flowchart of BOA

In the butterfly adjusting operator, it upgrades the location of monarch butterfly in Subpopulation2 as:

$$x_{j,k}^{t+1} = \begin{cases} x_{best,k}^t & rand \leq p \\ x_{r_3,k}^t & rand > p \& rand \leq BAR, \\ x_{i,k}^{t+1} + \alpha \times (dx_k - 0.5) & rand > p \& rand > BAR \end{cases} \quad (2)$$

Let $x_{j,k}^{t+1}$ be the k th component of x_j in generation $t + 1$; likewise $x_{best,k}^t$ indicates the k th component of x_{best} in generation t , i.e., the optimal position for Land1 and Land2 monarch butterflies, $x_{r_3,k}^t$ signifies the k th component of x_{r_3} in generation t , the monarch butterfly r_3 is arbitrarily chosen from Sub-population2, also BAR indicates the adjustment rate. When BAR is lesser when compared to the rand arbitrary value, the k th component of x_j at $t + 1$ is upgraded, in which α indicates the weight factor and $\alpha = S_{max}/t^2$, Let S_{max} be the maximal walk steps. In (2), dx represents the walk steps of j butterfly which are evaluated by the Levy fight thus $x = Levy(x_j^t)$.

The presented CBOA method depends on the incorporation of chaotic maps in the typical BOA. The major phases of the presented model can be given in the following.

- a) Invoke the chaotic map to update butterfly locations rather than utilizing arbitrary parameters hence it will enhance the CBOA accuracy. They would be adapted by substituting r^2 with C_j as:

$$x_i^{t+1} = x_i^t + (C_j \times g^* - x_i^t) \times f_i \quad (3)$$

$$x_i^{t+1} = x_i^t + (C_j \times x_{j'} - x_k^t) \times f_i \quad (4)$$

whereas C_j represents the chaotic map and $j = 1, 2, \dots, 10$. Noted that the C_j value is a chaotic value, created by ten chaotic maps are substituted by r values for getting optimal outcomes in accuracy and minimal fitness when compared to original algorithm which uses arbitrary value.

- b) Transfer CBOA to binary CBOA: Employing the binary CBOA would characterise the searching space in binary values. Hence, the binary CBOA could adoptively search the feature space for optimal feature integration and is predicted to be very simple when compared to the continuous version. Binary CBOA can be given as follows:

$$x_i^{t+1} = \begin{cases} 1 & \text{if } (s(x_i^{t+1})) \geq rand() \\ 0 & \text{otherwise} \end{cases} \quad (5)$$

Let s be a transfer function, $rand()$ represents an arbitrary value made from uniform distribution $[0,1]$ and x_i^{t+1} indicates the upgraded solutions.

$$s(x_i^{t+1}) = \frac{1}{1 + \exp^{10(x_i^{t+1} - 0.5)}} \quad (6)$$

Different from the standard BOA, wherever the solution was upgraded from the exploring space nearby to a continuing value place, in the CBOA, the searching space was demonstrated as a dimensional Boolean lattice. Besides, the solution was upgraded on the corner of the hypercube. In addition, to solve this issue of selecting or not, a given parameter and binary solution vectors were implemented; one relates to the parameter being chosen for comprising the new dataset, and zero relates to anything else. In binary techniques, one uses the step vector for evaluating the possibility of altering a place. The transmission function significantly influences the balance between exploitation and exploration. During the FS technique, if the size of the feature vector was large, the count of various features combined would inclines, for instance, a huge space for exhaustive research. The presented hybrid technique was utilized to achieve this resolve to explore the feature space vigorously and make the right combination of

features. The FS falls into multi-objective issues as it requires satisfying many objectives to receive better solutions that minimize the subset of the FS and, concurrently, maximize the accuracy of the outcome for providing a classifier.

Based on what came before, the fitness function (FF) for finding solutions in this state was made so that the two goals could be met in a balanced way.

$$fitness = \alpha \Delta_R(D) + \beta \frac{|Y|}{|T|} \quad (7)$$

$\Delta_R(D)$ refers the classifier error rate. $|Y|$ stands for the size of subset which this approach chooses and $|T|$ entire number of features involved from the existing datasets. α defines the parameter $\in [0, 1]$ comparing with the weight of error rate of classification respectively but $\beta = 1 - \alpha$ signifies the significance of decrease feature. The classification efficacy was allowed a vital weight rather than the number of chosen features. If the evaluation function is only regarded as the classification accuracy, the outcomes are neglected of solutions that are comprised of the same accuracy but minimally chosen features that serve as essential aspects of decreasing the dimensionality issue.

3.3 SFO-SSAE Based Classification Model

Finally, the SFO-SSAE based classification model gets executed to determine the proper class labels for the educational data. The building block of deep networks for unsupervised learning features is a single AE [23]. It is another kind of ANN model and is architecturally determined by the output, input and hidden layers that compose a decoder and an encoder. In, the encoder transmits the data matrix to a hidden depiction with a tunable number of neural units, followed by a non-linear activation. The procedure can be expressed by Eq. (8).

$$h = f(x) = \sigma(W_1^T x + b_1) \quad (8)$$

In which, $\sigma(\cdot)$ indicates the activation function, W_1 represents a weight matrix and b_1 denotes a bias vector. Let Relu, sigmoid and tanh be widely employed. During the decoder process, the deterministic mapping $g(\cdot)$ maps the hidden depiction back to recreate the x' input space as:

$$x' = g(h) = \sigma(W_2^T h + b_2) \quad (9)$$

Whereas b_2 & W_2 represents the bias vector and weight matrix of the decoder. The trained AE aim is to discover the $\theta = W_1, W_2, b_1, b_2$ parameters which minimize the recreation loss among the output data X' and input data X . The objective function is determined by:

$$\arg \min_{\theta} J_{AE}(\theta) = \frac{1}{N} \sum_{i=1}^N \|x_i - x'_i\|^2 + \lambda (\|W_1\|_2 + \|W_2\|_2) \quad (10)$$

Let λ be a standardization coefficient of the weight decay term, i.e., added to avoid over-fitting. The constraint representative power of a single AE results from the simplest shallow structural characteristics. Stimulated by the biological method of the human visual cortex, the conventional SAE can be generated by stacking AE consecutively, taking the output of the hidden unit of the prior layers as the input to the upper layers. Fig. 3 displays the framework of SAE. AE was initially presented according to the concept of reduction dimension and would lose the capacity to manually learn features if there were further hidden layer neurons when compared to input neurons. An SAE can be attained by adding a few sparse limitations to the conventional AE that could suppress all the outputs of hidden layer nodes. To attain this, the training objective of SAE can be expressed as follows:

$$\arg \min_{\theta} \int_{SAE} (\theta) = \frac{1}{N} \sum_{i=1}^N \|x_i - x'_i\|^2 + \lambda(\|W_1\|_2 + \|W_2\|_2) + \beta \sum_{j=1}^d KL(\rho \|\hat{\rho}_j) \quad (11)$$

Here $\hat{\rho}_j$ represents the average activation values of each trained instance on the j th hidden nodes and it is limited by KL divergence to be closer to the sparse variable ρ . β control the weights of sparse penalty. Next, an SSAE is attained by presenting sparse limitations on every single AE of the SAE.

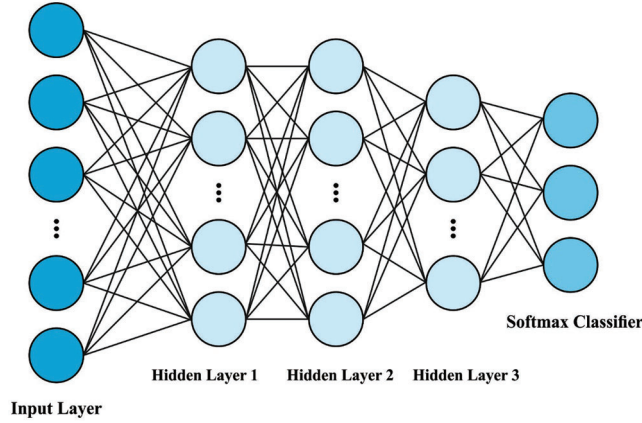


Figure 3: SAE structure

The SFO algorithm is utilized to determine the hyperparameters involved in the SSAE model. The SFO is a new, nature inspired meta heuristic approach, i.e., modelled after a group of hunting sailfish. It displays more competitive performances than widespread meta-heuristic models. The summary of SFO is demonstrated in the following. During the SFO method, the sailfish are considered as candidate solutions and the position of the sailfish in the searching space represents the variable of the problems. The location of i th sailfishes in k th searching iteration is represented as $SF_{i,k}$ and its equivalent fitness can be evaluated using $f(SF_{i,k})$. Sardine is the other important participant in the SFO method. Also, it is considered that a school of sardine is shifting in the searching space. The location of i th sardines is represented as S_i and its equivalent fitness can be evaluated using by $f(S_i)$. During SFO model, the sailfish occupying the optimal location is chosen as an elite sailfish that affects acceleration and maneuverability of the sardine at the time of attack. In addition, the location of injured sardines in all the iterations is chosen as an optimal location for collective hunting by the sailfish. The presented method's aim is to avoid formerly discarded solutions from being elected again. Injured sardines and Elite sailfish are upgraded according to the Eq. (12).

$$Y_{newSF}^i = Y_{eliteSF}^i - \lambda_i \times \left(random(0, 1) \times \left(\frac{Y_{eliteSF}^i - Y_{injuredS}^i}{2} \right) - Y_{currentSF}^i \right), \quad (12)$$

In which $Y_{currentSF}^i$ represents the present location of sailfish and arbitrary value in the range of [0,1].

The λ_i variable represents the coefficients in the i th iteration and the values are acquired by (13):

$$\lambda_i = 2 \times rand(0, 1) \times SD - SD, \quad (13)$$

Let SD be the sardine density that represents the number of sardines in all the iterations. The SD variable can be acquired by Eq. (14):

$$SD = 1 - \left(\frac{N_{SF}}{N_{SF} + N_S} \right), \quad (14)$$

Whereas N_S & N_{SF} represents the number of sardines and sailfish, respectively. During the hunting process, sardines is injured or not tired and sailfish are energetic. Sardines could rapidly escape. But, with continuous hunting, the strength of sailfish attacks would progressively decrease. In the meantime, sardines would become tired and the alertness of the position of sailfish would also decrease. Consequently, the sardines are hunted. According to the algorithmic procedure, the novel location of sardines Y_{newS}^i is upgraded according to Eq. (15):

$$Y_{newS}^i = random(0, 1) \times (Y_{eliteSF}^i - Y_{oldS}^i + ATP), \quad (15)$$

Now, Y_{oldS}^i represents the older location of the sardine and arbitrarily value in the range of [0,1]. ATP signifies the sailfish attack power. The ATP variable is expressed by Eq. (16):

$$ATP = B \times (1 - (2 \times ltr \times \varepsilon)) \quad (16)$$

Here, B & ε represents coefficient that is utilized for reducing the attack power linearly from B to 0 as well as ltr indicates the iteration count. Since the attack power of sailfish reduces over the hunting time [24], this reduction promotes the convergence of the search. Once ATP is greater, e.g., larger than 0.5, the location of each sardine is upgraded. On the other hand, α sardines with variables β upgraders their locations. The number of sardines upgrades their location is defined by Eq. (17):

$$\alpha = N_S \times ATP, \quad (17)$$

In the equation, N_S represents the number of sardines in all the iterations. The number of parameters of the sardine which upgrader their locations is attained by Eq. (18)

$$\beta = d_i \times ATP, \quad (18)$$

While d_i represents the number of parameters in the i th iteration. Once sardines are hunted, its fitness should be greater than the sailfish. In this condition, the location of sailfish Y_{SF}^i is upgraded by the newest location of the hunted sardine Y_S^i for promoting the hunting of novel sardines:

$$Y_{SF}^i = Y_S^i \text{ if } f(S_i) < f(SF_i). \quad (19)$$

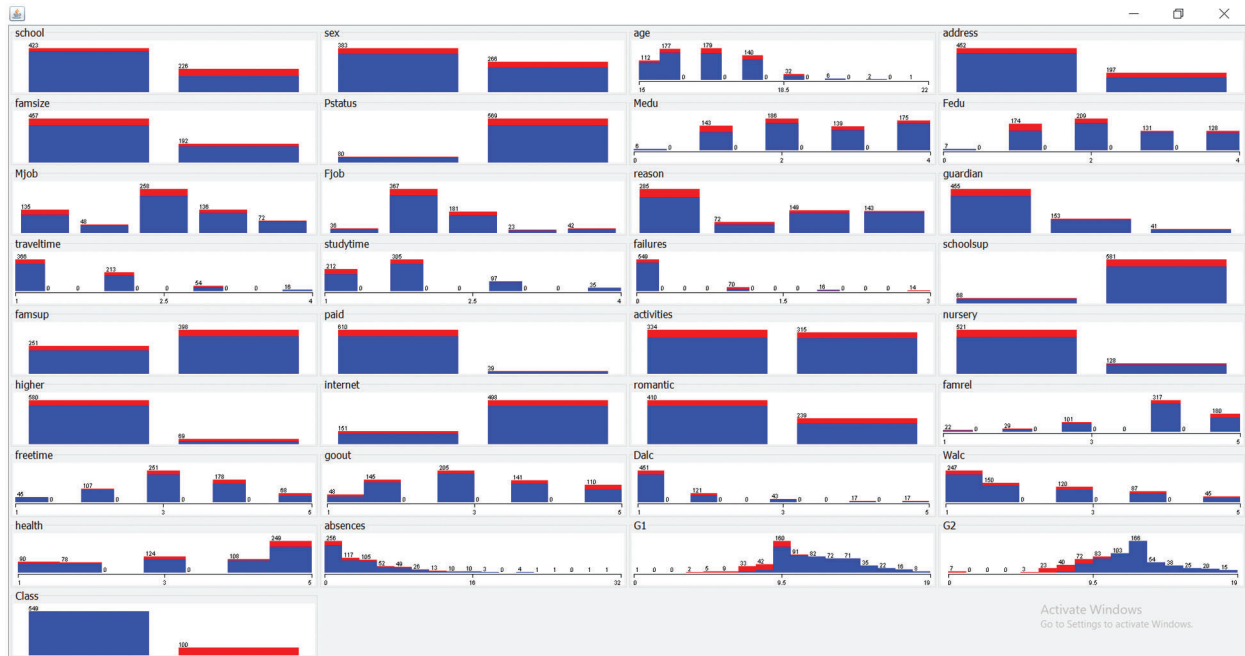
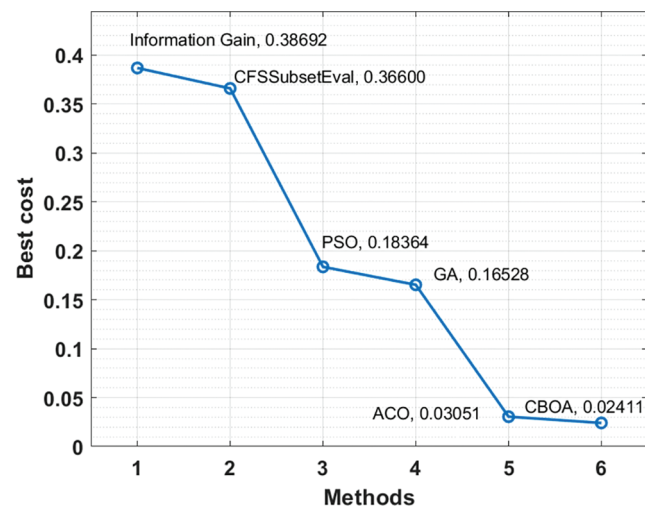
4 Experimental Validation

The benchmark dataset from the UCI repository is used to test the MOFSS-ODL model's performance. The dataset comprises 649 instances with 33 features and two classes. Table 1 demonstrates the details of dataset decryption. Fig. 4 shows the frequency distribution of the attributes involved in the dataset.

Fig. 5 Investigate the best cost analysis of the CBOA with other FS models. The results showed that the information gain and CFS techniques have obtained poor performance, with the best costs of 0.38692 and 0.36600. At the same time, the PSO and GA techniques have attained moderate best costs of 0.18364 and 0.16528, respectively. The CBOA method, on the other hand, has led to better performance at the minimum best cost of 0.02411.

Table 1: Dataset description

Description	Values
Number of instances	649
Number of features	33
Number of class	21
Data sources	[25]

**Figure 4:** Frequency distribution of attributes in dataset**Figure 5:** FS analysis of CBOA technique

The confusion matrices generated by the MOFSS-ODL model on the applied dataset under five distinct runs are in Fig. 6. The figures show that the MOFSS-ODL model has classified the instances into two classes effectively. For instance, with run-1, the MOFSS-ODL model has classified 538 instances into class 0 and 87 instances into class 1. At the same time, with run-2, the MOFSS-ODL method has classified 538 instances into class 0 and 86 instances into class 1. Also, with run-3, the MOFSS-ODL approach has classified 540 instances into class 0 and 86 instances into class 1. Concurrently, with run-4, the MOFSS-ODL technique has classified 538 instances into class 0 and 88 instances into class 1. Simultaneously, with run-5, the MOFSS-ODL system has classified 542 instances into class 0 and 88 instances into class 1.

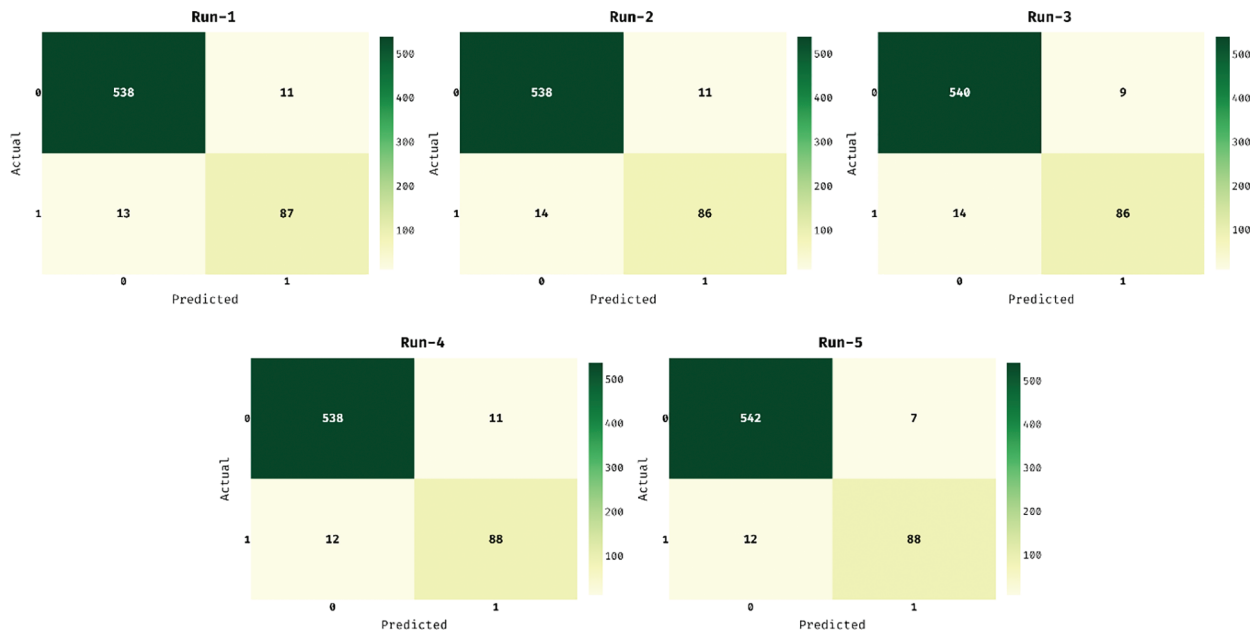


Figure 6: Confusion matrix of MOFSS-ODL model with distinct runs

The values in the confusion matrices are transformed in the form of TP, TN, FP and FN in Table 2.

Table 2: Confusion matrix of MOFSS-ODL model

No. of runs	TP	TN	FP	FN
Run-1	538	87	13	11
Run-2	538	86	14	11
Run-3	540	86	14	9
Run-4	538	88	12	11
Run-5	542	88	12	7

Table 3 offers a detailed classification result analysis of the MOFSS-ODL model under five distinct runs [26–29]. The experimental results reported that the MOFSS-ODL model has accomplished effective classification performance. For instance, with run-1, the MOFSS-ODL model has classified the instances with the $prec_n$, $reca_l$, $F_{measure}$, $accu_y$ and kappa of 0.9764, 0.9800, 0.9782, 0.9630 and

0.8231 respectively. In line with, with run-2, the MOFSS-ODL manner has classified the instances with the $prec_n$, $reca_l$, $F_{measure}$, $accu_y$ and kappa of 0.9746, 0.9800, 0.9773, 0.9615 and 0.8203 respectively. Moreover, with run-3, the MOFSS-ODL technique has classified the instances with the $prec_n$, $reca_l$, $F_{measure}$, $accu_y$ and kappa of 0.9747, 0.9836, 0.9791, 0.9646 and 0.8257 respectively. Furthermore, with run-4, the MOFSS-ODL approach has classified the instances with the $prec_n$, $reca_l$, $F_{measure}$, $accu_y$ and kappa of 0.9782, 0.9800, 0.9791, 0.9646 and 0.8259 respectively. Finally, with run-5, the MOFSS-ODL algorithm has classified the instances with the $prec_n$, $reca_l$, $F_{measure}$, $accu_y$ and kappa of 0.9783, 0.9872, 0.9828, 0.9707 and 0.8367 respectively.

Table 3: Result analysis of MOFSS-ODL model with different runs

No. of runs	Precision	Recall	F-measure	Accuracy	Kappa
Run-1	0.9764	0.9800	0.9782	0.9630	0.8231
Run-2	0.9746	0.9800	0.9773	0.9615	0.8203
Run-3	0.9747	0.9836	0.9791	0.9646	0.8257
Run-4	0.9782	0.9800	0.9791	0.9646	0.8259
Run-5	0.9783	0.9872	0.9828	0.9707	0.8367
Average	0.9764	0.9822	0.9793	0.9649	0.8263

Fig. 7 investigates the average classification outcomes analysis of the MOFSS-ODL model on the test dataset [30–35]. The figure depicted that the MOFSS-ODL methodology has resulted in maximal average $prec_n$, $reca_l$, $F_{measure}$, $accu_y$ and kappa of 0.9764, 0.9822, 0.9793, 0.96499 and 0.8263.

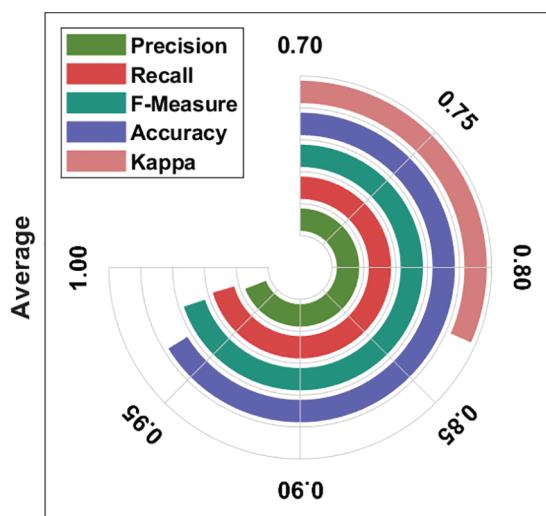


Figure 7: Average analysis of MOFSS-ODL model with different measures

Fig. 8 provides a comparative $prec_n$ and $reca_l$ analysis of the MOFSS-ODL model with recent methods. The figure portrayed that the RT and RRBFN models have obtained lower $prec_n$ and $reca_l$ values. In line with, the MLP and DT manners have reached to somewhat superior $prec_n$ and $reca_l$ values. Along with that, the LR, RF and ACO-LR models have resulted in considerable $prec_n$ and $reca_l$ values. However, the

MOFSS-ODL model has gained improved outcome with the maximum $prec_n$ and $reca_l$ of 97.83% and 98.72% respectively.

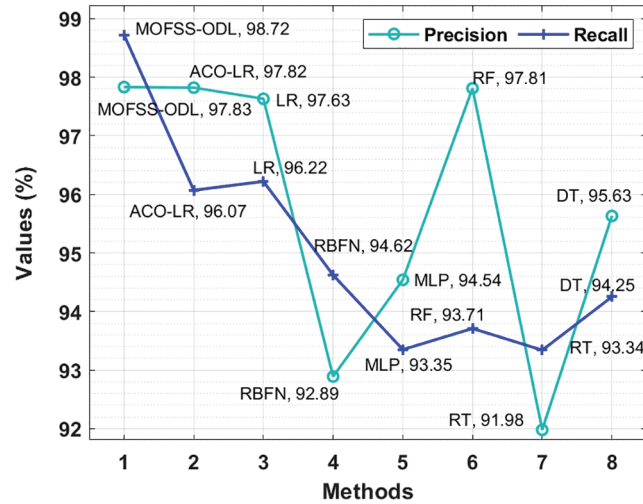


Figure 8: Precision and Recall analysis of MOFSS-ODL model

Fig. 9 offers a comparative $F_{measure}$ and Kap_p analysis of the MOFSS-ODL manner with recent techniques. The figure outperformed that the RT and RBFN manners have reached lesser $F_{measure}$ and Kap_p values. Besides, the MLP and DT models have reached slightly improved $F_{measure}$ and Kap_p values. At the same time, the LR, RF and ACO-LR models have resulted in considerable $F_{measure}$ and Kap_p values. However, the MOFSS-ODL model has reached higher outcome with the maximal $F_{measure}$ and Kap_p of 98.28% and 82.63% respectively.

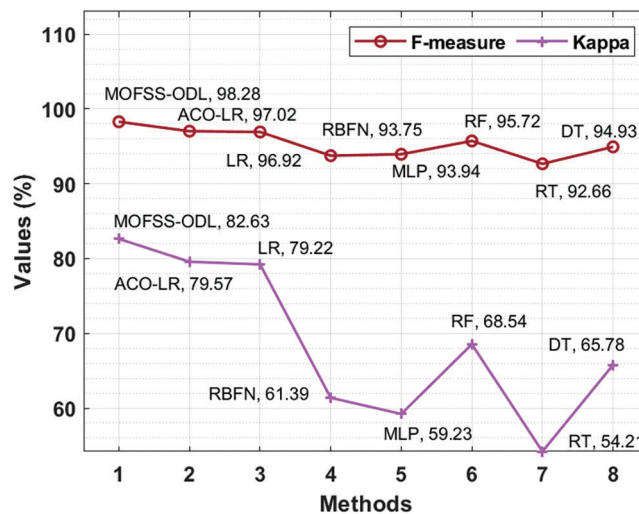


Figure 9: F-measure and Kappa analysis of MOFSS-ODL model

Accuracy analysis of the MOFSS-ODL technique with recent manners takes place in Fig. 10. The figure shows that the RBFN, MLP and RT techniques have obtained lower $accu_y$ of 89.52%, 89.67% and 87.67% respectively. Followed by the RF and DT models have attained slightly enhanced $accu_y$ of 92.60% and

91.37% respectively. Moreover, the ACO-LR and LR models have achieved moderate $accu_y$ of 94.91% and 94.76% respectively. However, the MOFSS-ODL model has resulted in a maximum $accu_y$ of 97.07%.

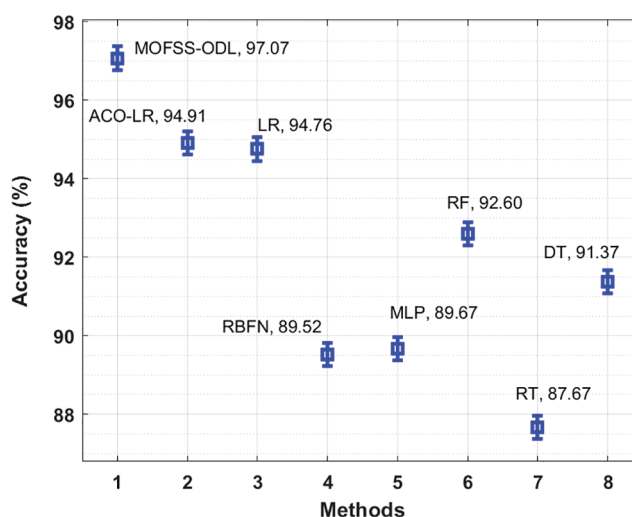


Figure 10: Accuracy analysis of MOFSS-ODL technique with existing approaches

After examining the tables and figures, it can be obvious that the MOFSS-ODL approach has accomplished effective outcomes on students' performance analysis.

5 Conclusion

In this study, an effective MOFSS-ODL technique was designed to predict students' performance. The proposed MOFSS-ODL technique encompasses IF-based outlier detection, CBOA-based feature selection, SSAE-based classification, and SFO-based parameter optimization. Besides, the utilization of CBOA-based feature selection and SFO-based parameter optimization help to accomplish improved students' performance prediction outcomes. To validate the enhanced predictive outcome of the MOFSS-ODL technique, a series of simulations were implemented, and the outcomes are inspected in several dimensions. The experimental results pointed out the improved performance of the MOFSS-ODL technique over recent approaches in terms of several evaluation measures. In future, the predictive performance of the MOFSS-ODL technique will be enhanced by using the clustering approaches and hybrid algorithms for feature selection on educational datasets to predict students' achievement.

Funding Statement: The authors received no specific funding for this study.

Conflicts of Interest: The authors declare that they have no conflicts of interest to report regarding the present study.

References

- [1] R. Asif, A. Merceron, S. A. Ali and N. G. Haider, "Analyzing undergraduate students' performance using educational data mining," *Computers & Education*, vol. 113, no. 1, pp. 177–194, 2018.
- [2] A. Bogarín, R. Cerezo and C. Romero, "Discovering learning processes using inductive miner: A case study with learning management systems (LMSs)," *Psicothema*, vol. 3, no. 2, pp. 322–329, 2018.

- [3] T. Kavitha, P. P. Mathai and C. Karthikeyan, "Deep learning-based capsule neural network model for breast cancer diagnosis using mammogram images," *Interdisciplinary Sciences: Computational Life Sciences*, vol. 14, no. 3, pp. 113–129, 2021.
- [4] C. Romero and S. Ventura, "Educational data mining and learning analytics: An updated survey," *Wiley Interdisciplinary Reviews: Data Mining and Knowledge Discovery*, vol. 10, no. 3, pp. 1–10, 2020.
- [5] B. T. Geetha, A. V. R. Mayuri, T. Jackulin, J. L. Aldo Stalin and V. Anitha, "Pigeon inspired optimization with encryption based secure medical image management system," *Computational Intelligence and Neuroscience*, vol. 2022, no. 2, pp. 1–13, 2022.
- [6] B. Jaishankar, S. Vishwakarma, A. Pundir, I. Patel and N. Arulkumar, "Blockchain for securing healthcare data using squirrel search optimization algorithm," *Intelligent Automation & Soft Computing*, vol. 32, no. 3, pp. 1815–1829, 2022.
- [7] S. Neelakandan, "Large scale optimization to minimize network traffic using MapReduce in big data applications," in *Int. Conf. on Computation of Power, Energy Information and Communication (ICCPEIC)*, India, pp. 193–199, 2016.
- [8] M. Injadat, A. Moubayed, A. B. Nassif and A. Shami, "Systematic ensemble model selection approach for educational data mining," *Knowledge-Based Systems*, vol. 200, no. 1, pp. 1–18, 2020.
- [9] M. Hardas, "Optimization of peak to average power reduction in OFDM," *Journal of Communication Technology and Electronics*, vol. 62, no. 2, pp. 1388–1395, 2017.
- [10] R. Farah Sayeed, S. Princey and S. Priyanka, "Deployment of multicloud environment with avoidance of ddos attack and secured data privacy," *International Journal of Applied Engineering Research*, vol. 10, no. 9, pp. 8121–8124, 2015.
- [11] M. Akour, H. Alsghaier and O. Al Qasem, "The effectiveness of using deep learning algorithms in predicting students' achievements," *Indonesian Journal of Electrical Engineering and Computer Science*, vol. 19, no. 1, pp. 387–393, 2020.
- [12] J. L. Harvey and S. A. Kumar, "A practical model for educators to predict students' performance in K-12 education using machine learning," in *2019 IEEE Symp. Series on Computational Intelligence (SSCI)*, India, pp. 3004–3011, 2019.
- [13] F. Orji and J. Vassileva, "Using machine learning to explore the relation between student engagement and students' performance," in *IEEE 2020 24th Int. Conf. Information Visualisation (IV)*, India, pp. 480–485, 2020.
- [14] J. Xu, K. H. Moon and M. Van Der Schaar, "A machine learning approach for tracking and predicting students' performance in degree programs," *IEEE Journal of Selected Topics in Signal Processing*, vol. 11, no. 5, pp. 742–753, 2017.
- [15] A. Hamoud, A. S. Hashim and W. A. Awadh, "Predicting students' performance in higher education institutions using decision tree analysis," *International Journal of Interactive Multimedia and Artificial Intelligence*, vol. 5, no. 1, pp. 26–31, 2018.
- [16] M. Hussain, W. Zhu, W. Zhang, S. M. R. Abidi and S. Ali, "Using machine learning to predict student difficulties from learning session data," *Artificial Intelligence Review*, vol. 52, no. 1, pp. 381–407, 2019.
- [17] G. Reshma, C. Al-Atroshi, V. K. Nassa, B. Geetha and S. Neelakandan, "Deep learning-based skin lesion diagnosis model using dermoscopic images," *Intelligent Automation & Soft Computing*, vol. 31, no. 1, pp. 621–634, 2022.
- [18] H. Waheed, S. U. Hassan, N. R. Aljohani, J. Hardman, S. Alelyani *et al.*, "Predicting academic performance of students from VLE big data using deep learning models," *Computers in Human Behavior*, vol. 104, no. 2, pp. 1–10, 2022.
- [19] C. P. D. Cyril, J. Rene Beulah, N. Subramani and A. Harshavardhan, "An automated learning model for sentiment analysis and data classification of twitter data using balanced CA-SVM," *Concurrent Engineering*, vol. 29, no. 4, pp. 386–395, 2021.
- [20] S. Neelakandan, A. K. Nanda, A. M. Metwally, M. Santhamoorthy and M. S. Gupta, "Metaheuristics with deep transfer learning enabled detection and classification model for industrial waste management," *Chemosphere*, vol. 308, no. 20, pp. 1–15, 2022.

- [21] M. Sundaram, S. Satpathy and S. Das, "An efficient technique for cloud storage using secured de-duplication algorithm," *Journal of Intelligent & Fuzzy Systems*, vol. 42, no. 2, pp. 2969–2980, 2021.
- [22] P. Ezhumalai and D. Paul Raj, "A deep learning modified neural network (dlmnn) based proficient sentiment analysis technique on twitter data," *Journal of Experimental & Theoretical Artificial Intelligence*, vol. 18, no. 2, pp. 1–15, 2022.
- [23] P. V. Rajaram, "Intelligent deep learning based bidirectional long short term memory model for automated reply of e-mail client prototype," *Pattern Recognition Letters*, vol. 152, pp. 340–347, 2021.
- [24] S. B. Pokle, "Analysis of ofdm system using dct-pts-slm based approach for multimedia applications," *Cluster Computing*, vol. 22, no. 2, pp. 4561–4569, 2019.
- [25] C. Saravanakumar, R. Priscilla, B. Prabha, A. Kavitha and C. Arun, "An efficient on-demand virtual machine migration in cloud using common deployment model," *Computer Systems Science and Engineering*, vol. 42, no. 1, pp. 245–256, 2022.
- [26] S. Mishra, P. Mohan, "Digital mammogram inferencing system using intuitionistic fuzzy theory," *Computer Systems Science and Engineering*, vol. 41, no. 3, pp. 1099–1115, 2022.
- [27] G. Liu, H. Bao and B. Han, "A stacked autoencoder-based deep neural network for achieving gearbox fault diagnosis," *Mathematical Problems in Engineering*, vol. 2018, no. 12, pp. 1–15, 2018.
- [28] P. Santhosh Kumar, B. Sathya Bama, S. Neelakandan, C. Dutta and D. Vijendra Babu, "Green energy aware and cluster-based communication for future load prediction in IoT," *Sustainable Energy Technologies and Assessments*, vol. 52, no. 12, pp. 1–12, 2022.
- [29] S. Neelakandan, M. A. Berlin and S. Tripathi, "IoT-based traffic prediction and traffic signal control system for smart city," *Soft Computing*, vol. 25, no. 8, pp. 12241–12248, 2021.
- [30] S. Thangakumar and K. Bhagavan, "Ant colony optimization-based feature subset selection with logistic regression classification model for education data mining," *International Journal of Advanced Science and Technology*, vol. 29, no. 3, pp. 1–14, 2020.
- [31] V. Ramalakshmi, "Honest auction-based spectrum assignment and exploiting spectrum sensing data falsification attack using stochastic game theory in wireless cognitive radio network," *Wireless Personal Communications-an International Journal*, vol. 102, no. 4, pp. 799–816, 2018.
- [32] M. Prakash and C. Saravana Kumar, "An authentication technique for accessing de-duplicated data from private cloud using one time password," *International Journal of Information Security and Privacy*, vol. 11, no. 2, pp. 1–10, 2017.
- [33] V. D. Ambeth Kumar, S. Malathi, A. Kumar and K. C. Veluvolu, "Active volume control in smart phones based on user activity and ambient noise," *Sensors*, vol. 20, no. 15, pp. 1–13, 2020.
- [34] I. Kaur, V. K. Nassa, T. Kavitha, P. Mohan and S. Velmurugan, "Maximum likelihood-based estimation with quasi oppositional chemical reaction optimization algorithm for speech signal enhancement," *International Journal of Information Technology*, vol. 14, no. 6, pp. 3265–3275, 2022.
- [35] S. Satpathy, A. Padthe, V. Goyal and B. K. Bhattacharyya, "Method for measuring supercapacitor's fundamental inherent parameters using its own self-discharge behavior: A new steps towards sustainable energy," *Sustainable Energy Technologies and Assessments*, vol. 53, no. 10, pp. 1–15, 2022.

SURVEY ON COMPARISON OF CNN WITH RNN

¹Anju Markose, ²Dr. P Rama, ³Dr. S. Chakravarthi

¹Research Scholar, ²Assistant Professor, ^{1,2}Computer Science and Engineering, Bharath Institution of Higher Education and Research, Chennai, India. ¹anjumarkose@gmail.com, ²ramaponnuvarman@gmail.com

³Associate Professor, Computer Science and Engineering, Panimalar Engineering College, Chennai, India. chakra2603@gmail.com

ABSTRACT

In this paper, a survey on the recurrent and its powerful behaviour. There are mainly two important types of deep neural networks Convolutional Neural Networks and Recurrent Neural Networks. This paper try to compare the impact of both CNN and RNN. Although it has been shown that CNN and RNN models obtain good performance, often superior to other state-of-the-art techniques, they suffer from some important drawbacks, including a very long training time and limitations on the number of context words that can be taken into account in practice. Recent extensions to recurrent neural network models have been developed in an attempt to address these drawbacks. This paper gives an overview of the most important things regarding RNN and CNN.

Keywords—CNN, RNN, ConvNet, LSTM, ReLU.

I. INTRODUCTION

Convolutional Neural networks are designed to process data through multiple layers of arrays. This type of neural networks is used in applications like image recognition or face recognition. The primary difference between CNN and any other ordinary neural network is that CNN takes input as a two-dimensional array and operates directly on the images rather than focusing on feature extraction which other neural networks focus on. The dominant approach of CNN includes solutions for problems of recognition. Top companies like Google and Facebook have invested in research and development towards recognition projects to get activities done with greater speed. Recurrent neural networks is a type of deep learning-oriented algorithm, which follows a sequential approach. In neural networks, we always assume that each input and output is independent of all other layers. These type of neural networks are called recurrent because they perform mathematical computations in sequential manner.

II. CONVOLUTIONAL NEURAL NETWORKS

A **Convolutional Neural Network (ConvNet/CNN)** is a Deep Learning algorithm which can take in an input image, assign importance (learnable weights and biases) to various aspects/objects in the image and be able to differentiate one from the other. The pre-processing required in a ConvNet is much lower as compared to other classification algorithms. While in primitive methods filters are hand-engineered, with enough training, ConvNets have the ability to learn these filters/characteristics.

ConvNet is able to successfully capture the Spatial and Temporal dependencies in an image through the application of relevant filters. The architecture performs a better fitting to the image dataset due to the reduction in the number of parameters involved and reusability of weights. In other words, the network can be trained to understand the sophistication of the image better.

There are various architectures of CNNs available which have been key in building algorithms which power and shall power AI as a whole in the foreseeable future. Some of them have been listed below:

1. LeNet

2. AlexNet
3. VGGNet
4. GoogLeNet
5. ResNet
6. ZFNet

III. RECURRENT NEURAL NETWORKS

RNN works on the principle of saving the output of a particular layer and feeding this back to the input in order to predict the output of the layer. Below is how you can convert a Feed-Forward Neural Network into a Recurrent Neural Network. In a feed-forward neural network, the decisions are based on the current input. It doesn't memorize the past data, and there's no future scope. Feed-forward neural networks are used in general regression and classification problems.

IV. WORKING OF RNN

RNNs are a powerful and robust type of neural network, and belong to the most promising algorithms in use because it is the only one with an internal memory.

A recurrent neural network (RNN) is a special type of an artificial neural network adapted to work for time series data or data that involves sequences. Ordinary feed forward neural networks are only meant for data points, which are independent of each other. However, if we have data in a sequence such that one data point depends upon the previous data point, we need to modify the neural network to incorporate the dependencies between these data points. RNNs have the concept of 'memory' that helps them store the states or information of previous inputs to generate the next output of the sequence.

The logic behind an RNN is to save the output of the particular layer and feed it back to the input in order to predict the output of the layer.

Below is a simple example of how you can convert a Feed-Forward Neural Network into a Recurrent Neural Network (RNN).

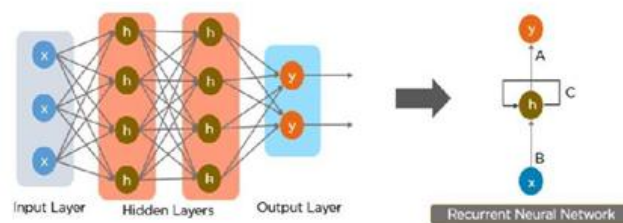


Fig 4.1. RNN

On the left side of the image, represent the following:

- X - is the input layer.
- h - is the hidden layer and it holds the information for the previous output and feeds it back to itself. y - is the output layer
- A, B, C are the parameters to improve the output of the model.

The Activation Function

We can use any activation function we like in the recurrent neural network. Common choices are:

- ☐ Sigmoid function
- ☐ Tanh function
- ☐ Relu function

Types of RNNs

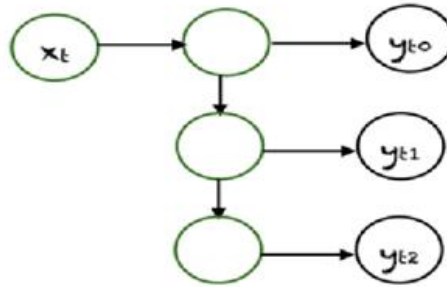
There are different types of recurrent neural networks with varying architectures. Some examples are:

1) One To One



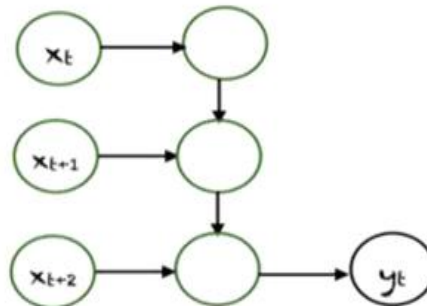
Here there is a single pair. Traditional neural networks employ a one to one architecture.

2) One To Many



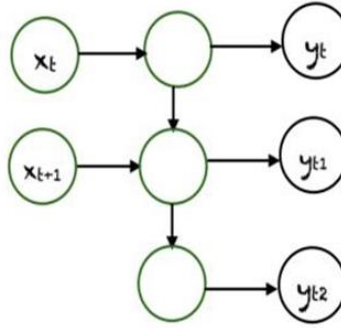
In one to many networks, a single input can produce multiple outputs. Music generation is an example area, where one to many networks are employed.

3) Many To One



In this case many inputs from different time steps produce a single output.

4) Many To Many



There are many possibilities for many to many.

B. Different RNN Architectures

There are different variations of RNNs that are being applied practically in machine learning problems:

Bidirectional recurrent neural networks (BRNN)

In BRNN, inputs from future time steps are used to improve the accuracy of the network. It is like having knowledge of the first and last words of a sentence to predict the middle words.

1) Gated Recurrent Units (GRU)

These networks are designed to handle the vanishing gradient problem. They have a reset and update gate. These gates determine which information is to be retained for future predictions.

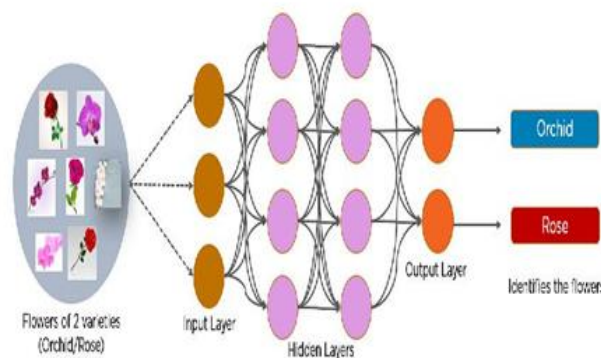
2) Long Short Term Memory (LSTM)

LSTMs were also designed to address the vanishing gradient problem in RNNs. LSTM use three gates called input, output and forget gate. Similar to GRU, these gates determine which information to retain.

V. WORKING OF CNN.

A convolutional neural network is a feed-forward neural network that is generally used to analyze visual images by processing data with grid-like topology. It's also known as a ConvNet. A convolutional neural network is used to detect and classify objects in an image.

Fig 5.1. CNN



Layers in a Convolutional Neural Network

A convolution neural network has multiple hidden layers that help in extracting information from an image. The four important layers in CNN are:

1. Convolution layer
2. ReLU layer
3. Pooling layer

4. Fully connected layer

Convolutional Neural Network Design :

The construction of a convolutional neural network is a multi-layered feed-forward neural network, made by assembling many unseen layers on top of each other in a particular order.

It is the sequential design that give permission to CNN to learn hierarchical attributes.

In CNN, some of them followed by grouping layers and hidden layers are typically convolutional layers followed by activation layers.

The pre-processing needed in a ConvNet is kindred to that of the related pattern of neurons in the human brain and was motivated by the organization of the Visual Cortex.

Difference between CNN and RNN

CNN	RNN
It is suitable for spatial data such as images.	RNN is suitable for temporal data, also called sequential data.
CNN is considered to be more powerful than RNN.	RNNs include less feature compatibility when compared to CNN.
This network takes fixed size inputs and generates fixed size outputs.	RNN can handle arbitrary input/output lengths.
CNN is a type of feed-forward artificial neural network with variations of multilayer perceptrons designed to use minimal amounts of preprocessing.	RNN unlike feed forward neural networks - can use their internal memory to process arbitrary sequence of inputs.

Table 5.1. Comparison of CNN and RNN

RNN or CNN: Which one is Better?**Type of input data**

While RNNs are suitable for handling temporal or sequential data, CNNs are suitable for handling spatial data (images). Though both models work a bit similarly by introducing sparsity and reusing the same neurons and weights over time (in case of RNN) or over different parts of the image (in case of CNN).

Computing power

Since both RNN and CNN are used for different purposes by the data scientists and deep learning researchers, it might not be appropriate to compare their computational ability. Though if we had to, CNN would be more powerful than RNN. That's mainly because RNN has less feature compatibility and it has the ability to take arbitrary output/input lengths which can affect the total computational time and efficiency. On the other hand, CNN takes fixed input and gives a fixed output which allows it to compute the results at a faster pace.

Architecture

Convolutional neural networks use the connectivity patterns available in neurons. Inspired by the visual cortex of the brain, CNNs have numerous layers and each one is responsible for detecting a specific set of features in the image. The combined output of all the layers helps CNNs identify and classify images.

Recurrent neural networks use time-series information to identify patterns between the input and output. The memory of RNN algorithms allows them to learn more about long-term dependencies in data and understand the whole context of the sequence while making the next prediction.

CONCLUSION

We found that RNNs perform well and robust in a broad range of tasks except when the task is essentially a keyphrase recognition task as in some sentiment detection and question-answer matching settings. In addition, hidden size and batch size can make DNN performance vary dramatically. This suggests that optimization of these two parameters is crucial to good performance of both CNNs and RNNs

They apply to different data and different purposes, so there's no exact comparison on powerfulness. The RNN is used to predict continuous or time step data, including natural language. The CNN is used for multidimensional data, like image or video.

REFERENCES

- [1] Sai Yeshwanth Chaganti, Ipseeta Nanda, Koteswara Rao Pandi, Niraj Kumar, "Image Classification using SVM and CNN," in 2020 IEEE Xplore.
- [2] Turan Goktug Altundogan, Mehmet Karakose, "Image Processing and Deep Neural Image Classification Based Physical Feature Determiner for Traffic Stakeholders," in 2019 IEEE.
- [3] Zhiyong Dong, Sheng Lin, "Research on image classification based on Capsnet," 2019 IEEE 4th Advanced Information Technology, Electronic and Automation Control Conference, IEEE, 2019.
- [4] Mrs. Arpana Mahajan, Dr. Sanjay Chaudhary, "Categorical Image Classification Based On Representational Deep Network (RESNET)," in 2019 IEEE Third International Conference on Electronics Communication and Aerospace Technology, IEEE, 2019.
- [5] Shyava Tripathi, Rishi Kumar, "Image Classification using small Convolutional Neural Network" in 2019, IEEE.
- [6] Yunyan Wang, Chongyang Wang, Lengkun Luo, Zhigang Zhou, "Image Classification Based on transfer Learning of Convolutional neural network" in 2019 38th Chinese Control Conference, IEEE, 2019.
- [7] Santisudha Panigrahi, Anuja Nanda, Tripti Swarnkar, "Deep Learning approach for Image Classification," in 2018 2nd International Conference on Data Science and Business Analytics, IEEE, 2018.
- [8] Md Tohidul Islam, B.M. Nafiz Karim Siddique, Sagidur Rahman, Taskeed Jabid, "Image Recognition with Deep Learning," in 2018 ICIIBMS, IEEE, 2018.

- [9] Aditya Vailaya, Mário A. T. Figueiredo, Anil K. Jain, Hong-Jiang Zhang, “Image Classification for Content-Based Indexing,” in 2001 IEEE TRANSACTIONS ON IMAGE PROCESSING, IEEE, 2001
- [10] Ardhendu Bandhu, Sanjiban Sekhar Roy, “Classifying multi-category images using Deep Learning : A Convolutional Neural Network Model,” in 2017 2nd IEEE International Conference On Recent Trends in Electronics Information & Communication Technology, IEEE, 2017.
- [11] Deepika Jaswal, Sowmya.V, K.P.Soman, “Image Classification Using Convolutional Neural Networks,” in 2014, IJSER.
- [12] S. Regina Lourdhugugan, Dr. Hanumanthappa, Dr. S. Kavitha, “Event Image Classification using Deep Learning,” in 2018 International Conference on Soft-computing and Network Security, IEEE, 2018.
- [13]. Rozenwald MB, Galitsyna AA, Sapunov GV, Khrameeva EE, Gelfand MS. A machine learning framework for the prediction of chromatin folding in Drosophila using epigenetic features. PeerJ Comput Sci. 2020;6:307.
- [14]. Amrit C, Paaup T, Aly R, Lavric M. Identifying child abuse through text mining and machine learning. Expert Syst Appl. 2017;88:402–18.
- [15]. Hossain E, Khan I, Un-Noor F, Sikander SS, Sunny MSH. Application of big data and machine learning in smart grid, and associated security concerns: a review. IEEE Access. 2019;7:13960–88.
- [16]. Crawford M, Khoshgoftaar TM, Prusa JD, Richter AN, Al Najada H. Survey of review spam detection using machine learning techniques. J Big Data. 2015;2(1):23.



Efficient Multi-Replica Cloud Data Integrity Checking Method Based on Enhanced PRF

Anju Susan George & A. Shajin Nargunam

To cite this article: Anju Susan George & A. Shajin Nargunam (2022): Efficient Multi-Replica Cloud Data Integrity Checking Method Based on Enhanced PRF, IETE Journal of Research, DOI: [10.1080/03772063.2022.2122608](https://doi.org/10.1080/03772063.2022.2122608)

To link to this article: <https://doi.org/10.1080/03772063.2022.2122608>



Published online: 25 Sep 2022.



Submit your article to this journal [↗](#)



View related articles [↗](#)



View Crossmark data [↗](#)

RESEARCH ARTICLE



Efficient Multi-Replica Cloud Data Integrity Checking Method Based on Enhanced PRF

Anju Susan George  and A. Shajin Nargunam

Department of Computer Science and Engineering, Noorul Islam Centre for Higher Education, Thuckalay, Kanyakumari, 629180 Tamil Nadu, India

ABSTRACT

Cloud storage is vital nowadays due to its scalability and availability. Clients can save their information on cloud without sustaining a local replica. To maintain privacy, the owners can confirm the integrity of the outsourced information. Users allow third-party auditors to prove the honesty of the data saved on the cloud server. Data integrity checking, plays a crucial role in safeguarding the user's data, particularly when kept in public clouds such as Microsoft Azure. To ensure the availability of stored data, users prefer multiple copies of data at multiple locations. Honesty checking of multiple copies can also be guaranteed with integrity checking techniques. Even though various scholars have proposed several multi-replica truthfulness checking schemes, many possess computational overhead during honesty verification. In this paper, an enhanced puncturable pseudorandom function is proposed to bring down the third-party auditor's processing overhead, as well as the cloud server during proof verification and proof generation of replica data blocks. The scheme supports dynamic updating of stored data in the cloud server with less communication overhead for insertion/modification and deletion. An indistinguishability obfuscation-based program is also used to preserve the confidentiality of the data stored.

KEYWORDS

Cloud computing; Cloud security; Data integrity; Dynamic updating; Multi-replica verification; Puncturable pseudorandom function

1. INTRODUCTION

With the emergence of big data and its applications, cloud storage and services are regularly used by an increasing number of users. Cloud computing is a distributed computing system with a virtual platform that is widely used for big data depository and data handling. The major cloud services include IaaS, PaaS and SaaS, which provide storage and computing services, a platform or environment for developing software and software services, respectively. Private, public, community and hybrid clouds form different deployment models which help individuals to store their data for various purposes. Cloud computing uses a pay-as-you-go model for payment.

The security or privacy of the data kept inside the cloud computing platform is a serious challenge. Because their data has been outsourced to cloud service providers, customers have no direct control over it. Several data integrity checking methods [1] have been developed to guarantee the truthfulness of the information outsourced.

Nowadays, to provide redundancy, multiple clones of outsourced data are being placed with cloud service providers [2, 3]. Here, instead of storing only the original

data on a single server, numerous replicas of information are stored across multiple servers. Multiple copies of cloud information storage are mainly because of catastrophic failures or any other database failures of the primary server, thus providing disaster recovery. Hence multi-replica storage systems provide persistency, availability and expandability of stored data.

Data replication makes it more difficult to confirm the privacy and honesty of the data since we need to authenticate all of the clones kept on separate servers. Various public verification schemes were developed by many scholars to check the multiple copies stored on multiple servers. Third-party auditors are delegated to validate the stored replicas so as to reduce the load of users.

Figure 1 shows a fundamental depiction of a multi-replica cloud system.

Dynamic updating of data in cloud storage is also supported in some schemes with multi-replication. Dynamic updating operations include insertion of data, deletion of data and modification of information in the already stored cloud data. Some schemes support multi-cloud storage, which is more complicated and needs much consideration.

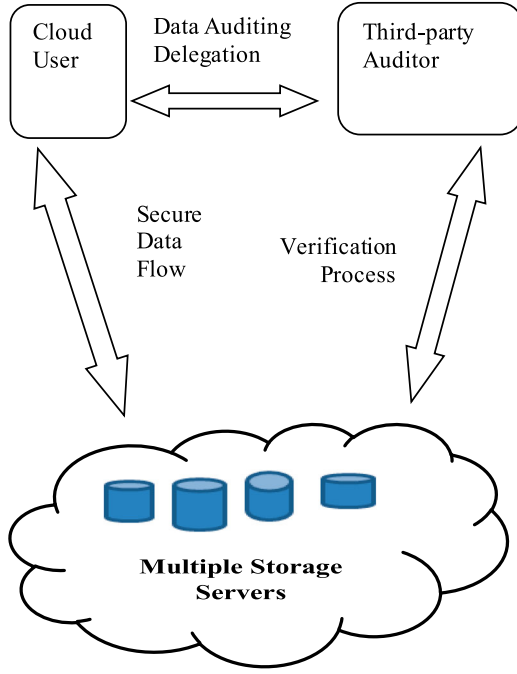


Figure 1: Fundamental representation of multi-replica system

To validate the honesty of the data warehoused on multiple servers, the proposed scheme offers an enhanced puncturable pseudorandom function. The system divides the entire file into several blocks, each of which is divided into sectors. An obfuscation program is generated by the user to offer the security of the information stored. The output of the enhanced pseudorandom function of each block is sent to the third-party auditor, which can be used for verification purposes. The servers can execute the obfuscation program to compute the proof of data saved on many servers. The enhanced pseudorandom function is generated by the file tag, block tag and the corresponding block for verification with the help of a key ε . When the user has to check the originality of the data stored on cloud servers, he can delegate a third-party auditor for the purpose. Then the output for the enhanced pseudorandom function is sent to the third-party auditor along a protected channel by the user. The third-party auditor will generate a pseudorandom permutation key p_1 for each audit and compute the signature of the corresponding blocks for verification. The signature consists of the output of the enhanced pseudorandom function and the pseudorandom permutation key encrypted with the user's public key. At the time of replica generation, a pseudorandom number is generated and concatenated with each block of the file. The pseudorandom number will be different for each replica stored on various servers. The construction of the suggested method is shown in Figure 2.

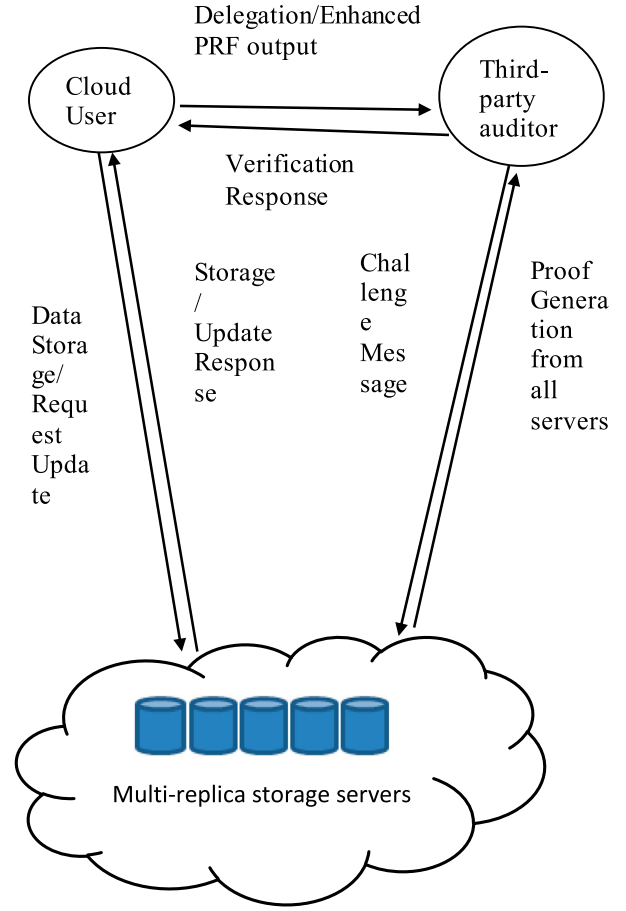


Figure 2: Enhanced PRF multi-replica scheme

Our Contributions: The following are the three phases in which we have contributed to this paper:

- (1) Our scheme implements an enhanced pseudorandom permutation function which reduces the third-party auditor's proof verification time as well as, lessens the cloud server's proof generation time and the tag generation time.
- (2) Our scheme supports dynamic updating, modification and deletion of the stored data in the cloud server with less communication overhead and checks the data integrity on the modifications.
- (3) Our scheme verifies all replica blocks at once, irrespective of the number of replicas. Also, the approach employs the indistinguishability obfuscation principle to protect user's data.

Paper organization: The remaining part of the paper is organized as follows: Section 2 frames the related work. Section 3 offers a comprehensive elucidation of the suggested method. Section 4 gives the execution and results of the suggested method. The advantages of our system are shown in this section, which compares the proposed

scheme to three prevailing schemes. Section 5 is a summary of the entire study.

2. RELATED WORK

Remote information truthfulness checking concepts are suggested by several scholars [4]. The most extensively used integrity verification concepts are the PDP approach suggested by Ateniese *et al.* [5], the POR scheme introduced by Juels and Kaliski [6], and its modifications [7]. The security technique proposed by Zhu *et al.* [7] uses a multiprover zero-knowledge evidence process that satisfies completeness, expertise coherence, and zero-knowledge features. Additionally, the performance optimization mechanisms for the scheme are expressed by presenting an effective way of picking appropriate parameters to reduce users' and storage service beneficiaries' computation costs. ArmKnecht *et al.* [1] introduce the concept of outsourced proofs of retrievability (OPOR), wherein the users have the ability to delegate the performance and verification of POR with the cloud provider to an external auditor. For OPOR, a formal framework and a security model is suggested. Also, the scheme suggests a basic process for converting a public POR to an OPOR. Indistinguishability obfuscation (*iO*) [8] concept maintains the functionality of jumbled software programs. In 2019, Sun *et al.* [9] suggested a puncturable pseudorandom function-based efficient *iO* approach. Many scholars propose dynamic auditing schemes [10] and privacy-preserving verification schemes [11, 12].

Multi-replica schemes are also proposed by various scholars [13, 14] to provide reliability and availability. The multi-replica PDP scheme suggested by Liu *et al.* [15] was based on the Merkle hash tree. Earlier multi-replica schemes did not support dynamic updating, but today many strategies are introduced with dynamic updating [15]. Bian and Chang [2] offer a certificate-less verifiable data possession approach for multiple copies and clouds. The method builds a tangible protocol whose protection can be demonstrated using the classic Computational Diffie-Hellman (CDH) assumption. A novel CAA (Compressed Authentication Array) based data structure for multi-replica verification has been introduced by Peng *et al.* [16]. Guo *et al.* [17] proposed a secure authenticated multi-replica verification tree scheme which brings down the storage cost of the tree. The scheme supports batch verification also.

Some schemes support multi-cloud storage [18, 19]. The first ID-based multi-cloud storage scheme was proposed by Wang [20]. Peng *et al.* [21] fixed the security flaws

in Wang scheme. Li *et al.* [22] suggested a multi-cloud storage that offers a new identity-based PDP system that supports multiple replicas. This method is the first IDPDP scheme that supports multi-replica and multi-cloud servers. In this method, all replicas are distributed to several cloud-based servers. These servers work collectively to keep the users' information. The truthfulness of all replicas can be verified simultaneously with the help of homomorphic verifiable tags. The Computation Diffie-Hellman (CDH) hard problem evidenced the security of the method.

Wang *et al.* [23] suggested a flexible and effective remote information integrity method using an Id-based PDP scheme. Based on the permission of the original user, the suggested technique can perform private remote data honesty verification, deputized remote server truthfulness checking, and public remote server truthfulness checking. Li *et al.* [24], suggested a data truthfulness verification approach which possesses high communication overhead and also, the protocol is not entirely identity-based. Ji *et al.* [25] suggested a method in order to address these two flaws, by implementing a tag-aggregating technique and a flexible data-splitting system. Using the certificateless signature technique, Li *et al.* [26] unveiled a novel RDPC procedure for verifying the data integrity revealed among a cluster. To guarantee that the right public keys are selected during data integrity verification, every user's public key is connected with their distinct identity. As a result, the certificate is no longer required, and the issue of key escrow is also resolved. Focusing on the homomorphic hash function, Yan *et al.* [27] introduced a new effective RDPC method. Relying on a basic security framework, the novel system is safe and efficient against forgery, replace, and replay attacks. Also, Yan *et al.* [28] introduced an innovative RDPC system with the authorized validator, where the data owner names a particular verifier to confirm the accuracy of the data.

A multi-replica multi-cloud certificate-less verification system constructed on blockchain technology was introduced by Yang [29]. The dynamic hashing table and update log table are used in this method to accomplish dynamic updates of group user information and identity monitoring. All clones are stored on various cloud servers, allowing for simultaneous auditing of their integrity. Chang *et al.* [30] suggested a novel PoR protocol named the admissible POR method with additional constraint conditions. The method considers whether any protected PoR technique is likely to construct a secure network scripting strategy and, if so, under what circumstances. To address the shortcomings of the original Usable Cloud Storage Auditing (UCSA) protocol

proposed by Chen *et al.* [31], Wang *et al.* [32] presented an Improved UCSA (iUCSA) protocol. A secure Cloud Server Auditing (CSA) protocol is a strategy that is equipped with cloud storage system elements to check whether the user's saved data is secure or not. CSPs can also use this protocol to demonstrate the reliability of their services, gaining new customers.

Zhou *et al.* [33] present a multiple-copy verifiable information possession for cloud-based Electronic Medical Record (EMR) systems that protects EMR data integrity and privacy. The method creates a one-of-a-kind dynamic system that enhances the Merkle Hash Tree for multiple copy storage while also achieving comprehensive dynamics quickly and safely for data updates. Furthermore, the idea uses a random masking technique to construct identifiable duplicate chunks of one block. The architecture prohibits a validator from obtaining health records via challenge responses while simultaneously prohibiting unwanted access to the material.

3. PROPOSED SYSTEM

3.1 Overview

The proposed method is constructed based on the notion of [8] and [9]. The scheme uses an enhanced puncturable pseudorandom function to assure the originality of the data warehoused inside the cloud server. With this approach, the hash value of the whole file need not be calculated each time to check the honesty of the data file, but to calculate only the hash value of the data block to be checked. In our approach, the safety of the data that has been stored will be ensured by the obfuscation program generated by the user. The enhanced puncturable pseudorandom function uses the hash value of the file tag, the block to be checked and the corresponding block tag with the help of the key ε . The file tag and block tag values are precomputed so as to reduce the computational overhead. The approach reduces the computing burden on both the TPA and the server side. Apart from honesty checking, the scheme supports dynamic updating, modification and deletion with less communication overhead.

3.2 Bilinear Pairing

Consider that G_1 and G_2 are two multiplicative groups of identical prime order p . Allow g_1 to be the generator of G_1 and g_2 be the generator of G_2 . If a function $e: G_1 \times G_1 \rightarrow G_2$ has the following characteristics, it is called a bilinear map. The properties are:

Bilinearity: $e(g^u, g^v) = e(g, g)^{uv}$, for all $g, b \in G_1$ and all $u, v \in Z_p$.

Non-Degeneracy: It is stated as, for the generator g_1 in G_1 , $e(g_1, g_1) \neq 1$.

Effective Calculation: $e(g, b)$ can be effectively calculated for every $g, b \in G_1$.

3.3 System Construction

A user U , a third-party auditor TPA, and a cloud server C encompass the suggested technique. The ensuing eight algorithms are involved in the methodology:

Setup: This algorithm generates the confidential parameter cp and the public parameter pu by selecting a security parameter ω . A signing key pair (scp, spu) is first selected by the user and then takes $k_1, k_2 \in Z_p$ as two random elements which can be used for replica generation and block tag computation respectively. Also, N number of arbitrary components y_1, \dots, y_N are selected by the user. Now the user calculates: $\sigma = g_1^{k_2} \in G_1$. A pseudorandom permutation $e_{key}()$ and a pseudorandom function $Y_{key}()$ are determined by the user. The confidential parameter cp is given as (k_2, scp) and the public parameter pu is given as $(\sigma, spu, y_1, \dots, y_N)$.

ReplicaGen: The user is the one who executes this algorithm. The user generates replica blocks for n number of servers, $\{S_i\}_{i=1,2,\dots,n}$. The user divides each replica of the information file F_i into r number of blocks, $F_i = (b_{i1}, b_{i2}, \dots, b_{ir})$, ie $\{b_j\}_{j=1,2,\dots,r}$. Each block is fragmented into s number of sectors. The original file F_i is named by the user with a random element, $g' \in Z_p$, and is used as the file identifier for identifying the file. The replica generation for n servers is as follows:

- For each server S_i and for each data block b_{ij} , a pseudorandom number, ρ_{ij} is generated, $\rho_{ij} = e(k_1, g'^{i||j||\omega})$
- The user then computes $\eta_{ij} = b_{ij} + \rho_{ij}$. Here the pseudorandom number ρ_{ij} generated for block b_{ij} and server S_i , is added with the corresponding block b_{ij} of the corresponding server S_i .
- The file replica for server S_i is given as, $g' = (\eta_{i1}, \eta_{i2}, \dots, \eta_{ir})$, $i = 1, 2, \dots, n$.

Store: The user performs this algorithm as well. The algorithm computes a file tag used to determine the text information's coding scheme inside files for each file and also calculates the corresponding block tags. A file tag

$t = g||r|| y_1, \dots y_N ||\text{Sig}()$ is the user's calculation, where $\text{sig}() = \text{sig}_{scp}(g||r|| y_1, \dots y_N)$ is a strong signature system. Then, a block tag $\{c_j\}_{j=1,2,\dots,\dots,r}$ is produced by the user for each data block for the file g :

$$c_j = \left(h(j||g) \cdot \prod_{l=1}^s \cup_l b_j \right)$$

in which, $h(): \{0,1\}^* \rightarrow G_1$ represents the cryptographic hash function and $\prod_{l=1}^s \cup_l b_j$ is an aggregated tag $\in G_1$ for the information blocks of the similar index number in all copies.

The information, including the file tag, block tags and the obfuscated files are subsequently outsourced to the server by the user.

Audit: This algorithm makes use of an enhanced PRF (puncturable pseudorandom function) in order to verify the honesty of the information kept inside the cloud. The cloud user picks an *enhanced PRF key* ε and uses the signing key pair (scp, spu) for each server S_i . The user then creates an obfuscation program, $\mathcal{Z} = iO(\text{Audit}_{\varepsilon, spu})$. This program will be sent to the server for executing the proof generation and the *enhanced PRF key*, ε is dispatched to the third-party auditor for verification along a protected network.

The third-party auditor produces a challenge message $\{p_1, p_2\}$ and sends the challenge to the cloud server in order to verify the originality of the data kept inside the cloud server, where p_1 is the key to the pseudorandom permutation and p_2 is the key to the pseudorandom function. For each audit, the third-party auditor chooses a pseudorandom element p_1 .

The $\text{Audit}_{\varepsilon, spu}$ can be computed as follows:

Audit_{ε, spu}:
 Input: $t, \{j\}, c_j, p_1, p_2$
 Constants: ε, spu
 Compute $H = \text{EPRF}(\varepsilon, h(j||t||c_j||p_2))$
 Output $\text{Sig}_{spu}(H||p_1)$

Proof: This algorithm is managed by the cloud server. When the server obtains the challenge message $\{p_1, p_2\}$ from the TPA, it first searches the warehoused files for the file's matching data block. The server will then calculate the matching data block's proof Prf and deliver it to the TPA.

For proof generation, the server chooses the corresponding file tag t , block tag c_j , the parameter ρ_{ij} and the public parameters. In addition to this, the aggregated

tag $\prod_{l=1}^s \cup_l b_j$ for the information blocks of the similar index number is computed. Also, the server computes the pseudorandom function $\hat{Y}_{key}()$, i.e. $\hat{Y}_{p2}(g||j||t)$ and the pseudorandom permutation $\hat{c}_{key}()$, i.e. $\hat{c}_{p1}(g||j||t)$. Finally, the proof, Prf will be generated:

$$Prf = \mathcal{Z}(t, \{j\}, c_j, p_1, p_2)$$

The proof or evidence Prf is obtained by the TPA from the cloud server.

Verify: This algorithm is managed by TPA. After receiving Prf from the server in the cloud, TPA calculates the pseudorandom permutation $\hat{c}_{p1}(g||j||t)$ and pseudorandom function $\hat{Y}_{p2}(g||j||t)$ and the truthfulness of the data is confirmed by means of the ensuing equation:

$$H = \text{EPRF}(\varepsilon, h(j||t||c_j||p_2))$$

$$Prf = \text{Sig}_{spu}(H||p_1)$$

If this verification is truthful, it outputs 1 otherwise 0.

Update: This algorithm is performed by the user. The algorithm is an update request to the cloud server by the user. The request includes either of the three data block operations: modification, insertion or deletion, on file copies stored on the cloud server. A request for file update is sent to the cloud server by the user as follows:

$$(g, blockop, b_{ij}, c_j, b_{ij}', c_j')$$

where g is the file identifier, $blockop$ is the data block operation (modification, insertion or deletion) to be performed on the data block, b_{ij} and c_j are the original data block and the actual block tag correspondingly and b_{ij}' and c_j' are the new information block and the new block tag to be updated respectively.

ExecUpdate: This algorithm is managed by the cloud server. With this algorithm, the cloud server performs all of the updates requested by the user. When the *Update* request is obtained by the cloud server, it executes the *ExecUpdate* algorithm. For the file identifier g , the corresponding data block operations will be executed. The data block b_{ij} is replaced by b_{ij}' and the data block tag c_j will be replaced with c_j' . The output of this algorithm will be an updated file with parameters, (g, b_{ij}', c_j') . After any block operation, the user implements the challenge protocol to ensure that the operations are accomplished correctly. Thus, the enhanced PRF has to be implemented by the TPA to update one data block.

4. PERFORMANCE ANALYSIS

This section elaborates on the execution and performance of the proposed methodology. The first part of our implementation has made a comparative assessment of the suggested scheme and Wei Guo *et al.* [17] scheme, based on parameters comprising time taken for generating tags, generating proof, verification and generating replicas. The experiment was simulated on a 64-bit Windows 10 PC with an Intel® Core™ i5-7300HQ processor at 2.50 GHz and SSD with 8GB. Jar files as well as a JDK file with version 1.8 are the libraries being utilized. A 256-bit key-sized elliptic curve is used in our methodology. An average of 10 trials are executed for simulation of each parametric measurement.

In our scheme, a sustained size of 1 MB file is presented. The computation overhead of tag generation time is measured first in the method. Figure 3 depicts the comparative assessment of tag generation time of our method and the scheme in Ref. [17]. In this phase, the user can pre-compute $h(j||g)$ and a lookup table can be constructed to execute the operations in our scheme. To verify all the replicas, only one set of tags is computed. Thus, our method is unaffected by the number of replica blocks, unlike in scheme [17], which is affected by the number of replica blocks. Our approach has an average of 8 s to generate the tag, which is less than the scheme mentioned in Ref. [17].

Figure 4 depicts the time to generate proof of our method and the method in Ref. [17]. To provide the evidence of the data warehoused inside the cloud server, our technique employs an *enhanced PRF*. In the proof generation phase, the server is computing $\zeta(t, \{j\}, c_j, p_1, p_2)$, where c_j and t are pre-computed, thereby the server's computing load is reduced. The exponential operations are also less.

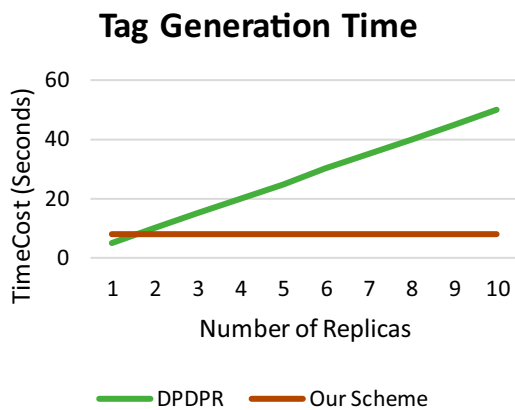


Figure 3: Time to generate tag for method [17] and proposed scheme

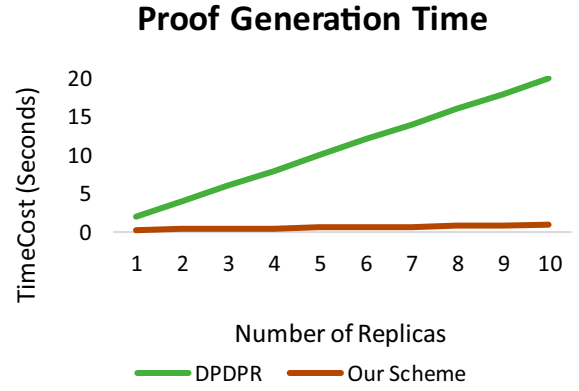


Figure 4: Time to generate proof for method [17] and proposed scheme

Also, a complete file hash value need not be calculated each time to check the honesty of the data file, but only the hash value of the data blocks to be examined is calculated. The proof generation time for three replica blocks for our scheme is 0.4 s, which is less than the scheme mentioned in Ref. [17].

Figure 5 depicts the verification overhead of our approach and the method in Ref. [17]. In this phase, the TPA is verifying the signature $Sig_{spu}(H || p_1)$. The time needed for verification in our scheme is constant and is 0.18 s, which is less than that of the scheme given in Ref. [17]. This is because the verification time required in the scheme mentioned in Ref. [17] depends on the number of replica blocks, whereas our scheme does not depend on the number of replica blocks.

Figure 6 depicts the time to generate a replica, of our scheme and the scheme in Ref. [17]. In this phase, the user computes $\eta_{ij} = b_{ij} + \rho_{ij}$ to generate the replica

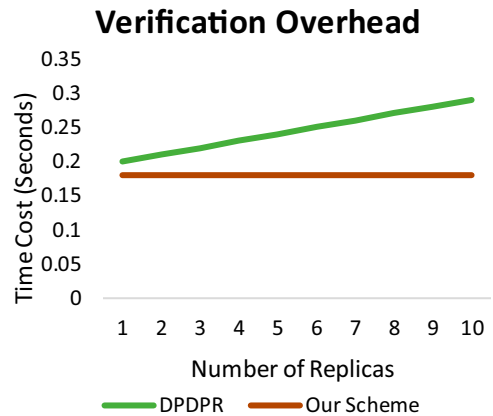


Figure 5: Time to verify proof for method [17] and proposed scheme

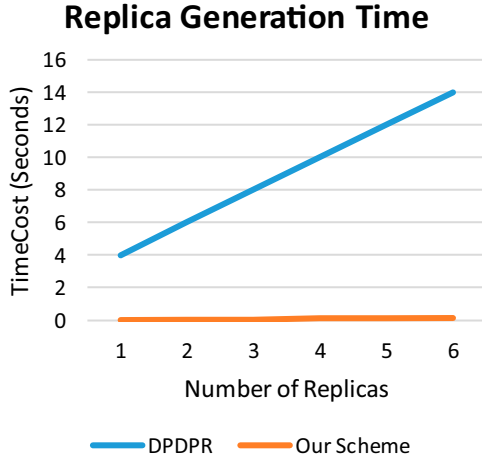


Figure 6: Time to generate replica for method [17] and proposed scheme

Table 1: Comparative analysis of similar existing methods based on replica numbers

		Performance Metrics							
		TagGen (s)		ProofGen (s)		Verification Time (s)		ReplicaGen (s)	
Replica numbers	References	3	4	3	4	3	4	3	4
1	17	30	38	0.63	0.85	0.6	0.9	0.07	0.09
2	19	10	10	0.6	0.62	0.25	0.25	0.08	0.1
3	9	15	20	8	10	0.22	0.23	8	10
4	Proposed	8	8	0.48	0.56	0.18	0.18	0.08	0.1

blocks. The time for generating three replicas in our scheme is 0.08 s, which is less than that required for the scheme given in Ref. [17].

Table 1 presents a comparative analysis of current methods that are similar and a proposed strategy based on the number of replicates. In order to analyze the methods, four metrics are chosen: time to generate tag, time to generate proof, time to verify proof and time to generate replica. The analysis depicts that our proposed scheme has less time to generate tags, proof, verify and replica generation when compared to all other methods. We compared our scheme with Liu *et al.* [15], Peng *et al.* [21] and Guo *et al.* [17]. Our scheme has a constant tag generation time and verification time of 8 and 0.18 s, respectively. The scheme does not depend on the number of replica blocks to compute tag and verify proof of the blocks. Eventhough the number of replica blocks affect proof computation and replica creation; the execution time is negligible for our scheme when related to other similar existing methods.

The second part of our implementation has been a comparative study between the proposed scheme and the Liu

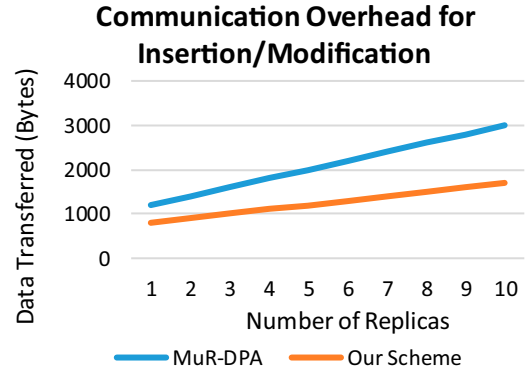


Figure 7: Communication overhead for insertion/modification

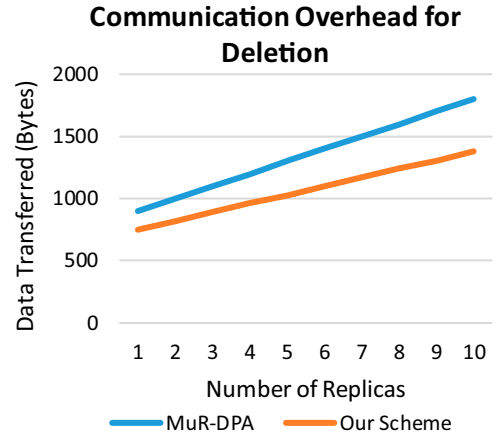


Figure 8: Communication overhead for deletion

et al. [15] scheme based on the communication overhead for “dynamic updates”. The parameters chosen are insertion/modification and deletion.

Figure 7 depicts the communication burden for “insertion/modification” operations of our approach and the method in Ref. [15]. The communication overhead of our scheme for three replica blocks needs only 1000 bytes, which is less than that of the scheme mentioned in Ref. [15].

Figure 8 depicts the communication overhead required for “deletion” operation, of our approach and the method in Ref. [15]. The communication burden of our scheme for three replica blocks needs only 890 bytes, which is less than that of the scheme mentioned in Ref. [15].

5. CONCLUSIONS AND FUTURE WORK

In this paper, an enhanced puncturable pseudorandom function is presented to decrease the computational burden during the proof creation and verification

of multiple-replicas. Bilinear pairings are used for the implementation. The scheme verifies all replica blocks at once without depending on the number of replicas. The proposed scheme can attain privacy for all replicas with the help of an indistinguishability obfuscation program produced by the user. Less communication overhead is possessed by the scheme at the time of dynamic updating.

As a future work, we can further extend our experiments with batch verification of users using an enhanced puncturable pseudorandom function.

DISCLOSURE STATEMENT

No potential conflict of interest was reported by the author(s).

ORCID

Anju Susan George  <http://orcid.org/0000-0001-7904-5348>

REFERENCES

1. F. ArmKnecht, J. M. Bohli, G. Karame, and W. Li, "Outsourcing proofs of retrievability," *IEEE Transactions on Cloud Computing*, Vol. 9, no. 1, pp. 286–301, 2021. DOI:10.1109/TCC.2018.2865554
2. G. Bian, and J. Chang, "Certificateless provable data possession protocol for the multiple copies and clouds case," *IEEE Access*, Vol. 8, pp. 102958–70, 2020. doi:10.1109/ACCESS.2020.2999208
3. Z. Hao, and N. Yu, "A multiple-replica remote data possession checking protocol with public verifiability", in *Second International Symposium on Data Privacy and E-Commerce*, IEEE 2010.
4. Y. Yu, J. B. Ni, M. H. Au, H. Y. Liu, H. Wang, and C. X. Xu, "Improved security of a dynamic remote data possession checking protocol for cloud storage," *Expert Syst. Appl.*, Vol. 41, no. 17, pp. 7789–96, Jun. 2014. DOI:10.1016/j.eswa.2014.06.027
5. G. Ateniese, R. Burns, R. Curtmola, J. Herring, I. Kissner, Z. Peterson, and D. Song, "Provable data possession at untrusted stores," in *Proceedings of the 14th ACM conference on CCS*, 2007, pp. 598–609.
6. A. I. Juels, and B. S. Kaliski. "Pors: proofs of retrievability for large files", in *Proceedings of the 14th ACM conference on CCS*, 2007, pp. 583–97.
7. Y. Zhu, *et al.*, "Cooperative provable data possession for integrity verification in multi-cloud storage," *IEEE Transactions in Parallel and Distributed Systems*, Vol. 23, no. 12, pp. 2231–44, Dec. 2012. DOI:10.1109/TPDS.2012.66
8. Y. Zhang, C. Xu, X. Liang, H. Li, Y. Mu, and X. Zhang, "Efficient public verification of data integrity for cloud storage systems from indistinguishability obfuscation," *IEEE Trans. Inf. Forensics Secur.*, Vol. 12, no. 3, pp. 676–88, Mar. 2017. DOI:10.1109/TIFS.2016.2631951
9. L. Sun, C. Xu, Y. Zhang, and K. Chen, "An efficient iO-based data integrity verification scheme for cloud storage," *Science China Information Services*, Vol. 62, pp. 059101:1–059101:3, May 2019.
10. C. Erway, *et al.*, "Dynamic provable data possession," *ACM Transactions on Information and System Security (TISSEC)*, Vol. 17, no. 4, pp. 213–222, Apr. 2015. DOI:10.1145/2699909
11. S. Aldossary, and W. Allen, "Data security, privacy, availability and integrity in cloud computing: issues and current solutions," *International Journal of Advanced Computer Science and Applications*, Vol. 7, no. 4, pp. 485–98, 2016. DOI:10.14569/IJACSA.2016.070464
12. B. Shao, C. Bian, Y. Wang, S. Su, and C. Guo, "Dynamic data integrity auditing method supporting privacy protection in vehicular cloud environment," *IEEE Access*, Vol. 6, pp. 43785–97, 2018. DOI:10.1109/ACCESS.2018.2863270
13. J. Lin, X. Li, X. Jia, and K. Ren, "Multiple-replica integrity auditing schemes for cloud data storage," in *Concurrency computation: practice and experience*, John Wiley and Sons Ltd., Vol. 33, no.7, pp. 1–14, 2019.
14. M. Yi, J. Wei, and L. Song, "Efficient integrity verification of replicated data in cloud computing system," *Computers and Security. Elsevier*, Vol. 65, pp. 202–212, 2017. DOI:10.1016/j.cose.2016.11.003
15. C. Liu, *et al.*, "MuR-DPA: Top-down levelled multi-replica merkle hash tree based secure public auditing for dynamic big data storage on cloud," *IEEE Trans. Comput.*, Vol. 64, no. 9, pp. 2609–22, Sept. 2015. DOI:10.1109/TC.2014.2375190
16. S. Peng, F. Zhou, J. Li, Q. Wang, and Z. Xu, "Efficient, dynamic and identity-based remote data integrity checking for multiple replicas," *J. Netw. Comput. Appl.*, Vol. 134, pp. 72–88, May 2019. DOI:10.1016/j.jnca.2019.02.014
17. W. Guo, *et al.*, "Dynamic proof of data possession and replication with tree sharing and batch verification in the cloud," *IEEE Transactions on Services Computing*, Vol. 15, no. 4, pp. 1813–1824, Sept. 2020. doi:10.1109/TSC.2020.3022812.
18. J. Chang, B. Shao, Y. Ji, and G. Bian, "Efficient identity-based provable multi-copy data possession in multi-cloud storage, revisited," *IEEE Commun. Lett.*, Vol. 24, no. 12, pp. 2723–27, 2020. DOI:10.1109/LCOMM.2020.3013280
19. X. Pei, *et al.* "Ensuring replication-based data Integrity and availability in multicloud storage", in *17th International Conference on SNPD*, IEEE, 2016.
20. H. Wang, "Identity- based distributed provable data possession in multicloud storage," *IEEE Transactions on*

- Services Computing*, Vol. 8, no. 2, pp. 328–40, 2015. DOI:10.1109/TSC.2014.1
21. S. Peng, F. Zhou, Q. Wang, Z. Xu, and J. Xu, “Identity-based public multi-replica provable data possession,” *IEEE Access*, Vol. 5, pp. 26990–7001, Nov. 2017. DOI:10.1109/ACCESS.2017.2776275
 22. J. Li, H. Yan, and Y. Zhang, “Efficient identity-based provable multi-copy data possession in multi-cloud storage,” *IEEE Transactions on Cloud Computing*, Vol. 14, no.1, pp. 71–81, Jul. 2019. DOI: 10.1109/TCC.2019.2929045.
 23. H. Wang, D. He, and S. Tang, “Identity-based proxy-oriented data uploading and remote data integrity checking in public cloud,” *IEEE Trans. Inf. Forensics Security*, Vol. 11, no. 6, pp. 1165–76, Jun. 2016. DOI:10.1109/TIFS.2016.2520886
 24. J. Li, H. Yan, and Y. Zhang, “Identity-based privacy preserving remote data integrity checking for cloud storage,” *IEEE Syst. J.*, Vol. 15, no. 1, pp. 577–85, Mar. 2021. DOI:10.1109/JSYST.2020.2978146
 25. Y. Ji, B. Shao, J. Chang, and G. Bian, “Flexible identity-based remote data integrity checking for cloud storage with privacy preserving property,” *Cluster. Comput.*, Vol. 25, pp. 337–49, 2022. DOI:10.1007/s10586-021-03408-y.
 26. J. Li, H. Yan, and Y. Zhang, “Certificateless public integrity checking of group shared data on cloud storage,” *IEEE Transactions on Services Computing*, Vol. 14, no. 1, pp. 71–81, Jan.-Feb. 2021. DOI:10.1109/TSC.2018.2789893.
 27. H. Yan, J. Li, J. Han, and Y. Zhang, “A novel efficient remote data possession checking protocol in cloud storage,” *IEEE Trans. Inf. Forensics Secur.*, Vol. 12, no. 1, pp. 78–88, Jan. 2017. DOI:10.1109/TIFS.2016.2601070.
 28. H. Yan, J. Li, and Y. Zhang, “Remote data checking with a designated verifier in cloud storage,” *IEEE Syst. J.*, Vol. 14, no. 2, pp. 1788–97, Jun. 2020. DOI:10.1109/JSYST.2019.2918022.
 29. X. Yang, X. Pei, M. Wang, T. Li, and C. Wang, “Multi-replica and multi-cloud data public audit scheme based on blockchain,” *IEEE Access*, Vol. 8, pp. 144809–22, Aug. 2020. DOI:10.1109/ACCESS.2020.3014510
 30. J. Chang, B. Shao, Y. Ji, M. Xu, and R. Xue, “Secure network coding from secure proof of retrievability,” *Sci. China Inform. Sci.*, Vol. 64, no. 12, pp. 229–301, May 2021. DOI:10.1007/s11432-020-2997-0
 31. F. Chen, *et al.*, “Towards usable cloud storage auditing,” *IEEE Trans. Parallel Distrib. Syst.*, Vol. 31, no. 11, pp. 2605–17, Nov. 2020. DOI:10.1109/TPDS.2020.2998462
 32. H. Wang, L. Feng, Y. Ji, B. Shao, and R. Xue, “Toward usable cloud storage auditing, revisited,” *IEEE Systems Journal*, Vol. 99, pp. 693–700, 2021. DOI:10.1109/JSYST.2021.3055021.
 33. L. Zhou, A. Fu, Y. Mu, H. Wang, S. Yu, and Y. Sun, “Multicopy provable data possession scheme supporting data dynamics for cloud-based electronic medical record system,” *Journal of Information Sciences*, Vol. 545, pp. 254–76, Aug. 2020. DOI:10.1016/j.ins.2020.08.031

AUTHORS



Anju Susan George received BE degree in information technology from Periyar University, Salem, India, in 2003 and received ME degree in computer science and engineering from Anna University, India, in 2010. She is currently pursuing PhD in computer science and engineering from Noorul Islam Centre for Higher Education, deemed to be University, Thuckalay, India, in the area of cloud security. She is working as Associate Professor with the department of information technology, APJ Abdul Kalam Technological University, Kerala, India. Her research interest include cryptography, network security, and cloud security.

Corresponding author. E-mail: anju@vjcet.org



A Shajin Nargunam received master of computer applications from Bharathidasan University, Trichy, India, in 1995, received ME degree in computer science and engineering from Anna University, India, in 2002 and received PhD degree in computer science and engineering from NIT, Calicut, India in 2008. He is currently working as Professor and Dean – Academics with the department of computer science and engineering at Noorul Islam Centre for Higher Education, Thuckalay, India. His research interest include cryptography, network security, fog computing, and cloud computing.

E-mail: shajin@niuniv.com



Workplace Bullying, Engagement and Employability: Moderating Role of Organization-Based Self-Esteem

Nimmi P. M.¹ · Geetha Jose² · Maria Tresita Paul Vincent³ · Anjali John⁴

Accepted: 12 July 2022

© The Author(s), under exclusive licence to Springer Science+Business Media, LLC, part of Springer Nature 2022

Abstract

The present research paper aims to examine the influence of workplace bullying on employee work outcomes in terms of employee engagement and perceived internal employability. The paper also analyses the moderating role of organization-based self-esteem (OBSE) in the relationship between workplace bullying and employee work outcomes. The authors relied on cross-sectional data from teaching faculty across universities and colleges in South India to validate hypotheses empirically. The proposed model was tested using Warp-PLS and PROCESS macro in SPSS. The study reported a significant negative influence of workplace bullying on perceived internal employability and employee engagement. The study also found that OBSE positively moderated the negative relationship between workplace bullying and employee work outcomes in terms of engaging employees and perceived employability. The unique aspect of this research is that it is the first time the moderating role of OBSE is discussed in bullying literature. The study puts across OBSE as a positive organization related construct that can nullify the negative impacts of workplace bullying. OBSE is a crucial resource in annualizing the negative effect of bullying in the workplace. Policymakers should imbibe OBSE as a crucial factor in the policies and ethics of their organization for enhancing employee engagement and employability.

Keywords Workplace bullying · Perceived internal employability · Employee engagement · Organization-based self-esteem · Indian faculty

✉ Nimmi P. M.
nimmimohandas1985@gmail.com

Geetha Jose
josegeetha@gmail.com

Maria Tresita Paul Vincent
maria.tresi@gmail.com

Anjali John
anjalijohn1990@gmail.com

¹ SCMS Cochin School of Business, Kochi, Kerala, India

² Bharatmata Institute of Management, Kochi, Kerala, India

³ Sardar Vallabhbhai Patel International School of Textiles & Management, Coimbatore, Tamil Nadu, India

⁴ Marthoma College of Management, Perumbavoor, India

Introduction

Daily interactions in the workplace establish critical grounds based on which organizational members are respected or not as respected. These interactions are also vital aspects that transfer the sense of belongingness and worth to the members (Nguyen et al., 2019). This unique sense of significance derived from interactions is at the heart of the human experience and psychological needs (Rogers & Ashforth, 2017). During such social exchanges, negative interactions may occur like workplace bullying, incivility, abusive supervision, deviance, harassment, emotional abuse, and social undermining (Mao et al., 2019; Jacobsen et al., 2018). Amongst these, even after 30 years of research, bullying remains a prominent issue that workplaces must solve (Agarwala, 2018; Krishna & Soumyaja, 2020). Workplace bullying is established as a serious work demand and has received much attention in the organizational psychology and behaviour literature in the last decade (Agarwala, 2018; Arshad & Ismail, 2018; Bartlett & Bartlett, 2011; Conway et al., 2021; Gardner et al., 2016; Glambek et al., 2018; Gupta, 2013; Hogh et al., 2021; Nielsen & Einarsen, 2012; Rai & Agarwal, 2017; Tuckey et al., 2017; Verkuil et al., 2015).

In India, teaching as a profession is considered noble; despite this, 'Indian academia' reports a high rate of workplace bullying (Agarwala, 2018; Gupta, 2013; Krishna & Soumyaja, 2020). Workplace bullying is described as a category of harassing behaviour that employees may be subjected to at any stage of their career, regardless of their membership in a protected class based on gender, ethnicity, age, etc. (Leymann, 1990). The repercussion of workplace bullying in academia is often reflected in the behaviour towards other stakeholders in an immediate environment like students. This vicious spillover effect may also be reflected in other work outcomes (Krishna & Soumyaja, 2020). However, research examining outcomes of workplace bullying literature in Indian academia is comparatively less (Agarwala, 2018; Gupta, 2013; Krishna & Soumyaja, 2020). Recent research identified that the literature on workplace bullying in India lacks studies on the antecedents and consequences of workplace bullying at the national, societal, and cultural levels, emphasizing future research in this direction (Gupta et al., 2020). Given these gaps in bullying literature in Indian academia, the present study is a modest attempt to address how workplace bullying influences work outcomes among Indian academics.

Adverse effects of bullying affect the organizational sustainability of higher educational institutions (Muazzam et al., 2020). Organizational sustainability is associated with how engaged/associated employees are with their work and organization (Glavas, 2012; Zayed et al., 2020). Activities that demoralize employees' enthusiasm for the organization can negatively impact organizational sustainability and growth. Moreover, workplace victimization can lead to absence of employees, reduced morale and motivation, and reduced productivity (Law et al., 2011). Although studies on workplace bullying and adverse work outcomes, like turnover intention (Coetzee & van Dyk, 2018), workplace incivility (Meires, 2018), and deviant behaviours (Sarwar et al., 2020), have yielded an understanding of the negative impact of bullying. The impact of workplace bullying and its relationship with positive work outcomes remain underexplored (Rai & Agarwal, 2017). While workplace bullying can have profound consequences in the work purview, it is vital to comprehend further workplace bullying and its interactions with positive outcomes in the work domain, like employee engagement and internal employability.

Sustainable growth of organizations is achieved by developing human resources and having a positive mindset at work. A highly engaged workforce is quintessential for the success of an organization. Commitment and belongingness towards the organization are evident while

assessing employees' perceived internal employability as it indicates whether employees plan to continue with the organization (Nimmi et al., 2020). From an employee perspective, an optimum balance between resources and demands is essential for a sustainable career.

Perceived internal employability is an indicator of increased productivity and higher retention of employees (Sánchez-Manjavacas et al., 2014). A greater sense of employability is associated with career satisfaction and wellbeing (Gowan, 2012). Employees with higher internal employability perceptions are confident that they are competent and competitive. Referred to as employees' alignment of current and future career prospects within the company, perceived employability is affected by individual differences. External realities relating to work and work environment help to nurture or hinder perceived internal employability (Cerdin et al., 2020). Uncertainties and contingencies at work results in less cognitive resources for employees which can negatively impact their internal employability perceptions (Cerdin et al., 2020).

Employee engagement can be defined as a *“positive, active, work-related psychological state operationalized by the maintenance, intensity, and direction of cognitive, emotional, and behavioral energy”* (Shuck et al., 2017, p. 269). Kahn conceptualizes engagement as harnessing selves in one's work roles cognitively, physically, and emotionally, driving in-role behaviours (May et al., 2004). The psychological conditions of meaningfulness, safety and availability has to be met for engaging the employees (Kahn, 1990). Research revealed that psychological conditions influence the overall employee engagements. (Allen & Rogelberg, 2013). Engagement creates a psychological connectedness with employees' work, and engaged employees encompass high levels of energy and are enthusiastic about their work. They also often get fully engrossed in their work and execute their role and responsibilities at a higher quality level. In organisations harmful social stressors like workplace bullying causes disengagement and disrupts the organisational productivity, increased intent to quit and decreased employee performance (Trépanier et al., 2013; Serban et al., 2022). Thus, when the psychological conditions are not met in the organizations, it can affect the employee's psychological health. Employee disengagement is a prominent indicator of such poor psychological health in employees.

Resource theory literature (Hobfoll, 2012) highlights the importance of resource caravans and resource passageways for a sustainable career. Bullying is characterized as a job demand that drains out the positive resources in an employee. More and more resources are needed to buffer the drain of resources. Theoretically, the study draws from the conservation of resources theory to decipher how workplace bullying negatively influences employee engagement and internal employability and how an organizational resource could mitigate this negative effect. The study proposes that developing organization-based self-esteem can potentially protect employees from the detrimental effects of bullying. Practically, this study provides insights into mitigating the adverse effects of bullying in the workplace and how organizations can play a role. The purpose of our paper is thus two-fold. First, to see if bullying negatively predicts employee engagement and perceived internal employability among academics in India as a case. Second, to look into whether OBSE moderates the negative relationships between the above said variables.

Theoretical Framework

Our study is positioned on the conservation of resource theory (COR theory). According to COR theory, *“people strive to retain, protect, and build resources and that what is threatening to them is the potential or actual loss of these valued resources,* Hobfoll (1989,

p.513)”. COR theory introduces resource passageways, representing how the external environment, including work and non-work environment, can promote or hinder one’s resource gain. In this study, we place bullying as a job demand. The job demand ought to have a depleting role on job resources. At a work setting, employee engagement and perceived internal employability are considered an outcome of resource perceptions. The study proposes that bullying as a job demand depletes the job resources and negatively impacts engagement and internal employability. The study then places OBSE as a resource passageway instigated within an employee by the organization. Thus, developed self-esteem in employees protects and safeguard them against incivility experienced by them at the workplace.

Literature Review and Hypothesis Development

Workplace Bullying and Employee Engagement

Personnel engagement is conceptualized as “the harnessing of organization members’ to their work roles; i.e., in engagement, people express and employ physically, cognitively, and emotionally during role performances (Kahn, 1990, 694)”. Engagement is about the willingness to invest oneself and expend an open effort to help the employer succeed. Employee engagement consists of three facets: trait engagement, behaviour engagement, and psychological state engagement (Macey & Schneider, 2008). Employee engagement is a crucial competitive advantage factor in human resource management practices (Albrecht et al., 2015). Saks (2019), in his study on the antecedents and consequences of employee engagement, stated a positive and significant relationship of employee engagement with job performance, organization commitment, and organizational citizenship behaviour. Employee engagement can be better understood by understanding the sources creating employee engagement.

The COR theory gets aligned with this perspective. The demands and resources employees collect in the organization play a vital role in engaging them. This is because employees’ intrinsic and extrinsic motivation gets strongly influenced by these demands and resources, which results in their engagement level (Nazir & Islam, 2017; Tesi, 2021). Workplace bullying covers a set of negative behaviours aimed toward an individual at the workplace (Einarsen et al., 2009). Bullying acts as a job demand that drains out the resources of an employee and negatively impacts the positive job outcomes of employees. Workplace bullying is primarily defined as “*repetitive acts of harassment, such as social isolation and verbal abuse, which one or more perpetrators commit over an extended period (six months or more)*” (Einarsen et al., 2020, p.22). There are a series of negative consequences of workplace bullying (Coetzee & van Dyk, 2018; Meires, 2018; Sarwar et al., 2020). Engagement with work or organization is the result of actual or anticipated resource gain enhancing energetic resources. The washout of resources due to bullying can reduce engagement with the organization. Based on previous empirical findings (e.g., Einarsen et al., 2018; Meriläinen et al., 2019; Park & Ono, 2017), based on the above discussions, we hypothesize that workplace bullying is negatively related to engagement, especially employee engagement.

H1: Workplace bullying negatively predicts employee engagement

Workplace Bullying and Perceived Internal Employability

Employability perception is defined as an individual's perception of his or her chances of attaining and maintaining employment (Vanhercke et al., 2014). Assessing employability perceptions is essential as employees' perceptions rather than reality activate their cognitions and behaviours (Vanhercke et al., 2014; Nimmi et al., 2020). There are two dimensions of perceived employability, namely, perceived internal employability and perceived external employability. According to Rothwell and Arnold (2007), internal employability is the perceived value of the occupation with the current employer or within the labour market. In contrast, external employability reflects the perceived value of employment in the external labour market.

Research reveal that, employability is a key job resource, impacting the subjective career success and job performance within organizations. (Bozionelos et al., 2016). The COR theory places perceived employability as a vital resource (Kirves, 2014) to enable an individual to adapt to the changing work environment (Baruch, 2014; Baruch & Rousseau, 2019) and as an individual coping mechanism for job security and a sustainable career (Donald et al., 2020). Perceived employability is considered an outcome of interactions between structural factors (Job market and Organisational) and internal factors (Berntson, 2008). Several factors like training, work experience, interpersonal relationships, and constructs like, protean career attitude, and spirituality affect the employability perceptions of a person (Cortellazzo et al., 2020; Groot & Van Den Brink, 2000; Nimmi et al., 2020; Nimmi et al., 2021). Organizational factors like HRM practices are associated with perceived internal employability (Akkermans et al., 2020). Perceived internal employability explains organizational outcomes like desired commitment, loyalty, adaptability, and productivity (Sánchez-Manjavacas et al., 2014). It is an indicator of enhanced commitment towards the organization and output of developmental activities provided by the organization. However, work demands like workplace bullying, which deplete resources, have a detrimental effect on internal employability as different bullying activities manifest into different adverse outcomes. Bullying depletes the resources like self-esteem, self-confidence, physical and mental health, trust in the organization and colleagues (Krishna & Soumyaja, 2020). As these resources see a downfall, workplace bullying can be detrimental to the internal employability perceptions of individuals and job insecurity (Krishna & Soumyaja, 2020). Thus, we hypothesize that,

H2: Workplace bullying negatively predicts perceived internal employability.

The Moderating Role of OBSE

Pierce et al. (1989) introduced the concept of organization-based self-esteem as a multifaceted phenomenon. Organization-based self-esteem (OBSE) is defined as "the degree to which an individual believes him/herself to be capable, significant, and worthy as an organizational member." The concept elaborates self-esteem, which has been studied in the individual context, to an organizational context where one's self-evaluation of his/her worthiness as an organizational member is assessed. High OBSE indicates individuals consider themselves as essential and competent enough to be employable in that particular organization (Pierce & Gardner, 2004) and are highly satisfied with the treatment in the particular organization. OBSE is a self-concept (personal resource)

developed at the individual level, based on social exchange within the organization. According to Xanthopoulou et al. (2007), personal resources moderate the link between job demands and work outcomes. In this context, employees who enjoy a stronger sense of self-esteem can be expected to exhibit a stronger sense of performance than their low self-esteem counterparts (Paul V & Devi, 2018, 2020).

Recent research has revealed that psychological empowerment substantially affects employee engagement (Joo et al., 2019). OBSE is an essential psychological empowerment resource for employees. In the organizational context, people with high self-esteem or high levels of OBSE may be less responsive to adverse effects than employees with low levels of OBSE (Hui & Lee, 2000). When threatened by a hostile work atmosphere, employees with high OBSE may cope more than employees having low OBSE (Arshadi & Damiri, 2013). The theoretical explanation for the moderating role of OBSE comes from its role as a resource passageway. First is that OBSE acts as a resource caravan passageway helps to maintain resource caravan by compensating for resources lost at the job (Hobfoll, 2012). OBSE moderates the relationship as ‘*resource passageway function*’ as it can diminish the side effects of adverse workplace habits. So OBSE helps an individual to cope up with the negative impacts of workplace bullying. Based on the assumptions we propose,

H3: OBSE positively moderates the negative relationship between Workplace bullying and employee engagement; such that the negative relationship between workplace bullying and employee engagement is weaker for those who are high in OBSE.

H4: OBSE positively moderates the negative relationship between Workplace bullying and perceived internal employability; such that the negative relationship between workplace bullying and internal employability is weaker for those who are high in OBSE.

So based on the propositions a theoretical model was framed, depicted in Fig. 1 which was theoretically tested,

Methodology

Methods and Participants

The core aim of this study was to investigate the linkage between workplace bullying with employee engagement and employability. It also examined how OBSE moderates the relationship mentioned above among university teachers.

The population of the study constitutes permanent teachers employed with recognised Indian universities and their affiliated colleges spread across Kerala and Tamil Nadu, in South India. Convenience sampling was chosen for the study considering the special interventions of Covid 19 pandemic. The methodological rigour followed in this study can subdue the apprehensions of choosing convenience sampling method in this cross-sectional study. Limiting respondents to the above criteria made OBSE, employee engagement, and employability relevant issues for the individual. An online survey was floated through the mail. Participants were assured strict academic usage of collected data and anonymity of their responses. Screening 269 reverted responses, nine were cast off due to incompleteness, resulting in a sample size of 260.

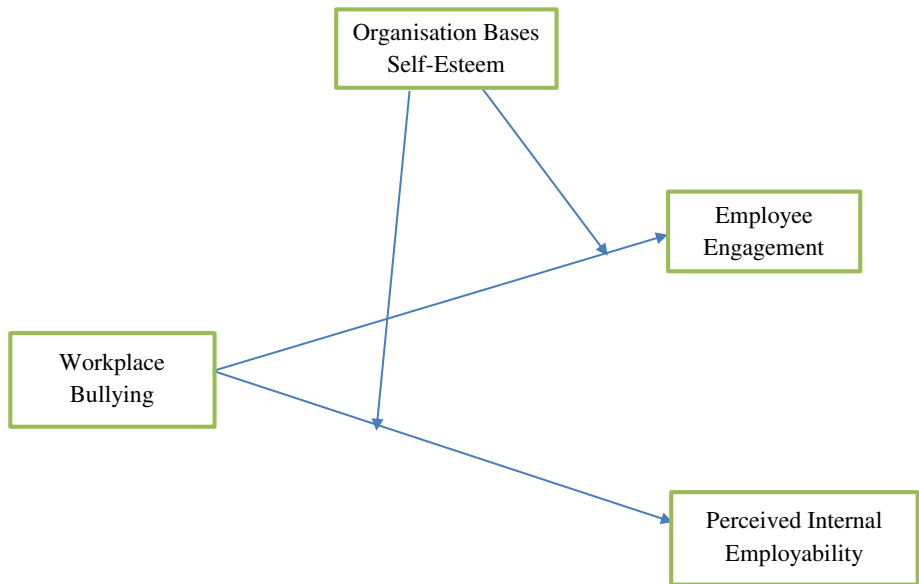


Fig. 1 Proposed theoretical model

Measures

Perceived Internal Employability was assessed via 4-items based on the scale developed by Rothwell and Arnold (2007). The perceived value of occupation in the current organization (internal employability) with four items. A sample item was “*Even if there was downsizing in this organization, I am confident that I would be retained.*”

Organisation Based Self-Esteem was assessed with a ten-item scale developed by Pierce et al. (1989). A sample item was “*I am taken seriously around here*”.

Employee engagement was assessed using a UWES -9 developed by Schaufeli et al. (2006) containing 9 items. A sample item is “*I feel happy when I am working intensely*”.

Workplace bullying was assessed using a Short Negative Acts Questionnaire containing 9 items developed by Notelaers, Hoel, van der Heijden and Einarsen et al. (2018). A sample item is “*in the past six months I experienced persistent criticism about my work and effort*”.

Control Variables

Gender, total experience, years of experience in the current organization were controlled in the study as previous studies have denoted the impact of these variables on outcome variables (Pierce et al., 1989; Donald et al., 2019).

Data Analysis Strategy

The Warp PLS was used to conduct confirmatory factor analysis (CFA), examining adopted study measures' measurement model and validity. Thus, confirming the discriminant and convergent validity of the instrument items. Subsequently, using the PRO-CESS macro in SPSS 23.0 (Hayes, 2013) with 5000 bootstrapped samples following Preacher and Hayes (2008), the structural equation model (SEM) was performed to test the hypothesized moderation model. Out of 260 respondents, 161 were female, and 99 were male. Also, 35% of teachers were below 25 years, 26% were between 26 and 35 years, 21% were between 36 and 45 years, 7% were between 46 and 55 years, and the remaining 11% were above the age of 55 years.

Further analysis was done in two stages. In the first stage, Harmon's single factor test was applied to check for common method bias. Initial descriptive tests were conducted using SPSS software. Then the reliability and validity of the scales were assured. The reliability of the scales was assessed using Cron-Bach alpha values. In the second stage of the study, the hypotheses were tested using structural equation modelling using Warp-PLS. The moderation effects were assessed using SPSS Macro- Hayes Model Template 1.

Results and Analysis

Descriptive Statistics

The fit of the proposed model depicted in Fig. 1 was tested with Warp-PLS v.6.0 statistical software (Kock, 2015). Each of the constructs like Bullying, OBSE are represented by latent factors. And each latent factors were assessed using specific scale items. Fit Indices are provided in Table. 1, which permits an acceptable fit for the model.

The mean, standard deviation, and correlations (Table 2) indicated a reliable correlation for the variables under study.

The convergent and discriminant validity was assessed using average extracted variance (AVE) and maximum shared variance (MSV); which found to be above threshold levels and approves validity and reliability tests for the measures (Table. 3). The

Table 1 Fit indices

Fit Index	Value	Threshold limit
Average path coefficient (APC)	0.350	$P < 0.001$
Average R-squared (ARS)	0.276	$P < 0.001$
Average adjusted R-squared (AARS)	0.261	$P < 0.001$
Average block VIF (AVIF)	3.34	acceptable if ≤ 5 , ideally ≤ 3.3
Average full collinearity VIF (AFVIF)	2.00	acceptable if ≤ 5 , ideally ≤ 3.3
Tenenhaus GoF (GoF)	0.443	small > 0.1 , medium > 0.25 , large > 0.36
Sympton's paradox ratio (SPR)	0.750	acceptable if > 0.7 , ideally = 1
R-squared contribution ratio (RSCR)	0.950	acceptable if > 0.9 , ideally = 1
Nonlinear bivariate causality direction ratio (NLBCDR)	0.750	acceptable if > 0.7
Statistical suppression ratio (SSR)	0.720	acceptable if > 0.7

Table 2 Correlation table

	1	2	3	4	5	6	7	Mean	S.D
1. Bullying								1.932	0.787
2. Perceived Employability	-.165*							3.842	749
3. OBSE	-.428**	.573**						4.146	0.721
4. Engagement	-.269**	.721**	.696**					4.04	0.818
5. Gender	-.093	.085	.002	.163				na	na
6. Total experience	-.251*	.042	.263**	.232*	.034			8.581	6.931
7. Experience in current Organization	-.102	.143	.052	.199*	.142	.531**		3.901	3.991

**, Correlation is significant at the 0.01 level (2-tailed)

*, Correlation is significant at the 0.05 level (2-tailed)

Table 3 Measurement model statistics

Constructs	Type	CR	AVE	Cronbach	VIF
1. Workplace Bullying	Reflective	0.902	0.708	0.877	1.293
2. Perceived Employability	Reflective	0.871	0.677	0.814	2.093
3. OBSE	Reflective	0.924	0.754	0.889	2.331
4. Engagement	Reflective	0.91	0.717	0.867	2.313

reliability of the constructs (Cron-Bach values) was above the accepted threshold (Workplace Bullying - 0.87, OBSE - 0.89, Perceived Internal Employability - 0.87, Employee Engagement - 0.86).

Hypothesis Testing

In order to assess the direct effects, path analysis was conducted with workplace bullying as the predictor and employee engagement and perceived internal employability as outcomes in Warp-PLS. The direct effects were assessed from the structural model. The study found a significant negative effect of workplace bullying on employee engagement (-0.269^{**}) and employability (-0.312^{**}). So, hypothesis 1 and 2 are accepted.

To test the moderating hypotheses, PROCESS method (Preacher and Hayes (2004, 2008)) was used as indirect effect can be deducted from it. Bootstrapping procedure was followed with around 5000 samples to give 95% confidence interval (CI) with indirect effect estimates. The codes for moderation analysis were captured from SPSS - Hayes Macro output and graphical representation were created with MS- Excel. Lastly, regarding the moderating hypotheses, H3 and H4, the indirect outcome of workplace bullying on perceived internal employability was significant for OBSE ($\beta=0.318^{**}$) and on employee engagement was significant for OBSE ($\beta=0.468^{**}$). The positive moderating role of OBSE is represented in the Figs. 2 and 3. Further Tables 4 and 5 depicts the interaction effect of Work place Bullying on Internal employability and Employee engagement. The direct effect of Bullying on Engagement and Internal Employability in the presence of OBSE as well interaction (moderation effect) effect is evident from the tables.

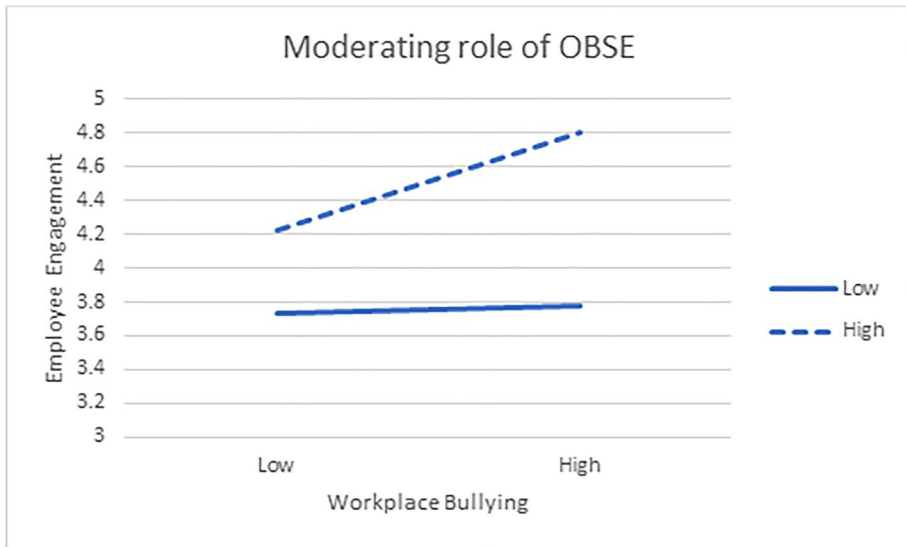


Fig. 2 Moderating role of OBSE in Bullying – Engagement

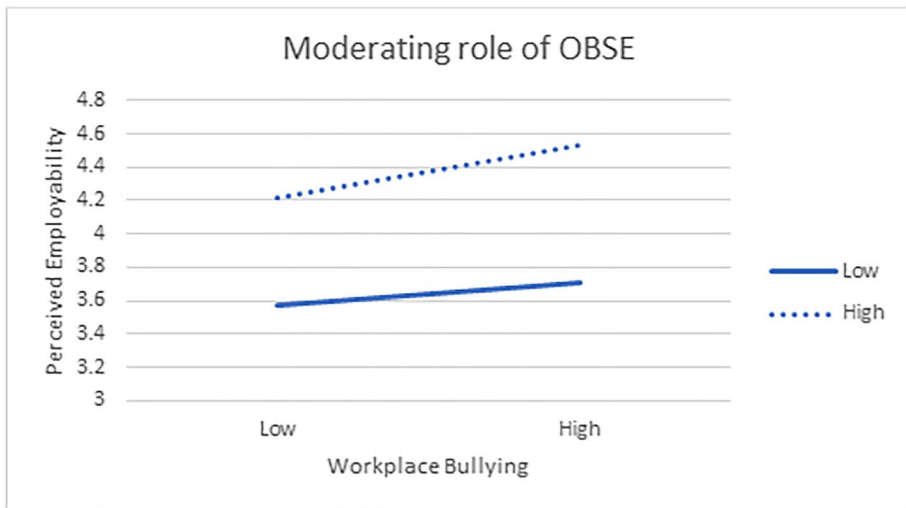


Fig. 3 Moderating role of OBSE in Bullying – Employability

Discussion

The purpose of this paper was two-fold. First, to see whether workplace bullying has a detrimental effect on internal employability perceptions and employee engagement. Second, to see whether OBSE has a positive effect on the above-mentioned relationships. We found support for H1 (workplace bullying negatively predicts employee engagement) and H2

Table 4 Interaction effect of OBSE and bullying on employee engagement

Predictor	Beta	SE	t	p	LLCI	ULCI
Constant	1.32	1.01	1.3	0.03	0.68	3.34
Bullying	-0.22	0.34	-0.65	0.05	-0.84	-0.25
OBSE	0.63	0.23	2.62	0.0002	0.36	0.89
Bullying*OBSE	0.46	0.08	0.244	0.04	0.27	0.85

Dependent Variable: Employee engagement

Table 5 Interaction effect of OBSE and bullying on perceived internal employability

Predictor	Beta	SE	t	p	LLCI	ULCI
Constant	1.49	1.07	1.38	0.17	1.18	2.23
Bullying	-0.21	0.36	-0.27	0.05	-0.78	-0.31
OBSE	0.61	0.32	2.39	0.01	0.36	0.88
Bullying*OBSE	0.32	0.08	0.97	0.03	0.27	0.64

Dependent Variable: Perceived Internal Employability

(workplace bullying negatively predicts perceived internal employability). The moderating hypothesis put forward was also accepted. That means OBSE moderated the relationship of workplace bullying with employee engagement as well as perceived internal employability. Our study was in response to a call by Park and Ono (2017) on more representation of reports from the impact of bullying on employees belonging to different cultures and occupations. The support to H1 addresses calls by Park and Ono, 2017 and Rai and Agarwal, 2017 on the under-representation of the effects of workplace bullying in different cultural contexts and also the organization-level outcomes of workplace bullying.

Our findings of the detrimental effect of workplace bullying on engagement and employability are in line with the JD-R theory claiming the negative impact of workplace bullying on work outcomes. The potential explanation of the negative impact of workplace bullying is that bullying could act as a workplace demand that can mitigate the energy and resources of the individual. This drain of resources may lead to a decreased level of engagement within the organization activities as well as perceiving low internal employability. The moderating role of OBSE is very much evident from the regression coefficient and Figs. 2 and 3. For those employees who have high OBSE, even when facing bullying experiences their engagement at work and internal employability seems to be high. This means the adverse effects of bullying are buffered by the high OBSE levels.

Theoretical Implications

The study looks into the impact of workplace bullying on important work outcomes from a multi-theoretic perspective. Major factors that reflect the sustainability of an organization are the internal employability and engagement of its employees. The study is the first among to look into the impact of bullying on employability. The study is significant from a socio-cultural perspective as India has a collectivist culture with high power distance (Hofstede, 1980). A negative association was found in lieu of the JD-R model and COR model. Prior research on workplace bullying has not checked the buffering role of OBSE. The most significant

theoretical implication of our study comes from the moderating role of OBSE. Organization based self-esteem acts as a source passage that alleviates the negative impacts of bullying in workplace domain. OBSE is an unswerving reflection of the self-perceived value that an individuals have in an organisational environment. Employees who perceive high OBSE, perceive themselves as important in the organisation and find meaning in the work they do. This is reflected in their future employment perceptions within the organisation. This will be directly reflected in their behaviours which is in lieu with the policies of the organisation and valued within organization. It is believed that these may result in employees' deriving intrinsic satisfaction, coupled with reinforcing their self-esteem (Pierce et al., 1989).

Practical Implications

The deleterious effects of workplace bullying may reflect on the sustainable growth of organizations. The cues from the employees who perceive bullying shall be seriously taken up by HR managers and supervisors to support them and help them relieve the negative emotions. The study calls for interventions conducted at the organization level that can convey the value system within the organization and restrain individuals from bullying manifestations. It is pertinent to develop a work culture that nurtures creativity as well as employability rather than mitigating them. The study also voices the need to develop a harmonious relationship at work. Such an atmosphere is necessary to ensure employees that their jobs are not at stake. The importance of developing OBSE in an organization is conveyed through the article by looking into the buffering role of OBSE on the negative impacts of workplace bullying. The effects of employer brand image regarding their warmth and competence on employee engagement is influenced by their employee characteristics (e.g., experience and role) (Davies et al., 2018). Thus, organizations should provide the teachers with a supportive environment (Gallagher et al., 2021) through OBSE to enhance their positive affirmations with their role and experience accumulation, to enhance their brand image and employee engagement.

Limitations and Future Research

Future research could include observer ratings to examine how much they predict incremental variance over and above self-reports, which could be collected at multiple time points. Likewise, a longitudinal research design to attain more knowledge on causal relationships. Cultural differences may exist in academic settings in different countries, so the validation of models in different nations is a possibility. Also, another scope is to capture the difference in outcome on temporary and permanent employees who are subjected to bullying. Various personal and organization level moderators could be considered to buffer the negative impacts of bullying. Further studies also could come up with how bullying impacts external employability and turnover intentions.

Conclusion

In conclusion, our study and model constitute an important step toward understanding the outcomes of workplace bullying. The study also investigated the moderating role of OBSE in the relationship of bullying at the workplace to that of employee engagement,

and employability. We found that OBSE positively moderates both the relationships. This research work adds to the research on workplace bullying and organizational outcomes in academia. We also provide implications of our findings for employees in academics.

Declarations

Conflict of Interest There is no conflict of Interest between the authors.

References

- Agarwala, T. (2018). Bullying and career consequences in the academy: Experiences of women faculty. In A. M. Broadbridge & S. L. Fielden (Eds.), *Research handbook of diversity and careers* (pp. 241–255). Edward Elgar Publishing.
- Akkermans, J., Richardson, J., & Kraimer, M. L. (2020). The Covid-19 crisis as a career shock: Implications for careers and vocational behavior. *Journal of Vocational Behavior*, 119, 103434.
- Albrecht, S. L., Bakker, A. B., Gruman, J. A., Macey, W. H., & Saks, A. M. (2015). Employee engagement, human resource management practices and competitive advantage: An integrated approach. *Journal of Organizational Effectiveness: People and Performance*, 2, 7–35.
- Allen, J. A., & Rogelberg, S. G. (2013). Manager-led group meetings: A context for promoting employee engagement. *Group & Organization Management*, 38(5), 543–569. <https://doi.org/10.1177/1059601113503040>
- Arshad, R., & Ismail, I. R. (2018). Workplace incivility and knowledge hiding behavior: Does personality matter? *Journal of Organizational Effectiveness: People and Performance*, 5, 278–288.
- Arshadi, N., & Damiri, H. (2013). The relationship of job stress with turnover intention and job performance: Moderating role of OBSE. *Procedia-Social and Behavioral Sciences*, 84, 706–710.
- Bartlett, J. E., & Bartlett, M. E. (2011). Workplace bullying: An integrative literature review. *Advances in Developing Human Resources*, 13, 69–84.
- Baruch, Y. (2014). The development and validation of a measure for protean career orientation. *The International Journal of Human Resource Management*, 25(19), 2702–2723. <https://doi.org/10.1080/09585192.2014.896389>
- Baruch, Y., & Rousseau, D. M. (2019). Integrating psychological contracts and ecosystems in career studies and management. *Academy of Management Annals*, 13(1), 84–111. <https://doi.org/10.5465/annals.2016.0103>
- Berntson, E. (2008). Employability perceptions: Nature, determinants, and implications for health and well-being (Doctoral dissertation, Psykologiska institutionen).
- Bozionelos, N., Kostopoulos, K., Van der Heijden, B., Rousseau, D. M., Bozionelos, G., Hoyland, T., Miao, R., Marzec, I., Jędrzejowicz, P., Epitropaki, O., Mikkelsen, A., Scholarios, D., & Van der Heijde, C. (2016). Employability and job performance as links in the relationship between mentoring receipt and career success: A study in SMEs. *Group & Organization Management*, 41(2), 135–171. <https://doi.org/10.1177/1059601115617086>
- Cerdin, J., Liao, Y., & Sharma, K. (2020). The role of temporal focus, dispositional employability, and training on the perceived internal career prospects of talents. *The International Journal of Human Resource Management*, 31(9), 1106–1133. <https://doi.org/10.1080/09585192.2019.1711441>
- Coetzee, M., & van Dyk, J. (2018). Workplace bullying and turnover intention: Exploring work engagement as a potential mediator. *Psychological Reports*, 121, 375–392.
- Conway, P. M., Høgh, A., Balducci, C., & Ebbesen, D. K. (2021). Workplace bullying and mental health. *Pathways of Job-Related Negative Behaviour*, 101–128.
- Cortellazzo, L., Bonesso, S., Gerli, F., & Batista-Foguet, J. M. (2020). Protean career orientation: Behavioral antecedents and employability outcomes. *Journal of Vocational Behavior*, 116, 103343.
- Davies, G., Mete, M., & Whelan, S. (2018). When employer brand image aids employee satisfaction and engagement. *Journal of Organizational Effectiveness: People and Performance*, 5, 64–80.
- Donald, W. E., Baruch, Y., & Ashleigh, M. (2019). The undergraduate self-perception of employability: Human capital, careers advice, and career ownership. *Studies in Higher Education*, 44(4), 599–614.
- Donald, W. E., Baruch, Y., & Ashleigh, M. J. (2020). Striving for sustainable graduate careers: Conceptualization via career ecosystems and the new psychological contract. *Career Development International*, 25, 90–110. <https://doi.org/10.1108/CDI-03-2019-0079>

- Einarsen, S., Hoel, H., & Notelaers, G. (2009). Measuring exposure to bullying and harassment at work: Validity, factor structure and psychometric properties of the negative acts questionnaire-revised. *Work and Stress*, 23, 24–44.
- Einarsen, S., Skogstad, A., Rørвик, E., Lande, Å. B., & Nielsen, M. B. (2018). Climate for conflict management, exposure to workplace bullying and work engagement: A moderated mediation analysis. *The International Journal of Human Resource Management*, 29, 549–570.
- Einarsen, S. V., Hoel, H., Zapf, D., & Cooper, C. L. (2020). The concept of bullying and harassment at work: The European tradition. In *Bullying and harassment in the workplace* (pp. 3–53). CRC Press.
- Gallagher, C. M., Hughes, I. M., & Keith, M. G. (2021). From social burden to support elicitation: Development and validation of a new measure of workplace support elicitation experiences. *Journal of Business and Psychology*. <https://doi.org/10.1007/s10869-021-09769-w>
- Gardner, D., O'Driscoll, M., Cooper-Thomas, H. D., Roche, M., Bentley, T., Catley, B., & Trenberth, L. (2016). Predictors of workplace bullying and cyber-bullying in New Zealand. *International Journal of Environmental Research and Public Health*, 13(5), 448.
- Glabek, M., Skogstad, A., & Einarsen, S. (2018). Workplace bullying, the development of job insecurity and the role of laissez-faire leadership: A two-wave moderated mediation study. *Work & Stress*, 32(3), 297–312.
- Glavas, A. (2012). Employee engagement and sustainability: A model for implementing meaningfulness at and in work. *Journal of Corporate Citizenship*, 46, 13–29.
- Gowan, M. A. (2012). Employability, well-being and job satisfaction following a job loss. *Journal of Managerial Psychology*, 27, 780–798. <https://doi.org/10.1108/02683941211280157>
- Groot, W., & Van Den Brink, H. M. (2000). Overeducation in the labor market: a meta-analysis. *Economics of Education Review*, 19(2), 149–158.
- Gupta, R. (2013). Prevalence of workplace bullying and its impact on workplace well-being in academia. *Indian Journal of Health and Wellbeing*, 4, 503–505.
- Gupta, P., Gupta, U., & Wadhwa, S. (2020). Known and unknown aspects of workplace bullying: A systematic review of recent literature and future research agenda. *Human Resource Development Review*, 19(3), 263–308. <https://doi.org/10.1177/1534484320936812>
- Hayes, A. F. (2013). *Introduction to mediation, moderation, and conditional Process analysis: A regression-based approach*. Guilford Press.
- Hobfoll, S. E. (1989). Conservation of resources: a new attempt at conceptualizing stress. *American Psychologist*, 44(3), 513.
- Hobfoll, S. E. (2012). Conservation of resources and disaster in cultural context: The caravans and passageways for resources. *Psychiatry: Interpersonal & Biological Processes*, 75(3), 227–232.
- Hofstede, G. (1980). Culture and organizations. *International Studies of Management & Organization*, 10(4), 15–41.
- Hogh, A., Clausen, T., Bickmann, L., Hansen, Å. M., Conway, P. M., & Baernholdt, M. (2021). Consequences of workplace bullying for individuals, organizations and society. *Pathways of job-related negative behaviour*, 177–200.
- Hui, C., & Lee, C. (2000). Moderating effects of organization-based self-esteem on organizational uncertainty: Employee response relationships. *Journal of Management*, 26(2), 215–232.
- Jacobsen, D. P., Nielsen, M. B., Einarsen, S., & Gjerstad, J. (2018). Negative social acts and pain: Evidence of a workplace bullying and 5-HTT genotype interaction. *Scandinavian Journal of Work, Environment & Health*, 44(3), 283–290.
- Joo, B.-K. (B.), Bozer, G., & Ready, K. J. (2019). A dimensional analysis of psychological empowerment on engagement. *Journal of Organizational Effectiveness: People and Performance*, 6(3), 186–203.
- Kahn, W. A. (1990). Psychological conditions of personal engagement and disengagement at work. *Academy of Management Journal*, 33(4), 692–724. <https://doi.org/10.5465/256287>
- Kirves, K. E. (2014). Perceived employability. Antecedents, trajectories and well-being consequences (Doctoral dissertation). University of Tampere and University of KU Leuven. <https://lirias.kuleuven.be/1963479?limo=0>. Accessed 08.05.2021.
- Kock, N. (2015). Common method bias in PLS-SEM: A full collinearity assessment approach. *International Journal of e-Collaboration (ijec)*, 11(4), 1–10.
- Krishna, A., & Soumyaja, D. (2020). Playing safe games – thematic analysis of victims' perspectives on gendered bullying in academia. *Journal of Aggression, Conflict and Peace Research*, 12(4), 197–208. <https://doi.org/10.1108/JACPR-03-2020-0478>
- Law, R., Dollard, M. F., Tuckey, M. R., & Dormann, C. (2011). Psychosocial safety climate as a lead indicator of workplace bullying and harassment, job resources, psychological health and employee engagement. *Accident Analysis & Prevention*, 43(5), 1782–1793.
- Leymann, H. (1990). Mobbing and psychological terror at workplaces. *Violence and Victims*, 5, 119–126.
- Macey, W. H., & Schneider, B. (2008). *The Meaning of Employee Engagement*, 1, 3–30.

- Mao, C., Chang, C. H., Johnson, R. E., & Sun, J. (2019). Incivility and employee performance, citizenship, and counterproductive behaviors: Implications of the social context. *Journal of Occupational Health Psychology*, 24(2), 213.
- May, D. R., Gilson, R. L., & Harter, L. M. (2004). The psychological conditions of meaningfulness, safety and availability and the engagement of the human spirit at work. *Journal of Occupational and Organizational Psychology*, 77(1), 11–37. <https://doi.org/10.1348/096317904322915892>
- Meires, J. (2018). The essentials: Using emotional intelligence to curtail bullying in the workplace. *Urologic Nursing*, 38(3), 150–154.
- Meriläinen, M., Kõiv, K., & Honkanen, A. (2019). Bullying effects on performance and engagement among academics. *Employee Relations*, 41(6), 1205–1223.
- Muazzam, A., Anjum, A., & Visvizi, A. (2020). Problem-focused coping strategies, workplace bullying, and sustainability of HEIs. *Sustainability*, 12, 10565.
- Nazir, O., & Islam, J. U. (2017). Enhancing organizational commitment and employee performance through employee engagement: An empirical check. *South Asian Journal of Business Studies*, 6(1), 98–114. <https://doi.org/10.1108/SAJBS-04-2016-0036>
- Nguyen, D. T., Teo, S. T., Grover, S. L., & Nguyen, N. P. (2019). Respect, bullying, and public sector work outcomes in Vietnam. *Public Management Review*, 21(6), 863–889.
- Nielsen, M. B., & Einarsen, S. (2012). Outcomes of exposure to workplace bullying: A meta-analytic review. *Work & Stress*, 26(4), 309–332.
- Nimmi, P. M., Zakkariya, K. A., & Nezzin, R. (2020). Insight to impact: The effect of protean career attitude on employability perceptions of IT professionals. *Colombo Business Journal*, 11(1), 1–23.
- Nimmi, P.M., Binoy, A.K., Joseph, G. & Suma, R. (2021). Significance of developing spirituality among management students: Discerning the impact on psychological resources and wellbeing. *Journal of Applied Research in Higher Education*. Vol. ahead-of-print No. ahead-of-print. <https://doi.org/10.1108/JARHE-10-2020-0372>.
- Park, J. H., & Ono, M. (2017). Effects of workplace bullying on work engagement and health: The mediating role of job insecurity. *The International Journal of Human Resource Management*, 28(22), 3202–3225.
- Paul V. M. T., & Devi, N. U. (2018). Psychological capital, outcome expectation and job performance: A mediated model of innovative work behavior. *International Journal for Research in Engineering Application & Management*, 1, 52–60.
- Paul V. M. T., & Devi, N. U. (2020). Family incivility and entrepreneurial success of MSMEs: Moderating role of psychological capital. *South Asian Journal of Marketing and Management Research*, 10, 35–45.
- Pierce, J. L., & Gardner, D. G. (2004). Self-esteem within the work and organizational context: A review of the organization-based self-esteem literature. *Journal of Management*, 30(5), 591–622.
- Pierce, J. L., Gardner, D. G., Cummings, L. L., & Dunham, R. B. (1989). Organization-based self-esteem: Construct definition, measurement, and validation. *Academy of Management Journal*, 32(3), 622–648.
- Preacher, K. J., & Hayes, A. F. (2004). SPSS and SAS procedures for estimating indirect effects in simple mediation models. *Behavior Research Methods, Instruments, & Computers*, 36(4), 717–731.
- Preacher, K. J., & Hayes, A. F. (2008). Asymptotic and resampling strategies for assessing and comparing indirect effects in multiple mediator models. *Behavior Research Methods*, 40(3), 879–891.
- Rai, A., & Agarwal, U. A. (2017). Linking workplace bullying and work engagement: The mediating role of psychological contract violation. *South Asian Journal of Human Resources Management*, 4(1), 42–71.
- Rogers, K. M., & Ashforth, B. E. (2017). Respect in organizations: Feeling valued as "we" and "me". *Journal of Management*, 43(5), 1578–1608.
- Rothwell, A., & Arnold, J. (2007). Self-perceived employability: Development and validation of a scale. *Personnel Review*, 36(5), 23–41.
- Saks, A. M. (2019). Antecedents and consequences of employee engagement revisited. *Journal of Organizational Effectiveness: People and Performance*, 6(1), 19–38.
- Sánchez-Manjavacas, A., Saorín-Iborra, M., & Willoughby, M. (2014). Internal employability as a strategy for key employee retention. *Innovar*, 24(53), 7–22.
- Sarwar, A., Naseer, S., & Zhong, J. Y. (2020). Effects of bullying on job insecurity and deviant behaviors in nurses: Roles of resilience and support. *Journal of Nursing Management*, 28(2), 267–276.
- Schaufeli, W. B., Bakker, A. B., & Salanova, M. (2006). The measurement of work engagement with a short questionnaire: A cross-national study. *Educational and Psychological Measurement*, 66(4), 701–716.
- Serban, A., Rubenstein, A. L., Bosco, F. A., Reina, C. S., & Grubb, L. K. (2022). Stressors and social resources at work: Examining the buffering effects of LMX, POS, and their interaction on employee attitudes. *Journal of Business and Psychology*, 37(4), 717–734.
- Shuck, B., Osam, K., Zigarmi, D., & Nimon, K. (2017). Definitional and conceptual muddling: Identifying the positionality of employee engagement and defining the construct. *Human Resource Development Review*, 16(3), 263–293. <https://doi.org/10.1177/1534484317720622>

- Tesi A. (2021). Moving forward to social workers' work engagement: Framing the regulatory modes and the job demands-resources model, *Journal of Workplace Behavioral Health*. <https://doi.org/10.1080/15555240.2021.1931260>.
- Trépanier, S. G., Fernet, C., & Austin, S. (2013). Workplace bullying and psychological health at work: The mediating role of satisfaction of needs for autonomy, competence and relatedness. *Work & Stress*, 27(2), 123–140.
- Tuckey, M. R., Li, Y., & Chen, P. Y. (2017). The role of transformational leadership in workplace bullying: Interactions with leaders' and followers' job characteristics in a multi-level study. *Journal of Organizational Effectiveness: People and Performance*, 4(3), 199–217.
- Vanhercke, D., De Cuyper, N., Peeters, E., & De Witte, H. (2014). Defining perceived employability: A psychological approach. *Personnel Review*, 43(4), 592–605. <https://doi.org/10.1108/PR-07-2012-0110>
- Verkuil, B., Atasayi, S., & Molendijk, M. L. (2015). Workplace bullying and mental health: a meta-analysis on cross-sectional and longitudinal data. *PloS One*, 10(8), e0135225.
- Xanthopoulou, D., Bakker, A. B., Demerouti, E., & Schaufeli, W. B. (2007). The role of personal resources in the job demands-resources model. *International Journal of Stress Management*, 14(2), 121.
- Zayed, M., Jauhar, J., Mohaidin, Z., & Murshid, M. A. (2020). Effects of inter-organizational justice on dimensions of organizational citizenship Behaviours: A study on Kuwait ministries' employees. *Management and Labour Studies*, 45(4), 444–470.

Publisher's Note Springer Nature remains neutral with regard to jurisdictional claims in published maps and institutional affiliations.



Application of grey-fuzzy logic for the optimization of drilling parameters for coir fibre reinforced composite

Snobin Mathew, K. Shunmugesh *

Department of Mechanical Engineering, Viswajyothi College of Engineering & Technology, Vazhakulam, India

ARTICLE INFO

Article history:

Available online 22 August 2022

Keywords:

Coir fibre reinforced composite
Grey relational analysis
Fuzzy logic algorithm
Thrust force and delamination factor

ABSTRACT

Coir Fibre Reinforced Composite (CFRC) materials have possible applications in different areas like auto, aviation, structural designing, sports, wind energy and so forth. Yet, CFRC drilling stances numerous issues that decline the nature of openings. The issues which influence the nature of boring are the over measuring, delamination factor, and the harshness of the openings. To acquire the best and ideal machining quality we should think about ideal boundaries of drilling. In this work, Taguchi's L27 symmetrical cluster is utilized to perform drilling of CFRC composite plate. Fuzzy and Grey fuzzy analysis on MATLAB is also conducted to confirm the optimum values for drill diameter, spindle rotary speed and feed rate of drill. The wear rate of the tool, material removal rate from the composite and roughness of the surface are measured and optimized using the MATLAB analysis. Examination of difference (ANOVA) is utilized to observe the rate commitment of the penetrating boundaries and observed that rate of feed is the most powerful variable in boring of CFRC composites. In this investigation, the multi-objective issue is changed over into a solitary objective improvement involving GRA method and further vulnerabilities in the dim result are diminished by fuzzy relational hypothesis.

Copyright © 2022 Elsevier Ltd. All rights reserved.

Selection and peer-review under responsibility of the scientific committee of the International Conference on Processing and Characterization of Materials.

1. Introduction

Now a days, biodegradable based composites have greater important and have large applications in our society. Coir Fibre Reinforced Composite (CFRC) materials have applications in the field of aerospace, marine activities, industries etc. So that, during its application it is necessary to drill it to make holes. Sometime it may cause harms like fibre pull out, roundness mistakes, delamination and interlaminar break engendering [1–4]. The destruction in the perfectly ordered stacked layers of composite is a significant danger to penetrating of openings that should be basically decreased and this effect is commonly called delamination of composites. The feed power and cutting boundaries have connection and it was gotten by multivariable direct relapse and contrasted and the exploratory outcomes [5–8]. Tsao and Chiu [9] investigated the conceivable outcomes of sans delamination penetrating in materials of composites. A complete examination of delamination being used of different types of drills, for example, centre drill,

saw drill, candle drill, centre drill and step drill was made to foresee basic push force at the beginning of delamination and contrasted and the contort drill. The information boring boundaries are to be recognized and upgraded to such an extent that these issues are limited [9–12]. As of late, dim social examination is utilized for advancement of info penetrating boundaries for accomplishing great quality result execution attributes. Notwithstanding, in different other machining applications like EDM, welding, processing, turning, surface imperfection too dark social advancement is involved [13–16].

In this work, an exploratory examination is conveyed utilizing a milling machining system for boring our CFRC plates. The investigation was done based on Taguchi's L27 symmetrical exhibit of tests. The significant info penetrating boundaries were picked as feed rate, axle speed and drill diameter and the reactions specifically, apparatus wear rate, removal of material rate and surface roughness. The numerous presentation qualities that were determined are, section delamination, exit delamination and the unconvencionality of bored openings. To limit the upsides of all the previously mentioned exhibition attributes, an ideal mix of information it is expected to penetrate boundaries. The grey fuzzy relation is utilized for streamlining of boring boundaries that limits the

* Corresponding author.

E-mail address: shunmugesh@vjcet.org (K. Shunmugesh).

penetrating harms. ANOVA is utilized to find the exceptionally powerful boring parameter(s) that adds to a top-notch item.

2. Experimental description

CFRC plates which we used for our analysis were produced by laying up coir fibre and epoxy sap applying layer by layer. The image of the material is displayed in the Fig. 1.the plate thickness is limited to 12 mm and the drill openings are of diameters of 6 mm, 8 mm and 10 mm. The boring apparatus utilized in trial and error was made of fast steel (HSS). The three set varieties of feed rate and axle speed picked for this trial and error is displayed in Table 1. The investigations are arranged according to Taguchi's L27 symmetrical cluster of trials. Subsequently-three set, three factorial level framework is utilized in all this work. The exploratory arrangement utilized in the current review is displayed in Fig. 2. The penetrating investigations were completed on vertical CNC milling machine with initially fixed cutting conditions. The push power and force of each of the 27 investigations were estimated utilizing piezo-electric dynamometer. The bored plate is captured utilizing Nikon D-200 camera. This image of the infiltrated openings was dealt with to CorelDRAW programming and the most outrageous width of the hurt zone of the drilled opening is estimated. And the picture of the bored openings was taken care of coreldraw programming and the greatest distance across of the

Table 1
Parameters and values.

Factor	SET 1	SET 2	SET 3
Axle Speed (RPM)	2500	4000	5500
Rate of Feed (mm/min)	50	40	30
Drill Bit Dia (mm)	6	8	10

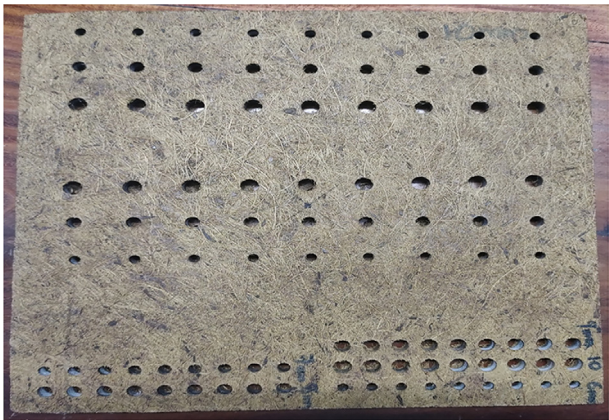


Fig. 2. Drilled CFRC Composite.



Fig. 1. CNC Drilling of CFRC a) 6 mm drill bit diameter. b) 8 mm drill bit diameter. c) 10 mm dill bit diameter.

harmful zone of the penetrated opening is estimated. The surface roughness was measured by using Mitutoyo Surface Roughness Tester.

3. Grey relational coefficient analysis

In grey relational analysis, first of all we convert the output parameters like surface roughness, material removal rate and tool wear rate into normalized values. This stage of grey analysis is called pre-processing stage. The result of this conversion is a normalized value which is in the range of zero to one (Fig. 3). The next step is to calculate the deviation range by subtracting normalized value from one. From the deviation sequence we can find the coefficient grey relation for the corresponding output parameters. The average of these values gives the grey coefficient for corresponding set of input parameters of feed rate, speed of spindle and diameter of the drill. Higher the value of coefficient greater the optimization of values. Table 2 and 3 gives the grey relation coefficient for the sets of input parameters.

4. Fuzzy analysis

Fuzzy based analysis method is an artificial intelligence method used for the analysis of any machining operation. In this analysis grey fuzzy analysis using MATLAB software is used. Mandhani MATLAB analysis is used and its methodology is shown in Fig. 3. The main advantage of fuzzy analysis over grey analysis is that, it is completely a programming software so that the result is accurate and easy to calculate. Grey fuzzy integration is used in our analysis for the better result with negligible errors. 5 membership function is used for input as well as for the output parameters. The linguistic membership functions operate very low, low, medium, high and very high are used here. The rules are generated based on these 5 membership functions. The generation rules and membership functions are shown in Figs. 4 and 5.

5. Result and discussion

5.1. Calculating the grey relational coefficient

The results we obtained from the analysis and testing are first used to calculate the grey relational grade. Here Microsoft Excel sheet software is used to calculate it. Grey relation can be easily calculated using simple equations and mathematics. The equations are fed into an Excel sheet and the result is generated in it. The result is shown in Table 2 and 3. Higher the value of grey coefficient greater its rank for optimization.

5.2. Execution of Grey-Fuzzy based method

The first stage of fuzzy analysis is to generate the membership function for input and output parameters. The five-membership function generated for the given parameters are shown in Fig. 4. The best set of parameters is obtained from the value corresponding to the maximum value of GFRG. These main effect values are plotted in Fig. 5 for the machining input and output parameters in table number 3.

5.3. Grey-fuzzy reasoning analysis

MATLAB apparatus is utilized for acquiring the grey fuzzy result. The three-sided enrolment work is applied for every one of the five grey coefficients, each with five participation capacities and a commonplace plot is displayed in Fig. 5 shows the participation work for the grey grade. The grey result is isolated into five number of enrolment capacities. A bunch of rules were composed for actuating the fuzzy inference system (FIS) and the FIS is assessed to anticipate the grey fuzzy grades for each of the 27 trials. Table 3 shows the grey fuzzy relational grade and its organization has gotten from the anticipated upsides of FIS. On contrasting the aftereffects of Tables 3 and 4, clearly there is an improvement in the upsides of grey fuzzy grade. Hence, the vulnerability of information is decreased. Likewise, it is affirmed that the examination number 12 has the ideal blend of info penetrating boundaries. Here 4 sources of info (MRR, TWR, SR1 and SR2) and one result (GFRG) fuzzy relational framework is utilized. The grey relational coeffi-

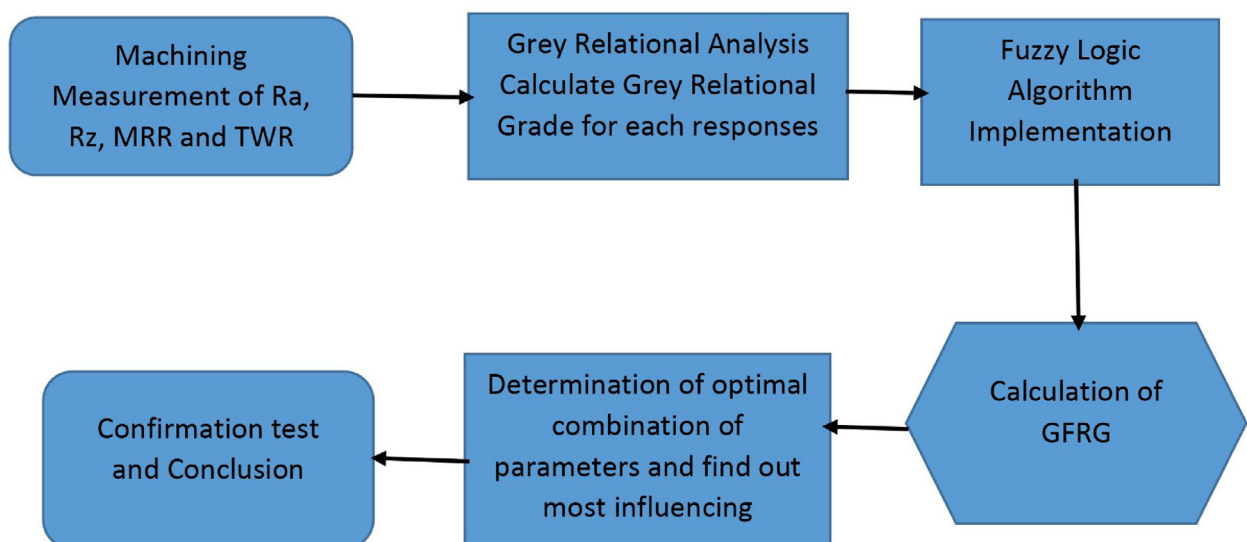


Fig. 3 Proposed Grey – Fuzzy Method

Fig. 3. Proposed Grey – Fuzzy Method.

Table 2
Standards of normalised.

Sl. No	INPUT PARAMETERS			OUTPUT RESPONSES				DATA PRE-PROCESSING			
	Spindle Speed (rpm)	Feed Rate (mm/min)	Drill Diameter (mm)	MRR	Surface Roughness (Ra) (μm)	Surface Roughness (Rz) (μm)	TWR	MRR	Surface Roughness (Ra) (μm)	Surface Roughness (Rz) (μm)	TWR
1	2500	30	6	0.2703	4.3279	15.4852	0.0092	0	0.8363	0.8363	0.86
2	2500	30	8	0.4167	4.1858	14.9769	0.0103	0.26	0.9851	0.9851	0.84
3	2500	30	10	0.5405	4.2299	15.1345	0.0119	0.48	0.939	0.939	0.81
4	2500	40	6	0.3571	4.7199	16.8878	0.0146	0.1543	0.4256	0.4256	0.76
5	2500	40	8	0.5	4.5409	16.2475	0.0162	0.408	0.6131	0.6131	0.73
6	2500	40	10	0.7143	4.7824	17.1114	0.0195	0.7886	0.3601	0.3601	0.67
7	2500	50	6	0.4167	4.9415	17.6806	0.0455	0.26	0.1935	0.1935	0.19
8	2500	50	8	0.6	4.6418	16.6083	0.0439	0.5856	0.5074	0.5074	0.22
9	2500	50	10	0.8333	4.967	17.7721	0.0558	1	0.1667	0.1667	0
10	4000	30	6	0.2703	4.3279	15.4852	0.0043	0	0.8363	0.8363	0.95
11	4000	30	8	0.3846	4.2142	15.0786	0.0049	0.2031	0.9554	0.9554	0.94
12	4000	30	10	0.5405	4.1716	14.9261	0.0038	0.48	1	1	0.96
13	4000	40	6	0.3571	4.6546	16.654	0.0092	0.1543	0.494	0.494	0.86
14	4000	40	8	0.5357	4.4983	16.095	0.0054	0.4714	0.6577	0.6577	0.93
15	4000	40	10	0.7143	4.5125	16.1458	0.0141	0.7886	0.6429	0.6429	0.77
16	4000	50	6	0.4167	4.7867	17.1267	0.0303	0.26	0.3557	0.3557	0.47
17	4000	50	8	0.625	4.5835	16.3999	0.0309	0.63	0.5685	0.5685	0.46
18	4000	50	10	0.8333	4.7994	17.1724	0.0444	1	0.3423	0.3423	0.21
19	5500	30	6	0.2703	4.3563	15.5868	0.0022	0	0.8065	0.8065	0.99
20	5500	30	8	0.4054	4.2725	15.2869	0.0016	0.24	0.8943	0.8943	1
21	5500	30	10	0.5405	4.4131	15.7901	0.0038	0.48	0.747	0.747	0.96
22	5500	40	6	0.3571	4.7668	17.0555	0.0016	0.1543	0.3765	0.3765	1
23	5500	40	8	0.5357	4.5978	16.4507	0.0038	0.4714	0.5536	0.5536	0.96
24	5500	40	10	0.7143	4.7824	17.1114	0.0049	0.7886	0.3601	0.3601	0.94
25	5500	50	6	0.4348	5.1219	18.326	0.0184	0.2922	0.0045	0.0045	0.69
26	5500	50	8	0.625	4.9244	17.6196	0.0227	0.63	0.2113	0.2113	0.61
27	5500	50	10	0.8333	5.1261	18.3413	0.0363	1	0	0	0.36

Table 3
Grey relational coefficient and grey reasoning grade.

Sl. No	DEVAIATION SEQUENCE				GREY RELATIONAL COEFFICIENT				Weighted Grey Relational Grade	Rank
	MRR	Surface Roughness (Ra) (μm)	Surface Roughness (Rz) (μm)	TWR	MRR	Surface Roughness (Ra) (μm)	Surface Roughness (Rz) (μm)	TWR		
1	1	0.1637	0.1637	0.14	0.3333	0.7534	0.7534	0.7813	0.655	11
2	0.74	0.0149	0.0149	0.16	0.4032	0.9711	0.9711	0.7576	0.900	3
3	0.52	0.061	0.061	0.19	0.4902	0.8912	0.8912	0.7246	0.836	5
4	0.8457	0.5744	0.5744	0.24	0.3715	0.4654	0.4654	0.6757	0.535	17
5	0.592	0.3869	0.3869	0.27	0.4579	0.5638	0.5638	0.6494	0.592	14
6	0.2114	0.6399	0.6399	0.33	0.7028	0.4386	0.4386	0.6024	0.493	19
7	0.74	0.8065	0.8065	0.81	0.4032	0.3827	0.3827	0.3817	0.382	25
8	0.4144	0.4926	0.4926	0.78	0.5468	0.5037	0.5037	0.3906	0.466	20
9	0	0.8333	0.8333	1	1	0.375	0.375	0.3333	0.361	27
10	1	0.1637	0.1637	0.05	0.3333	0.7534	0.7534	0.9091	0.805	7
11	0.7969	0.0446	0.0446	0.06	0.3855	0.918	0.918	0.8929	0.910	2
12	0.52	0	0	0.04	0.4902	1	1	0.9259	0.975	1
13	0.8457	0.506	0.506	0.14	0.3715	0.497	0.497	0.7813	0.592	15
14	0.5286	0.3423	0.3423	0.07	0.4861	0.5936	0.5936	0.8772	0.688	9
15	0.2114	0.3571	0.3571	0.23	0.7028	0.5833	0.5833	0.6849	0.617	13
16	0.74	0.6443	0.6443	0.53	0.4032	0.4369	0.4369	0.4854	0.453	21
17	0.37	0.4315	0.4315	0.54	0.5747	0.5367	0.5367	0.4808	0.518	18
18	0	0.6577	0.6577	0.79	1	0.4319	0.4319	0.3876	0.417	24
19	1	0.1935	0.1935	0.01	0.3333	0.721	0.721	0.9804	0.807	6
20	0.76	0.1057	0.1057	0	0.3968	0.8256	0.8256	1	0.884	4
21	0.52	0.253	0.253	0.04	0.4902	0.664	0.664	0.9259	0.751	8
22	0.8457	0.6235	0.6235	0	0.3715	0.445	0.445	1	0.630	12
23	0.5286	0.4464	0.4464	0.04	0.4861	0.5283	0.5283	0.9259	0.661	10
24	0.2114	0.6399	0.6399	0.06	0.7028	0.4386	0.4386	0.8929	0.590	16
25	0.7078	0.9955	0.9955	0.31	0.414	0.3343	0.3343	0.6173	0.429	23
26	0.37	0.7887	0.7887	0.39	0.5747	0.388	0.388	0.5618	0.446	22
27	0	1	1	0.64	1	0.3333	0.3333	0.4386	0.368	26

cient for MRR, TWR, SR1 and SR2 are contributions to the fuzzy framework. The phonetic participation work Extremely Low, Low, Medium, High and Exceptionally High are utilized to connote the grey relational coefficient of enter factors.

6. Taguchi analysis and ANOVA

The Taguchi L27 analysis is also done in this experiment and the result obtained is used to compare it with the experimentally

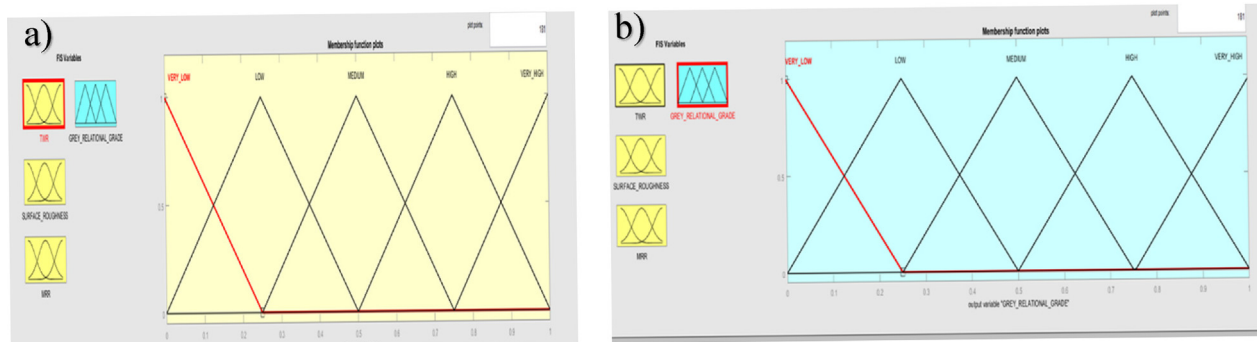


Fig. 4. Membership Functions Generation Using Mamdani Method a) Input Parameters b) Output Response.

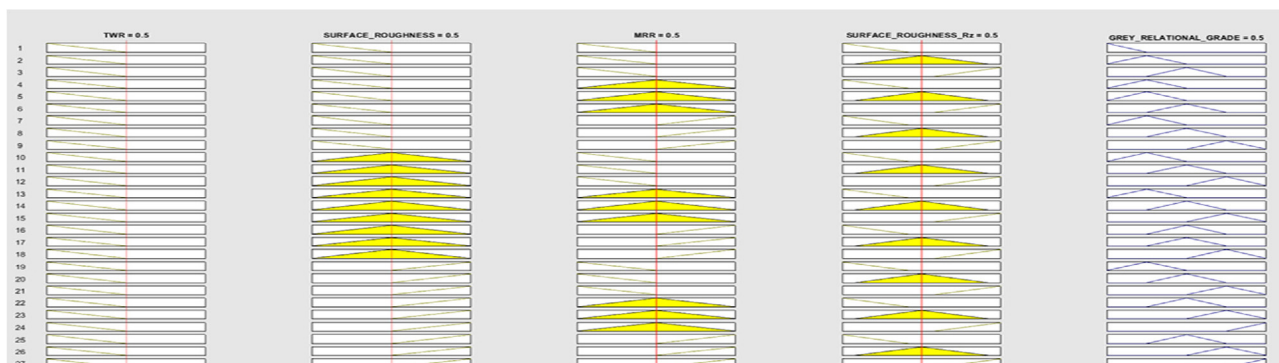


Fig. 5. Rule viewer for fuzzy system.

Table 4a

Response table for signal to noise ratios.

SET	SPINDLE SPEED	FEED RATE	DRILL DIA
1	−5.897	−4.260	−6.604
2	−5.133	−5.490	−5.090
3	−5.914	−7.194	−5.250
Delta	0.782	2.935	1.514
Rank	3	1	2

Table 4b

Response table for means.

SET	SPINDLE SPEED	FEED RATE	DRILL DIA
1	0.5749	0.7375	0.5424
2	0.6298	0.5792	0.6252
3	0.5964	0.4844	0.6335
Delta	0.0550	0.2531	0.0912
Rank	3	1	2

obtained result. The Table 4 shows the ratio of signal to noise and mean response table of Taguchi and this analysis gives that the better performance is obtained for the combination of parameters same as that obtained in fuzzy grey analysis.

The graphical representation of result is shown in Figs. 6 and 7, which shows that the parameters vary linearly with grey fuzzy coefficient. But non-linearity is present in practical situation due to external factors during the drilling CFRC composites. The error should be minimum in order to obtain the optimum performance. In Fig. 6 grade decreases linearly with increase in feed rate and increases with increase in drill diameter. But the spindle speed was varied non directionally.

7. Conclusion

The Coir Fibre Reinforced Composites (CFRC) was manufactured by hand layup method and it drilled by using CNC machine. The output parameters like tool wear rate, removal rate of material and surface roughness were measured during and after the drilling. Coming to the analysis side, in order to obtain the individually optimized drilling parameters, grey fuzzy analysis and Taguchi L27 methods were used. At conclusion, the optimized input parameters combination obtained for grey fuzzy analysis are: feed rate-30 mm/min, spindle axis speed-4000 RPM and drill diameter-10 mm. so we can conclude that, the output characteristics of CFRC composites are highly influenced by the input parameters like feed rate, spindle axle speed, and diameter of the drill. So, in order to obtain an optimum condition, this parameter should be optimized. Fuzzy analysis is the best method for machining parameter optimization because of its simplicity and fast response.

CRediT authorship contribution statement

Snobin Mathew: Writing – original draft, Conceptualization, Methodology, Software. **K. Shunmugesh:** Supervision, Writing – review & editing.

Data availability

Data will be made available on request.

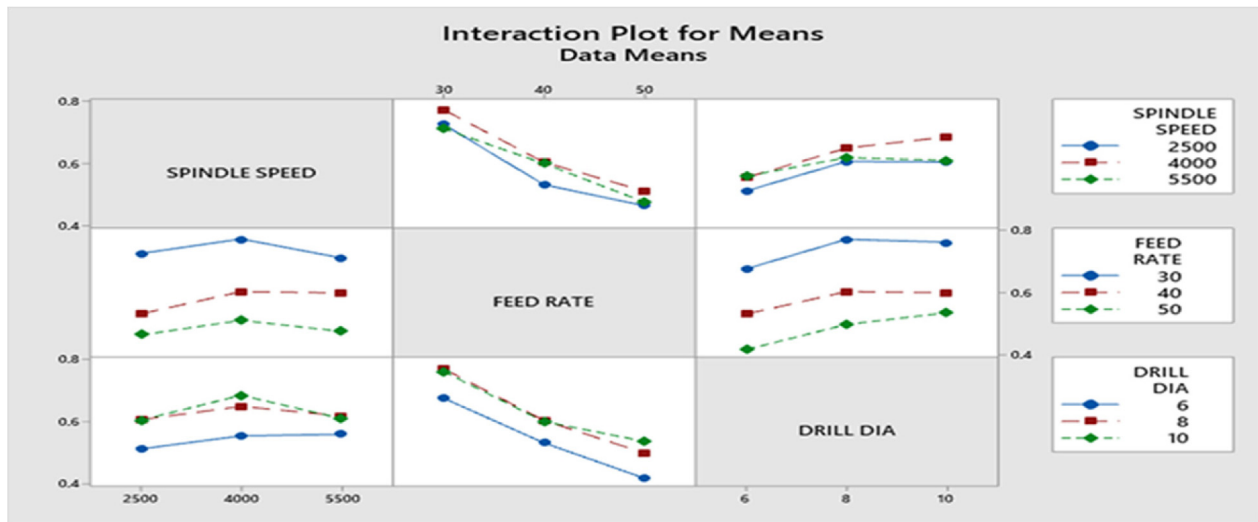


Fig. 6. Data Mean Grade Interaction Plot.



Fig. 7. Data Mean Grade Plot.

Declaration of Competing Interest

The authors declare that they have no known competing financial interests or personal relationships that could have appeared to influence the work reported in this paper.

References

- [1] A. Kumar, D. Saurav, S.S. Mahapatra, Multi- objective optimization in drilling of CFRP (polyester) composites: application of a fuzzy harmony search (HS) algorithm, *Meas.* 77 (2016) 222–239, <https://doi.org/10.1016/j.measurement.2015.09.015>.
- [2] G. Anand, N. Alagumurthi, K. Palanikumar, N. Venkateshwaran, R. Elansezhain, Influence of drilling process parameters on hybrid vinyl ester composite, *Mater. Manuf. Process* 33 (12) (2018) 1299–1305.
- [3] B. Latha, V.S. Senthilkumar, Modeling and analysis of surface roughness parameters in drilling GFRP composites using fuzzy logic, *Mater. Manuf. Process.* 25 (2010) 817–827, <https://doi.org/10.1080/10426910903447261>.
- [4] J. Xu, L. Zhou, M. Chen, F. Ren, Experimental study on mechanical drilling of carbon/epoxy composite-Ti6Al4V stacks, *Mater. Manuf. Process* 34 (2019) 715–725, <https://doi.org/10.1080/10426914.2019.1594275>.
- [5] S. Tom, J. Babu, P. Jose, Experimental studies on effect of process parameters on delamination in drilling GFRP composites using Taguchi method, *Proc. Mater. Sci.* 6 (2014) 1131–1142, <https://doi.org/10.1016/j.mspro.2014.07.185>.
- [6] G.Z. Keh, C.L. Tan, W.M.M. Irina, A.I. Azmi, K.W. Leong, M.N.M. Radzi, Delamination analyses of GFRP composites under high speed conditions and various drill geometries, *Adv. Mater. Res.* 1133 (2018) 126–130.
- [7] K. Dhiraj, K.K. Singh, Z. Redouane, Experimental investigation of delamination and surface roughness in the drilling of GFRP composite material with different drills, *Adv. Manuf. Polym. Compos. Sci.* 2 (2) (2016) 47–56, <https://doi.org/10.1080/20550340.2016.1187434>.
- [8] A. Krishnamoorthy, S.R. Boopathy, K. Palanikumar, J.P. Davim, Application of grey fuzzy logic for the optimization of drilling parameters for CFRP composites with multiple performance characteristics, *Meas.* 45 (2012) 1286–1296, <https://doi.org/10.1016/j.measurement.2012.01.008>.
- [9] C.C. Tsao, Y.C. Chiu, Evaluation of drilling parameters on thrust force in drilling carbon fiber reinforced plastic (CFRP) composite laminates using compound core-special drills, *Int. J. Mach. Tools. Manuf.* 51 (2011) 740–744, <https://doi.org/10.1016/j.ijmachtools.2011.05.004>.
- [10] D. Kumar, K. Singh, An approach to damage free composite machining: a review, *Adv. Compos. Mater.* 24 (2015) 49–63, <https://doi.org/10.1080/09243046.2014.928966>.
- [11] R.A. Kishore, R. Tiwari, P.K. Rakesh, I. Singh, N. Bhatnagar, Investigation of drilling in fibre-reinforced plastics using response surface methodology, *Proc. IMechE Part B: J. Eng. Manuf.* 225 (2011) 453–457, <https://doi.org/10.1177/2041297510394051>.
- [12] K.V. Vinod, G. Venkateswarlu, Optimization of process parameters in drilling of GFRP composite using Taguchi method, *J. Mater. Res. Technol.* 3 (1) (2014) 35–41, <https://doi.org/10.1016/j.jmrt.2013.10.007>.
- [13] K. Shunmugesh, K. Panneerselvam, Optimization of machining process parameters in drilling of CFRP using multi-objective Taguchi technique,

- TOPSIS and RSA techniques, Polym. Compos. 25 (3) (2017) 185–191, <https://doi.org/10.1177/096739111702500301>.
- [14] G. Anand, N. Alagumurthi, R. Elansezhian, K. Palanikumar, N. Venkateshwaran, Investigation of drilling parameters on hybrid polymer composites using grey relational analysis, regression, fuzzy logic and ANN models, J. Braz. Soc. Mech. Sci. Eng. 214 (2018) 1–20, <https://doi.org/10.1007/s40430-018-1137-1>.
- [15] C.L. Tan, A.I. Azmi, N. Muhammad, Delamination and surface roughness analyses in drilling hybrid carbon/glass composite, Mater. Manuf. Process 31 (2016) 1366–1376, <https://doi.org/10.1080/10426914.2015.1103864>.
- [16] A. Madhan Kumar, K. Jayakumar, Mechanical and drilling characterization of biodegradable PLA particulate green composites, J. Chin. Inst. Eng. 45 (5) (2022) 437–452, <https://doi.org/10.1080/02533839.2022.2061602>.



Artificial intelligence based tool condition monitoring for digital twins and industry 4.0 applications

Padmakumar Muthuswamy¹ · Shunmugesh K²

Received: 5 July 2022 / Accepted: 15 September 2022

© The Author(s), under exclusive licence to Springer-Verlag France SAS, part of Springer Nature 2022

Abstract

The high demand for machining process automation has placed real-time tool condition monitoring as one of the top priorities of academic and industrial scholars in the past decade. But the presence of numerous known and unknown machining variables and challenging operating conditions such as high temperature and pressure makes it a daunting task. However, recent advancements in sensor and digital technologies have enabled in-process condition monitoring and real-time process optimization a highly accurate, robust, and effective process. Hence, the objective of the article is to provide a summary of the factors influencing the performance of cutting tools, critical machining variables to be monitored, techniques applied to monitor tool conditions, and artificial intelligence algorithms used to predict tool performance by analyzing and reviewing the literature. The future direction of intelligent cutting tools and how they would help in building the foundation for advanced smart factory ecosystems such as digital twins and Industry 4.0 are also discussed.

Keywords Condition monitoring · Smart factory · Intelligent cutting tools · Digital twins · Sensors · Automation · Industry 4.0 · Artificial Intelligence

Nomenclature

MRR	Material Removal Rate
PVD	Physical Vapor Deposition
CVD	Chemical Vapor Deposition
CBN	Cubic Boron Nitride
PCD	Polycrystalline Diamond
MQL	Minimum Quantity Lubrication
OEE	Overall Equipment Effectiveness
DSA	Dynamic Signal Analyzer
FFT	Fast Fourier Transform
SVM	Support Vector Machine
HMM	Hidden Markov Model
RBF	Radius Basis Function
BPNN	Back Propagation Neural Network

ANN	Artificial Neural Networks
PCBN	Polycrystalline Cubic Boron Nitride
CNN	Convolutional Neural Network
FL	Fuzzy Logic
AISI	American Iron and Steel Institute
RA	Regression Analysis
AI	Artificial Intelligence
DTA	Decision Tree Algorithm
DFT	Discrete Fourier Transform
RF	Random Forest
DC	Direct current
CNC	Computer Numerical Control
GA	Genetic Algorithm
RMS	Root Mean Square
RDC	Ring-Down Count
BPNN	Back Propagation Neural Network
CCD	Charged Coupled Device
CMOS	Complementary Metal-Oxide Semiconductor
HMM	Hidden Markov Model
PCA	Principal Component Analysis
ANFIS	Adaptive Neuro-Fuzzy Inference System
RVM	Relevance Vector Machine
ELM	Extreme Learning Machines
NN	Neural Networks

✉ Padmakumar Muthuswamy
mpadmakumar86@gmail.com

Shunmugesh K
shunmugesh@gmail.com

¹ Technology Centre (KSSPL GES), Kennametal India Ltd,
560073 Bangalore, India

² Department of Mechanical Engineering, Viswajyothi College
of Engineering and Technology, 686670 Kochi, India

CNN	Convolution Neural Networks
RNN	Recurrent Neural Networks
GLCM	Gray-Level Co-occurrence Matrix
IoT	Internet of Things

1 Introduction

Machining is a traditional manufacturing process in which a hard tool is used to remove material from a relatively softer workpiece in the form of chips. Although the process seems simpler, multiple complex events such as shearing, ploughing, rubbing, and elastic and plastic deformation simultaneously occur at the tool-chip interface from the moment the tool starts engaging with the workpiece [1]. In addition, high temperature and pressure at a very small region make it highly difficult to observe the cutting zone. Hence, monitoring the condition of a cutting tool and predicting its behaviors is a challenging process. But observing the cutting zone to precisely evaluate the operating temperature, pressure, and stress that acts on the tool and fluctuations in their value is important to analyze and forecast the life of the tool.

In metal cutting, the relative motion of the cutting tool over the workpiece to remove material also results in friction which induces tool wear. As machining progresses, the degradation of tool properties due to high temperature, friction, and pressure at the interface region of the tool and chip further accelerate the wear rate. It results in frequent tool replacement and can lead to sudden failure of the tool that can damage the workpiece and make the other cutting edges unusable. In addition, using a worn tool negatively affects the surface finish and dimensional accuracy of the workpiece. Currently, changing the tool at the end of its life is performed by the machine operator mostly based on experience or through the knowledge gained by performing trial runs. But predicting the tool change time while machining a variety of parts that are made of different types of materials is nearly impossible. Hence an effective condition monitoring system is required to predict tool life to factor in the dynamically changing work environment to improve productivity and eliminate scrapping of expensive workpiece components. In general, the three major objectives to monitor the conditions of cutting tools are the accurate prediction of the end of tool life to avoid unplanned downtime, compensating cutting parameters to maintain machining accuracy, and preventing sudden tool failure to avoid workpiece scrapping [2].

Generally, the direct (or offline) and indirect (or online) tool condition monitoring techniques are used to measure the wear rate and predict the end of tool life [3]. In the direct technique, typically, the tool is removed from the machine and the wear rate is observed using an optical microscope

[4], while different types of sensors signal outputs such as temperature, forces, power, and vibration are used in the indirect techniques [5]. Radioactivity and electrical resistance method are other direct measurement techniques reported in the literature. Although the direct method is time-consuming and affects productivity, it can provide accurate data on the wear rate. In addition, it also gives additional insight into the type of wear and prominent wear mechanism which can be used to develop new tools and coatings with superior performance. However, the major advantage of developing a condition monitoring technique is the possibility of automating the machining process and dynamically controlling the parameters to get the required machining qualities. Besides, the recent trend to support Industry 4.0 setup such as intelligent automation, digital twins, and smart factory ecosystem has resulted in manufacturing industries looking for an advanced manufacturing solution that can assist in error-free decision making which brings up the following questions,

- Q1. What are the techniques used in condition monitoring of cutting tools?
- Q2. How does Artificial Intelligence benefit condition monitoring of cutting tools?
- Q3. How condition monitoring and Artificial Intelligence can transform traditional manufacturing into a smart factory ecosystem?

Hence, the objective of the investigation is to answer the research queries by scrutinizing, evaluating, and organizing the literature. A narrative or descriptive review approach was followed. The Sect. 1 introduces the subject and lists the research questions to be addressed. The Sect. 2 covers the fundamentals of metal cutting such as factors influencing tool life and tool performance. The answers to the research queries Q1, Q2, and Q3 are addressed through Sects. 3, 4, and 5, respectively. The key takeaway and future direction of the research area are summarized in Sect. 6, and the article concludes with Sect. 7.

2 Factors influencing tool life

Although the term “tool life” has various definitions, in general, it can be described as the amount of time a cutting tool can be utilized effectively and efficiently. Flank wear is the commonly seen wear in metal cutting. The uniform scar-like pattern that is formed on the flank of the tool below the main cutting edge is the flank wear, while the wear pattern on the flank seen below the corner radius (or nose) is the nose wear [6]. Friction and abrasive action between the tool and workpiece cause flank and nose wear. Crater wear is another

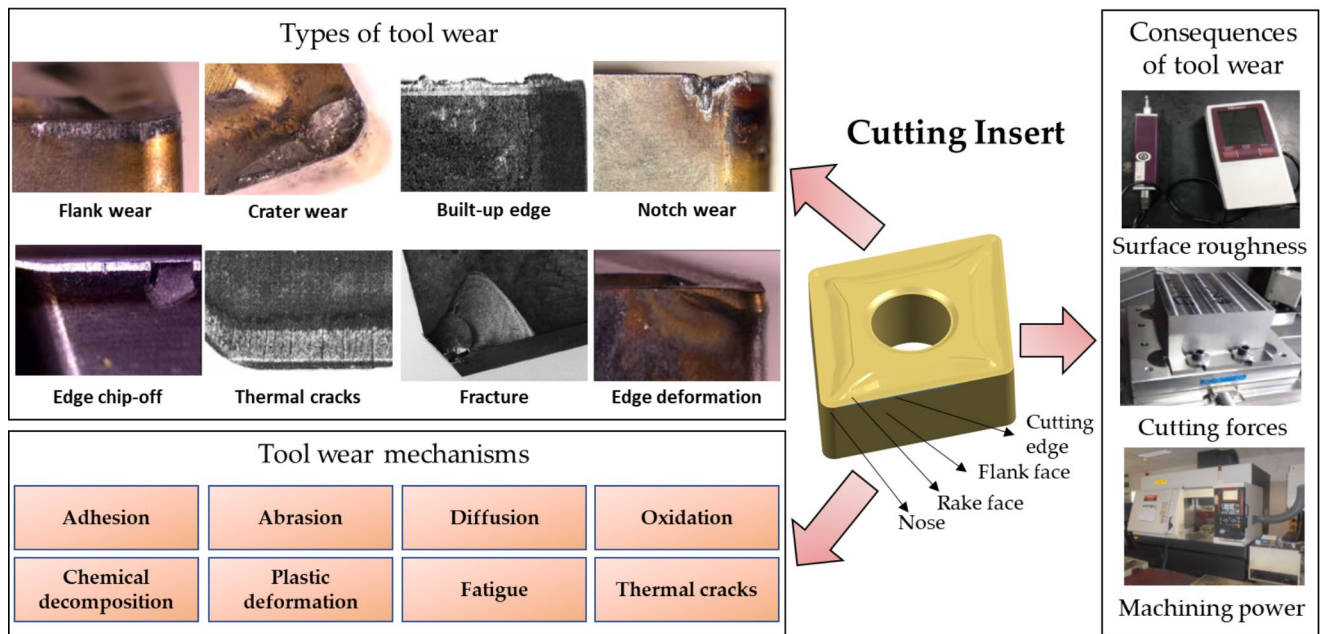


Fig. 1 Tool wear and its consequences

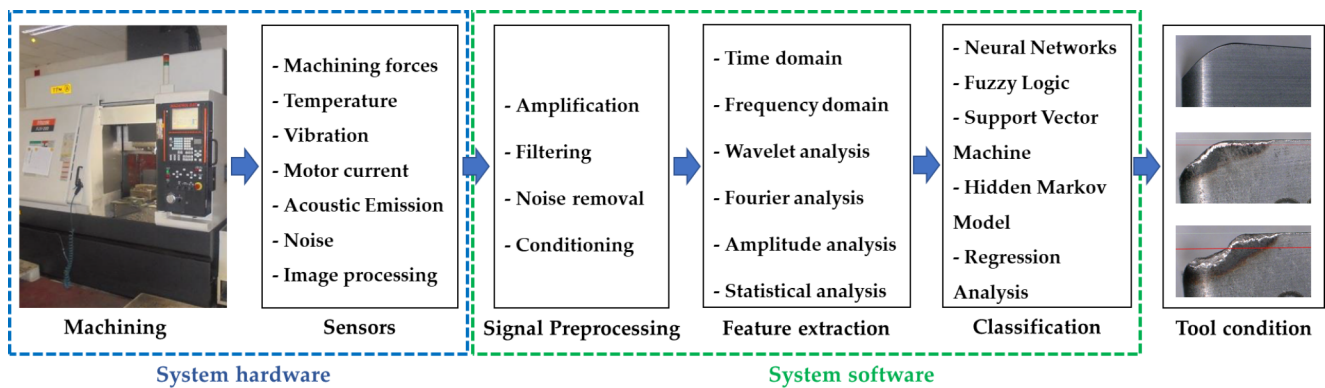


Fig. 2 Various stage of tool-condition monitoring system

major wear type that is formed primarily due to the continuous flow of chips over the tool rake face which results in abrasion and appears like a scooped surface on the rake side of the tool [7]. Although a tool also experiences other types of wear such as notch wear, built-up-edge, micro-chipping, thermal cracks, and thermal deformation, the most common wear types are flank, nose, and crater wear. However, irrespective of the type of wear, it is important to continuously monitor tool life to get the required machining accuracy on the workpiece. The life of a tool predominantly depends on important factors such as cutting parameters (cutting speed, feed, and depth of cut), tool geometry, tool material, workpiece material, and coolant usage. Hence, for efficient tool condition monitoring, it is crucial to understand the effect of these factors on the machining condition and the type of signals that the variation in each factor would send out.

Additionally, as the influence of these factors is similar for all the three major machining operations such as turning, milling, and drilling, a thorough knowledge of it helps in building a flexible condition monitoring system that can be used for all metal cutting operations. The types of tool wear, wear mechanism, and the consequences of tool wear are illustrated in Fig. 1.

2.1 Cutting parameters

The relative velocity between the tool and workpiece is the cutting speed. In other words, it can be stated as the speed at which the workpiece moves past the cutting edge and is usually measured in meters per minute (m/min). In turning the tool remains stationary, and the rotation of the workpiece is measured as the cutting speed, while in milling and drilling

(although a stationary tool is used if drilling is performed in a lathe) usually the workpiece is stationary, and the rotation of the tool is measured as the cutting speed. Generally, the selection of cutting speed is a function of tool and work material. However, irrespective of the tool or work material, operating the tools at high cutting speeds increase the temperature at the tool-chip interface as the time available to dissipate heat away from the cutting zone (primary and secondary shear zone) is reduced [8]. A high heat concentration at the cutting zone has a negative effect on the tool life. Especially, this behavior is highly evident in machining work materials with low thermal conductivity such as titanium and nickel-based alloys that are typically machined at low cutting speeds [8, 9]. However, high cutting zone temperature also tends to soften the work material and allows easy penetration of the tool into the workpiece which reduces the cutting forces and improves the tool stability [8]. Tools made of ceramic materials that have exceptional hot hardness, chemical inertness, and wear resistance properties make use of this work-softening effect and operate at high cutting speeds which improves machining productivity. As a rule of thumb, increasing the cutting speed by 20% decreases the tool life by around 50%, while increasing it by 50% results in an 80% reduction in tool life. However, operating the tool at a very low cutting speed results in chatter which can also drastically reduce the performance of a tool. Hence it is critical to operate the tools at optimum cutting speed to improve its life.

The velocity at which the tool is advanced into the workpiece is the feed rate. It is commonly measured in millimeters per revolution (mm/rev) in the case of turning and drilling, and millimeters per tooth (mm/tooth) in milling. An increase in the feed rate increases the chip thickness and material removal rate which results in higher cutting forces and power consumption [10–12]. Cutting speed and feed have a significant influence on the surface roughness and the quality of the machined surface [10–15]. Studies have shown that with the higher feeds, there is an increasing trend in the surface roughness values (lower the better) which is predominantly due to the formation of wider and deeper surface peaks on the workpiece [1, 8, 10, 11]. However, increasing the cutting speeds reduces the surface roughness as the lower cutting forces (due to the high cutting zone temperature that softens the work material) give marginally better stability to the tool. Using a low feed rate results in higher friction between the tool and workpiece which reduces the tool life. Hence it is always recommended to operate the tool at a feed rate that is larger than the size of the edge hone radius.

The perpendicular distance from the surface of the workpiece to the uncut surface up to which the tool penetrates is the depth of cut. Generally, it is measured along the axis

of the tool (also called axial depth of cut) and determines the length of the cutting edge that engages with the workpiece. However, in milling, additionally, the engagement of the tool along the radial direction is also measured which is termed as the radial depth of cut. Increasing the depth of cut increases the amount of material removed (Material Removal Rate or MRR) which results in higher machining power and forces. Besides, it is the third significant factor next to cutting speed and feed that affects the tool life and surface roughness [12]. Studies have shown that increasing the cutting speed and feed negatively affects tool life and surface finish. In addition, apart from influencing the cutting forces, it affects vibration, noise, and cutting zone temperature which can also lead to catastrophic breakage of the tool. Hence selecting an optimum cutting parameter is critical to improving the overall machinability.

2.2 Tool geometry

The cutting tool geometry has a major influence on the forces, temperature, chip formation, and tool life and can be classified into micro and macro geometries [1]. Micro-geometry refers to the shape of the cutting edge that is formed between the flank and rake face of a cutting tool. The micro-geometry increases the strength and stability of the cutting edge and prevents it from chip-off and sudden breakage [10]. Hone radius, T-land or chamfer, and a combination of hone and chamfer are the micro-geometries that are typically provided to a cutting edge [1, 16]. Studies have shown that in addition to micro-geometry, the symmetry of the cutting-edge hone radius (K-factor) also shows a major role in influencing the quality of machined surface, machining power, and cutting forces [11, 17]. In addition, reducing the area of contact between the tool and workpiece results in lower cutting forces and machining power due to lower friction and reduced resistance to tool motion [18]. The macro-geometry of a tool denotes the other geometrical features such as shape, profile, tool nose radius, rake angles, and clearance angle [1]. Typically, tools with sharp or smaller hone radii result in lower cutting forces as the tool penetrates the workpiece with ease. However, it also results in a weaker cutting edge that is prone to chip-off or breakage. In addition, the macro-geometrical features also have a significant influence on the magnitude and direction of forces. Hence an optimum micro and macro geometry must be selected based on the work material and the operating conditions to improve the performance of the tool.

2.3 Tool material

The type of material and its composition determine the critical properties of a tool such as hardness, toughness,

compressive strength, hot hardness, chemical inertness, fracture toughness, and wear resistance. Each of these properties holds a notable impact on the life of the tool. In general, a tool with higher hardness has superior wear resistance which in turn gives higher tool life. However, lack of toughness could result in sudden breakage of the tool, especially while machining parts with irregular surfaces or interruptions. Carbon steel was one of the most popular tool materials during the pre-world war industrial era which later gave rise to alloy steels and tool steels. But currently, tungsten carbide has almost replaced them as the preferred material in cutting tool manufacturing due to its superior hardness and toughness [19]. Based on the work material, as a tool with optimum hardness and toughness is required, the tool material is alloyed with suitable additives (mixed carbide) to get other required properties. In addition, to address some of the complex machining requirements, tools with a tougher base material and harder coatings such as PVD or CVD coated tungsten carbide tools are also used. However, as super-hard materials such as ceramics, CBN (Cubic Boron Nitride), and PCD (Polycrystalline Diamond) tools have higher hardness and thermal resistance than tungsten carbide, they give relatively longer life to the tool and can be operated at elevated cutting parameters.

2.4 Workpiece material

Apart from cutting parameters and tool condition, the life of a cutting tool is also influenced by the chemical composition, alloying elements, microstructure, and mechanical properties of the workpiece. Generally, machining a harder work material requires a stronger geometry such as rounded or chamfered cutting edge, while a sharper edge (low edge hone radius) is preferred to machine softer work material. The resultant friction due to the relative motion between the tool work material and the abrasive action due to the flow of chips over the tool results in wear. In addition, the work material with low thermal conductivity (as the generated heat remains at the tool-chip interface) and strain hardening properties (as the strength of the material increases due to machining-induced plastic deformation) negatively influences tool life and increases cutting force and machining power which requires a different machining strategy [10]. Similarly, materials such as titanium alloys, tool steels, stainless steels, hardened steels, and other super-alloys are categorized as difficult-to-cut materials as they promote rapid tool wear, higher machining forces, higher cutting power, and specific cutting energy which reduces their machinability.

2.5 Coolant condition

Usage of coolant is another critical factor that impacts tool life. Excessive heat on the cutting edge tends to weaken the tool material and accelerate the wear rate [20–22]. Applying coolant while machining reduces the temperature at the cutting zone and removes heat from the cutting edge. Thermally induced wear mechanisms such as thermal cracks and cutting-edge deformation are some commonly seen wear mechanisms if no or inadequate coolant is used. In addition, coolant also acts as a lubricant that reduces friction between the tool and workpiece [20]. Studies have shown that different coolant techniques such as high-pressure coolant, Minimum Quantity Lubrication (MQL), and cryogenic coolant can increase the tool life by many times.

Literature studies show that there is no one tool to solve all the machining-related challenges. However, optimizing the cutting parameters, selecting tools with appropriate microgeometry, optimum rake angles, application of coolant, and coated tools can assist in overcoming most of the challenges. Nevertheless, irrespective of the type of tool, work material, or machining parameters, a worn tool or a tool that is nearing the end of life would always show certain characteristics such as variation in the forces, power consumption, vibration, or noise that can be analyzed for the condition monitoring of tools which are discussed in the following sections.

3 Condition monitoring of cutting tools

Condition monitoring refers to the process of studying the variation in the behavior of tools to predict the potential fault developing in the system and is the first step in predictive and preventive maintenance. Studies have shown that unscheduled machine maintenance can significantly reduce the Overall Equipment Effectiveness (OEE) of production units which can lead to revenue loss and poor product quality [23]. Hence condition monitoring techniques can be used to find information on machine health, efficiency, downtime, and wear and tear of parts, which can help in improving maintenance strategies and OEE. The stages of a tool condition monitoring system are shown in Fig. 2. By studying the various tool or machine signals that are sent out during machining such as a sudden increase in noise, vibration, or power consumption, an experienced machine operator can easily identify if the tool has reached the end of life. However, with the increased demand to automate the manufacturing processes, advanced sensors are embedded on the tool to precisely capture these signals, analyze them online, and send corrective actions to improve the performance of the tool.

Usually, a Dynamic Signal Analyzer (DSA) is used to process the digital signals. Compared to general data acquisition and time domain analysis, a DSA focuses on the dynamic aspect of the signals such as frequency response, dynamic range, total harmonic distortion, phase match, and amplitude flatness [24] by using various technologies for processing the digital signal. Among them, the most fundamental and popular technology is Fast Fourier Transform (FFT) which is used to transform the time domain signals into the frequency domain to identify vibration peaks with less computational efforts and complexities. It is the standard and most applied frequency analysis technique for fault diagnosis and an FFT-based spectrum analyzers are commonly used to measure low-frequency or mechanical vibration. In FFT analyzer, the technique used in processing of the vibration signal plays a key role in successful vibration analysis of machines. Spectrum analysis based on FFT is the basis of traditional signal analysis [25]. By analyzing the frequencies and their harmonics, the source of vibration and the type of problem, and even its root cause can be identified. The benefit of FFT is its speed, which it gets by decreasing the number of calculations needed to analyze a waveform. However, its disadvantage is the restricted range of waveform data that can be transformed and the need to apply a window weighting function to the waveform to compensate for spectral leakage [26]. The disadvantage can be overcome by using Discrete Fourier Transform (DFT) but with a compromise on the speed. The various signals that give the precise condition of the tool and their interpretations are discussed in the following sections.

3.1 Machining forces

The forces generated in machining is a combination of tangential, radial, and axial force components that are measured with reference to the cutting tool. The force that acts along the axis of the tool is the axial force, while the force that acts on the cutting edge and tangent to the tool is the tangential force. The radial force acts at right angles to the tangential force. As a rule of thumb tangential force is usually the maximum of the three, followed by radial and axial force. However, the magnitude and direction of the force changes based on the machining operation and the tool's micro and macro-geometry. Any slight variation in the cutting conditions such as changes in cutting parameters [27], micro-geometry, macro-geometry, and tool wear has a major influence on the forces [28]. However, in an industrial machining condition, as constant cutting parameters and machining conditions are usually used throughout the machining process, any differences in the forces can be associated to wear and the rate of wear can be accurately measured using a strain-gauge

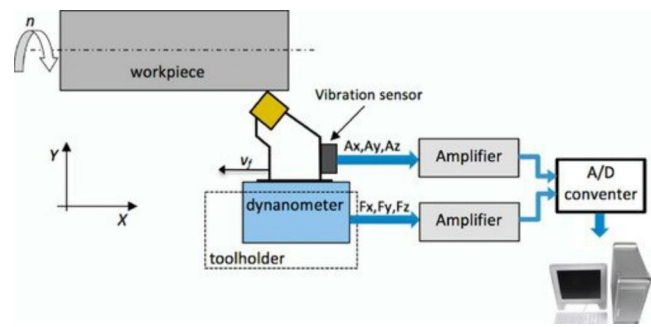


Fig. 3 Schematic of force and vibration measurement setup in turning [34]

or piezoelectric dynamometer. The schematics of force and vibration measurement in turning is shown in Fig. 3.

A tool with a sharp or keener edge produces lower forces as shearing of work material happens with ease. But gradually the tool starts losing its sharpness which increases the cutting forces and induces stress on the tool and workpiece [29]. Higher cutting-edge stress leads to micro-chip-off, edge fracture, and premature tool wear [9]. Hence, by continuously monitoring the cutting force, the wear rate of the tool and breakage can be predicted accurately [30]. Nouri et al. [31] have developed a technique to monitor the real-time tool wear in end mills by measuring the forces. They have observed that any changes in the tool geometry due to higher wear or edge chipping results in variation in the wear parameter which is a function of tangential and radial forces. By conducting experiments on various materials, they have proved that it is possible to track tool wear in real-time. Using Support Vector Machine (SVM), Hidden Markov Model (HMM), and Radius Basis Function (RBF) algorithms as base classifiers, Wang et al. [32] have predicted the tool wear using force sensors in machining titanium alloy with more than 99% accuracy.

Similarly, using Back Propagation Neural Network (BPNN), Özel and Nadgir [33] have successfully developed a model to predict flank wear of CBN cutting tools based on dynamometer forces and concluded that flank wear is highly sensitive to cutting forces. Twardowski and Wiciak-Pikuła [34] have monitored cutting forces and vibration signals and used Artificial Neural Networks (ANN) to measure tool wear in turning and have reported that wear prediction based on cutting force components showed slightly better accuracy than using vibration signals. In a similar study, Wang et al. [35] have used the SVM regression algorithm and monitored forces and vibration to develop a virtual tool wear sensing model. While most of the studies were focused on measuring the tool wear rate, Cho et al. [36] have used a dynamometer to measure cutting forces and correlated them with spindle power and developed a tool breakage detection technique using the SVM algorithm. They have reported a

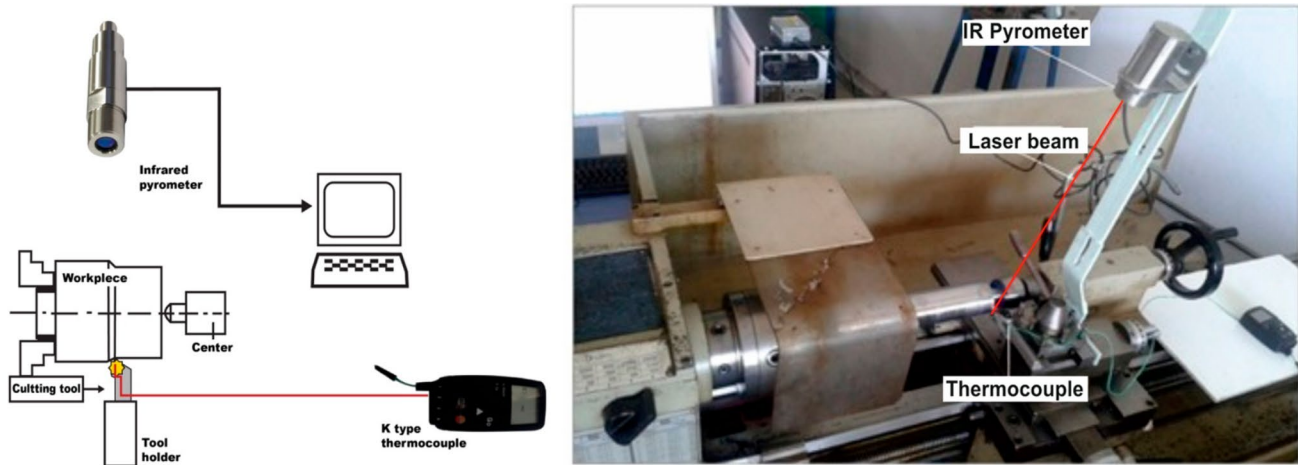


Fig. 4 Temperature measurement using thermocouple and IR pyrometer [43]

75% accuracy in the breakage prediction using force measurement technique while combining it with spindle power gave an accuracy of around 99%. From the literature, it can be safely concluded that cutting forces increases with an increase in tool wear, and a sudden surge in the force is a commonly observed behavior before tool breakage.

3.2 Temperature

Machining is the process of removing unwanted material from the workpiece in the form of chips using a sharp cutting tool. In metal cutting, heat generation happens at the primary shear zone due to deformation of the material, secondary deformation zone at which the material is sheared and pulled away, and due to friction between the tool and workpiece which creates an enormous amount of heat at the tool-chip interface zone (cutting zone). The cutting zone temperature is a critical factor in machining that plays a major role in determining wear rate, tool life, and surface quality of the machined surface [37]. In addition, a high cutting zone temperature also affects residual stress, hardness, and surface roughness of the workpiece [16]. Machining parameters such as cutting speed, feed, depth of cut, and usage of coolant, property of work material such as hardness, and microstructure, and tool conditions such as micro and macro geometry of the tool and the thermal conductivity of tool and workpiece influences cutting zone temperature [38]. Several studies have shown that increase in the machining parameters rises the temperature at the tool-chip interface which lowers the tool life significantly [39, 40]. Additionally, using different coolant strategies to remove heat from the cutting zone can extend the tool life by many folds [21, 22, 41, 42]. Such studies show the importance of temperature measurement to predict tool life accurately. A temperature measurement setup in turning using both

thermocouple and infrared (IR) pyrometer used by Kus et al. [43] is shown in Fig. 4.

Inserted thermocouples, tool-workpiece thermocouples, embedded thermocouples, infrared radiation methods, thermo-sensitive paints, and metallurgic techniques to study variation in microstructure or hardness are some of the popular techniques used in temperature measurements [44]. Kulkarni et al. [45] studied the correlation between cutting parameters and cutting temperature in machining AISI 304 stainless steels using a tool-work thermocouple. They have reported that tool-chip interface temperature increases for an increase in cutting speed and feed rate. Jiang et al. [46] developed a cutting temperature model to predict tool and workpiece temperature in interrupted cutting. By conducting validation testing on 1045 steel using thermocouples to continuously monitor the temperature on the tool and workpiece they have reported a good agreement between the actual and predicted temperature. A thin film thermocouple embedded PCBN cutting tool was used by Li et al. [47] for the real-time monitoring of tool wear in turning AISI O2 tool steel. Apart from the correlation between the variation in cutting zone temperature and the dynamometer forces they have reported that increasing the feed and depth of cut increases the cutting temperature. An increase in the flank wear and maximum cutting temperature was also observed when the cutting time was increased, and a significant increase in the temperature was seen after tool chip-off. Using infrared thermography, machine vision, and Convolutional Neural Network (CNN) techniques, Brili et al. [48] have monitored wear on turning tools by taking thermographic images of inserts immediately after machining and classified it into no, low, medium, high wear with an accuracy of more than 96%. Kuntoğlu and Sağlam [49] performed a Fuzzy Logic (FL) based study to compare the effectiveness of acoustic emission, current, temperature,

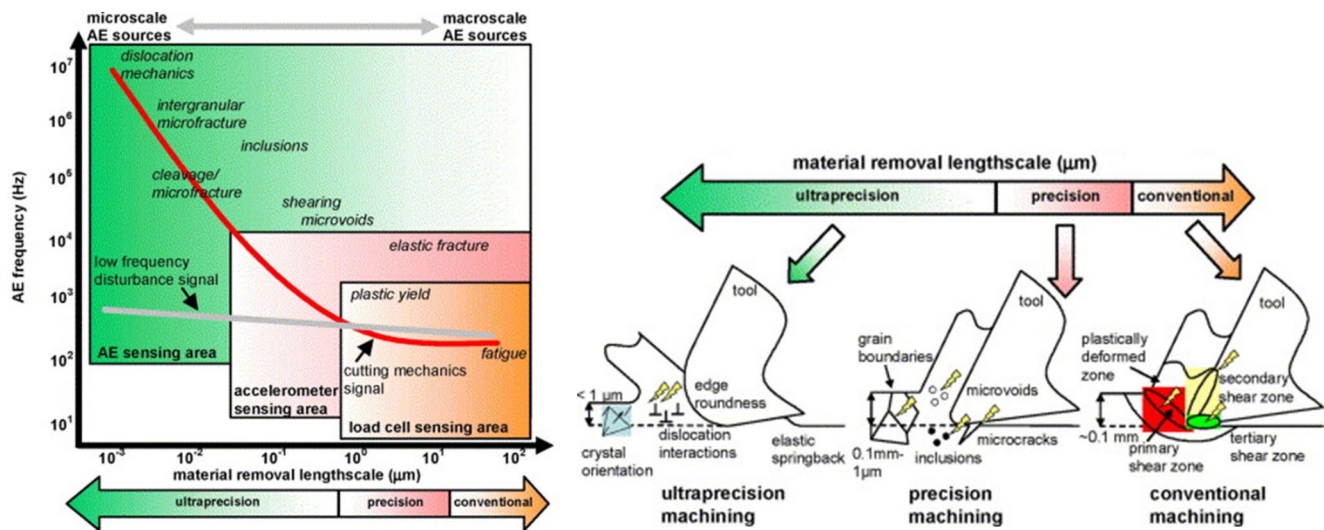


Fig. 5 Sources of AE in metal cutting [75]

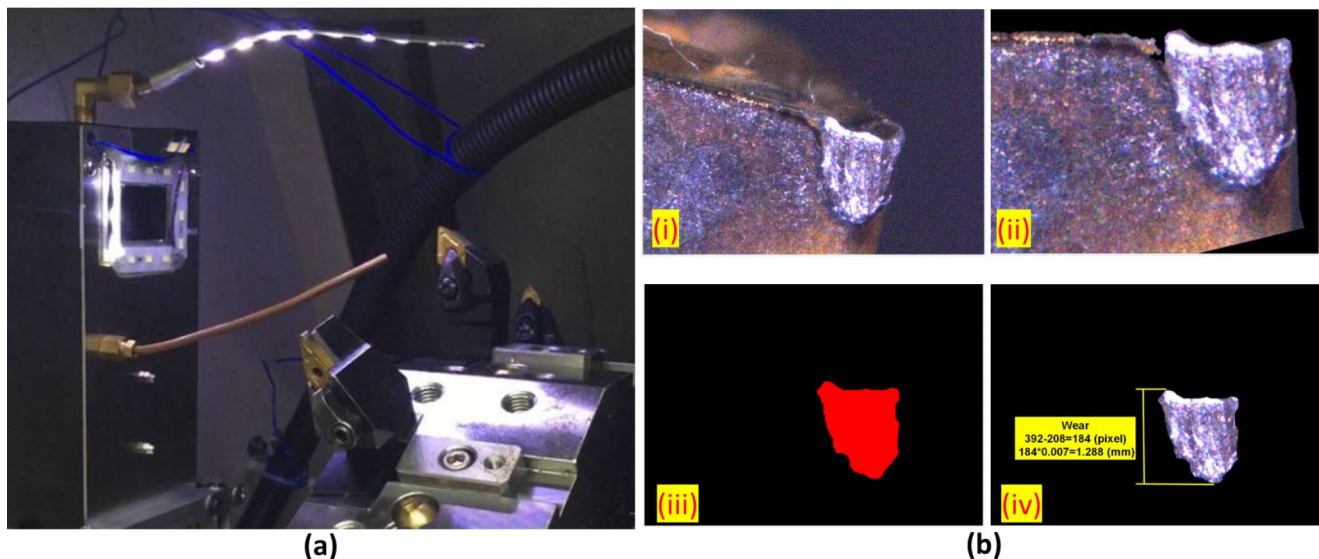


Fig. 6 (a) Vision based condition monitoring system and (b) key stages of image processing [94]

force, and vibration signals in predicting flank wear in dry turning of AISI 5140. They have concluded that acoustic emission and temperature signals showed good correlation in predicting flank wear than the other techniques. Korkut et al. [50] have compared the tool temperature measured using K-type thermocouple and prediction based on Regression Analysis (RA) and ANN models for various cutting parameters in turning. They have reported that the prediction accuracy of AI algorithms is accurate to the experimental values.

3.3 Vibration

Vibration is a commonly observed but undesirable phenomenon in machining that occurs due to the dynamic motion

of the tool over the workpiece. The most common sources of vibration in machining are poor machine rigidity, weak fixturing, irregularities in the workpiece, broken or worn tools, and operating the tool at unrecommended cutting parameters. Studies have also shown that the variation in chip thickness due to differences in the engagement of tool and workpiece at the entry, middle, and exit also influences vibration [14]. Reduction in tool performance, poor surface finish, high noise, rapid tool wear, and sudden breakage of the tool are the consequences of vibration in machining. Hence, monitoring the vibration signals using an accelerometer sensor is one of the widely used techniques to get an insight into the tool condition. In metal cutting, independent vibration occurs due to machine and machine components,

while the dependent vibration is a function of the machining process itself. Chatter is another commonly seen phenomenon that occurs in machining due to the harmonic imbalance between the tool and workpiece [51].

Generally, the amplitude of vibration increases if the tool wear increases which can be used to monitor and predict tool life. Identification of the right frequency range for the rate of tool wear is the main challenge in predicting tool wear using vibration signals. Previous studies show the frequency range of a typical machining operation is in the range of 0 to 8 kHz [52]. However, the right frequency range that is sensitive to the tool wear must be established based on the tool and work condition to accurately predict tool wear. Jiang et al. [53] have divided the vibration frequency signals into different segments through which the various stages of wear progression including micro-breakage can be predicted. Krishnakumar et al. [54] have used a drilling tool mounted with a 3-axis accelerometer sensor for continuous monitoring of tool wear and Decision Tree Algorithm (DTA) and ANN to classify tool wear. They have reported that the prediction accuracy of both the algorithms in correlating the condition of drill and vibration signals was around 95%. By conducting a turning study using vibration and force measurement sensors, Dimla and Lister [55] reported that the tangential force and vibration signals are highly sensitive to the tool wear. They have applied time series and FFT algorithm to analyze force and vibration signals and correlate it to tool wear monitoring. A tool with larger wear experiences higher frictional forces which increases the vibration amplitudes [56]. Rao et al. [57] have used vibration signals measured using laser Doppler vibrometer in milling Ti-6Al-4 V to predict tool wear and surface roughness. They have reported that the prediction accuracy of Grey Prediction Model GM (1, N) was higher than SVM. The AI algorithms such as ANN, FL, and RA require a large volume of training data and it is not possible to add or delete the old data, whereas the GM (1, N) models allow it. Patra et al. [58] have used a three-axis accelerometer to capture vibration signals in drilling and used ANN models to predict tool life in terms of the number of holes drilled. Ghani et al. [59] have reported lower vibration at higher cutting speeds and the magnitude of the vibration is higher in the direction of the main cutting force rather than the direction of radial force. Besides, for the same tool wear, an increase in vibration was seen when the feed or depth of cut is increased. The tool condition monitoring studies using vibration signals show a good correlation and accuracy in predicting tool wear similar to the force measurement studies. As any minor change in the cutting edge would significantly influence the behavior of the tool, studying the vibrational signature to monitor the tool condition gives a good result.

3.4 Spindle and feed motor current

A worn-out tool increases the machining forces and cutting power due to higher friction between the tool and workpiece. Especially, the root-mean-square value shows an increasing trend as the tool wear progresses. For instance, the time domain waveform, variational mode decomposition, and amplitude-frequency of current signals show a profound difference for a sharp and worn tool that can be used to monitor tool wear [60]. Yuan et al. [60] have used these signals along with Random Forest (RF) recognition model to establish a relationship between the signals and tool wear. As a spindle acts as a connecting member between the tool and the motor, any change in the tool condition directly affects the spindle motor power. A load meter is used to monitor the spindle motor and as it can be placed far away from the tool and workpiece, the setup is more suitable for tool condition monitoring in an industrial environment.

In machining, with an increase in the flank wear, all the three force components increase. Especially, there is a profound increase in the main cutting force and feed motor current. As a dynamometer setup is expensive and difficult to use in industrial applications Szecsi [61] has developed a low-cost condition monitoring system by measuring the DC motor current of a CNC lathe. However, Salgado and Alonso [62] have stated that feed and radial forces are highly sensitive to tool wear. They have developed a tool condition monitoring technique based on the feed motor current and trained the system using Genetic Algorithm (GA) and FL. Ghosh et al. [63] have also proved that relatively simpler and cost-effective current and voltage sensors along with ANN can be an effective tool condition monitoring techniques than can substitute costly dynamometers. In addition, the immunity of spindle motor current to external disturbances such as noise, the technique is more accurate than a vibration sensor [64]. Justo et al. [65] have used the current signals from the spindle and feed motor to train the ANN model and predict tool wear in drilling. However, few studies show that the current signal from the motor contains noise and the minute fluctuation in forces that arises due to tool wear can be lost during filtering [66, 67]. The interruptions in the signal due to an increase in motor temperature, fluctuations arising due to movable motor parts, and sensitivity of the device while using smaller tools that consume relatively low power are a few other challenges reported [50].

3.5 Acoustic emission (AE)

Acoustic emission is a high-frequency, low-amplitude elastic stress wave that is generated due to the rapid release of strain energy from localized sources within a material [68].

In metal cutting, when a tool penetrates the workpiece and the material undergoes plastic deformation, the ultrasonic vibration that is released due to the interaction between the tool, chip, and the workpiece is the acoustic emission. The major advantage of the technique over the force or vibration measuring technique is its superior signal-to-noise ratio, sensitivity, and its capability to operate at frequencies that can effectively eliminate noise from external sources [69]. Each characteristic of an AE signal and its type (burst or continuous type) give an insight into the metal cutting mechanism through which it is possible to track tool wear and chip formation [70]. Studies have shown that the catastrophic tool failure can be effectively identified by the burst type of AE signal and the magnitude of its RMS value [71]. Kannatey-Asibu and Dornfeld [72] assessed the β distribution to characterize the root mean square value of AE signal to study the rate of tool wear, while Gabriel et al. [73] have shown that the skew (S_B) and kurtosis (K_B) of AE signal can be used for the same. Mukhopadhyay et al. [74] have also reported that b-parameter, skewness, and kurtosis can be effective indicators of tool wear. Hence, AE is one of the best techniques in developing an accurate process monitoring system due to its ability to detect microscopic deformation even in a relatively loud manufacturing shopfloor [75].

Through a comprehensive review, Moriwaki [76] has identified fracture, friction between two surfaces, plastic deformation of materials, and interaction of tool with microstructural features such as voids, grain boundaries, and dislocation as the few of the sources of AE. The various sources of AE in ultra-precision, precision, and conventional machining and its frequency range are shown in Fig. 5. Several studies have been conducted in the past to identify the AE signal features and their relationship with the wear rate and type of tool failure. Mathew et al. [77] have demonstrated that AE signal characteristics such as Ring-Down Count (RDC) and RMS voltage can be used to accurately monitor tool wear in milling cutters. Similarly, Hassan et al. [78] have proved that AE signals can be used to detect tool chipping in a relatively shorter time. Bhuiyan et al. [79] have found that the AE signals from the turning operation are continuous and transient which is related to the wear on tool and plastic deformation of work material, while the burst type of signals are from chips and crack propagation. However, the unprocessed AE signal from a metal cutting operation consists of a wide range of frequencies that denotes occurrences of various events which must be filtered. From the turning study, they have concluded that an increase in the amplitude of the AE signal is associated with increasing tool wear, while the increase in its frequency is associated with increasing material removal. Olufayo and Hossein [80] have estimated the life of an end milling tool by acquiring AE signals. The signals were processed using

wavelet transform and applied Back Propagation Neural Network (BPNN) model. Many studies [81–83] have successfully utilized AE signals to identify chatter, observe tool wear, and predict tool breakage. However, a high degree of cautiousness is required while extracting and analyzing the data as factors such as interrupted machining, hard spots and voids on the workpiece, and tool runout can distort the signals which lead to faulty analysis.

3.6 Noise

Some studies show sound signals emitted during a machining process can be correlated to tool wear. As wear progresses in the tool, it increases the area of contact between the tool and workpiece which results in higher friction [9]. This also increases the frequency of noise emanated from the machining process. The amplitude of the sound frequency and pitch that are recorded using a microphone can provide information about the state of tool wear [62]. Any variation in the machining parameters such as cutting speed, feed, and depth of cut has a certain frequency range which influences the overall noise generated during machining [84]. In the case of condition monitoring of tools, it can be presumed that any change in the machining condition results in disturbance to the frequency. Lu and Kannatey-Asibu [85] have found a close relationship between the noise and vibration signals of a new and worn tool. Studies have shown that the frequency range between 0 and 2 kHz is usually emitted by the various sources in the surroundings and the range between 2 and 20 kHz can be used for the tool wear monitoring. For instance, Sadat and Raman [86] have studied the frequency range between 2.75 and 3.75 kHz, while Silva et al. [87] selected the range around 2.5 kHz. However, in the study conducted by Kopač and Šali [88], they have observed a clear difference in the amplitude of noise generated by a new tool and a worn tool for the same cutting parameters. They have also used a range between 6 and 20 kHz and reported that the range also depends on the cutting parameters. An increase in cutting forces due to higher tool wear increases the resonance of the spindle. Liu et al. [89] have shown that the noise emitted due to spindle resonance can be a source for monitoring the tool wear with the help of three-layered backpropagation ANN algorithm. Similarly, Madhusudana et al. [90] have extracted sound signals from face milling operation and used discrete wavelet transform and SVM for feature extraction and wear classification, respectively. Raja et al. [91] have used the Competitive Neural Network model to classify flank wear in turning into initial, medium, and severe wear. By combining image and noise sensors, Manan et al. [92] have developed a condition monitoring system that can differentiate a sharp, partially worn, and fully worn turning tool. But the noise level in machining varies

based on numerous factors. Hence, a trial run to find the reference frequency of noise for the various combinations of cutting parameters, workpiece material, tool material, and tool condition and appropriate noise cancellation methods to filter the ambient noise is required to improve the prediction accuracy of the noise measurement technique.

3.7 Image processing

Image processing is an optical system that imparts advanced techniques such as machine vision, artificial intelligence, and pattern recognition to monitor tool wear in real-time. The technique combines the accuracy of the direct method of tool condition monitoring and the in-process capabilities of the indirect method of monitoring. There are four major stages involved in the tool condition monitoring system using the image processing technique. Image acquisition using a CCD (Charged Coupled Device), or CMOS (Complementary Metal-Oxide Semiconductor) camera is the first and the most common technique to capture the image of the tool. Image pre-processing is the next step that is performed to adjust contrast, noise filtering, and picture enhancement to eliminate the noises such as micro-chips, burr, dirt, coolant, and oil from the image. In image segmentation and edge detection, the worn portion of the tool is differentiated from the unworn portion by slicing the picture into segments. Morphological operation is the final stage in which the wear profile is mapped accurately [93].

Sun and Yeh [94] have developed a machine vision-based real-time tool wear monitoring system that can detect fracture, built-up edge, chip-off, and flank wear. The in-process vision-based tool wear monitoring system and the various important stages of image processing are shown in Fig. 6. The technique used for lighting is one of the critical steps in any vision-based system as it influences the quality of the image [95]. It is preferred to take the pictures of the insert from at least four different positions, to avoid the influence of shadow region on the tool wear measurement [96]. The other possibilities of the image processing technique include comparing the images taken before and after machining to calculate the surface area and volume of the worn region on the tool and projecting reference lines on the tool surface to measure curvature and tangent values [97]. While most of the studies have focused on monitoring the tool life when the tool is stationary, using a high-speed camera Wang et al. [98] have demonstrated that tool wear can be measured when the tool is rotating. Tiwari et al. [99] have built a system to predict flank wear by correlating cutting force and the texture feature images of the machined surface with a high level of accuracy. Although the vision-based condition monitoring studies looks promising, the high cost and low accuracy of the setup is a drawback. However, the detection

accuracy can be improved by using suitable machine learning and artificial intelligence-based algorithms which gives future direction to the technique.

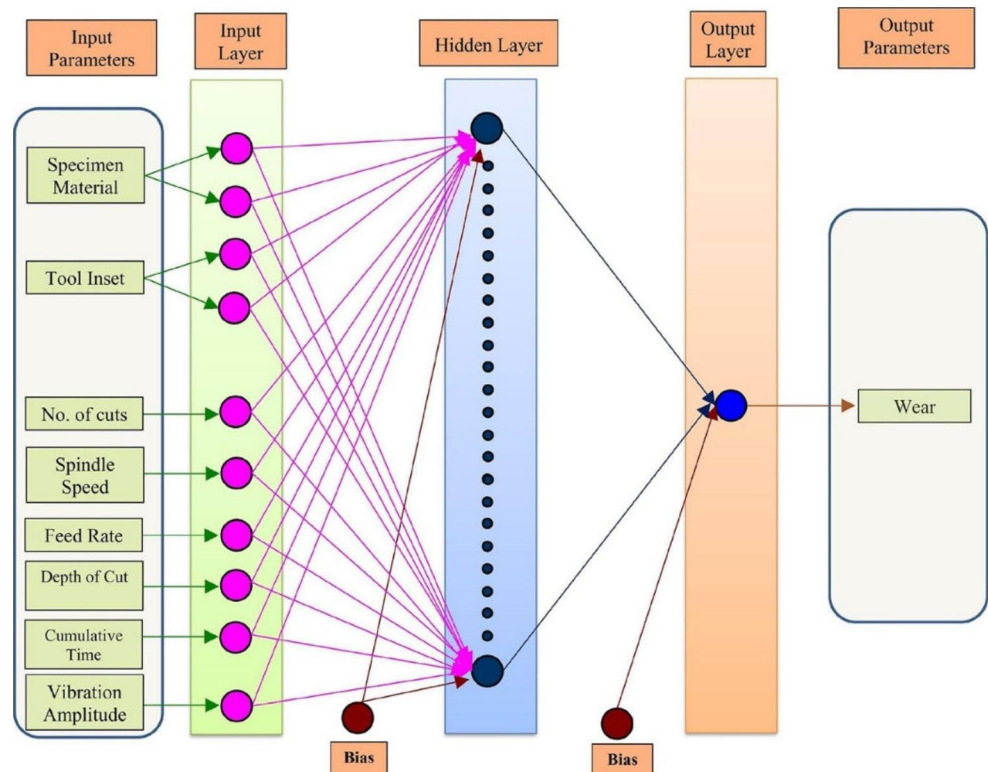
3.8 Other techniques

Few scholars have applied other novel and unconventional techniques such as ultrasonic methods [100, 101], stress/strain measurement [102], torque [103], surface roughness [104, 105] and shape mapping [106] for condition monitoring of cutting tools. Although they have successfully predicted the tool life using such methods, further comprehensive studies must be performed to understand the accuracy, feasibility, and reliability of such techniques in a real-life industrial environment.

4 Artificial intelligence for condition monitoring

If condition monitoring is the physical layer of the intelligent tools that comprises of various sensor technologies to observe the variation in machining condition, Artificial Intelligence (AI) is the software or analysis part of the system to make decisions from the data and provide corrective actions to improve the tool performance or predict failure. Besides, appropriate data acquisition and signal processing systems that act as an intermediary between the physical and decision-making layers must also be used to extract the appropriate signal features and differentiate them from external noise. Statistical moments, amplitude analysis, wavelet transform, Fourier analysis, time and frequency domain, automatic feature extraction, and representation learning are some of the signal processing techniques reported in the literature [107]. Literature study shows that numerous AI techniques are used in condition monitoring of tools. However, most of the studies are based on four techniques, Artificial Neural Network (ANN), Fuzzy logic, Hidden Markov Model (HMM), and Support Vector Machine (SVM) which are discussed in the following sections. Besides, there are other less used techniques such as Regression, Principal Component Analysis (PCA), Adaptive Neuro-Fuzzy Inference System or Adaptive Network-based Fuzzy Inference System (ANFIS), Bayesian Networks, Control charts (also called Shewhart charts or Process Behavior Charts), C-Means clustering, Ensembles, Genetic algorithm, K-star algorithm, Relevance Vector Machine (RVM), and Extreme Learning Machines (ELM) [108].

Fig. 7 Architecture of artificial neural network model [110]



4.1 Neural network or artificial neural network

Artificial Neural Network (ANN) which is sometimes simply termed as Neural Networks (NN) is one of the most popular and commonly applied computation models that take inspiration from the human brain's processing technique to solve complex mathematical problems. Apart from its versatility, flexibility, and processing speed, the technique is popular for its ability to model even non-linear relationships. Convolution Neural Networks (CNN) and Recurrent Neural Networks (RNN) are the other two types of Neural Networks. The model consists of several connected processing elements called nodes which behaves like artificial neurons to perform predefined activities. Typically, the model contains input and output layers and one or more hidden layers. Each layer contains numerous neurons which are interconnected with the adjacent layers. The appropriate selection of the number of neurons and hidden layers is crucial in using ANN. The connection strength between the neurons is termed as weights and it decides the amount of influence an input has on the output. Bias is an additional parameter that adjusts the output along with the weighted sum of the input to the neuron. Weights and biases improve the connection strength between the neurons. Training is one of the key requirements of ANN so that it can perform the tasks by modifying the weights linked with the connections between neurons. The training process helps in adjusting weights till the output from ANN matches with the target output which

is called supervised learning [109]. The architecture of the ANN model used by Baig et al. [110] to predict tool life in turning is shown in Fig. 7.

The ANN is termed the black-box model as it can approximate any function but does not give any insight into the structure of the function. Hence the decision-making does not depend on the understanding of the system. However, this approach helps in condition monitoring of cutting tools where it is difficult to establish analytical models to correlate sensor signals and wear, as the relationship between the input and output parameters in machining is highly complex and non-linear [111]. Hence, an appropriate training algorithm and a large volume of training data are critical for the performance of the model. The major drawback of ANN is the prediction accuracy drops if a smaller number of training data is used. In addition, the selection of the appropriate number of hidden layers and neurons also contributes to the prediction accuracy. ANN can be categorized as static and dynamic networks. The static network has no feedback or delay, and the signals move from the input layer to the output layer through the hidden layers in one direction. But in a dynamic network, all the layers have a feedback loop and hence the output is not just related only to the input but also to the previous inputs, outputs, and even the state of the network which makes it highly accurate in solving complex problems [112].

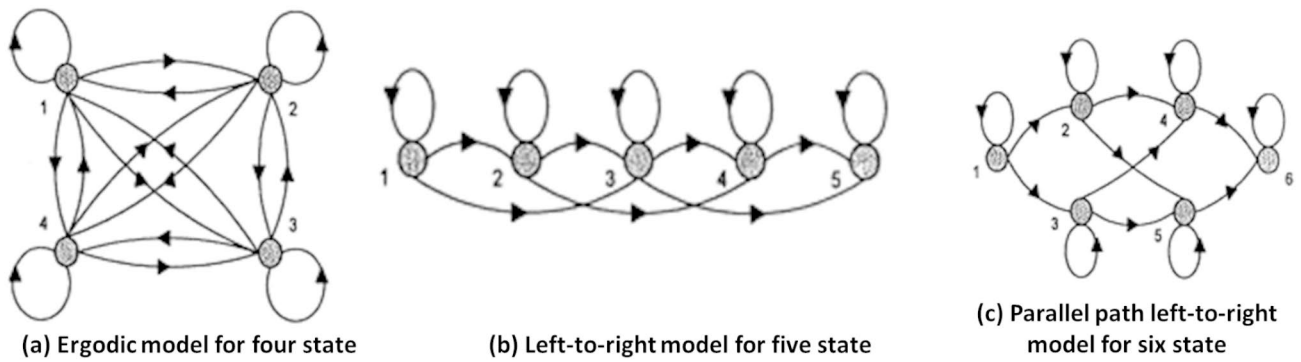


Fig. 8 Types of hidden Markov models [123]

4.2 Fuzzy logic

Fuzzy logic is a logical reasoning model to make decisions in the presence of ambiguity. The model allows multiple possible logic that is fairly accurate rather than fixed and exact. In a Boolean data type, the truth value of logic is represented either as “True” or “False” which are represented as “1” or “0”. But in a real-world scenario providing answers to questions such as skin color or food taste cannot be 0 or 1. In such scenarios, the degree of truth is the logical outcome. Fuzzy logic allows intermediate values between 0 and 1 based on the degree of truth which is more appropriate for real-world situations [113]. This allows the technique to model uncertainty similar to the human way of thinking, reasoning, and perception [114]. The process of mapping a given input to an output using knowledge-based rules (fuzzy logic) is the fuzzy inference based on which decisions are made [115]. A fuzzy inference system involves input and output membership functions, logical operations, and if-then condition statements. In classic engineering models, the input variables are real numbers that are processed using mathematical functions to provide a crisp numerical output. But fuzzy logic uses linguistic sets such as low, medium, or high, and the relationship is built using condition statements to derive a crisp output by defuzzification. The logic of using linguistic sets allows fuzzy logic to be more intuitive which resembles the way humans think. The various steps involved in a fuzzy inference process are, fuzzifying the input variables, defining membership functions, rule evaluation, aggregation of rule output, and defuzzification [116]. Numerous studies have successfully implemented fuzzy logic in condition monitoring of tools [117, 118] due to its ability to provide the results in a wide range of scale.

4.3 Hidden markov model

The Hidden Markov Model (HMM) is a statistical model that is applied to explain the development of observable

events which are dependent on the factors that cannot be observed directly and hence the association is based on the probability distribution. It is one of the popular statistical methods for time series data analysis. In the technique, the system that is modeled is assumed as a process with unknown parameters and identifies the unknown parameters from the observable parameters. In terms of wear monitoring of cutting tools, the sensor signals are the observable event while the tool wear is the hidden state [119]. According to Markov’s assumption, the future state depends only on the present state and not on the past states. It can accurately model and simulate the source from the observed data and is one of the successful models in signal processing, text recognition, and speech recognition [120]. Based on the probability density distribution an HMM model can be classified into continuous and discrete models [121]. Wang et al. [122] have used HMM technique to detect sharp and worn tools with an accuracy of more than 95%. The three types of HMM are the ergodic model, left-to-right model, and parallel path left-to-right model and are shown in Fig. 8 [123]. The left-to-right HMM technique is preferred for tool condition monitoring as the property of the model, the next state is always equal or greater than the current state that agrees well to the state of tool wear which does not decrease with an increase in time [124]. Similar to ANN, a huge volume of data is required to train an HMM which is one of the downsides of the technique.

4.4 Support vector machine

Support vector machines (SVMs) are a type of supervised machine learning algorithm used for classification and regression problems [125]. It is highly flexible in modeling diverse sources of data and can learn from the training data and make a generalization which is used to correctly predict outcomes with higher accuracy [126]. The data points that are close to the hyperplane are support vectors and the goal of SVM is to find the line or hyperplane that divides the

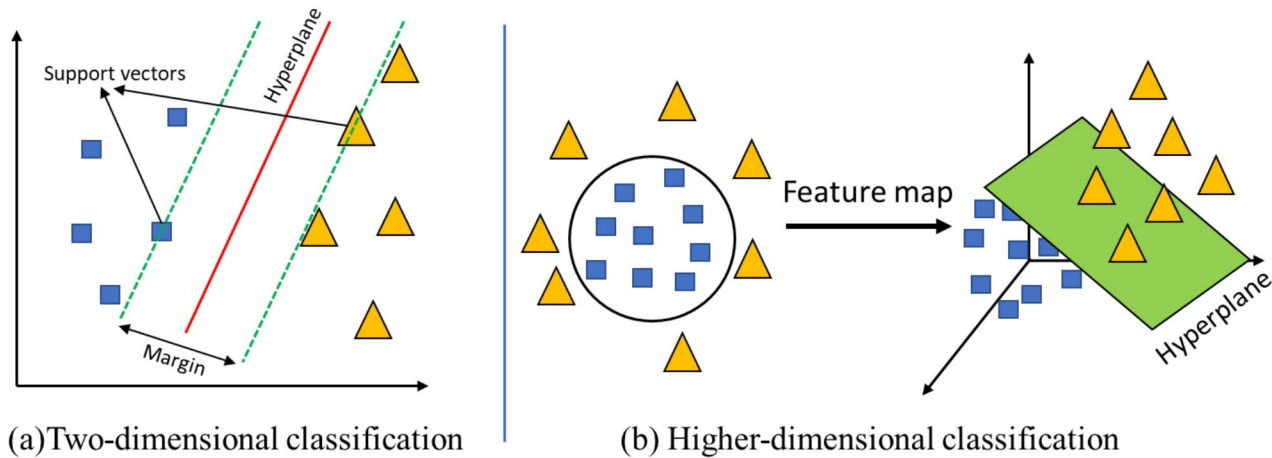


Fig. 9 A hyperplane in SVM algorithm

datasets into two classes. In linear-SVM, a hyperplane separates the datasets by drawing a straight line while the datasets that cannot be separated by a straight line are non-linear-SVM. A kernel function is used to transform the inseparable non-linear data into a higher-dimensional space where it is possible to separate them. The technique is highly effective in cases where the number of dimensions is greater than the number of samples. A hyperplane in two-dimensional and higher-dimensional SVM algorithms is shown in Fig. 9.

The SVM algorithm picks the hyperplane with a maximum margin between datasets to give the best classification. As SVM is a supervised model, it takes the benefit of prior tool wear knowledge to create a hyperplane that has a maximum margin between the datasets [127]. Bhat et al. [128] have converted the image of machined surface to a gray-level co-occurrence matrix (GLCM) to correlate the data with tool wear. By applying the SVM algorithm they have concluded that the GLCM features show a polynomial response rather than Gaussian. Yu and Zhou [129] have successfully applied the SVM technique to separate AE signals and noise signals with more than 98% accuracy. In the tool wear study conducted by monitoring the cutting forces, Wang et al. [130] have reported that the accuracy of Differential Evolution-SVM is superior to the Empirical Selection-SVM, and its processing time is lesser than the grid search-SVM. Although the accuracy of the technique is very good and is highly efficient while having smaller and cleaner datasets, the training data required is too high for larger data sets, and the efficiency drops if the data has noise and overlapping points.

5 Smart manufacturing, digital twins, and industry 4.0

The recent developments in Industry 4.0 technologies, an acronym given to the set of data-driven digital technologies such as Internet of Things (IoT), Big data, cloud computing, digital twins, and Artificial Intelligence have enabled digitizing the manufacturing industries to provide a high level of automation, improved productivity, efficiency, and flexibility [131]. The first and foremost step in the automation of the machining process is real-time condition monitoring and predicting the state of cutting tools. However, the real challenge in condition monitoring lies in the numerous process variables such as tool material, coatings, work material, and cutting parameters, each of which has a significant influence and complex interaction on tool life. Despite the challenges, an intelligent machine tool that can provide accurate and reliable tool condition monitoring techniques is the foundation of smart manufacturing and Industry 4.0 ecosystem. In addition, by maximizing the usage of tools, reducing work-piece scraps, lowering the machining cost, and optimizing the process parameters to reduce energy consumption a reliable condition monitoring system can support sustainable machining.

Moreover, the advent of digital twins, a technology that marries the physical and virtual world has the potential to further improve process monitoring, prediction, and optimization possibilities. A digital twin is a virtual model that reflects the live state of a physical system or a process accurately by combining the data collected through sensors and processed through mathematical models. Apart from simulating the conditions of a physical system in a virtual space, the technology can be used to give commands and control the physical space from the digital environment. The concept of twinning can be traced back to World War II

war rooms in which large maps with the current position of ships pinned to it were used to make strategies and NASA's Apollo space mission in which a spaceship in the earth was used to mirror the condition of the one in orbit. Although not a novel technology altogether, digit twinning has gained attraction in the past years due to the recent advancements in computational, networking, and digital technologies.

In the case of machining and tool condition monitoring, a live connection can be established between the machining process and its virtual twin. The various sensors that are fitted into the machine collect the process and machine condition data which are used to replicate the physical process in the virtual world. The data is a mixture of information such as state of tool wear, temperature, pressure, forces, motor power, humidity, coolant condition, drive units, work material properties, and other relevant machining data. The three major modules of a machining twin are the virtual twins of CNC equipment, machine behavior, and its mechanics which can be collectively used for various requirements. Process monitoring, simulation and control, performance improvement and optimization studies, and manipulation of actuators and sensors can be performed on the virtual model based on the sensory data using Artificial Intelligence algorithms which can be applied back to the physical machine. The optimized process parameters can be fed back to the physical system to improve the process efficiency. The highest level of accuracy and fidelity can be achieved by continuously monitoring the entire physical system using the virtual model. The real benefit of a digital twin is its capability to simulate the entire machining process (not just the tool wear signals), collect real-time data, and establish a two-way connection between the physical and the virtual system. With the massive amount of machining data collected from the system, appropriate digital technologies such as IoT, big data analytics, cloud computing, machine learning, and cyber physical system can empower manufacturing to an unprecedented level. Additionally, the seamless integration, communication, and data exchange between the physical and digital systems have the potential to develop intelligent manufacturing of the future.

6 Key takeaways and future directions

Excessive wear and sudden breakage of tools can severely affect productivity and can damage the workpiece, both of which can result in losses. Traditionally, machining industries rely on the experience of the machine operator (which is subjective) or by calculating the reference life of tools by conducting trial runs to monitor life and replace tools. But it is difficult to monitor tool life in small and medium scale machining industries that deal with varieties of parts that

have different sizes, shapes, and materials. In addition, both, under-utilization, and over-utilization of tools result in loss to the machining industries. However, studies have shown that a suitable condition monitoring system can give up to 40% cost savings by fully utilizing the life of cutting tools and reducing machine downtime.

Hence, sensor-based indirect tool condition monitoring techniques can help in in-process monitoring of tool wear and reduce machine downtime. However, selecting the right sensor and a suitable AI technique is a challenge. For instance, studies have shown that force and vibration-based techniques are highly sensitive even for minor variations in the cutting edge which can effectively be used to monitor tool wear. But the high cost of a dynamometer, size limitations of parts or tools that can be mounted over it, and its impact on the rigidity of machine structure and fixtures make it a practically unviable option, especially in industrial environments. Similarly, the position of vibration and acoustic emission sensors must be close to the cutting zone to accurately capture the signals which are challenging as the sensor position could interrupt the machining process. Although predictions based on temperature measurement have shown promising results, the performance of the system is questionable in challenging applications such as coolant, blindness to cutting zone due to longer chips, and difficulties in monitoring cutting zone in multipoint cutting tools. In addition, the current models are developed based on a certain fixed machining condition, whereas the system may not have the ability to adapt to the changes in cutting parameters or machining condition in industrial applications which may result in failure. Similarly, the distortion and disturbance to signals by external factors in noise and spindle/feed motor current measurement are high in a machining shop floor. This shows that the detection accuracy of the indirect measurement technique is generally much lower than the direct techniques in industrial applications and finding an appropriate place in the tool to position the sensors without disturbing the machining operation and losing the critical sensor signals is a daunting task. But image processing can give accuracies close to the direct measurement, and as the camera can be placed away from the cutting area, the technique does not interfere with the machining process. But the high setup cost, the requirement to stop the machining process to inspect wear, and the time taken to measure tool wear in the multipoint tools such as milling cutter is a challenge. However, even with such challenges, the technique looks promising and can give superior accuracies when used along with machine learning and artificial intelligence-based algorithms which can offset the time loss to a certain extent.

Nevertheless, finding an accurate, cost-effective, and reliable in-process tool condition monitoring is a multi-decade

long search that is still ongoing. The general drawback of most of the existing techniques is that they are too expensive, have poor accuracy, or cannot be used in an industrial environment. But an in-process tool condition monitoring technique is a necessity rather than a luxury to support smart manufacturing and Industry 4.0 ecosystem and in digitizing the manufacturing shop floor. Hence, the following are suggested as the potential key areas for future research,

- The development of advanced wireless miniature smart sensors (that can independently perform data collection, data processing, and establish communication to an external system such as an edge or cloud server) to suit the industrial environment that also has a high level of prediction accuracy is a future direction to address the current challenges in data acquisition.
- A cost-effective smart tool setup integrated with sensors and signal processing system supplied as a package by the tool manufacturers can increase industrial acceptance.
- A multisensory-based condition monitoring system in which each sensor measures a certain signal type and a suitable signal-processing algorithm such as a sensor fusion algorithm and integrated computational intelligence to combine the signals to improve the overall monitoring accuracy of the indirect measurement technique can be developed.
- The development of reliable and robust data processing setups and superior self-learning AI algorithms to effectively filter the noise signals can improve the data processing efficiency and overall performance.
- In addition, a cost-effective interoperable condition monitoring system that can be used for all types of machining operations is another area of research that has immense potential.

Nevertheless, the condition monitoring techniques combined with the digital revolution are poised to give numerous benefits such as higher productivity, flexibility, part quality, reduction in cost and process time, automated machining operation, superior preventive maintenance capability, and in turn higher profits to the businesses.

7 Conclusion

Metal cutting tools play a critical role in the manufacturing supply chain and monitoring the tool life in real-time to fully utilize it until its end of life can reduce the overall cost of machining and facilitate process automation. Although research on tool condition monitoring techniques is an ongoing research topic for many decades, it has not

got widespread acceptance in the machining industries. High initial cost, the accuracy of the system, difficulties in mounting sensors in an industrial machining setup, and the non-availability of a universal system for all machining operations such as turning, milling, drilling, and so on and variation in parts (workpiece) are a few of the potential challenges that must be addressed. Using multiple sensor signals can improve the accuracy and reliability of the system which may invariably increase the setup cost. However, the reduction in the cost of sensors drastically over the last few years, and the invention of advanced smart sensors shows a promising future for multi-sensor systems. In addition, further focus on the development of tailor-made smart sensors, advanced signal acquisition, processing techniques, and Artificial Intelligence algorithms specifically for the tool condition monitoring applications is a potential area of study. The review shows that Artificial Neural Network, Fuzzy logic, Hidden Markov Model, and Support Vector Machine are popular AI algorithms used for decision making.

Apart from monitoring the state of the tool, predicting the remaining useful life using prognostics modules can be a direction for future studies. Nevertheless, with the recent advancements in artificial intelligence and Industry 4.0 technologies such as the Internet of Things and Big data analytics, the tool condition monitoring system acts as the foundation for them. With the introduction of such advanced technologies, the automated and digitized production system of the past decade is rapidly evolving into intelligent data-driven setups. Hence, leveraging the technologies such as big data analytics to reveal the hidden patterns in the monitoring signals can help in better understanding the process and making quick data-driven decisions. Additionally, it also has immense potential in converting traditional manufacturing into a digital (data-driven), intelligent, and sustainable manufacturing setup that is reliable, robust, and cost-effective.

Funding The authors received no financial support for the research, authorship, and/or publication of this article.

Data availability The authors confirm that the data supporting the findings of this study are available within the article [and/or] its supplementary materials.

Code availability Not applicable.

Statements and declarations

Competing interests The authors have no relevant financial or non-financial interests to disclose.

Ethics approval Not applicable.

Consent to participate Not applicable.

Consent for publication Not applicable.

Disclaimer This disclaimer informs readers that the views, thoughts, and opinions expressed in the article belong solely to the authors, and they do not purport to reflect the opinions, views, policies, or positions of authors' employer, affiliates, organization, committee, or other group or individual.

References

- Muthuswamy, P., Nagarajan, S.K.: Experimental Investigation on the Effect of Different Micro-Geometries on Cutting Edge and Wiper Edge on Surface Roughness and Forces in Face Milling. *Lubricants*. **9**(10), 102 (2021). <https://doi.org/10.3390/lubricants9100102>
- Mohanraj, T., Shankar, S., Rajasekar, R., Sakthivel, N.R., Pramanik, A.: Tool condition monitoring techniques in milling process—a review. *J. Mater. Res. Technol.* **9**(1), 1032–1042 (2020). <https://doi.org/10.1016/j.jmrt.2019.10.031>
- Lister, P.M., Barrow, G.: Tool Condition Monitoring Systems. In: Davies B.J. (eds) *Proceedings of the Twenty-Sixth International Machine Tool Design and Research Conference*. Palgrave, London. (1986). https://doi.org/10.1007/978-1-349-08114-1_36
- Atli, A.V., Urhan, O.Ä.U., Z. H. A. N., Ertürk, S.A.R.P., Sönmez, M.: A computer vision-based fast approach to drilling tool condition monitoring. *Proceedings of the Institution of Mechanical Engineers, Part B: Journal of Engineering Manufacture*, **220**(9), 1409–1415. (2006). <https://doi.org/10.1243/09544054JEM412>
- Nitin Ambhore, D., Kamble, S., Chinchani, V., Wayal: Tool Condition Monitoring System: A Review, *Materials Today: Proceedings*, Volume 2, Issues 4–5, Pages 3419–3428, (2015). <https://doi.org/10.1016/j.matpr.2015.07.317>
- Padmakumar, M., Dinakaran, D.: Investigation on the effect of cryogenic treatment on tungsten carbide milling insert with 11% cobalt (WC–11%Co). *SN Appl. Sci.* **2**, 1050 (2020). <https://doi.org/10.1007/s42452-020-2872-3>
- Manoj Kumar, B.V., Ram Kumar, J., Basu, B.: Crater wear mechanisms of TiCN–Ni–WC cermets during dry machining. *International Journal of Refractory Metals and Hard Materials*, Volume 25, Issues 5–6, 2007, Pages 392–399, <https://doi.org/10.1016/j.jrmhm.2006.12.001>
- Padmakumar, M., Vijaya Ganesa Velan, M.: Machinability analysis in high speed turning of Ti–6Al–4V alloy and investigation of wear mechanism in AlTiN PVD coated tungsten carbide tool, *Engineering Research Express*, Volume 3, Number 4, 045011. <https://doi.org/10.1088/2631-8695/ac2e12>
- Ezugwu, E.O., Wang, Z.M.: Titanium alloys and their machinability—a review. *J. Mater. Process. Technol.* **68**(3), 262–274 (1997). [https://doi.org/10.1016/S0924-0136\(96\)00030-1](https://doi.org/10.1016/S0924-0136(96)00030-1)
- Padmakumar, M., Arunachalam, M.: Analyzing the effect of cutting parameters and tool nose radius on forces, machining power and tool life in face milling of ductile iron and validation using finite element analysis. *Eng. Res. Express*. (2020). <https://doi.org/10.1088/2631-8695/abala1>
- Padmakumar, M., Shiva Pradeep, N.: Effect of cutting edge form factor (K-factor) on the performance of a face milling tool. *CIRP J. Manuf. Sci. Technol.* **31**, 305–313 (2020). <https://doi.org/10.1016/j.cirpj.2020.06.004>
- Padmakumar, Muthuswamy: A novel wiper insert design and an experimental investigation to compare its performance in face milling. *Adv. Mater. Process. Technol.* (2022). <https://doi.org/10.1080/2374068X.2022.2034310>
- Shunmugesh, K., Panneerselvam, K.: Multi-performance optimization of micro-drilling using Taguchi technique based on membership function. *Indian J. Eng. Mater. Sci.* **25**, 383–390 (2018)
- Shunmugesh, K., Panneerselvam, K.: Optimization of drilling process parameters via Taguchi, TOPSIS and RSA techniques. *Arch. Metall. Mater.* **62**(3), 1803–1812 (2017). DOI: <https://doi.org/10.1515/amm-2017-0273>
- Shunmugesh, K., Panneerselvam, K.: Multi-response Optimization in Drilling of Carbon Fiber Reinforced Polymer Using Artificial Neural Network Correlated to Meta-heuristics Algorithm, *Procedia Technology*, Volume 25, Pages 955–962, (2016). <https://doi.org/10.1016/j.protcy.2016.08.187>
- Muthuswamy, P.: Influence of micro-geometry of wiper facet on the performance of a milling insert: an experimental investigation and validation using numerical simulation. *Sādhanā Volume 47, Article number: 140.* (2022). <https://doi.org/10.1007/s12046-022-01912-4>
- Shiva Pradeep, N., Padmakumar, M., Sarada, B.N.: Experimental investigation to assess the effects of trumpet hone on tool life and surface quality in milling of AISI4140 steel, *FME Transactions*, Volume 47, Issue 3, Pages 437–441. (2019). <https://doi.org/10.5937/fmet1903437s>
- Padmakumar, Muthuswamy: Investigation on sustainable machining characteristics of tools with serrated cutting edges in face milling of AISI 304 Stainless Steel, *Procedia CIRP*, Volume 105, Pages 865–871, (2022). <https://doi.org/10.1016/j.procir.2022.02.143>
- Padmakumar, M., Dinakaran, D.: A review on cryogenic treatment of tungsten carbide (WC–Co) tool material, *Materials and Manufacturing Processes*, Volume 36, Issue 6, Pages 637–659. (2021). <https://doi.org/10.1080/10426914.2020.1843668>
- Vijaya Ganesa Velan, M., Subha Shree, M., Muthuswamy, P.: Effect of cutting parameters and high-pressure coolant on forces, surface roughness and tool life in turning AISI 1045 steel, *Materials Today: Proceedings*, Volume 43, Part 1, 2021, Pages 482–489, <https://doi.org/10.1016/j.matpr.2020.12.020>
- Subha Shree, M., Vijaya Ganesa Velan, M., Padmakumar, M.: Experimental Investigation on Effect of High Pressure Coolant with Various Cutting Speed and Feed on Surface Roughness in Cylindrical Turning of AISI 1060 Steel Using Carbide Insert, *Advanced Materials Research*, Volume 984–985, Pages 3–8, (2014). <https://doi.org/10.4028/www.scientific.net/AMR.984-985.3>
- Subha Shree, M., Raguraman, K.: Experimental Investigation on Effect of High Pressure Coolant with Various Cutting Speed and Feed on Cutting Force and Tool Life in Cylindrical Turning of AISI 1060 Steel Using Carbide Insert. *Int. J. Appl. Eng. Res.* **10**(55) (2015). <https://doi.org/10.2139/ssrn.3963657>
- Murugesan, S., Sudharsanan, T., Murugesan, V.: P Muthuswamy. Overall Equipment Effectiveness (OEE) analysis and improvement in a spinning unit. *International Journal of Applied Engineering Research*, Vol. 10, No. 55, 2015, Special Issues, <https://doi.org/10.2139/ssrn.4032186>
- Andrew, S., Basics, D.S.A.: *Crystal Instruments*, (2016). <https://www.crystalinstruments.com/dynamic-signal-analysis-basics>, accessed on 7 Sep 2022
- Malla, C., Panigrahi, I.: Review of Condition Monitoring of Rolling Element Bearing Using Vibration Analysis and Other Techniques. *J. Vib. Eng. Technol.* **7**, 407–414 (2019). <https://doi.org/10.1007/s42417-019-00119-y>
- Instruments, D.: Waveform analysis using the fourier transform. (1995). https://www.dataq.com/resources/pdfs/article_pdfs/an11.pdf, accessed on 7 Sep 2022

27. Shunmugesh, R., Rajasekar, C., Moganapriya, Karthik., V.: Optimization of machining force and delamination factor of GFRP in dry drilling process using taguchi method, *Advances in Natural and Applied Sciences*, Vol. 11, Issue 8, Pages220–230. (2017)
28. Monroy Vazquez, K.P., Giardini, C., Ceretti, E.: Cutting Force Modeling. In: The International Academy for Production Engineering, Laperrière L., Reinhart G. (eds) *CIRP Encyclopedia of Production Engineering*. Springer, Berlin, Heidelberg. (2014). https://doi.org/10.1007/978-3-642-20617-7_6399
29. Sathish Kumar, N., Padmakumar, M.: An experimental study of applying various cutting edges on wiper milling inserts in face milling AISI 1070 steel. *Int. J. Mech. Industrial Eng.* **2**(4), 257–262 (2013). <https://doi.org/10.47893/IJMIE.2013.1107>
30. Oraby, S.E., Hayhurst, D.R.: Development of models for tool wear force relationships in metal cutting. *Int. J. Mech. Sci.* Volume. **33**(2), 125–138 (1991). [https://doi.org/10.1016/0020-7403\(91\)90062-8](https://doi.org/10.1016/0020-7403(91)90062-8)
31. Mehdi Nouri, B.K., Fussell, et al.: Real-time tool wear monitoring in milling using a cutting condition independent method. *Int. J. Mach. Tools Manuf.* **89**, 1–13 (2015). <https://doi.org/10.1016/j.ijmachtools.2014.10.011>
32. Wang, G., Yang, Y., Li, Z.: Force Sensor Based Tool Condition Monitoring Using a Heterogeneous Ensemble Learning Model. *Sensors*. **14**(11), 21588–21602 (2014). <https://doi.org/10.3390/s141121588>
33. Tugrul Özel, A., Nadgir: Prediction of flank wear by using back propagation neural network modeling when cutting hardened H-13 steel with chamfered and honed CBN tools. *Int. J. Mach. Tools Manuf.* **42**, 287–297 (2002). [https://doi.org/10.1016/S0890-6955\(01\)00103-1](https://doi.org/10.1016/S0890-6955(01)00103-1)
34. Twardowski, P., Wiciak-Pikuła, M.: Prediction of Tool Wear Using Artificial Neural Networks during Turning of Hardened Steel. *Materials*. **12**(19), 3091 (2019). <https://doi.org/10.3390/ma12193091>
35. Jinjiang Wang, J., Xie, R., Zhao, L., Zhang, L., Duan: Multi-sensory fusion based virtual tool wear sensing for ubiquitous manufacturing, *Robotics and Computer-Integrated Manufacturing*, Volume 45, Pages 47–58, (2017). <https://doi.org/10.1016/j.rcim.2016.05.010>
36. Sohyung Cho, S., Asfour, A., Onar, N., Kaundinya: Tool breakage detection using support vector machine learning in a milling process. *Int. J. Mach. Tools Manuf.* **45**(3), 241–249 (2005). <https://doi.org/10.1016/j.ijmachtools.2004.08.016>
37. Wang, Z., Rahman, M.: 11.10 - High-Speed Machining, Editor(s): Saleem Hashmi, Gilmar Ferreira Batalha, Chester J. Van Tyne, Bekir Yilbas, *Comprehensive Materials Processing*, Elsevier, Pages 221–253, ISBN 9780080965338, (2014). <https://doi.org/10.1016/B978-0-08-096532-1.01113-4>
38. Ueda, T.: Cutting Temperature. In: The International Academy for Production Engineering, Laperrière L., Reinhart G. (eds) *CIRP Encyclopedia of Production Engineering*. Springer, Berlin, Heidelberg. (2014). https://doi.org/10.1007/978-3-642-20617-7_6412
39. Conradie, P.J.T., Oosthuizen, G.A., Treurnicht, N.F., Shaaalane, A., A: Overview of work piece temperature measurement techniques for machining of Ti6Al4V. *S. Afr. J. Ind. Eng.* **23**(2), 116–130 (2012)
40. Pavel Kovac, M., Gostimirovic, D., Rodic, B., Savkovic: Using the temperature method for the prediction of tool life in sustainable production, *Measurement*, Volume 133, Pages320–327, (2019). <https://doi.org/10.1016/j.measurement.2018.09.074>
41. Çağrı, V., Yıldırım, M., Sarıkaya, T., Kivak, A., Şirin: The effect of addition of hBN nanoparticles to nanofluid-MQL on tool wear patterns, tool life, roughness and temperature in turning of Ni-based Inconel 625, *Tribology International*, Volume 134, Pages443–456, (2019). <https://doi.org/10.1016/j.triboint.2019.02.027>
42. Jinfu Zhao, Z., Liu: Influences of coating thickness on cutting temperature for dry hard turning Inconel 718 with PVD TiAlN coated carbide tools in initial tool wear stage. *J. Manuf. Process.* **56**, 1155–1165 (2020). <https://doi.org/10.1016/j.jmapro.2020.06.010>
43. Kus, A., Isik, Y., Cakir, M.C., Coşkun, S., Özdemir, K.: Thermocouple and Infrared Sensor-Based Measurement of Temperature Distribution in Metal Cutting. *Sensors* 2015, 15, 1274–1291. <https://doi.org/10.3390/s150101274>
44. Akhil, C.S., Ananthavishnu, M.H., Akhil, C.K., et al.: Measurement of Cutting Temperature during Machining, *IOSR Journal of Mechanical and Civil Engineering*, Volume 13, Issue 2, Version I (Mar. - 108–122. (2016)
45. Kulkarni, A., Joshi, G., Karekar, A., Sargade, V.: Investigation on cutting temperature and cutting force in turning AISI 304 austenitic stainless steel using AlTiCrN coated carbide insert. *Int. J. Mach. Mach. Mater.* **15**, 3–4 (2014). <https://doi.org/10.1504/ijmmm.2014.060546>
46. Fulin Jiang, Z., Liu, Y., Wan, Z., Shi: Analytical modeling and experimental investigation of tool and workpiece temperatures for interrupted cutting 1045 steel by inverse heat conduction method. *J. Mater. Process. Technol.* **213**(6), 887–894 (2013). <https://doi.org/10.1016/j.jmatprotec.2013.01.004>
47. Li, T., Shi, T., Tang, Z., Liao, G., Duan, J., Han, J., He, Z.: Real-time tool wear monitoring using thin-film thermocouple. *J. Mater. Process. Technol.* **288**, 116901 (2021). <https://doi.org/10.1016/j.jmatprotec.2020.116901>
48. Brili, N., Ficko, M., Klančnik, S.: Tool Condition Monitoring of the Cutting Capability of a Turning Tool Based on Thermography. *Sensors*. **21**(19), 6687 (2021). <https://doi.org/10.3390/s21196687>
49. Mustafa Kuntoğlu, H., Sağlam: Investigation of signal behaviors for sensor fusion with tool condition monitoring system in turning, *Measurement*, Volume 173, 108582, (2021). <https://doi.org/10.1016/j.measurement.2020.108582>
50. Ihsan Korkut, A., Acir, M., Boy: Application of regression and artificial neural network analysis in modelling of tool-chip interface temperature in machining, *Expert Systems with Applications*, Volume 38, Issue 9, Pages 11651–11656, (2011). <https://doi.org/10.1016/j.eswa.2011.03.044>
51. Teti, R., Jemielniak, K., O'Donnell, G., Dornfeld, D.: Advanced monitoring of machining operations, *CIRP Annals*, Volume 59, Issue 2, Pages 717–739, (2010). <https://doi.org/10.1016/j.cirp.2010.05.010>
52. Bonifacio, M.E.R., Diniz, A.E.: Correlating tool wear, tool life, surface roughness and tool vibration in finish turning with coated carbide tools, *Wear*, Volume 173, Issues 1–2, 1994, Pages137–144, [https://doi.org/10.1016/0043-1648\(94\)90266-6](https://doi.org/10.1016/0043-1648(94)90266-6)
53. Jiang, C.Y., Zhang, Y.Z., Xu, H.J., Annals, C.I.R.P.: Volume 36, Issue 1, Pages 45–48, (1987). [https://doi.org/10.1016/S0007-8506\(07\)62550-5](https://doi.org/10.1016/S0007-8506(07)62550-5)
54. Krishnakumar, P., Rameshkumar, K., Ramachandran, K.I.: Tool Wear Condition Prediction Using Vibration Signals in High Speed Machining (HSM) of Titanium (Ti-6Al-4V) Alloy, *Procedia Computer Science*, Volume 50, Pages270–275, (2015). <https://doi.org/10.1016/j.procs.2015.04.049>
55. Dimla, D.E., Lister, P.M.: On-line metal cutting tool condition monitoring.: I: force and vibration analyses. *Int. J. Mach. Tools Manuf.* **40**(5), 739–768 (2000). [https://doi.org/10.1016/S0890-6955\(99\)00084-X](https://doi.org/10.1016/S0890-6955(99)00084-X)
56. Scheffer, C., Kratz, H., Heyns, P.S., Klocke, F.: Development of a tool wear-monitoring system for hard turning. *Int. J. Mach. Tools Manuf.* **43**(10), 973–985 (2003). [https://doi.org/10.1016/S0890-6955\(03\)00110-X](https://doi.org/10.1016/S0890-6955(03)00110-X)
57. Rao, K.V., Kumar, Y.P., Singh, V.K., et al.: Vibration-based tool condition monitoring in milling of Ti-6Al-4V using an optimization model of GM(1,N) and SVM. *Int. J. Adv. Manuf. Technol.* **115**, 1931–1941 (2021). <https://doi.org/10.1007/s00170-021-07280-3>
58. Patra, K., Jha, A., Szalay, T.: “Tool condition monitoring in micro-drilling using vibration signals and artificial neural network:

- Subtitle: TCM in micro-drilling using vibration signals," 2017 International Conference on Industrial Engineering, Applications and Manufacturing (ICIEAM), pp. 1–5, doi: (2017). <https://doi.org/10.1109/ICIEAM.2017.8076196>
59. Ghani, A.K., Choudhury, I.A., Husni: Study of tool life, surface roughness and vibration in machining nodular cast iron with ceramic tool. *J. Mater. Process. Technol.* **127**(1), 17–22 (2002). [https://doi.org/10.1016/S0924-0136\(02\)00092-4](https://doi.org/10.1016/S0924-0136(02)00092-4)
 60. Yuan, J., Liu, L., Yang, Z., et al.: Tool wear condition monitoring by combining spindle motor current signal analysis and machined surface image processing. *Int. J. Adv. Manuf. Technol.* **116**, 2697–2709 (2021). <https://doi.org/10.1007/s00170-021-07366-y>
 61. Tamas Szecsi: A DC motor based cutting tool condition monitoring system. *J. Mater. Process. Technol. Volumes. 92–93* (1999). Pages 350–354 [https://doi.org/10.1016/S0924-0136\(99\)00182-X](https://doi.org/10.1016/S0924-0136(99)00182-X)
 62. Salgado, D.R., Alonso, F.J.: An approach based on current and sound signals for in-process tool wear monitoring. *Int. J. Mach. Tools Manuf.* **47**, 2140–2152 (2007). <https://doi.org/10.1016/j.ijmachtools.2007.04.013>
 63. Ghosh, N., Ravi, Y.B., Patra, A., et al.: Estimation of tool wear during CNC milling using neural network-based sensor fusion, *Mechanical Systems and Signal Processing*, Volume 21, Issue 1, Pages 466–479, (2007). <https://doi.org/10.1016/j.ymssp.2005.10.010>
 64. Stavropoulos, P., Papacharalampopoulos, A., Vasiliadis, E., et al.: Tool wear predictability estimation in milling based on multi-sensorial data. *Int. J. Adv. Manuf. Technol.* **82**, 509–521 (2016). <https://doi.org/10.1007/s00170-015-7317-6>
 65. Justo García-Sanz-Calcedo, SALGADO, D.R., Alfonso, G., GONZALEZ: Drilling Projects by Tool Condition Monitoring System. *Eng. Trans.* **64**(4), 555–561 (2016)
 66. Ryo Koike, K., Ohnishi, T., Aoyama: A sensorless approach for tool fracture detection in milling by integrating multi-axial servo information, *CIRP Annals*, Volume 65, Issue 1, Pages 385–388, (2016). <https://doi.org/10.1016/j.cirp.2016.04.101>
 67. Rizal, M., Ghani, J., Nuawi, M., Che, H.: A review of sensor system and application in milling process for tool condition monitoring. *Res. J. Appl. Sci. Eng. Technol.* **7**(10), 2083–2097 (2014). <https://doi.org/10.19026/rjaset.7.502>
 68. António João de Melo Martins Araújo, The generation mechanisms of acoustic emission in metal cutting, Doctoral Thesis:, University of South Wales. (2006)
 69. Jemielniak, K., Arrazola, P.J.: Application of AE and cutting force signals in tool condition monitoring in micro-milling. *CIRP J. Manufact. Sci. Technol.* **1**(2), 97–102 (2008). <https://doi.org/10.1016/j.cirpj.2008.09.007>
 70. Sunilkumar Kakade, L., Vijayaraghavan, R., Krishnamurthy, In-process tool wear and chip-form monitoring in face milling operation using acoustic emission., *Journal of Materials Processing Technology*, Volume 44, Issues 3–4, Pages 207–214, (1994). [https://doi.org/10.1016/0924-0136\(94\)90433-2](https://doi.org/10.1016/0924-0136(94)90433-2)
 71. Jemielniak, K., Otman, O., Tool failure detection based on analysis of acoustic emission signals, *Journal of Materials Processing Technology*, Volume 76, Issues 1–3, Pages 192–197, (1998). [https://doi.org/10.1016/S0924-0136\(97\)00379-8](https://doi.org/10.1016/S0924-0136(97)00379-8)
 72. Kannatey-Asibu, E., Dornfeld, D.A., A study of tool wear using statistical analysis of metal-cutting acoustic emission, *Wear*, Volume 76, Issue 2, Pages 247–261, (1982). [https://doi.org/10.1016/0043-1648\(82\)90009-6](https://doi.org/10.1016/0043-1648(82)90009-6)
 73. Gabriel, V., Matusky, J., Prusek, A., Zizka, J. "Study of machining process by acoustic emission method." In Proceedings of the IV International Conference on Monitoring and Automatic Supervision in Manufacturing, Miedzeszyn, CIRP, pp. 143–148. (1995)
 74. Mukhopadhyay, C.K., Jayakumar, T., Raj, B., Venugopal, S., Statistical Analysis of Acoustic Emission Signals Generated During Turning of a Metal Matrix Composite, *Journal of the Brazilian Society of Mechanical Sciences and Engineering* **34** (2), 2012, pp. 145–154. (2012)
 75. Lee, D.E., Hwang, I., Valente, C.M.O., Oliveira, J.F.G., Dornfeld, D.A.: Precision manufacturing process monitoring with acoustic emission. *Int. J. Mach. Tools Manuf.* **46**(2), 176–188 (2006). <https://doi.org/10.1016/j.ijmachtools.2005.04.001>
 76. Moriwaki, T.: Application of acoustic emission measurement to sensing of wear and breakage of cutting tool. *Bull. Japan Soc. Precision Eng.* **17**(3), 154–160 (1983)
 77. Mathew, M.T., Pai, P.S., Rocha, L.A.: An effective sensor for tool wear monitoring in face milling: Acoustic emission. *Sadhana.* **33**, 227–233 (2008). <https://doi.org/10.1007/s12046-008-0016-3>
 78. Hassan, M., Sadek, A., Attia, M.H., Thomson, V.: Intelligent machining: real-time tool condition monitoring and intelligent adaptive control systems. *J. Mach. Eng.* **18**(1), 5–17 (2018)
 79. Bhuiyan, M.S.H., Choudhury, I.A., Dahari, M., Nukman, Y., Dawal, S.Z., Application of acoustic emission sensor to investigate the frequency of tool wear and plastic deformation in tool condition monitoring, *Measurement*, Volume 92, Pages 208–217, (2016). <https://doi.org/10.1016/j.measurement.2016.06.006>
 80. Olufayo, O., Abou-El-Hossein, K.: Tool life estimation based on acoustic emission monitoring in end-milling of H13 mould-steel. *Int. J. Adv. Manuf. Technol.* **81**, 39–51 (2015). <https://doi.org/10.1007/s00170-015-7091-5>
 81. Richard, Y., Chiou, Steven, Y., Liang: Analysis of acoustic emission in chatter vibration with tool wear effect in turning. *Int. J. Mach. Tools Manuf.* **40**, 927–941 (2000). [https://doi.org/10.1016/S0890-6955\(99\)00093-0](https://doi.org/10.1016/S0890-6955(99)00093-0)
 82. Neslušan, M., Mičeta, B., Mičietová, A., Čilliková, M., Mrkvica, I., Detection of tool breakage during hard turning through acoustic emission at low removal rates, *Measurement*, Volume 70, Pages 1–13, (2015). <https://doi.org/10.1016/j.measurement.2015.03.035>
 83. Chengdong Wang, Z., Bao, P., Zhang, W., Ming, M., Chen, Tool wear evaluation under minimum quantity lubrication by clustering energy of acoustic emission burst signals, *Measurement*, Volume 138, Pages 256–265, (2019). <https://doi.org/10.1016/j.measurement.2019.02.004>
 84. Weller, E.J., Schrier, H.M., Weichbrodt, B. "What sound can be expected from a worn tool?" 525–534. (1969)
 85. Lu, M.-C., Kannatey-Asibu, E. Jr.: Analysis of sound signal generation due to flank wear in turning. *J. Manuf. Sci. Eng.* **124**(4), 799–808 (2002)
 86. Abdul, B., Sadat, S., Raman: Detection of tool flank wear using acoustic signature analysis. *Wear.* **115**(3), 265–272 (1987). [https://doi.org/10.1016/0043-1648\(87\)90216-X](https://doi.org/10.1016/0043-1648(87)90216-X)
 87. Silva, R.G., Reuben, R.L., Baker, K.J., Wilcox, S.J.: Mech. Syst. Signal Process. **12**(2), 319–332 (1998). <https://doi.org/10.1006/mssp.1997.0123> Tool wear monitoring of turning operations by neural network and expert system classification of a feature set generated from multiple sensors
 88. Kopač, J., Šali, S., Tool wear monitoring during the turning process, *Journal of Materials Processing Technology*, Volume 113, Issues 1–3, Pages 312–316, (2001). [https://doi.org/10.1016/S0924-0136\(01\)00621-5](https://doi.org/10.1016/S0924-0136(01)00621-5)
 89. Liu, M.K., Tseng, Y.H., Tran, M.Q.: Tool wear monitoring and prediction based on sound signal. *Int. J. Adv. Manuf. Technol.* **103**, 3361–3373 (2019). <https://doi.org/10.1007/s00170-019-03686-2>
 90. Madhusudana, C.K., Kumar, H., Narendranath, S.: Face milling tool condition monitoring using sound signal. *Int. J. Syst. Assur. Eng. Manag.* **8**, 1643–1653 (2017). <https://doi.org/10.1007/s13198-017-0637-1>
 91. Raja, J., Lim, W., Venkateses, C.: Tool Condition Monitoring using Competitive Neural Network and Hilbert-Huang Transform. *Asian J. Sci. Res.* **6**, 703–714 (2013). <https://doi.org/10.3923/ajsr.2013.703.714>

92. Mannan, M.A., Kassim, A.A., Jing, M.: Application of image and sound analysis techniques to monitor the condition of cutting tools. *Pattern Recognit. Lett.* **21**(11), 969–979 (2000). [https://doi.org/10.1016/S0167-8655\(00\)00050-7](https://doi.org/10.1016/S0167-8655(00)00050-7)
93. Dutta, S., Pal, S.K., Mukhopadhyay, S., Sen, R.: Application of digital image processing in tool condition monitoring: A review. *CIRP J. Manuf. Sci. Technol.* **6**, 212–232 (2013). <https://doi.org/10.1016/j.cirpj.2013.02.005>
94. Sun, W.-H., Yeh, S.-S.: Using the Machine Vision Method to Develop an On-machine Insert Condition Monitoring System for Computer Numerical Control Turning Machine Tools. *Materials*. **11**(10), 1977 (2018). <https://doi.org/10.3390/ma11101977>
95. Barreiro, J., Castejón, M., Alegre, E., Hernández, L.K.: Use of descriptors based on moments from digital images for tool wear monitoring. *International Journal of Machine Tools and Manufacture*, Volume 48, Issue 9, 2008, Pages 1005–1013, <https://doi.org/10.1016/j.ijmachtools.2008.01.005>
96. Weckenmann, A., Nalbantic, K.: Precision Measurement of Cutting Tools with two Matched Optical 3D-Sensors. *CIRP Annals*, Volume 52, Issue 1, Pages 443–446, (2003). [https://doi.org/10.1016/S0007-8506\(07\)60621-0](https://doi.org/10.1016/S0007-8506(07)60621-0)
97. Jurkovic, J., Korosec, M., Kopac, J.: New approach in tool wear measuring technique using CCD vision system. *Int. J. Mach. Tools Manuf.* **45**(9), 1023–1030 (2005). <https://doi.org/10.1016/j.ijmachtools.2004.11.030>
98. Wang, W., Wong, Y.S., Hong, G.S.: Flank wear measurement by successive image analysis. *Computers in Industry*. **56**(8–9), 816–830 (2005). <https://doi.org/10.1016/j.compind.2005.05.009>
99. Tiwari, K., Shaik, A., Arunachalam, N.: Tool wear prediction in end milling of Ti-6Al-4V through Kalman filter-based fusion of texture features and cutting forces. *Procedia Manuf.* **26**, 1459–1470 (2018). <https://doi.org/10.1016/j.promfg.2018.07.095>
100. Lange, J., Abu-Zahra, N.: Tool Chatter Monitoring in Turning Operations Using Wavelet Analysis of Ultrasound Waves. *Int. J. Adv. Manuf. Technol.* **20**, 248–254 (2002). <https://doi.org/10.1007/s001700200149>
101. Dinakaran, D., Sampathkumar, S., Sivashanmugam, N.: An experimental investigation on monitoring of crater wear in turning using ultrasonic technique. *Int. J. Mach. Tools Manuf.* **49**, 1234–1237 (2009). <https://doi.org/10.1016/j.ijmachtools.2009.08.001>
102. Scheffer, C., Heyns, P.S.: Wear monitoring in turning operations using vibration and strain measurements. *Mechanical Systems and Signal Processing*, Volume 15, Issue 6, Pages 1185–1202, (2001). <https://doi.org/10.1006/mssp.2000.1364>
103. Bulent Kaya, C., Oysu, H.M., Ertunc: Force-torque based on-line tool wear estimation system for CNC milling of Inconel 718 using neural networks. *Adv. Eng. Softw.* **42**, 76–84 (2011). <https://doi.org/10.1016/j.advengsoft.2010.12.002>
104. Haicheng Yu, K., Wang, R., Zhang, et al. An Improved Tool Wear Monitoring Method Using Local Image and Fractal Dimension of Workpiece, Volume 2021, Article ID 9913581, <https://doi.org/10.1155/2021/9913581>
105. Zeng, W., Jiang, X., Blunt, L.: Surface characterisation-based tool wear monitoring in peripheral milling. *Int. J. Adv. Manuf. Technol.* **40**, 226–233 (2009). <https://doi.org/10.1007/s00170-007-1352-x>
106. Zhang, C., Zhou, L.: Modeling of tool wear for ball end milling cutter based on shape mapping. *Int. J. Interact. Des. Manuf.* **7**, 171–181 (2013). <https://doi.org/10.1007/s12008-012-0176-6>
107. Kuntoğlu, M., Aslan, A., Pimenov, D.Y., et al.: A Review of Indirect Tool Condition Monitoring Systems and Decision-Making Methods in Turning: Critical Analysis and Trends. *Sensors*. **21**(1), 108 (2021). <https://doi.org/10.3390/s21010108>
108. Zhou, Y., Xue, W.: Review of tool condition monitoring methods in milling processes. *Int. J. Adv. Manuf. Technol.* **96**, 2509–2523 (2018). <https://doi.org/10.1007/s00170-018-1768-5>
109. Haykin, S.: “Neural networks: a comprehensive foundation.” Mc Millan, New Jersey (2010): 1–24. (1999)
110. Baig, R.U., Javed, S., Khaisar, M., Shakoor, M., Raja, P.: Development of an ANN model for prediction of tool wear in turning EN9 and EN24 steel alloy. *Adv. Mech. Eng.* (2021). <https://doi.org/10.1177/16878140211026720>
111. Özden, G., Mata, F., Öteyaka, M.: Artificial neural network modeling for prediction of cutting forces in turning unreinforced and reinforced polyamide. *J. Thermoplast. Compos. Mater.* **34**, 353–363 (2019). <https://doi.org/10.1177/0892705719845712>
112. Hadiyan, P.P., Moeini, R., Ehsanzadeh, E.: Application of static and dynamic artificial neural networks for forecasting inflow discharges, case study: Sefidroud Dam reservoir, *Sustainable Computing: Informatics and Systems*, Volume 27, 100401, (2020). <https://doi.org/10.1016/j.suscom.2020.100401>
113. Kamthan, S., Singh, H.: “Hierarchical Fuzzy Logic for Multi-Input Multi-Output Systems,” in *IEEE Access*, vol. 8, pp. 206966–206981, (2020). <https://doi.org/10.1109/ACCESS.2020.3037901>
114. Abraham, A.: Rule-based expert systems. In: Sydenham, P.H., Thorn, R. (eds.) *Handbook of Measuring System Design*, pp. 909–919. Oklahoma State University, Stillwater, OK, USA (2005)
115. Alavi, N.: Date grading using rule-based fuzzy inference system. *Int. J. Agricultural Technol.* **8**, 1243–1254 (2012)
116. Cuka, B., Kim, D.-W.: Fuzzy logic based tool condition monitoring for end-milling, *Robotics and Computer-Integrated Manufacturing*, Volume 47, Pages 22–36, (2017). <https://doi.org/10.1016/j.rcim.2016.12.009>
117. Marek Balazinski, E., Czogala, K., Jemielniak, J., Leski, Tool condition monitoring using artificial intelligence methods, *Engineering Applications of Artificial Intelligence*, Volume 15, Issue 1, Pages 73–80, (2002). [https://doi.org/10.1016/S0952-1976\(02\)00004-0](https://doi.org/10.1016/S0952-1976(02)00004-0)
118. Cuneyt Aliustaoglu, H., Metin Ertunc, H., Ocak, Tool wear condition monitoring using a sensor fusion model based on fuzzy inference system, *Mechanical Systems and Signal Processing*, Volume 23, Issue 2, Pages 539–546, (2009). <https://doi.org/10.1016/j.ymssp.2008.02.010>
119. Scheffer, C., Engelbrecht, H., Heyns, P.S.: A comparative evaluation of neural networks and hidden Markov models for monitoring turning tool wear. *Neural Comput. & Applic.* **14**, 325–336 (2005). <https://doi.org/10.1007/s00521-005-0469-9>
120. Monica Franzese, A., Iuliano, Hidden Markov Models, Editor(s): Shoba Ranganathan, Michael Gribskov, Kenta Nakai, Christian Schönbach, *Encyclopedia of Bioinformatics and Computational Biology*, Academic Press, Pages 753–762, (2019). <https://doi.org/10.1016/B978-0-12-809633-8.20488-3>
121. Chen, F.R., Wilcox, L.D., Bloomberg, D.S.: A comparison of discrete and continuous hidden Markov models for phrase spotting in text images, *Proceedings of 3rd International Conference on Document Analysis and Recognition*, pp. 398–402 vol.1, doi: (1995). <https://doi.org/10.1109/ICDAR.1995.599022>
122. Wang, L., Mehrabi, M., Kannatey-Asibu, E.: Hidden Markov Model-based Tool Wear Monitoring in Turning. *J. Manuf. Sci. Eng.* **124**, 651–658 (2002). <https://doi.org/10.1115/1.1475320>
123. Huseyin, M., Ertunc, K.A., Loparo, Hasan Ocak, Tool wear condition monitoring in drilling operations using hidden Markov models (HMMs), *International Journal of Machine Tools and Manufacture*. **41**(9), 1363–1384, (2001). [https://doi.org/10.1016/S0890-6955\(00\)00112-7](https://doi.org/10.1016/S0890-6955(00)00112-7)
124. Subakan, Y.C., Traa, J., Smaragdis, P., Hsu, D., Method of moments learning for left-to-right Hidden Markov models, 2015 IEEE Workshop on Applications of Signal Processing to Audio and Acoustics (WASPAA), pp. 1–5, doi: (2015). <https://doi.org/10.1109/WASPAA.2015.7336940>

125. Vapnik, V.N.: The Nature of Statistical Learning Theory. Statistics for Engineering and Information Science. Springer, New York, NY (2000). https://doi.org/10.1007/978-1-4757-3264-1_1
126. Zouhri, W., Homri, L., Dantan, J.Y.: Identification of the key manufacturing parameters impacting the prediction accuracy of support vector machine (SVM) model for quality assessment. *Int. J. Interact. Des. Manuf.* **16**, 177–196 (2022). <https://doi.org/10.1007/s12008-021-00807-8>
127. Sun, J., Rahman, M., Wong, Y.S., Hong, G.S.: Multiclassification of tool wear with support vector machine by manufacturing loss consideration. *Int. J. Mach. Tools Manuf.* **44**(11), 1179–1187 (2004). <https://doi.org/10.1016/j.ijmachtools.2004.04.003>
128. Bhat, N.N., Dutta, S., Vashisth, T., et al.: Tool condition monitoring by SVM classification of machined surface images in turning. *Int. J. Adv. Manuf. Technol.* **83**, 1487–1502 (2016). <https://doi.org/10.1007/s00170-015-7441-3>
129. Yu, Y., Zhou, L.: Acoustic emission signal classification based on support vector machine. *TELKOMNIKA Indonesian Journal of Electrical Engineering.* **10**(5), 1027–1032 (2012). <https://doi.org/10.11591/telkomnika.v10i5.1387>
130. Wang, G., Xie, Q., Zhang, Y.: Tool condition monitoring system based on support vector machine and differential evolution optimization. *Proceedings of the Institution of Mechanical Engineers, Part B: Journal of Engineering Manufacture.* **231**, 805–813. (2016). <https://doi.org/10.1177/0954405415619871>
131. Raja Santhi, A., Muthuswamy, P.: Influence of Blockchain Technology in Manufacturing Supply Chain and Logistics. *Logistics.* **6**, 15. (2022). <https://doi.org/10.3390/logistics6010015>

Publisher's note Springer Nature remains neutral with regard to jurisdictional claims in published maps and institutional affiliations.

Springer Nature or its licensor holds exclusive rights to this article under a publishing agreement with the author(s) or other rightsholder(s); author self-archiving of the accepted manuscript version of this article is solely governed by the terms of such publishing agreement and applicable law.

Transient Thermal Analysis on Rotary Friction Welding of 15CDV6 Aerospace Steel

Anchana Padmakumar^{1,2} ·

Ajith Puthuparambil Madhavan¹  · Joby Joseph³ ·

Shunmugesh Kailasamani⁴

Received: 24 January 2022 / Accepted: 5 September 2022
© The Indian Institute of Metals - IIM 2022

Abstract Friction welding is a solid-state joining method that does not require the workpieces to be melted. The thermo-mechanical mechanism during the rotary friction welding process of 15CDV6 alloy steel is analyzed using a finite element model in the ANSYS workbench. During the frictional stage, the effects of friction pressure, rotating speed, and friction time on maximum temperature along the interface were investigated. The experiments were conducted on 16 mm diameter and 65 mm length of 15CDV6 alloy steel to evaluate the numerical model. The model has achieved 94% accuracy and is useful to predict the temperature distribution for a set of parameters to obtain better weld quality.

Keywords Rotary friction welding · 15CDV6 alloy steel · Finite element analysis · Temperature distribution · Corona bond

1 Introduction

Rotary Friction Welding (RFW) is a common solid-state joining technique for both similar and different materials such as steel, aluminum alloys, nickel-based alloys, and other technical materials. Recent RFW research has revealed the popularity and uses of the friction welding process, and a thorough investigation is required before the method can be used to join large-scale structures like generator rods/pipes and nuclear power plants [1].

The development of the corona bond and the extrusion are the two stages of the friction welding cycle [2]. The corona bond generation is the first step, during which the temperature and stress field is changing constantly. The expulsion of flash is the final phase, in which both the temperature and the stress field remain constant. The word “corona bond” describes the morphology of the joint as it originates, develops, and fills out the interface before plasticized material extrudes as a flash. The first point at which corona begins to form is influenced by the welding conditions. The material deformation and heat generation have a great impact on the microstructure and performance of the welded joint. As a result, it's important to evaluate the heat generation that occurs during Rotary Friction welding, and simulation becomes an effective instrument.

15CDV6 alloy steel is low-alloy steel with high strength. This alloy possesses a high strength-to-weight ratio, as well as excellent toughness and weldability. The rods are attached to the missile rocket motor casings using friction welding. Roll cages, rocket motor casings, track and push-rods, uprights, pressure tanks, subframes, wishbones, and suspension components are some of the other main usages for 15CDV6 alloy steel.

Feng et al. [2] performed Rotary Friction Welding (RFW) on rod specimens, a more common RFW structure, in which

✉ Ajith Puthuparambil Madhavan
ajithpm@cet.ac.in

¹ Department of Mechanical Engineering, College of Engineering Trivandrum, Thiruvananthapuram, Kerala 695016, India

² APJ Abdul Kalam Technological University, Trivandrum, Kerala 695 016, India

³ Department of Mechanical Engineering, Mar Athanasius College of Engineering, Kothamangalam, Kerala 686666, India

⁴ Department of Mechanical Engineering, Viswajyothi College of Engineering and Technology, Muvattupuzha, Kerala 686670, India

the friction heat distributions are evaluated using a MATLAB environment, and the model is verified by the initiation position and evolution of the corona bond generated at the interface. The thermo-mechanical coupling process corresponding to corona bond evolution during RFW was modeled by Feng et al. [3]. They developed a friction coefficient model and SUS304 was picked up as the base metal.

Asif et al. [4] studied the temperature distribution and axial shortening during friction welding of duplex stainless steel by developing a 3D FEM model and experimentally validated it. It can be concluded that the frictional stage and upsetting stage of the welding process have more impact on temperature and axial shortening respectively. Li et al. [5] developed an analytical model to study the heat generation and temperature field during the initial stage of rotary friction welding. The model is very helpful for the selection of welding parameters. Kong et al. [6] developed a 3D coupled thermomechanical finite element model to study the thermal history, weld flash formation, and temperature distribution of dissimilar joints between A312 stainless steel pipe to A105 forged steel bar. They experimentally validated the model according to heating time and upsetting time. Li et al. [7] analyzed the low-pressure RFW process of D50Re steel using DEFORM software. The predicted distribution of the contact between workpieces, temperature distribution, stress distribution, and strain distribution, torque, axial shortening under three different simulation conditions, which consider no thermal expansion coefficient (TE), real TE coefficient, and equivalent TE coefficient respectively were compared to each other and experimental data.

To predict the temperature field for the entire weld, Jedraśiak et al. [8] developed an implicit FE thermal model of LFW. The distribution pattern and time evolution of the heat input, as well as the capacity to withstand substantial axial shortening and heat loss to the flash, are critical criteria for the thermal model. With a computationally efficient finite element analysis, Jedraśiak and Shercliff [9] simulated heat generation on Ti alloy linear friction welding. Bouarroudj et al. [10] optimized the friction time required to reach the forging temperature at the interface required for weld joint formation, which would be around 950 °C for most of the steels. This period is defined by the process variables rotation speed, friction force, type to be welded materials, friction coefficient, etc.

Li and Wang [11] employed ABAQUS to simulate the coupled thermo-mechanical process using a comprehensive finite element model of continuous drive friction welded mild steel. The mild steel simulation and experiment results are indeed very identical. Li et al. [12] established a slide-stick friction transition criterion and later adopted analytical models to characterize heat generation and temperature field, which may also provide a theoretical basis for welding parameter selection. The maximum temperature at the

friction interface confirms the models' reliability, and the difference between experimental and estimated findings at the transition moment is approximately 6%. To understand the thermal consequences, Seli et al. [13] investigated the mechanical characteristics of mild steel and aluminum welded rods, and an explicit one-dimensional finite difference approach was employed to model the joint's heating and cooling temperature distribution. The suggested finite difference approach will help in the design of weld parameters as well as provide a better knowledge of the friction welding process. During the linear friction welding of Ti–6Al–4V workpieces, Anthony et al. [14] used experimentally validated models to study the impacts of process inputs on temperature fields, material flow, and surface contamination removal. Using ABAQUS/explicit and a two-dimensional (2D) model, Pengkang et al. [15] studied the transient temperature field and flash during linear friction welding (LFW) between Ti–6.5Al–3.5Mo–1.5Zr–0.3Si (TC11) and Ti–4Mo–4Cr–5Al–2Sn–2Zr (TC17).

Reddy et al. [16] studied the effect of process parameters friction force, forge force, rotational speed, and burn-off length on hardness and microstructure of friction welded 15CDV6 alloy steel. From the optimization, it is recommended that rotation speed and burn-off length are the two most significant parameters to weld 15CDV6 alloy steel of 17 mm diameter round rods. Ajith et al. [17] investigated the effect of friction pressure, upsetting pressure, and speed of rotations on the mechanical and metallurgical properties and corrosion resistance of UNS S32205 DSS joints by friction welding.

Friction welding is a welding technique in which heat is generated by the direct conversion of mechanical energy to thermal energy at the interface of the workpieces without the need for electricity or heat from other sources. The primary processes during FW are temperature evolution and joint plastic deformation, which influence the removal of impurities such as oxide particles from the weld zone and consequently control the weld quality. The effects of various welding parameters on temperature distribution along the axial direction of friction welded joints were studied using a 3D FEM model in this work. An experimental study was also conducted by joining two similar 15CDV6 alloy steel rods to validate the simulation results.

2 Material and Methods

2.1 Material

15CDV6 alloy steel rods with a diameter of 16 mm and a length of 65 mm were employed in this study. Table 1 [18] shows the chemical composition of the sample.

Table 1 Chemical compositions of 15CDV6 alloy steel used in experimental studies

Element	C	Si	Mn	Cr	Mo	V	Fe
Min (%wt.)	0.12–0.18	0.13	0.8–1.0	1.25–1.5	0.80–1.0	0.20–0.3	Bal.

Table 2 Young's modulus and thermal conductivity of 15CDV6 alloy steel

Temperature	Young's modulus (GPa)	Thermal conductivity (W/mK)
50	208	26.99
100	205	28.33
200	199	30.49
300	191	31.79
400	181	32.15
500	170	31.72
600	157	30.83
700	143	29.88
800	129	29.23
900	114	29.08
1000	99.3	29.47
1100	84.9	30.27

Table 3 Specific heat and thermal expansion coefficient of 15CDV6 alloy steel

Temperature	Specific heat (J/KgK)	Thermal expansion coefficient ($10^{-6}/K$)
50	461.6	14.102
100	480.32	14.25
200	517.16	14.57
300	558.16	14.88
400	607.56	15.2
500	670.68	15.51
600	758.72	15.83
700	759	16.15
800	760.56	16.47
900	707.08	16.79
1000	691.4	17.12
1100	690.12	17.44

2.1.1 Material Properties

The temperature-dependent material properties of 15CDV6 alloy were calculated by using the JMatPro code. The Young's modulus and thermal conductivity of 15CDV6 alloy are listed in Table 2 and the specific heat capacity and thermal expansion coefficient are listed in Table 3.

Table 4 Parameters for Johnson cook material model

A (MPa)	B (MPa)	C	n	m	$\dot{\epsilon}_0$
790	943.88	.11	0.2408	0.477	1

2.1.2 Material Model

For finite element modeling, the Johnson–cook model was chosen to calculate flow stress. The following equation explains the relationship between flow stress and strain hardening, strain rate hardening, and temperature softening:

$$\sigma = (A + B\epsilon^n)(1 + C \ln \dot{\epsilon}^*)(1 - T^{*m}) \quad (1)$$

The elastic–plastic, viscosity, and thermal softening terms of the Johnson–Cook model are described by the first, second, and third brackets of Eq. (1) respectively. In Eq. (1), σ is the equivalent flow stress, ϵ is the equivalent plastic strain, A is the yield stress at reference temperature and reference strain rate, B is the coefficient of strain hardening, n is the strain hardening exponent, C and m are the material constants which represent the coefficient of strain rate hardening and thermal softening exponent, respectively, $\dot{\epsilon}^* = \dot{\epsilon}/\dot{\epsilon}_0$ is the dimensionless strain rate ($\dot{\epsilon}$ is the strain rate, while $\dot{\epsilon}_0$ is the reference strain rate), and T^* is the homologous temperature and expressed as

$$T^* = \frac{T - T_{\text{ref}}}{T_m - T_{\text{ref}}} \quad (2)$$

where T is the current absolute temperature, T_m is the melting temperature, and T_{ref} is the reference temperature ($T \geq T_{\text{ref}}$) [19–23].

The procedure for computing the constants of the Johnson–Cook model from JMatPro stress flow curves involves the following steps [4, 22]:

- The value of A is calculated from the yield stress of the metal given in Table 4, that is, $A = 790$ MPa.
- At $T = T_{\text{ref}}$, and $\dot{\epsilon} = \dot{\epsilon}_0$, the curve $\ln(\sigma - A)$ versus $\ln(\epsilon)$ is plotted. The values of B and n are extracted from the intercept and slope of this plot, respectively.
- Substituting the values of A , B , and n in Eq. (1) and assuming $T = T_{\text{ref}}$ which eliminates the thermal softening term, the strain rate coefficient (C) is obtained from the slope of the graph $[\sigma/(A + B\epsilon^n)]$ versus $\ln(\dot{\epsilon})$.
- At $\dot{\epsilon} = \dot{\epsilon}_0$, the viscosity term is eliminated. The exponent m is obtained from the slope of the graph $\ln[1 - \{\sigma$

$/(A + B\epsilon^n)\}$ versus $\ln[(T - T_{\text{ref}})/(T_m - T_{\text{ref}})]$. The material-dependent constants A , B , C , n , and m are given in Table 4.

In ANSYS software, there is an option to provide the material model and temperature-dependent properties.

2.2 Thermal Model

The classical Coulomb's friction law is used to describe the friction behavior at a low temperature which relates to shear stress at contact and axial pressure [3]:

$$\tau = \mu P \quad (3)$$

where τ is the shear stress at the frictional contact, μ the coefficient at friction, and P the contact pressure. At this stage, the coefficient of friction is simplified as a constant, 0.5. At higher temperatures, the material yield strength decreases rapidly, the interface shear strength is dominant at the frictional interface and is given by the Von Mises yield criterion as:

$$\tau_{\text{shear}} = \frac{\sigma_y}{\sqrt{3}} \quad (4)$$

where τ_{shear} is the flow shear stress and σ_y is the equivalent flow stress.

According to Amontons' law, the heat generated by friction between the workpiece is given by

$$q = \mu p \omega r \quad (5)$$

where q is the heat generated due to friction, ω the angular velocity, and r the workpiece radius.

After the material yields, friction at the interface becomes independent of pressure and visco-plastic friction is dominant at the interface. At this stage, equivalent flow stress takes the value of shear stress of the material, and heat generation is given by

$$q = \tau_s \omega r \quad (6)$$

where τ_s is the yield shear stress, ω the angular velocity, and r the workpiece radius.

3 Numerical Modeling

3.1 FE Modeling of Rotary Friction Welding

For the simulation of rotary friction welding, the ANSYS software was employed and a coupled thermomechanical transient method was selected. The software was provided temperature-dependent material properties. The temperature distribution along the axial direction of a friction welded

joint for various process parameters is the focus of this simulation.

3.2 FE Model and General Assumptions

The software ANSYS was used to create a 3D finite element model. Each part was constructed with a diameter of 16 mm and a length of 65 mm. The computations were first carried out with a coarser mesh. Even though the solution got converged, the results produced were not within the permitted experimental tolerance. Later, mesh refinement was performed until the solution was independent of mesh refinements and could be considered acceptable. As shown in Fig. 1, the material was categorized into two sections for meshing purposes: a tetragonal-shaped interface region around an 8 mm length was created with a meshing size of 0.8 mm, and a meshing size of 2 mm was designed away from the weld location. The pressure and heat generated at the weld interface were presumed to be uniform for RFW analysis. Initially, the parts to be welded were in contact. The work holding devices were not considered in the model.

3.3 Boundary Conditions and Simulation Settings

The pressure was applied to the non-contact face of the non-rotating component, which was parallel to the frictional interface. Heat loss owing to convection, conduction, and radiation were all included in the thermal boundary conditions. Throughout the analysis, the material emissivity was set to 0.4 and the heat transfer coefficient was set at 25 W/m²K [4, 6, 24].

Table 5 shows the welding parameters chosen for friction welding of 15CDV6 alloy steel. Three sets of parameters were used in the simulations to investigate the impacts of axial pressure, rotation speed, and friction time on the RFW process. In group I, the process was concentrated at 1500 rpm with an 8-s friction time, and the axial pressure was altered for each run. At constant axial pressure and friction time, different rotation speeds were investigated in

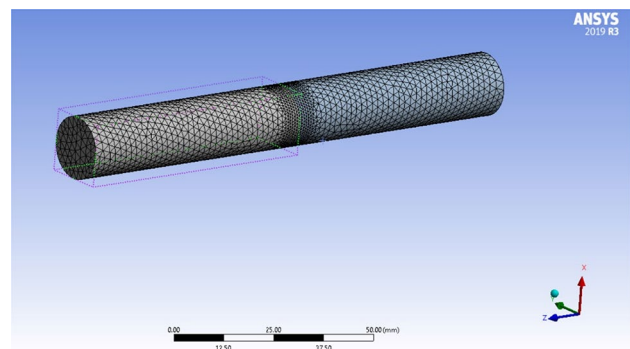
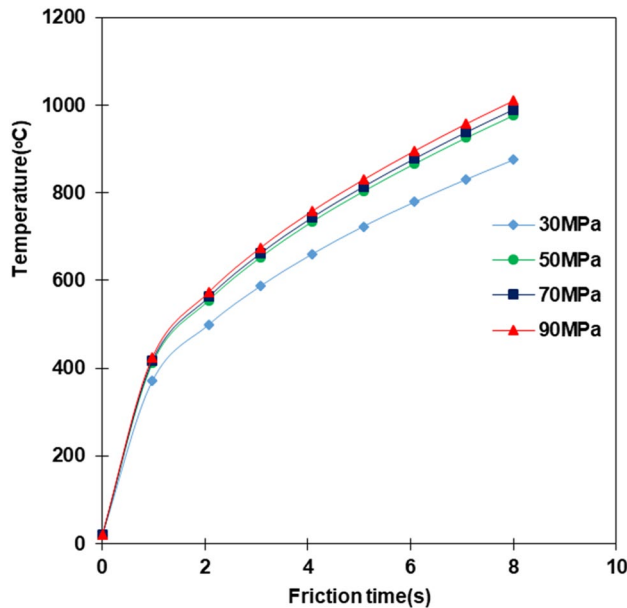


Fig. 1 Complete mesh geometry of the material model

Table 5 The welding parameters selected for simulation

Parameters	Rotation speed (rpm)	Friction pressure (MPa)	Friction time (s)
Group I	1500	30, 50, 70, 90	8
Group II	1250, 1500, 1750, 2000	50	8
Group III	1500	50	7, 8, 9, 10

**Fig. 2** The effect of friction pressure on the temperature evolution at the weld interface

group II. To evaluate the influence of friction time, the axial pressure and rotation speed were held constant in group III. In the above three cases, the friction pressure and upsetting pressure were considered to be the same. The loading was applied in two load steps, the friction stage was considered as the first step and the upsetting stage was considered as the second step. Also, the automatic time stepping options were selected for decreasing the simulation time. The cooling stage was not considered in this study.

4 Results and Discussion

In this study, a simulation of RFW of 15CDV6 alloy steel rods was conducted. Experiments were carried out to predict the accuracy of the developed FEM model.

4.1 Effect of Friction Pressure

The effect of friction pressure on the temperature evolution in the frictional stage of the RFW method is shown in Fig. 2. The maximum temperature distribution is at 90 MPa friction pressure and the minimum is at 30 MPa. During the

initial period of the frictional stage, the temperature profile follows the same path for all the values of friction pressure. Afterward, the variation in the pattern of temperature distribution is easily identifiable. The temperature at the interface increases as welding progresses, and reaches a maximum at the end of the frictional stage. The temperature evolution at the joint is identical for different axial pressure, and the peak temperature increases with the increase in the friction pressure. This is because friction pressure has a significant impact on material softening which leads to the temperature rise during the friction stage of the friction welding process.

Figure 3a–d represents the effect of friction pressure on temperature distribution at 1500 rpm, 8 s friction time, and 50 MPa upsetting pressure. The temperature distribution is symmetric and steadily declines from the peak value to either side of the weld interface. This is due to the use of similar materials in the welding process. It's also worth noting that when the friction pressure rises, the temperature rises in the frictional stage and the maximum temperature is at 90 MPa. It can be concluded that friction pressure has a major contribution to heat generation and temperature gradient.

4.2 Effect of Speed of Rotation

The peak temperature during friction welding rises as the rotational speed rises. At 50 MPa friction pressure, 50 MPa upsetting pressure, and 8 s friction time, Figs. 4 and 5a–d show the effect of rotation speed on interface temperature distribution during the frictional stage. The temperature rises rapidly for all rotating speeds during the early stage and reaches its highest value at the end of the friction stage. This is due to the effect of material strain rate on rotation speed, which has a considerable impact on material flow stress.

The temperature starts at 22 °C and quickly rises to 500 °C. For this time period, the temperature profiles for different rotation speeds almost coincide with each other, and after 3 s, a differentiable variation is observed. The minimum temperature profile is for 1250 rpm and the maximum profile is for 2000 rpm.

4.3 Effect of Friction Time

Figure 6a–d depicts the temperature distribution of friction welds at various friction times at 1500 rpm and 50 MPa friction pressure. Friction time is the period at which frictional

Fig. 3 The effect of friction pressure on temperature field at 1500 rpm and 8 s friction time, and 50 MPa upsetting pressure

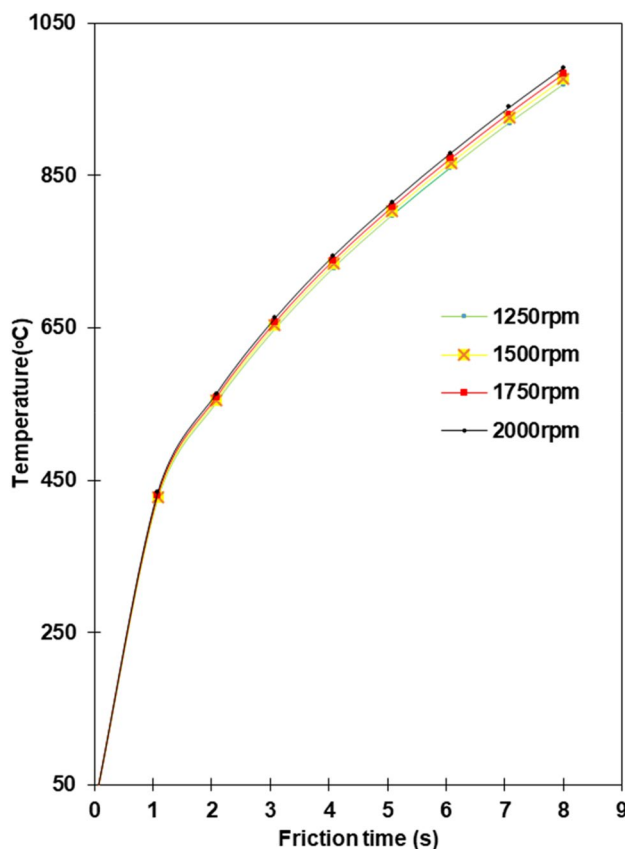
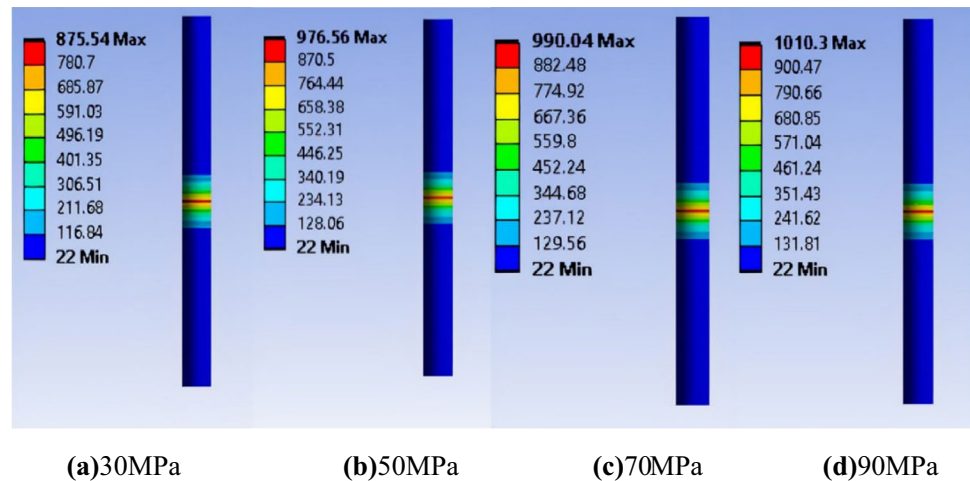


Fig. 4 The effect of rotating speed on the temperature evolution at the weld interface

heat is applied across the weld interface. With rising friction time, the maximum temperature generated during friction welding increases.

Figure 7a–c depicts the axial distribution of temperature fields for the same joint at 1500 rpm and 90 MPa axial pressure to understand the temperature profile distribution over time. The initial contact formed at the interface is not exactly

at the center and is a distance away along the radial direction. The non-uniform heat generation causes incomplete contact between the workpieces.

From Fig. 7a–c, the maximum heat generated in the early phases is not directly in the middle of the weld zone. i.e., the temperature distribution in the plastically deformed zone at the interface is not uniform. At 8 s, the heat dispersion indicates a consistent distribution in both directions. It can be seen that as the friction duration increases, the width of each zone expands symmetrically. The evolution of radial temperature distributions at the weld interface at 1500 rpm under 90 MPa forging pressure is depicted in Fig. 8. The simulated temperature fields during the frictional stage in Fig. 7 provide the basis for these observations. Friction welding is divided into two stages: the corona bond evolution stage and the extrusion stage. The plastic flow of the material happens during the corona bond evolution stage as the temperature rises. The maximum temperature along the radial direction is not in the middle of the joint and it is in between the radius of the circular section. The initial joint is formed at the interface, where the maximum temperature occurs.

5 Experimental Validation

The welding experiments were conducted on 15CDV6 alloy steel based on the parameters given in Table 4 to validate the simulated results. Rotary friction welding equipment, spm-FW-01 with a maximum diameter of 20 mm was used in the experiment. Figure 9 shows the experimental setup of rotary friction welding (@CEMAJOR, Annamalai University). To avoid the effect of surface roughness, the faying surfaces of the rod specimens were polished and cleaned. During the friction welding process, an infrared thermometer measuring from -50 to 1800 °C with a USB PC interface and adjustable emissivity from 0.10 to 1.0 in non-contact mode was

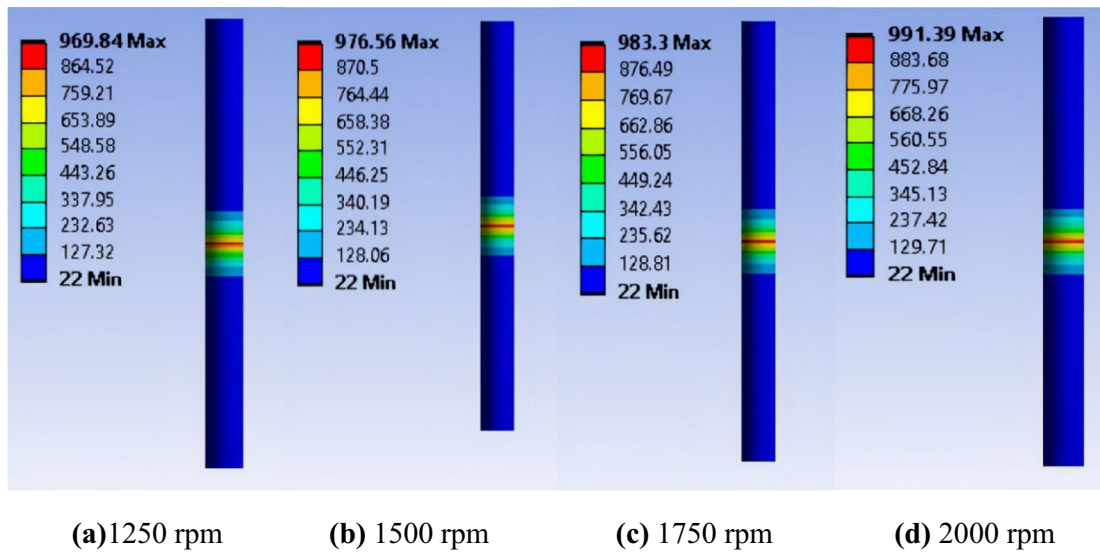


Fig. 5 The effect of rotation speed on temperature field at 50 MPa friction pressure, 50 MPa upsetting pressure and 8 s friction time

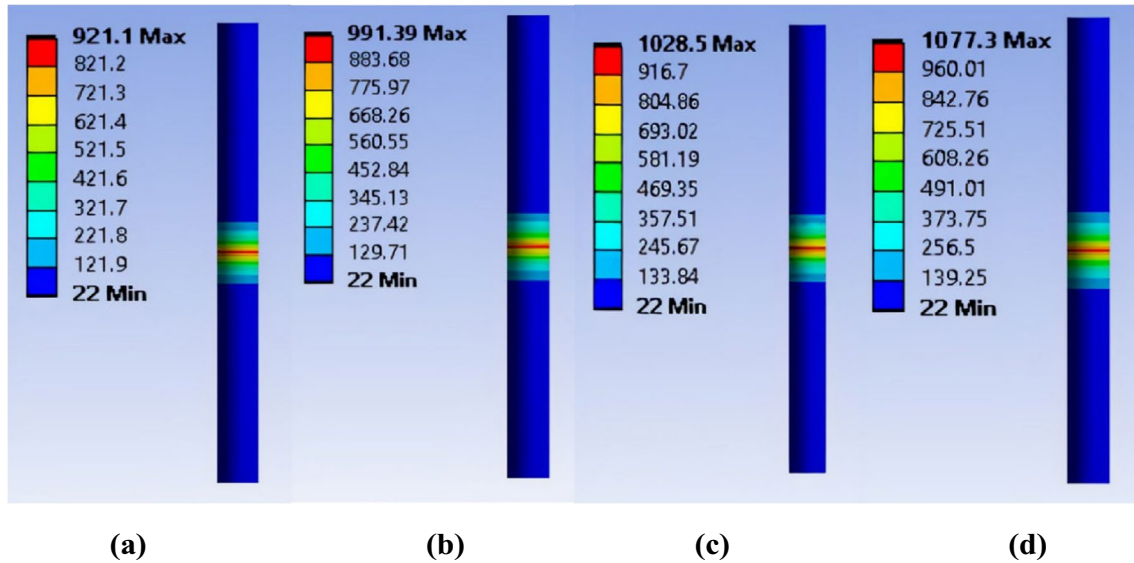


Fig. 6 The effect of friction time on temperature field at 1500 rpm and 50 MPa friction pressure

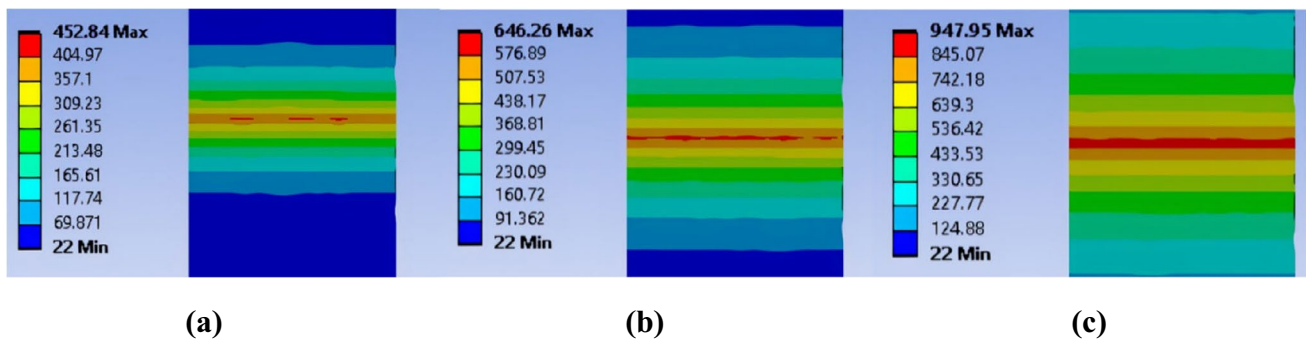


Fig. 7 The effect of friction time on heat distribution along the interface at 1500 rpm under 90 MPa axial pressure

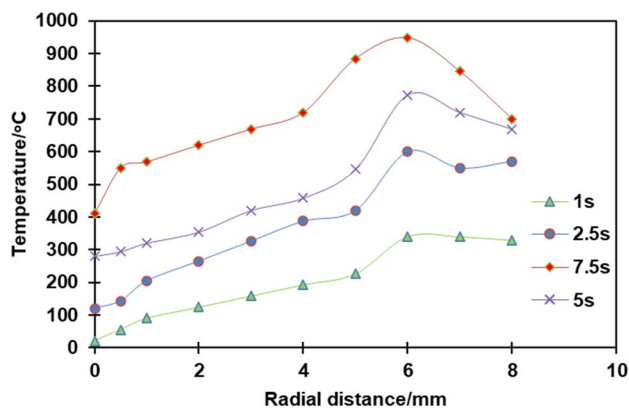


Fig. 8 Evolution of the interface temperature distributions of a weld at 1500 rpm under 90 MPa forging pressure

utilized to determine the temperature distribution. The infra-red thermometer was calibrated before measuring. Along the weld interface region, the temperature was measured. The

Fig. 9 Experimental setup of rotary friction welding (@ CEMAJOR, Annamalai University)



model's accuracy was confirmed by comparing experimental and simulated findings. The parameters used were the same as that of the simulation. Table 6 explains the experimental and simulated peak temperatures of the friction weld interface of 15CDV6 alloy steel. Overall, the model has achieved around 94% of accuracy. It can be concluded that the assumptions made during the simulation greatly affect the accuracy of the model.

Figure 10a–c compares the experimental and simulated peak temperature during the friction welding process for variation in axial pressure, rotation speed, and friction time respectively. There is a good agreement between simulated and experimental results.

6 Conclusions

Rotary friction welding of 15CDV6 alloy steel was simulated using a 3D non-linear finite element model in ANSYS. The effects of friction pressure, rotating speed,

Table 6 Experimental and simulated peak temperatures of friction welded 15CDV6 alloy steel

Exp. No	Group 1				Group 2				Group 3			
	1	2	3	4	5	6	7	8	9	10	11	12
Experimental peak temperatures (°C)	860.7	970.23	995.1	1010	935.6	967.2	971.4	980.6	906.8	971.6	998.3	1065.9
Simulated peak temperatures (°C)	875.54	976.56	990.04	1010.3	969.84	976.56	983.3	991.39	921.1	991.39	1028.5	1077.3

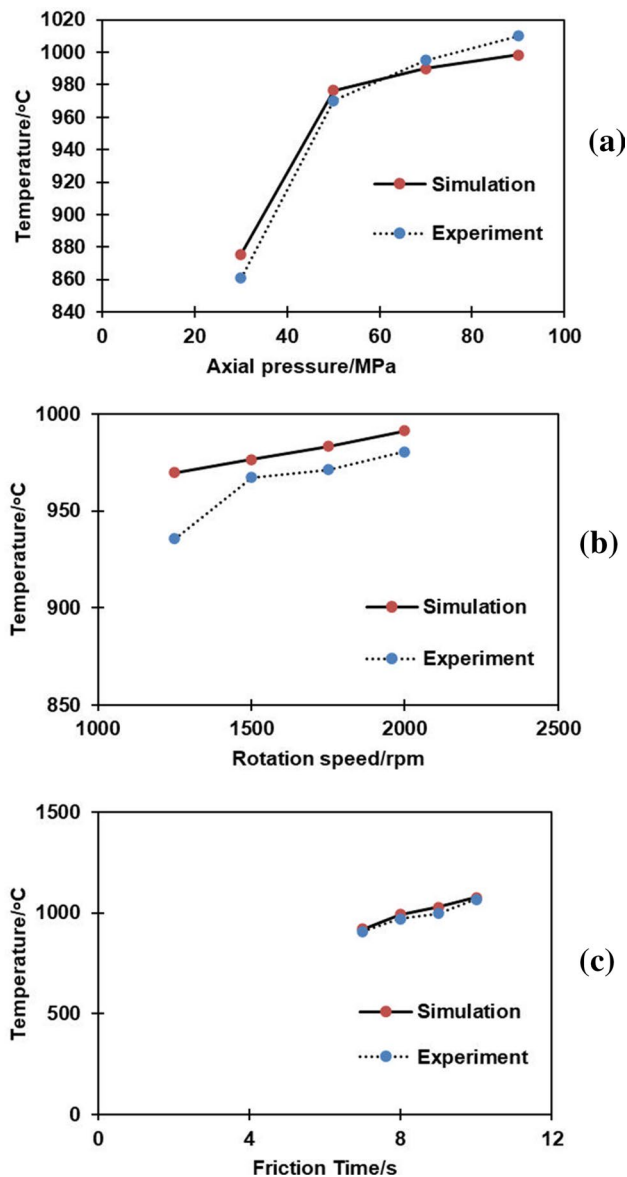


Fig. 10 The comparison of maximum temperature obtained from experimental and simulation for group I, II, and III parameters

and friction time on the temperature profile was studied using experiment and simulation and the following conclusions were drawn:

- (1) Numerical simulation of rotary friction welding using ANSYS Workbench has been carried out. The simulation results of temperature distributions along the axial direction and maximum temperature along with the interface at different axial pressure, rotating speed and friction time show a good agreement with actual experimental results. The maximum temperatures are much below the melting point of the material.

- (2) With increasing the axial pressure, rotating speed, and friction time, the temperature across the weld joint increases.
- (3) The temperature profile on both sides of the weld joint shows a similar pattern. This is due to the joining of similar materials.
- (4) As the friction time increases, the peak temperature developed increases up to the friction stage and starts decreasing slightly during the upsetting stage. This is due to the extrusion of highly plasticized material.
- (5) The model has achieved 94% accuracy. This model can be used to predict the welding parameters to obtain better weld quality.

Acknowledgements The authors gratefully acknowledge the support from the All India Council for Technical Education(AICTE), under the scheme of the AICTE Doctoral Fellowship (ADF).

Funding Not applicable.

Data Availability Not applicable.

Code Availability Not applicable.

Declarations

Conflict of interest The authors declare no competing interest.

Ethics Approval Not applicable.

Consent to Participate Not applicable.

Consent for Publication The consent to submit this paper has been received explicitly from all co-authors.

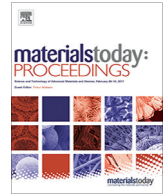
References

1. Lei B, Shi Q, Yang L, Liu C, Pan J and Chen G, *J Manuf Process* **56** (2020) 643. <https://doi.org/10.1016/j.jmapro.2020.05.034>
2. Jin F, Li J, Liu P, Nan X, Li X, Xiong J and Zhang F, *J Manuf Process* **46** (2019) 286. <https://doi.org/10.1016/j.jmapro.2019.09.008>
3. Jin F, Li J, Du Y, Nan X, Shi J, Xiong J and Zhang F, *J Manuf Process* **45** (2019) 595. <https://doi.org/10.1016/j.jmapro.2019.08.001>
4. Asif, M M, Shrikrishana K A and Sathiya P, *Eng Sci Technol Int J* **18** (2015) 704. <https://doi.org/10.1016/j.jestch.2015.05.002>
5. Li W, Liu Y, Jiang S, Luan Q, Li Y, Gu B and Shi Z, *Int J Light Mater Manuf* **2** (2019) 31. <https://doi.org/10.1016/j.ijlmm.2018.10.002>
6. Kong Y S, Cheepu M and Park Y W, *Trans Indian Inst Met* **73** (2020) 1433. <https://doi.org/10.1007/s12666-020-01900-4>
7. Li P, Li J and Dong H, *J Manuf Process* **25** (2017) 181. <https://doi.org/10.1016/j.jmapro.2016.12.003>
8. Jedrasiak P and Shercliff H R, *Mater Des* **177** (2019) 107833. <https://doi.org/10.1016/j.matdes.2019.107833>

9. Jedrasiak P and Shercliff H R, *J Mater Process Technol* **263** (2019) 207. <https://doi.org/10.1016/j.jmatprotec.2018.07.031>
10. Bouarroudj E O, Chikh S, Abdi S and Miroud D, *Appl Therm Eng* **110** (2017) 1543. <https://doi.org/10.1016/j.applthermaleng.2016.09.067>
11. Li W and Wang F, *Mater Sci Eng A* **528** (2011) 5921. <https://doi.org/10.1016/j.msea.2011.04.001>
12. Li P, Li J, Li X, Xiong J, Zhang F and Liang L, *J Adhes Sci Technol* **29** (2015) 1246. <https://doi.org/10.1080/01694243.2015.1022499>
13. Seli H, Noh M Z, Ahmad A I, Rachman E and Ahmad Z A, *J Alloys Compd* **506** (2010) 703. <https://doi.org/10.1016/j.jallcom.2010.07.047>
14. McAndrew A R, Colegrove P A, Addison A C, Flipo B C D and Russell M J, *Mater Des* **66** (2015) 183. <https://doi.org/10.1016/j.matdes.2014.10.058>
15. Zhao P, Fu L and Zhong D, *Comput Mater Sci* **92** (2014) 325. <https://doi.org/10.1016/j.commatsci.2014.05.062>
16. Reddy D R, Laxminarayana P, Reddy G C M and Reddy G M S, *Int J Eng Manuf* **6** (2016) 38. <https://doi.org/10.5815/ijem.2016.05.05>
17. Ajith P M, Sathiya P and Aravindan S, *Friction* **2** (2014) 82. <https://doi.org/10.1007/s40544-014-0042-6>
18. Srinivasan L, Mohammad Chand K, Deepan Bharathi Kannan T, Sathiya P and Biju S, *Trans Indian Inst Met* **71** (2018) 373. <https://doi.org/10.1007/s12666-017-1166-y>
19. Lin Y C and Chen X, *Mater Design* **32** (2011) 1733. <https://doi.org/10.1016/j.matdes.2010.11.048>
20. Lin Y C, Chen X and Liu G, *Mater Sci Eng A* **527** (2010) 6980. <https://doi.org/10.1016/j.msea.2010.07.061>
21. Samantaray D, Mandal S and Bhaduri A K, *Comput Mater Sci* **47** (2009) 568. <https://doi.org/10.1016/j.commatsci.2009.09.025>
22. Koyee R D, Schmauder S, Heisel U and Eisseler R, *Prod Manuf Res* **3** (2015) 36. <https://doi.org/10.1080/21693277.2014.990539>
23. Text O R, Buzyurkin A E, Gladky I L and Publishing P, *J Appl Mech Tech Phys* **56** (2015) 330. <https://doi.org/10.1134/S0021894415020194>
24. Kosky P, Balmer R, Keat W and Wise G, *Chapter 14—Mechanical Engineering*. Explor Eng (Fifth Ed) (2021), p 317. <https://doi.org/10.1016/B978-0-12-415891-7.00012-1>

Publisher's Note Springer Nature remains neutral with regard to jurisdictional claims in published maps and institutional affiliations.

Springer Nature or its licensor holds exclusive rights to this article under a publishing agreement with the author(s) or other rightsholder(s); author self-archiving of the accepted manuscript version of this article is solely governed by the terms of such publishing agreement and applicable law.



Multi response optimization and regression analysis of milling parameters of jute fibre reinforced epoxy composite

S. Harigovind, K. Shunmugesh *

Department of Mechanical Engineering, Viswajyothi College of Engineering & Technology, Vazhakulam, India

ARTICLE INFO

Article history:
Available online 1 September 2022

Keywords:
Composites
Grey Relational Analysis
Jute
Material Removal Rate
Green Composite

ABSTRACT

Multi response optimization is a tool for decision making when a number of characters are to be simultaneously considered. Multicriteria analysis helps in choosing the most feasible outcome from a finite set of available data. It is concerned with ranking of various alternatives for a particular case across all criteria. The use of organic materials to derive composites is very popular these days due to the environmental impact caused by artificial and synthetic composites. Organic or green composites are preferred by manufacturers due to their cost effectiveness, strength to weight ratio, durability etc. Jute is one of the cheapest and easily available organic fibres available. In this particular study we are concerned with the analysis of machining process of a jute fibre reinforced epoxy composite. Machining of a composite sheet results in matrix cracking, fibre pull-out, delamination etc. So, it is important to optimize various cutting parameters to obtain the most feasible results. The main objective of this study is to optimize 3 cutting parameters (output parameters) surface roughness (Ra & Rz), material removal rate and tool wear rate. To obtain these output values input parameters feed rate, spindle speed and depth of cut are varied. The Taguchi L27 orthogonal array is chosen and grey relational analysis is used to get the optimum performance parameters, that is, minimum surface roughness and Tool Wear Rate (TWR) and maximum Material Removal Rate (MRR). Regression analysis is also done to obtain empirical formulas for each parameter.

Copyright © 2022 Elsevier Ltd. All rights reserved.

Selection and peer-review under responsibility of the scientific committee of the International Conference on Processing and Characterization of Materials.

1. Introduction

In material engineering a composite is a combination of different materials with different chemical and mechanical properties. Main feature of composites is their capacity to obtain different properties according to the need of the user[1,2]. Different combination of constituents is used for different applications. Nowadays composites are used for many applications including automobile engineering, aerospace engineering etc. Most of the materials used for composite manufacturing have inorganic origins. But most of these composites suffer from wear, thermal degradation etc. So nowadays natural fibres are used to replace these artificial constituents. These materials are light weight, environment friendly, high specific strength etc[3–5]. But most of the natural materials used in making composites are fibrous in nature. This is not desir-

able when considering the machinability of these materials. This will result in fibre pull out, delamination etc. Thus, at normal conditions natural fibres have high surface roughness[6–8].

These problems can be diminished to a certain extent with the help of optimization of machining parameters. Taguchi method can be successfully implemented for this purpose. Taguchi analysis is being constantly being implemented in manufacturing and design sectors due to its capability in delivering quality goods. Taguchi's L27 or L9 methods can be used for the analysis of the machining parameters of the composite materials. L27 helps in more sophisticated analysis with 27 test results. 3 input parameters are varied to obtain different values of 3 output parameters. In study of composite manufacturing and machining this method can be effectively employed to obtain the most desirable input values for spindle speed, feed rate, depth of cut etc to obtain most desirable output[9–14].

Many applications including matlab, minitab etc can be used to carry out Taguchi's analysis. Minitab is extensively used in statistical analysis. The most important aspect of this software is its sim-

* Corresponding author.

E-mail address: shunmugesh@vjcet.org (K. Shunmugesh).

plicity. Main effect plots can be developed using this software which make this study more effective and easier to understand.

The main purpose of this study is to carry out machining of jute composite using CNC machine and to analyse the effect of inputs on the outputs such as MRR, Ra, Rz and TWR.

2. Material and methods

2.1. Jute

Jute is one of the most abundantly available natural fibre in nature. And India is one of its major manufacturers of jute. Jute fibre has good tensile strength and very low extensibility. Another advantage of jute as a natural fibre is its biodegradability. It also shows very good strength to weight ratio. Jute is one of the cheapest natural fibre available in the market. Its adhesion properties with epoxy resins are appreciable. The jute fiber is procured from Go Green products, Chennai.

2.2. Epoxy resin

Epoxy resin is one of the most abundantly used adhesives in making of composites. It has good compatibility with wide range of materials. The thermal properties of epoxy resins are also good. They can obtain good mechanical properties when cured at higher temperatures. They also show appreciable strength under bending and tension. The finishing given by epoxy after curing diminishes fibre pull-out of the composite to a certain extent. The mixing ratio of resin and hardener are 10:1. Commercially available epoxy LY556 and hardener HY951 are used in the composite.

2.3. Hand layup process

Hand layup process is one of the simplest and commonly used method for manufacturing simple composites. The composite is manufactured layer by layer, by applying epoxy resin between each layer of jute fibre cloth. The manufacturing process can be explained by following steps.

- Applying release gel to the mould.
- Mixing the epoxy resin with a hardener thoroughly.
- Applying the epoxy resin to the mould and using rollers to remove air bubbles present in the layer.
- Placing jute first jute layer over this epoxy layer.
- Applying epoxy resin to the top of the jute.
- Repeating the above cycle.

2.4. Machining process

The machining was carried out in a Jyoti VMC – 4301 CNC milling machine. The machine is shown in Fig. 1. The main parameters of this machine are.

- Spindle Motor Power – 7.5/5.5 KW
- Machine Weight – 3300 kg
- No. of Tools – 12
- Table Size – 600 mm × 300 mm
- Max. Spindle Speed – 10000 rpm
- Cutting Feed – 10 m/min

The jute epoxy composite was held on the table using an angle plate. The machining process is shown in Fig. 2. The machining was done with the help of a 6 mm diameter end milling cutter. 3 sides of the composite were machined by varying the depth of cut from 0.25 mm to 0.75 mm with an interval of 0.25 mm. The 3 feed rates



Fig. 1. Jyoti VMC 430.



Fig. 2. Machining Set-Up.

chosen were 0.25 mm/min, 0.5 mm/min and 0.75 mm/min. The speeds of spindles for the 3 levels were 2000 rpm, 4000 rpm, 6000 rpm as shown in Table 1..

Final product is shown in the Fig. 3. Total 27 results are obtained and they are tested using various equipment. The surface roughness was tested using a surface roughness testing machine. The tool wear rate was obtained through measurement of tool weight precisely after each milling operation.

3. Results and discussion

The values of Ra, Rz, Tool Wear Rate and Material Removal Rate are shown in the Table 2.. These values were fed into minitab and were subjected to analysis. The main advantage of analysis using

Table 1
Different stages of input variables.

Input parameters	Stage-1	Stage-2	Stage-3
Spindle speed (N) (rpm)	2500	4500	6500
Feed rate (f) (mm/min)	0.25	0.45	0.65
Depth of cut (d) (mm)	0.25	0.50	0.75

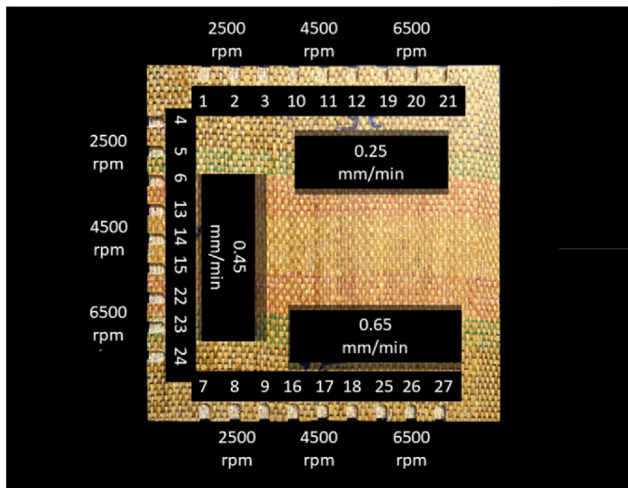


Fig. 3. Jute fibre composite.

minitab is the ability to generate main effect plot and to rank each test condition to get optimum condition.

3.1. Optimum condition for material removal rate

From the main effect plot in Fig. 4 it is obvious that the MRR increases with increase in feed rate, depth of cut and spindle speed. Hence maximum MRR is obtained at 6500 rpm speed, 0.75 mm depth of cut and 0.65 mm/min speed rate, that is test condition 27.

3.2. Optimum condition for Ra

From the main effect plot the optimum value of Ra is obtained 6500 rpm, 0.25 mm/min and depth of cut at.

0.50 mm. That its most desirable Ra values is obtained at test condition 20. The main effect plots are shown in Fig. 5.

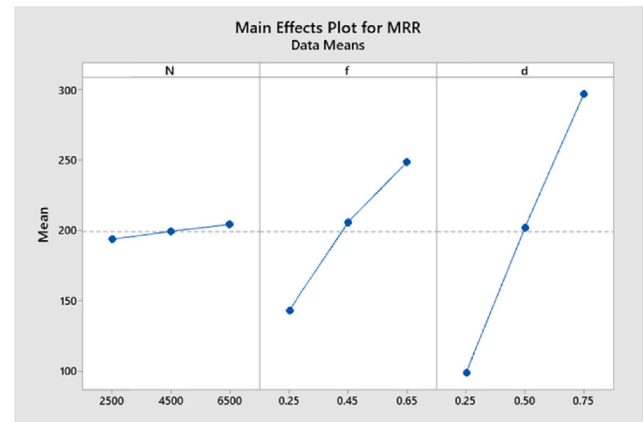


Fig. 4. Main effect plot for MRR.

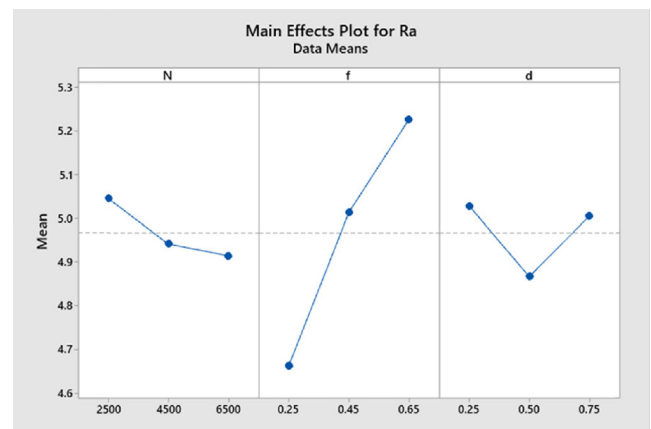


Fig. 5. Main effect plot for Ra.

Table 2

Results from experiments.

Sl. No	INPUT VARIABLES			OUTPUT VARIABLES			
	Spindle Speed (N) (rpm)	Feed Rate (f) (mm/min)	Depth of Cut (d) (mm)	MRR	Surface Roughness (Ra) (μm)	Surface Roughness (Rz) (μm)	TWR
1	2500	0.25	0.25	44	4.795	4.525	0.010
2	2500	0.25	0.50	132	4.661	4.399	0.011
3	2500	0.25	0.75	232	4.702	4.438	0.013
4	2500	0.45	0.25	95	5.165	4.875	0.015
5	2500	0.45	0.50	201	4.996	4.715	0.017
6	2500	0.45	0.75	307	5.224	4.930	0.020
7	2500	0.65	0.25	137	5.374	5.072	0.044
8	2500	0.65	0.50	250	5.091	4.805	0.043
9	2500	0.65	0.75	345	5.398	5.095	0.054
10	4500	0.25	0.25	53	4.774	4.505	0.005
11	4500	0.25	0.50	152	4.666	4.404	0.006
12	4500	0.25	0.75	232	4.626	4.366	0.005
13	4500	0.45	0.25	103	5.082	4.796	0.010
14	4500	0.45	0.50	206	4.934	4.657	0.006
15	4500	0.45	0.75	309	4.948	4.670	0.015
16	4500	0.65	0.25	152	5.207	4.914	0.030
17	4500	0.65	0.50	250	5.015	4.733	0.031
18	4500	0.65	0.75	340	5.219	4.925	0.043
19	6500	0.25	0.25	55	4.583	4.326	0.003
20	6500	0.25	0.50	147	4.504	4.251	0.003
21	6500	0.25	0.75	240	4.637	4.376	0.005
22	6500	0.45	0.25	103	4.971	4.691	0.003
23	6500	0.45	0.50	221	4.811	4.541	0.005
24	6500	0.45	0.75	309	4.986	4.705	0.006
25	6500	0.65	0.25	147	5.306	5.008	0.019
26	6500	0.65	0.50	260	5.120	4.832	0.023
27	6500	0.65	0.75	358	5.310	5.012	0.036

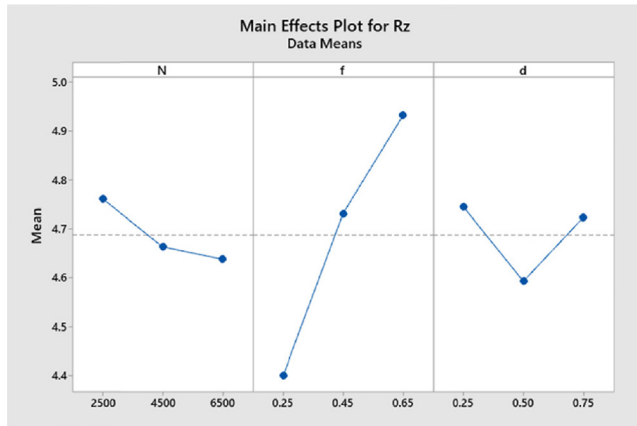


Fig. 6. Main effect plot for Rz.

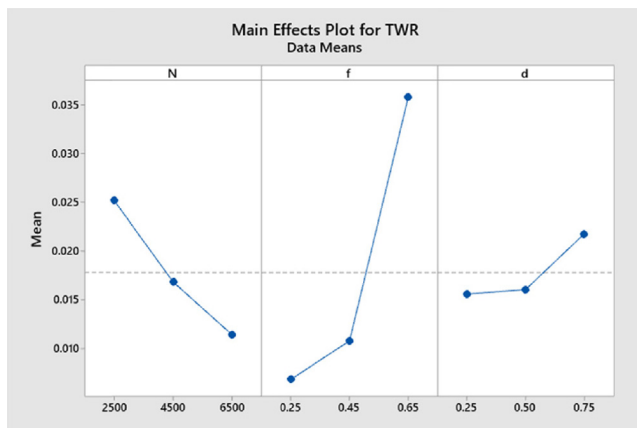


Fig. 7. Main effect plot for TWR.

3.3. Optimum condition for Rz

The main effect plot for surface roughness Rz is shown in Fig. 6. And the optimum condition is obtained at test condition 20. 6500 rpm spindle speed, 0.50 mm depth of cut and 0.65 mm/min feed rate.

3.4. Optimum condition for TWR

For minimum tool wear rate, the spindle speed should be maximum. And the depth of cut and feed rate should be minimum. The main effect plot for TWR is shown in Fig. 7. The optimum value of TWR is obtained at 6500 rpm, 0.25 mm/min feed rate and 0.25 mm depth of cut.

3.5. Grey relational analysis

The main function of Grey relational analysis is the generation of a single mathematical relation between the input parameters and each output parameters. Hence it results in a single objective function to obtain unique solution for each input parameter. Also, this result in the generation of unique Grey relational coefficient and grade. These values can be used to rank each test results and find the optimum case as shown in Table 3. Also, the main effect plot is generated for the Grey relational analysis as shown in Fig. 8. From the graph its obtained that the most optimum condition among the test results were speed at 6500 rpm, feed rate at 0.25 mm/min and depth of cut at 0.50 mm.

3.6. Mathematical modelling

$$MRR = -130.3 + 0.00266N + 264.18f + 396.79d \quad (1)$$

$$Ra = 4.5008 - 0.000033N + 1.414f - 0.04d \quad (2)$$

$$Rz = 4.2478 - 0.000031N + 1.334f - 0.0433d \quad (3)$$

$$TWR = -0.00545 - 0.000003N + 0.07241f + 0.01238d \quad (4)$$

Table 3
Grey relational analysis.

Sl. No	MRR	Surface Roughness (Ra) (μm)	Surface Roughness (Rz) (μm)	TWR	Weighted Grey Relational Grade	Rank
1	0	0.325105	0.325105	0.14	0.748304346	4
2	0.28125	0.175128	0.175128	0.16	0.719694099	8
3	0.6	0.221621	0.221621	0.19	0.641238141	11
4	0.164063	0.73904	0.73904	0.24	0.558923245	14
5	0.5	0.55007	0.55007	0.27	0.525417072	16
6	0.8375	0.80503	0.80503	0.33	0.435626794	22
7	0.296875	0.973004	0.973004	0.81	0.422003766	23
8	0.65625	0.656553	0.656553	0.78	0.421923875	24
9	0.959375	1	1	1	0.335653105	27
10	0.03125	0.301347	0.301347	0.05	0.774541539	3
11	0.34375	0.181366	0.181366	0.06	0.738272616	5
12	0.6	0.136373	0.136373	0.04	0.737969426	6
13	0.1875	0.646294	0.646294	0.14	0.595224908	13
14	0.515625	0.481319	0.481319	0.07	0.597134292	12
15	0.84375	0.496317	0.496317	0.23	0.515180337	17
16	0.34375	0.785772	0.785772	0.53	0.463943105	19
17	0.65625	0.571305	0.571305	0.54	0.461660628	20
18	0.940625	0.79927	0.79927	0.79	0.376082892	25
19	0.0375	0.088486	0.088486	0.01	0.902474925	1
20	0.328125	0	0	0	0.900943396	2
21	0.625	0.148477	0.148477	0.04	0.728111299	7
22	0.1875	0.521919	0.521919	0	0.676455961	9
23	0.5625	0.343447	0.343447	0.04	0.645531379	10
24	0.84375	0.538416	0.538416	0.06	0.556988732	15
25	0.328125	0.896861	0.896861	0.31	0.484237114	18
26	0.6875	0.688393	0.688393	0.39	0.456080681	21
27	1	0.90136	0.90136	0.64	0.371380565	26



Fig. 8. Main effect plot for grey relational grade.

4. Conclusion

A fibre was manufactured using hand layup process. And it was milled using a CNC machine. The analysis was conducted using Minitab software. The following conclusions were drawn from the experimental study:

1. Minimum Ra and Rz (Surface Roughness) was achieved at 6500 rpm, 0.25 mm/min and 0.50 mm depth of cut
2. Minimum TWR (Tool Wear Rate) was achieved at 6500 rpm, 0.25 mm/min and 0.25 mm depth of cut.
3. Maximum MRR (Material Removal Rate) was achieved at 6500 rpm, 0.65 mm/min and 0.75 mm depth of cut.
4. Overall optimum machining conditions through Grey Relational Analysis were at 6000 rpm, 0.25 mm/min and depth of cut at 0.25 mm.

CRediT authorship contribution statement

S. Harigovind: Writing – original draft, Conceptualization, Methodology, Software. **K. Shunmugesh:** Supervision, Writing – review & editing.

Data availability

Data will be made available on request.

Declaration of Competing Interest

The authors declare that they have no known competing financial interests or personal relationships that could have appeared to influence the work reported in this paper.

References

- [1] L. Gao, A. Adesina, S. Das, Properties of eco-friendly basalt fibre reinforced concrete designed by Taguchi method, *Constr. Build. Mater.* 302 (2021), <https://doi.org/10.1016/j.conbuildmat.2021.124161> 124161.
- [2] H. Chandekar, V. Chaudhari, S. Waigaonkar, A review of jute fiber reinforced polymer composites, *Mater. Today Proc.* 26 (2020) 2079–2082, <https://doi.org/10.1016/j.matpr.2020.02.449>.
- [3] H. Song, J. Liu, K. He, W. Ahmad, A comprehensive overview of jute fiber reinforced cementitious composites, *Case Stud. Constr. Mater.* 15 (2021) e00724.
- [4] A. Gabryelczyk, S. Ivanov, A. Bund, G. Lota, Taguchi method in experimental procedures focused on corrosion process of positive current collector in lithium-ion batteries, *Electrochim. Acta* 360 (2020), <https://doi.org/10.1016/j.electacta.2020.137011> 137011.
- [5] H. Singh, J.I. Singh, S. Singh, V. Dhawan, S.K. Tiwari, A brief review of jute fibre and its composites, *Mater. Today Proc.* 5 (14) (2018) 28427–28437, <https://doi.org/10.1016/j.matpr.2018.10.129>.
- [6] B. Rajeswari, K.S. Amirthagadeswaran, Experimental investigation of machinability characteristics and multi-response optimization of end milling in aluminium composites using RSM based grey relational analysis, *Meas* 1 (105) (2017 Jul) 78–86, <https://doi.org/10.1016/j.measurement.2017.04.014>.
- [7] A. Krishnamoorthy, S.R. Boopathy, K. Palanikumar, J.P. Davim, Application of grey fuzzy logic for the optimization of drilling parameters for CFRP composites with multiple performance characteristics, *Meas* 45 (5) (2012) 1286–1296, <https://doi.org/10.1016/j.measurement.2012.01.008>.
- [8] B.C. Gupta, *Statistical Quality Control: Using MINITAB, R, JMP and Python*, John Wiley & Sons, 2021.
- [9] Kenett RS, Zacks S. *Modern industrial statistics: With applications in R, MINITAB, and JMP*. John Wiley & Sons; 2021.
- [10] R. Çakıroğlu, A. Acır, Optimization of cutting parameters on drill bit temperature in drilling by Taguchi method, *Meas* 46 (9) (2013) 3525–3531, <https://doi.org/10.1016/j.measurement.2013.06.046>.
- [11] M.P. Jenarathanan, R. Jeyapaul, Optimisation of machining parameters on milling of GFRP composites by desirability function analysis using Taguchi method, *Int. J. Eng. Sci. Technol.* 5 (4) (2013) 22–36, <https://doi.org/10.4314/ijest.v5i4.3>.
- [12] B.U. Gowda, H.V. Ravindra, G.N. Prakash, P. Nishanth, G. Ugrasen, Optimization of process parameters in drilling of epoxy Si3N4 composite material, *Mater. Today Proc.* 2 (4–5) (2015) 2852–2861, <https://doi.org/10.1016/j.matpr.2015.07.300>.
- [13] K. Jayakumar, Comparative study of ball nose and flat end milling on A356 Alloy/SiC p metal matrix composite, *Trends Manuf. Eng. Manag.* (2021) 487–495, https://doi.org/10.1007/978-981-15-4745-4_43.
- [14] K. Jayakumar, Study of cutting force and surface roughness in ball nose end milling of vacuum hot pressed A356 alloy/SiCp metal matrix composite, *Mater. Today Proc.* 5 (2) (2018) 6526–6533, <https://doi.org/10.1016/j.matpr.2017.11.307>.

Study of discharge characteristics and multi objective optimisation of machining parameters in ultrasonic vibration assisted micro electrical discharge machining

Proc IMechE Part C:
J Mechanical Engineering Science
1–14
© IMechE 2023
Article reuse guidelines:
sagepub.com/journals-permissions
DOI: 10.1177/09544062231168775
journals.sagepub.com/home/pic
 SAGE

Leeba Varghese , Manesh Kailathuvalappil Kochunny and Jerin George

Abstract

Micro-EDM is a non-traditional manufacturing technique that uses the heat energy of the plasma to remove material. When there is a sufficient electric potential between two electrodes, the dielectric in between becomes ionised, resulting in the formation of a plasma channel. The net discharge energy produced is the result of the current and voltage present at the inter-electrode gap (IEG). The current and voltage waveforms obtained from the oscilloscope are used to calculate the discharge energy. A small part of this discharge energy gets converted as plasma temperature, which facilitates material removal in micro-EDM. Because plasma is the only source of heat, its properties must be studied. In the present study, Optical Emission Spectroscopy is used to calculate the temperature of the plasma. This article explores the scope of a hybrid micro EDM process, where an ultrasonic vibration is integrated to the tool electrode. A systematic approach using Response Surface Methodology is employed for modelling and analysis of plasma properties and material removal in micro EDM. Two types of input parameters were chosen: Voltage and pulse on time being the electrical parameters, and Amplitude and Frequency as the vibrational parameters. Dielectric used is deionised water. A single spark experiment was performed on Nitinol Shape Memory Alloy and tool used was of same material. Ultrasonic vibration was provided to the tool using a piezoelectric actuator. It was found that electrical parameters have a significant impact in determining plasma properties and material removal properties. Vibrational parameters play a vital impact in enhancing the crater's surface features.

Keywords

Micro-electrical discharge machining, electrical parameters, vibrational parameters, shape memory alloy, response surface methodology

Date received: 18 November 2022; accepted: 13 February 2023

Introduction

Micro EDM is a cutting-edge manufacturing technique that can remove material with sub-grain dimensions. Due to its non-contact nature, it causes minimal damage to the material and thus retains the material's properties.

Due to the heat energy of the plasma, which forms in the space between the tool and the workpiece, material removal occurs. Both the electrodes are immersed in a dielectric. A power supply circuit is utilised to apply an electric potential at the inter electrode gap (IEG) between the tool and workpiece. Primary electrons generated at the tool and those already present in the dielectric serve to start breakdown of the dielectric. A series of chemical reactions are initiated, releasing secondary electrons and a

plasma channel is created as a result of the breakdown of the dielectric. This sudden explosion of electrons appears as a spark and lasts for a few microseconds. These ions and electrons strike the tool and workpiece surfaces, melting and evaporating material from their surfaces, respectively. The pressure of the surrounding dielectric causes the plasma to collapse when the power is switched off. The dielectric flushes away the

Department of Mechanical Engineering, Government Engineering College, Thrissur, Kerala, India

Corresponding author:

Leeba Varghese, Research Scholar, Department of Mechanical Engineering, Government Engineering College, Ramavarmapuram, Thrissur 680009, Kerala, India.
Email: leebavarghese1982@gmail.com

molten metal, leaving a crater on the workpiece's surface.¹

After discharge, the dielectric deionises and regain the dielectric strength. Sometimes, even before the deionisation is complete, another discharge may take place either at the same spot or at a different location. This could be due to the non-uniform IEG because of the surface irregularities on both the workpiece and the tool. This results in further release of discharge energy, causing arcing, which may damage the surface at multiple locations.² Short circuit is also a flawed discharge caused by metal-to-metal contact. Potential difference reduces further and current flows through the point of contact.³ Material removal will not take place in this condition.

Even though many studies have been conducted on EDM technology, very few have dealt with analysing plasma discharges. Most of them are based on simulation as the physical measurement of plasma characteristics is challenging. Plasma, once formed, will last only for a few microseconds. Therefore, one has to rely on non-contact type measurement to study about plasma characteristics. This is done through optical emission spectroscopy.⁴

Breakdown of the dielectric depends on many factors, including pulse duration, inter-electrode gap length, the voltage applied and resistivity of the liquid.⁵ When dielectric flushing is applied, the probability of getting a proper spark is very low in micro-EDM. This is because the pulse duration is in the order of microseconds, and by the time a fresh dielectric occupies the inter-electrode gap, the on-time of the applied pulse will be over, and the chances of the dielectric getting deionised will reduce. Also, the IEG of a μ EDM is below $10\text{ }\mu\text{m}$, which will reduce effective dielectric flushing. A clean and debris-free dielectric at the IEG will produce a better spark. Pulsing the dielectric at the IEG causes cavitation bubbles and, later, micro jets, which effectively flush the debris at the gap.⁶

The plasma channel's hydrostatic pressure increases as the tool descend by adding acoustic pressure to the ambient dielectric pressure. This limits plasma channel growth and raises electron density (Ne). The tool electrode's high-frequency mobility enhances the kinetic energy. This raises the temperature of the plasma, causing more metal to melt from the workpiece surface.⁷

Micro EDM is a prominent manufacturing process in the machining of advanced materials like shape memory alloys (SMA) due to the increased material removal rate (MRR) and decreased surface roughness it provides. Nickel-titanium alloy, also known as Nitinol, is a SMA used in various industrial applications such as automotive, robotics, actuators, electronics and biomedical.⁸ They belong to a group of metallic alloys that can revert to their original state after undergoing a memory process that alternates between two transformation phases which is either

Table 1. EDS composition analysis of Nitinol.

Element	Weight %	Atomic %
TiK	44.8	49.8
NiK	55.2	50.2

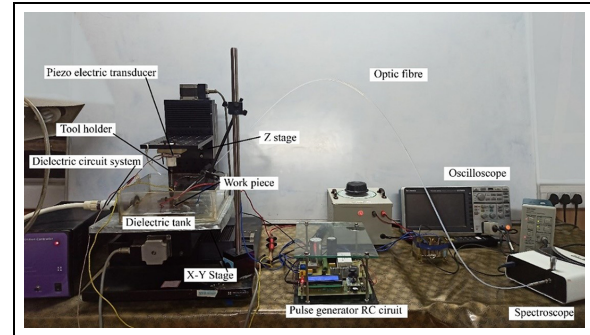


Figure 1. UV - EDM Experimental set up.

temperature or magnetic field dependent. In addition to the shape memory effect, good bifunctionality and biocompatibility make Ni Ti-based shape memory alloys (Nitinol), a suitable candidate for biomedical applications. However, it is a very difficult material to machine and calls for specialised manufacturing and finishing techniques. With Nitinol, EDM and laser cutting are frequently used techniques. The main problems are low material removal rate, high tool wear rate and low surface finish resulting in low fatigue strength of the product. This paper reports the significance of Ultrasonic Vibration Assisted micro EDM (UAmEDM) operating parameters in the characteristics of the plasma and thereby in the material removal rate of the process and surface finish of the workpiece.

Experimental details

Material used

The tool as well as workpiece used here is Nitinol. This was chosen so that migration of tool to the workpiece will not alter the properties of Nitinol. Energy Dispersive \times Ray Analysis (EDX) image is taken to check the composition of the workpiece, and the data obtained is shown in Table 1. Also, deionised water is used as the dielectric so that deposition of foreign particles on electrodes can be avoided during dielectric decomposition.

Experimental setup

An experimental setup was developed in-house as shown in Figure 1. A servo-controlled XYZ stage with a resolution of 1 micron was used. The dielectric tank is fitted on the *XY* axis. *Z* axis was provided

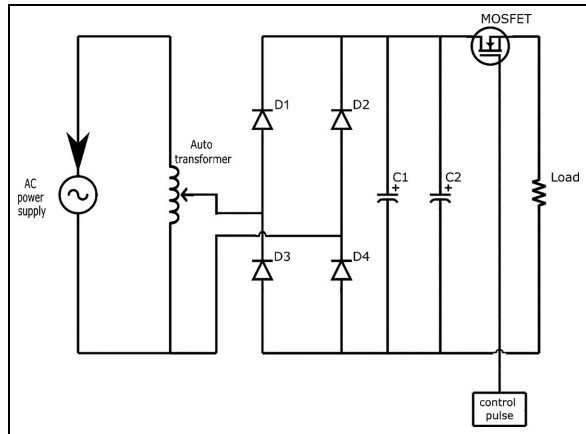


Figure 2. Pulse generator circuit.

with an emergency stop triggered by a feedback system. To set the spark gap, the tool was made to move in the Z axis. A micro position controller controls the movement of the axis through a software interface, Mach 3 Loader, a CNC control package capable of processing G codes.

The ultrasonic vibrations are generated by a piezoelectric actuator APA400M, manufactured by CEDRAT Technologies. The vibration is parallel to the direction of movement of the actuator with amplitude in the range of 0–10 μm . The output signal from the pulse generator is transmitted to the actuator through two twisted PTFE insulated AWG28 wires 100 mm long with a banana plug of diameter 1 mm. The actuator can vibrate through a frequency ranging from 0.05 to 500 kHz. It is fitted to a Teflon block for mechanical support, and the assembly is assumed to be infinitely stiff. The tool electrode is connected to the Teflon block. This is done so that when voltage is applied between the electrodes, the piezoelectric component remains safe. Also, the vibration signals are transmitted to the tool through the tool holder without loss.

The pulse generator circuit shown in Figure 2 is a hybrid circuit with the duration of the discharge waveform controlled by a transistor. An isolation transformer is used, which limits the input voltage to 110 V to protect the circuit. The discharge circuit consists of a full wave bridge rectifier that converts AC to DC. A filtering capacitor C1 is the voltage source that charges the capacitor C2, a storage capacitor. A control pulse unit and MOSFET control the pulse ON and OFF time. The tool was given negative polarity and the workpiece positive polarity.

Spark will be produced when the voltage applied becomes sufficient to split the dielectric at the inter-electrode gap (IEG). The zero-gap position is located using an inbuilt offline feedback system. Then the tool can be moved to the required position, and the required spark gap can be maintained. Tektronix TBS2000 series oscilloscope was used for monitoring current and voltage waveforms.

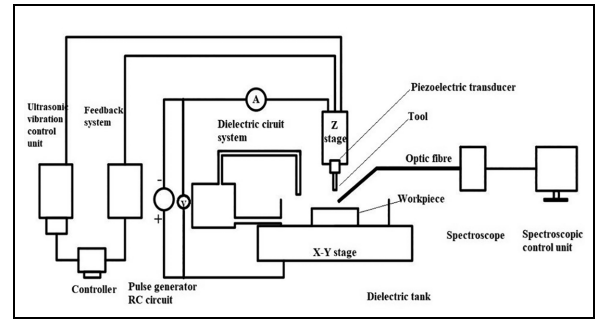


Figure 3. Schematic of UV-EDM Experiment set up.

The spectroscope used in the present study is HOLMARC Spectra G600 75F, with a wavelength range of 320–618 nm. It is equipped with a CCD camera, Toshiba TCD1304DG, to detect the light that comes in through the inbuilt micrometer-controlled variable slit on the spectroscope. Optical fibre with a core dia 1.5 mm and length of 1 m is used to capture the light produced at the spark. Spectra Analyte V2.26 is the software interface that displays the spectrum. The schematic of the experimental set up is shown in Figure 3.

Principle and methodology

Discharge energy

Plasma develops in three stages (1) Ignition phase, (2) Heating phase and (3) Removal phase.⁹ Once ionisation starts in the dielectric, its resistance to the flow of current starts to deteriorate.¹⁰ The applied potential difference drops and current starts to flow in the IEG. Thus, the discharge voltage obtained is always smaller than the open circuit voltage. A part of the thermal energy produced results in removal of material through melting and vapourisation.

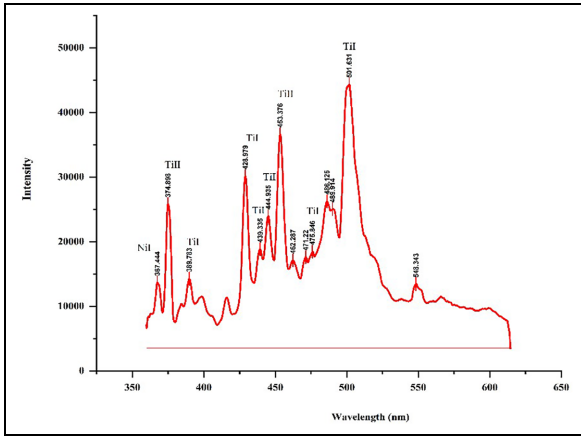
In a transistor based circuit, the net discharge energy produced at the IEG is the product of discharge voltage, instantaneous current and time.¹¹ Voltage and current waveforms were obtained for all combinations of voltage and pulse on time. In order to analyse the impact of ultrasonic vibration, the same set of experiments were repeated with an ultrasonic vibration of amplitude 5 μm and frequency 60 kHz at each discharge.

Plasma spectroscopy

The plasma formed due to the avalanche of electrons lasts only for a few microseconds, making direct temperature measurement quite challenging. Optical emission spectroscopy is used to capture light intensity generated by various elements in the plasma. Plasma formation and maintenance involve numerous chemical processes. These are ionisation, excitation, dissociation and elastic reactions as shown in Table 2.

Table 2. Reactions in plasma formation.

Sl No	Reaction	Collision type
1	$e + H_2O \Rightarrow e + H_2O$	Elastic Ionisation
2	$e + H_2O \Rightarrow e + e + H_2O +$	
3	$e + H_2O \Rightarrow e + e + OH +$	
4	$e + H_2O \Rightarrow e + e + O +$	Excitation
5	$e + H_2O \Rightarrow e + e + H +$	
6	$e + H_2O \Rightarrow e + e + H_2 +$	
7	$e + H_2 \Rightarrow e + e + H_2 +$	Attachment
8	$e + O_2 \Rightarrow e + e + O_2 +$	
9	$e + H_2O \Rightarrow e + OH$	
10	$e + OH \Rightarrow e + H_2O$	Attachment
11	$e + H_2O \Rightarrow e + H$	
12	$e + H \Rightarrow e + H_2O$	
13	$e + H_2O \Rightarrow HO + H-$	Attachment
14	$e + H_2O \Rightarrow H_2 + O-$	
15	$e + O_2 \Rightarrow O + O$	
16	$e + H_2O \Rightarrow H + OH-$	

**Figure 4.** Emission spectra.

Ions belonging to different species, which are formed from the ionisation of the dielectric as well as the dissociation at the electrodes, are liberated into the dielectric in the IEG.¹²

The diverse species absorb the energy released by the reactions during this stage, which excites them to a higher energy level. This occurs during the plasma's initialisation and expansion stages. These species return to their minimum energy stage as plasma tends to revert to its stable state. The fibre optics attached to the spectroscope capture the visible energy released.¹³ An in-line CCD camera processes the spectroscope images, and the emission spectra is plotted as displayed in Figure 4. Data from this emission spectrum is used to calculate temperature and electron density, which defines the characteristics of the plasma.

Temperature measurement. Temperature is determined using the Boltzmann line pair method. The spectrum obtained contains both continuum and line radiation.

Line radiation is due to the ions returning from an excited state to the initial state. This justifies the assumption of a local thermodynamic equilibrium (LTE) where ionisation reactions are reversible. Therefore, Maxwell-Boltzmann statistics is applied to describe the population at various energy levels of an atom. The absence of higher ionisation stages is also an indication of LTE. Continuum radiation is due to the free-bound electrons. Electrons may accelerate and escape from the control of the atom or may decelerate when they encounter some obstacle in their path. This causes continuum radiation, which may fall in any range of the electromagnetic spectrum.

According to Maxwell Boltzmann distribution, the number of particles present in the energy level, say, i th level, which is the most probable microstate, is given by

$$n_i = \frac{n_0 g_i}{Z} \exp\left(\frac{-E_i}{K_b T_e}\right) \quad (1)$$

In this case, the most probable microstate is the equilibrium microstate. Here, n_0 is the overall density of particles in plasma, g_i is the statistical weight of excited states, E_i is the excitation energy, Z is the partition function, K_b is the Boltzmann constant and T_e is electron temperature.

As the plasma is considered to be in LTE, electron temperature (T_e) is the same as the plasma temperature (T). During the upper to the lower-level transition of particles, the ε is the emission coefficient of the line emitted.

$$\varepsilon = \frac{1}{4} \frac{h_c}{\lambda} A_{ij} n_i \quad (2)$$

Where, A_{ij} is the transition probability from i to j . Replacing n_i in the equation;

$$\varepsilon = \frac{h_c n_0 g_i A_{ij}}{4 Z \lambda} \exp\left(-\frac{E_i}{K_b T_e}\right) \quad (3)$$

Considering two lines emitted from same species with wavelengths λ_1 and λ_2 , the ratio of their line intensity is obtained as;

$$\frac{I_1}{I_2} = \frac{\varepsilon_1}{\varepsilon_2} = \frac{g_1 A_1}{\lambda_1} \frac{\lambda_2}{g_2 A_2} \exp\left(\frac{E_2 - E_1}{K_b T_e}\right) \quad (4)$$

From equation (4), plasma temperature T_e ¹⁴

$$T_e = \frac{|E_2 - E_1|}{\left(\ln \frac{I_1 \lambda_1 A_2 g_2}{I_2 \lambda_2 A_1 g_1}\right) K_b} \quad (5)$$

Where E_i is the ionisation energy, A_1 is the transition probability, g_1 is the statistical weight of the excited level, and I_1 is the recorded emission line intensity at

wavelength λ_1 . E_2 , A_2 , g_2 and I_2 are similar functions at wavelength λ_2 , and K_b is the Boltzmann constant. NIST data¹⁵ can be used to determine the values of each of these parameters, with the exception of the radiant intensities I_1 and I_2 in equation (5). By using optical emission spectroscopy to quantify radiant fluxes, it is possible to determine the ratio between two intensities.

As the intensity ratios are taken from line radiations, there are chances of errors in temperature calculation if the intensity measurements are not accurate. Relatively small difference in excitation potential, and uncertainty in transition probability are also reasons for inaccuracy. Also, ground states and metastable states should be avoided since they are in the lower energy state and will tend to remain in that state for a longer period of time.

Electron density measurement. Electron density is measured from the spectral line, which is broadened as a result of collisions between perturbers in the region of emitting atoms. The acquired spectrum's line shape is influenced by electron density. It is determined using the spectral line radiation's Full Width at Half Maximum (FWHM). As the electron density increases, the line shape will broaden and shift from its theoretical position.

In EDM plasma, Stark broadening of the line radiation occurs due to collision between emitters and charged perturbers. Due to the motion of electrons and ions in the plasma channel, an electric field is developed inside the plasma, which directly influences the emitter's lines shape, and this is known as the Stark effect. In the present study, hydrogen Balmer lines (H_β) are used for electron density calculation as it is more sensitive to the Stark effect. Also, for densities up to 1017 cm^{-3} H_β line lies clearly separated from the underlying continuum as well as from the neighbouring lines. It was inferred from the literature that Lorentz fit, as shown in Figure 5 suits better for Stark broadening simulations and for calculating N_e , FWHM is used. The equation for calculating N_e is given by¹⁴,

$$N_e = C * \Delta\lambda_\beta^{3/2} \quad (6)$$

Where N_e electron density in cm^{-3} , C is excitation coefficient.

Material removal characteristics

Surface roughness. The quality of the finished surface is a crucial parameter in the micromachining of Nitinol. This is because the defects present on the surface may act as stress raisers and cause premature failure.¹⁶ All craters were measured five times using Mitutoyo, SURFTEST SJ-410 and the R_a value was averaged. The Standard used was ISO1997. Cut off length is

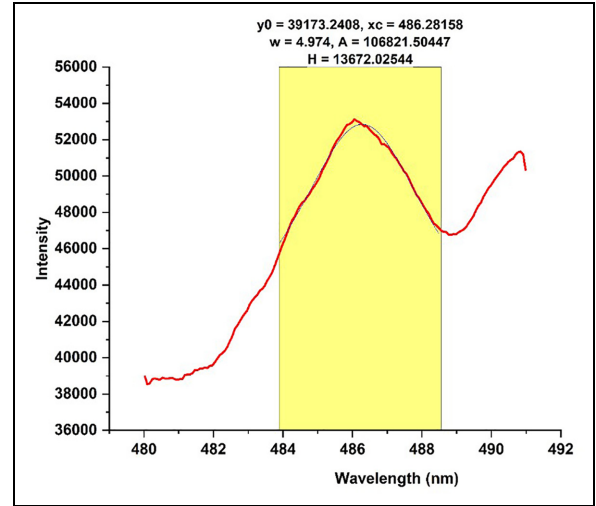


Figure 5. Lorentz fit.

0.25 mm, and the evaluation length is 0.5 mm. The filter used is Gaussian, which is used to eliminate wavelength above and below certain frequencies.

Diameter and depth of crater. Since the experiment performed was single spark experiments, the amount of material removed was very low. Therefore, the calculation of the Material Removal Rate (MRR) is irrelevant. Instead, the diameter and depth of the crater produced at each input condition are measured using a non-contact optical profilometer AEP Nanomap 1000 WL I. Three-dimensional topography is obtained, as shown in Figure 6(a). The diameter of the crater and its depth are measured from the cross-sectional data, as shown in Figure 6(b).

Results and discussion

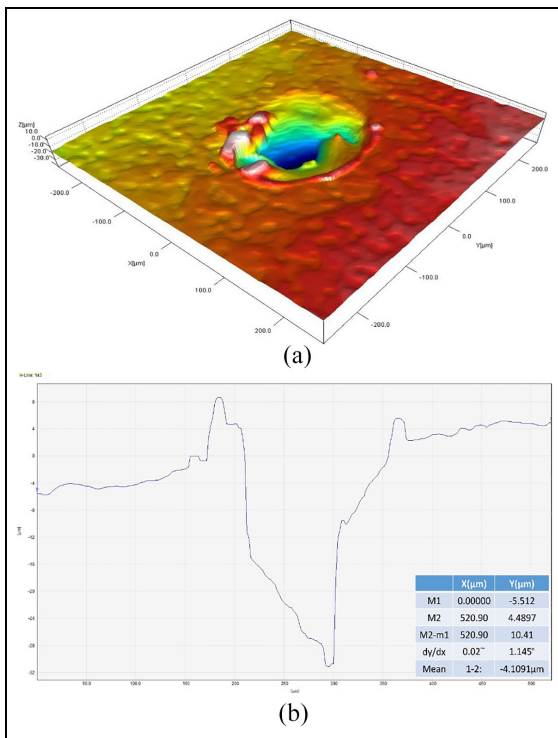
Estimation and analysis of Discharge Energy

Discharge energy was calculated for each combination of voltage and pulse on time from the current and voltage waveforms obtained from the oscilloscope. It can be seen from Table 3 that for all the nine combinations of voltage and pulse on time, the value discharge energy shows only a slight variation when ultrasonic vibration is applied.

Figure 7(a) to (i) shows the current and voltage waveforms at nine combinations of open circuit voltage and pulse on time, when ultrasonic vibration is not applied. In Figure 7(b) and (c), at an open circuit voltage of 40 V, it can be seen that, at a certain point during the discharge, the voltage drops instantly and current rises. This shows that the electrodes came in contact with each other, resulting in a short circuit. In such cases, material removal does not take place. When ultrasonic vibration is applied for the same values of voltage and pulse on time, the tool vibrates at a certain amplitude and this prevents occurrence of a

Table 3. Discharge energy and maximum current at different input conditions.

Sl no	Voltage (V)-T on (μ s)-Amplitude (μ m)-Frequency (kHz)	With vibration		Voltage-T on	Without vibration(μ j)	
		Discharge Energy (μ j)	Max Current (A)		Discharge Energy (μ j)	Max Current (A)
1	40-20-5-40	59.4	14	40-20	60.9	20
2	40-40-5-60	79	16	40-40	64.3	30
3	40-60-5-40	89.5	23	40-60	69.7	30
4	60-20-8-40	125	35	60-20	122	35
5	60-40-5-40	176	37	60-40	160	37
6	60-60-5-60	197	34	60-60	190	34
7	80-20-5-40	230	49	80-20	213	50
8	80-40-5-60	245	52	80-40	263	49
9	80-60-5-40	274	51	80-60	306	49

**Figure 6.** (a) 3D Topography of crater (b) Cross sectional data.

short circuit as can be seen in Figure 8(a) to (i). At higher values of discharge energy, the incidence of short circuit are comparatively lesser. This is because, at higher discharge energies, the break down voltage of the dielectric is reached at a comparatively higher inter electrode gap width. In the present experiment, instances of arcing were not observed.

The second set of experiments were conducted with ultrasonic vibration assisted tool electrode in micro EDM setup. Design-Expert is used for the design of experiments (DOE) and optimisation. Response surface methodology (RSM) generates DOE using the Box-Behnken design.¹⁷ Plasma temperature (T_e), electron density (N_e), surface roughness (SR), crater diameter and depth are response parameters. The input

Table 4. Process parameters and their levels.

Process parameters			
Tool electrode	Nitinol		
Work piece electrode	Nitinol		
Dielectric	De ionised water		
Polarity	Straight		
Levels	-1	0	1
Voltage (V)	40	60	80
T-on (μ s)	20	40	60
Amplitude (MU)	2	5	8
Frequency (kHz)	20	40	60

parameters employed in the current study along with their levels are listed in Table 4.¹⁸

The experiments are carried out according to run order at specified levels with two replications. The output responses, temperature, electron density, surface roughness and diameter and depth of crater are given in Table 5.

Response surface modelling (RSM) is used in this study to explore how the various UVEDM process parameters affect the output responses while establishing relationships between the parameters and various machining criteria.

An equation of the following kind describes the response surface in the general case¹⁹:

$$\begin{aligned}
 \text{Response} = & \beta_0 + \sum_{i=1}^k \beta_i x_i + \sum_{i=1}^k \beta_{ii} x_i^2 \\
 & + \sum_{i=1}^k \sum_{j=1}^k \beta_{ij} x_i x_j + \epsilon
 \end{aligned}
 \quad (7)$$

Where:

x_i = Coded levels of S quantitative process variables

β = second-order regression coefficients

Analysis of plasma characteristics

Estimation of electron temperature. Emission spectra of a spark produced at 60 V, 60 μ s on – time, with tool

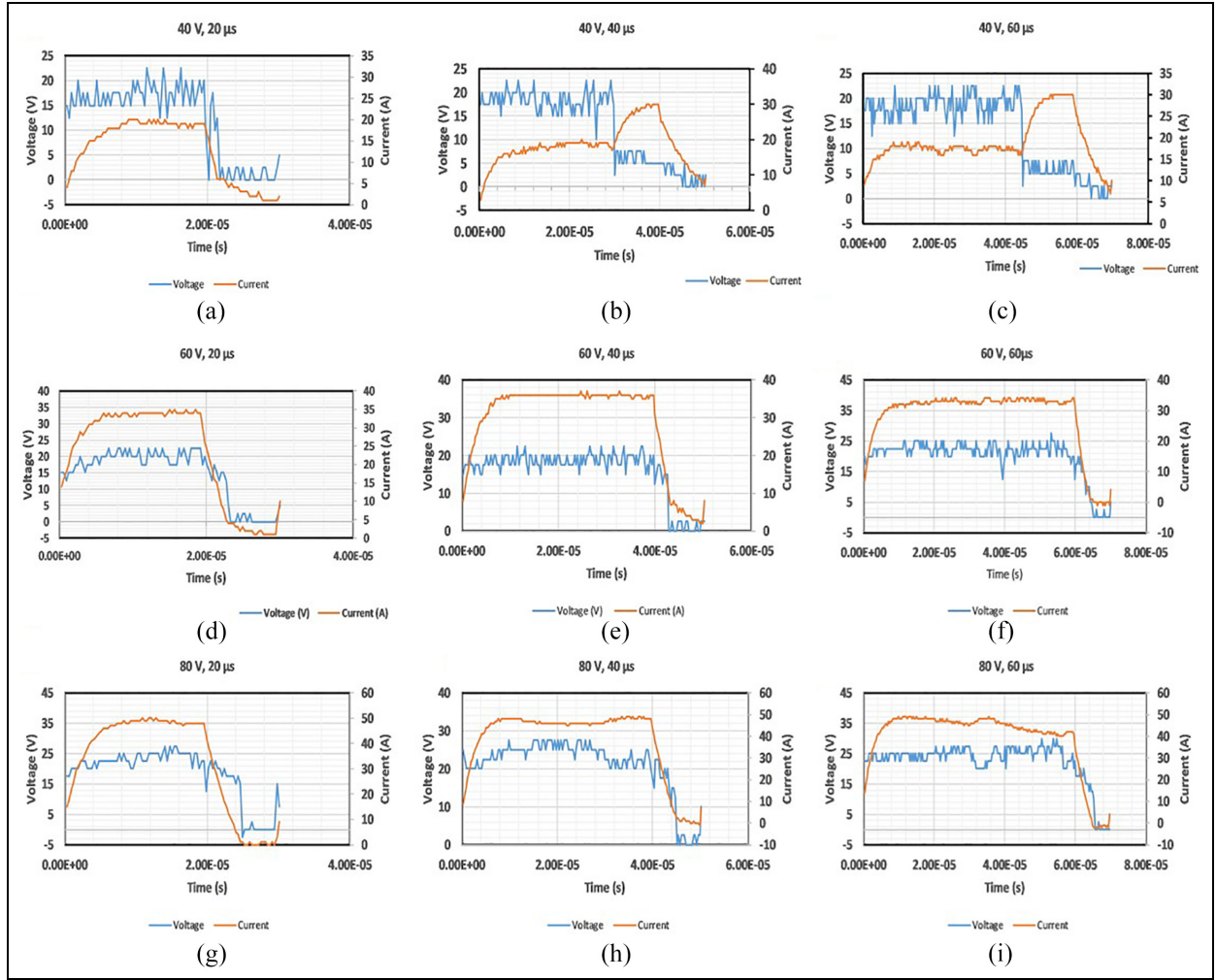


Figure 7. (a-i) Current and voltage waveforms at input conditions (without ultrasonic vibration).

vibrating at 20 kHz frequency and 5 μm amplitude is shown in Figure 4. The values of parameters in equations (5) and (6) from the NIST database, for a spectrum obtained is listed in Table 6. The singly ionised state of Titanium (TiI) is taken for the calculation. Plasma temperature varies between 3100 and 14,400 K, with an average of 8953.8 K.

Effect of machining conditions on electron temperature. The temperature analysis suggests that a quadratic model is significant as seen in Table 7. Voltage and On-time have a substantial influence on temperature. This is because the net energy developed increases with voltage and on time. In the interaction with voltage and on time with the vibrational parameters, it can be seen from Figure 9i (a) to (d) that the temperature initially tends to decrease and then reaches a maximum value.

The amplitude of vibration has a significant role in plasma temperature. A higher amplitude confines plasma to a smaller region, increasing its density and thus increasing the temperature. Frequency does not significantly influence plasma temperature. Therefore, the interaction of other parameters with frequency is insignificant, as shown in Figure 9i (e) and (f).

Estimation of electron density. Lorentz fit over the Hydrogen Balmer line with FWHM of 44.3 Å and $C = 3.30 \times 10^{14}$ is shown in Figure 5, and the electron density derived is $9.74\text{E} + 16\text{cm}^3$. The average electron density of UVEDM calculated from the study is $9.413\text{E} + 16\text{cm}^3$.

Effect of machining conditions on the electron density. Two Factor Interaction model is suggested for electron density with an F-value of 33.19 and p -value < 0.001 (Table 7). A higher pulse on time and frequency of vibration are the most relevant factors influencing electron density. A higher pulse on time facilitates more time for secondary electron emission, thus increasing electron density. The vibration frequency of the tool helps in the removal of debris from the inter-electrode gap, and therefore, a clearer dielectric is available for breakdown when the potential difference is applied. It also confines plasma to a smaller area. The significance of voltage and amplitude of vibration is relatively low. This could be because the voltage considered here is the open gap voltage, not the discharge voltage that is present in the IEG.²⁰ The

Table 5. Response table.

Trial	Input parameters				Output parameters				
	V (V)	T on (μ s)	Amp (μ m)	Fre (kHz)	Temp (K)	Electron density (cm^{-3})	Surface roughness (μ m)	Diameter (μ m)	Depth (μ m)
1	60	40	5	40	4623	9.35E+16	1.367333	162.21	23.5
2	80	20	5	40	12835.5	7.705E+16	1.284	237.5	25.08
3	40	40	5	20	7149	9.128E+16	1.7822	90	17.5
4	40	40	2	40	6090	8.224E+16	1.5664	110	16
5	80	60	5	40	12,345.5	1.024E+17	1.336	300	44.4315
6	40	20	5	40	7220	1.011E+17	1.342714	117.5	13.537
7	40	40	5	60	10,551.5	1.125E+17	1.0194	112.5	14.00285
8	60	40	2	60	10,186.5	9.803E+16	1.075714	156.25	24.052
9	60	40	2	20	5271	8.195E+16	1.83	150	24.4415
10	60	40	8	20	10,515.43	9.764E+16	1.5642	200.5	25.992
11	80	40	5	20	11,730.5	9.197E+16	1.6698	228.75	32.35
12	60	20	5	20	7447.5	9.996E+16	1.593	134.375	16.206
13	80	40	5	60	11,725.23	9.06E+16	0.915	283.75	36.772
14	40	60	5	40	10,792.89	9.357E+16	1.40275	151.075	24.869
15	40	40	8	40	11,243	1.117E+17	1.2244	140	16.1441
16	60	40	5	40	3108.85	9.75E+16	1.34375	160	25.3025
17	60	40	5	40	3075	8.495E+16	1.35225	192.62	24.108
18	60	20	8	40	7011.629	1.127E+17	1.2008	165.065	20.36325
19	80	40	2	40	12166	9.522E+16	1.431	207.5	35.578
20	60	40	8	60	6650	1.047E+17	0.832	197.5	25.8815
21	60	60	2	40	6900	1.323E+17	1.457	220.425	34.0315
22	60	20	2	40	9042.5	6.168E+16	1.412667	148.925	20.4405
23	60	60	8	40	14400	8.14E+16	1.19825	239.58	30.9225
24	60	60	5	20	9774.981	6.381E+16	1.7924	205.415	30.8588
25	80	40	8	40	11910.5	8.217E+16	1.233333	250.28	33.9695
26	60	60	5	60	11,833.5	1.373E+17	1.054	229.76	33.4585
27	60	20	5	60	6154.266	6.245E+16	0.976667	157.5	22.37

Table 6. Parameters used in equations (5) and (6).

Parameter	Line 1	Line 2
E_n (ev)	4.86	2.41
I_n	24129	26732
λ_n (nm)	475.919	519.209
A_n (s^{-1})	7.40E+07	3.86E+06
g_n	13	7
K_b (ev/K)	8.61733262E-5	
C	3.3E14	
λ_β (nm)	42.3921	

variation of electron density with respect to significant process parameters is shown in Figure 9(ii).

Effect of machining conditions on crater characteristics

Surface roughness. The values of surface roughness obtained in the experiment can be best predicted by a linear model, as shown in Table 8. Vibrational parameters play a more significant role compared to electrical parameters. The vibration of the tool electrode removes debris particles from the IEG and prevents them from getting adhered to the crater. This improves the surface roughness characteristics. The

rim of material produced at each crater surface and the tapered shape of the crater makes the measurement of surface roughness somewhat inaccurate. Post-processing operations are necessary to improve surface characteristics.²¹ The variation of surface roughness with respect to significant process parameters is given in Figure 10(i).

Diameter and depth. Linear models are suggested to predict the diameter and depth of the crater as shown in Table 8. The variation of material removal characteristics with respect to significant operational parameters is shown in Figure 10(ii) and (iii). Voltage and on-time contribute most to the material removal compared to the frequency and amplitude of tool vibration. As voltage and on time increase, the net energy produced at the plasma increases, thereby melting more material. The removal of debris from the inter electrode gap and thereby producing a clearer spark will certainly improve the material removal, but this effect will become more pronounced in multi spark experiment.

Confirmatory experiments were conducted at optimum machining parameters. The percentage error between the predicted value and experimental value was calculated as shown in Table 9. The values show reasonable reproducibility of the results.

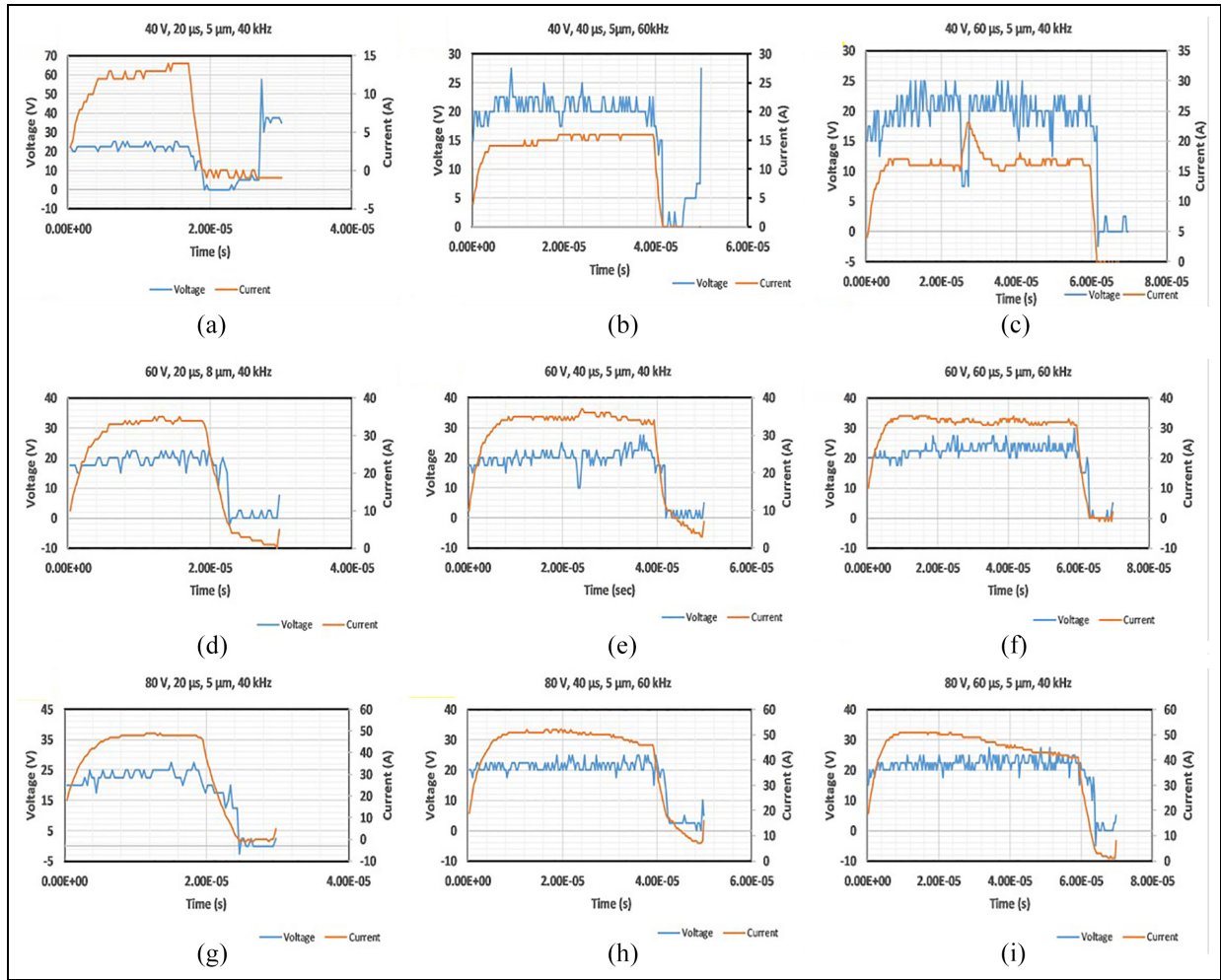


Figure 8. (a-i) Current and voltage waveforms at input conditions (with ultrasonic vibration).

Conclusion

The present work provides a deeper understanding of the discharge energy generated at the IEG in micro EDM. This initiates the chemical reactions, leading to the development of plasma channel. Phases of plasma development were identified, and the current that flows between the electrodes during the different phases was measured. This research provides information about how ultrasonic vibration affects plasma characteristics and material removal characteristics. Only a very small portion of the discharge energy appears as plasma temperature, which contributes to material removal. Plasma in micro-EDM is a transient heat source, and the heat flux distribution is Gaussian, as seen from the shape of the crater.

The factors influencing the plasma characteristics were studied by conducting single spark experiments. The conclusions obtained are summarised as follows.

1. Ultrasonic vibration does not significantly increase the discharge energy, but helps in improving material removal by reducing the

number of flawed discharges, thus improves the process stability.

2. Electrical parameters have a significant role in determining the characteristics of plasma. Higher voltage and longer pulse on time result in higher plasma temperature and electron density, thereby more material being removed. Vibrational parameters also contribute to improving plasma properties. This is because, due to vibration, plasma will be confined to a smaller area as the tool moves down in longitudinal vibration, and thus the kinetic energy of the electrons will be converted to temperature in this smaller area.
3. When it comes to surface roughness, the amplitude and frequency of tool vibration make a significant contribution due to efficient dielectric flushing caused by ultrasonic vibration. This prevents the adherence of molten debris particles on to the surface of the crater and thus reduces the surface roughness. An increase in voltage reduces surface roughness slightly but, with on time, it is found to increase, as more amount of molten metal is produced with increased discharge energy.

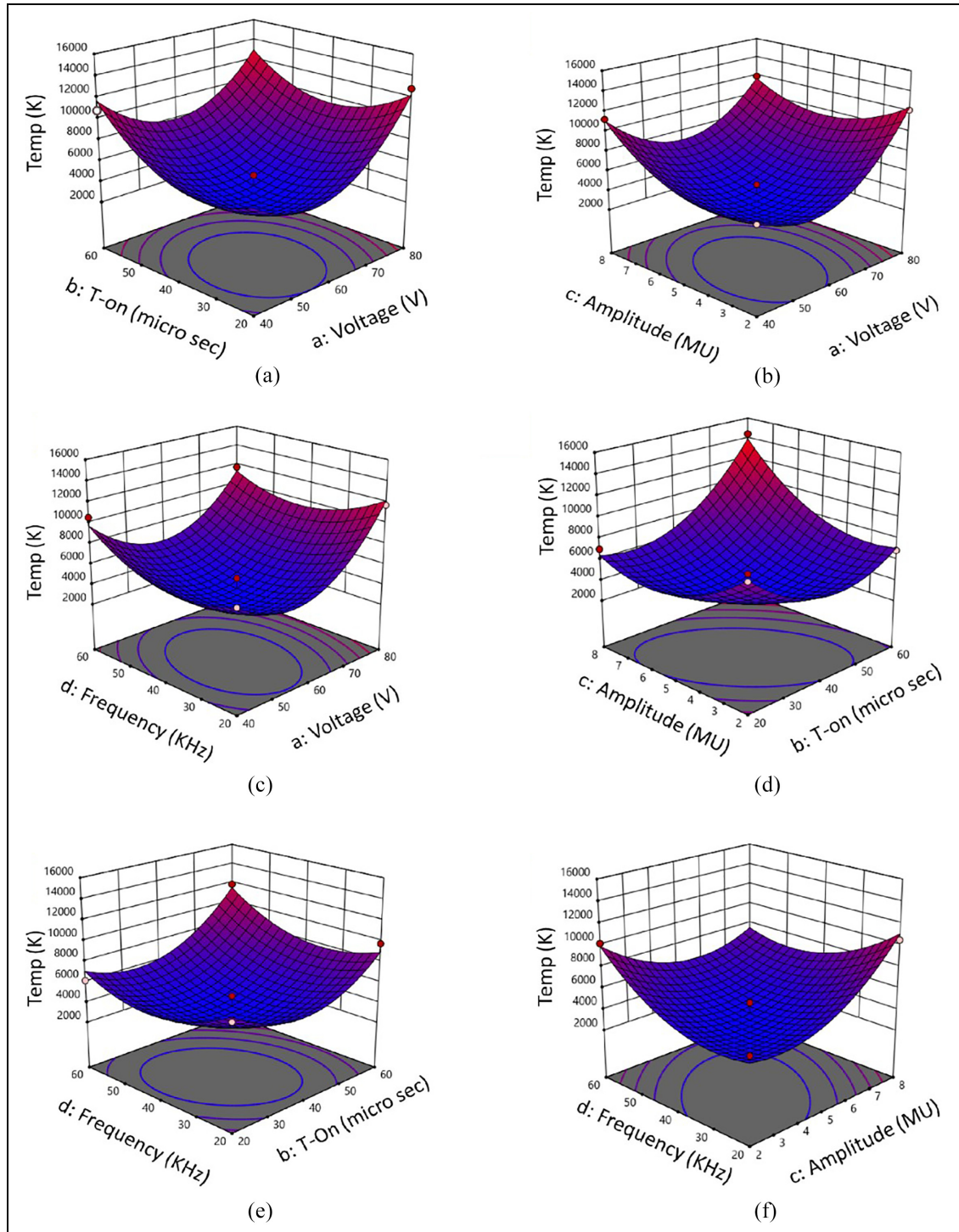


Figure 9. (Continued).

4. The diameter and depth of the crater is increased with increasing voltage and on time as this enhances the discharge energy. Vibrational parameters also indirectly contribute to material removal as they help to increase the plasma temperature and density. Also, an efficient dielectric flushing ensures that arcs or short

circuits does not happen, resulting in better material removal.

5. The depth of crater is not found to significantly increase with vibrational parameters. This may be because craters produced by a single spark are not sufficient to analyse vibrational parameters in terms of material removal.

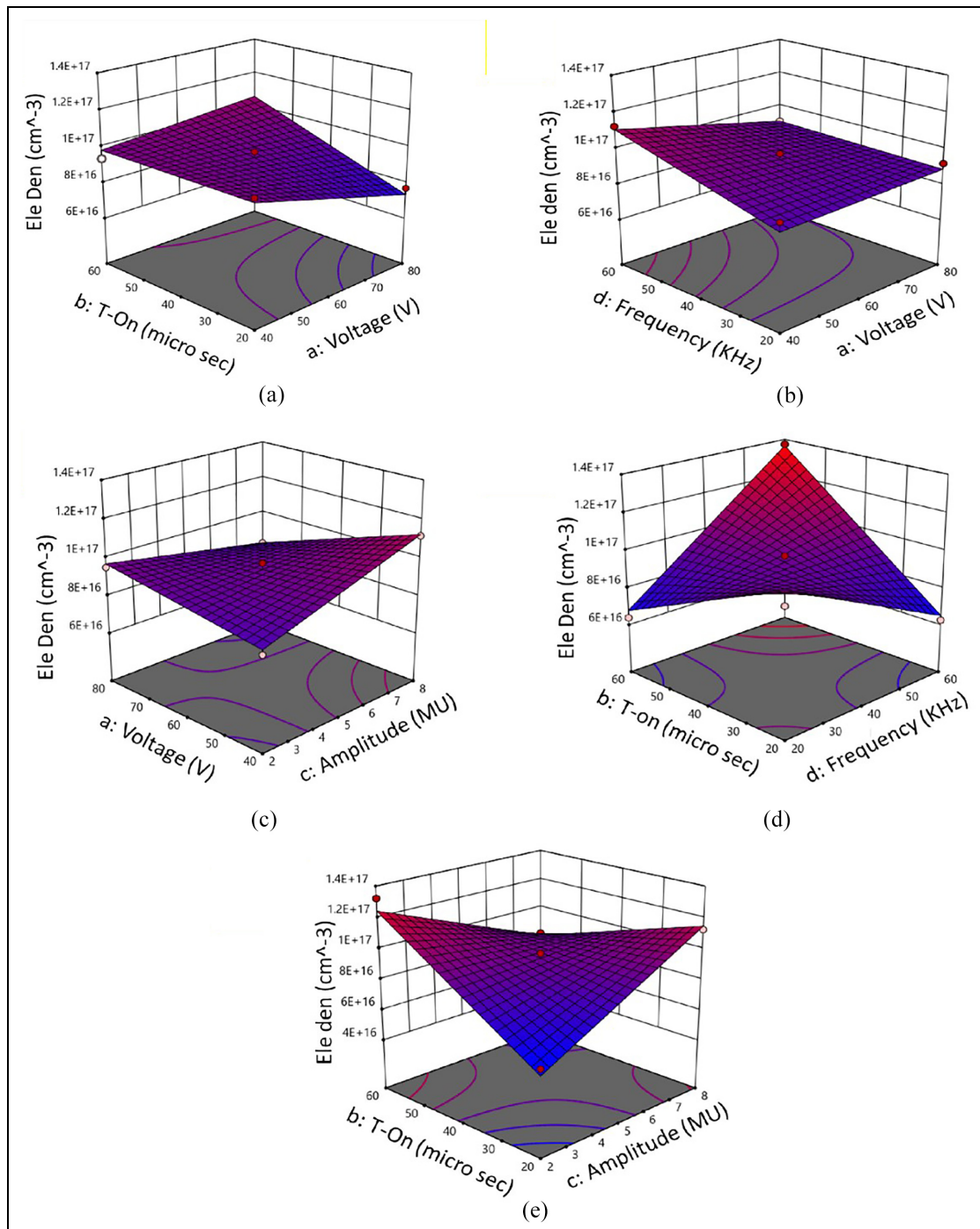


Figure 9. Response surface plots for (i) (a-f) Temperature (ii) (a-e) Electron Density.

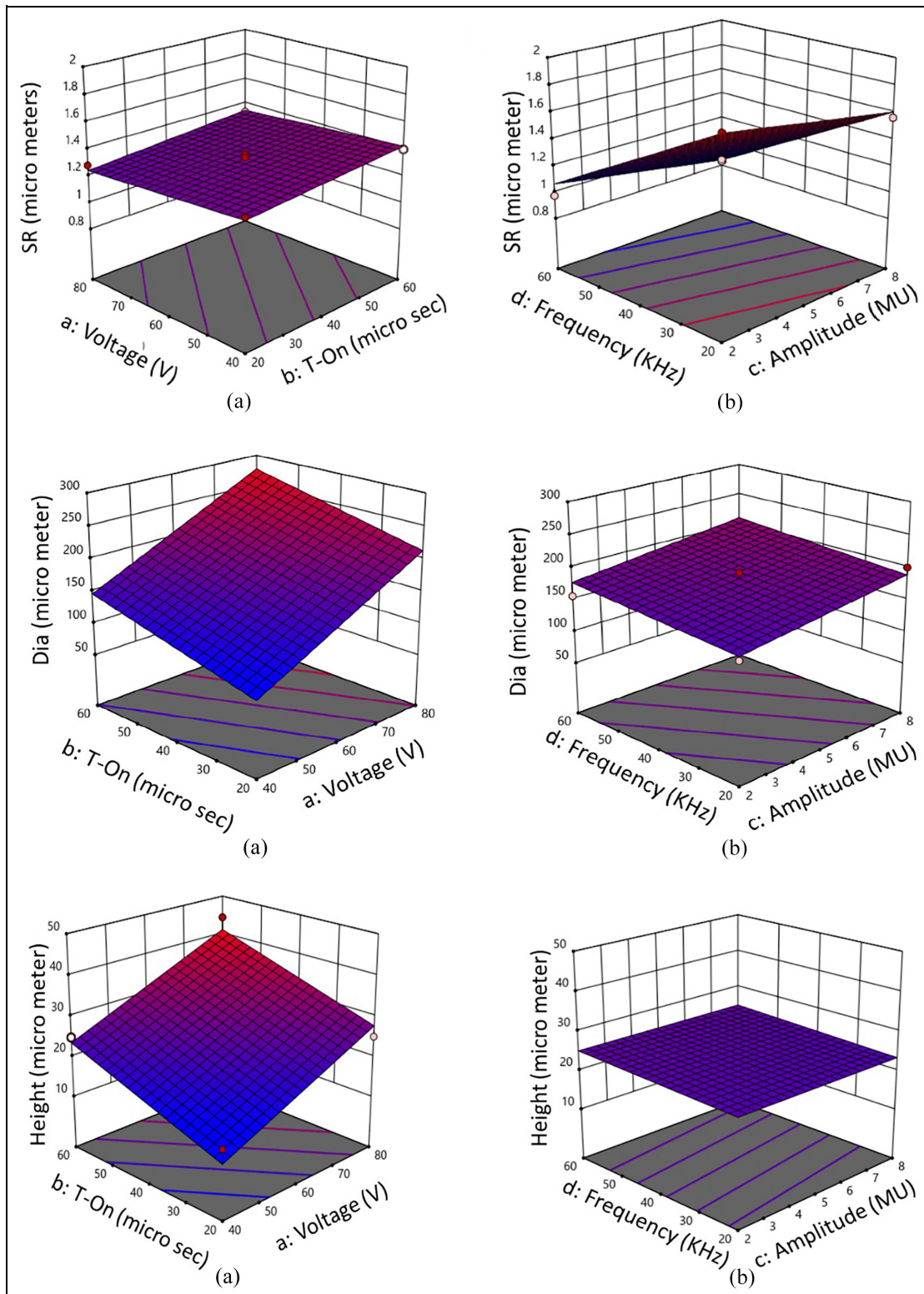


Figure 10. Response surface plots for (i) (a-b) Surface Roughness (ii) (a-b) Diameter of crater (iii) (a-b) Depth of crater.

Table 7. ANOVA results for temperature and electron density.

Output response: Temperature							
Source	Sum of squares	df	Mean square	F-value	p-Value	Percentage contribution	Order of significance
Model	2.45E+08	14	1.75E+07	24.88	< 0.0001	96.65	
Voltage	3.22E+07	1	3.22E+07	45.79	< 0.0001	12.70	4
T on	2.22E+07	1	2.22E+07	31.58	0.0001	8.76	7
Amplitude	1.22E+07	1	1.22E+07	17.26	0.0013	4.79	9
Frequency	2.26E+06	1	2.26E+06	3.22	0.0981	0.89	14
Voltage-T on	4.13E+06	1	4.13E+06	5.86	0.0323	1.63	11
Voltage-Amplitude	7.31E+06	1	7.31E+06	10.39	0.0073	2.88	10
Voltage-Frequency	2.90E+06	1	2.90E+06	4.12	0.065	1.14	12
T on-Amplitude	2.27E+07	1	2.27E+07	32.26	0.0001	8.95	6
T on-Frequency	2.81E+06	1	2.81E+06	3.99	0.069	1.11	13
Amplitude-Frequency	1.93E+07	1	1.93E+07	27.38	0.0002	7.60	8
Voltage ²	9.84E+07	1	9.84E+07	139.81	< 0.0001	38.80	1
T on ²	4.95E+07	1	4.95E+07	70.28	< 0.0001	19.50	2
Amplitude ²	3.33E+07	1	3.33E+07	47.33	< 0.0001	13.13	3
Frequency ²	2.58E+07	1	2.58E+07	36.66	< 0.0001	10.17	5
Residual	8.45E+06	12	7.04E+05			3.33	
Lack of Fit	6.89E+06	10	6.89E+05	0.8807	0.6406	2.71	
Pure Error	1.56E+06	2	7.82E+05			0.62	
Cor Total	2.54E+08	26				100.00	
Output response: Electron density							
Model	8.18E+33	10	8.18E+32	33.19	< 0.0001	95.40	
Voltage	2.34E+32	1	2.34E+32	9.47	0.0072	2.72	7
T on	7.65E+32	1	7.65E+32	31	< 0.0001	8.91	3
Amplitude	1.26E+32	1	1.26E+32	5.1	0.0383	1.47	9
Frequency	5.18E+32	1	5.18E+32	21.02	0.0003	6.04	4
Voltage-T on	2.70E+32	1	2.70E+32	10.93	0.0045	3.14	6
Voltage-Amplitude	4.51E+32	1	4.51E+32	18.29	0.0006	5.26	5
Voltage-Frequency	1.27E+32	1	1.27E+32	5.15	0.0374	1.48	8
T on-Amplitude	2.60E+33	1	2.60E+33	105.24	< 0.0001	30.25	2
T on-Frequency	3.08E+33	1	3.08E+33	124.84	< 0.0001	35.89	1
Amplitude-Frequency	2.05E+31	1	2.05E+31	0.8307	0.3756	0.24	10
Residual	3.95E+32	16	2.47E+31			4.60	
Lack of Fit	3.12E+32	14	2.23E+31	0.5429	0.8051	3.64	
Pure Error	8.22E+31	2	4.11E+31			0.96	
Cor Total	8.58E+33	26				100.00	

Table 8. ANOVA Results for surface roughness, diameter and depth of crater.

Output response: Surface roughness							
Source	Sum of squares	df	Mean square	F-Value	p-Value	Percentage contribution	Order of significance
Model	1.93	4	0.4821	138.66	< 0.0001	96.5	
Voltage	0.0183	1	0.0183	5.27	0.0317	0.915	4
T on	0.0331	1	0.0331	9.53	0.0054	1.655	3
Amplitude	0.1452	1	0.1452	41.75	< 0.0001	7.26	2
Frequency	1.73	1	1.73	498.09	< 0.0001	86.5	1
Residual	0.0765	22	0.0035			3.825	
Lack of Fit	0.0691	20	0.0035	0.935	0.638	3.455	
Pure Error	0.0074	2	0.0037			0.37	
Cor Total	2	26				100	
Output response: Diameter							
Model	68,650.05	4	17,162.51	56.8	< 0.0001	91.17	
Voltage	51,575.4	1	51,575.4	170.7	< 0.0001	68.50	1
T on	12,377.12	1	12,377.12	40.96	< 0.0001	16.44	2
Amplitude	3327.5	1	3327.5	11.01	0.0031	4.42	3
Frequency	1370.03	1	1370.03	4.53	0.0447	1.82	4
Residual	6647.12	22	302.14			8.83	
Lack of Fit	5982.55	20	299.13	0.9002	0.6512	7.95	
Pure Error	664.57	2	332.29			0.88	
Cor Total	75,297.17	26				100.00	
Output response: Depth							
Model	1486.8	4	371.7	92.89	< 0.0001	94.41	
Voltage	938.6	1	938.6	234.57	< 0.0001	59.60	1
T on	541.03	1	541.03	135.21	< 0.0001	34.35	2
Amplitude	0.1345	1	0.1345	0.0336	0.8562	0.01	4
Frequency	7.04	1	7.04	1.76	0.1984	0.45	3
Residual	88.03	22	4			5.59	
Lack of Fit	86.35	20	4.32	5.13	0.1754	5.48	
Pure Error	1.68	2	0.8409			0.11	
Cor Total	1574.83	26				100.00	

Table 9. Experimental results at optimum values of process parameters.

Voltage (V)	T-On (μ s)	Amplitude (μ)	Frequency (KHz)		Temperature (K)	Electron Density (cm^{-3})	Surface Roughness (μ m)	Diameter (μ m)	Depth (nm)
44.783	59.99	2.019	59.99	Optimum value	14,399.97	1.54E17	1.147	159.667	26.49
				Experimental value	14,531.26	8.162E16	1.231	156.25	24.05
				Percentage error	0.9035	-12.29	6.8	-2.28	-10.15



Declaration of conflicting interests

The author(s) declared no potential conflicts of interest with respect to the research, authorship, and/or publication of this article.

Funding

The author(s) received no financial support for the research, authorship, and/or publication of this article.

ORCID iDs

Leeba Varghese  <https://orcid.org/0000-0003-4153-1775>
 Manesh Kailathuvalappil Kochunny  <https://orcid.org/0000-0002-0788-5046>

References

1. Raju L and Hiremath SS. A state-of-the-art review on Micro Electro-discharge Machining. *Procedia Technol* 2016; 25: 1281–1288.
2. Kuriachen B and Mathew J. Spark radius modeling of resistance-capacitance pulse discharge in micro-electric discharge machining of Ti-6Al-4V: an experimental study. *Int J Adv Manuf Technol* 2016; 85: 1983–1993.
3. Yeo SH, Aligiri E, Tan PC, et al. A new pulse discriminating system for micro-EDM. *Mater Manuf Process* 2009; 24: 1297–1305.
4. Descoeudres A, Hollenstein C, Walder G, et al. Time- and spatially-resolved characterization of electrical discharge machining plasma. *Plasma Sources Sci Technol* 2008; 17: 024008.
5. Veda Prakash G, Kumar R, Saurabh K, et al. Comparative study of electrical breakdown properties of deionized water and heavy water under pulsed power conditions. *Rev Sci Instrum* 2016; 87: 015115.
6. Sabyrov N, Jahan MP, Bilal A, et al. Ultrasonic vibration assisted Electro-Discharge Machining (EDM)-an overview. *Materials* 2019; 12: 522.
7. Shabgard MR, Gholipour A and Mohammadpourfard M. Numerical and experimental study of the effects of ultrasonic vibrations of tool on machining characteristics of EDM process. *Int J Adv Manuf Technol* 2018; 96: 2657–2669.
8. Mwangi JW, Nguyen LT, Bui VD, et al. Nitinol manufacturing and micromachining: a review of processes and their suitability in processing medical-grade nitinol. *J Manuf Process* 2019; 38: 355–369.
9. Dhanik S, Joshi SS, Ramakrishnan N, et al. Evolution of EDM process modelling and development towards modelling of the micro-EDM process. *Int J Manuf Technol Manag* 2005; 7: 157.
10. Mujumdar SS, Curreli D, Kapoor SG, et al. Model-based prediction of plasma resistance, and discharge voltage and current waveforms in micro-electrodischarge machining. *J Micro Nanomanuf* 2016; 4: 011003.
11. Chu X, Feng W, Wang C, et al. Analysis of mechanism based on two types of pulse generators in micro-EDM using single pulse discharge. *Int J Adv Manuf Technol* 2017; 89: 3217–3230.
12. Mujumdar SS, Curreli D, Kapoor SG, et al. A model of micro electro-discharge machining plasma discharge in Deionized Water. *J Manuf Sci Eng* 2014; 136: 031011.
13. Macedo FTB, Wiessner M, Hollenstein C, et al. Fundamental investigation of dry electrical discharge machining (DEDM) by optical emission spectroscopy and its numerical interpretation. *Int J Adv Manuf Technol* 2017; 90: 3697–3709.
14. Nagahanumaiah Ramkumar J, Glumac N, et al. Characterization of plasma in micro-EDM discharge using optical spectroscopy. *J Manuf Process* 2009; 11: 82–87.
15. Atomic Spectra Database. *NIST*, <https://www.nist.gov/pml/atomic-spectra-database> (2009, accessed 6 October 2022).
16. Kapoor D. Nitinol for medical applications: a brief introduction to the properties and processing of nickel titanium shape memory alloys and their use in tents. *Johnson Matthey Technol Rev* 2017; 61: 66–76.
17. Sharma N, Raj T and Jangra KK. Parameter optimization and experimental study on wire electrical discharge machining of porous Ni₄₀Ti₆₀ alloy. *Proc IMechE, Part B: J Engineering Manufacture* 2017; 231: 956–970.
18. Varghese L, George J, Manesh KK, et al. Plasma characterization in ultrasonic vibration-assisted micro-electrical discharge machining (μ -EDM). In: Bhattacharyya B, Mathew J, Saravanakumar N, et al. (eds) *Advances in micro and nano manufacturing and Surface Engineering*. Singapore: Springer Nature, 2023, pp.13–21.
19. Marichamy S, Stalin B, Ravichandran M, et al. Optimization of machining parameters of EDM for α - β brass using response surface methodology. *Mater Today Proc* 2020; 24: 1400–1409.
20. Kliuev M, Florio K, Akbari M, et al. Influence of energy fraction in EDM drilling of Inconel 718 by statistical analysis and finite element crater-modelling. *J Manuf Process* 2019; 40: 84–93.
21. Heinz K, Kapoor SG, DeVor RE, et al. An investigation of magnetic-field-assisted material removal in Micro-EDM for nonmagnetic materials. *J Manuf Sci Eng* 2011; 133: 021002.



Modelling of micro-electrochemical machining parameters used for machining of holes on copper plate

S. Aravind, Somashekhar S. Hiremath^{*}

Department of Mechanical Engineering, Indian Institute of Technology Madras, Chennai, 600036, Tamilnadu, India

ARTICLE INFO

Keywords:

Electrochemical machining
Modelling
ANFIS
Material removal rate
Radial overcut
Circularity
Taper angle

ABSTRACT

The electrochemical machining is a non-conventional machining process based on the electrolysis principle. It is used to machine various features on conducting engineering materials with the required accuracy and precision. So an attempt has been made to machine micro-holes on a 300 μm thick copper plate as an anode and a hollow stainless steel tool electrode of 250 μm diameter as the cathode. The machining operation is performed on the in-house developed micro-ECM experimental setup with controlled machining parameters voltage, concentration, and duty factor varied in three levels. A full factorial experimental plan is used to study the output responses material removal rate (MRR), radial overcut (ROC), circularity, and taper angle (TA). Later an adaptive neuro-fuzzy inference system (ANFIS) model has been developed and shown the effectiveness of the developed model in the paper. The Sugeno fuzzy model has been used in ANFIS to generate the fuzzy rules required for the model. Out of 27 experiments, 22 machining data are used for training the model, and the remaining 5 machining data are used for testing the developed model. The average error observed between the ANFIS predicted values and experimental values of MRR is 12.56%, circularity is 43.09%, ROC is 13%, and TA is 27.53%, respectively.

1. Introduction

The electrochemical machining process is a non-conventional machining process used for machining conductive materials. The basic principle is anodic dissolution based on the Faradays laws of electrolysis. This process is widely employed in aerospace applications for manufacturing turbine blades with high aspect ratio holes, aerodynamic seals, gear wheels, and turbine blisks. The automotive applications include holes in fuel injection nozzles and bearings. The μ -ECM finds application in biomedical industries for the manufacturing of micro-needles, surgical tools and punches for tablets. It is also used in chemical industries for the manufacturing of micro-heat exchangers and micro-reactors [1]. Micro-drilling is one of the micromachining processes which is widely used in the manufacturing sector. The micro-drilling process requires material removal at the micro level to accomplish precision and accuracy. The conventional micro-machining process, micro-drilling faces difficulties in terms of tool wear, heat-affected zone, and tool rigidity. Micro-ECM process is an effective nonconventional process that has better MRR, machining accuracy, minimum tool wear, and independent of workpiece hardness, no heat-affected zones, and no machining forces.

The micro-ECM cell consists of an anode (workpiece electrode), cathode (tool electrode), electrolyte solution, and dc power supply. The anode and cathode are placed in the electrolyte solution separated by the inter-electrode gap (IEG). The process parameters affecting the process are given in Fig. 1 [2]. The tool electrode and workpiece electrodes used in μ -ECM should be electrically conductive. The tool electrode materials used in the micro-ECM process include platinum, brass, copper, stainless steel, titanium, tungsten, and molybdenum. The electrolytes used in the micro-ECM are potassium hydroxide (KOH), sodium chloride (NaCl), hydrochloric acid (HCl), sodium nitrate (NaNO_3), sulphuric acid (H_2SO_4), sodium bromide (NaBr), hydrogen fluoride (HF), nitric acid (HNO_3), and sodium hydroxide (NaOH). The electrolytes are selected based on the workpiece material to be machined. The micro-ECM process involves various process parameters and makes the process very complex. This complexity and non-linear parametric relations require the artificial intelligence-based modelling technique [3].

Adaptive Neuro-Fuzzy Interference System (ANFIS) is an artificial intelligence-based technique for modelling complex processes. This technique combines Artificial Neural Networks (ANN) and Fuzzy Logic (FL), which are two soft computing techniques [4].

The literatures related to the ANFIS modelling are detailed in the

^{*} Corresponding author.

E-mail address: somashekhar@iitm.ac.in (S.S. Hiremath).

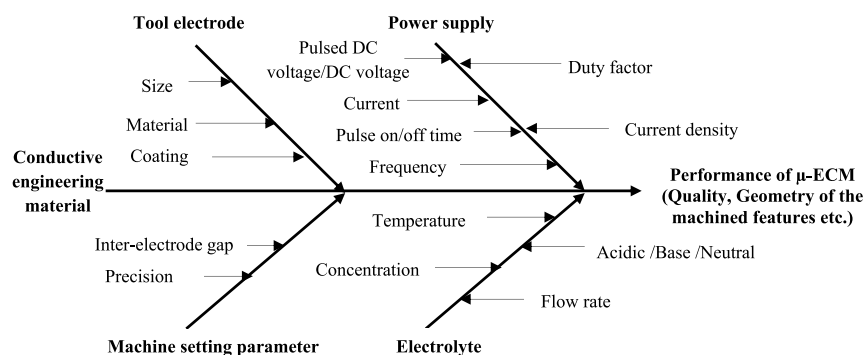


Fig. 1. Major parameters influencing the performance of the μ -ECM process.

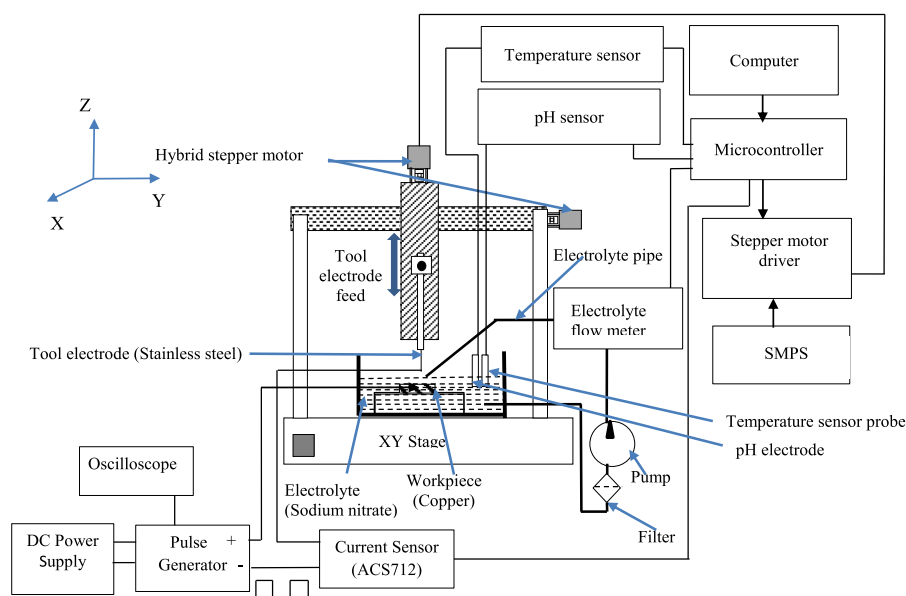


Fig. 2. Schematic of the developed micro-ECM experimental setup.

following section. Sharma et al. [5] developed ANFIS model for the output responses like material removal rate (MRR), surface roughness (SR), and tool wear rate (TWR) for machining of the Inconel 625 using copper tool electrode using electrical discharge machining (EDM). The accuracy of the ANFIS model predicted are 95.55% for MRR, 90.35% for TWR, and 97.82% for SR. Manikandan et al. [6] studied the machinability of LM6/SiC/Dunite Hybrid Metal Matrix Composites using the wire electric discharge machining process. The output responses selected are Material Removal Rate (MRR), Surface finish, overcut, circularity error and perpendicularity error. They adopted the GREY ANFIS modelling for predicting the overall response denoted by the term grey relational grade. The mean of absolute error percentage reported for ANFIS-GRG prediction is 0.04280%. Prasanth and Somashekhar [7] developed the predictive modelling in dry micro-drilling of titanium alloy using Ti-Al-N coated carbide tools using adaptive neuro-fuzzy inference system (ANFIS). The process parameters selected are cutting speed, feed, and pecking depth and the output responses selected are thrust force, burr height, and radial overcut. The mean absolute percentage error given by the ANFIS model for thrust force, burr height, and radial overcut are ANFIS model with MAPE of 5.27%, 5.17%, and 5.22%, respectively. Gangwar et al. [8] developed ANFIS model for surface roughness and MRR of chemically assisted magnetic abrasive finishing of AISI52100 alloy steel. The prediction accuracy of the developed ANFIS model for MRR and change in surface roughness is

96.45%. Ranjan et al. [9] studied the multi-sensor signals for the condition monitoring of the micro-drill bit of 0.4 mm diameter used in mechanical micro drilling operations by predicting the hole quality. They have developed an ANFIS models using time domains and wavelet packet features of the sensor signals for the prediction of the hole quality. Hole roundness error is taken as the output response for predicting the hole quality. The mean testing error reported by the ANFIS time domain model and wavelet packet features are 10% and 8% respectively.

The ANFIS model developed with the data is capable of predicting the output responses. The present article explains the ANFIS based simulation model developed and analyzed for the machining of holes on the copper plate using the electrochemical machining process. This study aim is to investigate the suitability of ANFIS in micro-ECM. The process parameters used for the machining process are voltage, concentration, and duty factor. The responses considered for the studies are material removal rate (MRR), radial overcut (ROC), circularity, and taper angle (TA).

2. Materials and methods

The experiments are performed on the in-house developed experimental setup. The experimental setup includes pulsed dc power supply unit, closed tool electrode feed mechanism, XY stage, electrolyte

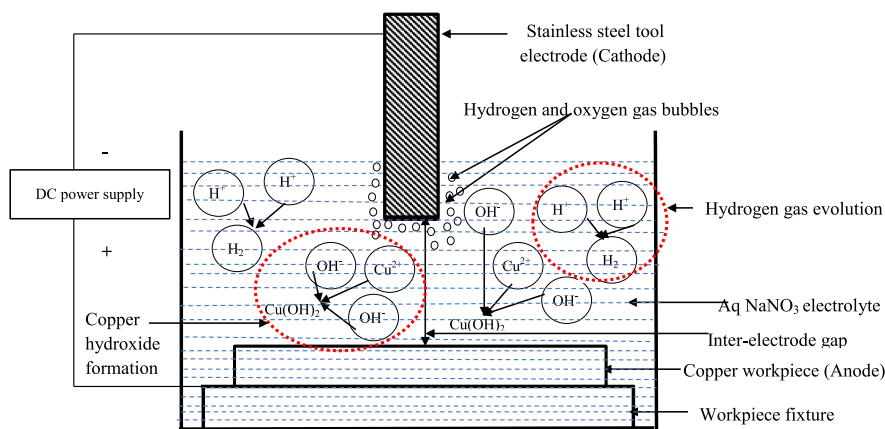
Fig. 3. Schematic of μ -ECM cell.

Table 1

Process parameters and levels for experiments.

Tool Material	Stainless steel hollow tube of 250 μ m diameter		
Workpiece Material	Copper (20 mm \times 20 mm \times 0.3 mm)		
Electrolyte	Aqueous solution of Sodium nitrate (NaNO_3)		
Inter Electrode Gap	0.05 mm		
Levels	-1	0	1
Machining parameters			
Voltage (V)	8	10	12
Electrolyte Concentration (wt %)	15	20	25
Duty Factor (%)	30	40	50

circulation system, and processing cell.

A detailed explanation of the developed experimental setup is available [10]. Fig. 2 depicts the schematic of the micro-ECM experimental setup.

2.1. Chemical reactions

The copper workpiece and a hollow stainless steel tool are the anode and cathode. The electrolyte is an aqueous solution of sodium nitrate.

Fig. 3 gives a schematic of μ -ECM cell reactions. The copper workpiece (Cu) (anode) oxidises, by losing the electrons as given in equation (1).



Also, the oxygen gas is evolved when aqueous NaNO_3 is used and is given in equation (2).



The water from the aqueous NaNO_3 electrolyte separates into OH^- ions and hydrogen (H_2) gas as per equation (3). The copper ions (Cu^{2+}) combine with hydroxyl ions (OH^-) to form copper hydroxide $\text{Cu}(\text{OH})_2$ (equation (4)).



The parameters, along with the levels taken for the experiments based on the full factorial experimental plan, are given in Table 1. The optical images of the holes machined with lower, medium, and higher parameter levels are presented in Fig. 4. The holes with lower top diameter of 807.167 μ m and bottom diameter of 786.625 μ m are

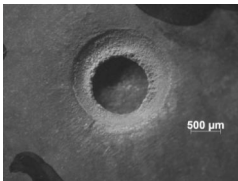
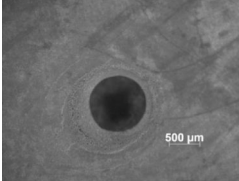
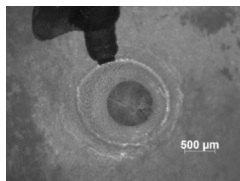
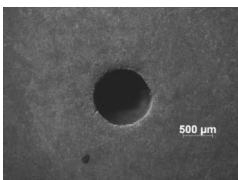
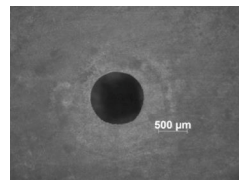
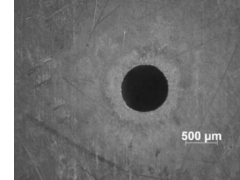
Lower parameter levels	Medium parameter levels	Higher parameter levels
Voltage :8 V Concentration:15 wt % C Duty Factor:30 %	Voltage :10 V Concentration:20 wt % C Duty Factor: 40 %	Voltage :12 V Concentration:25 wt % C Duty Factor:50 %
		
Top Dia. 1036.288 μ m	Top Dia.-946.889 μ m	Top Dia.-807.164 μ m
		
Bottom Dia:1030.979 μ m	Bottom Dia:937.257 μ m	Bottom Dia: 786.625 μ m

Fig. 4. Optical images of the machined hole.

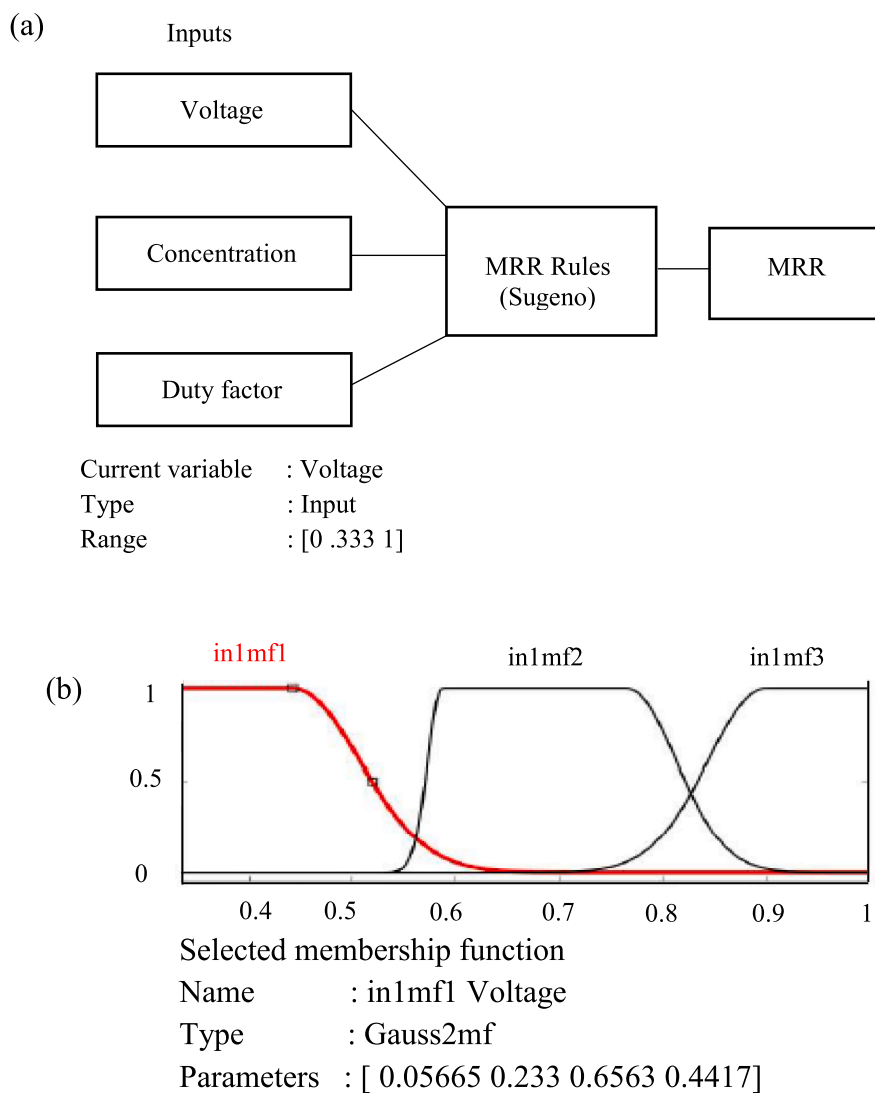


Fig. 5. (a) Representation of voltage for MRR (b) Membership function.

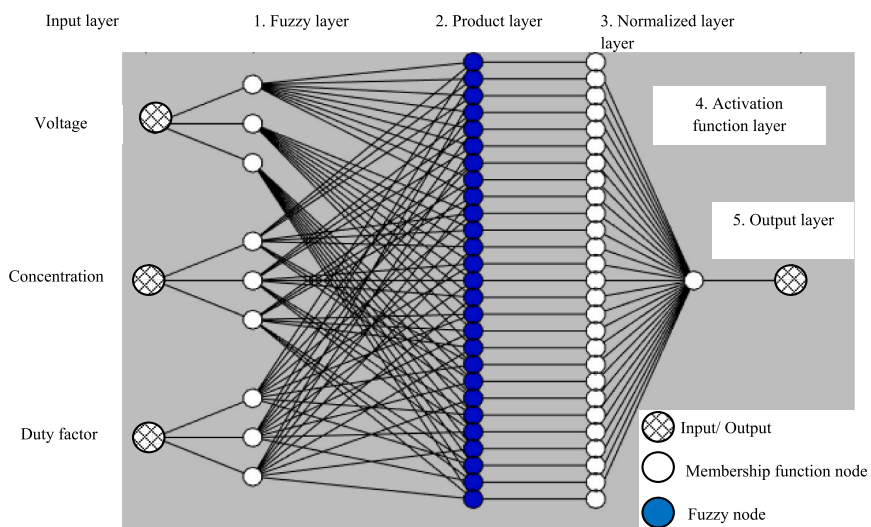


Fig. 6. ANFIS architecture with three inputs and one output.

Table 2

Parameters considered for ANFIS Modelling.

Response	Membership function	Error tolerance	Epoch
MRR	gauss2mf	0	1100
Circularity	gauss2mf	0	1775
ROC	gauss2mf	0	2100
TA	gauss2mf	0	2400

obtained at the higher process parametric combination. The detailed analysis of the machined holes is available in literature [10].

The MRR is calculated using equation (5). High precision weighing machine (Make: Mettler Toledo, model ME204E) is used for weighing the workpiece before and after machining.

$$MRR = \left(\frac{I_w - F_w}{t_m} \right) \mu g / s \quad \text{Eq. (5)}$$

Where, I_w is the initial weight, F_w is the final weight of the workpiece and t_m is the machining time.

Table 3

GRC values of process parameters and responses.

Expt no	V	C	DF	GRC Values						
				V	C	DF	MRR	C	ROC	TA
1	8	15	40	0.333	1	0.5	0.333	1	0.5	0.333
2	8	25	30	0.333	0.333	1	0.333	0.333	1	0.333
3	8	15	30	0.33	1	1	0.333	1	1	0.333
4	12	25	50	1	0.333	0.333	1	0.333	0.333	1
5	8	20	40	0.333	0.5	0.5	0.333	0.5	0.5	0.333
6	10	25	40	0.5	0.333	0.5	0.5	0.333	0.5	0.5
7	12	15	30	1	1	1	1	1	1	1
8	10	15	30	0.5	1	1	0.5	1	1	0.5
9	10	15	40	0.5	1	0.5	0.5	1	0.5	0.5
10	12	20	40	1	0.5	0.5	1	0.5	0.5	1
11	8	25	40	0.333	0.333	0.5	0.333	0.333	0.5	0.333
12	10	20	30	0.5	0.5	1	0.5	0.5	1	0.5
13	12	25	40	1	0.333	0.5	1	0.333	0.5	1
14	10	25	30	0.5	0.333	1	0.5	0.333	1	0.5
15	10	20	40	0.5	0.5	0.5	0.5	0.5	0.5	0.5
16	10	25	50	0.5	0.333	0.333	0.5	0.333	0.333	0.5
17	8	20	50	0.333	0.5	0.333	0.333	0.5	0.333	0.333
18	12	20	30	1	0.5	1	1	0.5	1	1
19	10	20	50	0.5	0.5	0.333	0.5	0.5	0.333	0.5
20	12	25	30	1	0.333	1	1	0.333	1	1
21	12	15	50	1	1	0.333	1	1	0.333	1
22	8	25	50	0.333	0.333	0.333	0.333	0.333	0.333	0.333
23	8	20	30	0.333	0.5	1	0.333	0.5	1	0.333
24	12	15	40	1	1	0.5	1	1	0.5	1
25	10	15	50	0.5	1	0.333	0.5	1	0.333	0.5
26	12	20	50	1	0.5	0.333	1	0.5	0.333	1
27	8	15	50	0.333	1	0.333	0.333	1	0.333	0.333

V: Voltage(V), C: concentration (wt %C), DF: Duty factor, MRR: Material removal rate, C: Circularity, ROC: Radial overcut, TA: Taper Angle.

Table 4

Experimental results of the training data.

Expt no	Voltage	Concentration	Duty Factor	Experimental results			
				MRR	Circularity	ROC	TA
1	8	15	40	19.7	0.968	234.300	3.830
2	8	25	30	14.5	0.961	256.000	0.610
3	8	15	30	15.6	0.947	393.140	0.510
4	12	25	50	66	0.976	278.580	1.960
5	8	20	40	18.2	0.981	383.750	0.640
6	10	25	40	91.8	0.943	320.930	2.090
7	12	15	30	37	0.974	279.510	5.140
8	10	15	30	27	0.947	340.080	4.390
9	10	15	40	42.8	0.985	375.490	0.740
10	12	20	40	46	0.98	288.870	2.320
11	8	25	40	15.4	0.906	193.110	0.780
12	10	20	30	21.5	0.981	274.800	0.940
13	12	25	40	61.6	0.97	254.330	2.940
14	10	25	30	27.5	0.975	280.530	0.160
15	10	20	40	34.6	0.982	348.440	0.920
16	10	25	50	52.8	0.967	280.310	3.990
17	8	20	50	28.3	0.981	406.880	1.560
18	12	20	30	44.4	0.981	260.440	0.500
19	10	20	50	48.8	0.974	271.540	1.780
20	12	25	30	25.9	0.968	206.570	0.720
21	12	15	50	42.4	0.974	368.410	1.490
22	8	25	50	11.2	0.968	273.120	1.010

MRR-material removal rate, ROC- radial overcut, TA-taper angle.

Table 5

Experimental and ANFIS predicted results of the testing data.

Expt no	V	C	DF	Experimental results				ANFIS Predicted results			
				MRR	C	ROC	TA	MRR	C	ROC	TA
1	8	20	30	47.3	0.969	241.11	0.480	44.711	1.056	241.11	0.46
2	12	15	40	32.3	0.947	361.72	1.320	32.340	1.292	361.72	1.93
3	10	15	50	73.3	0.964	247.82	2.260	49.154	1.375	247.82	1.60
4	12	20	50	43.8	0.95	289.84	0.930	38.853	1.487	289.84	0.39
5	8	15	50	19.7	0.952	208.94	0.120	22.259	1.627	208.94	0.12

V-Voltage(V),C-concentration (wt %C),DF: Duty factor, MRR-material removal rate, C- Circularity ROC- radial overcut, TA-taper angle.

Table 6

The deviation and error between the experimental and ANFIS predicted results.

Expt no	Deviation (Δ)				Error (%)			
	MRR	Circularity	ROC	TA	MRR	Circularity	ROC	TA
1	2.589	0.087	1.140	0.020	5.47	8.98	0.47	4.17
2	0.040	0.345	8.398	0.610	0.12	36.43	2.32	46.21
3	24.146	0.411	110.592	0.660	32.94	42.63	44.63	29.20
4	4.947	0.537	0.999	0.540	11.29	56.53	0.34	58.06
5	2.559	0.675	36.013	0.000	12.99	70.90	17.24	0.00
Average Error (%)					12.56	43.09	13.00	27.53

MRR-material removal rate, ROC- radial overcut, TA-taper angle.

The top and bottom images of the workpieces are acquired using a stereomicroscope (Zeiss Stemi 2000-C). The image captured is analyzed using Image J software (Version 1.51) to measure the top diameter, bottom diameter, area, and perimeter of the machined holes. The circularity index is calculated using equation (6).

$$C = 4\pi \frac{A}{p^2} \quad \text{Eq. (6)}$$

Where, A is the area of the machined hole, and p is the perimeter of the machined hole. The machined hole is said to be circular if the value of circularity is closer to one. Taper angle is calculated using equation (7).

$$TA = \tan^{-1} \left(\frac{D-d}{2h} \right) \text{ deg} \quad \text{Eq. (7)}$$

Where, D and d are the top and bottom diameter of the machined hole, h is the thickness of the workpiece.

2.2. Adaptive neuro-fuzzy inference system

The ANFIS was reported by Jang in 1993 [4] and is used for modelling. ANFIS algorithm combines the back-propagation algorithm and least square method to refine the parameters of following section.

2.2.1. Development of ANFIS model

The steps adopted in developing the ANFIS model are explained in this section. The ANFIS toolbox available in commercial software Matlab 2018a is used in the development of the model.

STEP 1: Normalize the inputs and outputs by the GRA method and find GRC [11]

The first step is to normalize the individual responses in the range of 0 and 1. The normalization is a three-step process, as explained below.

The target is to maximize the MRR and circularity and to minimize the ROC and TA. The normalized value for MRR and circularity is calculated using equation (8) and equation (9).

Larger the better for MRR

$$\eta_i = \left(\frac{MRR_i - MRR_{\min}}{MRR_{\max} - MRR_{\min}} \right) \quad \text{Eq. (8)}$$

Larger the better for circularity

$$\eta_i = \left(\frac{C_i - C_{\min}}{C_{\max} - C_{\min}} \right) \quad \text{Eq. (9)}$$

The normalized value for the ROC and TA is calculated using equation (10) and equation (11).

Smaller the better for ROC

$$\eta_i = \left(\frac{ROC_{\max} - ROC_i}{ROC_{\max} - ROC_{\min}} \right) \quad \text{Eq. (10)}$$

Smaller the better for TA

$$\eta_i = \left(\frac{TA_{\max} - TA_i}{TA_{\max} - TA_{\min}} \right) \quad \text{Eq. (11)}$$

Where η_i is the normalized value.

• Step 2-Deviation Sequence

Here the deviation of each normalized value of the individual responses from its desired value is calculated from equation (12).

$$\partial_i = |\eta_{\max} - \eta_i| \quad \text{Eq. (12)}$$

Where ∂_i is the deviation sequence, η_i is the normalized value and η_{\max} is the desired value, which is equal to 1.

• Step 3- Grey Relation Coefficient (GRC)

Grey Relation Coefficient (GRC) shows the relationship between the desired and normalized output responses, and it is calculated by equation (13).

$$\gamma_i = \left(\frac{\partial_{\min} + \xi \partial_{\max}}{\partial_i + \xi \partial_{\max}} \right) \quad \text{Eq. (13)}$$

Where γ_i is the GRC, ξ is distinguishing coefficient, $\xi = 0$ to 1, considered to be 0.5, ∂_i is the deviation sequence. For the process parameters the respective normalized value between 0 and 1 is determined by equation (14), equation (15), and equation (16).

$$(\eta_i)_V = \left(\frac{Max_V - V_i}{Max_V - Min_V} \right) \quad \text{Eq. (14)}$$

$$(\eta_i)_{Con} = \left(\frac{Max_{Con} - Con_i}{Max_{Con} - Min_{Con}} \right) \quad \text{Eq. (15)}$$

$$(\eta_i)_{DF} = \left(\frac{Max_{DF} - DF_i}{Max_{DF} - Min_{DF}} \right) \quad \text{Eq. (16)}$$

Where $(\eta_i)_V$, $(\eta_i)_{Con}$, and $(\eta_i)_{DF}$ are the normalized value for voltage, concentration, and duty factor. Max_V is the maximum value of voltage = 12 V, Min_V is the minimum value of voltage = 8 V, Max_{Con} is the maximum value of concentration = 25 wt% C, Min_{Con} is the minimum value of the concentration = 15 wt % C, Max_{DF} is the maximum value of the duty factor = 50%, and Min_{DF} is the minimum value of the duty factor = 30%.

The GRC values of voltage, concentration, and duty factor are also similarly determined by equation (9), and equation (10), respectively. The generated GRC values are given as input to the ANFIS model. The fuzzy inference systems (FIS) present in ANFIS toolbox are Mamdani and Sugeno models. The Sugeno model is taken in this study, and it accepts multiple inputs and gives single output at a time [12,13].

STEP2: Categorise the training and testing data of the individual responses and save them in two separate .dat files in notepad.

80% of data from the experiment is used for training, and 20% of data is used for testing. In this study, 22 experimental data is taken as the training data, and 5 experimental data is taken as the testing data.

STEP 3: Use evalfis function to predict the outputs by the FIS model created

Fig. 5 shows the representation of voltage for MRR with the membership function. The input variables in the model for MRR are voltage, concentration, and duty factor. The architecture of the ANFIS model with the three inputs (voltage, concentration, and duty factor) and one output (MRR) is given in Fig. 6.

The ANFIS model comprises of five layers known as fuzzy layer, product layer, normalized layer, activation function layer, and output layer [14,15]. The input layer consists of the inputs (voltage, concentration, and duty factor). This model takes three inputs and yield one output (MRR).

In the fuzzy layer, x , y , and z are the input nodes, and A_1 , B_1 , C_1 , A_2 , B_2 , C_2 and A_3 , B_3 , C_3 are the linguistic labels in the fuzzy logic theory. The membership relationship between the output and input functions of the fuzzy layer is given by equation (17), expressed as follows [12].

$$O_i^1 = \mu_{A_i}(x), i = 1, 2, 3 \quad \text{Eq. (17)}$$

Where μ_{A_i} is membership functions and O_i^1 is the output function. The membership function for the A_1 is selected from membership functions like linear (triangular and trapezoidal membership function) and non-linear (Gaussian membership function). The membership function consists of two Gaussian functions (gauss2mf) is selected in this study and is represented by equation 18–20. The gauss2mf takes the value between 0 and 1 [12].

$$\mu(x : \sigma_1, C_1, \sigma_2, C_2) = \exp \left[\frac{-(x - C_1)^2}{2\sigma_1^2} \right] \text{ when } x \leq C_1 \quad \text{Eq. (18)}$$

$$\mu(x : \sigma_1, C_1, \sigma_2, C_2) = 1 \text{ when } C_1 \leq x \leq C_2 \quad \text{Eq. (19)}$$

$$\mu(x : \sigma_1, C_1, \sigma_2, C_2) = \exp \left[\frac{-(x - C_1)^2}{2\sigma_1^2} \right] \text{ when } C_2 < x \quad \text{Eq. (20)}$$

Where C_1 , C_2 represents the width of the curve on the left and right sides and σ_1 , σ_2 represents the height of the curve on the left and right sides [12].

The membership function plot for the voltage generated based on equations (18)–(20) is given in Fig. 5. The C value and σ values range between 0 and 1. The σ values which reached $C = 1$ will proceed further in the learning process, and σ values reached $C = 0$ values will be eliminated.

The fuzzy and operators (AND, OR, and NOT) are the node functions in the product layer. In this study AND operator is used. The output of this layer is given by equation (21) [12].

$$O_i^2 = w_i = \mu_{A_i}(x) \times \mu_{B_i}(y) \times \mu_{C_i}(z), i = 1, 2, 3 \quad \text{Eq. (21)}$$

Where x , y , z are the input values.

The total number of fuzzy rules are generated by the membership function based on equation (22).

$$N_{(i)} = a^b \quad \text{Eq. (22)}$$

Where $N_{(i)}$ is the number of fuzzy rules, a = number of membership functions, and b is the number of input variables. In this study, there are three membership functions and three input variables that generate 27 fuzzy rules. The fuzzy rules are represented as follows.

If (V is in1mf1) and (C is in2mf1) and (DF is in3mf1) then (MRR is out1mf1)

If (V is in1mf1) and (C is in2mf1) and (DF is in3mf2) then (MRR is out1mf2)

In the normalized layer, the weight function is normalized by equation (23). The i th node calculates the degree of fulfilment of each rule w_i with respect to sum of all rules' degree of fulfilment [12].

$$O_i^3 = \bar{w}_i = \frac{w_i}{\sum w_i} i = 1, 2, 3, \dots, 27 \quad \text{Eq. (23)}$$

The activation function layer returns the defuzzified value. The input and output defuzzy relationship is given by equation (24) [12].

$$O_i^4 = \bar{w}_i f_i = \bar{w}_i (1 + x^{0.5} + y^{-1} + z^{-1.5})^2 \quad \text{Eq. (24)}$$

where f_i : output function of 3 non-linear input values x , y , z of i th node

The sum of all the inputs of layer 4 is the output of this fifth layer. This output is obtained from equation (25).

$$O_i^5 = \sum \bar{w}_i f_i = \frac{\sum w_i f_i}{\sum w_i} \quad \text{Eq. (25)}$$

The overall output is given by the layer 5 from equation (26).

$$Ep = \sum_{k=1}^{N(L)} dk - X_{k,p}^L \quad \text{Eq. (26)}$$

Where d_k is the k^{th} vector component of the desired output and $X_{k,p}^L$ is the k th component of the vector of actual output given by the ANFIS [12]. The back-propagation and hybrid algorithms are provided in the ANFIS model. In the back-propagation algorithm, the errors in each epoch are returned to the network and act like feedback which helps in self-correction and learning. The error tolerance and the number of epochs are to be specified in the model so that the training can be stopped upon reaching the error tolerance or the number of epochs. A similar method is carried out for the modelling of other responses like ROC, circularity, and TA. The parameters considered for ANFIS Modelling are given in Table 2.

3. Results and discussions

This section explains the results obtained by the ANFIS modelling. ANFIS simulation performed works in two steps. The first step is to train the model, followed by the testing of the model. In order to predict MRR, initially, the ANFIS model is trained with the available 22 sets of experimental data, and for testing the model, another five experimental data are used. The GRC values of process parameters and responses are

given in Table 3. Table 4 gives experimental results of the training data for the output responses like MRR, Circularity, ROC, and TA.

Table 5 gives experimental and ANFIS predicted results of the testing data for the output responses like MRR, circularity, ROC, and TA.

The deviation (Δ) is calculated as the absolute value of the difference between the ANFIS predicted value and the experimental value of the respective output responses. The error (%) is calculated as percentage of the ratio of deviation to the experimental value of the respective output responses. Table 6 gives the deviation and the error between the experimental and ANFIS predicted results the output responses like MRR, Circularity, ROC, and TA. The average error in the predicted values of the output responses is MRR-12.56%, Circularity-43.09%, ROC -13%, and TA-27.53%. The error is caused due to a lack of data set for training the model and complexity of the ECM process, which leads to the dynamic nature of the responses. ANFIS is expected to give error-less predictions with more training data as the training data results in better model learning.

4. Conclusions

This article explains the ANFIS modelling of the micro-ECM to predict the output responses like MRR, Circularity, ROC, and TA. The experimental data generated by the full factorial experiment is used in the study. Out of the 27 data, 22 data is used for training purposes, and the model is tested with the remaining 5 data. The average errors in the predicted responses are as follows.

- MRR-12.56%
- Circularity-43.09%,
- ROC -13.00%
- TA-27.53%

Declaration of competing interest

The authors declare that they have no known competing financial interests or personal relationships that could have appeared to influence the work reported in this paper.

Acknowledgments

Authors are grateful to the organizers of International Conference on Advances in Chemical and Material Science (ACMS-2022) organized by IICChE headquarters for giving an opportunity to submit this paper in the Journal of Indian Chemical Society as the special issue.

References

- [1] K.K. Saxena, J. Qian, D. Reynaerts, A review on process capabilities of electrochemical micromachining and its hybrid variants, *Int. J. Mach. Tool Manuf.* 127 (2018) 28–56, <https://doi.org/10.1016/j.ijmachtools.2018.01.004>.
- [2] B. Bhattacharyya, *Electrochemical Micromachining for Nanofabrication, MEMS and Nanotechnology*, William Andrew Publishing, New York, 2015, <https://doi.org/10.1016/C2014-0-00027-5>.
- [3] S. Sreepriya, K. Aparna, M.L. Vinila, Adaptive neuro-fuzzy approach to sodium chlorate cell modeling to predict cell pH for energy-efficient chlorate production, *Chem. Eng. Commun.* 208 (2) (2021) 256–270, <https://doi.org/10.1080/00986445.2019.1708740>.
- [4] J.R. Jang, ANFIS: adaptive-network-based fuzzy inference system, *IEEE Trans. Syst. Man Cybern.* 23 (1993) 665–685.
- [5] Sharma Deepesh, Bhowmick Arnab, Goyal Ashish, Enhancing EDM performance characteristics of Inconel 625 superalloy using response surface methodology and ANFIS integrated approach, *CIRP J. Manuf. Sci. Technol.* 37 (2022) 155–173, <https://doi.org/10.1016/j.cirpj.2022.01.005>.
- [6] N. Manikandan, K. Balasubramanian, D. Palanisamy, P.M. Gopal, D. Arulkirubakaran, J.S. Binoj, Machinability analysis and ANFIS Modelling on advanced machining of hybrid metal matrix composites for aerospace applications, *Mater. Manuf. Process.* 34 (2019) 16 1866–1881, <https://doi.org/10.1080/10426914.2019.1689264>.
- [7] P. Prashanth, S.S. Hiremath, Experimental and predictive modelling in dry micro-drilling of titanium alloy using ti-al-n coated carbide tools, *Int. J. Interact. Des. Manuf.* (2022), <https://doi.org/10.1007/s12008-022-01032-7>.
- [8] S. Gangwar, A. Singh, V.K. Pathak, Experimental investigation and ANFIS modelling of surface roughness and mrr during chemically assisted MAF of AISI52100 alloy steel, *Sadhana - Acad. Proc. Eng. Sci.* 47 (2022) 3, <https://doi.org/10.1007/s12046-022-01950-y>.
- [9] J. Ranjan, K. Patra, T. Szalay, M. Mia, M.K. Gupta, Q. Song, G. Krolczyk, R. Chudy, V.A. Pashnyov, D.Y. Pimenov, Artificial Intelligence-based hole quality prediction in micro-drilling using multiple sensors, *Sensors* 20 (3) (2020) 1–14, <https://doi.org/10.3390/s20030885>.
- [10] S. Aravind, Somashekhar, S. Hiremath, Design and development of IEG control and characterization of micro-holes generated using in-house developed μ -ECM setup, *Arabian J. Sci. Eng.* (2022), <https://doi.org/10.1007/s13369-021-06392-y>.
- [11] B.J. Madhavi, S.S. Hiremath, Machining and characterization of channels and textures on quartz glass using μ -ecdm process, *Silicon* 11 (2020) 2919–2931, <https://doi.org/10.1007/s12633-019-0083-6>.
- [12] Ishwar Bhiradi, Leera Raju, Somashekhar, S. Hiremath, Adaptive neuro fuzzy inference system (ANFIS): modelling, analysis, and optimisation of process parameters in the micro-EDM process, *Adv. Mater. Process. Technol.* 6 (1) (2020) 133–145, <https://doi.org/10.1080/2374068X.2019.1709309>.
- [13] Jinka Ranganayakulu, S Hiremath Somashekhar, Paul Lijo, Parametric analysis and a soft computing approach on material removal rate in electrochemical discharge machining, *Int. J. Manuf. Technol. Manag.* 24 (1–4) (2011) 23–39, <https://doi.org/10.1504/IJMTM.2011.046758>.
- [14] X.H. Suganthi, U. Natarajan, S. Sathiyamurthy, K. Chidambaram, Prediction of quality responses in micro-EDM process using an adaptive neuro-fuzzy inference system (ANFIS) model, *Int. J. Adv. Manuf. Technol.* 68 (1–4) (2013) 339–347, <https://doi.org/10.1007/s00170-013-4731-5>.
- [15] R. Teimouri, H. Sohrabpoor, Application of adaptive neuro-fuzzy inference system and cuckoo optimization algorithm for analyzing electro chemical machining process, *Front. Mech. Eng.* 8 (4) (2013) 429–442, <https://doi.org/10.1007/s11465-013-027>.



Tuning thermoelectric figure of merit in Ag doped nanostructured PbSnTeSe alloy by entropy and band engineering phenomena

Arun Raphel^{a,b}, P. Vivekanandhan^a, Arun Kumar Rajasekaran^c, S. Kumaran^{a,*}

^a Green Energy Materials and Manufacturing Research Group, Department of Metallurgical and Materials Engineering, National Institute of Technology, Tiruchirappalli, 620015 Tamil Nadu, India

^b Department of Mechanical Engineering, Viswajyothi College of Engineering and Technology, Ernakulam 686670, India

^c Cavendish Laboratory, Department of Physics, University of Cambridge, Cambridge CB3 0HE, United Kingdom

ARTICLE INFO

Keywords:

High entropy alloy
Thermoelectric material
Nanostructuring
Thermal conductivity
Band engineering

ABSTRACT

Advanced thermoelectric materials with novel chemistry and structure that exhibit superior functional properties are in high demand in today's scientific scenario. Engineered configurational entropy in bulk thermoelectric materials through complex chemical disorder is an emerging and potential approach to achieve exceptional thermoelectric properties over traditional material systems. In the current study, mechanical alloying (MA) and spark plasma sintering (SPS) were used to synthesize the high-density (>96%) nanocrystalline lead tin tellurium selenium (PbSnTeSe) high entropy alloy (HEA) with varied atomic concentrations of silver (Ag) doping (0–0.9 at %). The high entropy, band engineering and nanostructuring approach synergistically show a remarkable decrease to ultralow thermal conductivity (0.814 W/mK), resulting in a substantial increase in the power factor ($14.16 \times 10^{-4} \text{ W/mK}^2$). Thus, an excellent figure of merit ($ZT=0.891$) is achieved in PbSnTeSe doped with 0.9Ag HEA at 573 K, which is estimated as a 225% increase over the pristine PbSnTeSe HEA ($ZT=0.396$).

1. Introduction

Globally, an escalation in energy needs and greenhouse effects has become an intense threat to humans for a couple of decades. The exponentially increasing population, environmental impact due to the combustion of fossil fuels and dramatic decline in non-renewable energy resources have created severe unbalance in nature and society [1]. In this context, sustainable and highly efficient renewable energy technologies are profoundly potential and promising. Thus, research on these domains have been spearheaded in recent years [2]. Thermoelectric technology is an exciting and emerging for broader and niche technological applications among the several eco-friendly energy harvesting approaches. Thermoelectric materials are solid-state semiconductors that converts thermal energy into electrical energy directly pronounced by charge carriers [3]. The simplicity in energy conversion is further conceived by various appreciable factors such as scalability, long service span, noise-less operation, no carbon footprints, and zero maintenance cost [4]. Even though first-generation thermoelectric material systems like SiGe, Bi₂Te₃ and PbTe have been successfully commercialized, but with a limited figure of merit (ZT) [5–7]. Decreasing the phonon transport properties without reducing the

electrical conductivity and enhancing the electrical conductivity without disturbing thermal transport properties are challenging due to their contradicting nature.

In recent years, advancements in nanostructured strategies for lowering thermal conductivity via nano inclusions, nanocomposites and nano-scale device fabrications have significantly contributed towards improving thermoelectric performances [8,9]. Furthermore, developing an advanced thermoelectric materials with novel chemistry to achieve $ZT > 3$ is one of the primary goals of future-generation thermoelectric research. Lead telluride (PbTe) is a proven thermoelectric system in this class with a $ZT > 1.4$ at 750 K [10]. Chalcogenides-based solid solutions such as PbTe, PbSe, PbS (lead-based) and SnTe, SnSe, and SnS (tin-based), GeTe have been extensively investigated with improved thermoelectric properties [11–18]. Over the past years, Cu₂Se has evolved to be an encouraging material for thermoelectric applications with significantly higher ZT [19,20]. Recent advancements in carbon allotrope hybrid material development offer great attention due to lower lattice thermal conductivity. Alongwith good mechanical properties and flexible design make it a promising alternative to traditional bulk thermoelectric materials. [21,22].

Furthermore, substantial research were conducted to improve

* Corresponding author.

E-mail address: kumara@nitt.edu (S. Kumaran).

<https://doi.org/10.1016/j.mtcomm.2023.105880>

Received 25 November 2022; Received in revised form 12 March 2023; Accepted 22 March 2023

Available online 23 March 2023

2352-4928/© 2023 Elsevier Ltd. All rights reserved.

thermoelectric properties by synthesizing pseudo-binary alloys such as SnSe-SnS, PbSe-PbS, PbTe-PbS and pseudo-ternary alloys like PbTe-PbSe-PbS [23–27]. The chemical complexity and multiple phases in these multi-component alloys could significantly reduce the lattice thermal conductivity (K_{lat}) to a greater extent, but adversely affect the electrical transport properties. In this context, recent research has been focused on synthesizing advanced and interesting multi-component high entropy alloys (HEA) with four or more parental elements with near equiatomic ratio [28–31]. With compositional tailoring, HEAs show a high-mixing entropy (configurational entropy) and form a simple solid solution. HEA shows the severe distortion of the lattice with higher crystal structure symmetry and lower thermal conductivity, which is desirable to improve the ZT. Further, implementing various viable techniques, such as doping, nanostructuring and introducing point defects, could improve the power factor and lead to higher ZT. The potential of high entropy alloys were less explored for thermoelectric applications. However, thermoelectric HEA processing through melting, grinding and subsequent consolidation using sintering warrants prolonged processing duration of approximately 144 hrs in various stages [32,33]. Melt route synthesis of solid solutions possesses inherent challenges such as uneven grain size distribution, phase separation and disparity in melting point and vapor pressure, which leads to poor stoichiometry and detrimental thermoelectric properties [34]. Alloys synthesized via melt route require secondary processing methods such as mechanical grinding or crushing and compaction to achieve nano-scale features in a material.

Our ever first attempt to synthesize the nanocrystalline PbSnTeSe HEA via powder metallurgical route combining mechanical alloying (MA) and spark plasma sintering (SPS) have shown encouraging thermoelectric properties [35]. The single-phase alloys are facile synthesized in a shorter duration involving 5 hrs of MA and 11 min of SPS. Furthermore, it avoids many practical complexities and challenges involved in the melt route synthesis. Attempts to fine tune thermoelectric performance of PbSnTeSe HEA via potential doping of Bi and Na have shown significant improvement in ZT [36,37]. This is highly encouraging and attract research community towards carrying out more potential research in PbSnTeSe HEA to enhance ZT via atomic doping, band engineering, nanostructuring etc. This opens the way for promising researches in future to develop other doped systems of PbSnTeSe with an aim to push the ZT > 2 and thereby to create a revolutionary breakthrough in thermoelectric energy conversion technology.

In the present study, nanocrystalline PbSnTeSe HEA doped with Ag at different doping concentrations (0.3–0.9 at%) is facile synthesized by MA (5hrs) and SPS (11 min). The complex chemistry with good crystal structure symmetry, nanostructuring and band engineering via Ag doping synergistically contributes to achieving superior power factor and lower thermal conductivity leading to a high ZT of 0.891 at 573 K.

2. Materials and methods

2.1. Materials

The elemental powders such as Lead (Pb), Tin (Sn), Tellurium (Te) and Selenium (Se) along with Silver (Ag) as a dopant of 99.9% purity and particle size – 325 mesh (Loba Chemie, India) were used to synthesize p-type PbSnTeSe thermoelectric high entropy alloys. The nominal stoichiometry of PbSnTeSe doped with Ag is $(\text{PbSnTeSe})_{1-x}\text{Ag}_x$. Where X = 0, 0.3, 0.6 and 0.9 at%. For convenience, the PbSnTeSe alloys with varying Ag concentration (i.e. x = 0, 0.3, 0.6 and 0.9 at%) are named as base, 0.3Ag, 0.6Ag and 0.9Ag, respectively. The complete powder handling was carried out in high purity (99.999%) Argon (Ar) environment inside a glove box. The mixture powder was loaded into a high-energy ball mill (Fritsch Pulverisette, Germany), and mechanical alloying (MA) was executed for 5 hrs in a high-purity Ar atmosphere. MA was carried out at a ball-to-powder ratio of 15:1 with a milling speed of 300 rpm. The milling cycle involves 10 min milling and 20 min cooling.

2.2. Spark plasma sintering of Ag-doped PbSnTeSe HEA powder

Spark plasma sintering instrument (SPS 515, Dr. Sinter Lab, Japan) was used to consolidate the mechanically alloyed powder under a vacuum (<10 Pa). During the single-stage sintering process from room temperature (RT) to 325 °C, an uniaxial pressure of 50 MPa was maintained. After 325 °C, samples were retained in the same temperature for 5 min and then cooled to room temperature (RT). The instantaneous relative density (%) and densification rate (per sec) during SPS were estimated using the following relation [38].

$$\rho_n = \frac{d\rho_n}{dt_n} = \frac{\rho_{n+1} - \rho_{n-1}}{t_{n+1} - t_{n-1}}; \rho = \frac{L_0}{L} \rho_0 \quad (1)$$

Where, ρ_n represents the instantaneous relative density percentage at t_n (sec) time. The percentage of relative density of sample ρ was calculated from initial height L_0 (mm), instantaneous height L (mm), and initial density ρ_0 . Prior to sintering, the Z-axis displacement is set to zero. The density measurement of samples were carried out based on Archimede's principle.

2.3. X-ray diffraction and electron microscopy characterizations

X-ray diffractometer (Ultima III, Rigaku, Japan) with Cu-K α radiation ($\lambda = 1.54 \text{ \AA}$) was used to analyze the phase and structural features of mechanically alloyed and sintered samples. The lattice strain (%) and average crystal size were determined using the Williamson and Hall relation in both powder and sintered samples. The following relationship was used to estimate the crystallite size (D) from the diffracted peaks.

$$D = \frac{K\lambda}{\beta \cos \theta} + 4\epsilon \tan \theta \quad (2)$$

Where, K represents the shape factor ($K = 0.9$), λ represents the X-ray wavelength, β represents the full width half maximum corresponding to hkl planes (in radians), ϵ represents lattice strain and θ stands for the diffraction angle. The induced lattice strain (ϵ) was obtained from the following relation.

$$\epsilon = \frac{\beta}{4 \tan \theta} \quad (3)$$

The phase characteristics, elemental and dopant distribution of sintered samples were studied using a scanning electron microscope equipped with energy-dispersive X-ray spectroscopy (SEM-EDS) (Carl Zeiss, Germany).

2.4. Hall measurements and thermoelectric performance of nanostructured PbSnTeSe HEA doped with Ag

Van der Pauw's four-probe approach was used to measure the hall characteristics of the bulk sample (HMS 5000, Ecopia, USA). The absolute Seebeck coefficient and electrical conductivity measurements were carried out using the Seebeck coefficient and electrical resistivity measuring instrument (LSR-3, Linseis, Germany) under high purity helium (99.999%) atmosphere between 373 K and 573 K. The thermal diffusivity (D) of the bulk sample was calculated using the laser flash apparatus (LFA457, Netzsch, Germany). Differential scanning calorimetry (DSC) analysis was used to estimate the specific heat (C_p) of samples. The total thermal conductivity (k) was determined using the empirical formula $k = \rho D C_p$.

3. Results and discussion

3.1. XRD and electron microscopy characterization

X-ray diffraction (XRD) patterns of mechanically alloyed and

sintered PbSnTeSe HEA doped with Ag (0, 0.3, 0.6, and 0.9 at%) are shown in Fig. 1a. The diffracted peaks of milled and SPS bulk materials are indexed to a single-phase PbSnTeSe HEA with NaCl type FCC crystal structure in the Fm3-m space group (ICDD-PDF card number 01-071-6519) (Fig. 1d). The elemental powders experience substantial lattice distortion during milling, resulting in the formation of the PbSnTeSe alloy. Furthermore, due to the complex chemical gradient caused by multiple elements in the equiatomic ratio, the configurational entropy in the PbSnTeSe HEA significantly increases to achieve a single-phase solid solution in a shorter milling time. In spite, of possessing the single phase PbSnTeSe HEA, the Ag doping (0.3–0.9 at%) show significant variation in its lattice. This is evident from the shift of the principal plane (200) at the 2θ vicinity of 28.7° (Fig. 1b).

It is also confirmed that 5 hrs of milling favoring the nanostructuring of the powder particles, thus showing the significant variation in crystallite size and lattice strain, as evidenced by the peak broadening phenomena of the PbSnTeSe HEA. Table 1 shows that the average crystallite size of all sintered samples is < 60 nm. The lattice parameter

Table 1

Average crystallite size and lattice strain of sintered Ag-doped PbSnTeSe HEA.

Sample	Average crystallite size (nm)	Lattice strain (%)
Base	53 ± 0.24	0.171
0.3Ag	54 ± 0.76	0.167
0.6Ag	57 ± 0.30	0.160
0.9Ag	59 ± 0.57	0.156

of PbSnTeSe HEA with Ag doping (0–0.9 at%) shows a considerable variation. It is understood that increasing Ag doping concentration lower the PbSnTeSe HEA's lattice parameter from 6.229 \AA to 6.212 \AA (Fig. 1c). This is due to the atomic size difference between the parental elements and Ag, which causes lattice distortion in the base system. Further, with an increase in Ag doping concentration, configurational entropy can be enhanced in PbSnTeSe HEA, which can be referred from Appendix A: Electronic supplementary information (ESI).

Fig. 2a features the SEM image of sintered nanocrystalline 0.9Ag HEA captured in the backscattered electron (BSE) mode. The grey color

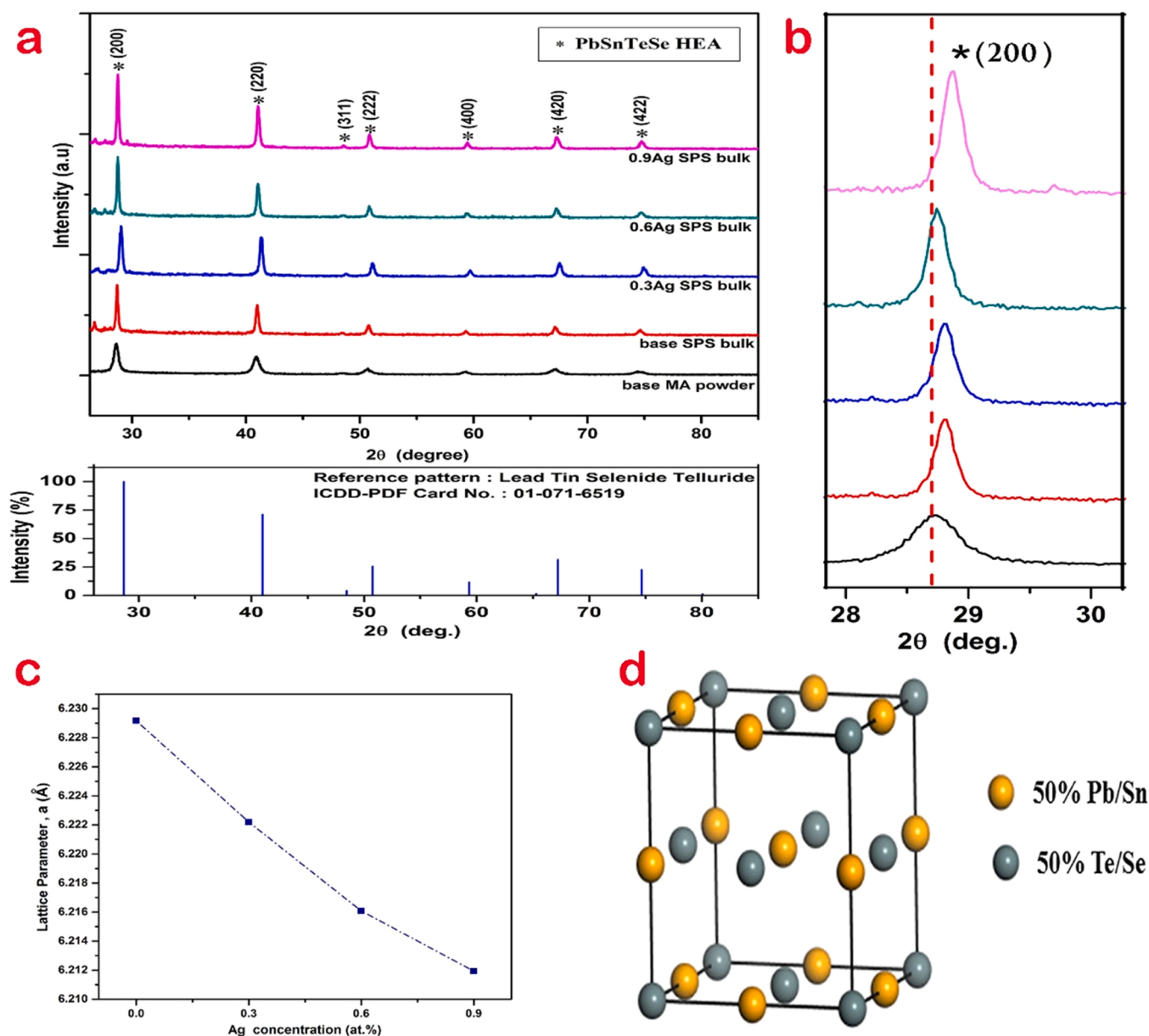


Fig. 1. a). XRD patterns of mechanically alloyed PbSnTeSe HEA powder and sintered PbSnTeSe HEA doped with Ag, b) Shift in (200) peak of PbSnTeSe HEA, c) Variation of the lattice parameter with Ag doping and d) Crystal structure of PbSnTeSe HEA.

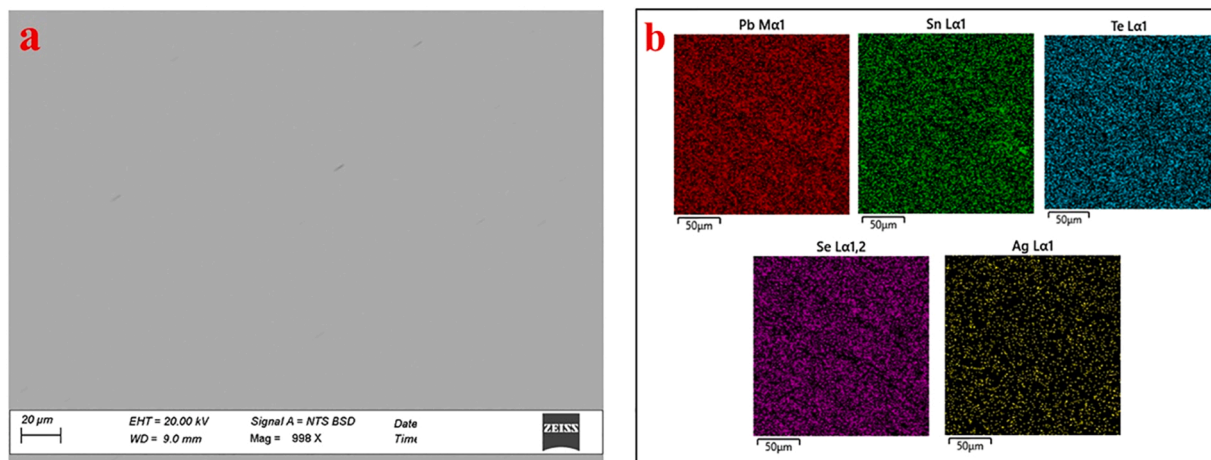


Fig. 2. a) BSE-SEM image, b) EDS mapping of spark plasma sintered 0.9Ag HEA bulk.

contrast of the SEM image depicts the uniform and homogeneous PbSnTeSe HEA phase. Thus, it confirms the single-phase nature of the alloy and complies with the XRD observation. The corresponding EDS elemental mapping (Fig. 2b) and spectrums (Fig. 3) affirm that the bulk sample's constituent elements and Ag dopant are distributed uniformly. Furthermore, the superior phase homogenization is confirmed by the narrow deviation of constituent elements to the nominal concentration made from EDS elemental quantification. In addition, it portrays that Ag dopant is distributed uniformly in the sintered PbSnTeSe HEA and it is quantified as 0.9 at%, which is in good agreement with its nominal concentration (inset to Fig. 3). Furthermore, composition analysis of all the samples portrays a similar trend with an increase in doping concentration of the Ag and closer agreement with the theoretical stoichiometry (Fig. A.1 of Electronic supplementary information).

3.2. Densification kinetics of HEA powder during spark plasma sintering

To further understand the sintering kinetics, the densification rate and instantaneous relative density profiles of nanostructured PbSnTeSe HEA powders with varying Ag doping concentration were recorded during SPS (Fig. 4). It depends on the various driving factors such as (i) applied load, (ii) stress induced on the powder particles, (iii) high-density electron migration, and (iv) momentary evolution of the plasma [35]. The entire densification process can be divided into three stages: primary (stage-I), intermediate (stage-II), and final (stage-III). Pressure and temperature are crucial in each regime for activating thermodynamical events of varying nature and momentum in order to

achieve better densification. The primary stage (RT to 125 °C) portrays the least densification rate synergistically attributed by the constant pressure imposed and the initial flow of high-density pulse current passing through the HEA powder volume. Concurrently, the applied pressure causes PbSnTeSe HEA powder particles to self-arrange inward (due to an azimuthal magnetic field), thus enhancing physical contacts within the powder volume [39,40]. Surface integration and mechanical interactions between the particles are greatly influenced by the surface energy of the powder particles at this point. As a result, it aids in forming a better passage for the pulsed, high-density current uniformly through the powder compact. Due to Joule heating, the pulse current (I) generated during SPS is delivered through the graphite die packed with powders, which is responsible for achieving the desired temperature. It is related to the root mean square of an instantaneous current density (I_{RMS}), which is mathematically represented by the following equation [41].

$$I_{RMS} = \sqrt{\frac{1}{\tau} \int_t^{t+\tau} I^2(t) dt} \quad (4)$$

Where, I and τ are the instantaneous current and time. Notably, the nanostructured powders processed through mechano-chemical synthesis exist with the boundary (amorphous region) and internal atomic disorder (defects) due to severe mechanical knocking. Therefore, the transient pulse current passes through the graphite die column, causing the overheating of the individual powder particles with the existing atomic and grain boundaries consequence in the skin effect, which leads to surface cleaning. Also, the wider chemical complexity and compositional gradient existence in the PbSnTeSe (i.e., Pb, Sn, Te, Se) and Ag dopant are expected to offer a high resistance towards the current consumption, thus consuming a higher current than that of the conductive monolithic powder. However, the surface melting and encapsulation that results from the momentary generation of plasma significantly reduce the surface energy of the HEA powder particles (Stage I). It develops the meting of the powder particle boundaries and forms the thinner amorphous layer with an increase in temperature with control pressure aided in the particle gliding. These factors significantly impact the solid-state atomic transport in the intermediate stage, which showcases the bulk deformation in the powder compact (marked as Stage-II in Fig. 4a). The major densification rate is attributed in this region by increasing the densification rate from 0.0045 s^{-1} at 125 °C to 0.0234 s^{-1} at 250 °C. This complements the corresponding drastic improvement in the relative density from 79% (125 °C) to 97% (250 °C) (Fig. 4b). The compact, in particular, exhibits remarkable creep, and subsequent hot forging phenomena lead to a higher densification rate. After 250 °C, a stable densification rate is observed in the final stage,

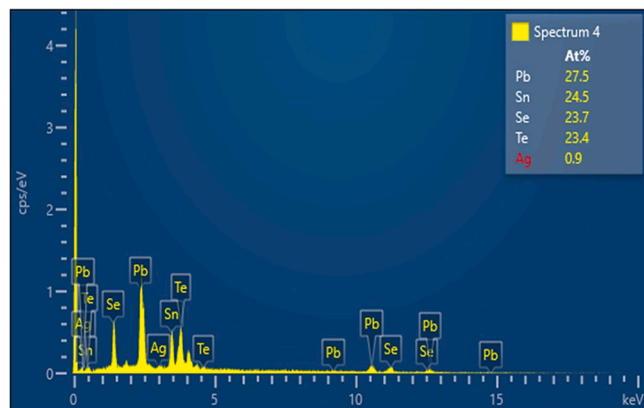


Fig. 3. EDS spectrum of spark plasma sintered 0.9Ag HEA (Inset: atomic concentration of constituent elements).

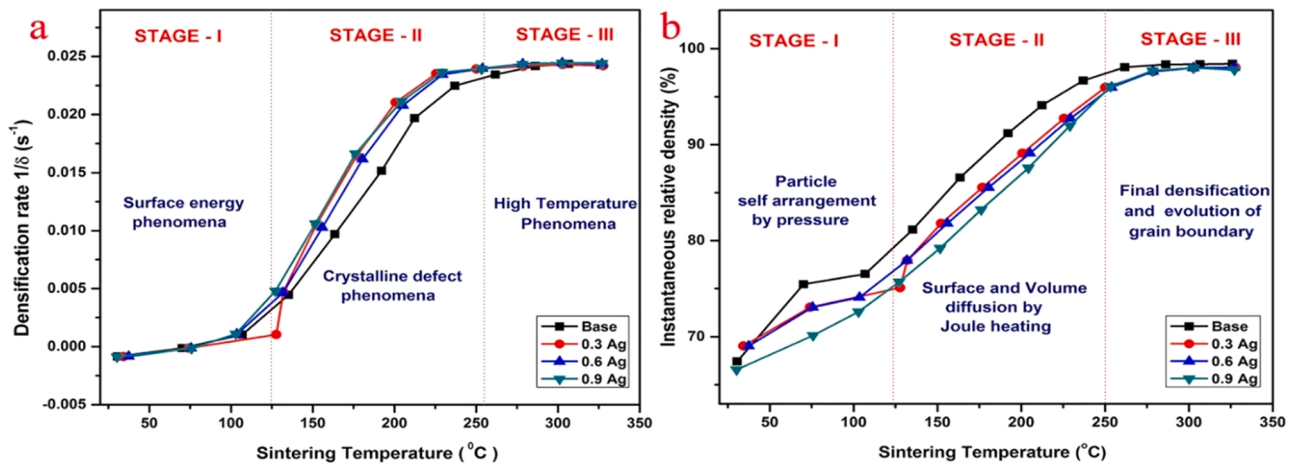


Fig. 4. SPS curves of PbSnTeSe doped with Ag a) Densification rate and b) Instantaneous relative density (%).

reflecting near-maximum densification with a relative density closer to 98.5%.

3.3. Hall measurements and thermoelectric properties of bulk nanocrystalline PbSnTeSe HEA samples with Ag doping

Table 2 summarises the ambient temperature carrier concentration and hall mobility characteristics of Ag-doped PbSnTeSe HEA samples. Hall coefficient values are recorded positively in all the HEA samples, which confirms that alloys are p-type semiconductors. The nanocrystalline PbSnTeSe HEA possesses a bulk carrier density of $1.80 \times 10^{19} \text{ cm}^{-3}$ and hall mobility of $368 \text{ cm}^2/\text{Vs}$. The recorded values provide the ideal compliance to be general semiconducting range. In PbSnTeSe HEA, raising the Ag doping concentration significantly increases the carrier concentration and decreases the hall mobility. The PbSnTeSe HEA doped with 0.9Ag achieves a superior carrier concentration of $1.34 \times 10^{20} \text{ cm}^{-3}$. The carrier mobility of the samples show the adverse trend of reduction with Ag doping concentration. The charge carrier mobility of the pristine PbSnTeSe HEA is $368 \text{ cm}^2/\text{Vs}$, which is reduced to $222 \text{ cm}^2/\text{Vs}$ by doping with 0.3 at% Ag. With Ag doping of 0.6 at% and 0.9 at%, the carrier mobilities are drastically reduced to $66.4 \text{ cm}^2/\text{Vs}$ and $63.5 \text{ cm}^2/\text{Vs}$, respectively. Even though bulk carrier concentration increases with Ag doping, the charge carrier mobility observed decreases, thus resulting in a significant reduction in electrical conductivity. With an increase in Ag concentration, lattice distortion significantly increases due to atomic size and mass difference created by the Ag atom relative to the parental elements. This is evident from the reduction in the lattice parameter of the alloy from 6.229 \AA to 6.212 \AA (Fig. 1c) quantified by the XRD analysis. The increase in lattice distortion and the introduction of point defects due to Ag atom doping could increase electron scattering centers. Furthermore, it gives the combined effect with the inherent grain boundaries and junctions scattering via the nanocrystalline nature in the alloy. Consequently, the mean free path of electrons remarkably decreases, thus reducing the electrical conductivity of the HEA. This can be understood from the significant decrease in the hall mobility from $368 \text{ cm}^2/\text{Vs}$ to $63.5 \text{ cm}^2/\text{Vs}$ when the Ag concentration is varied from

0 to 0.9 at%. The similar observation is reported in $\text{BiSb}_{1.5}\text{Te}_{1.5}\text{Se}$ HEA is doped with an Ag atom [33]. With a rise in Ag doping, the average Hall coefficient of the HEA samples drops from $+0.348 \text{ m}^3/\text{C}$ to $+0.0465 \text{ m}^3/\text{C}$.

Fig. 5a shows the absolute Seebeck coefficient (S) values for Ag-doped PbSnTeSe at temperatures ranging from 373 K to 573 K. All of the samples exhibit positive values, confirming the p-type semiconducting nature in the samples with holes as the majority of charge carriers. This observation complements the behavior recorded from the Hall measurement characteristics (Table 2).

In general, S values and carrier concentration data can be correlated to understand the density of state's effective mass of the charge carries considering the model on the single-parabolic band (SPB) with an acoustic-phonon scattering as an influential and dominating scattering mechanism as emphasized in the Fermi-Dirac statistics, the S and effective mass can be mathematically expressed respectively by Eq. (5) and Eq. (6) [41].

$$S = \left(\frac{k_B}{e} \right) \left\{ \left(\frac{(2 + \lambda) F_{1+\lambda}(\eta)}{(1 + \lambda) F_{\lambda}(\eta)} - \eta \right) \right\} \quad (5)$$

$$m^* = \frac{h^2}{2k_B T} \left[\frac{n}{4\pi F_{\frac{1}{2}}(\eta)} \right]^{2/3} \quad (6)$$

Where, k_B represents the Boltzmann constant, λ represents the scattering factor (i.e. in the case of acoustic phonon scattering $\lambda = 0$ and for ionized impurity scattering it is $\lambda = 2$), m^* corresponds to the effective mass, n is the carrier concentration and h is the Planck constant, $F_{\lambda}(\eta)$ is the Fermi-Dirac integral. The S values in pristine PbSnTeSe increase monotonically from $84 \text{ } \mu\text{V/K}$ at 373 K to $144 \text{ } \mu\text{V/K}$ at 573 K. Furthermore, the S values have a positive slope in the measurement range, indicating no bipolar phenomena in the synthesized HEAs. The higher configurational entropy and good crystal structure symmetry due to complex chemistry significantly increase the S value. With an increase in doping of Ag, S value increases to $150 \text{ } \mu\text{V/K}$ (0.3Ag) and $213 \text{ } \mu\text{V/K}$ (0.6Ag) at 573 K. This could be attributed to higher microscopic configurations, synergetic enhancement in the bandgap, the density of states (DOS), and effective mass of charge carriers [42–44]. This is due to the drastic reduction in the charge carrier mobility from $368 \text{ cm}^2/\text{Vs}$ to $63.5 \text{ cm}^2/\text{Vs}$ via increased effective mass and higher doping concentration from 0 to 0.9 at%. In the same operating temperature, the current observation is a two-fold increase in the S value of PbSnTeSe HEA that doped with La [32].

The electrical conductivity (σ) of the Ag-doped PbSnTeSe HEA is shown in Fig. 5b. It can be seen in all HEA samples, the steady decrease in σ up to 573 K. The σ of the base HEA decreases from $6.13 \times 10^4 \text{ S/m}$ at

Table 2
Hall measurement characteristics of bulk PbSnTeSe HEA doped with Ag.

Sample	Bulk carrier concentration (cm^{-3})	Carrier mobility (cm^2/Vs)	Average Hall coefficient (m^3/C)	Nature of semiconduction
base	1.80×10^{19}	368	+ 0.348	p-type
0.3Ag	3.31×10^{19}	222	+ 0.189	p-type
0.6Ag	7.74×10^{19}	66.4	+ 0.080	p-type
0.9Ag	1.34×10^{20}	63.5	+ 0.046	p-type

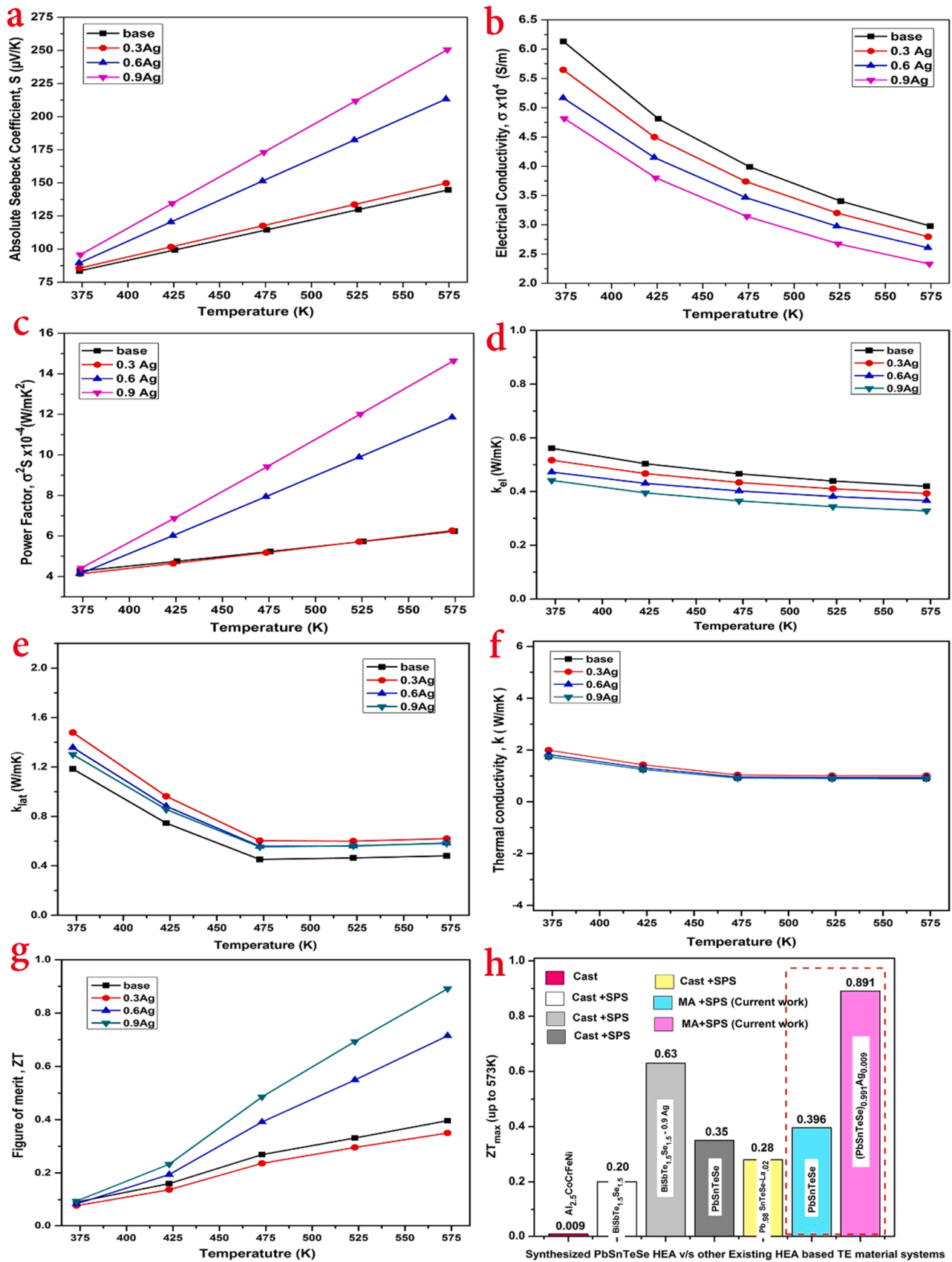


Fig. 5. Thermoelectric properties of sintered PbSnTeSe HEA doped with Ag a) Absolute Seebeck coefficient, b) Electrical conductivity, c) Power factor, d) electronic thermal conductivity, e) lattice thermal conductivity, f) total thermal conductivity, g) Figure of merit ZT and h) comparison of current ZT_{max} values with other thermoelectric HEA systems processed through different approaches.

373 K to a much lower value of 2.98×10^4 S/m at 573 K. In the 0.9Ag HEA, a peak reduction of 2.33×10^4 S/m is observed at 573 K. From Table 2, It is evident that, in addition to the increase in charge carrier concentration by increasing Ag doping concentration, there is a substantial reduction in charge carrier mobility. This implausible effect is mainly manipulated by the following phenomena: (i) higher configurational entropy and complex crystal structure, (ii) Enhancements in grain boundaries and junctions (i.e., nanostructuring approach) and (iii) Physical defects and imperfections in different types (i.e., Ag doping, porosity, and lattice misfit) [32,33]. These factors provide synergetic influence in reducing the charge carrier mobility by increasing scattering centers in bulk HEA samples. Furthermore, Ag doping significantly increases the charge carrier effective mass and substantially reduces the carrier velocity, causing a decrease in σ .

The thermal conductivity of base and Ag-doped nanocrystalline PbSnTeSe HEAs show a synergetic decrease in electronic and lattice thermal conductivity (i.e., k_{el} and k_{lat}) (Fig. 5d-e). The nanostructuring phenomena and charge carrier scattering by point defects (Ag atoms), an increase in Ag doping concentration in the HEA results in a significant reduction in k_{el} (Fig. 5d). Alongside, higher volume grain boundaries by nanostructuring and lattice distortion induced during MA also oppose the transport of the heat-carrying phonons to decrease k_{lat} . Also, the complex chemistry due to the high entropy phenomena results in anharmonicity and phonon-phonon scattering. This anharmonicity increases with the higher temperature gradient, thereby enhancing the phonon-phonon collision to achieve lower energy. This can increase the Umklapp scattering events at a higher temperature and reduce the k_{lat} further to < 0.6 W/mK (Fig. 5e). As a result, at the elevated temperatures of 573 K, the total thermal conductivity (k) of HEA samples is dramatically reduced to a lower range (i.e., 0.9 W/mK) (Fig. 5f).

The power factor ($S^2\sigma$) of the nanocrystalline PbSnTeSe HEA with Ag doping concentrations increases with temperature (Fig. 5c). The PbSnTeSe base HEA shows a power factor of 6.24×10^{-4} W/mK² at 573 K. The maximum power factor reported for the 0.9Ag HEA is 14.64×10^{-4} W/mK². The power factor of base HEA increases significantly as the Ag doping concentration rises. The substantial increase in the S value compliments the enormous increase in the power factor. The temperature-dependent figure of merit (ZT) of nanocrystalline PbSnTeSe HEA doped with Ag is shown in Fig. 5g. The ZT value of base PbSnTeSe HEA increases linearly as the temperature rises and reaching a maximum of 0.396 at 573 K. Notably, the higher ZT values of 0.714 and 0.891 at 573 K are observed in the 0.6Ag HEA and 0.9Ag HEA, respectively. The 0.6Ag and 0.9Ag HEAs possess remarkable enhancements of 180% and 225%, respectively, over the pristine PbSnTeSe HEA. The ZT for the systems are significantly higher when compared to pristine PbSnTeSe HEA (ZT = 0.35) and La-doped PbSnTeSe HEA (ZT = 0.28) doped alloys synthesized via melt and SPS route (ZT = 0.28) in same operating temperature range [32]. Furthermore, single phase alloy synthesis with very short processing time avoids many practical complexities and challenges involved in the melt route synthesis. [32–33, 44].

4. Conclusion

The monophase nanocrystalline PbSnTeSe HEA doped with Ag (0.3–0.9 at%) were developed via solid-state synthesis by mechanical alloying (MA) and spark plasma sintering (SPS). The following are the most significant findings.

- i. The short duration mechanical alloying for 5hrs significantly contributes to achieving the monophase PbSnTeSe HEA (solid solution) powder doped with varying Ag concentration (i.e., 0 – 0.9 at%).
- ii. SPS of PbSnTeSe HEA doped with Ag retained the phase stability and nanocrystalline nature with the average crystallite size < 60 nm with a high relative density ($>96\%$)

- iii. The XRD, SEM, and EDS composition analyses confirm the monophase nature of the HEAs and the uniform elemental distribution.
- iv. A high absolute Seebeck coefficient (250 μ V/K at 573 K) via Ag doping significantly increases the power factor (14.64×10^{-4} W/mK² in 0.9Ag HEA) than PbSnTeSe HEA (with a power factor of 6.24×10^{-4} W/mK²).
- v. With an increase in Ag doping from 0 to 0.9 at%, a notable increase in the charge carrier concentration from 1.80×10^{19} cm⁻³ to 1.34×10^{20} cm⁻³ and a substantial decrease in carrier mobility from 368 cm²/Vs to 63.5 cm²/Vs is observed. This indicates that effective mass of charge carrier increases with the Ag doping.
- vi. The superior power factor combined with lower thermal conductivity achieved a virtuous ZT of 0.891 at 573 K in 0.9Ag HEA.
- vii. This enhancement in the ZT is remarkably higher (225%) than the pristine PbSnTeSe HEA (ZT = 0.396).
- viii. Compared to other HEA thermoelectric systems processed through alternative routes, the nanostructured PbSnTeSe-Ag HEA synthesized using the current swift approach (MA and SPS) shows a substantial improvement in the ZT.

CRediT authorship contribution statement

Arun Raphael: Methodology, Investigation, Validation, Writing – original draft. **Vivekanandhan P:** Investigation, Validation, Supervision, Writing – review & editing. **Arun Kumar Rajasekaran:** Investigation, Validation. **Kumaran S:** Conceptualization, Methodology, Supervision, Validation, Resources, Project administration.

Declaration of Competing Interest

The authors declare that they have no known competing financial interests or personal relationships that could have appeared to influence the work reported in this paper.

Data Availability

Data will be made available on request.

Appendix A. Supporting information

Supplementary data associated with this article can be found in the online version at [doi:10.1016/j.mtcomm.2023.105880](https://doi.org/10.1016/j.mtcomm.2023.105880).

References

- [1] S.M. Pourkiaei, M.H. Ahmadi, M. Sadeghzadeh, S. Moosavi, F. Pourfayaz, L. Chen, M.A. Pour Yazdi, R. Kumar, Thermoelectric cooler and thermoelectric generator devices: a review of present and potential applications, modeling and materials, *Energy* 186 (2019), 115849, <https://doi.org/10.1016/j.energy.2019.07.179>.
- [2] H.S. Kim, W. Liu, Z. Ren, The bridge between the materials and devices of thermoelectric power generators, *Energy Environ. Sci.* 10 (2017) 69–85, <https://doi.org/10.1039/C6EE02488B>.
- [3] C. Li, F. Jiang, C. Liu, P. Liu, J. Xu, Present and future thermoelectric materials toward wearable energy harvesting, *Appl. Mater. Today* 15 (2019) 543–557, <https://doi.org/10.1016/j.apmt.2019.04.007>.
- [4] C. Gayner, K.K. Kar, Recent advances in thermoelectric materials, *Prog. Mater. Sci.* 83 (2016) 330–382, <https://doi.org/10.1016/j.pmatsci.2016.07.002>.
- [5] A. Mehdizadeh Dehkordi, M. Zebbarjadi, J. He, T.M. Tritt, Thermoelectric power factor: enhancement mechanisms and strategies for higher performance thermoelectric materials, *Mater. Sci. Eng.: R. Rep.* 97 (2015) 1–22, <https://doi.org/10.1016/j.mser.2015.08.001>.
- [6] C.-H. Su, Design, growth and characterization of PbTe-based thermoelectric materials, *Prog. Cryst. Growth Charact. Mater.* 65 (2019) 47–94, <https://doi.org/10.1016/j.pcrysgrow.2019.04.001>.
- [7] R. Murugasami, P. Vivekanandhan, S. Kumaran, R. Suresh Kumar, T. John Tharakan, Simultaneous enhancement in thermoelectric performance and mechanical stability of p-type SiGe alloy doped with Boron prepared by mechanical alloying and spark plasma sintering, *J. Alloy. Compd.* 773 (2019) 752–761, <https://doi.org/10.1016/j.jallcom.2018.09.029>.
- [8] X. Zhang, L.-D. Zhao, Thermoelectric materials: energy conversion between heat and electricity, *J. Mater.* 1 (2015) 92–105, <https://doi.org/10.1016/j.jmat.2015.01.001>.

- [9] A. Raphael, P. Vivekanandhan, S. Kumaran, High entropy phenomena induced low thermal conductivity in $\text{BiSbTe}_{1.5}\text{Se}_{1.5}$ thermoelectric alloy through mechanical alloying and spark plasma sintering, *Mater. Lett.* 269 (2020), 127672, <https://doi.org/10.1016/j.matlet.2020.127672>.
- [10] A.D. LaLonde, Y. Pei, H. Wang, G. Jeffrey Snyder, Lead telluride alloy thermoelectrics, *Mater. Today* 14 (2011) 526–532, [https://doi.org/10.1016/S1369-7021\(11\)70278-4](https://doi.org/10.1016/S1369-7021(11)70278-4).
- [11] H. Meng, M. An, T. Luo, N. Yang, 2 - Thermoelectric applications of chalcogenides, in: X. Liu, S. Lee, J.K. Furdyna, T. Luo, Y.-H. Zhang (Eds.), *Chalcogenide*, Woodhead Publishing, 2020, pp. 31–56, <https://doi.org/10.1016/B978-0-08-102687-8.00002-6>.
- [12] C. Gayner, K.K. Kar, W. Kim, Recent progress and futuristic development of PbSe thermoelectric materials and devices, *Mater. Today Energy* 9 (2018) 359–376, <https://doi.org/10.1016/j.mtener.2018.06.010>.
- [13] Y. Qin, Y. Xiao, D. Wang, B. Qin, Z. Huang, L.-D. Zhao, An approach of enhancing thermoelectric performance for p-type PbS: decreasing electronic thermal conductivity, *J. Alloy. Compd.* 820 (2020), 153453, <https://doi.org/10.1016/j.jallcom.2019.153453>.
- [14] L. Zhao, J. Wang, J. Li, J. Liu, C. Wang, J. Wang, X. Wang, High thermoelectric performance of Ag doped SnTe polycrystalline bulks via the synergistic manipulation of electrical and thermal transport, *Phys. Chem. Chem. Phys.* 21 (2019) 17978–17984, <https://doi.org/10.1039/C9CP03534F>.
- [15] L.-D. Zhao, C. Chang, G. Tan, M.G. Kanatzidis, SnSe: a remarkable new thermoelectric material, *Energy Environ. Sci.* 9 (2016) 3044–3060, <https://doi.org/10.1039/C6EE01755J>.
- [16] Q. Zhao, B. Qin, D. Wang, Y. Qiu, L.-D. Zhao, Realizing high thermoelectric performance in polycrystalline SnSe via silver doping and germanium alloying, *ACS Appl. Energy Mater.* 3 (2020) 2049–2054, <https://doi.org/10.1021/acsaem.9b01475>.
- [17] K.S. Bayikadi, R. Sankar, C.T. Wu, C. Xia, Y. Chen, L.-C. Chen, K.-H. Chen, F.-C. Chou, Enhanced thermoelectric performance of GeTe through in situ microdomain and Ge-vacancy control, *J. Mater. Chem. A* 7 (2019) 15181–15189, <https://doi.org/10.1039/C9TA03503F>.
- [18] W.-D. Liu, D.-Z. Wang, Q. Liu, W. Zhou, Z. Shao, Z.-G. Chen, High-performance GeTe-based thermoelectrics: from materials to devices, *Adv. Energy Mater.* 10 (2020), 2000367, <https://doi.org/10.1002/aenm.202000367>.
- [19] W.-D. Liu, L. Yang, Z.-G. Chen, Cu₂Se thermoelectrics: property, methodology, and device, *Nano Today* 35 (2020), 100938, <https://doi.org/10.1016/j.nantod.2020.100938>.
- [20] W.-D. Liu, L. Yang, Z.-G. Chen, J. Zou, Promising and eco-friendly Cu₂X-based thermoelectric materials: progress and applications, *Adv. Mater.* 32 (2020), 1905703, <https://doi.org/10.1002/adma.201905703>.
- [21] W.-D. Liu, Y. Yu, M. Dargusch, Q. Liu, Z.-G. Chen, Carbon allotrope hybrids advance thermoelectric development and applications, *Renew. Sustain. Energy Rev.* 141 (2021), 110800, <https://doi.org/10.1016/j.rser.2021.110800>.
- [22] M. Dargusch, W.-D. Liu, Z.-G. Chen, Thermoelectric generators: alternative power supply for wearable electrocardiographic systems, *Adv. Sci.* 7 (2020), 2001362, <https://doi.org/10.1002/advs.202001362>.
- [23] D. Wu, L.-D. Zhao, X. Tong, W. Li, L. Wu, Q. Tan, Y. Pei, L. Huang, J.-F. Li, Y. Zhu, M.G. Kanatzidis, J. He, Superior thermoelectric performance in PbTe–PbS pseudobinary: extremely low thermal conductivity and modulated carrier concentration, *Energy Environ. Sci.* 8 (2015) 2056–2068, <https://doi.org/10.1039/C5EE01147G>.
- [24] H. Wang, J. Wang, X. Cao, G.J. Snyder, Thermoelectric alloys between PbSe and PbS with effective thermal conductivity reduction and high figure of merit, *J. Mater. Chem. A* 2 (2014) 3169–3174, <https://doi.org/10.1039/C3TA14929C>.
- [25] Y.-M. Han, J. Zhao, M. Zhou, X.-X. Jiang, H.-Q. Leng, L.-F. Li, Thermoelectric performance of SnS and SnS–SnSe solid solution, *J. Mater. Chem. A* 3 (2015) 4555–4559, <https://doi.org/10.1039/C4TA06955B>.
- [26] Y.-M. Han, J. Zhao, M. Zhou, X.-X. Jiang, H.-Q. Leng, L.-F. Li, Thermoelectric performance of SnS and SnS–SnSe solid solution, *J. Mater. Chem. A* 3 (2015) 4555–4559, <https://doi.org/10.1039/C4TA06955B>.
- [27] B.R. Ortiz, J.M. Adamczyk, K. Gordiz, T. Braden, E.S. Toberer, Towards the high-throughput synthesis of bulk materials: thermoelectric PbTe–PbSe–SnTe–SnSe alloys, *Mol. Syst. Des. Eng.* 4 (2019) 407–420, <https://doi.org/10.1039/C8ME00073E>.
- [28] D.B. Miracle, O.N. Senkov, A critical review of high entropy alloys and related concepts, *Acta Mater.* 122 (2017) 448–511, <https://doi.org/10.1016/j.actamat.2016.08.081>.
- [29] E.J. Pickering, N.G. Jones, High-entropy alloys: a critical assessment of their founding principles and future prospects, *Int. Mater. Rev.* 61 (2016) 183–202, <https://doi.org/10.1080/09506608.2016.1180020>.
- [30] O.N. Senkov, G.B. Wilks, D.B. Miracle, C.P. Chuang, P.K. Liaw, Refractory high-entropy alloys, *Intermetallics* 18 (2010) 1758–1765, <https://doi.org/10.1016/j.intermet.2010.05.014>.
- [31] O.N. Senkov, G.B. Wilks, J.M. Scott, D.B. Miracle, Mechanical properties of Nb₂₅Mo₂₅Ta₂₅W₂₅ and V₂₀Nb₂₀Mo₂₀Ta₂₀W₂₀ refractory high entropy alloys, *Intermetallics* 19 (2011) 698–706, <https://doi.org/10.1016/j.intermet.2011.01.004>.
- [32] Z. Fan, H. Wang, Y. Wu, X. Liu, Z. Lu, Thermoelectric performance of PbSnTeSe high-entropy alloys, *Mater. Res. Lett.* 5 (2017) 187–194, <https://doi.org/10.1080/21663831.2016.1244116>.
- [33] Z. Fan, H. Wang, Y. Wu, X.J. Liu, Z.P. Lu, Thermoelectric high-entropy alloys with low lattice thermal conductivity, *RSC Adv.* 6 (2016) 52164–52170, <https://doi.org/10.1039/C5RA28088E>.
- [34] Y.F. Ye, Q. Wang, J. Lu, C.T. Liu, Y. Yang, High-entropy alloy: challenges and prospects, *Mater. Today* 19 (2016) 349–362, <https://doi.org/10.1016/j.matod.2015.11.026>.
- [35] A. Raphael, A.K. Singh, P. Vivekanandhan, S. Kumaran, Thermoelectric performance of nanostructured PbSnTeSe high entropy thermoelectric alloy synthesized via spark plasma sintering, *Phys. B: Condens. Matter* 622 (2021), 413319, <https://doi.org/10.1016/j.physb.2021.413319>.
- [36] A. Raphael, V. P. A.K. Singh, K. S. High entropy stabilization and band engineering driven high figure of merit in nanostructured PbSn_{0.875}TeSeBi_{0.125} alloy, *J. Solid State Chem.* 303 (2021), 122531, <https://doi.org/10.1016/j.jssc.2021.122531>.
- [37] A. Raphael, V. P. A.K. Rajasekaran, K. S. Tuning figure of merit in Na doped nanocrystalline PbSnTeSe high entropy alloy via band engineering, *Mater. Sci. Semicond. Process.* 138 (2022), 106270, <https://doi.org/10.1016/j.msssp.2021.106270>.
- [38] P. Vivekanandhan, R. Murugasami, S. Kumaran, Spark plasma assisted in-situ phase evolution and densification of nanocrystalline magnesium silicide – silicon germanium thermo-electric composite: pulse current effects and densification mechanisms, *Scr. Mater.* 146 (2018) 344–348, <https://doi.org/10.1016/j.scriptamat.2017.12.021>.
- [39] R. Orrù, R. Licheri, A.M. Locci, A. Cincotti, G. Cao, Consolidation/synthesis of materials by electric current activated/assisted sintering, *Mater. Sci. Eng. R: Rep.* 63 (2009) 127–287, <https://doi.org/10.1016/j.mser.2008.09.003>.
- [40] Z.-Y. Hu, Z.-H. Zhang, X.-W. Cheng, F.-C. Wang, Y.-F. Zhang, S.-L. Li, A review of multi-physical fields induced phenomena and effects in spark plasma sintering: fundamentals and applications, *Mater. Des.* 191 (2020), 108662, <https://doi.org/10.1016/j.matdes.2020.108662>.
- [41] Jae Ki Lee, Byungki Ryua, Sungjin Park, Ji. Hee Son, Jongho Park, Jeongin Jang, Min-Wook Oh, Su.Dong Park, Effect of microstructure on thermoelectric conversion efficiency in metastable δ -phase AgSbTe_2 , *Acta Mater.* 222 (2022), 117443.
- [42] R. Liu, H. Chen, K. Zhao, Y. Qin, B. Jiang, T. Zhang, G. Sha, X. Shi, C. Uher, W. Zhang, L. Chen, Entropy as a gene-like performance indicator promoting thermoelectric materials, *Adv. Mater.* 29 (2017), 1702712, <https://doi.org/10.1002/adma.201702712>.
- [43] B.G. Yacobi, *Semiconductor Materials: An Introduction to Basic Principles*, Springer, US, 2003, <https://doi.org/10.1007/b105378>.
- [44] S. Shafeie, S. Guo, Q. Hu, H. Fahlquist, P. Erhart, A. Palmqvist, High-entropy alloys as high-temperature thermoelectric materials, *J. Appl. Phys.* 118 (2015), 184905, <https://doi.org/10.1063/1.4935489>.



Finite element modelling of carbon fiber reinforced with vespel and honey-comb structure

K. Shunmugesh^{a,*}, Arun Raphel^a, T.G. Unnikrishnan^a, K.T. Akhil^b

^a Department of Mechanical Engineering, Viswajyothi College of Engineering and Technology, Vazhakulam, Kerala, India

^b HMT Machine Tools Ltd, Kalamassery, India

ARTICLE INFO

Article history:

Available online 30 August 2022

Keywords:

Carbon Fiber
Vespel SP-21
Finite Element Modelling

ABSTRACT

Carbon fiber is considered as a material of future. It has better mechanical properties when compared to metals like steel and aluminium. And its high strength to weight ratio makes it a promising component for modern buildings, spacecrafts etc. Carbon fiber has a low compressive to tensile strength ratio. Carbon fiber can't operate under high temperature conditions. Current work proposes a composite design which will help in shielding carbon fiber from high temperature. For this sole purpose we are using high temperature polyimide plastic, vespel SP-21 and high temperature epoxy resin eccobond 104. The manufacturing of the composite is done by vacuum bagging process. The manufactured composite is future heat treated to obtain high tensile strength. Using rules of mixture equations approximate equivalent properties of the composite is found and is used for finite element modelling of the composite. This model is used for the analysis of a single layer and double layer of the composite sheet. The stresses and elongation at the layers are analyzed. The optimum loads for single and double layer composite was found by trial and error method.

Copyright © 2022 Elsevier Ltd. All rights reserved.

Selection and peer-review under responsibility of the scientific committee of the International Conference on Processing and Characterization of Materials.

1. Introduction

Material engineering is one of the most rapidly evolving part of engineering sector. Material engineering is what allows us to find best combinations of materials that can be used for various purposes. Composites is an important part of material science, since it combines desirable properties of various materials. Composites are inevitable part of various developing parts of engineering technologies. The use of composites varies from cement used in construction works to carbon fiber composites used in spacecrafts. Designing composites helps in improving properties of it constituents and to protect them from their weaknesses[1–2].

Carbon fiber is considered as a material of future. It sports better mechanical properties when compared to metals like steel and aluminium. And its high strength to weight ratio makes it a promising component for modern buildings, spacecrafts etc[3–4]. But there are some difficulties in using carbon fiber directly for outer-space activities. Carbon fiber has a low compressive to tensile strength ratio. Operating above 150 °C may cause oxidation

of surface carbon layer and corresponding shrinkage of the sheet. Carbon fiber can't operate under high temperature conditions.

The available composites which allow us to use carbon fibers under higher temperature are costly and are only under development. Even though carbon fiber reinforced metal matrix composites exist in the market they never helps in full potential of carbon fibers and shows similar properties to that of metals[4–7].

Design of a new sandwich type composite in which we can utilize the high strength to weight ratio of carbon fiber while protecting it from high temperature exposure. The design includes use of heat repellent polyimide thermosetting plastic(vespel by dupoint) and resins that can be used at high temperature to improve the high temperature properties of the composite[8–9]. This design may help in enabling the use of carbon fiber under conditions of varying temperature, even from cryogenic level to temperatures above 200 °C without significant variation in the properties. This may help in using this composite even during space colonization due to its high strength to weight ratio and ability to operate under varying temperature range. Investigators have considered all the possibilities and alternatives of the design and its technical aspects and we infer that the system might be efficient[10–12].

* Corresponding author.

E-mail address: shunmugesh@vjcet.org (K. Shunmugesh).

By using 'rules of mixtures' equations for composite we generated approximate equivalent properties of the composite sheet is found out. These values are used to generate various deformations occurring in a composite bar under various loading conditions. An open software called FREECAD is used for the finite element modelling of the corresponding equivalent composite bar.

2. Abbreviations and notations

Various abbreviations and notations used in this research paper are given below.

2.1. Abbreviations

- CAD-Computer Aided Design
- FEM-Finite Element Modelling
- CF-Carbon Fibre

2.2. Notations

- E-elastic modulus
- f-volume fraction
- D-density
- α -thermal expansion coefficient

3. Constituents of the composite

3.1. Vespel® SP-21 sheet

Vespel is the trademark of a range of durable high-performance polyimide-based plastics manufactured by.

DuPont. It combines heat resistance, lubricity, dimensional stability, chemical resistance, and creep resistance, and can be used in hostile and extreme environmental conditions.

DuPont™ Vespel® SP-21 is graphite-enhanced with low-friction properties for use with or without lubrication in various applications. Vespel® SP-21 has maximum physical strength, elongation, and toughness. This contains 15 % graphite.

3.2. Carbon fiber sheet / unidirectional carbon fiber fabric

Carbon fiber and carbon fiber cloth consist of bulk, chopped fibers, continuous strands, or woven cloth forms of carbon. Carbon fiber fabrics are infused with epoxy resins to make composites.

3.3. Nomex honey comb

ANA aerospace grade Nomex® honeycomb core is manufactured from Nomex® paper sheets and is coated and bonded together with epoxy resin. Designed to offer users and designers high strength-to-weight properties at relatively low cost, Nomex® honeycomb is particularly suitable as a core material for production of sandwich structures requiring significant performance.

3.4. Epoxy eccobond 104 resin

Eccobond 104 is formulated using a black liquid and white powder creating a high strength epoxy adhesive. Main purpose of this advanced adhesive is to bond a variety of substrates including metals, glass, ceramic and thermoset plastic. This epoxy is designed for applications that require extremely high temperature exposure.

4. Methods and manufacturing

Vacuum bagging is a commonly used technique in composites, and for good reason. When done correctly, your part will have a nice, uniformly distributed compression about the surface of the layup. This in turn helps to minimize any voids (e.g. bubbles and wrinkles) in the build-up of layers. Also, when used with a porous substrate made of peel-ply and breather-cloth as we'll see, it assists in having the optimal ratio of resin to reinforcement (e.g. fibreglass, or carbon fiber, or Kevlar) by squeezing out the excess. The Fig. 1 shows the requirements of vacuum bagging process.

4.1. Steps to be followed

- Cutting of plastics
- Folding the cut plastic.
- Setting the other corners.
- Laying down the Sealing Tape
- Apply final sealing edge.
- Sealing the First Side
- Seal the Other Side
- Placing the Bag-Tube Connector.
- Layup
- Final vacuum bagging and heat treatment

4.2. Final product

The following Fig. 2 represents the cross section of the designed composite. The thickness is calculating as 10.95 mm. The resulting structure consists of 2 layers of Vespel® SP-21 sheets, 2 layers of Carbon Fiber Fabric and 3 layers of Nomex® honeycomb.

5. Results and discussions

Used simple modelling test in order to find how the material react to various tensile and compressive forces. For that we have calculated the equivalent mechanical properties of the composite bar. For that purpose, we used the 'rules of mixtures' equations.

5.1. Rules of mixtures

Elastic modulus of the equivalent composite bar.

$$E = E_1f_1 + E_2f_2 + E_3f_3 + \dots E_nf_n$$

Density of the equivalent composite bar.

$$D = D_1f_1 + D_2f_2 + D_3f_3 + \dots D_nf_n$$

The thermal expansion coefficient of the composite bar.

$$\alpha = \alpha_1f_1 + \alpha_2f_2 + \alpha_3f_3 + \dots \alpha_nf_n$$

where, 'f' is the volume fraction of each component for the below calculation the thickness of the epoxy layer is excluded. Since the length and breadth of every sheets of components are same as that of the composite, the volume fraction is directly proportional to the thickness of each layer.

Volume fraction of carbon fiber = $(1.3 \times 2) / 10.85 = 23.96 \%$.

Volume fraction of vespel = $(1.55 \times 2) / 10.85 = 28.57 \%$.

volume fraction of Nomex Honey Comb = $100 \% - (28.57 + 23.96) = 47.47 \%$.

5.2. Calculation of mechanical and physical properties

- o To calculate the Density, Young's modulus etc. the honey comb layer is considered to act like a single sheet infused with Resin.

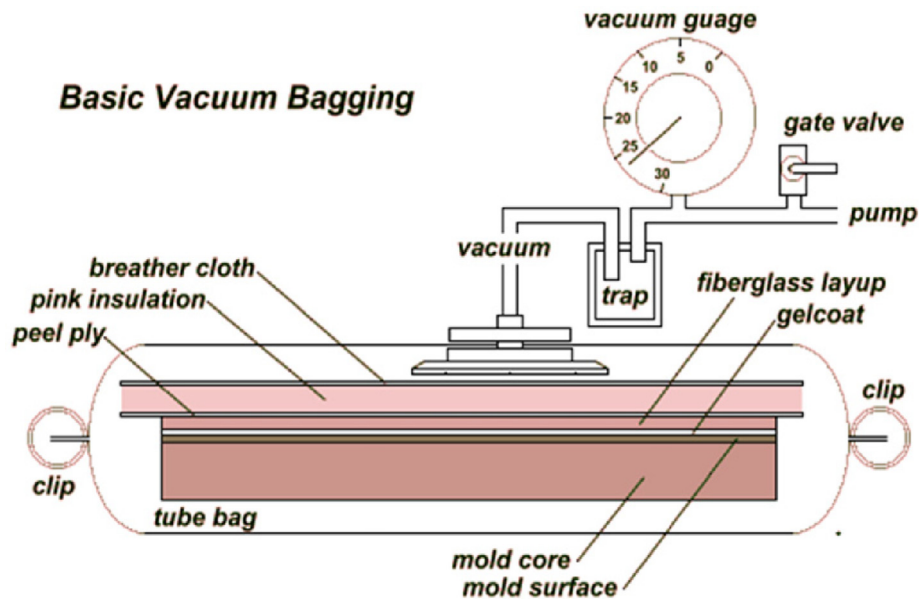


Fig. 1. Vacuum Bagging Set-up.

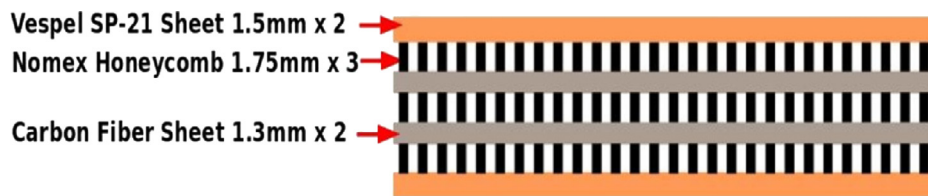


Fig. 2. Cross Section of Carbon Vespel composite.

- o All the properties of vespel, carbon fiber are after the treatment with epoxy resin at elevated temperature.

Equivalent Young's modulus of the composite = 46.83GPa.
 Approx. Density of the composite = 1510Kg/m³.
 Thermal expansion coefficient = 49 microm/m/k.
 Thermal conductivity = 11.32 W/m/K.

5.3. Modelling

Steps to be followed.

- o Model a rectangular sheet with 500 mm length and 250 mm width using 'part' tool.
- o Creating an N mesh around the sheet for the analysis purpose.
- o The material properties are entered manually.
- o The loading conditions are set according to our requirement.
- o The variation in the structure under the load is calculated by the Calculix tool available in the FEM menu of Free CAD.

5.4. Result

5.4.1. Limiting factors

- o Tensile strength of nomex honeycomb-60 MPa
- o Shear strength of carbon fiber -22.4 MPa
- o Maximum strain of carbon fiber -2.7 %

To obtain the optimum value of load for the sheet it was ensured that the maximum principal stress was under the tensile

strength of nomex honeycomb. And ensured shear stress developed was under the shear strength of carbon fiber.

5.4.2. Single layer under tension

a. Findings from The FEM Analysis.

The following findings were obtained by analysing Tables 1 to 4 and Figs. 3 to 14. And the optimum condition for the operation of the single and double layer composite is found. (1) Double layer 500x250mm sheet was tested under 100KN, 160KN & 200KN. (2) At 200KN the resultant maximum stress was less than the tensile strength of Honey comb layer. But shear stress developed was almost similar to maximum shear strength of carbon fiber. So it can't be used. (3) And by trial and error method 160KN is the optimum load for a double layer of the composite to avoid permanent deformation. (4) Single layer 500x250mm sheet was tested under 60KN, 80KN & 100KN. (5) Under 100KN the resultant maximum stress was higher than the tensile strength of Honey comb layer which means failure. (6) And by trial and error method 60KN is the optimum load for a single layer of the composite to avoid permanent deformation.

Table 1

Tensile load of 10⁵N is applied at one end of single layer composite.

Parameter	Value
Displacement	0.40 mm
Maximum Principal Stress	62.47 MPa
Shear Stress	23.66 Pa

Table 2

Tensile load of 60 KN is applied at one end of single layer composite.

Parameter	Value
Displacement	0.24 mm
Maximum Principal Stress	37.48 MPa
Shear Stress	14.20 MPa

Table 3

Tensile load of 10^5 N is applied at one end of double layer composite.

Parameter	Value
Displacement	0.40 mm
Maximum Principal Stress	51.51 MPa
Shear Stress	21.52 MPa

Table 4

Tensile load of 2×10^5 N is applied at one end of double layer composite.

Parameter	Value
Displacement	0.24 mm
Maximum Principal Stress	37.48 MPa
Shear Stress	14.20 MPa

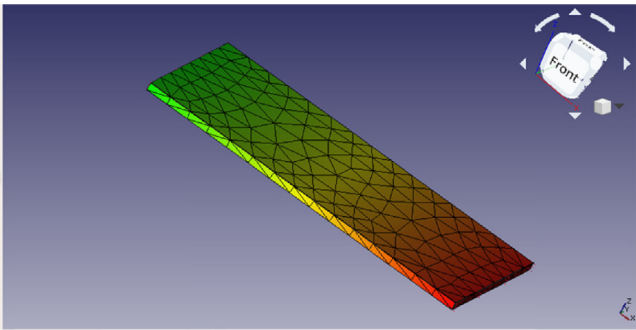


Fig. 3. Distribution of Displacement (1L – 100KN).

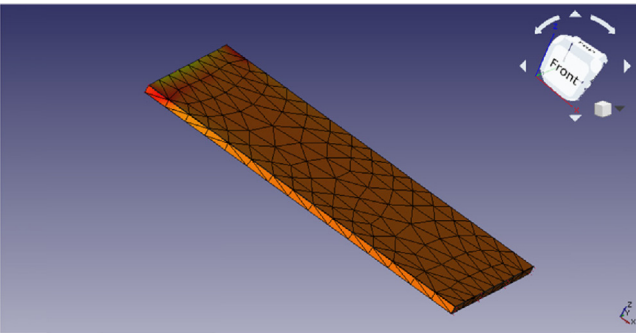


Fig. 4. Distribution of Principal Stress (1L – 100KN).

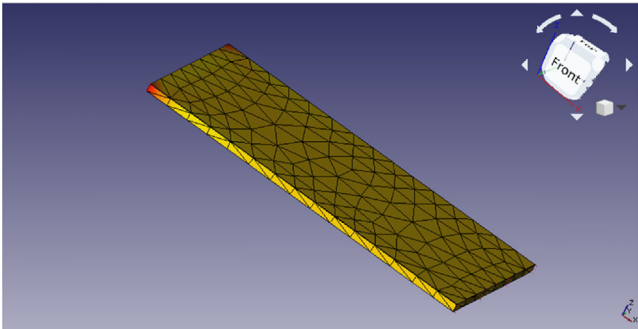


Fig. 5. Distribution of Shear Stress (1L – 100KN).

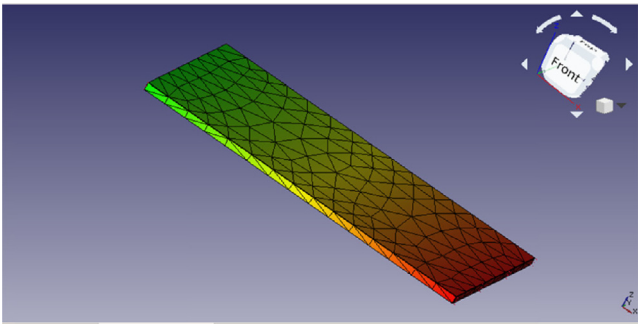


Fig. 6. Distribution of Displacement (1L – 60KN).

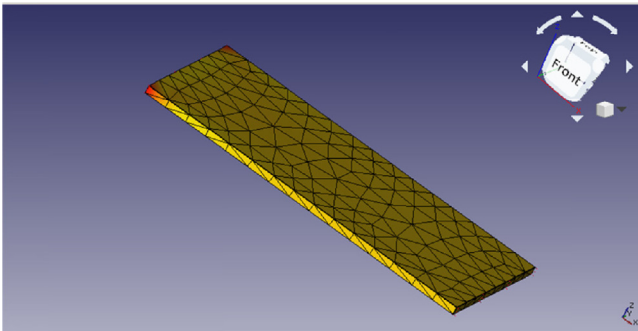


Fig. 7. Distribution of Principal Stress (1L – 60KN).

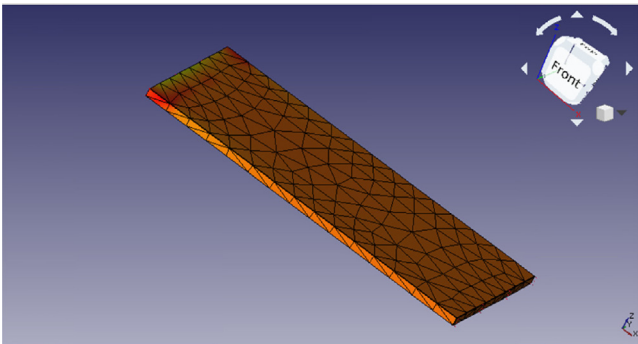


Fig. 8. Distribution of Shear Stress (1L – 60KN).

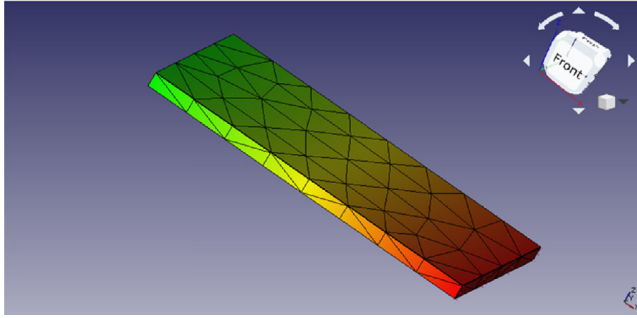


Fig. 9. Distribution of Displacement (2L – 100kN).

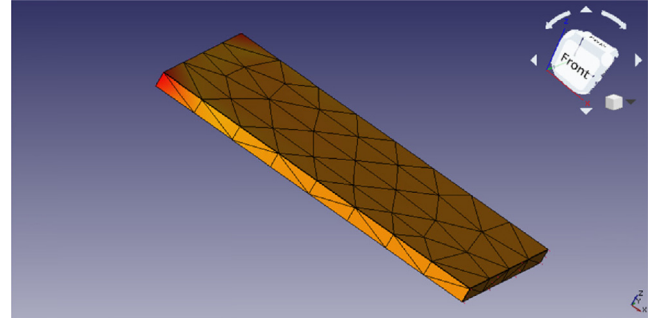


Fig. 13. Distribution of Principal Stress (2L – 200kN).

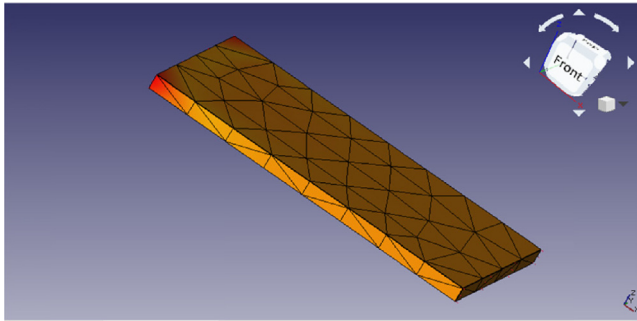


Fig. 10. Distribution of Principal Stress (2L – 100kN).

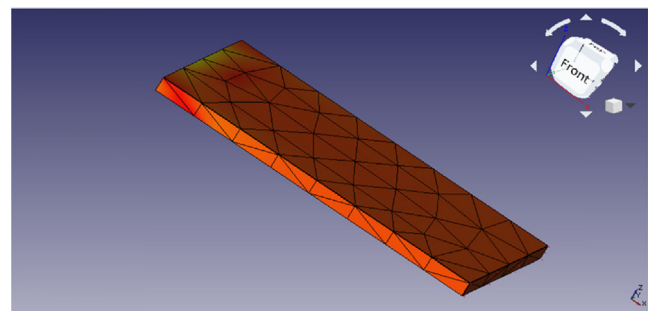


Fig. 14. Distribution of Shear Stress (2L – 200kN).

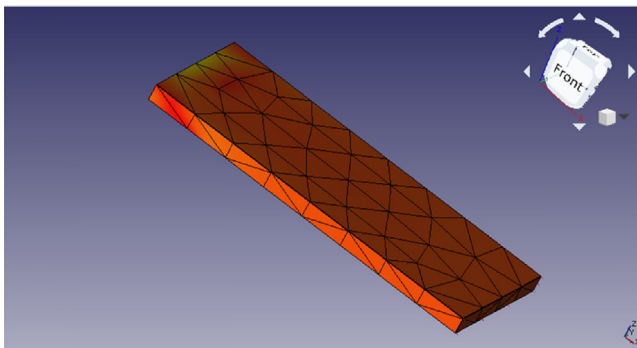


Fig. 11. Distribution of Shear Stress (2L – 100kN).

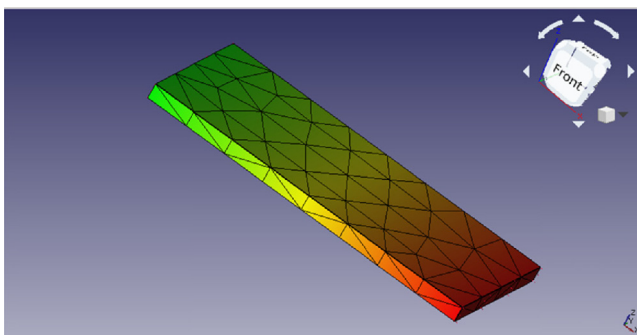


Fig. 12. Distribution of Displacement (2L – 200kN).

- b. 100000 N at right end when left end is fixed.
- c. 60000 N at right end when left end is fixed.

5.4.3. Two layer under tension

- a. 100000 N at right end when left end is fixed.
- b. 200000 N at right end when left end is fixed.

6. Conclusion

The finite element modelling of the carbon fiber reinforced with epoxy and vespel honey comb structure composite was done and following conclusions are drawn. This model was used to the analysis of a single layer and double layer of the composite sheet. The performance of the newly designed composite was studied under various tensile loads. And it helped in finding the durability of the composite material in a variety of conditions. The newly designed composite shows good performance under tension and compression. The production of the composite can be economical only if it is produced at a large scale. From the Finite Element Analysis, it can be concluded that the composite has potential applications where the 4 thin edges of the composite sheets is fixed. On bending it has been observed that the ultimate strength depends on the thickness of vespel layer. Increasing thickness of the composite reduced the flexibility and cost of the product. Rather than bending the sheets for use it will be desirable to mould the vespel sheet according to the use.

CRediT authorship contribution statement

K. Shunmugesh: Conceptualization, Writing – review & editing.
Arun Raphel: Methodology, Software. **T.G. Unnikrishnan:** Methodology, Software. **K.T. Akhil:** Writing – review & editing.

Data availability

Data will be made available on request.

Declaration of Competing Interest

The authors declare that they have no known competing financial interests or personal relationships that could have appeared to influence the work reported in this paper.

References

- [1] P. Bhatt, A. Goe, Carbon fibres: production, properties and potential use, *Mater. Sci. Res. India* 14 (1) (2017) 52–57, <https://doi.org/10.13005/msri/140109>.
- [2] F. Zhou, J. Zhang, S. Song, D. Yang, C. Wang, Effect of temperature on material properties of carbon fiber reinforced polymer (CFRP) tendons: experiments and model assessment, *Mater.* 12 (7) (2019) 1025, <https://doi.org/10.3390/ma12071025>.
- [3] I.L. Kalnin, in: *Fracture of Composite Materials*, Springer Netherlands, Dordrecht, 1982, pp. 465–475.
- [4] S. Wang, Z.H. Chen, W.J. Ma, Q.S. Ma, Influence of heat treatment on physical-chemical properties of PAN-based carbon fiber, *Ceram. Int.* 32 (3) (2006) 291–295, <https://doi.org/10.1016/j.ceramint.2005.02.014>.
- [5] Summerscales J, Virk AS, Hall W. Enhanced rules-of-mixture for natural fibre reinforced polymer matrix (nfrp) composites (comment on lau et al. in volume 136). *Compos Part B: Engineering*. 2019; 167–9. <https://doi.org/10.1016/j.compositesb.2018.10.021>
- [6] D. Zenkert, *The handbook of sandwich construction*, Eng. Mater. Advisory Services (1997).
- [7] Y. Shibuya, J. Zhang, Y. Sato, J. Yanagimoto, Evaluation of the mechanical properties and deformability of metal-based composite sheets made of thin stainless-steel sheets and carbon fiber reinforced plastics, *Int. J. Mater. Form* 15 (4) (2022) 1–3, <https://doi.org/10.1007/s12289-022-01661-z>.
- [8] M. Hasan, J. Zhao, Z. Jiang, Micromanufacturing of composite materials: a review, *Int. J. Extrem. Manuf.* 1 (1) (2019), <https://doi.org/10.1088/2631-7990/ab0f74> 012004.
- [9] Gohar S, Hussain G, Ali A, Ahmad H. Mechanical performance of honeycomb sandwich structures built by FDM printing technique. *J Thermoplast Compos Mater* 2021 :0892705721997892. <https://doi.org/10.1177/0892705721997892>
- [10] B.R. Reddy, K. Ramji, Modeling and evaluation of effective elastic properties of carbon nanotubes reinforced carbon fiber/epoxy multiscale composites, *Mater. Today: Proc.* 21 (2020) 1099–1103, <https://doi.org/10.1016/j.matpr.2020.01.056>.
- [11] M.V. Mousavi, H. Khoramshad, The effect of hybridization on high-velocity impact response of carbon fiber-reinforced polymer composites using finite element modeling, Taguchi method and artificial neural network, *Aerosp. Sci. Technol.* 94 (2019), <https://doi.org/10.1016/j.ast.2019.105393> 105393.
- [12] Malekimoghadam R, Icardi U. Prediction of mechanical properties of carbon nanotube-carbon fiber reinforced hybrid composites using multi-scale finite element modelling. *Compos Part B: Engineering*. 2019; 177:107405. <https://doi.org/10.1016/j.compositesb.2019.107405>.



Contents lists available at ScienceDirect

Materials Today: Proceedings

journal homepage: www.elsevier.com/locate/matpr

Experimental investigation on mechanical properties of Kenaf fibre reinforced epoxy composites with annona squamosa powder

Lokasani Bhanuprakash ^{a,*}, N. Manikandan ^b, Arun Raphel ^c, Georgekutty S. Mangalathu ^d

^a Department of Mechanical Engineering, MLR Institute of Technology, Dundigal, Hyderabad, Telangana 500043, India

^b Department of Mechanical Engineering, School of Engineering, Mohan Babu University, Tirupati, Andhra Pradesh, India

^c Department of Mechanical Engineering, Viswajyothi College of Engineering and Technology, Muvattupuzha, Kerala 686670, India

^d Department of Mechanical Engineering, Mar Athanasius College of Engineering, Kothamangalam, Kerala 686666, India

ARTICLE INFO

Article history:

Available online xxxx

Keywords:

Polymer Composites
Kenaf Fibres
Epoxy Composites
Mechanical Properties

ABSTRACT

The adoption of biodegradable and environmentally-friendly composite materials is gaining momentum in diverse engineering sectors due to their growing popularity. The present investigation focuses on analysing the influence of fibre treatment on the mechanical properties of hybrid composites made of Kenaf fibres and epoxy matrix. The fibre is subjected to NaOH treatment initially, which is subsequently followed by a comprehensive drying process. The second scenario involves the utilisation of custard apple seed powder, a biodegradable filler material, to modify the matrix. The utilisation of microscopy is employed as a means to analyse the modified fibres and to identify any potential surface alterations that may have taken place. Following this, epoxy composites are fabricated by utilising modified and unmodified Kenaf fibres through a basic hand layup method with vacuum bagging. The composites that have been prepared are subsequently evaluated for their characteristics through tensile and flexural measurements, in compliance with the applicable ASTM standards.

Copyright © 2023 Elsevier Ltd. All rights reserved.

Selection and peer-review under responsibility of the scientific committee of the International Conference on Advancements in Materials and Manufacturing.

1. Introduction

The *Hibiscus cannabinus* plant species is the source of Kenaf fibre, which is a type of natural fibre [1]. The subject matter has garnered considerable significance and scrutiny owing to its diverse advantageous characteristics and potential applications [2]. Kenaf fibre is widely recognised for its environmentally conscious and sustainable attributes in the field of sustainability [3]. The resource in question is characterised by rapid renewability, as the plant species in question can be cultivated and harvested within a relatively brief timeframe of approximately four to five months. This renders it a feasible substitute for other natural fibres and synthetic materials that possess a greater ecological footprint [4]. Kenaf fibre possesses biodegradability, implying its ability to undergo natural decomposition without causing persistent environmental contamination. The aforementioned attribute holds significant importance in the mitigation of waste and advancement of the circular economy [5]. The mechanical properties of Kenaf fibre

are noteworthy, particularly in terms of its strength and stiffness, rendering it a viable option for a range of structural applications. Upon integration into composite materials, such as those composed of epoxy, it serves to augment their mechanical properties, inclusive of tensile strength, flexural strength, and impact resistance. Kenaf fibre exhibits a relatively lower weight profile in comparison to conventional materials such as glass fibres or metals [6]. This attribute renders it highly coveted in contexts where the reduction of weight is imperative, such as in the manufacturing of automotive parts and the construction of aerospace frameworks [7]. The low density of the material is a contributing factor to the enhancement of fuel efficiency and energy conservation. Kenaf fibre exhibits remarkable thermal insulation characteristics. The natural barrier against heat transfer is a beneficial feature in the context of construction materials, insulation products, and energy-efficient building designs [8]. The sound absorption properties of Kenaf fibre can be attributed to its fibrous structure [9]. This technology exhibits a high degree of efficacy in attenuating sound waves, rendering it a viable option for employment in diverse settings such as automotive cabin environments, architectural acoustics, and sound insulation materials. The moisture resistance of

* Corresponding author.

E-mail address: bhanuprakash.lokasani@mlrinstitutions.ac.in (L. Bhanuprakash).

<https://doi.org/10.1016/j.matpr.2023.06.247>

2214-7853/Copyright © 2023 Elsevier Ltd. All rights reserved.

Selection and peer-review under responsibility of the scientific committee of the International Conference on Advancements in Materials and Manufacturing.

Kenaf fibre is noteworthy, as it exhibits a commendable ability to resist moisture absorption [10–11]. The material exhibits notable resistance to swelling and degradation in humid conditions, thereby augmenting its robustness and steadfastness in various domains, including furniture, packaging, and outdoor constructions [12]. To summarise, Kenaf fibre presents numerous benefits such as sustainability, biodegradability, strength, lightweight, thermal insulation, sound absorption, moisture resistance, versatility, agricultural benefits, and cost-effectiveness. The aforementioned attributes render it a valuable and auspicious substance in diverse sectors, thereby facilitating the transition towards more ecologically sustainable practices [13].

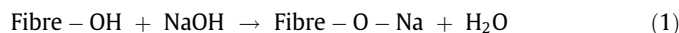
The versatile applications of composites derived from kenaf fibres can be employed across diverse fields. The utilisation of Kenaf fibre composites is a viable option in the production of various automotive components, including but not limited to door panels, dashboards, and seat backs. The utilisation of Kenaf fibre composites as a substitute for traditional building materials such as roofing tiles, siding and decking is a promising prospect. The utilisation of Kenaf fibre composites in the manufacturing of packaging materials such as food containers and shipping boxes is feasible. Kenaf fibre composites exhibit promising characteristics for application in the production of furniture, including chairs, tables, and desks. Kenaf fibre composites have the potential to be utilised in the manufacturing of diverse sports equipment, such as golf clubs, tennis rackets, and baseball bats. To sum up, it can be inferred that kenaf fibre composites present a number of benefits in comparison to traditional reinforcement materials. The aforementioned advantages render them a persuasive substitute for a diverse array of use cases across various sectors.

2. Improving mechanical properties of Kenaf fibre composite

2.1. Alkaline treatment

The chemical modification of natural fibres is frequently accomplished through the utilisation of alkaline treatment. The aforementioned treatment is known to have a noteworthy impact on augmenting the surface properties of fibres through the modification or interruption of hydrogen bonds that are responsible for the fundamental structural stability of the fibre system. The application of alkali treatment on kenaf fibre (KF) has been subject to extensive research and analysis [14]. The elimination of diverse constituents, including lignin, oils, and wax, which form a coating on the external surface of the fibre cell wall, is a significant outcome of the alkali treatment. The elimination of certain substances results in a surface of the fibre that is cleaner and more refined. Furthermore, the alkaline treatment procedure induces depolymerization of cellulose within the fibre, leading to the exposure of shorter-length crystallites. The process of depolymerization is aided by the existence of an aqueous solution of sodium hydroxide (NaOH). The addition of NaOH facilitates the ionisation process of hydroxyl groups, resulting in the generation of alkoxide species. The generation of alkoxide species serves as an additional factor in the modification of both the fibre morphology and surface characteristics in the course of alkaline processing. To summarise, the chemical modification of natural fibres such as kenaf fibre is frequently achieved through the utilisation of alkaline treatment. The aforementioned treatment has been observed to enhance the surface roughness of fibres by means of disrupting hydrogen bonds and eliminating substances such as lignin, oils, and wax from the outermost layer of the fibre cell wall. Furthermore, the process of alkaline treatment results in the depolymerization of cellulose, thereby facilitating the accessibility of shorter-length crystallites. The ionisation of hydroxyl groups is facilitated by the existence

of aqueous sodium hydroxide, leading to the creation of alkoxide species and consequent alteration of the fibre structure.



The application of alkaline treatment on natural fibres, such as kenaf fibre, has noteworthy effects on multiple aspects, including the extraction of cellulosic fibrils, lignin, and hemicellulosic components, as well as the level of polymerization. The immersion of fibres in a solution of sodium hydroxide (NaOH) of a specific concentration for a predetermined duration is a widely used and uncomplicated method for achieving fibre treatment. The predominant focus of research in this particular field has been to examine the impact of NaOH concentration and treatment duration on the strength and properties of the fibres that have undergone treatment. The significance of the NaOH solution concentration utilised in the treatment procedure is pivotal in ascertaining the degree of chemical reactions and alterations taking place within the fibre architecture. The extent of fibre modification is influenced by the treatment duration, which provides ample opportunity for the NaOH to interact with the fibre components. A considerable amount of scholarly literature has investigated the influence of NaOH concentration and treatment duration on the mechanical characteristics of treated fibres. However, only a restricted number of investigations have delved into the effects of treatment temperature on these properties. The temperature employed during the process of fibre treatment has the potential to impact both the velocity and magnitude of chemical reactions, as well as the degree of NaOH infiltration into the fibre architecture. The treatment of fibres has a consequential impact on their mechanical properties, including tensile strength, flexural strength, and impact resistance. To summarise, the application of alkaline treatment on natural fibres, such as kenaf fibre, has significant implications on the extraction of cellulosic fibrils, lignin, and hemicellulosic components, as well as the degree of polymerization. The treatment of fibres through immersion in NaOH solution at specific concentrations and durations is a widely used technique. Most research has concentrated on investigating the impact of NaOH concentration and treatment duration on fibre strength. However, only a few studies have examined the consequences of treatment temperature on the mechanical properties of the treated fibres. Comprehending and enhancing these parameters hold significant importance in customising the characteristics of kenaf fibre and maximising its potential in diverse applications.

Alavudeen et al. utilized a 5%, 10%, and 15% concentration of NaOH solution on two kinds of woven KF at room temperature for 2 h, 4 h, 6 h, and 8 h. According to their findings, a ten percent NaOH treatment for eight hours had the optimum effect on the mechanical characteristics of KF [15].

Fiore et al. performed an alkaline treatment on KF, changing the treatment time (48 h and 144 h) while keeping the NaOH concentration at 6% [16]. According to their findings, KF treated for 48 h has improved characteristics and all contaminants have been eliminated. Meanwhile, fracture propagation is visible in the KF treated for 144 h, indicating that the fibre has been severely damaged, leading to decreased tensile strength. Ikhwan Ibrahim et al. investigated the effect of 2%, 4%, 6%, and 8% concentrations of NaOH solution on a single kenaf fibre and found that 6% NaOH concentration improves the young modulus, tensile strength, and percentage fracture strain when compared to an untreated single kenaf fibre [17].

Overall, the alkaline treatment has been documented to primarily include the use of NaOH solution, and so this treatment has a few significant effects on the fibre. When the surface roughness or surface area is increased, better mechanical interlocking between fibre and matrix can be achieved. The alkaline treatment exposes the cellulose on the fibre surface, which increases the

number of available reaction sites. Excess delignification of the natural fibre, which destroys or weakens it, can be caused by a higher proportion of alkali concentration. The tensile strength of the composite formed has been discovered to substantially diminish when the NaOH concentration is increased above a specific percentage.

3. Experimental procedure

The present experimental investigation involved the use of bidirectional Kenaf fibres procured from Fibre Region, Chennai, India. The choice of epoxy resin as the matrix material was based on its advantageous processability, cross-linking properties, and mechanical characteristics. The manufacturer's (Fine Finish Organics Pvt Ltd, Mumbai, India) instructions were followed for room temperature curing, utilising a resin-to-hardener ratio of 100:34.

3.1. Fibre treatments

The kenaf fibres were subjected to surface modifications through the utilisation of alkali (NaOH) and sodium lauryl sulphate (SLS). Regarding the alkali treatment, the fibres were subjected to immersion in solutions of sodium hydroxide (NaOH) with different concentrations and durations. A comprehensive water rinsing procedure was conducted to eliminate any surplus sodium hydroxide present on the surface of the fibre. The ultimate stage of the washing process entailed the utilisation of aqueous solution consisting of acetic acid in a diluted form. Two critical parameters were selected to facilitate the examination of composite properties amidst the numerous factors that impact chemical treatment. The fibre surface morphology was found to be significantly impacted by solution concentration and treatment duration, which were identified as key factors. The phenomenon of a positive impact resulting from the increase in solution concentration up to a certain threshold, followed by a sudden decline in this effect, has been documented. The present investigation involved the application of a 6% concentrated NaOH solution on kenaf fibres for a duration of 3 h under ambient conditions.

3.2. Matrix modification with fillers

The matrix is modified using custard apple seed powder. The properties of the final composite are also influenced by the quantity of filler particles incorporated. In general, the incorporation of additional filler particles into a composite material is known to enhance its strength and stiffness. However, this improvement may come at the expense of reduced ductility and increased brittleness. It gave a satisfying result (increased tensile and flexural strength) at 4 wt% concentration.

3.3. Hand Lay-up process

The process of producing kenaf fibre composites involved the utilisation of a hand-layup technique, which was executed in accordance with the subsequent procedure: The mould was filled with Kenaf fibres, and subsequently, the resin was combined with the hardener. After the composites were left to cure for a duration of 24 h, they underwent a subsequent post-curing process in an oven at a temperature of 50 °C for a period of one hour.

3.4. Mechanical testing

3.4.1. Tensile strength

The measurement of tensile strength was conducted, which is a crucial characteristic for the utilisation of composite materials in

structural applications. The aforementioned attribute denotes the capacity of a substance to endure fracture when subjected to a stretching force. The ASTM: D-638–10 procedure was employed to determine the tensile strength of the composites, with a cross-head speed of 1 mm/min. The mean value of five specimens was documented.

3.4.2. Flexural strength

The study involved the execution of flexural strength tests utilising an UNITEK 94100, (Blue Star Engineering & Electronics, India) universal testing machine and a three-point bending fixture in accordance with the ASTM: D-790–10 standard. The experiments were conducted utilising a crosshead velocity of 1 mm per minute. The distance separating the supports was established at 48 mm, in accordance with the prescribed standard, utilising a ratio of 16:1.

4. Results and discussion

4.1. Tensile strength analysis

The application of NaOH treatment on Kenaf fibres has been observed to considerably enhance their tensile characteristics. The alkaline treatment of natural fibres, such as Kenaf, is a common practice that involves the use of NaOH (sodium hydroxide). The surface roughness of Kenaf fibres can be enhanced through an alkaline treatment utilising NaOH. The intervention perturbs the hydrogen bonds present in the fibre architecture, thereby inducing alterations in the surface morphology. The augmentation of surface roughness results in an improvement of the interfacial adhesion between the fibres and the matrix material. The load vs displacement curve for untreated and treated fibres is provided in Fig. 1 and the strength values are listed in Table 1.

The process of eliminating impurities from the surface of fibres involves the utilisation of NaOH as a depolymerizing agent during alkaline treatment. The process of partially removing lignin, oils, wax, and other substances that coat the outer section of the fibre cell wall leads to the attainment of cleaner and purer fibre surfaces. The depolymerization of cellulose within fibres can be induced through treatment with NaOH, resulting in the exposure of crystallites of reduced length. The aforementioned alteration in structure amplifies the fiber's capacity to transmit load and enhances its overall strength. The morphology of Kenaf fibres undergoes notable alterations as a result of the alkaline treatment with NaOH. The fibre surface undergoes modifications as observed through microscopic analysis, including heightened roughness, elimination of coatings, and enhanced fibre integrity. The application of NaOH treatment on Kenaf fibres has been observed to augment their tensile strength. The enhancement of interfacial bonding and overall strength of fibres is attributed to the disruption of hydrogen bonds, elimination of impurities, and depolymerization of cellulose [7]. The enhancement of the tensile modulus is observed subsequent to the NaOH treatment, which is indicative of an improvement in the fibres' stiffness or rigidity. The augmentation of surface roughness and enhancement of fibre integrity result in amplified load transfer and heightened resistance to deformation. The optimisation of treatment parameters is a critical factor in determining the degree of enhancement in tensile properties. Specifically, the concentration and duration of the NaOH treatment are key factors that play a significant role in this regard. Research has demonstrated that in order to attain the highest possible improvement in both tensile strength and modulus, it is necessary to establish the ideal NaOH concentration and treatment duration. In general, the utilisation of NaOH for alkaline treatment of Kenaf fibres is a viable approach for enhancing their tensile characteristics. The aforementioned treatment methodology serves to augment the

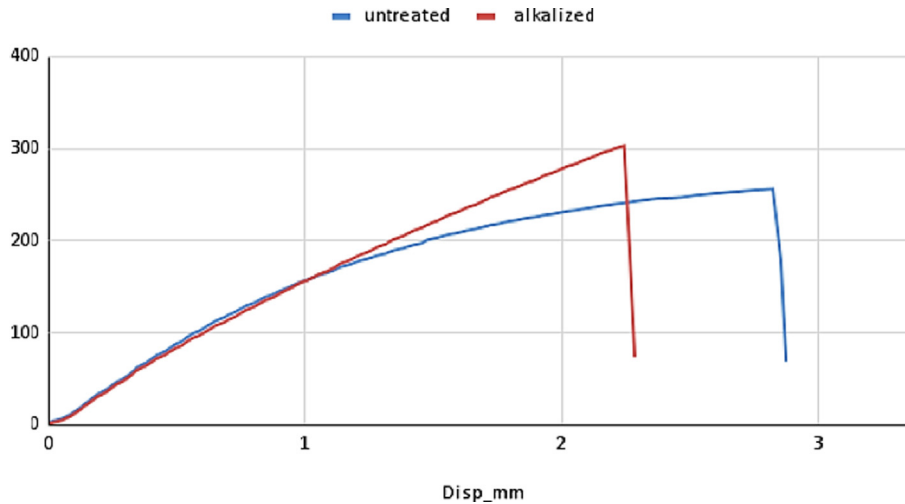


Fig. 1. Tensile test results of untreated (blue line) and treated fibre (red line) reinforced composites. (For interpretation of the references to colour in this figure legend, the reader is referred to the web version of this article.)

Table 1
Tensile Strength Analysis.

Type	Matrix	Soak time, temp, concentration	Maximum load (kN)
Single Kenaf (treated)	Epoxy	3hr, Room Temp, 6% NaOH	0.3031
Single Kenaf (untreated)	Epoxy		0.2563

surface roughness, eliminate impurities, facilitate cellulose depolymerization, and ultimately engender superior interfacial bonding between the fibres and the matrix. The enhancements lead to a rise in tensile strength and modulus, rendering the processed Kenaf fibres more appropriate for a range of applications that necessitate high-performance composite materials.

4.2. Flexural strength analysis

The mechanical property of flexural strength plays a crucial role in determining a material's capacity to endure bending or deformation when subjected to a flexural load. Treatment with sodium

hydroxide (NaOH) can lead to a substantial enhancement in the flexural strength of kenaf fibre (Fig. 2 and Table 2). The following are comprehensive notes pertaining to the enhancement of flexural strength characteristics of kenaf fibre that has undergone NaOH treatment. The surface of kenaf fibres undergoes chemical alterations as a result of NaOH treatment, leading to surface modification. The NaOH solution facilitates the degradation of the lignin, waxes, and oils that form a coating on the outer cell wall of the fibre. Consequently, the aforementioned process induces a partial elimination of said substances, thereby leading to an increase in surface roughness of the fibre. The treatment with NaOH results in the disruption of hydrogen bonds that are responsible for maintaining the structural integrity of the cellulose in kenaf fibre. The aforementioned procedure involves the depolymerization of cellulose and subsequent exposure of the shorter crystallites present within the fibre. Consequently, the accessibility of the fibre for interaction with the matrix material is enhanced. The altered surface morphology of kenaf fibres enhances the interfacial adhesion and bonding with the matrix material, commonly epoxy resin. The augmentation of the fiber–matrix interface facilitates the efficient transmission of stress during flexural loading, thereby leading to a notable enhancement in flexural strength. The

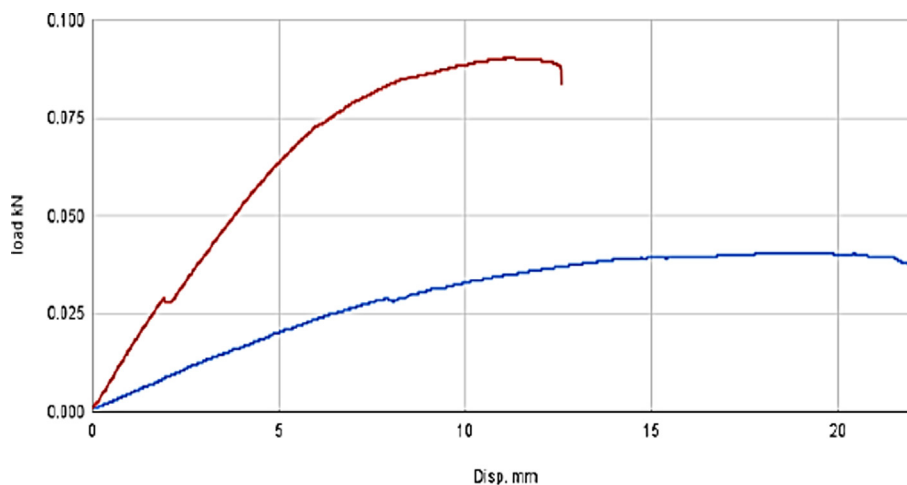


Fig. 2. Flexural Strength results of untreated (blue line) and treated fibres (red line) reinforced epoxy composites. (For interpretation of the references to colour in this figure legend, the reader is referred to the web version of this article.)

Table 2
Flexural Strength of untreated and treated fibres.

Type	Matrix	Soak time, temp, concentration	Maximum load (kN)
Single Kenaf (treated)	Epoxy	3hr, Room Temp, 6%NaOH	0.0905
Single Kenaf (untreated)	Epoxy		0.0405

morphology of kenaf fibres is affected by the treatment with NaOH, resulting in morphological changes. The augmentation of surface roughness and the exposure of additional active sites on the fibre surface facilitate superior mechanical interlocking with the matrix. The observed alterations in morphology are a significant factor in enhancing the flexural strength of the composite material. The enhancement of flexural strength is significantly affected by the concentration and duration of the NaOH treatment, which are deemed as crucial treatment parameters. Research has demonstrated that an optimal concentration of NaOH and duration of treatment exist, beyond which a reduction in flexural strength may occur. The identification of suitable treatment parameters is of utmost importance in order to attain the intended improvement in flexural characteristics. The reinforcement effect is observed in the composite material due to the incorporation of treated kenaf fibres. The incorporation of these elements results in enhanced flexural characteristics of the composite, owing to their supplementary strength and stiffness. The optimisation of the fibre-matrix interaction results in an effective transfer of loads, thereby minimising the likelihood of fibre debonding or failure [17]. The evaluation of the flexural strength of composites reinforced with kenaf fibres is conventionally conducted through the utilisation of standardised testing approaches, such as ASTM D790.

4.3. Tensile strength analysis for modified matrix

The Tensile strength properties of kenaf fibre can be significantly improved through a combination of fibre treatment with sodium hydroxide (NaOH) and the addition of custard apple powder filler particles to the matrix. The application of NaOH treatment has been observed to enhance the surface roughness of fibres through the disruption of the hydrogen bonds responsible for maintaining the structural integrity of the fibres. The process eliminates extraneous substances, such as lignin, oils, and wax, from the external layer of the fibre cell wall. The treatment process leads to depolymerization of cellulose present in the fibre, thereby enhancing the accessibility and exposure of the fibre surface. The

forementioned alterations result in an improved interfacial bonding between the fibre and matrix, thereby augmenting the mechanical characteristics of the composite material [17]. The utilisation of custard apple powder, which is obtained from the seeds of the custard apple fruit, as a biodegradable filler material in the epoxy matrix is a viable option. The incorporation of filler particles into the matrix enhances the mechanical and thermal characteristics of the composite material.

The incorporation of custard apple powder into the matrix results in a reinforcement effect, leading to an improvement in both strength and stiffness.

Moreover, it aids in diminishing the total expenditure on materials due to its cost-effectiveness and environmentally sustainable nature as a filling alternative.

Optimisation of the filler particles' size, shape, and concentration can be undertaken to attain the intended properties. The present study investigates the synergistic effect on flexural strength. The flexural strength properties of a composite material are enhanced through a synergistic effect resulting from the incorporation of NaOH-treated kenaf fibres and custard apple powder filler particles. The application of NaOH treatment enhances the interface between the fibre and matrix, thereby facilitating superior transfer of stress and distribution of load between the two components [16].

The augmentation of surface roughness and the elimination of impurities serve to improve the adhesion between the fibres and the epoxy matrix.

Incorporating custard apple powder filler particles into the matrix results in a reinforcement of the material, leading to an enhancement in its strength and stiffness.

The enhancement of interfacial adhesion and overall composite performance is attributed to the optimised concentration and dispersion of the filler particles. The flexural strength properties of composites can be enhanced considerably by incorporating custard apple powder filler particles into the epoxy matrix and subjecting kenaf fibres to alkaline treatment using NaOH (Fig. 3). The aforementioned methodology presents a sustainable and economical resolution for augmenting the mechanical efficacy of composites made of kenaf fibres and polymer.

5. Conclusions

- The application of NaOH treatment results in a notable enhancement of the tensile properties of Kenaf fibres.
- The utilisation of sodium hydroxide (NaOH) for alkaline treatment is a prevalent technique for natural fibres, such as Kenaf.

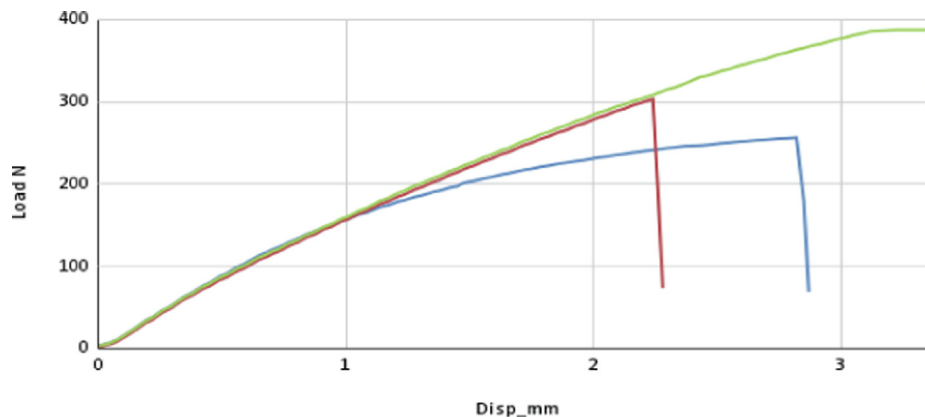


Fig. 3. Tensile Strength results of untreated fibre (blue), treated fibre (red) and matrix modified composite (green) specimens. (For interpretation of the references to colour in this figure legend, the reader is referred to the web version of this article.)

- The application of NaOH treatment results in an augmentation of the surface roughness of Kenaf fibres.
- The alteration of the fibre surface morphology is a result of the breakdown of hydrogen bonds caused by alkaline treatment utilising NaOH.
- Enhanced interfacial adhesion between the matrix material and Kenaf fibres can be achieved through an increase in surface roughness.
- The flexural strength of kenaf fibre is significantly improved through treatment with sodium hydroxide (NaOH).
- The application of NaOH induces surface-level chemical modifications in kenaf fibres, which entail the breakdown of lignin, waxes, and oils that envelop the outer cell wall of the fibre.
- The process of treatment involves the disruption of hydrogen bonds and depolymerization of cellulose, which leads to the exposure of shorter crystallites within the fibre. This, in turn, enhances the accessibility of the fibre for interaction with the matrix material.
- The modification of the surface morphology of kenaf fibres has been observed to improve the interfacial adhesion and bonding with the matrix, specifically with epoxy resin.
- The enhancement in flexural strength can be attributed to the efficient stress transmission facilitated by an improved fiber-matrix interface during flexural loading.

CRediT authorship contribution statement

Lokasani Bhanuprakash: . **N. Manikandan:** Validation, Formal analysis. **Arun Raphael:** Validation, Methodology. **Georgekutty S. Mangalathu:** Writing – review & editing.

Data availability

Data will be made available on request.

Declaration of Competing Interest

The authors declare that they have no known competing financial interests or personal relationships that could have appeared to influence the work reported in this paper.

References

- [1] R. Ayadi, M. Hanana, R. Mzid, L. Hamrouni, M.L. Khouja, A. Salhi Hanachi, *Hibiscus cannabinus L.-kenaf: a review paper*, J. Nat. Fibers 14 (4) (2017) 466–484.
- [2] M.D. Hossain, M.M. Hanafi, H. Jol, A.H. Hazandy, Growth, yield and fiber morphology of kenaf (*Hibiscus cannabinus L.*) grown on sandy bris soil as influenced by different levels of carbon, Afr. J. Biotechnol. 10 (50) (2011) 10087–10094.
- [3] F.D. Wilson, M.Y. Menzel, Kenaf (*Hibiscus cannabinus*), roselle (*Hibiscus sabdariffa*), Econ. Bot. 18 (1964) 80–91.
- [4] N. Saba, M.T. Paridah, M. Jawaid, Mechanical properties of kenaf fibre reinforced polymer composite: A review, Constr. Build. Mater. 76 (2015) 87–96.
- [5] M. Ramesh, Kenaf (*Hibiscus cannabinus L.*) fibre based bio-materials: A review on processing and properties, Prog. Mater. Sci. 78 (2016) 1–92.
- [6] G. Sun, D. Chen, G. Zhu, Q. Li, Lightweight hybrid materials and structures for energy absorption: a state-of-the-art review and outlook, Thin-Walled Struct. 172 (2022).
- [7] H. Sosiati, Y.A. Shofie, A.W. Nugroho, Tensile properties of Kenaf/E-glass reinforced hybrid polypropylene (PP) composites with different fiber loading, EVERGREEN Joint Journal of Novel Carbon Resource Sciences & Green Asia Strategy 05 (02) (2018) 1–5.
- [8] S.S. Chandel, V. Sharma, B.M. Marwah, Review of energy efficient features in vernacular architecture for improving indoor thermal comfort conditions, Renew. Sustain. Energy Rev. 65 (2016) 459–477.
- [9] A.S. Ismail, M. Jawaid, J. Naveen, Void content, tensile, vibration and acoustic properties of kenaf/bamboo fiber reinforced epoxy hybrid composites, Materials 12 (13) (2019) 2094.
- [10] N.S.N. Arman, R.S. Chen, S. Ahmad, Review of state-of-the-art studies on the water absorption capacity of agricultural fiber-reinforced polymer composites for sustainable construction, Constr. Build. Mater. 302 (2021).
- [11] A.M. Edeerozey, H.M. Akil, A.B. Azhar, M.Z. Ariffin, Chemical modification of kenaf fibers, Mater. Lett. 61 (10) (2007) 2023–2025.
- [12] S. Kalia, B.S. Kaith, I. Kaur, Pretreatments of natural fibers and their application as reinforcing material in polymer composites—a review, Polym. Eng. Sci. 49 (7) (2009) 1253–1272.
- [13] P. Ramesh, B.D. Prasad, K.L. Narayana, Influence of montmorillonite clay content on thermal, mechanical, water absorption and biodegradability properties of treated kenaf fiber/PLA-hybrid biocomposites, Silicon 13 (1) (2021) 109–118.
- [14] A.G.N. Abbas, F.N.A.A. Aziz, K. Abdan, N.A. Mohd Nasir, M.N. Norizan, Kenaf fibre reinforced cementitious composites, Fibers 10 (1) (2022) 3.
- [15] A. Alavudeen, N. Rajini, S. Karthikeyan, M. Thiruchitrambalam, N. Venkateshwareen, Mechanical properties of banana/kenaf fiber-reinforced hybrid polyester composites: effect of woven fabric and random orientation, Mater. Des. 1980–2015 (66) (2015) 246–257.
- [16] V. Fiore, G. Di Bella, A. Valenza, The effect of alkaline treatment on mechanical properties of kenaf fibers and their epoxy composites, Compos. B Eng. 68 (2015) 14–21.
- [17] M.I. Ibrahim, R. Dolah, M. Zuhri, S. Sharif, M. Hassan, Chemical treatment evaluation of tensile properties for single Kenaf fiber, J. Adv. Res. Appl. Mech 32 (2016) 9–14.

Article

Topological Study on Triazine-Based Covalent-Organic Frameworks

Tony Augustine and Santiago Roy *

Department of Mathematics, Vellore Institute of Technology, Vellore 632014, India

* Correspondence: roy.santiago@vit.ac.in

Abstract: Most of the research has evidenced that there is a strong natural correlation among the chemical properties of molecular structures. This study analyses supramolecular chemistry and investigates topological indices of supramolecular structures called triazine-based covalent-organic frameworks. The use of degree-based topological indices on these chemical molecular structures can aid material scientists in better understanding their chemical and biological properties, thus compensating for the lack of chemical tests. This study aims to theoretically examine the triazine-based covalent-organic frameworks (TriCF) utilizing degree-based topological indices, specifically multiplicative topological indices and entropy measures. A detailed comparison of the computed topological indices of the aforementioned chemical structures is described using graphical depiction.

Keywords: triazine-based covalent-organic frameworks; degree-based topological indices; entropy measures; graph-theoretical approach



Citation: Augustine, T.; Roy, S. Topological Study on Triazine-Based Covalent-Organic Frameworks. *Symmetry* **2022**, *14*, 1590. <https://doi.org/10.3390/sym14081590>

Academic Editor: Jan Cz. Dobrowolski

Received: 1 July 2022

Accepted: 24 July 2022

Published: 2 August 2022

Publisher's Note: MDPI stays neutral with regard to jurisdictional claims in published maps and institutional affiliations.



Copyright: © 2022 by the authors. Licensee MDPI, Basel, Switzerland. This article is an open access article distributed under the terms and conditions of the Creative Commons Attribution (CC BY) license (<https://creativecommons.org/licenses/by/4.0/>).

1. Introduction

Chemical graph theory integrates graph theory and chemistry in an area of mathematics. After obtaining insight into the physical features of chemical substances, graph theory is employed mathematically to model them [1]. For centuries, graph theory and chemistry have been interlinked and well connected. Various investigations in both disciplines have created extraordinarily strong linkages between mathematics and chemistry, resulting in the emergence of a scientific field known as chemical graph theory. The first instances of chemical graphs are from the late eighteenth century, when Isaac Newton's ideas influenced chemistry's perspectives. Even though research into atom interactions accelerated during that century, chemical bonds were not discovered [1]. As a result, the initial application of chemical graphs was to depict hypothetical forces between molecules and atoms [2].

In this study, we consider a triazine-based covalent organic polymer (TriCF) as a chemical graph. The TriCF structure is one of the supermolecular families in the field of supermolecular chemistry [3]. Supramolecular chemistry, or the "chemistry of molecular assemblages and the intermolecular connection", is one of the most popular and rapidly growing disciplines of chemistry, emphasising going "above" molecular chemistry. It is the study of systems that comprise several molecular assemblies with the goal of understanding their structure, function and attributes. Supramolecular chemistry investigates molecular self-assembly, protein folding, molecular recognition, host-guest chemistry, mechanically interlocked molecular architectures and dynamic covalent chemistry, among other phenomena. It is highly interdisciplinary in nature, attracting biologists, environmental scientists, physicists, biochemists, theoreticians and crystallographers in addition to chemists. Supramolecular chemistry's potential to lead to modern technologies has sparked recent research [3]. Supramolecular chemistry is still a young field that is rapidly evolving thanks to contributions from the range of fields given above. Supramolecular chemistry emerged at the turn of the century as a breakthrough approach to deal with chemical substances and concepts, utilising capabilities beyond the bounds of single

molecules. Supramolecular chemistry has already demonstrated the enormous potential for designing intelligent molecules and gadgets. The next generation of advanced machines is projected to be based on molecular electronics and photonics. This field has recently focused on the development of molecular devices capable of sensing, photo switching, separation, motion, and transport [3–5].

The triazines have a six-membered planar benzene-like ring with three nitrogens replacing the carbons. The locations of the nitrogen atoms distinguish the three isomers of triazine [6]. Two well-known triazine structures are melamine and cyanuric chloride. Melamine, a white, odourless, crystalline, and nontoxic hetero-aromatic molecule, is a chemical commodity used as a raw ingredient in a variety of everyday products that must meet stringent durability and wear resistance standards [2,6]. Cyanuric chloride (2,4,6-trichloro-1,3,5-triazine) is a versatile multifunctional reagent that has been widely employed in bioconjugation as well as the production of insecticides, brighteners and reactive dyes. Triazine-based covalent organic polymers (COPs) are a growing sub-class of porous organic framework materials made from triazine or nitrile-containing precursors by covalent bonding. The synthesis of triazine-based covalent-organic frameworks (see Figure 1) using melamine and cyanuric chloride is discussed by Wen et al. [6]. TriCF denotes the as-prepared covalent-organic frameworks. TriCF has a lamellar structure and is extremely thermo-stable. It is a novel synthesized brand-new lubricant [6]. There are currently no studies in the literature on the computation of topological indices of TriCF's structure. The results of this study could be applied to future triazine-based covalent organic frameworks that are designed and manufactured [6].

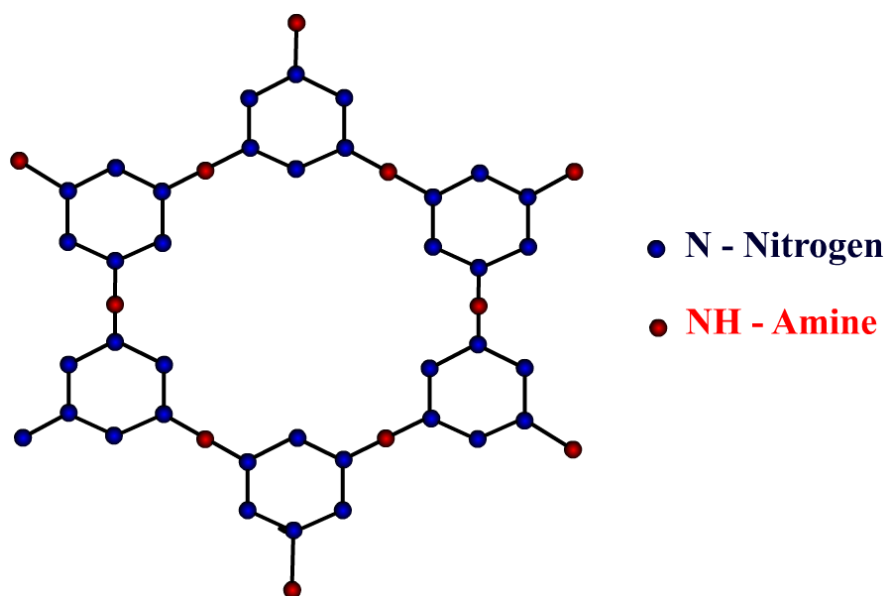


Figure 1. TriCF Structure.

The topological index of a molecule structure is a numerical quantity that quantifies the molecular structure and its branching pattern in a non-empirical way [7]. In this juncture, the topological index can be thought of as a score function that converts each chemical structure into a real number and then uses that number as a descriptor for the molecule under investigation. For grasping the links between the molecular structure and the prospective physicochemical features, chemical engineers use various well-known indices. The topological indices may be used in drug design, molecular QSPR/QSAR analysis, thermodynamics and other fields [4–8]. For instance, it has been demonstrated that there is a strong association between the boiling points and heats of production of specific classes of isomeric octanes and the atom bond connectivity index. Chemical compounds, materials and pharmaceuticals are represented as (molecular) graphs in theoretical

chemistry, with each vertex representing an atom of the molecule structure and each edge implying covalent bonds between two atoms [8].

In an effort to describe the complexity of graphs, graph entropy was developed. Although it was initially developed to illustrate the complexity of information transmission and communication, it currently has numerous important applications in a variety of scientific fields, including physical dissipative structures, biological systems, engineering fields and others [8]. Graph entropies can be divided into two categories: deterministic and probabilistic [7–10]. Since it is frequently used in a variety of fields, including communication and the characterisation of chemical structures, this work focuses on the probabilistic category [9,11]. Statistical techniques are further divided into intrinsic and extrinsic groups. In intrinsic measures, a graph is divided into parts with similar structural similarities, and a probability distribution over those parts is discovered. For extrinsic measurements, vertices or edges in the graph are given a probability function [11]. Applying an entropy function to this probability distribution function yields the numerical value of probabilistic measurements of graph complexity [7–13].

2. Preliminaries and Mathematical Terminologies

In this paper, we consider γ to be a connected graph. The vertex set and edge set are denoted by the symbols $|V(\gamma)| = \mathcal{P}$ and $|E(\gamma)| = \mathcal{Q}$, respectively. In order to create multiplicative topological indices and degree-based entropy measurements for the TriCF structure, the research uses edge-partition techniques.

The research shows various degree-based topological descriptors and multiplicative degree-based topological descriptors, which can be seen in Table 1 [10–22] and Table 2 [23–31], respectively.

Table 1. Degree-based topological indices.

Randić Index	$R(G) = \sum_{uv \in E(G)} \left[\frac{1}{\sqrt{d_u d_v}} \right]$
Reciprocal Randić Index	$RR(G) = \sum_{uv \in E(G)} [\sqrt{d_u d_v}]$
Reduced Reciprocal Randić Index	$RRR(G) = \sum_{uv \in E(G)} [\sqrt{(d_u - 1)(d_v - 1)}]$
First Zagreb Index	$M_1(G) = \sum_{uv \in E(G)} [d_u + d_v]$
Second Zagreb Index	$M_2(G) = \sum_{uv \in E(G)} [d_u \times d_v]$
Reduced Second Zagreb Index	$RM_2(G) = \sum_{uv \in E(G)} [(d_u - 1)(d_v - 1)]$
Hyper Zagreb Index	$HM(G) = \sum_{uv \in E(G)} [d_u + d_v]^2$
Augmented Zagreb Index	$AZ(G) = \sum_{uv \in E(G)} \left[\frac{d_u \times d_v}{d_u + d_v - 2} \right]^3$
Harmonic Index	$H(G) = \sum_{uv \in E(G)} \left[\frac{2}{d_u + d_v} \right]$
Sum Connectivity Index	$SC(G) = \sum_{uv \in E(G)} \frac{1}{\sqrt{d_u + d_v}}$
Geometric Arithmetic Index	$GA(G) = \sum_{uv \in E(G)} \frac{2\sqrt{d_u d_v}}{d_u + d_v}$
Inverse Sum Index	$IS(G) = \sum_{uv \in E(G)} \frac{d_u d_v}{d_u + d_v}$
Albertson Index	$Alb(G) = \sum_{uv \in E(G)} u - v $

Table 1. *Cont.*

Symmetric Division Index	$AZI(G) = \sum_{uv \in E(G)} \frac{d_u^2 + d_v^2}{d_u d_v}$
Atom Bond Connectivity Index	$ABC(G) = \sum_{uv \in E(G)} \sqrt{\frac{d_u + d_v - 2}{d_u d_v}}$

Table 2. Multiplicative degree-based topological indices.

Randić Index	$R(G) = \prod_{uv \in E(G)} \left[\frac{1}{\sqrt{d_u d_v}} \right]$
Reciprocal Randić Index	$RR(G) = \prod_{uv \in E(G)} [\sqrt{d_u d_v}]$
Reduced Reciprocal Randić Index	$RRR(G) = \prod_{uv \in E(G)} [\sqrt{(d_u - 1)(d_v - 1)}]$
First Zagreb Index	$M_1(G) = \prod_{uv \in E(G)} [d_u + d_v]$
Second Zagreb Index	$M_2(G) = \prod_{uv \in E(G)} [d_u \times d_v]$
Reduced Second Zagreb Index	$RM_2(G) = \prod_{uv \in E(G)} [(d_u - 1)(d_v - 1)]$
Hyper Zagreb Index	$HM(G) = \prod_{uv \in E(G)} [d_u + d_v]^2$
Augmented Zagreb Index	$AZ(G) = \prod_{uv \in E(G)} \left[\frac{d_u \times d_v}{d_u + d_v - 2} \right]^3$
Harmonic Index	$H(G) = \prod_{uv \in E(G)} \left[\frac{2}{d_u + d_v} \right]$
Sum Connectivity Index	$SC(G) = \prod_{uv \in E(G)} \frac{1}{\sqrt{d_u + d_v}}$
Geometric Arithmetic Index	$GA(G) = \prod_{uv \in E(G)} \frac{2\sqrt{d_u d_v}}{d_u + d_v}$
Inverse Sum Index	$IS(G) = \prod_{uv \in E(G)} \frac{d_u d_v}{d_u + d_v}$
Albertson Index	$Alb(G) = \prod_{uv \in E(G)} u - v $
Symmetric Division Index	$AZI(G) = \prod_{uv \in E(G)} \frac{d_u^2 + d_v^2}{d_u d_v}$
Atom Bond Connectivity Index	$ABC(G) = \prod_{uv \in E(G)} \sqrt{\frac{d_u + d_v - 2}{d_u d_v}}$

3. Methodology

The computations in this study are carried out using graph theoretical technologies, namely the edge partition method, and analytical methods. The molecular structures of the TriCF are described using Chem Draw Ultra, and numerical results are visualized using Origin.

4. Main Results

In this section, the authors present key findings of the study. A schematic of triazine-based covalent-organic frameworks synthesis can be formed into any kind of structure, such as a linear chain, parallelogram, hexagonal shape, etc. Linear chain triazine-based covalent-organic frameworks, parallelogram triazine-based covalent-organic frameworks, and hexagonal triazine-based covalent-organic frameworks are here denoted as TriCF(r), TriCF(r,s), and TriCF(r), respectively. Figures 2–4 show the 2D structure of linear chain,

parallelogram, hexagonal TriCF structures respectively. Figure 5 shows the unit cell of TriCF and explains the edge partition method. In this work, based on the growth of TriCF, the authors categorized it into three kinds. In particular, γ_1 , γ_2 and γ_3 are linear chain TriCF structures, parallelogram TriCF structures and hexagonal TriCF structures, respectively.

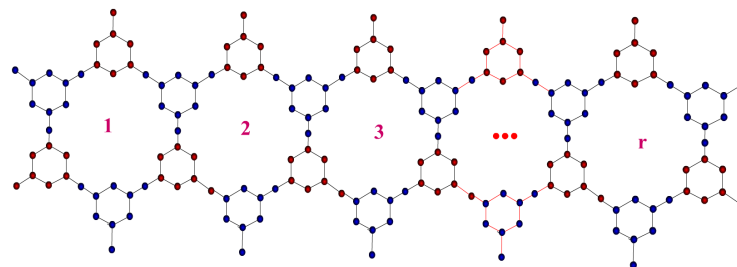


Figure 2. Linear chain TriCF structure.

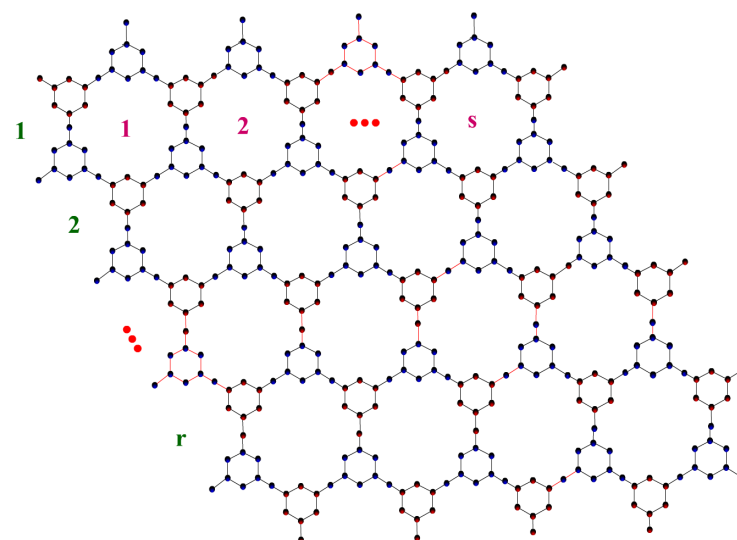


Figure 3. Parallelogram TriCF structure.

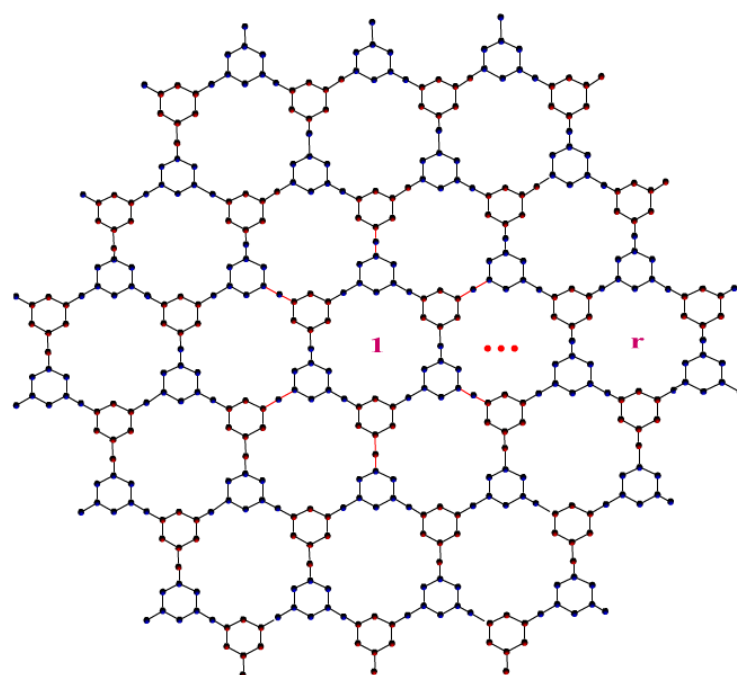


Figure 4. Hexagonal TriCF structure.

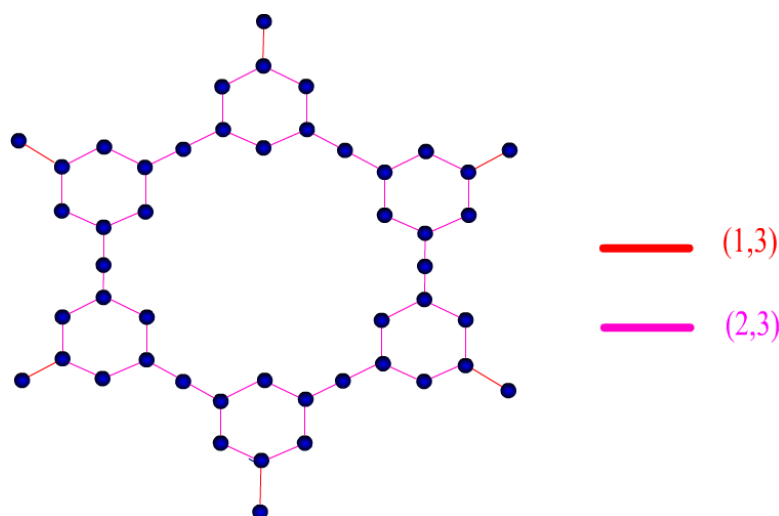


Figure 5. Edge partition of unit cell of TriCF structure.

- The total number of vertices and edges of γ_1 is depicted as $\mathcal{P} = 33r + 15$ and $\mathcal{Q} = 36r + 18$, respectively. In addition, the edge set has two edge partitions. The first edge partition contains edges with the following values: $2r + 4$; $d_{\mathcal{Q}_1}(u) = 1$, $d_{\mathcal{Q}_1}(v) = 3$ and $34r + 14$ edges make up the second edge partition, where $d_{\mathcal{Q}_1}(u) = 2$, $d_{\mathcal{Q}_1}(v) = 3$.
- The total number of vertices and edges of γ_2 is depicted as $\mathcal{P} = (13s + 20)r + 18s + 3$ and $\mathcal{Q} = (18s + 18)r + 18s$, respectively. In addition, the edge set has two edge partitions. The first edge partition contains edges with the following values: $2r + 2s + 2$; $d_{\mathcal{Q}_2}(u) = 1$, $d_{\mathcal{Q}_2}(v) = 3$ and $(18s + 16)r + 16s - 2$ edges make up the second edge partition, where $d_{\mathcal{Q}_2}(u) = 2$, $d_{\mathcal{Q}_2}(v) = 3$.
- The total number of vertices and edges of γ_3 is depicted as $\mathcal{P} = 45r^2 + 3r$ and $\mathcal{Q} = 54r^2$, respectively. In addition, the edge set has two edge partitions. The first edge partition contains edges with the following values: $6r$; $d_{\mathcal{Q}_3}(u) = 1$, $d_{\mathcal{Q}_3}(v) = 3$ and $54r^2 - 6r$ edges make up the second edge partition, where $d_{\mathcal{Q}_3}(u) = 2$, $d_{\mathcal{Q}_3}(v) = 3$.

Table 3 below illustrates how the structure's edges are divided.

Table 3. Edge partition of γ .

γ	(1,3)	(2,3)	$\mathcal{Q}()$	$\mathcal{P}()$
γ_1	$2r + 4$	$34r + 14$	$36r + 18$	$36r + 15$
γ_2	$2r + (2s + 2)$	$(18s + 16)r + 16s - 2$	$(18s + 18)r + 18s$	$(13s + 20)r + 18s + 3$
γ_3	$6r$	$54r^2 - 6r$	$54r^2$	$45r^2 + 3r$

4.1. Degree-Based Topological Indices of TriCF Structure

Theorem 1. Let γ_1 be a linear chain TriCF structure with dimension r . Then,

1. $R(\gamma_1) = \frac{\sqrt{3}(17\sqrt{2}r + 7\sqrt{2} + 2r + 4)}{3}$.
2. $RR(\gamma_1) = 2\sqrt{3}(17\sqrt{2}r + 7\sqrt{2} + r + 2)$.
3. $RRR(\gamma_1) = \sqrt{2}(34r + 14)$.
4. $M_1(\gamma_1) = 178r + 86$.
5. $M_2(\gamma_1) = 210r + 96$.
6. $RM_2(\gamma_1) = 68r + 28$.
7. $HM(\gamma_1) = 882r + 414$.
8. $AZ(\gamma_1) = \frac{1115r}{4} + \frac{251}{2}$.

9. $H(\gamma_1) = \frac{73r}{5} + \frac{38}{5}$.
10. $SC(\gamma_1) = r + 2 + \frac{\sqrt{5}(34r + 14)}{5}$.
11. $GA(\gamma_1) = \frac{1}{5} \left(2\sqrt{3} (34\sqrt{10}r + 14\sqrt{10} + 5r + 10) \right)$.
12. $IS(\gamma_1) = \frac{423r}{10} + \frac{99}{5}$.
13. $AZI(\gamma_1) = \frac{241r}{3} + \frac{131}{3}$.
14. $Alb(\gamma_1) = 38r + 22$.
15. $ABC(\gamma_1) = \frac{2\sqrt{3r+6}}{3} + \sqrt{17r+7}$.

Proof. Let γ_1 be a linear chain TriCF structure with $\mathcal{P}()$ and $\mathcal{Q}()$ (see Table 3). We have conducted edge partitions of γ_1 based on the vertex degree, and the following results are obtained by applying those edge partitions in the definitions of degree-based topological indices (Table 1).

1.
$$\begin{aligned} R(\gamma_1) &= \frac{1}{\sqrt{1 \times 3}}(2r + 4) + \frac{1}{\sqrt{2 \times 3}}(34r + 14) \\ &= \frac{\sqrt{3}(2r + 4)}{3} + \frac{\sqrt{6}(34r + 14)}{6} \\ &= \frac{\sqrt{3}(17\sqrt{2}r + 7\sqrt{2} + 2r + 4)}{3}. \end{aligned}$$
2. $RR(\gamma_1) = \sqrt{1 \times 3}(2r + 4) + \sqrt{2 \times 3}(34r + 14) = 2\sqrt{3} (17\sqrt{2}r + 7\sqrt{2} + r + 2)$.
3. $RRR(\gamma_1) = \sqrt{0}(2r + 4) + \sqrt{2}(34r + 14) = \sqrt{2}(34r + 14)$.
4. $M_1(\gamma_1) = 4(2r + 4) + 5(34r + 14) = 178r + 86$.
5. $M_2(\gamma_1) = 3(2r + 4) + (6)(34r + 14) = 210r + 96$.
6. $RM_2(\gamma_1) = (0)(2)(2r + 4) + (1)(2)(34r + 14) = 68r + 28$.
7. $HM(\gamma_1) = (1 + 3)^2(2r + 4) + (2 + 3)^2(34r + 14) = 882r + 414$.
8.
$$\begin{aligned} AZ(\gamma_1) &= \left(\frac{1 \times 3}{(1 + 3 - 2)} \right)^3 (2r + 4) + \left(\frac{2 \times 3}{(2 + 3 - 2)} \right)^3 (34r + 14) \\ &= \frac{1115r}{4} + \frac{251}{2}. \end{aligned}$$
9.
$$\begin{aligned} H(\gamma_1) &= \frac{2}{4}(2r + 4) + \frac{2}{5}(34r + 14) \\ &= \frac{73r}{5} + \frac{38}{5}. \end{aligned}$$
10.
$$\begin{aligned} SC(\gamma_1) &= \frac{1}{\sqrt{1+3}}(2r + 4) + \frac{1}{\sqrt{2+3}}(34r + 14) \\ &= r + 2 + \frac{\sqrt{5}(34r + 14)}{5}. \end{aligned}$$
11.
$$\begin{aligned} GA(\gamma_1) &= 2 \left(\frac{\sqrt{1 \times 3}}{1 + 3} \right) (2r + 4) + 2 \left(\frac{\sqrt{2 \times 3}}{2 + 3} \right) (34r + 14) \\ &= \sqrt{3}(2r + 4) + \frac{2\sqrt{30}(34r + 14)}{5} \\ &= \frac{2\sqrt{3}(34\sqrt{10}r + 14\sqrt{10} + 5r + 10)}{5}. \end{aligned}$$

$$\begin{aligned}
12. \quad IS(\gamma_1) &= \frac{1 \times 3}{1+3}(2r+4) + \frac{2 \times 3}{2+3}(34r+14) \\
&= \frac{423r}{10} + \frac{99}{5}. \\
13. \quad AZI(\gamma_1) &= \left(\frac{1+9}{1 \times 3}\right)(2r+4) + \left(\frac{4+9}{2 \times 3}\right)(34r+14) \\
&= \frac{241r}{3} + \frac{131}{3}. \\
14. \quad Alb(\gamma_1) &= 2(2r+4) + 1(34r+14) \\
&= 38r+22. \\
15. \quad ABC(\gamma_1) &= \sqrt{\frac{1+3-2}{1 \times 3}}(2r+4) + \sqrt{\frac{2+3-2}{2 \times 3}}(34r+14) \\
&= \frac{2\sqrt{3r+6}}{3} + \sqrt{17r+7}.
\end{aligned}$$

□

Theorem 2. Let γ_2 be a parallelogram TriCF structure with dimensions r and s . Then, the degree-based topological indices are:

$$\begin{aligned}
1. \quad R(\gamma_2) &= \frac{((9s+8)r+8s-1)\sqrt{3}\sqrt{2}}{3} + \frac{\sqrt{3}(2r+2s+2)}{3}. \\
2. \quad RR(\gamma_2) &= ((18s+16)r+16s-2)\sqrt{3}\sqrt{2} + 2\sqrt{3}(r+s+1). \\
3. \quad RRR(\gamma_2) &= \sqrt{2}((18s+16)r+16s-2). \\
4. \quad M_1(\gamma_2) &= (90s+88)r+88s-2. \\
5. \quad M_2(\gamma_2) &= (108s+102)r+102s-6. \\
6. \quad RM_2(\gamma_2) &= (36s+32)r+32s-4. \\
7. \quad HM(\gamma_2) &= (450s+432)r+432s-18. \\
8. \quad AZ(\gamma_2) &= \frac{(576r+539)s}{4} + \frac{539r}{4} - \frac{37}{4}. \\
9. \quad H(\gamma_2) &= \frac{(36s+37)r}{5} + \frac{37s}{5} + \frac{1}{5}. \\
10. \quad SC(\gamma_2) &= r+s+1 + \frac{\sqrt{5}((18s+16)r+16s-2)}{5}. \\
11. \quad GA(\gamma_2) &= \frac{((36s+32)r+32s-4)\sqrt{3}\sqrt{10}}{5} + 2\sqrt{3}(r+s+1) \\
12. \quad IS(\gamma_2) &= \frac{(216s+207)r}{10} + \frac{207s}{10} - \frac{9}{10}. \\
13. \quad Alb(\gamma_2) &= (18s+20)r+20s+2. \\
14. \quad AZI(\gamma_2) &= \frac{(117r+124)s}{3} + \frac{124r}{3} + \frac{7}{3}. \\
15. \quad ABC(\gamma_2) &= \frac{2\sqrt{3r+3s+3}}{3} + \sqrt{(9s+8)r+8s-1}.
\end{aligned}$$

Proof. Let γ_2 be a parallelogram TriCF structure with $\mathcal{P}()$ and $\mathcal{Q}()$ as taken from Table 3. We have conducted edge partitions of γ_2 based on the vertex degree, and the following results are obtained by applying those edge partitions in the definitions of degree-based topological indices (Table 1).

$$\begin{aligned}
1. \quad (\gamma_2) &= \frac{1}{\sqrt{1 \times 3}}(2r+2s+2) + \frac{1}{\sqrt{2 \times 3}}((18s+16)r+16s-2) \\
&= \frac{\sqrt{3}(2r+2s+2)}{3} + \frac{\sqrt{6}((18s+16)r+16s-2)}{6} \\
&= \frac{((9s+8)r+8s-1)\sqrt{3}\sqrt{2}}{3} + \frac{\sqrt{3}(2r+2s+2)}{3}. \\
2. \quad RR(\gamma_2) &= \sqrt{1 \times 3}(2r+2s+2) + \sqrt{2 \times 3}((18s+16)r+16s-2) \\
&= \sqrt{3}(2r+2s+2) + \sqrt{6}((18s+16)r+16s-2) \\
&= ((18s+16)r+16s-2)\sqrt{3}\sqrt{2} + 2\sqrt{3}(r+s+1).
\end{aligned}$$

3. $RRR(\gamma_2) = \sqrt{(1-1)(3-1)}(2r+2s+2) + \sqrt{(2-1)(3-1)}((18s+16)r+16s-2)$
 $= \sqrt{2}((18s+16)r+16s-2).$
4. $M_1(\gamma_2) = (1+3)(2r+2s+2) + (2+3)((18s+16)r+16s-2)$
 $= 8r+88s-2+5(1s+16)r$
 $= (90s+88)r+88s-2.$
5. $M_2(\gamma_2) = (1 \times 3)(2r+2s+2) + (2 \times 3)((18s+16)r+16s-2)$
 $= 6r+102s-6+6(18s+16)r$
 $= (108s+102)r+102s-6.$
6. $RM_2(\gamma_2) = ((1-1)(3-1))(2r+2s+2) + ((2-1)(3-1))((18s+16)r+16s-2)$
 $= 2(18s+16)r+32s-4$
 $= (36s+32)r+32s-4.$
7. $HM(\gamma_2) = ((1+3)^2)(2r+2s+2) + ((2+3)^2)((18s+16)r+16s-2)$
 $= 32r+432s-18+25(18s+16)r$
 $= (450s+432)r+432s-18.$
8. $AZ(\gamma_2) = \left(\frac{1 \times 3}{(1+3-2)}\right)^3 (2r+2s+2) + \left(\frac{2 \times 3}{(2+3-2)}\right)^3 ((18s+16)r+16s-2)$
 $= \frac{27r}{4} + \frac{539s}{4} - \frac{37}{4} + 8(18s+16)r$
 $= \frac{(576r+539)s}{4} + \frac{539r}{4} - \frac{37}{4}.$
9. $H(\gamma_2) = \left(\frac{2}{1+3}\right)(2r+2s+2) + \left(\frac{2}{2+3}\right)((18s+16)r+16s-2)$
 $= r + \frac{37s}{5} + \frac{1}{5} + \frac{2(18s+16)r}{5}$
 $= \frac{(36s+37)r}{5} + \frac{37s}{5} + \frac{1}{5}.$
10. $SC(\gamma_2) = \frac{1}{\sqrt{1+3}}(2r+2s+2) + \frac{1}{\sqrt{2+3}}((18s+16)r+16s-2)$
 $= r+s+1 + \frac{\sqrt{5}((18s+16)r+16s-2)}{5}.$
11. $GA(\gamma_2) = 2\left(\frac{\sqrt{1 \times 3}}{1+3}\right)(2r+2s+2) + 2\left(\frac{\sqrt{2 \times 3}}{2+3}\right)((18s+16)r+16s-2)$
 $= \sqrt{3}(2r+2s+2) + \frac{2\sqrt{30}((18s+16)r+16s-2)}{5}$
 $= \frac{((36s+32)r+32s-4)\sqrt{3}\sqrt{10}}{5} + 2\sqrt{3}(r+s+1).$
12. $IS(\gamma_2) = \left(\frac{1 \times 3}{1+3}\right)(2r+2s+2) + \left(\frac{2 \times 3}{2+3}\right)((18s+16)r+16s-2)$
 $= \frac{3r}{2} + \frac{207s}{10} - \frac{9}{10} + \frac{6(18s+16)r}{5}$
 $= \frac{(216s+207)r}{10} + \frac{207s}{10} - \frac{9}{10}.$
13. $Alb(\gamma_2) = 2(2r+2s+2) + 1((18s+16)r+16s-2)$
 $= 4r+2s+2+(18s+16)r$
 $= (18s+20)r+20s+2.$
14. $AZI(\gamma_2) = \left(\frac{1+9}{1 \times 3}\right)(2r+2s+2) + \left(\frac{4+9}{2 \times 3}\right)((18s+16)r+16s-2)$
 $= \frac{20r}{3} + \frac{124s}{3} + \frac{7}{3} + \frac{13(18s+16)r}{6}$
 $= \frac{(117r+124)s}{3} + \frac{124r}{3} + \frac{7}{3}.$
15. $ABC(\gamma_2) = \sqrt{\frac{1+3-2}{1 \times 3}}(2r+2s+2) + \sqrt{\frac{2+3-2}{2 \times 3}}((18s+16)r+16s-2)$
 $= \frac{2\sqrt{3r+3s+3}}{3} + \sqrt{\frac{(18s+16)r}{2}} + 8s-1$
 $= \frac{2\sqrt{3r+3s+3}}{3} + \sqrt{(9s+8)r+8s-1}.$

□

Theorem 3. Let γ_3 be a hexagonal TriCF structure with dimension r . Then,

1. $R(\gamma_3) = \sqrt{3}r(9\sqrt{2}r - \sqrt{2} + 2).$
2. $RR(\gamma_3) = 6\sqrt{3}r(9\sqrt{2}r - \sqrt{2} + 1).$
3. $RRR(\gamma_3) = \sqrt{2}(54r^2 - 6r).$
4. $M_1(\gamma_3) = 270r^2 - 6r.$
5. $M_2(\gamma_3) = 324r^2 - 18r.$
6. $RM_2(\gamma_3) = 108r^2 - 12r.$
7. $HM(\gamma_3) = 1350r^2 - 54r.$
8. $AZ(\gamma_3) = -\frac{111}{4}r + 432r^2.$
9. $H(\gamma_3) = \frac{3}{5}r + \frac{108}{5}r^2.$
10. $SC(\gamma_3) = 3r + \frac{\sqrt{5}(54r^2 - 6r)}{5}.$
11. $GA(\gamma_3) = \frac{6\sqrt{3}r(18\sqrt{10}r - 2\sqrt{10} + 5)}{5}.$
12. $IS(\gamma_3) = -\frac{27}{10}r + \frac{324}{5}r^2.$
13. $AZI(\gamma_3) = 117r^2 + 7r.$
14. $Alb(\gamma_3) = 54r^2 + 6r.$
15. $ABC(\gamma_3) = \sqrt{3}\sqrt{9r^2 - r} + 2\sqrt{r}.$

Proof. Let γ_3 be a hexagonal TriCF structure with $\mathcal{P}()$ and $\mathcal{Q}()$ as given in Table 3. We have conducted edge partitions of γ_3 based on the vertex degree, and the following results are obtained by applying those edge partitions in the definitions of degree-based topological indices (Table 1).

1.
$$\begin{aligned} R(\gamma_3) &= \frac{1}{\sqrt{1 \times 3}}(6r) + \frac{1}{\sqrt{2 \times 3}}(54r^2 - 6r) \\ &= 2\sqrt{3}r + \frac{\sqrt{6}(54r^2 - 6r)}{6} \\ &= \sqrt{3}r(9\sqrt{2}r - \sqrt{2} + 2). \end{aligned}$$
2.
$$\begin{aligned} RR(\gamma_3) &= \sqrt{1 \times 3}(6r) + \sqrt{2 \times 3}(54r^2 - 6r) \\ &= 6\sqrt{3}r + \sqrt{6}(54r^2 - 6r) \\ &= 6\sqrt{3}r(9\sqrt{2}r - \sqrt{2} + 1). \end{aligned}$$
3.
$$\begin{aligned} RRR(\gamma_3) &= \sqrt{(1-1)(3-1)}(6r) + \sqrt{(2-1)(3-1)}(54r^2 - 6r) \\ &= \sqrt{2}(54r^2 - 6r). \end{aligned}$$
4.
$$\begin{aligned} M_1(\gamma_3) &= (1+3)(6r) + (2+3)(54r^2 - 6r) \\ &= 270r^2 - 6r. \end{aligned}$$
5.
$$\begin{aligned} M_2(\gamma_3) &= (1 \times 3)(6r) + (2 \times 3)(54r^2 - 6r) \\ &= 324r^2 - 18r. \end{aligned}$$
6.
$$\begin{aligned} RM_2(\gamma_3) &= ((1-1)(3-1))(6r) + ((2-1)(3-1))(54r^2 - 6r) \\ &= 108r^2 - 12r. \end{aligned}$$
7.
$$\begin{aligned} HM(\gamma_3) &= ((1+3)^2)(6r) + ((2+3)^2)(54r^2 - 6r) \\ &= 1350r^2 - 54r. \end{aligned}$$
8.
$$\begin{aligned} AZ(\gamma_3) &= \left(\frac{1 \times 3}{1+3-2}\right)^3(6r) + \left(\frac{2 \times 3}{2+3-2}\right)^3(54r^2 - 6r) \\ &= -\frac{111}{4}r + 432r^2. \end{aligned}$$
9.
$$\begin{aligned} H(\gamma_3) &= \frac{2}{1+3}(6r) + \frac{2}{2+3}(54r^2 - 6r) \\ &= \frac{3}{5}r + \frac{108}{5}r^2. \end{aligned}$$

10. $SC(\gamma_3) = \frac{1}{\sqrt{1+3}}(6r) + \frac{1}{\sqrt{2+3}}(54r^2 - 6r)$
 $= 3r + \frac{\sqrt{5}(54r^2 - 6r)}{5}.$
11. $GA(\gamma_3) = 2\left(\frac{\sqrt{1 \times 3}}{1+3}\right)(6r) + 2\left(\frac{\sqrt{2 \times 3}}{2+3}\right)(54r^2 - 6r)$
 $= 6\sqrt{3}r + \frac{2\sqrt{30}(54r^2 - 6r)}{5}$
 $= \frac{6\sqrt{3}r(18\sqrt{10}r - 2\sqrt{10} + 5)}{5}.$
12. $IS(\gamma_3) = \left(\frac{1 \times 3}{1+3}\right)(6r) + \left(\frac{2 \times 3}{2+3}\right)(54r^2 - 6r)$
 $= -\frac{27}{10}r + \frac{324}{5}r^2.$
13. $AZI(\gamma_3) = \left(\frac{1+9}{1 \times 3}\right)(6r) + \left(\frac{4+9}{2 \times 3}\right)(54r^2 - 6r)$
 $= 117r^2 + 7r.$
14. $Alb(\gamma_3) = 2(6r) + 1(54r^2 - 6r)$
 $= 54r^2 + 6r.$
15. $ABC(\gamma_3) = \sqrt{\frac{1+3-2}{1 \times 3}}(6r) + \sqrt{\frac{2+3-2}{2 \times 3}}(54r^2 - 6r)$
 $= 2\sqrt{r} + \sqrt{27r^2 - 3r}$
 $= \sqrt{3}\sqrt{9r^2 - r} + 2\sqrt{r}.$

□

4.2. Multiplicative Degree-Based Topological Indices of TriCF Structure

Theorem 4. Let γ_1 be a linear chain TriCF structure with dimension r . Then, the degree-based multiplicative indices are

1. $R(\gamma_1) = \left(\frac{\sqrt{3}}{3}\right)^{2r+4} \left(\frac{\sqrt{6}}{6}\right)^{34r+14}.$
2. $RR(\gamma_1) = (\sqrt{3})^{2r+4} (\sqrt{6})^{34r+14}.$
3. $M_1(\gamma_1) = 4^{(2r+4)} 5^{(34r+14)}.$
4. $M_2(\gamma_1) = 3^{2r+4} 6^{34r+14}.$
5. $HM(\gamma_1) = 16^{2r+4} 25^{34r+14}.$
6. $AZ(\gamma_1) = \left(\frac{27}{8}\right)^{2r+4} 8^{34r+14}.$
7. $H(\gamma_1) = \left(\frac{1}{2}\right)^{2r+4} \left(\frac{2}{5}\right)^{34r+14}.$
8. $SC(\gamma_1) = \left(\frac{1}{2}\right)^{2r+4} \left(\frac{\sqrt{5}}{5}\right)^{34r+14}.$
9. $GA(\gamma_1) = \left(\frac{\sqrt{3}}{2}\right)^{2r+4} \left(\frac{2\sqrt{6}}{5}\right)^{34r+14}.$
10. $IS(\gamma_1) = \left(\frac{3}{4}\right)^{2r+4} \left(\frac{6}{5}\right)^{34r+14}.$
11. $AZI(\gamma_1) = \left(\frac{10}{3}\right)^{2r+4} \left(\frac{13}{6}\right)^{34r+14}.$
12. $Alb(\gamma_1) = 2^{2r+4}.$
13. $ABC(\gamma_1) = \left(\frac{\sqrt{6}}{3}\right)^{2r+4} \left(\frac{\sqrt{2}}{2}\right)^{34r+14}.$

Proof. Let γ_1 be a linear chain TriCF structure with vertices $\mathcal{P}()$ and $\mathcal{Q}()$ (see Table 3). We have conducted edge partitions of γ_1 based on the vertex degree, and the following results are obtained by applying those edge partitions in the definitions of multiplicative degree-based topological indices (Table 2).

1.
$$R(\gamma_1) = \left(\frac{1}{1 \times 3}\right)^{(2r+4)} \left(\frac{1}{2 \times 3}\right)^{(34r+14)}$$
$$= \left(\frac{\sqrt{3}}{3}\right)^{2r+4} \left(\frac{\sqrt{6}}{6}\right)^{34r+14}.$$
2.
$$RR(\gamma_1) = (\sqrt{1 \times 3})^{(2r+4)} (\sqrt{2 \times 3})^{(34r+14)} = (\sqrt{3})^{2r+4} (\sqrt{6})^{34r+14}.$$
3.
$$M_1(\gamma_1) = (1+3)^{(2r+4)} (2+3)^{(34r+14)} = 4^{(2r+4)} 5^{(34r+14)}.$$
4.
$$M_2(\gamma_1) = (1 \times 3)^{(2r+4)} (2 \times 3)^{(34r+14)} = 3^{2r+4} 6^{34r+14}.$$
5.
$$HM(\gamma_1) = ((1+3)^2)^{(2r+4)} ((2+3)^2)^{(34r+14)}$$
$$= 16^{2r+4} 25^{34r+14}.$$
6.
$$AZ(\gamma_1) = \left(\left(\frac{1 \times 3}{1+3-2}\right)^3\right)^{(2r+4)} \left(\left(\frac{2 \times 3}{2+3-2}\right)^3\right)^{(34r+14)}$$
$$= \left(\frac{27}{8}\right)^{2r+4} 8^{34r+14}.$$
7.
$$H(\gamma_1) = \left(\frac{2}{1+3}\right)^{(2r+4)} \left(\frac{2}{2+3}\right)^{(34r+14)}$$
$$= \left(\frac{1}{2}\right)^{2r+4} \left(\frac{2}{5}\right)^{34r+14}$$
8.
$$SC(\gamma_1) = \left(\frac{1}{\sqrt{1+3}}\right)^{(2r+4)} \left(\frac{1}{\sqrt{2+3}}\right)^{(34r+14)}$$
$$= \left(\frac{1}{2}\right)^{2r+4} \left(\frac{\sqrt{5}}{5}\right)^{34r+14}.$$
9.
$$GA(\gamma_1) = \left(2\left(\frac{\sqrt{1 \times 3}}{1+3}\right)\right)^{(2r+4)} \left(2\left(\frac{\sqrt{2 \times 3}}{2+3}\right)\right)^{(34r+14)}$$
$$= \left(\frac{\sqrt{3}}{2}\right)^{2r+4} \left(\frac{2\sqrt{6}}{5}\right)^{34r+14}.$$
10.
$$IS(\gamma_1) = \left(\frac{1 \times 3}{1+3}\right)^{(2r+4)} \left(\frac{2 \times 3}{2+3}\right)^{(34r+14)}$$
$$= \left(\frac{3}{4}\right)^{2r+4} \left(\frac{6}{5}\right)^{34r+14}.$$
11.
$$AZI(\gamma_1) = \left(\frac{1+9}{1 \times 3}\right)^{(2r+4)} \left(\frac{4+9}{2 \times 3}\right)^{(34r+14)}$$
$$= \left(\frac{10}{3}\right)^{2r+4} \left(\frac{13}{6}\right)^{34r+14}.$$
12.
$$Alb(\gamma_1) = (2)^{(2r+4)} (1)^{(34r+14)} = 2^{2r+4}.$$
13.
$$ABC(\gamma_1) = \left(\sqrt{\frac{1+3-2}{1 \times 3}}\right)^{(2r+4)} \left(\sqrt{\frac{2+3-2}{2 \times 3}}\right)^{(34r+14)}$$
$$= \left(\frac{\sqrt{6}}{3}\right)^{2r+4} \left(\frac{\sqrt{2}}{2}\right)^{34r+14}.$$

□

Theorem 5. Let γ_2 be a parallelogram TriCF structure with dimensions r and s . Then, the multiplicative degree-based topological indices are

1. $R(\gamma_2) = \left(\frac{\sqrt{3}}{3}\right)^{2r+2s+2} \left(\frac{\sqrt{6}}{6}\right)^{(18s+16)r+16s-2}$.
2. $RR(\gamma_2) = (\sqrt{3})^{2r+2s+2} (\sqrt{6})^{(18s+16)r+16s-2}$.
3. $M_1(\gamma_2) = 4^{2r+2s+2} 5^{(18s+16)r+16s-2}$.
4. $M_2(\gamma_2) = 3^{2r+2s+2} 6^{(18s+16)r+16s-2}$.
5. $HM(\gamma_2) = 16^{2r+2s+2} 25^{(18s+16)r+16s-2}$.
6. $AZ(\gamma_2) = \left(\frac{27}{8}\right)^{2r+2s+2} 8^{(18s+16)r+16s-2}$.
7. $H(\gamma_2) = \left(\frac{1}{2}\right)^{2r+2s+2} \left(\frac{2}{5}\right)^{(18s+16)r+16s-2}$.
8. $SC(\gamma_2) = \left(\frac{1}{2}\right)^{2r+2s+2} \left(\frac{\sqrt{5}}{5}\right)^{(18s+16)r+16s-2}$.
9. $GA(\gamma_2) = \left(\frac{\sqrt{3}}{2}\right)^{2r+2s+2} \left(\frac{2\sqrt{6}}{5}\right)^{(18s+16)r+16s-2}$.
10. $IS(\gamma_2) = \left(\frac{3}{4}\right)^{2r+2s+2} \left(\frac{6}{5}\right)^{(18s+16)r+16s-2}$.
11. $Alb(\gamma_2) = 2^{2r+2s+2}$.
12. $AZI(\gamma_2) = \left(\frac{10}{3}\right)^{2r+2s+2} \left(\frac{13}{6}\right)^{(18s+16)r+16s-2}$.
13. $ABC(\gamma_2) = \left(\frac{\sqrt{6}}{3}\right)^{2r+2s+2} \left(\frac{\sqrt{2}}{2}\right)^{(18s+16)r+16s-2}$.

Proof. Let γ_2 be a parallelogram TriCF structure with vertex and edge set \mathcal{P} and \mathcal{Q} , respectively (Table 3). We have conducted edge partitions of γ_2 based on the vertex degree (Table 3), and the following results are obtained by applying those edge partitions in the definitions of multiplicative degree-based topological indices (Table 2).

1. $R(\gamma_2) = \left(\frac{1}{\sqrt{1 \times 3}}\right)^{(2r+2s+2)} \left(\frac{1}{\sqrt{2 \times 3}}\right)^{(18s+16)r+16s-2}$
 $= \left(\frac{\sqrt{3}}{3}\right)^{2r+2s+2} \left(\frac{\sqrt{6}}{6}\right)^{(18s+16)r+16s-2}$.
2. $RR(\gamma_2) = (\sqrt{1 \times 3})^{(2r+2s+2)} (\sqrt{2 \times 3})^{(18s+16)r+16s-2}$
 $= (\sqrt{3})^{2r+2s+2} (\sqrt{6})^{(18s+16)r+16s-2}$.
3. $M1(\gamma_2) = (1+3)^{(2r+2s+2)} (2+3)^{(18s+16)r+16s-2}$
 $= 4^{2r+2s+2} 5^{(18s+16)r+16s-2}$.
4. $M2(\gamma_2) = (1 \times 3)^{(2r+2s+2)} (2 \times 3)^{(18s+16)r+16s-2}$
 $= 3^{2r+2s+2} 6^{(18s+16)r+16s-2}$.
5. $HM(\gamma_2) = ((1+3)^2)^{(2r+2s+2)} ((2+3)^2)^{(18s+16)r+16s-2}$
 $= 16^{2r+2s+2} 25^{(18s+16)r+16s-2}$.
6. $AZ(\gamma_2) = \left(\left(\frac{1 \times 3}{(1+3-2)}\right)^3\right)^{(2r+2s+2)} \left(\left(\frac{2 \times 3}{(2+3-2)}\right)^3\right)^{(18s+16)r+16s-2}$
 $= \left(\frac{27}{8}\right)^{2r+2s+2} 8^{(18s+16)r+16s-2}$.

$$\begin{aligned}
7. \quad H(\gamma_2) &= \left(\frac{2}{1+3}\right)^{(2r+2s+2)} \left(\frac{2}{2+3}\right)^{(18s+16)r+16s-2} \\
&= \left(\frac{1}{2}\right)^{2r+2s+2} \left(\frac{2}{5}\right)^{(18s+16)r+16s-2}. \\
8. \quad SC(\gamma_2) &= \left(\frac{1}{\sqrt{1+3}}\right)^{(2r+2s+2)} \left(\frac{2}{\sqrt{2+3}}\right)^{(18s+16)r+16s-2} \\
&= \left(\frac{1}{2}\right)^{2r+2s+2} \left(\frac{\sqrt{5}}{5}\right)^{(18s+16)r+16s-2}. \\
9. \quad GA(\gamma_2) &= \left(2\left(\frac{\sqrt{1 \times 3}}{1+3}\right)\right)^{(2r+2s+2)} \left(2\left(\frac{\sqrt{2 \times 3}}{2+3}\right)\right)^{(18s+16)r+16s-2} \\
&= \left(\frac{\sqrt{3}}{2}\right)^{2r+2s+2} \left(\frac{2\sqrt{6}}{5}\right)^{(18s+16)r+16s-2}. \\
10. \quad IS(\gamma_2) &= \left(\frac{1 \times 3}{1+3}\right)^{(2r+2s+2)} \left(\frac{2 \times 3}{2+3}\right)^{(18s+16)r+16s-2} \\
&= \left(\frac{3}{4}\right)^{2r+2s+2} \left(\frac{6}{5}\right)^{(18s+16)r+16s-2}. \\
11. \quad Alb(\gamma_2) &= (2)^{(2r+2s+2)} (1)^{(18s+16)r+16s-2} \\
&= 2^{2r+2s+2}. \\
12. \quad AZI(\gamma_2) &= \left(\frac{1+9}{1 \times 3}\right)^{(2r+2s+2)} \left(\frac{4+9}{2 \times 3}\right)^{(18s+16)r+16s-2} \\
&= \left(\frac{10}{3}\right)^{2r+2s+2} \left(\frac{13}{6}\right)^{(18s+16)r+16s-2}. \\
13. \quad ABC(\gamma_2) &= \left(\sqrt{\frac{(1+3-2)}{(1 \times 3)}}\right)^{(2r+2s+2)} \left(\sqrt{\frac{(2+3-2)}{(2 \times 3)}}\right)^{(18s+16)r+16s-2} \\
&= \left(\frac{\sqrt{6}}{3}\right)^{2r+2s+2} \left(\frac{\sqrt{2}}{2}\right)^{(18s+16)r+16s-2}.
\end{aligned}$$

□

Theorem 6. Let γ_3 be a hexagonal TriCF structure with dimension r . Then, the multiplicative degree-based topological indices are

$$\begin{aligned}
1. \quad R(\gamma_3) &= \left(\frac{\sqrt{3}}{3}\right)^{6r} \left(\frac{\sqrt{6}}{6}\right)^{54r^2-6r}. \\
2. \quad RR(\gamma_3) &= (\sqrt{3})^{6r} (\sqrt{6})^{54r^2-6r}. \\
3. \quad M_1(\gamma_3) &= 4^{6r} 5^{54r^2-6r}. \\
4. \quad M_2(\gamma_3) &= 3^{6r} 6^{54r^2-6r}. \\
5. \quad HM(\gamma_3) &= 16^{6r} 25^{54r^2-6r}. \\
6. \quad AZ(\gamma_3) &= \left(\frac{27}{8}\right)^{6r} 8^{54r^2-6r}. \\
7. \quad H(\gamma_3) &= \left(\frac{1}{2}\right)^{6r} \left(\frac{2}{5}\right)^{54r^2-6r}. \\
8. \quad SC(\gamma_3) &= \left(\frac{1}{2}\right)^{6r} \left(\frac{\sqrt{5}}{5}\right)^{54r^2-6r}.
\end{aligned}$$

$$\begin{aligned}
9. \quad GA(\gamma_3) &= \left(\frac{\sqrt{3}}{2}\right)^{6r} \left(\frac{2\sqrt{6}}{5}\right)^{54r^2-6r}. \\
10. \quad IS(\gamma_3) &= \left(\frac{3}{4}\right)^{6r} \left(\frac{6}{5}\right)^{54r^2-6r}. \\
11. \quad AZI(\gamma_3) &= 2340r^3 - 260r^2. \\
12. \quad Alb(\gamma_3) &= 2^{6r}. \\
13. \quad ABC(\gamma_3) &= \left(\frac{\sqrt{6}}{3}\right)^{6r} \left(\frac{\sqrt{2}}{2}\right)^{54r^2-6r}.
\end{aligned}$$

Proof. Let γ_3 be a hexagonal TriCF structure. The cardinality of vertices $\mathcal{P}()$ and edges $\mathcal{Q}()$ are given in Table 3. We have conducted edge partitions of γ_3 based on the vertex degree, and the following results are obtained by applying those edge partitions in the definitions of multiplicative degree-based topological indices (Table 2).

$$\begin{aligned}
1. \quad R(\gamma_3) &= \left(\frac{1}{\sqrt{1 \times 3}}\right)^{6r} \left(\frac{1}{\sqrt{1 \times 3}}\right)^{54r^2-6r} \\
&= \left(\frac{\sqrt{3}}{3}\right)^{6r} \left(\frac{\sqrt{6}}{6}\right)^{54r^2-6r}. \\
2. \quad RR(\gamma_3) &= (\sqrt{1 \times 3})^{6r} (\sqrt{2 \times 3})^{54r^2-6r} \\
&= (\sqrt{3})^{6r} (\sqrt{6})^{54r^2-6r}. \\
3. \quad M_1(\gamma_3) &= (1+3)^{6r} (2+3)^{54r^2-6r} \\
&= 4^{6r} 5^{54r^2-6r}. \\
4. \quad M_2(\gamma_3) &= (1 \times 3)^{6r} (2 \times 3)^{54r^2-6r} \\
&= 3^{6r} 6^{54r^2-6r}. \\
5. \quad HM(\gamma_3) &= ((1+3)^2)^{6r} ((2+3)^2)^{54r^2-6r} \\
&= 16^{6r} 25^{54r^2-6r}. \\
6. \quad AZ(\gamma_3) &= \left(\left(\frac{1 \times 3}{1+3-2}\right)^3\right)^{6r} \left(\left(\frac{1 \times 3}{1+3-2}\right)^3\right)^{54r^2-6r} \\
&= \left(\frac{27}{8}\right)^{6r} 8^{54r^2-6r}. \\
7. \quad H(\gamma_3) &= \left(\frac{2}{1+3}\right)^{6r} \left(\frac{2}{2+3}\right)^{54r^2-6r} \\
&= \left(\frac{1}{2}\right)^{6r} \left(\frac{2}{5}\right)^{54r^2-6r}. \\
8. \quad SC(\gamma_3) &= \left(\frac{1}{\sqrt{1+3}}\right)^{6r} \left(\frac{1}{\sqrt{2+3}}\right)^{54r^2-6r} \\
&= \left(\frac{1}{2}\right)^{6r} \left(\frac{\sqrt{5}}{5}\right)^{54r^2-6r}. \\
9. \quad GA(\gamma_3) &= \left(2\left(\frac{\sqrt{1 \times 3}}{1+3}\right)\right)^{6r} \left(2\left(\frac{\sqrt{2 \times 3}}{2+3}\right)\right)^{54r^2-6r} \\
&= \left(\frac{\sqrt{3}}{2}\right)^{6r} \left(\frac{2\sqrt{6}}{5}\right)^{54r^2-6r}. \\
10. \quad IS(\gamma_3) &= \left(\frac{1 \times 3}{1+3}\right)^{6r} \left(\frac{2 \times 3}{2+3}\right)^{54r^2-6r} \\
&= \left(\frac{3}{4}\right)^{6r} \left(\frac{6}{5}\right)^{54r^2-6r}.
\end{aligned}$$

$$\begin{aligned}
11. \quad AZI(\gamma_3) &= \left(\frac{1+9}{\sqrt{1 \times 3}} \right)^{6r} \left(\frac{4+9}{\sqrt{2 \times 3}} \right)^{54r^2-6r} \\
&= \left(\frac{10}{3} \right)^{6r} \left(\frac{13}{6} \right)^{54r^2-6r} . \\
12. \quad Alb(\gamma_3) &= (2)^{6r} (1)^{54r^2-6r} \\
&= 2^{6r} . \\
13. \quad ABC(\gamma_3) &= \left(\sqrt{\frac{(1+3-2)}{(1 \times 3)}} \right)^{6r} \left(\sqrt{\frac{(2+3-2)}{(2 \times 3)}} \right)^{54r^2-6r} \\
&= \left(\frac{\sqrt{6}}{3} \right)^{6r} \left(\frac{\sqrt{2}}{2} \right)^{54r^2-6r} .
\end{aligned}$$

□

4.3. Degree-Based Entropy Measures

This section explains how to calculate entropy values using Shannon's method by creating the probability function using degree-based topological indices. To calculate probabilistic entropy, we utilised Shannon's model because it is the most popular approach [7,11,13,31]. The entropy measured using that topological index X is given by

$$E_X(\gamma) = \log(X(\gamma)) - \frac{1}{X(\gamma)} \left(\sum_{uv \in E(\gamma)} f(e) \log(f(e)) \right)$$

By using the first Zagreb index to calculate the entropy value for the TriCF structure, the calculation procedure is illustrated.

First Zagreb entropy for linear chain TriCF molecular graph,

$$\begin{aligned}
EM_1(\gamma_1) &= \log(M_{1\gamma_1}) - \frac{1}{M_{1\gamma_1}} \sum_{uv \in \mathcal{Q}(\gamma_1)} (d_{\mathcal{Q}}(u) + d_{\mathcal{Q}}(v)) \log(d_{\mathcal{Q}}(u) + d_{\mathcal{Q}}(v)) \\
&= \log(178r + 86) - \frac{1}{178r + 86} ((2r + 4)(1 + 3) \log(1 + 3)) + (34r + 14)(2 + 3) \log(2 + 3) \\
&\log(178r + 86) - \frac{8(2r + 4) \log(2) + 5(34r + 14) \log(5)}{178r + 86}
\end{aligned}$$

After simplifying this, we obtain

$$EM_1(\gamma_1) = \frac{(89r + 43) \log(89r + 43) + (81r + 27) \log(2) + (-85r - 35) \log(5)}{89r + 43}.$$

The general entropy expression of each TriCF chemical network would be too long to provide as theorems. By using the above mentioned procedure, it is simple to construct any degree-based entropies expression with regard to each topological index.

5. Numerical Computation

The numerical results of degree-based topological descriptors utilizing entropy measures generated for three different TriCF structures are shown in this section, with the values of the variable r & s ranging from 1 to 10. For a graphical comparison of the computed topological descriptors, these values were plotted using the Origin 2020 b software. Tables 4–6 summarize the results. Figure 5 shows this trend as three-dimensional graphical representations. The difference between each topological index for a specific structure can be seen in these 3D plots. The 3D plots can also be used to compare the behavior of a given index for the three different structures that are being researched in this article. The following tables and figures examine various entropies in numerical and graphical forms for all the different structures of the TriCF molecular graph.

Table 4. Numerical values for degree-based entropies of linear chain TriCF structure.

r	$ER(\gamma_1)$	$ERR(\gamma_1)$	$EM_1(\gamma_1)$	$EM_2(\gamma_1)$	$EHM(\gamma_1)$	$EAZ(\gamma_1)$	$EH(\gamma_1)$	$ESC(\gamma_1)$	$EGA(\gamma_1)$	$EIS(\gamma_1)$	$EAZI(\gamma_1)$	$EAlb(\gamma_1)$
1	4.5044	5.6303	3.9868	3.9726	3.9812	3.9658	3.9862	3.9883	3.9866	3.9805	3.9776	3.9557
2	5.2513	6.1719	4.498	4.4866	4.4935	4.4812	4.4975	4.4993	4.4978	4.4929	4.4903	4.4718
3	5.7778	6.5215	4.8347	4.8244	4.8306	4.8196	4.8342	4.8358	4.8345	4.8301	4.8277	4.8107
4	6.1886	6.78	5.0861	5.0765	5.0823	5.072	5.0857	5.0871	5.0859	5.0818	5.0795	5.0634
5	6.527	6.9853	5.2868	5.2777	5.2832	5.2734	5.2864	5.2878	5.2867	5.2827	5.2805	5.265
6	6.8151	7.1555	5.4539	5.4451	5.4504	5.4409	5.4535	5.4549	5.4538	5.45	5.4478	5.4327
7	7.0662	7.301	5.5971	5.5884	5.5936	5.5844	5.5967	5.598	5.5969	5.5932	5.591	5.5763
8	7.2888	7.4279	5.7222	5.7138	5.7189	5.7098	5.7219	5.7232	5.7221	5.7185	5.7163	5.7018
9	7.4889	7.5406	5.8335	5.8252	5.8302	5.8212	5.8331	5.8344	5.8334	5.8298	5.8277	5.8134
10	7.6706	7.6418	5.9336	5.9254	5.9303	5.9215	5.9332	5.9345	5.9335	5.9299	5.9278	5.9137

Table 5. Numerical values for degree-based entropies of parallelogram TriCF structures.

(r, s)	$ER(\gamma_2)$	$ERR(\gamma_2)$	$EM_1(\gamma_2)$	$EM_2(\gamma_2)$	$EHM(\gamma_2)$	$EAZ(\gamma_2)$	$EH(\gamma_2)$	$ESC(\gamma_2)$	$EGA(\gamma_2)$	$EIS(\gamma_2)$	$EAZI(\gamma_2)$	$EAlb(\gamma_2)$
1	3.174	4.8518	5.5761	5.7236	7.167	6.002	3.1002	3.1974	4.7498	4.1288	4.8203	4.0944
2	4.1165	5.8451	6.5653	6.7262	8.1634	7.0083	4.0707	4.1733	5.7395	5.1257	5.7797	5.037
3	4.7315	6.479	7.1974	7.3639	8.7985	7.6474	4.695	4.7998	6.3718	5.7611	6.3991	5.649
4	5.1945	6.952	7.6695	7.8391	9.2722	8.1235	5.1625	5.2686	6.844	6.235	6.8638	6.1092
5	5.5676	7.3313	8.0482	8.2199	9.6519	8.5048	5.5381	5.6451	7.2227	6.6149	7.2375	6.48
6	5.8805	7.6486	8.365	8.5382	9.9696	8.8235	5.8528	5.9604	7.5396	6.9325	7.5508	6.7912
7	6.1504	7.9216	8.6376	8.812	10.2428	9.0975	6.1238	6.2319	7.8123	7.2059	7.8208	7.0596
8	6.3877	8.1613	8.8771	9.0523	10.4827	9.3381	6.362	6.4705	8.0517	7.4458	8.0582	7.2957
9	6.5996	8.3751	9.0907	9.2665	10.6967	9.5525	6.5745	6.6833	8.2653	7.6598	8.2701	7.5066
10	6.791	8.568	9.2834	9.4599	10.8897	9.746	6.7664	6.8754	8.4581	7.8529	8.4615	7.6971

Table 6. Numerical values for degree-based entropies of hexagonal TriCF structures.

r	$ER(\gamma_3)$	$ERR(\gamma_3)$	$EM_1(\gamma_3)$	$EM_2(\gamma_3)$	$EHM(\gamma_3)$	$EAZ(\gamma_3)$	$EH(\gamma_3)$	$ESC(\gamma_3)$	$EGA(\gamma_3)$	$EIS(\gamma_3)$	$EAZI(\gamma_3)$	$EAlb(\gamma_3)$
1	3.9819	3.984	3.9868	3.9726	3.9812	3.9658	3.9862	3.9883	3.9866	3.9805	3.9776	3.9557
2	5.3714	5.3727	5.3741	5.3669	5.3713	5.3635	5.3738	5.3749	5.374	5.3709	5.369	5.3564
3	6.1836	6.1845	6.1854	6.1806	6.1835	6.1783	6.1852	6.186	6.1854	6.1833	6.1819	6.1731
4	6.7596	6.7603	6.761	6.7573	6.7595	6.7557	6.7608	6.7614	6.7609	6.7593	6.7583	6.7515
5	7.2062	7.2068	7.2074	7.2045	7.2062	7.2031	7.2072	7.2077	7.2073	7.2061	7.2052	7.1997
6	7.5711	7.5716	7.5721	7.5697	7.5711	7.5686	7.572	7.5724	7.5721	7.571	7.5703	7.5656
7	7.8796	7.8801	7.8805	7.8784	7.8796	7.8774	7.8804	7.8807	7.8804	7.8795	7.8789	7.8749
8	7.8796	8.1472	8.1476	8.1457	8.1468	8.1449	8.1475	8.1478	8.1475	8.1467	8.1462	8.1427
9	8.3825	8.3828	8.1476	8.3815	8.3825	8.3808	8.3831	8.3834	8.3831	8.3824	8.3819	8.3788
10	8.5933	8.5936	8.5939	8.5925	8.5933	8.5918	8.5938	8.5941	8.5939	8.5933	8.5928	8.59

6. Conclusions

In this study, degree-based topological indices have been computed using the multiplicative and entropy measures. These indices allow chemists to predict a variety of molecular compound qualities without the need for costly or time-consuming tests. For instance, from Figure 6, reverse Randić has a greater impact on the initial structure than other indices if we analyse the entropy measures. As a result, the computed results may be extremely important in forecasting TriCF system features. This is a novel synthesized lubricant, and so far, no physicochemical properties have been experimentally studied. Therefore, this current study will help the researchers to make further progress. We have also computed the topological indices for this TriCF structure for future utilization. This paper also includes a graphical depiction and a numerical comparison of the computed results, which is helpful for both theoretical chemists and professionals in the field.

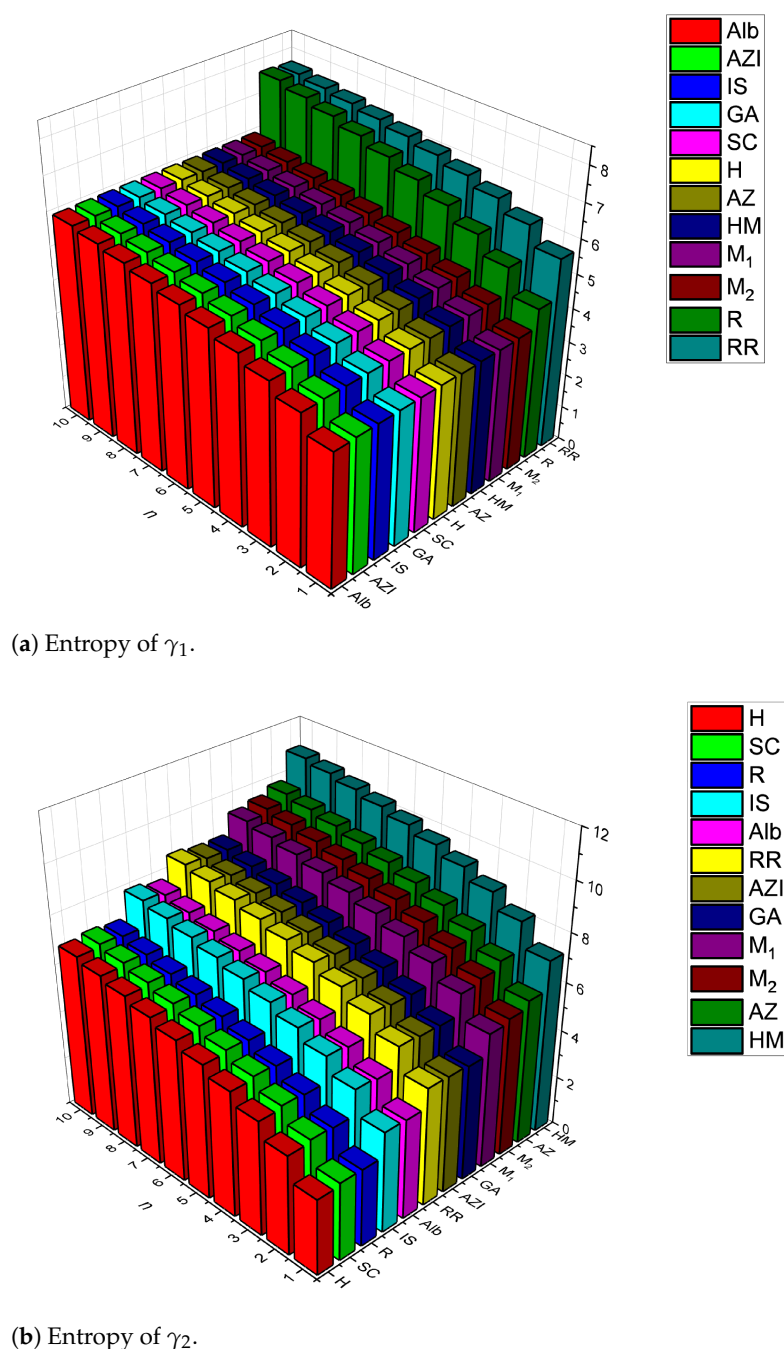
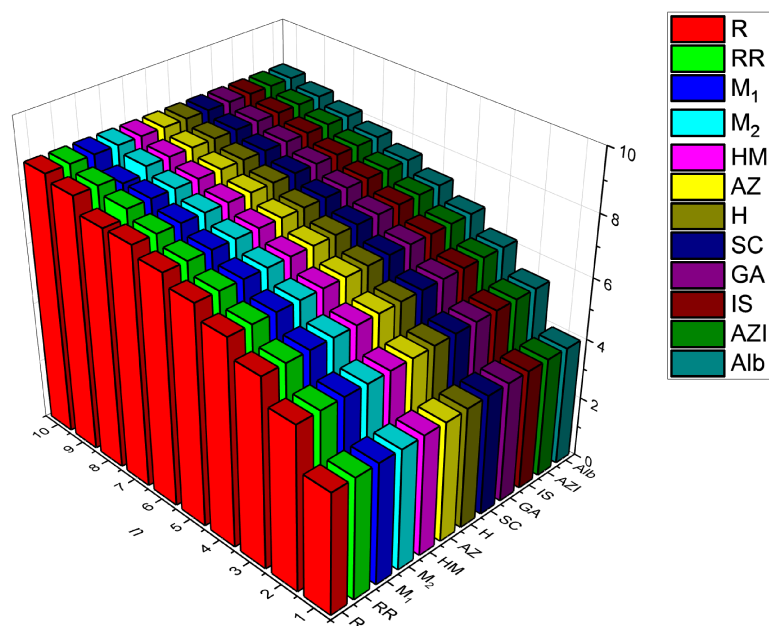


Figure 6. Cont.



(c) Entropy of γ_3 .

Figure 6. Comparison of entropy measures for TriCF structures.

Author Contributions: T.A. contributes for conceptualization, software, methodology and writing original draft. S.R. contributes for supervision, validation, formal analysis, review and editing. All authors have read and agreed to the published version of the manuscript.

Funding: This research work is supported by Vellore Institute of Technology, Vellore- 632014.

Institutional Review Board Statement: Not applicable.

Informed Consent Statement: Not applicable.

Data Availability Statement: Not applicable.

Acknowledgments: The authors wish to thank the management of Vellore Institute of Technology, Vellore- 632014, for their continuous support and encouragement to carry out this research work.

Conflicts of Interest: The authors declare no conflicts of interest.

References

- Yirik, M.A.; Colpan, K.E.; Schmidt, S.; Sorokina, M.; Steinbeck, C. Review on Chemical Graph Theory and Its Application in Computer-Assisted Structure Elucidation. *Chemistry* **2021**, *Preprints*. [\[CrossRef\]](#)
- Hasan, AL-Abayechi, M.M.; AL-Zuhairi, A.J.; AL-Baiati, M.N. Synthesis and Identification of a Novel Hyper Branched Polymers Containing Melamine Derivative. *IOP Conf. Ser. Mater. Sci. Eng.* **2019**, *571*, 012092. [\[CrossRef\]](#)
- Kotresh, T.M.; Ramani, R.; Jana, N.; Minu, S.; Shekar, R.I.; Ramachandran, R. Supermolecular Structure, Free Volume, and Glass Transition of Needleless Electrospun Polymer Nanofibers. *ACS Appl. Polym. Mater.* **2021**, *3*, 3989–4007. [\[CrossRef\]](#)
- Liu, J.-B.; Ali, H.; Shafiq, M.K.; Munir, U. On Degree-Based Topological Indices of Symmetric Chemical Structures. *Symmetry* **2018**, *10*, 619. [\[CrossRef\]](#)
- Balasubramanian, K. Mathematical and Computational Techniques for Drug Discovery: Promises and Developments. *Curr. Top. Med. Chem.* **2018**, *18*, 2774–2799. [\[CrossRef\]](#)
- Wen, P.; Zhang, C.; Yang, Z.; Dong, R.; Wang, D.; Fan, M.; Wang, J. Triazine-Based Covalent-Organic Frameworks: A Novel Lubricant Additive with Excellent Tribological Performances. *Tribol. Int.* **2017**, *111*, 57–65. [\[CrossRef\]](#)
- Rahul, M.P.; Clement, J.; Singh Junias, J.; Arockiaraj, M.; Balasubramanian, K. Degree-Based Entropies of Graphene, Graphyne and Graphdiyne Using Shannon's Approach. *J. Mol. Struct.* **2022**, *1260*, 132797. [\[CrossRef\]](#)
- Huilgol, M.I.; Sriram, V.; Balasubramanian, K. Structure—Activity Relations for Antiepileptic Drugs through Omega Polynomials and Topological Indices. *Mol. Phys.* **2022**, *120*, e1987542. [\[CrossRef\]](#)
- Devillers, J.; Balaban, A.T. *Topological Indices and Related Descriptors in QSAR and QSPAR*; CRC Press: Boca Raton, FL, USA, 2000.
- Balasubramanian, K. Combinatorics, Big Data, Neural Network & AI for Medicinal Chemistry & Drug Administration. *Lett. Drug Des. Discov.* **2021**, *18*, 943–948. [\[CrossRef\]](#)

11. Sabirov, D.S.; Shepelevich, I. S. Information Entropy in Chemistry: An Overview. *Entropy* **2021**, *23*, 1240. [\[CrossRef\]](#)
12. Chaudhry, F.; Shoukat, I.; Afzal, D.; Park, C.; Cancan, M.; Farahani, M. R. M-Polynomials and Degree-Based Topological Indices of the Molecule Copper(I) Oxide. *J. Chem.* **2021**, *2021*, 6679819. [\[CrossRef\]](#)
13. Mowshowitz, A.; Dehmer, M. Entropy and the Complexity of Graphs Revisited. *Entropy* **2012**, *14*, 559–570. [\[CrossRef\]](#)
14. Kavitha, S. R. J.; Abraham, J.; Arockiaraj, M.; Jency, J.; Balasubramanian, K. Topological Characterization and Graph Entropies of Tessellations of Kekulene Structures: Existence of Isentropic Structures and Applications to Thermochemistry, Nuclear Magnetic Resonance, and Electron Spin Resonance. *J. Phys. Chem. A* **2021**, *125*, 8140–8158. [\[CrossRef\]](#)
15. Arockiaraj, M.; Paul, D.; Klavžar, S.; Clement, J.; Tigga, S.; Balasubramanian, K. Relativistic Distance Based and Bond Additive Topological Descriptors of Zeolite RHO Materials. *J. Mol. Struct.* **2022**, *1250*, 131798. [\[CrossRef\]](#)
16. Gutman, I. Degree-Based Topological Indices. *Croat. Chem. Acta* **2013**, *86*, 351–361. [\[CrossRef\]](#)
17. Arockiaraj, M.; Clement, J.; Tratnik, N. Mostar Indices of Carbon Nanostructures and Circumscribed Donut Benzenoid Systems. *Int. J. Quantum Chem.* **2019**, *119*, e26043. [\[CrossRef\]](#)
18. Kanna, M. R.; Mamta, D.; Indumathi, R. S. Computation of Topological Indices of Triglyceride. *Glob. J. Pure Appl. Math.* **2017**, *13*, 1631–1638.
19. Randić, M. Characterization of Molecular Branching. *J. Am. Chem. Soc.* **1975**, *97*, 6609–6615. [\[CrossRef\]](#)
20. Schultz, H.P. Topological Organic Chemistry. 1. Graph Theory and Topological Indices of Alkanes. *J. Chem. Inf. Model.* **1989**, *29*, 227–228. [\[CrossRef\]](#)
21. Kazemi, R. Entropy of Weighted Graphs with the Degree-Based Topological Indices as Weights. *MATCH Commun. MATCH Commun. Math. Comput. Chem* **2016**, *76*, 69–80.
22. Ahmad, A.; Elahi, K.; Hasni, R.; Nadeem, M.F. Computing the Degree Based Topological Indices of Line Graph of Benzene Ring Embedded in P-Type-Surface in 2D Network. *J. Inf. Optimiz. Sci.* **2019**, *40*, 1511–1528. [\[CrossRef\]](#)
23. Wang, S.; Wei, B. Multiplicative Zagreb Indices of K-Trees. *Discret. Appl. Math.* **2015**, *180*, 168–175. [\[CrossRef\]](#)
24. Kulli, V.R. Multiplicative Hyper-Zagreb Indices and Coindices of Graphs: Computing These Indices of Some Nanostructures. *Int. Res. J. Pure Algebra* **2016**, *6*, 342–347.
25. Kulli, V.R.; Stone, B.; Wang, S.; Wei, B. Generalised Multiplicative Indices of Polycyclic Aromatic Hydrocarbons and Benzenoid Systems. *Z. Naturforsch. A* **2017**, *72*, 573–576. [\[CrossRef\]](#)
26. Kwun, Y. C.; Virk, A. R.; Nazeer, W.; Rehman, M. A.; Kang, S. M. On the Multiplicative Degree- Based Topological Indices of Silicon-Carbon Si₂C₃-I [p,q] and Si₂C₃-II. *Symmetry* **2018**, *10*, 320–330. [\[CrossRef\]](#)
27. Bhanumathi, M.; Rani, K.E.J. On Multiplicative Sum Connectivity Index, Multiplicative Randic Index and Multiplicative Harmonic Index of Some Nanostar Dendrimers. *Int. J. Eng. Sci. Adv. Comput. Bio-Technol.* **2018**, *9*, 52–67. [\[CrossRef\]](#)
28. Mahboob, A.; Mahboob, S.; Jaradat, M. M. M.; Nigar, N.; Siddique, I. On Some Properties of Multiplicative Topological Indices in Silicon-Carbon. *J. Math.* **2021**, *2021*, 1–10. [\[CrossRef\]](#)
29. Kulli, R. Multiplicative Connectivity Indices of TUC₄C₈. *J. Math. Comput. Sci.* **2016**, *7*, 599–605.
30. Guangyu, L.; Hussain, S.; Khalid, A.; Ishtiaq, M.; Siddiqui, M.K.; Cancan, M.; Imran, M. Topological Study of Carbon Nanotube and Polycyclic Aromatic Nanostar Molecular Structures. *Polycycl. Aromat. Compd.* **2021**, 1–21. [\[CrossRef\]](#)
31. Hussain, Z.; Ijaz, N.; Tahir, W.; Butt, M.T.; Talib, S. Calculating Degree Based Multiplicative Topological Indices of Alcohol. *SSRN Electron. J.* **2018**. [\[CrossRef\]](#)

Article

Topological Properties and Entropy Calculations of Aluminophosphates

Jeyaraj Sahaya Vijay ¹, Santiago Roy ^{1,*}, Bheeter Charles Beromeo ¹, Mohamad Nazri Husin ^{2,*}, Tony Augustine ¹, R.U. Gobithaasan ² and Michael Easuraja ³

- ¹ School of Advanced Sciences, Vellore Institute of Technology, Vellore 632 014, India; sahayavijay.j@vit.ac.in (J.S.V.); charlesbheeter@vit.ac.in (B.C.B.); tony.augustine@vit.ac.in (T.A.)
² Special Interest Group on Modelling and Data Analytics (SIGMDA), Faculty of Ocean Engineering Technology and Informatics, Universiti Malaysia Terengganu, Kuala Nerus 21030, Terengganu, Malaysia; gr@umt.edu.my
³ Department of Chemistry, Arul Anandar College, Karumathur 625 514, India; easuraja@aactni.edu.in
* Correspondence: roy.santiago@vit.ac.in (S.R.); nazri.husin@umt.edu.my (M.N.H.)

Abstract: Topological indices are invariant numerical quantities of a graph that give facts about the structure of graphs and are found to be very helpful in predicting the physical properties of aluminophosphates. The characteristics of aluminophosphates are similar to the characteristics of zeolites. Two examples of current applications are natural gas dehydration and humidity sensors. Researchers in chemistry and materials science are synthesizing new frameworks. There are many layers and holes in these substances. The technique used to predict natural behaviors among the physicochemical characteristics of chemical molecules in their basic network is known as topological indices. This study explains the vertex version of distance-based topological indices, the entropy of topological indices and their numerical analysis.

Keywords: aluminophosphates; vertex-based molecular descriptors; cut method; Shannon's method; correlation coefficient

MSC: 05C09; 05C92; 92E10



Citation: Vijay, J.S.; Roy, S.; Beromeo, B.C.; Husin, M.N.; Augustine, T.; Gobithaasan, R.U.; Easuraja, M. Topological Properties and Entropy Calculations of Aluminophosphates. *Mathematics* **2023**, *11*, 2443. <https://doi.org/10.3390/math11112443>

Academic Editor: Hilal Ahmad

Received: 21 April 2023

Revised: 17 May 2023

Accepted: 18 May 2023

Published: 25 May 2023



Copyright: © 2023 by the authors. Licensee MDPI, Basel, Switzerland. This article is an open access article distributed under the terms and conditions of the Creative Commons Attribution (CC BY) license (<https://creativecommons.org/licenses/by/4.0/>).

1. Introduction

Aluminophosphate is an essential crystalline microporous material. Due to its well-defined pore structures and high porosities, it has high permeability and selectivity [1,2]. It is available at low prices and provides synthesis and accessibility for various applications. Especially in catalyst preparation, it is used to improve catalyst efficiency and, in process development, to recognize the reaction mechanism [3]. To introduce a particular characteristic, appropriate metals in the periodic table can incorporate aluminophosphates due to their outstanding pore attributes and hydrophilic nature [4]. Accordingly, among solid catalysts, silico aluminophosphate has a worldwide market of billions of USD per annum [5,6]. Moreover, because of water adsorption properties, potential aluminophosphates are available with a superior pore volume greater than 14% in contrast to zeolite frameworks. Therefore, studying their core structure in a thorough conceptual banner is becoming essential to increase aluminophosphates' porosity, efficiency and stability for enhanced applications.

Such aluminophosphate materials can be structurally represented using molecular graphs, in which the vertices stand for atoms and the edges stand for chemical bonds. To extract topological information from such graphs, one can utilize theoretical graph quantifiers, which in turn give valuable functions that have perfect linear relationships with various properties of such materials through graph invariants or, more commonly, structure descriptors.

Quantitative structure–activity relationships (QSAR) and quantitative structure–property relationships (QSPR) can be supported by topological indices, which are among the structural descriptors that provide numerical functions of the structure of a molecule. The derived variables can be used to calculate the chemical and biological properties of the materials. The complex systems of such materials that are difficult to define due to their complexity can be viewed as an objective numerical variable that characterizes them. The numerical variable that describes the networks of these structural applications is called the topological index of a molecular structure. One of the most significant and efficient structural descriptors in the field of advanced materials is the fact that the mathematical functions that can be generated using various graph theoretical approaches can be used to predict the properties of these materials. They are often an addition to quantum chemistry calculations that need a good deal of computing [7–22]. A wide range of indices can be used in research to understand the relationships between structure and properties.

It should be mentioned that very little progress has been made in the inclusion of topological descriptors that are based purely on the connectivity to chemistry-specific characteristics, such as various indicators [23–35], especially for very heavy atoms in such materials for which relativistic impacts are essential.

In a well-known 1948 study [36], the author first introduced the idea of entropy, declaring that the entropy of a probability distribution is known as a measure of unpredictability. Entropy was used to assess the structural details of graphs and chemical networks. Rachhevsky et al. introduced in 1955 the idea of graph entropy based on categorizing vertex orbits [37]. In many disciplines, there has been an increase in the use of graph entropy. Information theory was used in biology and chemistry after initial linguistics and electrical engineering applications. Spontaneous communication is one of the essential innovations [38–43]. Network structural information content was calculated using Shannon’s entropy formula [36] in light of this realization. This technique was used to examine living systems using graphs. Graphs are used to investigate biological and chemical networks [44].

This paper studies a set of weighted topological descriptors for chemical molecules. We also investigated how the perfect linear relationship in QSPR and QSAR models can be improved by assigning optimal weights to the vertices of the structure to obtain a realistic topology. Models that include structural instabilities and other quantum chemistry-derived features that control the overall structural stability of chemical substances have also been explored.

2. Computational Theoretical Technique

A graph $G = (V(G), E(G))$, where $V(G)$ is the set of all the vertices of G and $E(G)$ is the set of all the edges of G . The cardinality of $V(G)$ and $E(G)$ is denoted by $|V(G)| = M$ and $|E(G)| = N$, respectively. The number of edges incident to u is represented by the degree of a vertex u . It is denoted as $d_G(u)$. The length of the shortest uv -path is called the distance $d_G(u, v)$ between two vertices $u, v \in V(G)$. We used $d(v)$ and $d(u, v)$ for $d_G(v)$ and $d_G(u, v)$, respectively, in this study.

To count the vertices and evaluate which quantity is closest to the end vertices of $e = uv$, we must first recall the two numbers based on vertices and edge distance functions.

- $n_u(e) = |t \in V(G) : d(u, t) < d(v, t)|$
- $n_v(e) = |t \in V(G) : d(v, t) < d(u, t)|$

Further, we list the distance-based and bond additive topological indices in Table 1 derived from the below-mentioned quantitative metrics, such as distance and closeness.

Table 1. Vertex version of distance-based molecular descriptors.

Molecular Descriptors	Mathematical Formula
Wiener Index [16]	$WI_v(G) = \sum_{\{u,v\} \subseteq V(G)} d(u,v)$
Vertex–Szeged Index [9]	$Sz_v(G) = \sum_{e=uv \in E(G)} n_u(e)n_v(e)$
Vertex–Padmakar–Ivan Index [11]	$PI_v(G) = \sum_{e=uv \in E(G)} n_u(e) + n_v(e)$
Vertex–Mostar Index [45]	$Mo_v(G) = \sum_{e=uv \in E(G)} n_u(e) - n_v(e) $

With Matlab programming, the provided distance-based and bond additive topological indices could be successfully calculated based on the Djoković–Winkler relationship by finding the equivalence classes of graph structures. For any two edges $e_1 = ab \in E(G)$ and $e_2 = cd \in E(G)$, if $d_G(a,c) + d_G(b,d) \neq d_G(a,d) + d_G(b,c)$ then $e_1 \Theta e_2$ is called a Djoković–Winkler relation Θ [46,47]; these play a key role in our analytical computation. The graph G that may be isometrically embedded into a hypercube is called a partial cube. Bipartite graphs with transitive Djoković–Winkler relation Θ or cut method [48] can be used to describe partial cubes [47]. Let Θ^* -class be the transitive closure of the Djoković–Winkler relation Θ .

The relation Θ is also transitive and hence an equivalence relation if molecular graph G is a partial cube [49]. Let K be a partial cube with its Θ -classes $\mathcal{F}(K) = \{F_1, F_2, \dots, F_r\}$. Let $TI \in \{WI_v, WI_e, W_{ve}, Sz_v, Sz_e, Sz_{ve}, PI_v, S, Gut, Mo, Mo_e, Mo_t, w^+ Mo, w^+ Mo_e, w^+ Mo_t, w^* Mo, w^* Mo_e, w^* Mo_t\}$, Then $TI(K) = \sum_{i=1}^k (TI(K/F_i))$ [49].

In this article, we use the following methods to compute distance-based molecular descriptors (see Table 1): [8,49,50]

1. $WI_v(G/F_i) = n_1(F_i)n_2(F_i)$
2. $Sz_v(G/F_i) = |F_i|(n_1(F_i)n_2(F_i))$
3. $PI_v(G/F_i) = |F_i|(n_1(F_i) + n_2(F_i))$
4. $Mo_v(G/F_i) = |F_i||n_1(F_i) - n_2(F_i)|$

3. Results and Discussion

This study discusses aluminophosphate-based molecular sieve structures and their perfect linear relationships with molecular descriptors. The high selectivity, more significant adsorption velocity, higher strength and increased anti-pollution ability produced by the shape and structural optimization increase the consumption effects of the molecular sieve.

Being the first extra-large-pore crystalline material ever made, the extra-large VPI-5, AIPO molecular sieve with 18-ring channels was discovered. The chain-building units used to build VPI-5 and AIPO- H_2 contain octahedral Al atoms (coordinated with four framework oxygens and two water molecules). The modest number of extra-large-pore microporous materials with 16-ring channels is very noteworthy. The synthesis of ITQ-51, a previously unreported extra-large-pore silico aluminophosphate (SAPO) with 16 ring openings, using the bulky aromatic proton sponge DMAN as an OSDA, is presented by Martinez-Franco et al. [51].

The pore openings of aluminophosphate-based molecular sieve structures T12MR (see Figure 1a), T16MR (see Figure 1b) and VPI-5 (see Figure 1c) [51] seem like n mesh. The layer is placed in an n, l, k -dimensional mesh known as a molecular sieve hexagonal mesh $mSHL(n, l, k)$. This layer can be easily stretched to several layers, as shown in Figure 2, and is denoted G , where G is considered a molecular sieve hexagonal mesh $mSHL(n, l, k)$ in this study.

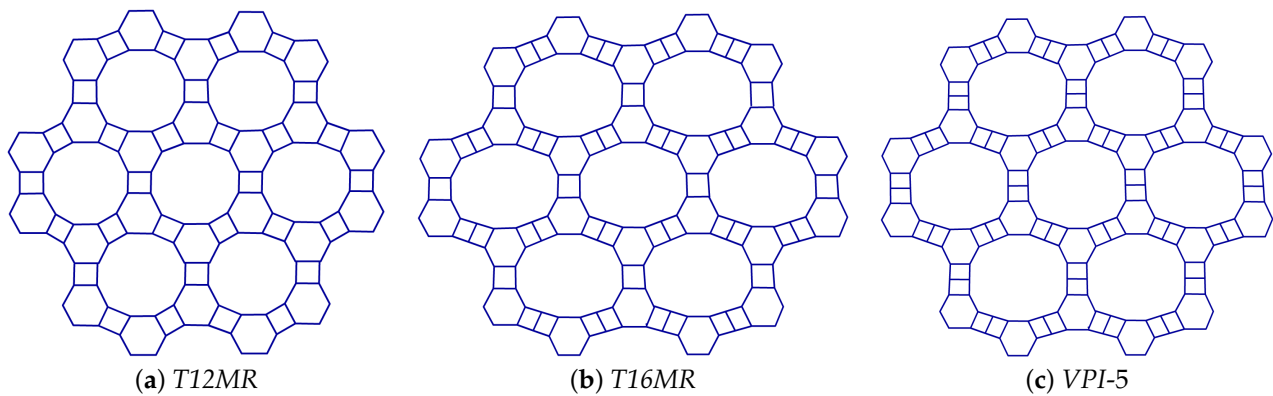


Figure 1. Aluminophosphate-based molecular sieve structures.

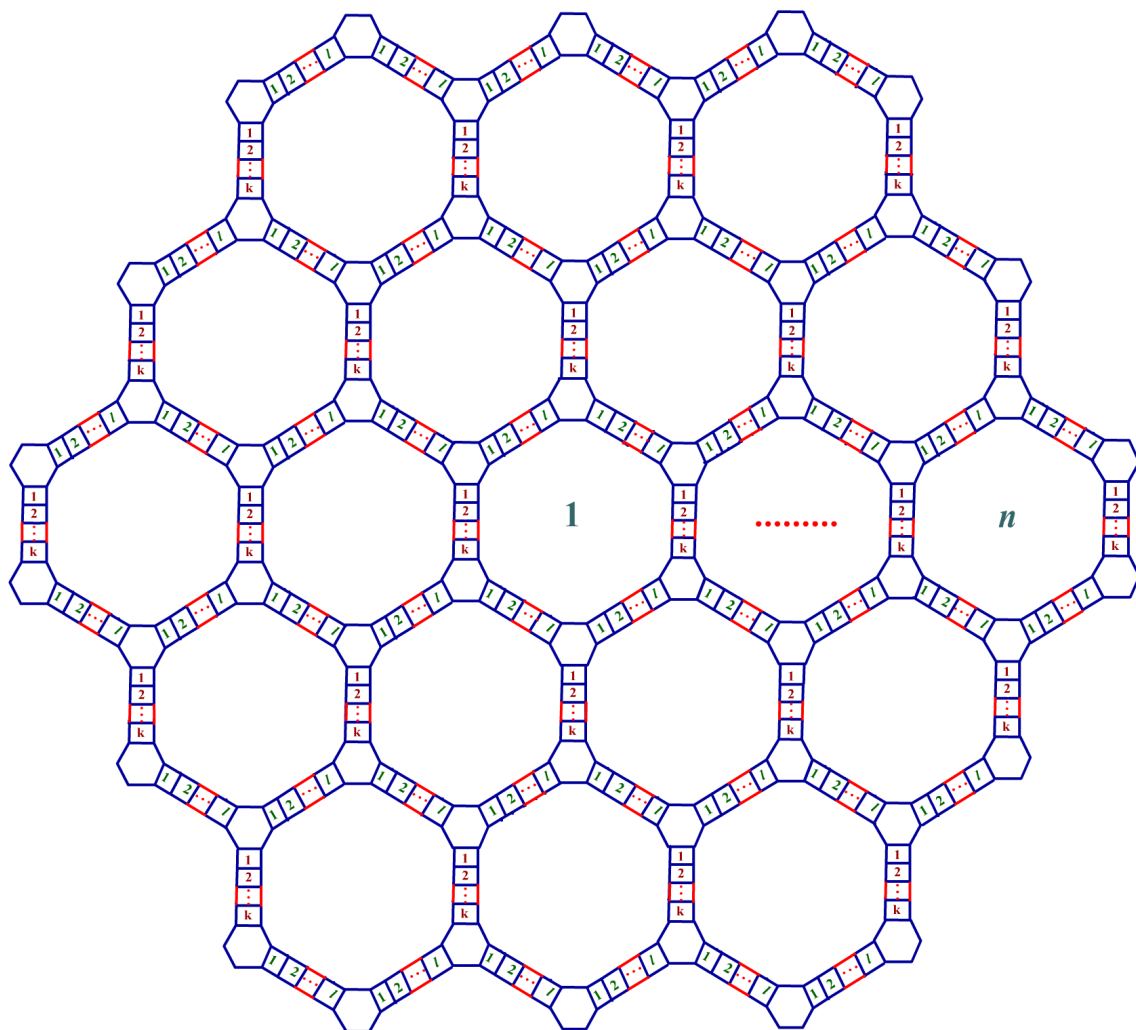


Figure 2. Aluminophosphate-based molecular sieve structure growth $mSHL(n, l, k)$.

3.1. Vertex Distance-Based Topological Indices

In this section, we present an analytical computation of some vertex versions of distance-based topological descriptors for molecular sieve hexagonal mesh $mSHL(n, l, k)$. We used Matlab version 2019 software for analytical computation and also used Flash 8 to construct molecular structure in this study.

Theorem 1. Let G be a molecular sieve hexagonal mesh $mSHL(n, l, k)$. Then

$$W_v(G) = \frac{2n}{45}(246k^3n^4 - 270k^3n^3 + 100k^3n^2 - 15k^3n - k^3 + 1476k^2ln^4 - 1230k^2ln^3 + 240k^2ln^2 + 60k^2ln - 6k^2l + 2754k^2n^4 - 1260k^2n^3 - 90k^2n^2 + 90k^2n - 9k^2 + 2952kl^2n^4 - 2265kl^2n^3 + 150kl^2n^2 + 285kl^2n - 42kl^2 + 11016kl n^4 - 3870kl n^3 - 1620kl n^2 + 450kl n + 144kl + 9882kn^4 + 1845kn^3 - 1630kn^2 - 345kn + 88k + 1968l^3n^4 - 1770l^3n^3 + 440l^3n^2 + 30l^3n - 8l^3 + 11,016l^2n^4 - 4455l^2n^3 - 990l^2n^2 + 405l^2n + 54l^2 + 19764ln^4 + 3690ln^3 - 3260ln^2 - 690ln + 176l + 11502n^4 + 9585n^3 + 1800n^2 - 270n - 72)$$

$$Sz_v(G) = \frac{n}{60(-1)^k}(174(-1)^kk - 195(-1)^{kn}n - 45(-1)^{3n}(-1)^k + 348(-1)^{kl} + 2070(-1)^{kn} - 810(-1)^{kn}n^2 - 1215(-1)^{kn}n^3 + 402(-1)^k - 30(-1)^{k^2} + 10(-1)^{k^3} - 204(-1)^{kl^2} - 76(-1)^{kl^3} - 45(-1)^k(-1)^n + 9120(-1)^{kn^2} + 29,700(-1)^{kn^3} + 81648(-1)^{kn^4} + 87480(-1)^{kn^5} - 288(-1)^{kkl} + 360(-1)^{kkn} + 100(-1)^{kln} - 45(-1)^{3n}(-1)^{k^2} + 15(-1)^{3n}(-1)^{k^3} - 90(-1)^{3n}(-1)^{kl^2} + 30(-1)^{3n}(-1)^{kl^3} + 270(-1)^{3n}(-1)^{kn^2} + 2025(-1)^{3n}(-1)^{kn^3} + 195(-1)^{kn}(-1)^{kn} + 810(-1)^{kn}kn^2 - 45(-1)^{kn}k^2n + 405(-1)^{kn}kn^3 - 45(-1)^{kn}k^3n - 60(-1)^{kn}l^2n - 1620(-1)^{kn}ln^3 - 240(-1)^{kl^2} - 96(-1)^{kl^2}l + 45(-1)^k(-1)^nk - 2760(-1)^{kkn^2} + 120(-1)^{k^2}n - 5870(-1)^{kkn^3} + 120(-1)^{k^3}n + 22476(-1)^{kkn^4} + 10(-1)^{k^4}n + 87480(-1)^{kkn^5} + 90(-1)^k(-1)^nl - 7520(-1)^{kln^2} + 3240(-1)^{kl^2}n - 10120(-1)^{kln^3} + 120(-1)^{kl^3}n + 54672(-1)^{kln^4} + 174960(-1)^{kln^5} - 180(-1)^k(-1)^nn + 810(-1)^{kn}(-1)^{kn^2} + 1215(-1)^{kn}(-1)^{kn^3} + 90(-1)^{kn}k^2n^2 + 675(-1)^{kn}k^2n^3 - 90(-1)^{kn}k^3n^2 + 135(-1)^{kn}k^3n^3 + 360(-1)^{kn}l^2n^2 - 540(-1)^{kn}l^2n^3 + 45(-1)^{3n}(-1)^{kk} - 45(-1)^k(-1)^nk^2 - 440(-1)^{k^2}n^2 + 15(-1)^k(-1)^nk^3 + 950(-1)^{k^2}n^3 - 520(-1)^{k^3}n^2 - 8060(-1)^{k^2}n^4 - 10(-1)^{k^3}n^3 + 160(-1)^{k^4}n^2 + 29160(-1)^{k^2}n^5 - 540(-1)^{k^3}n^4 - 630(-1)^{k^4}n^3 + 3240(-1)^{k^3}n^5 + 540(-1)^{k^4}n^4 + 90(-1)^{3n}(-1)^{kl} - 90(-1)^k(-1)^nl^2 + 440(-1)^{kl^2}n^2 + 30(-1)^k(-1)^nl^3 - 8940(-1)^{kl^2}n^3 + 200(-1)^{kl^3}n^2 - 36896(-1)^{kl^2}n^4 + 7380(-1)^{kl^3}n^3 + 116640(-1)^{kl^2}n^5 - 24704(-1)^{kl^3}n^4 + 25920(-1)^{kl^3}n^5 - 180(-1)^{3n}(-1)^{kn} + 270(-1)^k(-1)^n^2 + 2025(-1)^k(-1)^n^3 + 285(-1)^{kn}kn + 180(-1)^{kn}ln + 80(-1)^{kl^2}n^2 - 1480(-1)^{k^2}ln^2 - 120(-1)^{k^2}l^2n + 11720(-1)^{kl^2}n^3 + 4700(-1)^{k^2}ln^3 + 960(-1)^{k^3}ln^2 - 38000(-1)^{kl^2}n^4 - 13904(-1)^{k^2}ln^4 - 2520(-1)^{k^3}ln^3 + 38880(-1)^{kl^2}n^5 + 19440(-1)^{k^2}ln^5 + 2160(-1)^{k^3}ln^4 - 180(-1)^{3n}(-1)^{kkn} - 1170(-1)^k(-1)^nkn^2 + 30(-1)^k(-1)^nk^2n + 675(-1)^k(-1)^nkn^3 - 60(-1)^k(-1)^nk^3n - 360(-1)^{3n}(-1)^{kln} - 2340(-1)^k(-1)^nln^2 + 570(-1)^k(-1)^nl^2n + 1350(-1)^k(-1)^nl^3n - 330(-1)^k(-1)^nl^3n - 240(-1)^{kn}kl n - 90(-1)^{kn}(-1)^{k^2}n^2 - 675(-1)^{kn}(-1)^{k^2}n^3 + 90(-1)^{kn}(-1)^{k^3}n^2 - 135(-1)^{kn}(-1)^{k^3}n^3 - 360(-1)^{kn}(-1)^{kl^2}n^2 + 540(-1)^{kn}(-1)^{kl^2}n^3 + 3680(-1)^{kkl}n + 960(-1)^{k^2}l^2n^2 - 2520(-1)^{k^2}l^2n^3 + 2160(-1)^{k^2}l^2n^4 - 1170(-1)^{3n}(-1)^{kkn^2} + 30(-1)^{3n}(-1)^{k^2}n + 675(-1)^{3n}(-1)^{kkn^3} - 60(-1)^{3n}(-1)^{k^3}n - 150(-1)^k(-1)^nk^2n^2 - 225(-1)^k(-1)^nk^2n^3 + 90(-1)^k(-1)^nk^3n^2 - 75(-1)^k(-1)^nk^3n^3 - 2340(-1)^{3n}(-1)^{kl^2}n + 570(-1)^{3n}(-1)^{kl^2}n + 1350(-1)^{3n}(-1)^{kl^3}n - 330(-1)^{3n}(-1)^{kl^3}n - 240(-1)^k(-1)^nl^2n^2 - 900(-1)^k(-1)^nl^2n^3 + 960(-1)^k(-1)^nl^3n^2 - 600(-1)^k(-1)^nl^3n^3 - 285(-1)^{kn}(-1)^{kkn} - 180(-1)^{kn}(-1)^{kln} + 360(-1)^{kn}kl n^2 + 60(-1)^{kn}kl^2n + 60(-1)^{kn}k^2ln + 1080(-1)^{kn}kl n^3 + 800(-1)^{kkl}n^2 + 520(-1)^{kkl^2}n + 700(-1)^{k^2}ln - 8720(-1)^{kkl}n^3 - 120(-1)^{k^3}ln - 41552(-1)^{kkl}n^4 + 116640(-1)^{kkl}n^5 - 180(-1)^k(-1)^nkn - 360(-1)^k(-1)^nln - 150(-1)^{3n}(-1)^{k^2}n^2 - 225(-1)^{3n}(-1)^{k^2}n^3 + 90(-1)^{3n}(-1)^{k^3}n^2 - 75(-1)^{3n}(-1)^{k^3}n^3 - 240(-1)^{3n}(-1)^{kl^2}n^2 - 900(-1)^{3n}(-1)^{kl^2}n^3 + 960(-1)^{3n}(-1)^{kl^3}n^2 - 600(-1)^{3n}(-1)^{kl^3}n^3 - 810(-1)^{kn}(-1)^{kkn^2} + 45(-1)^{kn}(-1)^{k^2}n - 405(-1)^{kn}(-1)^{kkn^3} + 45(-1)^{kn}(-1)^{k^3}n + 60(-1)^{kn}(-1)^{kl^2}n - 360(-1)^{kn}kl^2n^2 + 1620(-1)^{kn}(-1)^{kl^3}n - 360(-1)^{kn}k^2ln^2 + 540(-1)^{kn}kl^2n^3 + 540(-1)^{kn}k^2ln^3 + 240(-1)^{kn}(-1)^{kkl}n + 1020(-1)^k(-1)^nkl n + 1680(-1)^{3n}(-1)^{kl^2}n^2 + 780(-1)^{3n}(-1)^{k^2}ln^2 - 900(-1)^{3n}(-1)^{kl^2}n^3 - 450(-1)^{3n}(-1)^{k^2}ln^3 - 360(-1)^{kn}(-1)^{kkl}n^2 - 60(-1)^{kn}(-1)^{kl^2}n - 60(-1)^{kn}(-1)^{k^2}ln - 1080(-1)^{kn}(-1)^{kkl}n^3 + 1020(-1)^{3n}(-1)^{kkl}n + 120(-1)^k(-1)^nkl n^2 - 300(-1)^k(-1)^nkl^2n - 210(-1)^k(-1)^nk^2ln - 900(-1)^k(-1)^nkl n^3 + 360(-1)^{kn}(-1)^{kl^2}n^2 + 360(-1)^{kn}(-1)^{k^2}ln^2 - 540(-1)^{kn}(-1)^{kl^2}n^3 - 540(-1)^{kn}(-1)^{k^2}ln^3 + 120(-1)^{3n}(-1)^{kkl}n^2 - 300(-1)^{3n}(-1)^{kl^2}n - 210(-1)^{3n}(-1)^{k^2}ln - 900(-1)^{3n}(-1)^{kkl}n^3 +$$

$$1680(-1)^k(-1)^n k l^2 n^2 + 780(-1)^k(-1)^n k^2 l n^2 - 900(-1)^k(-1)^n k l^2 n^3 - 450(-1)^k(-1)^n k^2 l n^3$$

$$PI_v(G) = \frac{n}{2(-1)^k} (9n - 2l - k + 3kn + 6ln + 3)(3(-1)^{3n}(-1)^k + (-1)^{kn}k - 4(-1)^k l + 12(-1)^k n - (-1)^{kn} + (-1)^{kn}(-1)^k + 6(-1)^k - 2(-1)^k k^2 + 3(-1)^k(-1)^n + 108(-1)^k n^2 - 16(-1)^k k n - 24(-1)^k l n - (-1)^{kn}(-1)^k k - (-1)^k(-1)^n k + 36(-1)^k k n^2 + 4(-1)^k k^2 n - 2(-1)^k(-1)^n l + 72(-1)^k l n^2 - (-1)^{3n}(-1)^k k - 2(-1)^{3n}(-1)^k l)$$

$$Mo_v(G) = \frac{1}{2} (2k^2 n - 4kn - 8ln - k^2 - 2l^2 - 2(-1)^n k - 80kn^2 - 72kn^3 + 324kn^4 - 4(-1)^n l - 160ln^2 + 12l^2 n - 144ln^3 + 648ln^4 + 24(-1)^n n + 3(-1)^n + 12n^2 + 84n^3 + 486n^4 + 2k + (-1)^n k^2 - 32k^2 n^2 - 4k^2 n^3 + 54k^2 n^4 + 4l - 8(-1)^l n^2 + 2(-1)^n l^2 + 16(-1)^l n^3 - 84l^2 n^2 - 88l^2 n^3 + 216l^2 n^4 - 36n + 36(-1)^n n^2 - 40kl n^2 - 160kl n^3 + 216kl n^4 - 4(-1)^n kn - 8(-1)^n ln - 4(-1)^n l^2 n + 16kl n - 16(-1)^l k^2 n^2 + 32(-1)^l k^2 n^3 + 2k^2 n - 4(-1)^n k^2 n^2 + 8l^2 n - 16(-1)^n l^2 n^2 - 8(-1)^n kln + 8kln - 16(-1)^n kln^2 - 3).$$

Proof. Let G be a molecular sieve hexagonal mesh $mSHL(n, l, k)$. Here the total number of vertices of G is denoted $M = 6n - 2kn - 4ln + 6kn^2 + 12ln^2 + 18n^2$ and the total number of edges of G is denoted $N = n^2(9k + 27) - l(-18n^2 + 6n) - n(3k - 3)$. The graph G that may be isometrically embedded into a hypercube is called a partial cube. Bipartite graphs with transitive Djoković–Winkler relation Θ or cut method can be used to describe partial cubes. Let Θ^* -class be the transitive closure of the Djoković–Winkler relation Θ .

Throughout this paper, we discussed two types of Θ^* -classes F_{mi} and F_{mi}^* on G , where $1 \leq m \leq 3$ are depicted in Figure 3. We show different directions of Θ^* -classes $Dd(Th)$ on $mSHL(2, 1, 1)$ in Figure 4. By applying $Dd(Th)$ on G , G is converted to quotient graphs Q , which is a complete bipartite graph K_2 (see Figure 5). Let $a_j b_j \in K_2$ and let $h(i)$ denotes the number of cut edges in G . To complete the analytical computation by using all mentioned Θ^* -classes (see Figure 4), we now divide the Θ^* -classes of G into two cases.

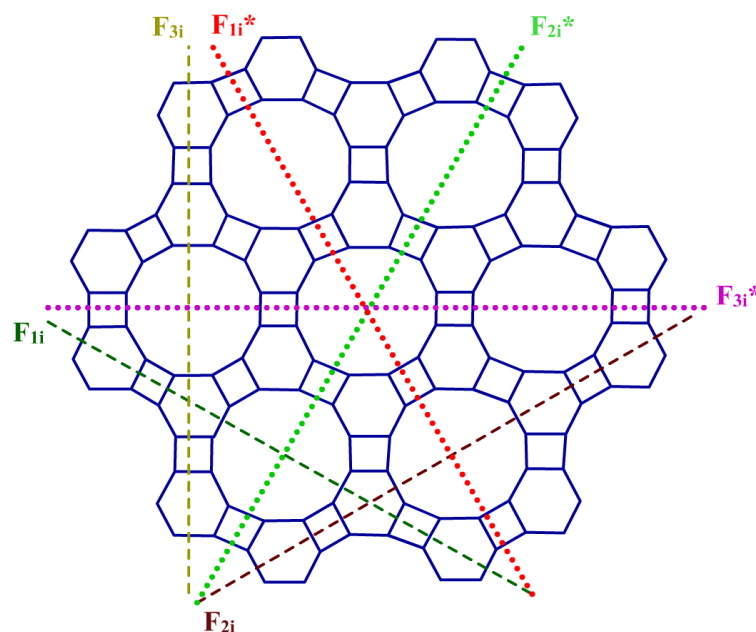


Figure 3. Two types of Θ^* -class F_{fi} and F_{fi}^* .

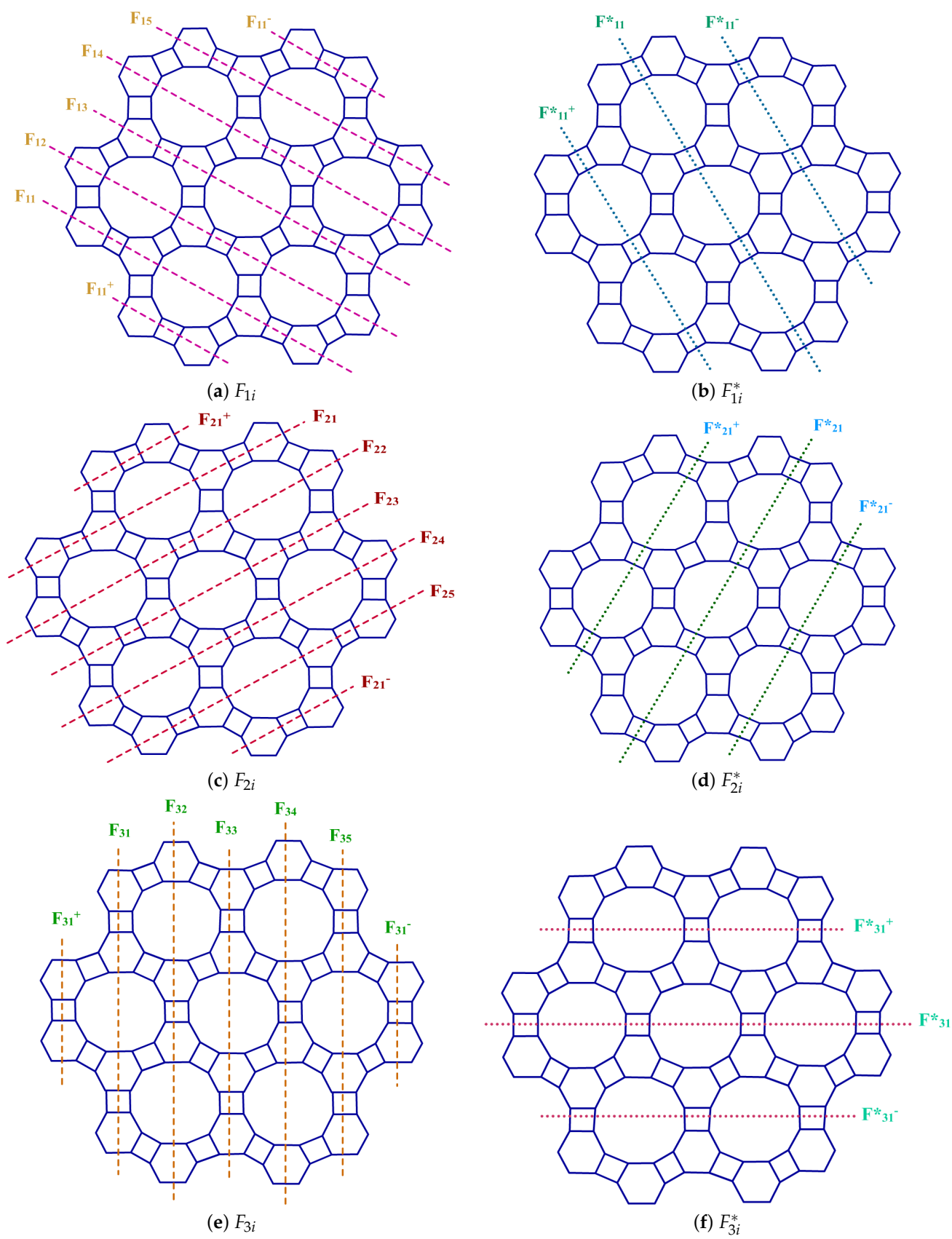


Figure 4. Different directions of Θ^* -classes.

Figure 5. Quotient graph Q .

Case (i): F_{mi} on G ; $\{F_{mi}|1 \leq m \leq 3\}$, $\{F_{mi}|1 \leq i \leq n-1\}$, $\{F_{mi}|n \leq i \leq 3n\}$.

For $1 \leq j \leq 4$, $1 \leq i \leq 4$, the vertex-weighted a_j , b_j and the strength-weighted $h(i)$ values on vertices of Q are defined below:

$$a_1 = (k+2l+3)i^2 + (2-l-k)i$$

$$a_2 = i(n(2k+6) + l(4n-1) + 1) - n(k-1) - 2ln^2 - n^2(k+3)$$

$$a_3 = (k+2l+3)i^2 + (2-2l)i$$

$$a_4 = i(4ln - k + n(2k+6) + 1) - l(2n^2 + 2n) + n(k+1) - n^2(k+3)$$

$$b_j = M - a_j, \text{ where } 1 \leq j \leq 4.$$

$$h(1) = li + 3i \quad h(2) = \frac{((-1)^i + 1)}{2}(3n - l + ln + 1) - \frac{((-1)^i - 1)}{2}(3n + ln)$$

$$h(3) = ki + 3i \quad h(4) = \frac{((-1)^i + 1)}{2}(3n - k + kn + 1) - \frac{((-1)^i - 1)}{2}(3n + kn)$$

Case (ii): F_{mi}^* on G ; $\{F_{mi}^*|1 \leq m \leq 3\}$, $\{F_{mi}^*|1 \leq j \leq n-1, (j-1)l+1 \leq i \leq jl\}$, $\{F_{mi}^*|nl-l+1 \leq i \leq nl\}$, $\{F_{mi}^*|1 \leq j \leq n-1, (j-1)k+1 \leq i \leq jk\}$ and $\{F_{mi}^*|nk-k+1 \leq i \leq nk\}$

For $5 \leq j \leq 8$, $5 \leq i \leq 6$, the vertex-weighted a_j , b_j and strength-weighted $h(i)$ values on vertices of Q are defined below:

$$a_5 = l(2j^2 - 2j + n(4j-2)) - (2j+2n)(l(j-1) - i + 1) + n(j(2k+6) + 2) - j(k-3) + j^2(k+3)$$

$$a_6 = n^2(3k+9) - l(-6n^2 + 4n) - n(k-5) + n(4i+4l-4ln-4)$$

$$a_7 = n(j(4l+6) + 2) - (2j+2n)(k(j-1) - i + 1) + j^2(2l+3) + k(j^2 - j + n(2j-2)) - j(2l-3)$$

$$a_8 = n^2(6l+9) - k(-3n^2 + 3n) + n(4i+4k-4kn-4) - n(2l-5)$$

$$b_j = M - a_j \text{ where } 5 \leq j \leq 8$$

$$h(5) = 2n + 2j \quad h(6) = 4n$$

By symmetry, we have $F_{mi^+} = F_{mi^-}$ and $F_{mi^+}^* = F_{mi^-}^*$, and $1 \leq m \leq 3$ (see Figure 4). Define,

$$\begin{aligned} (X(G), \circ) &= 2 \sum_{i=1}^{n-1} 2h(1)(a_1 \circ b_1) + h(3)(a_3 \circ b_3) + \sum_{i=n}^{3n} 2h(2)(a_2 \circ b_2) + h(4)(a_4 \circ b_4) + \\ &2 \left[2 \sum_{j=1}^{n-1} \sum_{i=(j-1)l+1}^{jl} h(5)(a_5 \circ b_5) + \sum_{i=ln-l+1}^{ln} h(6)(a_6 \circ b_6) \right] + 2 \sum_{j=1}^{n-1} \sum_{i=(j-1)k+1}^{jk} h(5)(a_7 \circ b_7) \\ &+ \sum_{i=kn-k+1}^{kn} h(6)(a_8 \circ b_8), \text{ where } (X, \circ) = (W_v, \times), (Sz_v, \times), (PI_v, +) \text{ and when } \\ (X, \circ) &= (W_v, \times), h(i) = 1, \text{ for } 1 \leq i \leq 6. \end{aligned}$$

$$\begin{aligned} Y(G) &= 2 \sum_{i=1}^{n-1} 2h(1)(b_1 - a_1) + h(3)(b_3 - a_3) + \sum_{i=n}^{2n-1} 2h(2)(b_2 - a_2) + h(4)(b_4 - a_4) + \\ &2 \left[2 \sum_{j=1}^{n-1} \sum_{i=(j-1)l+1}^{jl} h(5)(b_5 - a_5) + \sum_{i=\frac{1}{2}(n-l+ln+1)}^{\frac{1}{2}(n)(l+1)} h(6)(b_6 - a_6) + \sum_{i=\frac{1}{2}(ln-l+2)}^{\frac{ln}{2}} h(6)(b_6 - a_6) \right] \\ &+ 2 \sum_{j=1}^{n-1} \sum_{i=(j-1)k+1}^{jk} h(5)(b_7 - a_7) + \sum_{i=\frac{1}{2}(n-k+kn+1)}^{\frac{1}{2}(n)(k+1)} h(6)(b_8 - a_8) + \sum_{i=\frac{1}{2}(kn-k+2)}^{\frac{kn}{2}} h(6)(b_8 - a_8). \end{aligned}$$

Further, an analytical computation of $(X(G), \circ)$ and $Y(G)$ yields the results of Theorem 1.

□

3.2. Vertex Degree-Based Topological Indices

In this section, we implement degree-based molecular descriptors of G . Let G be broken into three different edge sets using the methodology of edge set partition (ESP) of molecular descriptors. For clarity, the ESPs of $mSHL(2, 1, 1)$ are shown in Figure 6.

The ESPs of G are $|esp(2, 2)| = 6n$, $|esp(2, 3)| = 12n$, $|esp(3, 3)| = ((18n^2 - 6n)l + (9k + 27)n^2 - (3k + 15)n)$.

The degree-based molecular descriptors [52–59] presented in Table 2 will help chemists to find the closure values of physiochemical properties by using statistical correlation.

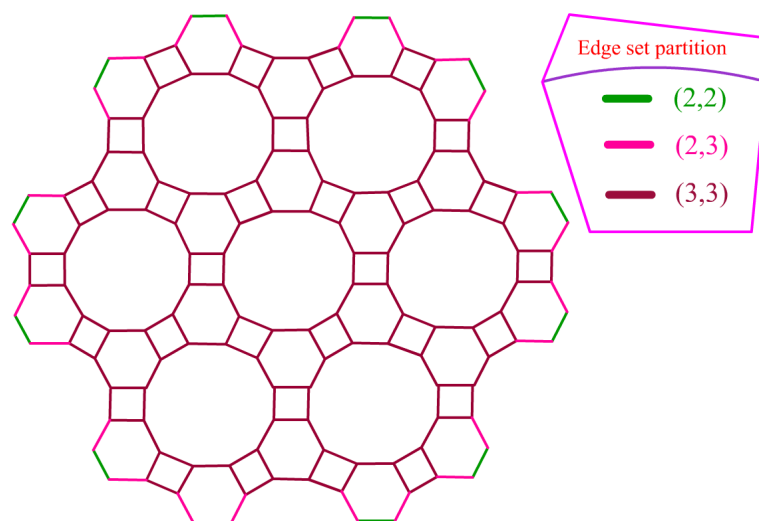


Figure 6. Edge set partitions (ESPs).

Table 2. Different types of vertex versions of degree-based molecular descriptors.

Molecular Descriptors	Mathematical Formula
First Zagreb Index	$M_1(G) = \sum_{uv \in E(G)} [d_u + d_v]$
Second Zagreb Index	$M_2(G) = \sum_{uv \in E(G)} [d_u \times d_v]$
Reduced Second Zagreb Index	$RM_2(G) = \sum_{uv \in E(G)} [(d_u - 1)(d_v - 1)]$
Hyper Zagreb Index	$HM(G) = \sum_{uv \in E(G)} [d_u + d_v]^2$
Augmented Zagreb Index	$AZ(G) = \sum_{uv \in E(G)} \left[\frac{d_u \times d_v}{d_u + d_v - 2} \right]^3$
Randić Index	$R(G) = \sum_{uv \in E(G)} \left[\frac{1}{\sqrt{d_u d_v}} \right]$
Reciprocal Randić Index	$RR(G) = \sum_{uv \in E(G)} [\sqrt{d_u d_v}]$
Reduced Reciprocal Randić Index	$RRR(G) = \sum_{uv \in E(G)} [\sqrt{(d_u - 1)(d_v - 1)}]$
Harmonic Index	$H(G) = \sum_{uv \in E(G)} \left[\frac{2}{d_u + d_v} \right]$
Sum Connectivity Index	$SC(G) = \sum_{uv \in E(G)} \frac{1}{\sqrt{d_u + d_v}}$

We obtain the expressions of degree-based molecular descriptors from Table 2 using the above edge set partitions.

Theorem 2. Let G be a molecular sieve hexagonal mesh $mSHL(n, l, k)$. Then

$$\begin{aligned} M_1(G) &= 6n(27n - 6l - 3k + 9kn + 18ln - 1) \\ M_2(G) &= 3n(81n - 18l - 9k + 27kn + 54ln - 13) \\ RM_2(G) &= 6n(18n - 4l - 2k + 6kn + 12ln - 5) \\ HM(G) &= 36n(27n - 6l - 3k + 9kn + 18ln - 4) \\ AZ(G) &= \frac{9n}{64}(2187n - 486l - 243k + 729kn + 1458ln - 191) \\ R(G) &= n(9n - 2l - k + 3kn + 6ln + 26^{\frac{1}{2}} - 2) \\ RR(G) &= 3n(27n - 6l - 3k + 9kn + 18ln + 46^{\frac{1}{2}} - 11) \\ RRR(G) &= 6n - 2l(-18n^2 + 6n) + 12(2^{\frac{1}{2}})n + 2n^2(9k + 27) - 2n(3k + 15) \\ H(G) &= \frac{n}{3}(18n - 4l - 2k + 6kn + 12ln + 11) \\ SC(G) &= n(9n - 2l - k + 3kn + 6ln + 26^{\frac{1}{2}} - 2). \end{aligned}$$

3.3. Degree-Based Entropy

In this section, we present the numerical analysis and the entropy stability of the given molecular descriptors in Table 2. Further, the section provides instructions on calculating entropy values according to Shannon's method by constructing a probability function from degree-based topological indices. We used Shannon's model to calculate probabilistic entropy because it is the most widely used method [55,59–62]. Using that topological index, the entropy K is calculated as follows:

$$E_k(G) = \log(K(G)) - \frac{1}{K(G)} \left(\sum_{uv \in E(G)} (f(e) \log(f(e))) \right)$$

By using $M_1(G)$ to calculate the entropy value for G , the calculation procedure is illustrated.

First Zagreb entropy for $mSHL(n, l, k)$

$$\begin{aligned} EM_1(G) &= \log(6n(27n - 6l - 3k + 9kn + 18ln - 1)) \\ &\quad - \frac{(6n)(2 + 2)\log(2 + 2) + (12n)(2 + 3)\log(2 + 3)}{6n(27n - 6l - 3k + 9kn + 18ln - 1)} \\ &\quad + \frac{((18n^2 - 6n)l + (9k + 27)n^2 - (3k + 15)n)(3 + 3)\log(3 + 3)}{6n(27n - 6l - 3k + 9kn + 18ln - 1)} \\ &= \log(6n(9kn + 18ln - 3k - 6l + 27n - 1)) - \frac{48n \log(2) + 60n \log(5)}{6n(9kn + 18ln - 3k - 6l + 27n - 1)} \\ &\quad + \frac{6((18n^2 - 6n)l + (9k + 27)n^2 - (3k + 15)n) \log(6)}{6n(9kn + 18ln - 3k - 6l + 27n - 1)} \end{aligned}$$

After simplifying this, we obtain

$$\begin{aligned} EM_1(G) &= \frac{((9k + 18l + 27)n - 3k - 6l - 1) \log(9((k + 2l + 3)n - \frac{k}{3} - \frac{2l}{3} - \frac{1}{9})n)}{(9k + 18l + 27)n - 3k - 6l - 1} \\ &\quad + \frac{6 \log(2) + 14 \log(3) - 10 \log(5)}{(9k + 18l + 27)n - 3k - 6l - 1} \end{aligned}$$

However, concerning each topological index, its method and 3D plot of entropy (see Figure 7), as mentioned above, can generate any degree-based entropy expressions.

3.4. Numerical Results

The numerical values of distance- and degree-based molecular descriptors utilizing entropy measures generated for G are given in Tables 3 and 4 with the values of the variables n , l and k ranging from 1 to 10.

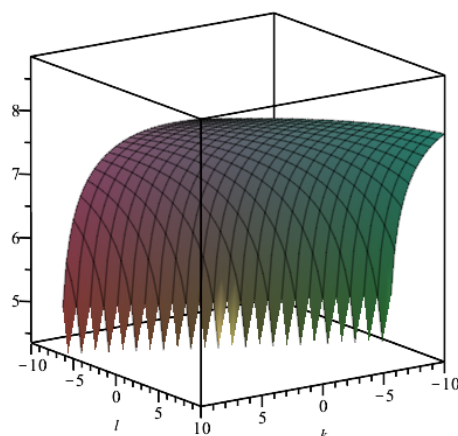


Figure 7. Three-dimensional plot of EM_1 .

Table 3. Numerical values for distance-based molecular descriptors.

(n, l, k)	(1, 1, 1)	(2, 2, 2)	(3, 3, 3)	(4, 4, 4)	(5, 5, 5)
$WI_v(G)$	3024	270,000	4,668,072	37,920,768	198,934,944
$Sz_v(G)$	12,096	2,180,550	59,575,584	665,112,240	4,487,610,096
$PI_v(G)$	1728	59,976	560,592	2,819,448	10,144,560
$Mo_v(G)$	576	27,684	265,776	1,385,064	4,916,352
(n, l, k)	(6, 6, 6)	(7, 7, 7)	(8, 8, 8)	(9, 9, 9)	(10, 10, 10)
$WI_v(G)$	784,272,816	2,527,739,928	7,013,962,368	17,335,729,008	39,076,777,008
$Sz_v(G)$	21,585,912,126	82,522,470,576	264,389,591,088	743,053,567,968	1,873,931,558,022
$PI_v(G)$	28,958,688	71,033,760	154,482,768	308,200,032	571,213,080
$Mo_v(G)$	14,290,380	34,549,680	76,122,576	149,955,648	280,858,740

Table 4. Numerical values for degree-based molecular descriptors.

(n, l, k)	(1, 1, 1)	(2, 2, 2)	(3, 3, 3)	(4, 4, 4)	(5, 5, 5)
$M_1(G)$	264	1716	5328	12,072	22,920
$M_2(G)$	366	2514	7902	17,988	34,230
$RM_2(G)$	150	1092	3474	7944	15,150
$HM(G)$	1476	10,080	31,644	72,000	136,980
$AZ(G)$	485.71875	3226.78125	10,068.46875	22,856.0625	43,434.84375
$R(G)$	17.899	101.798	305.6969	683.5959	1290
$RR(G)$	131.3939	856.7878	2662	6034	11,457
$RRR(G)$	82.9706	561.9411	1761	4004	7615
$H(G)$	13.66666667	71.33333333	209	462.6666667	868.3333333
$SC(G)$	17.899	101.798	305.6969	683.5959	1290
(n, l, k)	(6, 6, 6)	(7, 7, 7)	(8, 8, 8)	(9, 9, 9)	(10, 10, 10)
$M_1(G)$	38,844	60,816	89,808	126,792	172,740
$M_2(G)$	58,086	91,014	134,472	189,918	258,810
$RM_2(G)$	25,740	40,362	59,664	84,294	114,900
$HM(G)$	232,416	364,140	537,984	759,780	1,035,360
$AZ(G)$	73,650.09375	115,347.0938	170,371.125	240,567.4688	327,781.4063
$R(G)$	2177	3401	5015	7073	9629
$RR(G)$	19,418	30,404	44,899	63,391	86,364
$RRR(G)$	12,918	20,237	29,896	42,219	57,530
$H(G)$	1462	2279.666667	3357.333333	4731	6436.666667
$SC(G)$	2177	3401	5015	7073	9629

These values were plotted using the Origin 2020b for a graphical comparison (see Figures 8–10) of the computed topological descriptors below. The three-dimensional plots proved a comparison to the behavior of degree-based indices of G .

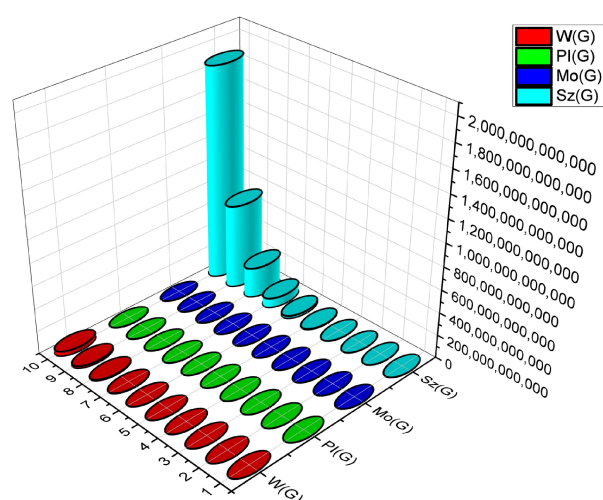


Figure 8. Comparison of graphical representation of distance-based molecular descriptors.

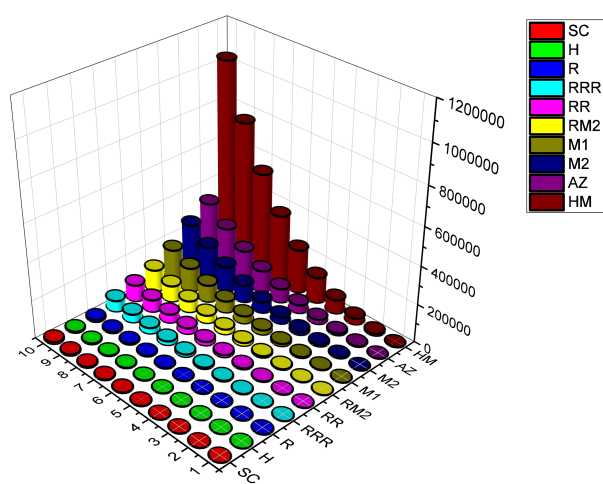


Figure 9. Comparison of graphical representation of degree-based molecular descriptors.

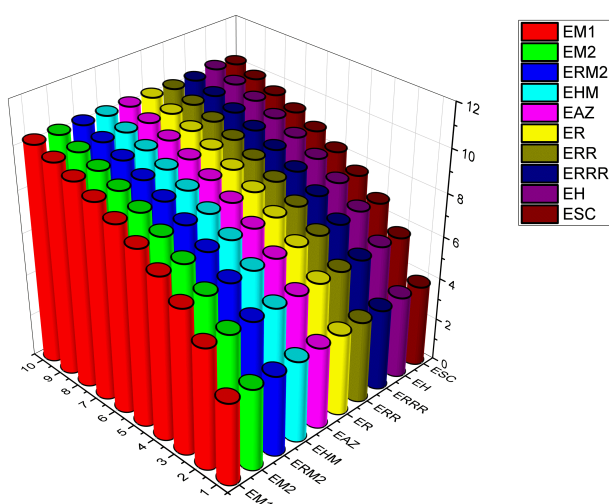


Figure 10. Comparison of entropy measures for G .

3.5. Statistical Correlation

All numerical values of molecular descriptors are approaches to the entropy properties of G (see Table 5). The correlation (r) gauge chart shows how strongly two quantitative variables are correlated. Pearson's correlation coefficient (r) is defined as follows.

$$r = \frac{\sum(t_i - t^-)(s_i - s^-)}{\sqrt{\sum(t_i - t^-)^2 \sum(s_i - s^-)^2}}.$$

where r = correlation coefficient,

t_i = values of the t -variable in a sample;

t^- = mean the values of the t -variable;

s_i = values of the s -variable in a sample;

s^- = mean the values of the s -variable.

We have shown the correlation (r) between degree-based descriptors (A) and degree entropy values (B) below in Table 6 and the correlation between A and B is denoted as $A \sim B$.

Table 5. Numerical values for degree-based entropies.

(n, l, k)	(1, 1, 1)	(2, 2, 2)	(3, 3, 3)	(4, 4, 4)	(5, 5, 5)	(6, 6, 6)	(7, 7, 7)	(8, 8, 8)	(9, 9, 9)	(10, 10, 10)
$EM_1(G)$	3.8625	5.6801	6.8006	7.6137	8.2525	8.7787	9.2262	9.6155	9.96	10.269
$EM_2(G)$	3.8383	5.6711	6.7961	7.6111	8.2507	8.7775	9.2253	9.6148	9.9594	10.2685
$ERM_2(G)$	3.7907	5.6552	6.7883	7.6064	8.2477	8.7753	9.2237	9.6135	9.9584	10.2677
$EHM(G)$	3.8404	5.6719	6.7965	7.6113	8.2509	8.7776	9.2254	9.6148	9.9595	10.2685
$EAZ(G)$	3.8576	5.678	6.7995	7.6131	8.2521	8.7784	9.226	9.6153	9.9599	10.2689
$ER(G)$	3.8599	5.6782	6.7995	7.6131	8.2521	8.7784	9.226	9.6153	9.9599	10.268
$ERR(G)$	3.862	5.6798	6.8005	7.6137	8.2525	8.7787	9.2262	9.6155	9.96	10.269
$EH(G)$	3.8928	5.7735	6.9177	7.7412	8.3854	8.9147	9.3642	9.7548	10.1002	10.4098
$ESC(G)$	3.8552	5.6756	6.7976	7.6113	8.2504	8.7769	9.2245	9.6138	9.9584	10.2674

Table 6. Statistical Correlation (r) between degree-based molecular descriptors and degree-based entropy values.

(n, l, k)	$M_1 \sim EM_1$	$M_2 \sim EM_2$	$RM_2 \sim ERM_2$	$HM \sim EHM$	$AZ \sim EAZ$
r	0.800895321	0.799930694	0.798222338	0.800014703	0.800664403
(n, l, k)	$R \sim ER$	$RR \sim ERR$	$RRR \sim ERRR$	$H \sim EH$	$SC \sim ESC$
r	0.822763752	0.80086312	0.800240768	0.798861487	0.801363561

The results show that vertex-based indices of this study have perfect linear relationships. As a result, all the indices mentioned in this study are extremely useful in determining the topological properties of $mSHL(n, l, k)$. As a result, the Randić index has a perfect linear relationship index for $mSHL(n, l, k)$. The effect of this paper, based on applications and properties, is beneficial in obtaining the scientific results of aluminophosphate structure for future studies.

4. Conclusions

This study computed synthetic structural descriptors for aluminophosphate-based molecular sieve structure $mSHL(n, l, k)$ using cut methods for vertex and edge-weighted molecular graphs. Entropy calculations for degree-based descriptors and linear correlation calculations for $mSHL(n, l, k)$ were carried out. Topological methods can also obtain quantitative data for phase transitions and other material alterations caused by chemical interactions, contaminants and heavy metal ions. The graphical presentation of this work, the linear correlation and the numerical comparison of the computed results will be helpful to theoretical chemists. This computational study is extremely useful in determining specific applications, such as the topological properties of the aluminophosphate structure. Further analyzing this study, we hope our results will support researchers in predicting the

NMR pattern for NMR signal processing. Moreover, it helps investigators to obtain new ideas in hypothetical and investigational NMR Spectroscopy [63–65].

Author Contributions: J.S.V.: Data collection, Writing of an original draft preparation, Visualization, Software, Methodology and Investigation. S.R.: Conceptualization, Supervision, Investigation, Reviewing and Editing. B.C.B.: Visualization, Investigation, Reviewing and Editing. M.N.H.: Visualization, Investigation. T.A.: Writing of an original draft preparation, Software. R.U.G.: Conceptualization, Investigation. M.E.: Visualization, Investigation. All authors have read and agreed to the published version of the manuscript.

Funding: We thank Universiti Malaysia Terengganu for providing funding support for this project (UMT/TAPE-RG/2021/55330).

Data Availability Statement: No data associated in the manuscript.

Acknowledgments: We thank Universiti Malaysia Terengganu for providing funding support for this project (UMT/TAPE-RG/2021/55330).

Conflicts of Interest: The authors declare no competing interests.

References

- Wang, Y.; Zou, X.; Sun, L.; Rong, H.; Zhu, G. A zeolite-like aluminophosphate membrane with molecular-sieving property for water desalination. *Chem. Sci.* **2018**, *9*, 2533–2539. [\[CrossRef\]](#)
- Yang, M.; Fan, D.; Wei, Y.; Tian, P.; Liu, Z. Recent progress in methanol-to-olefins (MTO) catalysts. *Adv. Mater.* **2019**, *31*, 1902181. [\[CrossRef\]](#)
- Huang, Z.; Seo, S.; Shin, J.; Wang, B.; Bell, R.G.; Hong, S.B.; Zou, X. 3D-3D topotactic transformation in aluminophosphate molecular sieves and its implication in new zeolite structure generation. *Nat. Commun.* **2020**, *11*, 3762. [\[CrossRef\]](#)
- Yu, J.; Xu, R. Insight into the construction of open-framework aluminophosphates. *Chem. Soc. Rev.* **2006**, *35*, 593–604. [\[CrossRef\]](#)
- Cheetham, A.K.; Férey, G.; Loiseau, T. Open-framework inorganic materials. *Angew. Chem. Int. Ed.* **1999**, *38*, 3268–3292.
- Liu, Z.; Xu, J.; Xu, M.; Huang, C.; Wang, R.; Li, T.; Huai, X. Ultralow-temperature-driven water-based sorption refrigeration enabled by low-cost zeolite-like porous aluminophosphate. *Nat. Commun.* **2022**, *13*, 193. [\[CrossRef\]](#)
- Gozalbes, R.; Doucet, J.P.; Derouin, F. Application of topological descriptors in QSAR and drug design: History and new trends. *Curr. Drug Targets-Infect. Disord.* **2002**, *2*, 93–102. [\[CrossRef\]](#)
- Arockiaraj, M.; Clement, J.; Tratnik, N.; Mushtaq, S.; Balasubramanian, K. Weighted Mostar indices as measures of molecular peripheral shapes with applications to graphene, graphyne and graphdiyne nanoribbons. *SAR QSAR Environ. Res.* **2020**, *31*, 187–208. [\[CrossRef\]](#)
- Gutman, I. A formula for the Wiener number of trees and its extension to graphs containing cycles. *Graph Theory Notes NY* **1994**, *27*, 9–15.
- Gutman, I.; Ashrafi, A.R. The edge version of the Szeged index. *Croat. Chem. Acta* **2008**, *81*, 263–266.
- Khadikar, P.V.; Karmarkar, S.; Agrawal, V.K. A novel PI index and its applications to QSPR/QSAR studies. *J. Chem. Inf. Comput. Sci.* **2001**, *41*, 934–949. [\[CrossRef\]](#) [\[PubMed\]](#)
- Khalifeh, M.H.; Yousefi-Azari, H.; Ashrafi, A.R.; Gutman, I. The edge Szeged index of product graphs. *Croat. Chem. Acta* **2008**, *81*, 277–281.
- Khalifeh, M.H.; Yousefi-Azari, H.; Ashrafi, A.R.; Wagner, S.G. Some new results on distance-based graph invariants. *Eur. J. Comb.* **2009**, *30*, 1149–1163. [\[CrossRef\]](#)
- Klein, D.J.; Lukovits, I.; Gutman, I. On the definition of the hyper-Wiener index for cycle-containing structures. *J. Chem. Inf. Comput. Sci.* **1995**, *35*, 50–52. [\[CrossRef\]](#)
- Schultz, H.P. Topological organic chemistry. 1. Graph theory and topological indices of alkanes. *J. Chem. Inf. Comput. Sci.* **1989**, *29*, 227–228. [\[CrossRef\]](#)
- Wiener, H. Structural determination of paraffin boiling points. *J. Am. Chem. Soc.* **1947**, *69*, 17–20. [\[CrossRef\]](#)
- Husin, M.N.; Ariffin, A. On the edge version of topological indices for certain networks. *Ital. J. Pure Appl. Math.* **2022**, *47*, 550–564.
- Liu, Y.; Rezaei, M.; Farahani, M.R.; Husin, M.N.; Imran, M. The Omega polynomial and the Cluj-Ilmenau index of an infinite class of the Titania Nanotubes $TiO_2(m, n)$. *J. Comput. Theor. Nanosci.* **2017**, *14*, 3429–3432. [\[CrossRef\]](#)
- Husin, M.N.; Zafar, S.; Gobithaasan, R.U. Investigation of Atom-Bond Connectivity Indices of Line Graphs Using Subdivision Approach. *Math. Probl. Eng.* **2022**, *2022*, 6219155. [\[CrossRef\]](#)
- Modabish, A.; Husin, M.N.; Alameri, A.Q.; Ahmed, H.; Alaeiyan, M.; Farahani, M.R.; Cancan, M. Enumeration of spanning trees in a chain of diphenylene graphs. *J. Discret. Math. Sci. Cryptogr.* **2022**, *25*, 241–251. [\[CrossRef\]](#)
- Asif, F.; Zahid, Z.; Husin, M.N.; Cancan, M.; Tas, Z.; Alaeiyan, M.; Farahani, M.R. On Sombor indices of line graph of silicate carbide $Si_2C_3 - I[p, q]$. *J. Discret. Math. Sci. Cryptogr.* **2022**, *25*, 301–310. [\[CrossRef\]](#)
- Ghani, M.U.; Campena FJ, H.; Pattabiraman, K.; Ismail, R.; Karamti, H.; Husin, M.N. Valency-Based Indices for Some Succinct Drugs by Using M-Polynomial. *Symmetry* **2023**, *15*, 603. [\[CrossRef\]](#)

23. Gutman, I.; Trinajstić, N. Graph theory and molecular orbitals. Total π -electron energy of alternant hydrocarbons. *Chem. Phys. Lett.* **1972**, *17*, 535–538. [\[CrossRef\]](#)
24. Estrada, E.; Torres, L.; Rodriguez, L.; Gutman, I. An atom-bond connectivity index: Modelling the enthalpy of formation of alkanes. *Indian J. Chem.* **1998**, *37A*, 849–855.
25. Randić, M. Characterization of molecular branching. *J. Am. Chem. Soc.* **1975**, *97*, 6609–6615. [\[CrossRef\]](#)
26. Zhou, B.; Trinajstić, N. On a novel connectivity index. *J. Math. Chem.* **2009**, *46*, 1252–1270. [\[CrossRef\]](#)
27. Vukičević, D.; Furtula, B. Topological index based on the ratios of geometrical and arithmetical means of end-vertex degrees of edges. *J. Math. Chem.* **2009**, *46*, 1369–1376. [\[CrossRef\]](#)
28. Albertson, M.O. The irregularity of a graph. *Ars Comb.* **1997**, *46*, 219–225.
29. Gutman, I.; Togan, M.; Yurttaş, A.; Cevik, A.S.; Cangul, I.N. Inverse problem for sigma index. *MATCH Commun. Math. Comput. Chem.* **2018**, *79*, 491e508.
30. Furtula, B.; Gutman, I. A forgotten topological index. *J. Math. Chem.* **2015**, *53*, 1184–1190. [\[CrossRef\]](#)
31. Vasilyev, A. Upper and lower bounds of symmetric division deg index. *Iran. J. Math. Chem.* **2014**, *5*, 91–98.
32. Hayat, S.; Imran, M.; Liu, J.B. An efficient computational technique for degree and distance based topological descriptors with applications. *IEEE Access* **2019**, *7*, 32276–32296. [\[CrossRef\]](#)
33. Hayat, S.; Ahmad, S.; Umair, H.M.; Wang, S. Distance property of chemical graphs. *Hacet. J. Math. Stat.* **2018**, *47*, 1071–1093. [\[CrossRef\]](#)
34. Hayat, S. Computing distance-based topological descriptors of complex chemical networks: New theoretical techniques. *Chem. Phys. Lett.* **2017**, *688*, 51–58. [\[CrossRef\]](#)
35. Shirdel, G.H.; Rezapour, H.; Sayadi, A.M. The hyper-Zagreb index of graph operations. *Iran. J. Math. Chem.* **2013**, *4*, 213–220.
36. Shannon, C.E. A mathematical theory of communication. *Bell Syst. Tech. J.* **1948**, *27*, 379–423. [\[CrossRef\]](#)
37. Rashevsky, N. Life, information theory and topology. *Bull. Math. Biophys.* **1955**, *17*, 229–235. [\[CrossRef\]](#)
38. Dehmer, M.; Grabner, M. The discrimination power of molecular identification numbers revisited. *MATCH Commun. Math. Comput. Chem.* **2013**, *69*, 785–794.
39. Ulanowicz, R.E. Quantitative methods for ecological network analysis. *Comput. Biol. Chem.* **2004**, *28*, 321–339. [\[CrossRef\]](#)
40. Imran, M.; Hayat, S. On counting polynomials of certain polyomino chains. *Bulg. Chem. Commun.* **2016**, *48*, 332–337.
41. Imran, M.; Hayat, S.; Shafiq, M.K. Computing omega and Sadhana polynomials of carbon nanotubes. *Optoelectron. Adv. Mater. Rapid Commun.* **2014**, *8*, 1218–1224.
42. Hayat, S.; Khan, S.; Khan, A.; Imran, M. Distance-based topological descriptors for measuring the π -electronic energy of benzenoid hydrocarbons with applications to carbon nanotubes. *Math. Methods Appl. Sci.* **2020**, early View. [\[CrossRef\]](#)
43. Morowitz, H.J. Some order-disorder considerations in living systems. *Bull. Math. Biophys.* **1955**, *17*, 81–86. [\[CrossRef\]](#)
44. Manzoor, S.; Siddiqui, M.K.; Ahmad, S. On entropy measures of molecular graphs using topological indices. *Arab. J. Chem.* **2020**, *13*, 6285–6298. [\[CrossRef\]](#)
45. Došlić, T.; Martinjak, I.; Škrekovski, R.; Tipurić Spužević, S.; Zubac, I. Mostar index. *J. Math. Chem.* **2018**, *56*, 2995–3013. [\[CrossRef\]](#)
46. Djoković, D.Ž. Distance-preserving subgraphs of hypercubes. *J. Comb. Theory Ser. B* **1973**, *14*, 263–267. [\[CrossRef\]](#)
47. Winkler, P.M. Isometric embedding in products of complete graphs. *Discret. Appl. Math.* **1984**, *7*, 221–225.
48. Nadjafi-Arani, M.J.; Klavzar, S. Cut method and Djoković–Winkler’s relation. *Electron. Notes Discret. Math.* **2014**, *45*, 153–157. [\[CrossRef\]](#)
49. Arockiaraj, M.; Clement, J.; Paul, D.; Balasubramanian, K. Relativistic distance-based topological descriptors of Linde type A zeolites and their doped structures with very heavy elements. *Mol. Phys.* **2021**, *119*, e1798529. [\[CrossRef\]](#)
50. Kavitha SR, J.; Abraham, J.; Arockiaraj, M.; Jency, J.; Balasubramanian, K. Topological characterization and graph entropies of tessellations of kekulene structures: Existence of isentropic structures and applications to thermochemistry, nuclear magnetic resonance and electron spin resonance. *J. Phys. Chem. A* **2021**, *125*, 8140–8158. [\[CrossRef\]](#)
51. Martínez-Franco, R.; Moliner, M.; Yun, Y.; Sun, J.; Wan, W.; Zou, X.; Corma, A. Synthesis of an extra-large molecular sieve using proton sponges as organic structure-directing agents. *Proc. Natl. Acad. Sci. USA* **2013**, *110*, 3749–3754. [\[CrossRef\]](#) [\[PubMed\]](#)
52. Balasubramanian, K. Combinatorics, big data, neural network & AI for medicinal chemistry & drug administration. *Lett. Drug Des. Discov.* **2021**, *18*, 943–948.
53. Sabirov, D.S.; Shepelevich, I.S. Information entropy in chemistry: An overview. *Entropy* **2021**, *23*, 1240. [\[CrossRef\]](#) [\[PubMed\]](#)
54. Chaudhry, F.; Shoukat, I.; Afzal, D.; Park, C.; Cancan, M.; Farahani, M.R. M-polynomials and degree-based topological indices of the molecule copper (i) oxide. *J. Chem.* **2021**, *2021*, 6679819. [\[CrossRef\]](#)
55. Mowshowitz, A.; Dehmer, M. Entropy and the complexity of graphs revisited. *Entropy* **2012**, *14*, 559–570. [\[CrossRef\]](#)
56. Arockiaraj, M.; Paul, D.; Klavžar, S.; Clement, J.; Tigga, S.; Balasubramanian, K. Relativistic distance based and bond additive topological descriptors of zeolite RHO materials. *J. Mol. Struct.* **2022**, *1250*, 131798. [\[CrossRef\]](#)
57. Gutman, I. Degree-based topological indices. *Croat. Chem. Acta* **2013**, *86*, 351–361. [\[CrossRef\]](#)
58. Arockiaraj, M.; Clement, J.; Tratnik, N. Mostar indices of carbon nanostructures and circumscribed donut benzenoid systems. *Int. J. Quantum Chem.* **2019**, *119*, e26043. [\[CrossRef\]](#)
59. Augustine, T.; Roy, S. Topological Study on Triazine-Based Covalent-Organic Frameworks. *Symmetry* **2022**, *14*, 1590. [\[CrossRef\]](#)
60. Sahaya Vijay, J.; Roy, S. Computation of Wiener Descriptor for Melamine Cyanuric Acid Structure. *Polycycl. Aromat. Compd.* **2023**, *1–15*. [\[CrossRef\]](#)

61. Rahul, M.P.; Clement, J.; Junias, J.S.; Arockiaraj, M.; Balasubramanian, K. Degree-based entropies of graphene, graphyne and graphdiyne using Shannon's approach. *J. Mol. Struct.* **2022**, *1260*, 132797. [[CrossRef](#)]
62. Hussain, Z.; Ijaz, N.; Tahir, W.; Butt, M.T.; Talib, S. Calculating Degree Based Multiplicative Topological indices of Alcohol. *Asian J. Appl. Sci. Technol.* **2018**, *2*, 132–139. [[CrossRef](#)]
63. Balasubramanian, K. Operator algebraic methods for NMR spectroscopy, I. Generation of NMR spin species. *J. Chem. Phys.* **1983**, *78*, 6358–6368. [[CrossRef](#)]
64. Balasubramanian, K. Topological and group theoretical analysis in dynamic NMR spectroscopy. *J. Phys. Chem.* **1982**, *86*, 4668–4674. [[CrossRef](#)]
65. Raza, Z.; Arockiaraj, M.; Maaran, A.; Kavitha SR, J.; Balasubramanian, K. Topological entropy characterization, NMR and ESR spectral patterns of coronene-based transition metal organic frameworks. *ACS Omega* **2023**, *8*, 13371–13383. [[CrossRef](#)] [[PubMed](#)]

Disclaimer/Publisher's Note: The statements, opinions and data contained in all publications are solely those of the individual author(s) and contributor(s) and not of MDPI and/or the editor(s). MDPI and/or the editor(s) disclaim responsibility for any injury to people or property resulting from any ideas, methods, instructions or products referred to in the content.

Article

On Neighborhood Degree-Based Topological Analysis over Melamine-Based TriCF Structure

Tony Augustine and Roy Santiago * 

Department of Mathematics, Vellore Institute of Technology, Vellore 632014, India

* Correspondence: roy.santiago@vit.ac.in

Abstract: Triazine-based covalent organic frameworks (TriCFs) were synthesized using melamine, and cyanuric acid is a brand-new synthetic lubricant, which is thermo-stable and possesses a lamellar structure. This article demonstrates how topological descriptors for the TriCF structure are precisely evaluated using the degree sum of the end vertex neighbors and also some molecular descriptors with multiplicative neighborhood degree sums are evaluated. Furthermore, the neighborhood entropy measures for the outcomes are provided. The results are compared using the graph theoretical method.

Keywords: triazine-based covalent organic frameworks; neighborhood-degree sum-based topological indices; entropy measures; graph-theoretical approach

MSC: 92E10; 05C09



Citation: Augustine, T.; Santiago, R. On Neighborhood Degree-Based Topological Analysis over Melamine-Based TriCF Structure. *Symmetry* **2023**, *15*, 635. <https://doi.org/10.3390/sym15030635>

Academic Editors: Sergei D. Odintsov and Juan Luis García Guirao

Received: 29 December 2022

Revised: 26 January 2023

Accepted: 31 January 2023

Published: 3 March 2023



Copyright: © 2023 by the authors. Licensee MDPI, Basel, Switzerland. This article is an open access article distributed under the terms and conditions of the Creative Commons Attribution (CC BY) license (<https://creativecommons.org/licenses/by/4.0/>).

1. Introduction

Chemical graph theory is the process of performing a thorough analysis to identify the key characteristics or meanings of chemical compounds graphically. It is the area of mathematics that combines graph theory and chemistry. In chemical graph theory, a compound's idiosyncrasies are mathematically described when an image of the mixture from X-ray or electron microscope diffraction is drawn into a plane and illuminated on its symmetry [1]. The chemical graph is a straightforward representation of a picture of a compound in which we suppose that the edges are bonds between atoms and the vertices are atoms. Understanding properties such as molecular structure, the kinetics of molecules, atoms, or electrons, chains or patterns of polymers, crystals and clusters, aromaticity, nuclear magnetic resonance (NMR) analysis, depicting orbitals, and electron behaviors are made possible by chemical graph theory. A few researchers who have introduced graph theory in chemistry are Ante Graovac, Alexandru Balaban, Haruo Hosoya, Iván Gutman, Nenad Trinajstić, and Milan Randić [2–4].

Graph theory connects mathematics and chemistry using a valuable tool called the topological index. A real number associated with a graph and determined by a certain rule is known as the topological index. This number is invariant for isomorphic graphs [5]. It describes the molecular structure's topology. These indices are crucial to the research of quantitative structure–property relationship/quantitative structure–activity relationship (QSPR/QSAR) since they may be used to predict various physiochemical characteristics and bioactivity, which aids in the development of new drugs. Its use in other sectors, including nanoscience and biotechnology, is equally impressive [6]. Topological indices have been used to numerically quantify various physical and chemical properties of various chemical and biological molecules, including the boiling point, anti-leishmanial action, acute toxicity, radical scavenging activity, and many more. Throughout the world, researchers are interested in this. Over the years, several vertex-degree-based topological indices have been developed [5,7].

Three nitrogen atoms replace the carbons in the triazines' six-membered planar ring, which is similar to that of benzene. The three isomers of triazine are distinguished by the positions of the nitrogen atoms [8]. The triazine structures of melamine and cyanuric chloride are two well-known examples. Melamine is a white, odorless, crystalline, nontoxic, hetero-aromatic compound utilized as a raw material in many daily products that must adhere to rigid standards for toughness and wear resistance. The synthesis of insecticides, brighteners, and reactive dyes have all benefited from the versatility and multifunctionality of cyanuric chloride (2,4,6-trichloro-1,3,5-triazine), a versatile reagent. Covalent bonding creates triazine-based covalent organic polymers (COPs), a developing subclass of porous organic framework materials. Ping Wen et al. explained the synthesis of triazine-based covalent organic frameworks (see Figure 1) utilizing melamine and cyanuric chloride [8]. The as-prepared covalent organic frameworks are referred to as TriCFs. They are exceptionally thermo-stable and possess a lamellar structure. This comprises a brand-new synthetic lubricant. The degree-based indices of this structure were studied by [9]. Currently, research on the computation of the TriCF neighborhood topological indices is needed in the literature. Future designed and produced triazine-based covalent organic frameworks could benefit from the findings of this study [8].

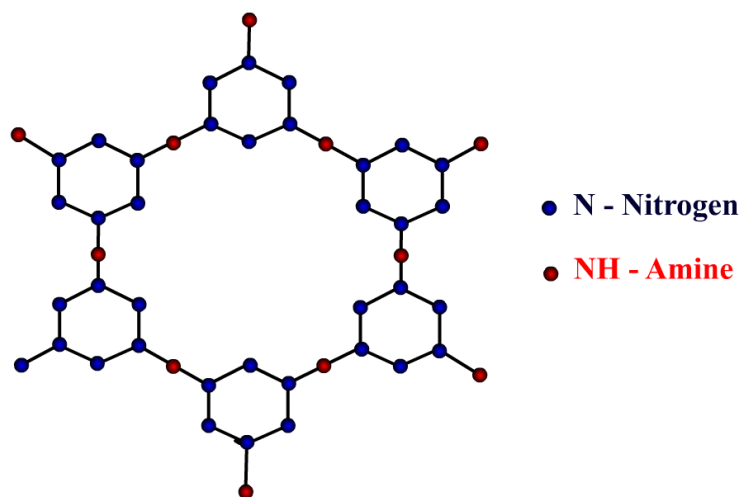


Figure 1. TriCFs' structure.

"The entropy of a probability distribution is regarded as a measure of the unpredictability of information content or a measure of the uncertainty of a system", Shannon famously wrote in his article from 1948, which established the term "entropy" [10]. Entropy later started to be applied to chemical networks and graphs. It was created for analyzing the structural data of chemical networks and graphs. There are intrinsic and extrinsic metrics for graph entropy, which correlates probability distributions with a graph's elements (vertices, edges, etc.). To estimate a network's structural information content, Shannon's entropy calculations have been applied [11]. This approach has been used to visualize live systems using graphs. Entropy measurements for graphs have also been widely used in structural chemistry, computer science, and biology [10]. Entropy network measures have a variety of uses, including quantitative structure characterization in structural chemistry and the investigation of biological or chemical aspects of molecular graphs using software [12–14].

2. Preliminaries and Mathematical Terminologies

In this study, we take γ as a connected graph. The letters \mathcal{P} and \mathcal{Q} stand for the vertex set (atoms) and edge set (bonds between atoms). Furthermore, $s_\gamma(u)$ stands for the total number of degrees of all vertices adjacent to u . Topological indices, which are graph-based descriptors, are often used to forecast the characteristics of chemical networks and systems. They are functions defined from a graph γ to a collection of real numbers \mathbb{R} . There are

primarily two kinds of topological indices. The first is a topological index based on degrees, while the second is based on distance. The motivation for using degree-based indices, also known as connectivity-based indices, comes from several research works showing that they are reliable for linking the physicochemical properties of various molecules.

Randić created the first legitimate degree-based index, which has now gained widespread acceptance as the Randić index [15]. Later, several degree-based metrics such as the Zagreb index, the atom bond connectivity index, the enhanced Zagreb index, and the geometric arithmetic index were created. Due to their excellent correlation capacity, these indices have drawn much attention [3]. Randić indices are often used to simulate molecules' physical and chemical characteristics, while Zagreb indices were developed to explore molecular complexity. A modified version of the Randić index called the "atom bond connectivity index" has shown a good correlation with the thermodynamic properties of alkanes [5]. Refer to [5] and the references there in for a thorough overview of the different degree-based topological indices.

Later, a significant number of researchers developed unique modifications to these indices that consider the neighboring degree sum for each vertex rather than the degree [16–18]. Let s_u represent the degree sum of the nearby vertices of the vertex u to define them broadly. The generic equation for bond additive and multiplicative variants of degree-sum-based indices may be written as

$$TI_s(\gamma) = \sum_{uv \in E(\gamma)} \phi(s_u, s_v) \quad (1)$$

and

$$TI_s^*(\gamma) = \prod_{uv \in E(\gamma)} \phi(s_u, s_v) \quad (2)$$

We used the edge partition approach, where the total number of edges for each structure is split into different groups according to the degrees of the end vertices of edges, to generate the degree-based indices. Similar to this, edges are divided into sections to determine degree-sum-based indices using the neighborhood degree sums of the end vertices of edges. This research employed edge partition approaches to derive multiplicative neighborhood degree sum topological indices and neighborhood degree-sum-based entropy measurements for the TriCF structure. We used Shannon's model to calculate the probabilistic entropy because it is the most widely used method [10–12]. The entropy measured using that topological index X is given by

$$E_X(\gamma) = \log(X(\gamma)) - \frac{1}{X(\gamma)} \left(\sum_{uv \in E(\gamma)} f(e) \log(f(e)) \right). \quad (3)$$

where $f(e)$ is the edge partition.

For vertices u and v , s_u and s_v denote the neighborhood degree sum of u and v . We now show various neighborhood degree-sum-based topological descriptors and neighborhood multiplicative degree-sum-based topological descriptors in Table 1 [19,20] and Table 2 [6,16–18,21–33], respectively.

Table 1. Neighborhood degree-sum-based topological indices.

Neighborhood First Zagreb Index	$NM_1(G) = \sum_{uv \in E(G)} [s_u + s_v]$
Neighborhood Second Zagreb Index	$NM_2(G) = \sum_{uv \in E(G)} [s_u \times s_v]$
Neighborhood Reduced Second Zagreb Index	$NRM_2(G) = \sum_{uv \in E(G)} [(s_u - 1)(s_v - 1)]$
Neighborhood Hyper Zagreb Index	$NHM(G) = \sum_{uv \in E(G)} [s_u + s_v]^2$
Neighborhood Augmented Zagreb Index	$NAZ(G) = \sum_{uv \in E(G)} \left[\frac{s_u \times s_v}{s_u + s_v - 2} \right]^3$

Table 1. *Cont.*

Neighborhood Randić Index	$NR(G) = \sum_{uv \in E(G)} \left[\frac{1}{\sqrt{s_u s_v}} \right]$
Neighborhood Reciprocal Randić Index	$NRR(G) = \sum_{uv \in E(G)} [\sqrt{s_u s_v}]$
Neighborhood Reduced Reciprocal Randić Index	$NRRR(G) = \sum_{uv \in E(G)} [\sqrt{(s_u - 1)(s_v - 1)}]$
Neighborhood Harmonic Index	$NH(G) = \sum_{uv \in E(G)} \left[\frac{2}{s_u + s_v} \right]$
Neighborhood Sum Connectivity Index	$NSC(G) = \sum_{uv \in E(G)} \frac{1}{\sqrt{s_u + s_v}}$
Neighborhood Geometric Arithmetic Index	$NGA(G) = \sum_{uv \in E(G)} \frac{2\sqrt{s_u s_v}}{s_u + s_v}$
Neighborhood Inverse Sum Index	$NIS(G) = \sum_{uv \in E(G)} \frac{s_u s_v}{s_u + s_v}$
Neighborhood Forgotten index	$NF(G) = \sum_{uv \in E(G)} s_u^2 + s_v^2$
Neighborhood Symmetric Division Index	$NSDI(G) = \sum_{uv \in E(G)} \frac{s_u^2 + s_v^2}{s_u s_v}$
Neighborhood Atom Bond Connectivity Index	$NABC(G) = \sum_{uv \in E(G)} \sqrt{\frac{s_u + s_v - 2}{s_u s_v}}$

Table 2. Multiplicative neighborhood degree-sum-based topological indices.

Multiplicative Neighborhood First Zagreb Index	$MNM_1(G) = \prod_{uv \in E(G)} [s_u + s_v]$
Multiplicative Neighborhood Second Zagreb Index	$MNM_2(G) = \prod_{uv \in E(G)} [s_u \times s_v]$
Multiplicative Neighborhood Reduced Second Zagreb Index	$MNRM_2(G) = \prod_{uv \in E(G)} [(s_u - 1)(s_v - 1)]$
Multiplicative Neighborhood Hyper Zagreb Index	$MNHM(G) = \prod_{uv \in E(G)} [s_u + s_v]^2$
Multiplicative Neighborhood Augmented Zagreb Index	$MNAZ(G) = \prod_{uv \in E(G)} \left[\frac{s_u \times s_v}{s_u + s_v - 2} \right]^3$
Multiplicative Neighborhood Randić Index	$MNR(G) = \prod_{uv \in E(G)} \left[\frac{1}{\sqrt{s_u s_v}} \right]$
Multiplicative Neighborhood Reciprocal Randić Index	$MNRR(G) = \prod_{uv \in E(G)} [\sqrt{s_u s_v}]$
Multiplicative Neighborhood Reduced Reciprocal Randić Index	$MNRRR(G) = \prod_{uv \in E(G)} [\sqrt{(s_u - 1)(s_v - 1)}]$
Multiplicative Neighborhood Harmonic Index	$MNH(G) = \prod_{uv \in E(G)} \left[\frac{2}{s_u + s_v} \right]$
Multiplicative Neighborhood Sum Connectivity Index	$MNSC(G) = \prod_{uv \in E(G)} \frac{1}{\sqrt{s_u + s_v}}$
Multiplicative Neighborhood Geometric Arithmetic Index	$MNGA(G) = \prod_{uv \in E(G)} \frac{2\sqrt{s_u s_v}}{s_u + s_v}$
Multiplicative Neighborhood Inverse Sum Index	$MNIS(G) = \prod_{uv \in E(G)} \frac{s_u s_v}{s_u + s_v}$
Multiplicative Neighborhood Forgotten index	$MNF(G) = \prod_{uv \in E(G)} s_u^2 + s_v^2$
Multiplicative Neighborhood Symmetric Division Index	$MNSDI(G) = \prod_{uv \in E(G)} \frac{s_u^2 + s_v^2}{s_u s_v}$
Multiplicative Neighborhood Atom Bond Connectivity Index	$MNABC(G) = \prod_{uv \in E(G)} \sqrt{\frac{s_u + s_v - 2}{s_u s_v}}$

3. Research Aim and Methodology

Chemical graph theory is a concept used in the mathematical chemistry field of topology. It gained popularity as its proponents presented several graph theory applications for the mathematical modeling of chemical characteristics [34,35]. Chemists have established through actual experimental data that a compound's physicochemical properties are closely related to its molecular structure. Later, additional graph-theoretical techniques were developed to describe various chemical compound properties. The idea of topological indices, specific network invariants, is an essential tool. In addition to the topological index, information entropy is a necessary tool for assessing the properties of chemical compounds. Due to its applicability, the notion, which was first applied to the communication system, has recently received respect in various scientific and technological sectors [10,12]. In chemistry, much research has been performed on the correspondence between the traditional concept of thermodynamics and the statistical mechanic's definition of entropy. The concept of information entropy may be considered a replacement for thermodynamic entropy due to its relationship to the Gibbs entropy formula employed in statistical mechanics [33,36]. They are thus primarily used in chemistry to characterize compounds' complexity, disorder, and other properties, such as phase transition energy. The relationship between information entropy and chemical properties, such as the variation in molecule stability caused by various arrangements of essential components, has been studied recently [13]. Shannon first introduced the concept of information entropy in communication networks, and the statement was purely based on terms used in that field. Later, it was changed to use it in other scientific domains [11].

In this article, we explore the multiplicative neighborhood-degree sum-based indices and neighborhood-degree sum-based indices of the TriCF structure. In addition, we calculate the entropies of these structures and also determine the numerical values, which aid in the investigation of the physiochemical characteristics of the TriCF structure.

This study's computations use graph theoretical technologies, precisely the edge partition method and analytical techniques. Chem Draw Ultra describes the TriCFs' molecular structures, and Origin displays the numerical outcomes.

4. Main Results

In this section, we present the key findings of the study. In this work, based on the growth of TriCFs, the authors categorized it into three kinds. In particular, γ_1 , γ_2 , and γ_3 are linear chain TriCF structures, parallelogram TriCF structures, and hexagonal TriCF structures, respectively. The schematic of the triazine-based covalent organic framework synthesis can be formed into any structure such as a linear chain, parallelogram, hexagonal, etc. Figures 2–4 show the 2D structure of a linear chain, parallelogram and hexagonal TriCF structures, respectively. Figure 5 shows the unit cell of the TriCF structure. In the linear chain TriCF structure, the unit cell is repeated r -times linearly (r columns). Similarly, in the parallelogram TriCF structure, the unit cells are arranged in the shape of a parallelogram structure. In hexagonal TriCF structures, the unit cells are placed in a hexagonal structure. It is easy to understand the growth from Figures 3 and 4. From this, we can find the edge partition, which is given in Table 3.

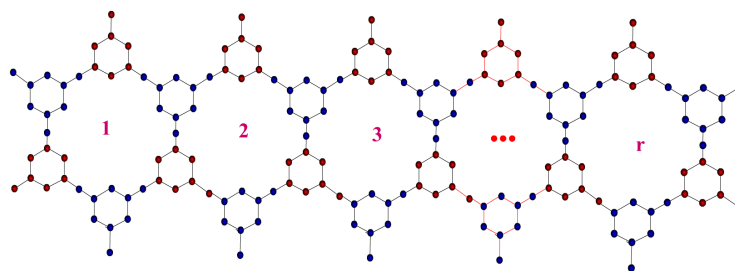


Figure 2. Linear chain TriCF structure.

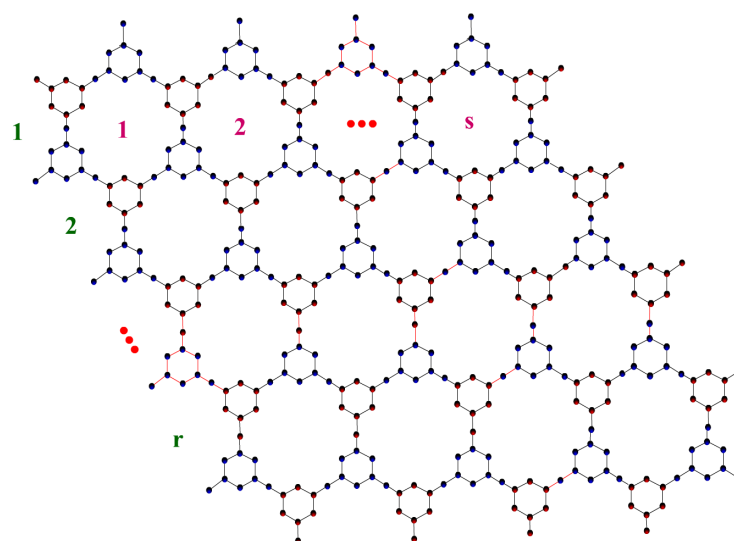


Figure 3. Parallelogram TriCF structure.

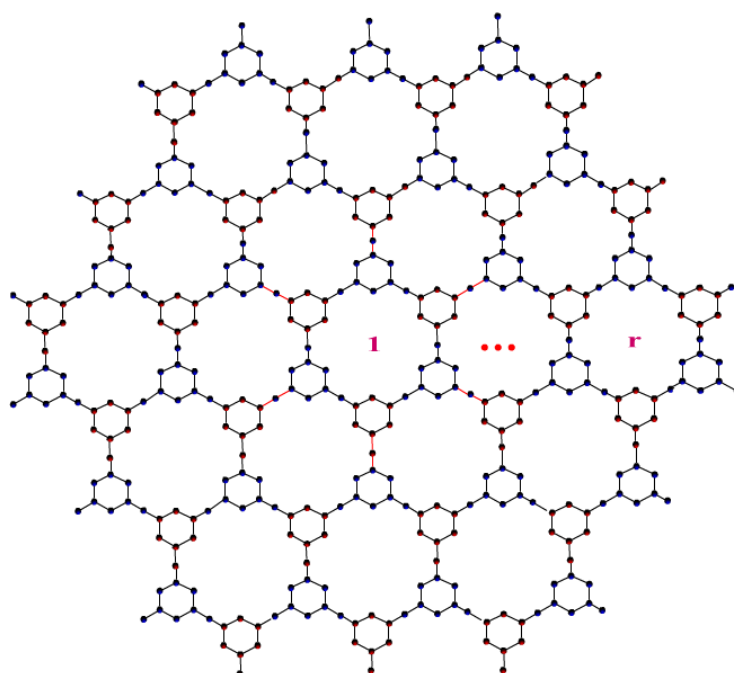


Figure 4. Hexagonal TriCF structure.

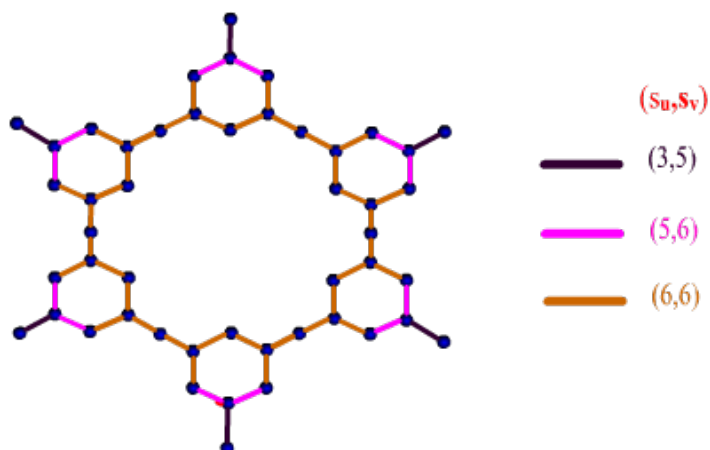


Figure 5. Neighborhood degree sum edge partition of the unit cell of the TriCF structure.

Table 3 below illustrates the total number of edges (\mathcal{Q}) and vertices (\mathcal{P}) and how the edges are partitioned in each structure.

Table 3. Edge partition of γ .

γ	(3, 5)	(5, 6)	(6, 6)	\mathcal{Q}	\mathcal{P}
γ_1	$2r + 4$	$4r + 8$	$30r + 6$	$36r + 18$	$36r + 15$
γ_2	$2(r + s + 1)$	$4(r + s + 1)$	$(18s + 12)r + 12s - 6$	$(18s + 18)r + 18s$	$(13s + 20)r + 18s + 3$
γ_3	$6r$	$12r$	$54r^2 - 18r$	$54r^2$	$45r^2 + 3r$

4.1. Neighborhood-Degree Sum-Based Topological Indices of TriCF Structure

Theorem 1. Let γ_1 be the Linear chain TriCF structure with dimension r . Then:

1. $NR(\gamma_1) = \frac{2(1 + \sqrt{2})(r + 2)\sqrt{15}}{15} + 5r + 1.$
2. $NRR(\gamma_1) = ((4r + 8)\sqrt{2} + 2r + 4)\sqrt{15} + 180r + 36.$
3. $NRRR(\gamma_1) = (4r + 8)\sqrt{2} + (8r + 16)\sqrt{5} + 150r + 30.$
4. $NM_1(\gamma_1) = 420r + 192.$
5. $NM_2(\gamma_1) = 1230r + 516.$
6. $NRM_2(\gamma_1) = 846r + 342.$
7. $NHM(\gamma_1) = 4932r + 2088.$
8. $NAZ(\gamma_1) = \frac{4263511r}{2700} + \frac{4311443}{6750}.$
9. $NH(\gamma_1) = \frac{137r}{22} + \frac{38}{11}.$
10. $NSC(\gamma_1) = \frac{(110r + 22)\sqrt{3}}{22} + \frac{(r + 2)(\sqrt{2} + \frac{8\sqrt{11}}{11})}{2}.$
11. $NGA(\gamma_1) = \frac{8(\sqrt{2} + \frac{11}{16})(r + 2)\sqrt{15}}{11} + 30r + 6.$
12. $NIS(\gamma_1) = \frac{4605r}{44} + \frac{1041}{22}.$
13. $NSDI(\gamma_1) = \frac{218r}{3} + \frac{112}{3}.$
14. $NF(\gamma_1) = 2472r + 1056.$
15. $NABC(\gamma_1) = \frac{(3\sqrt{6} + 6)\sqrt{5r + 10}}{15} + \frac{\sqrt{75r + 15}}{3}.$

Proof. Let γ_1 be a linear chain TriCF structure with \mathcal{P} and \mathcal{Q} (see Table 3). We performed edge partitions of γ_1 based on the neighborhood vertex degree sum. The following results were obtained by applying those edge partitions in the definitions of neighborhood degree sum-based topological indices (Table 1).

To provide the proofs, the neighborhood-degree sum-based topological indices of each TriCF linear chemical network would be too long to furnish in this paper. Hence, using the procedure mentioned below and Table 1, it is simple to construct any neighborhood-degree sum-based expression concerning each topological index.

The neighborhood-degree sum-based indices of the first Zagreb for a linear TriCF molecular graph is

$$\begin{aligned}
 NM_1(\gamma_1) &= (3 + 5)(2r + 4) + (5 + 6)(4r + 8) + (6 + 6)(30r + 6) \\
 &= (8)(2r + 4) + (11)(4r + 8) + (12)(30r + 6) \\
 &= 16r + 32 + 44r + 88 + 360r + 72 \\
 &= 420r + 192. \quad \square
 \end{aligned}$$

Theorem 2. Let γ_2 be the parallelogram TriCF structure with dimension r and s . Then, the neighborhood-degree sum-based topological indices are:

1. $NR(\gamma_2) = \frac{2(1+\sqrt{2})(r+s+1)\sqrt{15}}{15} + \frac{(45s+30)r}{15} + 2s - 1.$
2. $NRR(\gamma_2) = 4(r+s+1)(\sqrt{2} + \frac{1}{2})\sqrt{15} + (108s+72)r + 72s - 36.$
3. $NRRR(\gamma_2) = (4r+4s+4)\sqrt{2} + (8r+8s+8)\sqrt{5} + (90s+60)r + 60s - 30.$
4. $NM_1(\gamma_2) = (216s+204)r + 204s - 12.$
5. $NM_2(\gamma_2) = (648s+582)r + 582s - 66.$
6. $NRM_2(\gamma_2) = (450s+396)r + 396s - 54.$
7. $NHM(\gamma_2) = (2592s+2340)r + 2340s - 252.$
8. $NAZ(\gamma_2) = \frac{(11337408s+9980147)r}{13500} + \frac{9980147s}{13500} - \frac{1357261}{13500}.$
9. $NH(\gamma_2) = \frac{(66r+71)s}{22} + \frac{71r}{22} + \frac{5}{22}.$
10. $NSC(\gamma_2) = \frac{((66s+44)r+44s-22)\sqrt{3}}{22} + \frac{(r+s+1)(\sqrt{2} + \frac{8\sqrt{11}}{11})}{2}.$
11. $NGA(\gamma_2) = \frac{8(r+s+1)(\sqrt{2} + \frac{11}{16})\sqrt{15}}{11} + \frac{(396s+264)r}{22} + 12s - 6.$
12. $NIS(\gamma_2) = \frac{(2376r+2229)s}{44} + \frac{2229r}{44} - \frac{147}{44}.$
13. $NSDI(\gamma_2) = \frac{(216r+182)s}{3} + \frac{182r}{3} - \frac{34}{3}.$
14. $NF(\gamma_2) = (1296s+1176)r + 1176s - 120.$
15. $NABC(\gamma_2) = \frac{\sqrt{(45s+30)r+30s-15}}{3} + \frac{(3\sqrt{6}+6)\sqrt{5r+5s+5}}{15}.$

Proof. Let γ_2 be a parallelogram TriCF structure with \mathcal{P} and \mathcal{Q} be taken from Table 3. We performed edge partitions of γ_2 based on the neighborhood vertex degree sum, and the following results were obtained by applying those edge partitions in the definitions of neighborhood-degree sum-based topological indices (Table 1). To put forward the given proofs, the neighborhood-degree sum-based topological indices of each TriCF parallelogram chemical network would run into many pages. Hence, using the procedure mentioned below and Table 1, it is easy to construct any neighborhood-degree sum-based expression with regard to each topological index.

The neighborhood-degree sum-based indices of the second Zagreb for a parallelogram TriCF molecular graph is

$$\begin{aligned} NM_2(\gamma_2) &= (3 \times 5)2(r+s+1) + (5 \times 6)4(r+s+1) + (6 \times 6)((18s+12)r+12s-6) \\ &= 150r + 582s - 66 + 36(18s+12)r \\ &= (648s+582)r + 582s - 66. \quad \square \end{aligned}$$

Theorem 3. Let γ_3 be the hexagonal TriCF structure with dimension r . Then:

1. $NR(\gamma_3) = \frac{r(2\sqrt{15}\sqrt{2} + 2\sqrt{15} + 45r - 15)}{5}.$
2. $NRR(\gamma_3) = 6r(2\sqrt{15}\sqrt{2} + \sqrt{15} + 54r - 18).$
3. $NRRR(\gamma_3) = (4r+8)\sqrt{2} + (8r+16)\sqrt{5} + 150r + 30.$
4. $NM_1(\gamma_3) = 648r^2 - 36r.$
5. $NM_2(\gamma_3) = 1944r^2 - 198r.$
6. $NRM_2(\gamma_3) = 1350r^2 - 162r.$
7. $NHM(\gamma_3) = 7776r^2 - 756r.$
8. $NAZ(\gamma_3) = \frac{314928}{125}r^2 - \frac{1357261}{4500}r.$
9. $NH(\gamma_3) = \frac{15}{22}r + 9r^2.$
10. $NSC(\gamma_3) = \frac{3r(66\sqrt{3}r + 11\sqrt{2} + 8\sqrt{11} - 22\sqrt{3})}{22}.$

11. $NGA(\gamma_3) = \frac{3r(16\sqrt{15}\sqrt{2} + 11\sqrt{15} + 396r - 132)}{22}.$
12. $NIS(\gamma_3) = 162r^2 - \frac{441}{44}r.$
13. $NSDI(\gamma_3) = 108r^2 + 2r.$
14. $NF(\gamma_3) = 3888r^2 - 360r.$
15. $NABC(\gamma_3) = \left(\left(\frac{3\sqrt{2}}{5} + \frac{2\sqrt{3}}{5} \right) \sqrt{r} + \sqrt{3r^2 - r} \right) \sqrt{5}.$

Proof. Let γ_3 be a hexagonal TriCF structure \mathcal{P} and \mathcal{Q} given in Table 3. We performed edge partitions of γ_3 based on the neighborhood vertex degree sum, and the following results were obtained by applying those edge partitions in the definitions of neighborhood-degree sum-based topological indices (Table 1). To provide the proof, the neighborhood-degree sum-based topological indices of each TriCF hexagonal chemical network would be too long. Using the procedure mentioned below and Table 1, it is simple to construct any neighborhood-degree sum-based expression with regard to each topological index.

The neighborhood-degree sum-based indices of the forgotten indices for a hexagonal TriCF molecular graph is $NF(\gamma_3) = (9 + 25)(6r) + (25 + 36)(12r) + (36 + 36)(54r^2 - 18r) = (34)(6r) + (61)(12r) + (72)(54r^2 - 18r) = 3888r^2 - 360r.$ \square

4.2. Multiplicative Neighborhood-Degree Sum-Based Topological Indices of TriCF Structure

Theorem 4. Let γ_1 be the linear chain TriCF structure with dimension r . Then, the neighborhood-degree sum-based multiplicative indices are:

1. $MNR(\gamma_1) = \frac{1}{6^{30r+6}15^{4r+8}3^{30r+6}}.$
2. $MNRR(\gamma_1) = 2^{32r+10}3^{33r+12}5^{3r+6}.$
3. $MNRRR(\gamma_1) = 2^{7r+14}5^{32r+10}.$
4. $MNM_1(\gamma_1) = 8^{2r+4}11^{4r+8}12^{30r+6}.$
5. $MNM_2(\gamma_1) = 15^{2r+4}30^{4r+8}36^{30r+6}.$
6. $MNRM_2(\gamma_1) = 8^{2r+4}20^{4r+8}25^{30r+6}.$
7. $MNHM(\gamma_1) = 64^{2r+4}121^{4r+8}144^{30r+6}.$
8. $MNAZ(\gamma_1) = 2^{96r+30}3^{168r+12}5^{18-72r}.$
9. $MNH(\gamma_1) = \frac{1}{6^{30r+6}11^{4r+8}}.$
10. $MNSC(\gamma_1) = \frac{1}{1619177472 \cdot 2^{33r}3^{15r}11^{2r}}.$
11. $MNGA(\gamma_1) = \frac{1}{2^{34r+11}11^{4r+8}}.$
12. $MNIS(\gamma_1) = \left(\frac{15}{8} \right)^{2r+4} \left(\frac{30}{11} \right)^{4r+8} 3^{30r+6}.$
13. $MNSDI(\gamma_1) = \left(\frac{34}{15} \right)^{2r+4} \left(\frac{61}{30} \right)^{4r+8} 2^{30r+6}.$
14. $MNF(\gamma_1) = 34^{2r+4}61^{4r+8}72^{30r+6}.$
15. $MNABC(\gamma_1) = \frac{5^{12r}}{36000 \cdot 2^{16r}3^{28r}}.$

Proof. Let γ_1 be a linear chain TriCF structure with vertices \mathcal{P} and \mathcal{Q} (see Table 3). We performed edge partitions of γ_1 based on the neighborhood vertex degree sum, and the following results were obtained by applying those edge partitions in the definitions of multiplicative neighborhood-degree sum-based topological indices (Table 2). To provide the proofs, the multiplicative neighborhood-degree sum-based topological indices of each TriCF linear chemical network would be too long. By using the below-mentioned procedure and Table 2, it is simple to construct any multiplicative neighborhood-degree sum-based expression with regard to each topological index.

The multiplicative neighborhood-degree sum-based indices of the Randić indices for a linear TriCF molecular graph is $NMR(\gamma_1) = (9 + 25)^{(2*r+4)} (25 + 36)^{(4*r+8)} (36 + 36)^{(30*r+6)} = 34^{2r+4} 61^{4r+8} 72^{30r+6}$. \square

Theorem 5. Let γ_2 be the parallelogram TriCF structure with dimension r and s . Then, the multiplicative neighborhood-degree sum-based topological indices are:

1. $MNM_1(\gamma_2) = 8^{2r+2s+2} 11^{4r+4s+4} 12^{(18s+12)r+12s-6}$.
2. $MNM_2(\gamma_2) = 15^{2r+2s+2} 30^{4r+4s+4} 36^{(18s+12)r+12s-6}$.
3. $MNRM_2(\gamma_2) = 2^{14r+14s+14} 5^{36rs+28r+28s-8}$.
4. $MNHM(\gamma_2) = 64^{2r+2s+2} 121^{4r+4s+4} 144^{(18s+12)r+12s-6}$.
5. $MNAZ(\gamma_2) = \left(\frac{125}{8}\right)^{2r+2s+2} \left(\frac{1000}{27}\right)^{4r+4s+4} \left(\frac{5832}{125}\right)^{(18s+12)r+12s-6}$.
6. $MNR(\gamma_2) = \left(\frac{\sqrt{15}}{15}\right)^{2r+2s+2} \left(\frac{\sqrt{30}}{30}\right)^{4r+4s+4} \left(\frac{1}{6}\right)^{(18s+12)r+12s-6}$.
7. $MNRR(\gamma_2) = \left(\sqrt{15}\right)^{2r+2s+2} \left(\sqrt{30}\right)^{4r+4s+4} 6^{(18s+12)r+12s-6}$.
8. $MNRRR(\gamma_2) = 2^{7r+7s+7} 5^{18rs+14r+14s-4}$.
9. $MNH(\gamma_2) = \left(\frac{1}{4}\right)^{2r+2s+2} \left(\frac{2}{11}\right)^{4r+4s+4} \left(\frac{1}{6}\right)^{(18s+12)r+12s-6}$.
10. $MNSC(\gamma_2) = \left(\frac{\sqrt{2}}{4}\right)^{2r+2s+2} \left(\frac{\sqrt{11}}{11}\right)^{4r+4s+4} \left(\frac{\sqrt{3}}{6}\right)^{(18s+12)r+12s-6}$.
11. $MNGA(\gamma_2) = 8 \left(\frac{\sqrt{15}}{8}\right)^{2r+2s+2} \left(\frac{\sqrt{30}}{11}\right)^{4r+4s+4} \left(\frac{1}{2}\right)^{(18s+12)r+12s-6}$.
12. $MNIS(\gamma_2) = \left(\frac{15}{8}\right)^{2r+2s+2} \left(\frac{30}{11}\right)^{4r+4s+4} 3^{(18s+12)r+12s-6}$.
13. $MNSDI(\gamma_2) = \left(\frac{34}{15}\right)^{2r+2s+2} \left(\frac{61}{30}\right)^{4r+4s+4} 2^{(18s+12)r+12s-6}$.
14. $MNF(\gamma_2) = 34^{2r+2s+2} 61^{4r+4s+4} 72^{(18s+12)r+12s-6}$.
15. $MNABC(\gamma_2) = \left(\frac{\sqrt{10}}{5}\right)^{2r+2s+2} \left(\frac{\sqrt{30}}{10}\right)^{4r+4s+4} \left(\frac{\sqrt{10}}{6}\right)^{(18s+12)r+12s-6}$.

Proof. Let γ_2 be a parallelogram TriCF structure with vertex and edge set \mathcal{P} and \mathcal{Q} , respectively (Table 3). We performed edge partitions of γ_2 based on the neighborhood vertex degree sum (Table 3), and the following results were obtained by applying those edge partitions in the definitions of multiplicative neighborhood-degree sum-based topological indices (Table 2).

To provide the proofs, the multiplicative neighborhood-degree sum-based topological indices of each TriCF parallelogram chemical network would be too long. By using the below-mentioned procedure and Table 2, it is simple to construct any multiplicative neighborhood-degree sum-based expression with regard to each topological index.

Multiplicative neighborhood-degree-based indices of the first Zagreb for a parallelogram TriCF molecular graph is $MNM_1(\gamma_2) = (3 + 5)^{(2r+2s+2)} (5 + 6)^{(4r+4s+4)} (6 + 6)^{((18*s+12)r+12s-6)} = 8^{(2r+2s+2)} 11^{(4r+4s+4)} 12^{((18s+12)r+12s-6)}$. \square

Theorem 6. Let γ_3 be the hexagonal TriCF structure with dimension r . Then, the multiplicative neighborhood-degree sum-based topological indices are:

1. $MNM_1(\gamma_3) = 8^{6r} 11^{12r} 12^{54r^2-18r}$.
2. $MNM_2(\gamma_3) = 15^{6r} 30^{12r} 36^{54r^2-18r}$.
3. $MNRM_2(\gamma_3) = 8^{6r} 20^{12r} 25^{54r^2-18r}$.
4. $MNHM(\gamma_3) = 64^{6r} 121^{12r} 144^{54r^2-18r}$.

$$\begin{aligned}
5. \quad MN_{AZ}(\gamma_3) &= \left(\frac{125}{8}\right)^{6r} \left(\frac{1000}{27}\right)^{12r} \left(\frac{5832}{125}\right)^{54r^2-18r} \\
6. \quad MN_R(\gamma_3) &= \left(\frac{\sqrt{15}}{15}\right)^{6r} \left(\frac{\sqrt{30}}{30}\right)^{12r} \left(\frac{1}{6}\right)^{54r^2-18r} \\
7. \quad MN_{RR}(\gamma_3) &= \left(\sqrt{15}\right)^{6r} \left(\sqrt{30}\right)^{12r} 6^{54r^2-18r} \\
8. \quad MN_{RRR}(\gamma_3) &= \left(2\sqrt{2}\right)^{6r} \left(2\sqrt{5}\right)^{12r} 5^{54r^2-18r} \\
9. \quad MN_H(\gamma_3) &= \left(\frac{1}{4}\right)^{6r} \left(\frac{2}{11}\right)^{12r} \left(\frac{1}{6}\right)^{54r^2-18r} \\
10. \quad MN_{SC}(\gamma_3) &= \left(\frac{\sqrt{2}}{4}\right)^{6r} \left(\frac{\sqrt{11}}{11}\right)^{12r} \left(\frac{\sqrt{3}}{6}\right)^{54r^2-18r} \\
11. \quad MN_{GA}(\gamma_3) &= 8 \left(\frac{\sqrt{15}}{8}\right)^{6r} \left(\frac{\sqrt{30}}{11}\right)^{12r} \left(\frac{1}{2}\right)^{54r^2-18r} \\
12. \quad MN_{IS}(\gamma_3) &= \left(\frac{15}{8}\right)^{6r} \left(\frac{30}{11}\right)^{12r} 3^{54r^2-18r} \\
13. \quad MN_{SDI}(\gamma_3) &= \left(\frac{34}{15}\right)^{6r} \left(\frac{61}{30}\right)^{12r} 2^{54r^2-18r} \\
14. \quad MN_F(\gamma_3) &= 34^{6r} 61^{12r} 72^{30r+6} \\
15. \quad MN_{ABC}(\gamma_3) &= \left(\frac{\sqrt{10}}{5}\right)^{6r} \left(\frac{\sqrt{30}}{10}\right)^{12r} \left(\frac{\sqrt{10}}{6}\right)^{54r^2-18r}
\end{aligned}$$

Proof. Let γ_3 be a hexagonal TriCF structure. The cardinality of vertices \mathcal{P} and edges \mathcal{Q} is given in Table 3. We performed edge partitions of γ_3 based on the neighborhood vertex degree sum, and the following results were obtained by applying those edge partitions in the definitions of multiplicative neighborhood-degree sum-based topological indices (Table 2). To provide the proofs, the multiplicative neighborhood-degree sum-based topological indices of each TriCF hexagonal chemical network would be too long. By using the below-mentioned procedure and Table 2, it is simple to construct any multiplicative neighborhood-degree sum-based expression with regard to each topological index.

The multiplicative neighborhood-degree sum-based indices of the first Zagreb for a hexagonal TriCF molecular graph is $MN_{M1}(\gamma_3) = (3+5)^{(6r)}(5+6)^{(12r)}(6+6)^{(54r^2-18r)} = 8^{6r} 11^{12r} 12^{54r^2-18r}$.

□

4.3. Neighborhood-Degree Sum-Based Entropy Measures

This section discusses constructing the probability function using neighborhood-degree sum-based topological indices to compute the entropy values using Shannon's approach. The calculation procedure is illustrated below by using Equation (3) to calculate the entropy value of the first Zagreb index for the TriCF structure. Furthermore, Figure 6 is the 3D plot of the entropy of the first Zagreb index.

The first Zagreb entropy for the linear chain TriCF molecular graph is

$$\begin{aligned}
EN_{M1}(\gamma_1) &= \log(420r + 192) - \frac{(2r+4)(3+5)\log(3+5) + (4r+8)(5+6)\log(5+6) + (30r+6)(6+6)\log(6+6)}{420r + 192} \\
&= \log(420r + 192) - \frac{24(2r+4)\log(2) + 11(4r+8)\log(11) + 12(30r+6)\log(12)}{420r + 192}
\end{aligned}$$

After simplifying this, we obtain

$$ENM_1(\gamma_1) = \frac{(105r + 48) \log(35r + 16) + 18(r + 2)(\log(2) + \frac{5 \log(3)}{6} - \frac{11 \log(11)}{18})}{105r + 48}.$$

Figure 6 illustrates the entropy of the first Zagreb index of the TriCF linear chain structure using Maple 2020. Using the parameters r and s , we established a horizontal grid and, then, constructed a surface on top of that grid. This graph illustrates how the entropy values exhibit unique patterns corresponding to various causes. These graphs show various entropy features based on the parameters. We can regulate various variables and actions by varying the topological indices and entropy via these elements. Each TriCF chemical network's general entropy formulation is too lengthy to be given as a theorem. As mentioned above, the method makes it easy to generate any neighborhood-degree sum-based entropy expression for each topological index.

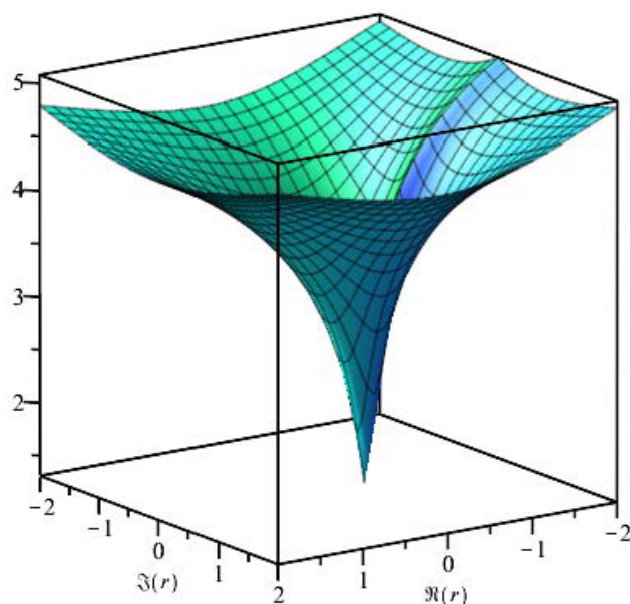


Figure 6. Three-dimensional plot of $ENM_1(\gamma_1)$.

5. Numerical Computation

This section displays the numerical outcomes of neighborhood-degree sum-based topological descriptors created for three distinct TriCF structures using entropy measurements. The values of the variables r and s range from 1 to 10. The generated topological descriptors were plotted using the Origin 2020 b application for a graphical comparison. The outcomes are summarized in Tables 4–6. Figure 5 depicts this tendency in three dimensions. These 3D charts illustrate the variation of each topological index for a particular structure. The behavior of a specific index for each of the three alternative structures that are the subject of this article can also be compared using 3D graphs. The following tables and figures analyze various entropies for all the possible structures of the TriCF molecular graph in numerical and graphical form.

Table 4. Numerical values for neighborhood-degree sum-based entropies of a linear chain TriCF structure.

$r \rightarrow$	1	2	3	4	5	6	7	8	9	10
$ER(\gamma_1)$	3.9779	4.4903	4.8276	5.0793	5.2803	5.4476	5.5908	5.7161	5.8274	5.9276
$ERR(\gamma_1)$	3.9814	4.4935	4.8306	5.0823	5.2831	5.4503	5.5936	5.7188	5.8301	5.9302
$ERRR(\gamma_1)$	3.977	4.4899	4.8274	5.0792	5.2802	5.4475	5.5908	5.7161	5.8274	5.9276
$EM_1(\gamma_1)$	3.9824	4.4943	4.8313	5.0829	5.2838	5.451	5.5942	5.7194	5.8307	5.9308
$EM_2(\gamma_1)$	3.9643	4.4795	4.818	5.0704	5.2718	5.4394	5.5828	5.7083	5.8197	5.92
$ERM_2(\gamma_1)$	3.9523	4.4698	4.8093	5.0623	5.2641	5.4319	5.5755	5.7011	5.8127	5.9131
$EHM(\gamma_1)$	3.9671	4.4818	4.82	5.0723	5.2736	5.4411	5.5845	5.71	5.8214	5.9216
$EAZ(\gamma_1)$	3.954	4.4712	4.8105	5.0634	5.2651	5.4329	5.5765	5.7021	5.8136	5.914
$EH(\gamma_1)$	9.1795	11.7376	14.0571	16.2695	18.4211	20.5336	22.6189	24.684	26.7338	28.7714
$ESC(\gamma_1)$	3.9868	4.498	4.8346	5.086	5.2867	5.4538	5.597	5.7222	5.8334	5.9335
$EGA(\gamma_1)$	3.9889	4.4998	4.8362	5.0876	5.2882	5.4553	5.5984	5.7236	5.8348	5.9349
$EIS(\gamma_1)$	3.9804	4.4927	4.8299	5.0816	5.2825	5.4497	5.5929	5.7182	5.8295	5.9296
$EAZI(\gamma_1)$	3.9882	4.4991	4.8357	5.087	5.2877	5.4548	5.5979	5.7231	5.8343	5.9344
$EF(\gamma_1)$	3.9696	4.4838	4.8218	5.074	5.2753	5.4427	5.5861	5.7115	5.8229	5.9231
$EABC(\gamma_1)$	4.5889	5.7275	6.6214	7.376	8.0385	8.6346	9.1802	9.6858	10.1586	10.6041

Table 5. Numerical values for the neighborhood-degree sum-based entropies of a parallelogram TriCF structure.

$(r, s) \rightarrow$	1	2	3	4	5	6	7	8	9	10
$ER(\gamma_2)$	−150.6809	−158.9867	−162.4445	−164.3874	−165.6278	−166.4793	−167.0923	−167.5486	−167.8965	−168.1668
$ERR(\gamma_2)$	−14.3228	−13.8865	−13.4802	−13.1369	−12.8428	−12.5861	−12.3585	−12.1542	−11.9688	−11.7991
$ERRR(\gamma_2)$	−9.3014	−8.7902	−8.3518	−7.9898	−7.6833	−7.4176	−7.1833	−6.9737	−6.7841	−6.6109
$EM_1(\gamma_2)$	3.9824	4.9654	5.595	6.0657	6.4434	6.7595	7.0317	7.2708	7.484	7.676
$EM_2(\gamma_2)$	3.9643	4.9536	5.5861	6.0584	6.4373	6.7543	7.0271	7.2667	7.4803	7.6731
$ERM_2(\gamma_2)$	3.9523	4.946	5.5804	6.0539	6.4335	6.751	7.0242	7.2641	7.4779	7.671
$EHM(\gamma_2)$	3.9671	4.9554	5.5875	6.0595	6.4382	6.7551	7.0278	7.2673	7.4808	7.6736
$EAZ(\gamma_2)$	4.3707	5.1949	5.7625	6.1985	6.5538	6.8541	7.1144	7.3444	7.5503	7.7368
$EH(\gamma_2)$	3.9796	4.9632	5.5932	6.0641	6.442	6.7584	7.0306	7.2698	7.4832	7.6757
$ESC(\gamma_2)$	3.9868	4.9683	5.5973	6.0675	6.4449	6.7609	7.0329	7.2718	7.485	7.6774
$EGA(\gamma_2)$	3.9889	4.9698	5.5984	6.0684	6.4457	6.7616	7.0335	7.2724	7.4855	7.6779
$EIS(\gamma_2)$	3.9804	4.9641	5.5941	6.0649	6.4427	6.759	7.0312	7.2703	7.4836	7.6762
$EAZI(\gamma_2)$	3.9509	4.944	5.5786	6.0523	6.4321	6.7497	7.0231	7.263	7.477	7.6701
$EF(\gamma_2)$	3.9696	4.957	5.5887	6.0605	6.439	6.7558	7.0284	7.2678	7.4814	7.6741
$EABC(\gamma_2)$	4.5889	7.071	9.4073	11.7079	14.002	16.3001	18.6062	20.2467	23.2467	25.5816

Table 6. Numerical values for the neighborhood-degree sum-based entropies of a hexagonal TriCF structure.

$r \rightarrow$	1	2	3	4	5	6	7	8	9	10
$ER(\gamma_3)$	3.9779	5.3687	6.1816	6.758	7.205	7.5701	7.8787	8.146	8.3818	8.5927
$ERR(\gamma_3)$	3.9814	5.37127	6.1834	6.7594	7.2061	7.5711	7.8796	8.1468	8.3825	8.5933
$ERRR(\gamma_3)$	3.977	5.3688	6.1818	6.7582	7.2052	7.5703	7.8789	8.1462	8.3819	8.5928
$EM_1(\gamma_3)$	3.9824	5.3717	6.1837	6.7597	7.2063	7.5712	7.8797	8.1469	8.3826	8.5934
$EM_2(\gamma_3)$	3.9643	5.3622	6.1773	6.7548	7.2024	7.568	7.8769	8.1445	8.3804	8.5914
$ERM_2(\gamma_3)$	3.9523	5.3561	6.1732	6.7518	7.2	7.5659	7.8752	8.1429	8.379	8.5902
$EHM(\gamma_3)$	3.9671	5.3636	6.1783	6.7556	7.203	7.5685	7.8773	8.1448	8.3807	8.5917
$EAZ(\gamma_3)$	3.954	5.3569	6.1738	6.7522	7.2003	7.5662	7.8754	8.1431	8.3792	8.5904
$EH(\gamma_3)$	9.1795	16.6571	23.3695	29.7961	36.0729	42.2578	48.3802	54.4577	60.5011	66.5179
$ESC(\gamma_3)$	3.9868	5.374	6.1853	6.7609	7.2073	7.5721	7.8804	8.1475	8.3831	8.5939
$EGA(\gamma_3)$	3.9889	5.3753	6.1862	6.7616	7.2078	7.5725	7.8808	8.1479	8.3834	8.5941
$EIS(\gamma_3)$	3.9804	5.3706	6.183	6.7592	7.2059	7.5709	7.8794	8.1466	8.3823	8.5932
$EAZI(\gamma_3)$	3.9882	5.3748	6.1859	6.7613	7.2077	7.5723	7.8807	8.1477	8.3833	8.5941
$EF(\gamma_3)$	3.9696	5.3649	6.1791	6.7562	7.2036	7.5689	7.8777	8.1452	8.381	8.592
$EABC(\gamma_3)$	4.5889	8.5204	12.4547	16.4326	20.4534	24.5118	28.6026	32.7216	36.8652	41.0305

Results and Discussion

If we examine the entropy measures in Figure 7a,c, we can see that the neighborhood harmonic (NH) significantly impacts the initial structure more than the other indices. At the same time, Figure 7b shows that the NABC outperforms the other entropy measures. The stability study of the generalized TriCF structure using numerical information entropy values and the derived entropy formulae are new findings that can connect Shannon's entropy with traditional thermodynamic entropy.

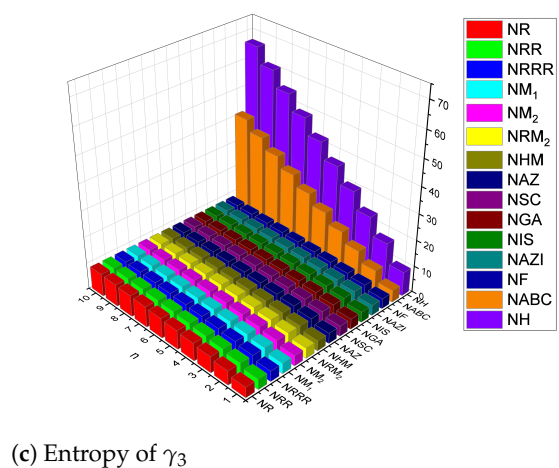
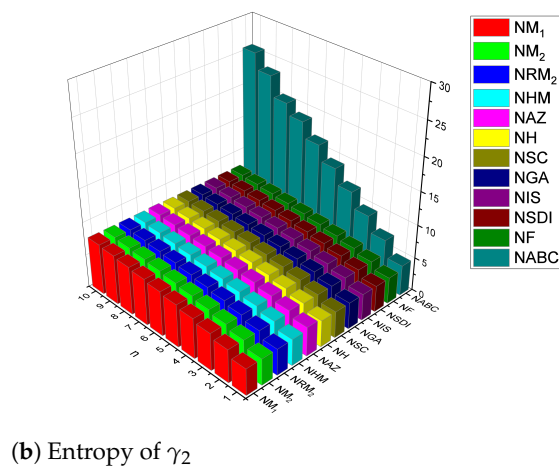
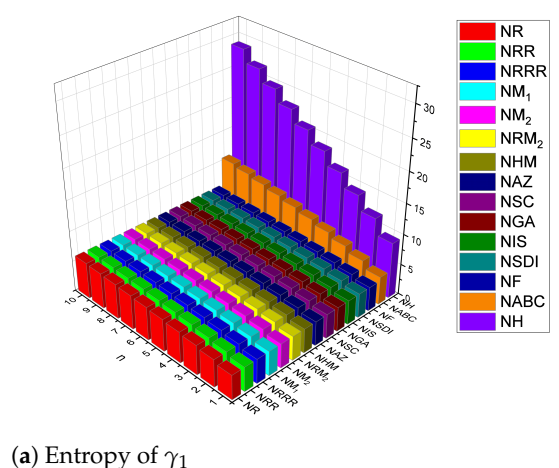


Figure 7. Comparison of entropy measures for TriCF structures.

In this study, we determined the neighborhood degree sum indices, multiplicative neighborhood degree sum indices, and entropy of TriCF structure using the neighborhood degree sum edge partition. From the computation and analysis, we obtained that the neighborhood harmonic indices and neighborhood ABC indices both have more impact than other indices and are highly correlated to the thermodynamic properties of the TriCF structures [16–18,22,23,37]. In the previous study [9], we determined degree-based indices, multiplicative degree-based indices, and the entropy values of the TriCF structure by the edge partition method based on the degrees of the end vertices and reciprocal Randić indices showed a higher impact. This will simulate molecules' physical and chemical characteristics [3,5,15] regarding the structure. Therefore, by employing degree-based and neighborhood degree-sum-based approaches, future researchers can easily compute the topological indices of upcoming TriCF structures, and also, these studies will help them produce different types of TriCF structures for different applications.

6. Conclusions

In this study, neighborhood-degree-based topological indices were computed using multiplicative and entropy measures. Using these indices, scientists can predict a range of molecular compound properties without requiring expensive or time-consuming studies. The computed findings are, therefore, crucial in predicting TriCF system properties. This is a newly synthesized lubricant whose physical, chemical, and experimental properties have yet to be investigated. As a result, the researchers will be able to advance their work with the support of this current study. For further use, we also generated the multiplicative neighborhood topological indices for the TriCF structure. Both theoretical chemists and industry experts will find this paper's graphical representation and numerical comparison of the computed findings beneficial. With the aid of the observations produced regarding the effectiveness of various indices, other researchers will be able to choose the indices more efficiently. The same classes, distance-based indices, QSAR, and QSPR, are being developed because they are also crucial for research.

Author Contributions: Conceptualization, T.A.; formal analysis, T.A.; methodology, T.A.; software, T.A.; supervision, R.S.; validation, T.A. and R.S.; visualization, T.A.; writing—original draft, T.A.; writing—review and editing, R.S. All authors have read and agreed to the published version of the manuscript.

Funding: This research was funded by Vellore Institute of Technology, Vellore.

Data Availability Statement: The authors declare that all data supporting the findings of this study are available within the article.

Conflicts of Interest: The authors declare no conflict of interest.

References

1. Mirajkar, K.G.; Morajkar, A.; Budihal, H.H. QSPR analysis of some chemical structures using KCD indices. *AIP Conf. Proc.* **2022**, *2385*, 030002. [\[CrossRef\]](#)
2. Nilanjan, D.; Nayeem, S.M.A.; Anita, P. F-index of some graph operations. *Discret. Math. Algorithms Appl.* **2016**, *8*, 1650025. [\[CrossRef\]](#)
3. Furtula, B.; Graovac, A.; Vukicevic, D. Augmented Zagreb index. *J. Math. Chem.* **2010**, *48*, 370–380. [\[CrossRef\]](#)
4. Furtula, B.; Gutman, I. Forgotten topological index. *J. Math. Chem.* **2015**, *53*, 1184–1190. [\[CrossRef\]](#)
5. Gutman, I. Degree-based topological indices. *Croat Chem. Acta.* **2013**, *86*, 351–361. [\[CrossRef\]](#)
6. Mondal, S.; Nilanjan, D.; Anita, P. QSPR analysis of some novel neighborhood-degree-based topological descriptors. *Complex Intell. Syst.* **2021**, *7*, 977–996. [\[CrossRef\]](#)
7. Huilgol, M.I.; Sriram, V.; Balasubramanian, K. Structure–Activity Relations for Antiepileptic Drugs through Omega Polynomials and Topological Indices. *Mol. Phys.* **2022**, *120*, 1987542. [\[CrossRef\]](#)
8. Wen, P.; Zhang, C.; Yang, Z.; Dong, R.; Wang, D.; Fan, M.; Wang, J. Triazine-Based Covalent-Organic Frameworks: A Novel Lubricant Additive with Excellent Tribological Performances. *Tribol. Int.* **2017**, *111*, 57–65. [\[CrossRef\]](#)
9. Augustine, T.; Roy, S. Topological Study on Triazine-Based Covalent-Organic Frameworks. *Symmetry* **2022**, *14*, 1590. [\[CrossRef\]](#)
10. Sabirov, D.S.; Shepelevich, I.S. Information Entropy in Chemistry: An Overview. *Entropy* **2021**, *23*, 1240. [\[CrossRef\]](#)

11. Rahul, M.P.; Clement, J.; Singh Junias, J.; Arockiaraj, M.; Balasubramanian, K. Degree-Based Entropies of Graphene, Graphyne and Graphdiyne Using Shannon's Approach. *J. Mol. Struct.* **2022**, *1260*, 132797. [\[CrossRef\]](#)
12. Mowshowitz, A.; Dehmer, M. Entropy and the Complexity of Graphs Revisited. *Entropy* **2012**, *14*, 559–570. [\[CrossRef\]](#)
13. Kavitha, S.R.J.; Abraham, J.; Arockiaraj, M.; Jency, J.; Balasubramanian, K. Topological Characterization and Graph Entropies of Tessellations of Kekulene Structures: Existence of Isentropic Structures and Applications to Thermochemistry, Nuclear Magnetic Resonance, and Electron Spin Resonance. *J. Phys. Chem. A* **2021**, *125*, 8140–8158. [\[CrossRef\]](#) [\[PubMed\]](#)
14. Mondal, S.; Nilanjan, D.; Anita, P. On neighborhood Zagreb index of product graphs. *J. Mol. Struct.* **2020**, *1223*, 129210. [\[CrossRef\]](#) [\[PubMed\]](#)
15. Randić, M. Characterization of molecular branching. *J. Am. Chem. Soc.* **1975**, *97*, 6609–6615. [\[CrossRef\]](#)
16. Sun, C.; Khalid, A.; Usman, H.; Ahmad, A.; Siddiqui, M.; Fufa, S.A. On Neighborhood-Degree-Based Topological Analysis of Polyphenylene Network. *Math. Probl. Eng.* **2022**, *2022*, 1951226. [\[CrossRef\]](#)
17. Mondal, S.; Nilanjan, D.; Anita, P. Topological properties of Graphene using some novel neighborhood-degree-based topological indices. *Int. J. Math. Ind.* **2019**, *11*, 1950006. [\[CrossRef\]](#)
18. Prosanta S.; Nilanjan, D.; Anita, P. On Some Neighbourhood Degree-Based Multiplicative Topological Indices and Their Applications. *Polycycl Aromat Compd.* **2022**, *42*, 7738–7753. [\[CrossRef\]](#)
19. Balasubramanian, K. Combinatorics, Big Data, Neural Network & AI for Medicinal Chemistry & Drug Administration. *Lett. Drug Des. Discov.* **2021**, *18*, 943–948. [\[CrossRef\]](#)
20. Hawkins, D.M.; Basak, S.C.; Shi, X. QSAR with few compounds and many features. *J. Chem. Inf. Comput. Sci.* **2001**, *41*, 663–670. [\[CrossRef\]](#)
21. Shanmukha, M.C.; Usha, A.; Siddiqui, M.K.; Shilpa, K.C.; Asare-Tuah, A. Novel Degree-Based Topological Descriptors of Carbon Nanotubes. *J. Chem.* **2021**, *2021*, 3734185. [\[CrossRef\]](#)
22. Kulli, V.R. Some new multiplicative geometric-arithmetic indices. *Journal of Ultra. Sci. Phys. Sci. A* **2017**, *29*, 52–57.
23. Wang, S.; Wei, B. Multiplicative Zagreb Indices of K-Trees. *Discrete Appl. Math.* **2015**, *180*, 168–175. 2014.08.017. [\[CrossRef\]](#)
24. Kulli, V.R. Multiplicative Hyper-Zagreb Indices and Coindices of Graphs: Computing These Indices of Some Nanostructures. *Int. Res. J. Pure Algebra* **2016**, *6*, 342–347.
25. Kulli, V.R.; Stone, B.; Wang, S.; Wei, B. Generalised Multiplicative Indices of Polycyclic Aromatic Hydrocarbons and Benzenoid Systems. *Z. Naturforsch. A* **2017**, *72*, 573–576. [\[CrossRef\]](#)
26. Kwun, Y.C.; Virk, A.R.; Nazeer, W.; Rehman, M.A.; Kang, S.M. On the Multiplicative Degree- Based Topological Indices of Silicon-Carbon Si₂C₃-I [p,q] and Si₂C₃-II. *Symmetry* **2018**, *10*, 320–330. [\[CrossRef\]](#)
27. Bhanumathi, M.; Rani, K.E.J. On Multiplicative Sum Connectivity Index, Multiplicative Randic Index and Multiplicative Harmonic Index of Some Nanostar Dendrimers. *Int. J. Adv. Sci. Eng. Sci. Adv. Comput. Bio-Technol.* **2018**, *9*, 52–67. [\[CrossRef\]](#)
28. Mahboob, A.; Mahboob, S.; Jaradat, M.M.M.; Nigar, N.; Siddique, I. On Some Properties of Multiplicative Topological Indices in Silicon-Carbon. *J. Math.* **2021**, *2021*, 4611199. [\[CrossRef\]](#)
29. Kulli, V.R. Multiplicative Connectivity Indices of TUC₄C₈. *J. Math. Comput. Sci.* **2016**, *7*, 599–605.
30. Kulli, V.R. Some New Fifth Multiplicative Zagreb Indices of PAMAM Dendrimers. *J. Glob. Res. Math. Arch.* **2018**, *5*, 82–86.
31. Mondal, S.; Nilanjan, D.; Anita, P. On Some General Neighborhood Degree Based Topological Indices. *Int. J. Appl. Math.* **2019**, *32*, 1037–1049. [\[CrossRef\]](#)
32. Weidong, Z.; Shanmukha, M.C.; Usha, A.; Farahan, M.R.; Shilpa, K.C. Computing SS Index of Certain Dendrimers. *J. Math.* **2021**, *2021*, 7483508. [\[CrossRef\]](#)
33. Gao, X.; Gallicchio, E.; Roitberg, A.E. The generalized Boltzmann distribution is the only distribution in which the Gibbs-Shannon entropy equals the thermodynamic entropy. *J. Chem. Phys.* **2019**, *151*, 034113. [\[CrossRef\]](#) [\[PubMed\]](#)
34. Bonchev, D. *Chemical Graph Theory: Introduction and Fundamentals*, 1st ed.; CRC Press: Boca Raton, FL, USA, 1991.
35. Ghorbani, M.; Hosseinzadeh, M.A. A new version of Zagreb indices. *Filomat* **2012**, *26*, 93–100. [\[CrossRef\]](#)
36. Rahul, M.P.; Clement, J. Topological characterization and entropy measures of large cavity cycloarene oligomers. *Eur. Phys. J. Plus.* **2022**, *137*, 1365. [\[CrossRef\]](#)
37. Mondal, S.; Nilanjan, D.; Anita, P. On some new neighborhood degree based indices. *Acta Chem. Iasi.* **2019**, *27*, 31–46. [\[CrossRef\]](#)

Disclaimer/Publisher's Note: The statements, opinions and data contained in all publications are solely those of the individual author(s) and contributor(s) and not of MDPI and/or the editor(s). MDPI and/or the editor(s) disclaim responsibility for any injury to people or property resulting from any ideas, methods, instructions or products referred to in the content.



Determination of Degree-Based Molecular Descriptors of Superphenalene and Supertriphenylene through M-Polynomial

Tony Augustine^a, S. Roy ^{a,1}, S. Govardhan^a, S. Prabhu^b

^aDepartment of Mathematics, School of Advanced Sciences, VIT University, Vellore 632014, India

^bDepartment of Mathematics, Rajalakshmi Engineering College, Chennai 602105, India

¹roy.santiago@vit.ac.in

Abstract:

The objective of this article is to obtain degree-based molecular descriptors for super-polycyclic aromatic compounds like superphenalene and supertriphenylene, which are built upon the foundational molecule hexabenzocoronene. These descriptors will offer quantitative insights into the connectivity and structural properties of these compounds by analysing their degree of connectivity. These super-polycyclic aromatic compounds have been the focus of several studies due to their unprecedented mechanical lead to their remarkable thermoelectric conductivities, making graphene an obvious choice to replace other common materials in a variety of applications. With the help of M-polynomial, we were able to generate numerous degree-based descriptors in this study.

Key Words: M-polynomial; Superphenalene; Supertriphenylene; Molecular descriptors; Super-polycyclic aromatic compounds.

1: Introduction

Polycyclic aromatic hydrocarbons (PAHs) are broad family of chemical compounds that are persistent environmental pollutants with unique structures and varying toxicity. They comprise two or more fused aromatic rings and have a wide range of toxicity. Hundreds of individual PAHs are released into the environment because of both anthropogenic and natural processes [1]. Hexabenzocoronene (HBC) should be referred to as a superbenzene because of its hexagonal symmetry and peripheral benzene rings that each equate to one sp^2 -carbon of benzene. Mullen's research group prepared super-PAHs in 2001 [2], incorporating well-known terminology for benzene substitution patterns, such as ortho, meta, and para. Superphenalene is essentially a PAH with the chemical formula $C_{96}H_{30}$, and it is widely believed to be composed of three trapped Hexa-peri-hexabenzocoronene (HBC) molecules. It is generally regarded as a structure consisting of three HBC molecules symmetrically associated around a central core [3].

These HBCs have been recognized as building blocks for molecular electronics since 2004, as they form self-assembled structures and nanotubes. The synthesis of HBCs has led to the formation of superacenes, such as supertriphenylene, through the cyclodehydrogenation of their corresponding twisted precursors [4].

In chemical graph theory, chemical structures are depicted as molecular graphs, which are simple graphs that illustrate the carbon atom skeleton of an organic molecule. The vertices of the molecular graph represent the carbon atoms, while the edges represent the carbon-carbon bonds [5]. A topological index, often referred to as a molecular structure descriptor, is a numerical value correlated with the chemical make-up of a molecule. These indices are employed to link chemical structure to a variety of physical attributes, chemical reactivity, or biological activity [5]. However, achieving consistent predictions often requires the use of multiple topological indices, as a single molecular graph may necessitate the identification of several indices.

The research conducted by Milan Randić et al. [6] focused on calculating the molecular resonance energy for superphenalene. They observed that as we move closer to the center of the molecule, the degree of difference between nearby rings decreases. Vandana Bhalla et al. [7] subsequently worked on the synthesis of supertriphenylene from triphenylene. In 2020, Prabhu et al. [8] conducted a study on the molecular structural characterization of both superphenalene and supertriphenylene. However, there has been no progress in computing degree-based topological indices using M-polynomials for super polycyclic aromatic hydrocarbons (PAHs) such as superphenalene and supertriphenylene. The following section will explain the computation of degree-based topological indices using M-polynomials and computing the corresponding mathematical expressions. Figure 1 illustrates the two-dimensional structure of Superphenalene and Supertriphenylene.

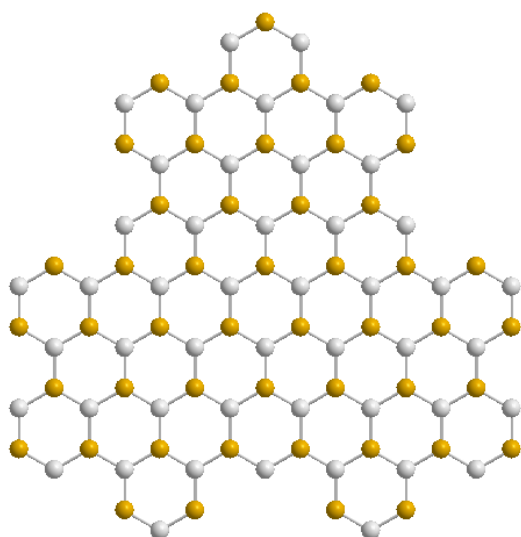
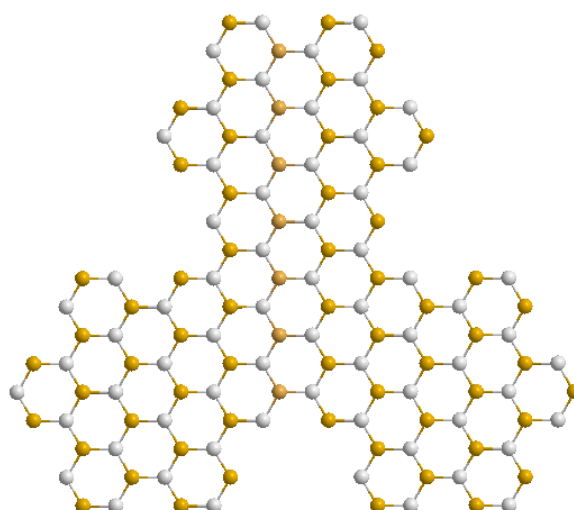


Figure 1: (a) Superphenalene SP(2);



(b) Supertriphenylene STP(2)

2: Mathematical Terminologies

We calculate the degree-based topological indices using the degree of the vertices of molecular graph. The M-polynomial was proposed as a substitute for the Hosoya polynomial by Deutsch et al. in [9]. The M-polynomial offers a distinct advantage as it carries significant information on degree-based graph invariants. In this context, Γ represents a simple connected graph, while V and Ω represent the vertex set and edge set, respectively. The degree of a vertex v in a graph Γ is denoted as $\deg \Gamma(v)$ and represents the number of edges adjacent to that vertex. Table 1 demonstrates the derivation of specific degree-based topological descriptors from M-polynomials.

The M-polynomial of a graph Γ is defined as,

$$M(\Gamma; u, v) = \sum_{\delta \leq i \leq j \leq \Delta} m_{ij}(\Gamma) u^i v^j \quad (1)$$

where $m_{ij}(\Gamma)$ is the number of edges $rs \in \Omega(\Gamma)$ such that $\{d_r, d_s\} = \{i, j\}$, $\delta = \min\{d_s | s \in V(\Gamma)\}$, and $\Delta = \max\{d_s | s \in V(\Gamma)\}$. Let $M(\Gamma; u, v) = f(u, v)$ and Table 1 shows expression of M-polynomial for different TI's, where.

$$\begin{aligned} D_u(f(u, v)) &= u \frac{\partial f(u, v)}{\partial u} \\ D_v(f(u, v)) &= v \frac{\partial f(u, v)}{\partial v} \\ S_u(f(u, v)) &= \int_0^u \frac{f(t, v)}{t} dt \\ S_v(f(u, v)) &= \int_0^v \frac{f(u, t)}{t} dt \\ J(f(u, v)) &= f(u, v) \\ Q_\alpha(f(u, v)) &= x^\alpha f(u, v), \alpha \neq 0 \end{aligned}$$

For more properties and applications on the above indices refer [10–20].

Table 1: The extraction of some degree-based topological descriptors from M-polynomials.

Topological Index	Extraction From $M(\Gamma; x, y)$
First Zagreb Index	$D_u + D_v(M(\Gamma; u, v)) _{u=v=1}$
Second Zagreb Index	$D_u D_v(M(\Gamma; u, v)) _{u=v=1}$

Modified Second Zagreb Index	$S_u S_v (M(\Gamma; u, v)) _{u=v=1}$
General Randić Index	$D_u^\alpha D_v^\alpha (M(\Gamma; u, v)) _{u=v=1}$
Inverse Randić Index	$S_u^\alpha S_v^\alpha (M(\Gamma; u, v)) _{u=v=1}$
Symmetric Division Index	$(D_u S_v + D_v S_u)(M(\Gamma; u, v)) _{u=v=1}$
Harmonic Index	$2S_u J(M(\Gamma; u, v)) _{u=1}$
Inverse Sum Index	$S_u J D_u D_v (M(\Gamma; u, v)) _{u=1}$
Augmented Zagreb Index	$S_u^3 Q_{-2} J D_u^3 D_v^3 (M(\Gamma; u, v)) _{u=1}$
Forgotten Index	$(D_u^2 + D_v^2)(M(\Gamma; u, v)) _{u=v=1}$
Reduced Second Zagreb Index	$(D_u - 1)(D_v - 1)(M(\Gamma; u, v)) _{u=v=1}$
Sigma Index	$(D_u - D_v)^2 (M(\Gamma; u, v)) _{u=v=1}$
Hyper-Zagreb Index	$(D_u + D_v)^2 (M(\Gamma; u, v)) _{u=v=1}$
Albertson Index	$(D_v - D_u)(M(\Gamma; u, v)) _{u=v=1}$

3: The Topological Descriptors for Superphenalene $SP(t)$

Let Γ_1 be a graph of superphenalene is represented as $SP(t)$, $t \geq 2$, Then the total number of vertices and edges of the superphenalene $SP(t)$ are $54t^2 - 72t + 24$ and $81t^2 - 120t + 45$ respectively. Table 2 gives the edge partition of $SP(t)$.

Table 2: The edge partition of $SP(t)$

(d_r, d_s) Where $rs \in \Omega(\Gamma_1)$	Total Number of Edges
(2, 2)	$12t - 6$
(2, 3)	$24t - 24$
(3, 3)	$81t^2 - 156t + 75$

Theorem 1. Let $SP(t)$, $t \geq 2$, be a superphenalene, Then $M(SP(t); u, v) = (12t - 6)u^2 v^2 + (24t - 24)u^2 v^3 + (81t^2 - 156t + 75)u^3 v^3$.

Proof: The intended outcome is achieved by using the definition of the M-Polynomial for $SP(t)$ as

$$\begin{aligned} M(SP(t)) &= \sum_{i \leq j} m_{ij} (SP(t)) u^i v^j \\ &= \sum_{2 \leq 2} m_{2,2} (SP(t)) u^2 v^2 + \sum_{2 \leq 3} m_{2,3} (SP(t)) u^2 v^3 + \sum_{3 \leq 3} m_{3,3} (SP(t)) u^3 v^3 \\ &= (12t - 6)u^2 v^2 + (24t - 24)u^2 v^3 + (81t^2 - 156t + 75)u^3 v^3. \end{aligned}$$

Figure 2 gives the 3D plot of M-polynomial for $SP(t)$.

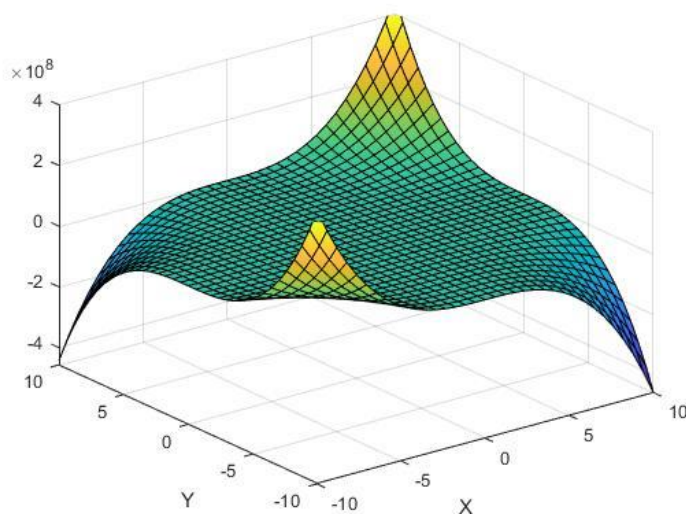


Figure 2: 3-dimensional plot of M-polynomial for $SP(t)$

Theorem 2. Let $SP(t)$, $t \geq 2$ be superphenalene. Then

- i. $M_1(SP(t)) = 486t^2 - 768t + 306.$
- ii. $M_2(SP(t)) = 729t^2 - 1212t + 507.$
- iii. $M_2^m(SP(t)) = 81t^2 - 140t + 65.$
- iv. $R_\alpha(SP(t)) = 4^\alpha(12t - 6) + 6^\alpha(24t - 24) + 9^\alpha(81t^2 - 156t + 75).$
- v. $RR_\alpha(SP(t)) = \frac{1}{4^\alpha}(12t - 6) + \frac{1}{6^\alpha}(24t - 24) + \frac{1}{9^\alpha}(81t^2 - 156t + 75).$
- vi. $SDD(SP(t)) = 162t^2 - 236t + 86.$
- vii. $H(SP(t)) = 243t^2 - 384t + 153.$
- viii. $I(SP(t)) = 54t^2 - 72t + 24.$

- ix. $AZI(SP(t)) = \frac{64t^2}{9} + \frac{14168t}{243} - \frac{12980}{243}.$
- x. $F(SP(t)) = 1458t^2 - 2400t + 990.$
- xi. $RM_2(t) = 324t^2 - 876t + 510.$
- xii. $\sigma(SP(t)) = 24t - 24.$
- xiii. $HM(SP(t)) = 2916t^2 - 4824t + 2004.$
- xiv. $A(SP(t)) = 24t - 24.$

Proof: Let $f(u, v) = M(SP(t); u, v) = (12t - 6)u^2v^2 + (24t - 24)u^2v^3 + (81t^2 - 156t + 75)u^3v^3$

By making use of Table 1 and Table 2, we get the required result.

$$\begin{aligned}
 D_u(f(u, v)) &= 2(12t - 6)u^2v^2 + 2(24t - 24)u^2v^3 + 3(81t^2 - 156t + 75)u^3v^3 \\
 D_v(f(u, v)) &= 2(12t - 6)u^2v^2 + 3(24t - 24)u^2v^3 + 3(81t^2 - 156t + 75)u^3v^3 \\
 D_u^2(f(u, v)) &= 4(12t - 6)u^2v^2 + 4(24t - 24)u^2v^3 + 9(81t^2 - 156t + 75)u^3v^3 \\
 D_v^2(f(u, v)) &= 4(12t - 6)u^2v^2 + 9(24t - 24)u^2v^3 + 9(81t^2 - 156t + 75)u^3v^3 \\
 D_u + D_v(f(u, v)) &= 4(12t - 6)u^2v^2 + 5(24t - 24)u^2v^3 + 6(81t^2 - 156t + 75)u^3v^3 \\
 D_u \cdot D_v(f(u, v)) &= 4(12t - 6)u^2v^2 + 6(24t - 24)u^2v^3 + 9(81t^2 - 156t + 75)u^3v^3 \\
 S_u(f(u, v)) &= (6t - 3)u^2v^2 + (12t - 12)u^2v^3 + (27t^2 - 52t + 25)u^3v^3 \\
 S_v(f(u, v)) &= (6t - 3)u^2v^2 + (8t - 8)u^2v^3 + (27t^2 - 52t + 25)u^3v^3 \\
 S_v \cdot S_u(f(u, v)) &= \frac{(6t - 3)}{2}u^2v^2 + (4t - 4)u^2v^3 + \frac{(27t^2 - 52t + 25)}{3}u^3v^3 \\
 D_u^\alpha \cdot D_v^\alpha(f(u, v)) &= 4^\alpha(12t - 6)u^2v^2 + 6^\alpha(24t - 24)u^2v^3 + 9^\alpha(81t^2 - 156t + 75)u^3v^3 \\
 S_u^\alpha \cdot S_v^\alpha(f(u, v)) &= \frac{(12t - 6)}{4^\alpha}u^2v^2 + \frac{(24t - 24)}{6^\alpha}u^2v^3 + \frac{(81t^2 - 156t + 75)}{9^\alpha}u^3v^3 \\
 S_v \cdot D_u(f(u, v)) &= (12t - 6)u^2v^2 + (16t - 16)u^2v^3 + (81t^2 - 156t + 75)u^3v^3 \\
 S_u \cdot D_v(f(u, v)) &= (12t - 6)u^2v^2 + (36t - 36)u^2v^3 + (81t^2 - 156t + 75)u^3v^3 \\
 Jf(u, v) &= f(u, u) = (12t - 6)u^4 + (24t - 24)u^5 + (81t^2 - 156t + 75)u^6 \\
 S_u \cdot Jf(u, v) &= f(u, u) = \frac{(12t - 6)}{4}u^4 + \frac{(24t - 24)}{5}u^5 + \frac{(81t^2 - 156t + 75)}{6}u^6 \\
 S_u J D_v D_v(f(u, v)) &= (12t - 6)u^4 + \frac{6}{5}(24t - 24)u^5 + \frac{3}{2}(81t^2 - 156t + 75)u^6 \\
 S_u^3 Q_{-2} J D_u^3 D_v^3(f(u, v)) &= 8(12t - 6) + 8(24t - 24) + \frac{729(81t^2 - 156t + 75)}{64}
 \end{aligned}$$

4: The Topological Descriptors for $STP(t)$

Let Γ_2 be a graph of Supertriphenylene is represented as $STP(t)$, $t \geq 2$. Then the total number of vertices and edges of the supertriphenylene $STP(t)$ are $72t^2 - 90t + 24$ and $108t^2 - 153t + 51$ respectively. Table 3 represents the edge partition of $SPT(t)$.

Table 3: The edge partition of $SPT(t)$.

(d_r, d_s) Where $rs \in \Omega(\Gamma_2)$	Total Number of Edges
(2, 2)	$18t - 12$
(2, 3)	$36t - 36$
(3, 3)	$108t^2 - 207t + 99$

Theorem 3. Let $STP(t)$, $t \geq 2$, be a supertriphenylene. Then, $M(STP(t); u, v) = (18t - 12)u^2v^2 + (36t - 36)u^2v^3 + (108t^2 - 207t + 99)u^3v^3$

Proof: Using Equation (1) for $STP(t)$, the desired result is obtained as follows,

$$\begin{aligned}
 M(STP(t); u, v) &= \sum_{i \leq j} m_{ij}(STP(t)) u^i v^j \\
 &= \sum_{2 \leq 2} m_{2,2}(STP(t)) u^2 v^2 + \sum_{2 \leq 3} m_{2,3}(STP(t)) u^2 v^3 + \sum_{3 \leq 3} m_{3,3}(STP(t)) u^3 v^3 \\
 &= (18t - 12)u^2 v^2 + (36t - 36)u^2 v^3 + (108t^2 - 207t + 99)u^3 v^3
 \end{aligned}$$

Figure 3 gives the 3D plot of M-polynomial for $STP(t)$.

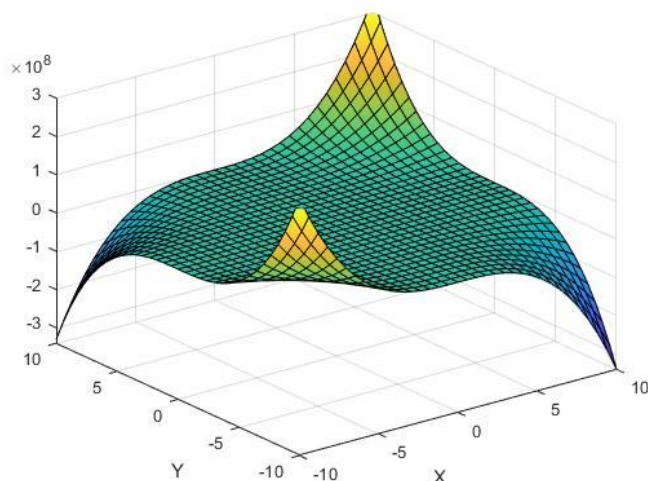


Figure 3: 3D plot of M-polynomial for STP(t)

Theorem 4. Let $STP(t)$, $t \geq 2$ be a supertriphenylene. Then

- i. $M_1(STP(t)) = 648t^2 - 990t + 366.$
- ii. $M_2(STP(t)) = 972t^2 - 1575t + 627.$
- iii. $M_2^m(STP(t)) = 12t^2 + 55t - 43.$
- iv. $R_\alpha(STP(t)) = 4^\alpha(18t - 12) + 6^\alpha(36t - 36) + 9^\alpha(108t^2 - 207t + 99).$
- v. $RR_\alpha(STP(t)) = \frac{1}{4^\alpha}(18t - 12) + \frac{1}{6^\alpha}(36t - 36) + \frac{1}{9^\alpha}(108t^2 - 207t + 99).$
- vi. $SDD(STP(t)) = 216t^2 - 300t + 96.$
- vii. $H(STP(t)) = 1296t^2 - 1980t + 732.$
- viii. $I(STP(t)) = 72t^2 - 90t + 24.$
- ix. $AZI(STP(t)) = \frac{256t^2}{27} + \frac{7276t}{81} - \frac{7072}{81}.$
- x. $F(STP(t)) = 1944t^2 - 3114t + 1218.$
- xi. $RM_2(STP(t)) = 432t^2 - 738t + 312.$
- xii. $\sigma(STP(t)) = 36t - 36.$
- xiii. $HM(STP(t)) = 3888t^2 - 6264t + 2472.$
- xiv. $A(STP(t)) = 36t - 36.$

Proof: Let $f(u, v) = M(STP(t); u, v) = (18t - 12)u^2v^2 + (36t - 36)u^2v^3 + (108t^2 - 207t + 99)u^3v^3$. Then by using Table 1 and Table 3 we obtain the necessary outcomes.

$$\begin{aligned}
 D_u(f(u, v)) &= 2(18t - 12)u^2v^2 + 2(36t - 36)u^2v^3 + 3(108t^2 - 207t + 99)u^3v^3 \\
 D_v(f(u, v)) &= 2(18t - 12)u^2v^2 + 3(36t - 36)u^2v^3 + 3(108t^2 - 207t + 99)u^3v^3 \\
 D_u^2(f(u, v)) &= 4(18t - 12)u^2v^2 + 4(36t - 36)u^2v^3 + 9(108t^2 - 207t + 99)u^3v^3 \\
 D_v^2(f(u, v)) &= 4(18t - 12)u^2v^2 + 9(36t - 36)u^2v^3 + 9(108t^2 - 207t + 99)u^3v^3 \\
 D_u + D_v(f(u, v)) &= 4(18t - 12)u^2v^2 + 5(36t - 36)u^2v^3 + 6(108t^2 - 207t + 99)u^3v^3 \\
 D_u \cdot D_v(f(u, v)) &= 4(18t - 12)u^2v^2 + 6(36t - 36)u^2v^3 + 9(108t^2 - 207t + 99)u^3v^3 \\
 S_u(f(u, v)) &= \frac{(18t - 12)}{2}u^2v^2 + \frac{(36t - 36)}{2}u^2v^3 + \frac{(108t^2 - 207t + 99)}{3}u^3v^3 \\
 S_v(f(u, v)) &= \frac{(18t - 12)}{2}u^2v^2 + \frac{(36t - 36)}{3}u^2v^3 + \frac{(108t^2 - 207t + 99)}{3}u^3v^3 \\
 S_v \cdot S_u(f(u, v)) &= \frac{(18t - 12)}{4}u^2v^2 + \frac{(36t - 36)}{6}u^2v^3 + \frac{(108t^2 - 207t + 99)}{9}u^3v^3 \\
 D_u^\alpha \cdot D_v^\alpha(f(u, v)) &= 4^\alpha(18t - 12)u^2v^2 + 6^\alpha(36t - 36)u^2v^3 + 9^\alpha(108t^2 - 207t + 99)u^3v^3 \\
 S_u^\alpha \cdot S_v^\alpha(f(u, v)) &= \frac{(18t - 12)}{4^\alpha}u^2v^2 + \frac{(36t - 36)}{6^\alpha}u^2v^3 + \frac{(108t^2 - 207t + 99)}{9^\alpha}u^3v^3 \\
 S_v \cdot D_u(f(u, v)) &= (18t - 6)u^2v^2 + \frac{2(36t - 36)}{3}u^2v^3 + (108t^2 - 207t + 99)u^3v^3 \\
 S_u \cdot D_v(f(u, v)) &= (18t - 12)u^2v^2 + \frac{3(36t - 36)}{2}u^2v^3 + (108t^2 - 207t + 99)u^3v^3 \\
 Jf(u, v) &= f(u, u) = (18t - 12)u^4 + (36t - 36)u^5 + (108t^2 - 207t + 99)u^6 \\
 S_u Jf(u, v) &= \frac{(18t - 12)}{4}u^4 + \frac{(36t - 36)}{5}u^5 + \frac{(108t^2 - 207t + 99)}{6}u^6 \\
 S_u J D_u D_v(f(u, v)) &= (18t - 12)u^4 + \frac{6(36t - 36)}{5}u^5 + \frac{3(108t^2 - 207t + 99)}{2}u^6 \\
 S_u^3 Q_{-2} J D_u^3 D_v^3(f(u, v)) &= 8(18t - 12) + 8(36t - 36) + \frac{729(108t^2 - 207t + 99)}{64}
 \end{aligned}$$

5: Numerical Results and Discussions

The statistical results for superphenalene and supertriphenylene are reported in this part, which are derived from the computation of degree-based topological descriptors with the help of *M*-polynomial. The degree-based topological indices for different values of *n* are given below for numerical comparison. These values are plotted using the ORIGIN 2020b software. Tables 4 and 5 give the numerical values and Figure 4 is its graphical representations.

Table 4: Numerical computation for TI's of SP(t).

t	M ₁ (Γ ₁)	M ₂ (Γ ₁)	M ₂ ^m (Γ ₁)	R _α (Γ ₁)	RR _α (Γ ₁)	SDD(Γ ₁)	H(Γ ₁)	I(Γ ₁)	AZI(Γ ₁)	F(Γ ₁)	RM ₂ (Γ ₁)	σ(Γ ₁)	HM(Γ ₁)	Alb(Γ ₁)
1	24	24	6	24	24	12	12	6	12	48	6	0	96	0
2	714	999	109	999	859	262	357	96	92	2022	414	24	4020	24
3	2376	3432	374	3432	3152	836	1188	294	186	6912	1470	48	13776	48
4	5010	7323	801	7323	6903	1734	2505	600	294	14718	3174	72	29364	72
5	8616	12672	1390	12672	12112	2956	4308	1014	416	25440	5526	96	50784	96
6	13194	19479	2141	19479	18779	4502	6597	1536	522	39078	8526	120	78036	120
7	18744	27744	3054	27744	26904	6372	9372	2166	703	55632	12174	144	111120	144
8	25266	37467	4129	37467	36487	8566	12633	2904	868	75102	16470	168	150036	168
9	32760	48648	5366	48648	47528	11084	16380	3750	1047	97488	21414	192	194784	192
10	41226	61287	6765	61287	60027	13926	20613	4704	1240	122790	27006	216	245364	216

Table 5: Numerical computation for TI's of STP(t).

t	M ₁ (Γ ₂)	M ₂ (Γ ₂)	M ₂ ^m (Γ ₂)	R _α (Γ ₂)	RR _α (Γ ₂)	SDD(Γ ₂)	H(Γ ₂)	I(Γ ₂)	A(Γ ₂)	F(Γ ₂)	RM ₂ (Γ ₂)	σ(Γ ₂)	HM(Γ ₂)	Alb(Γ ₂)
1	24	24	24	24	24	12	48	6	12	48	6	0	96	0
2	978	1365	115	1365	1155	360	1956	132	130	2766	564	36	5496	36
3	3228	4650	230	4650	4230	1140	6456	402	267	9372	1986	72	18672	72
4	6774	9879	369	9879	4429	2352	13548	816	424	19866	4272	108	39624	108
5	11616	17052	532	17052	16212	3996	23232	1374	599	34248	7422	144	68352	144
6	17754	26169	719	26169	25119	6072	35508	2076	793	52518	11436	180	104856	180
7	25188	37230	930	37230	35970	8580	50376	2922	1006	74676	16314	216	149136	216
8	33918	50235	1165	50235	48765	11520	67836	3912	1238	100722	22056	252	201192	252
9	43944	65184	1424	65184	63504	14892	87888	5046	1489	130656	28662	288	261024	288
10	55266	82077	1707	82077	80187	18696	110532	6324	1759	164478	36132	324	328632	324

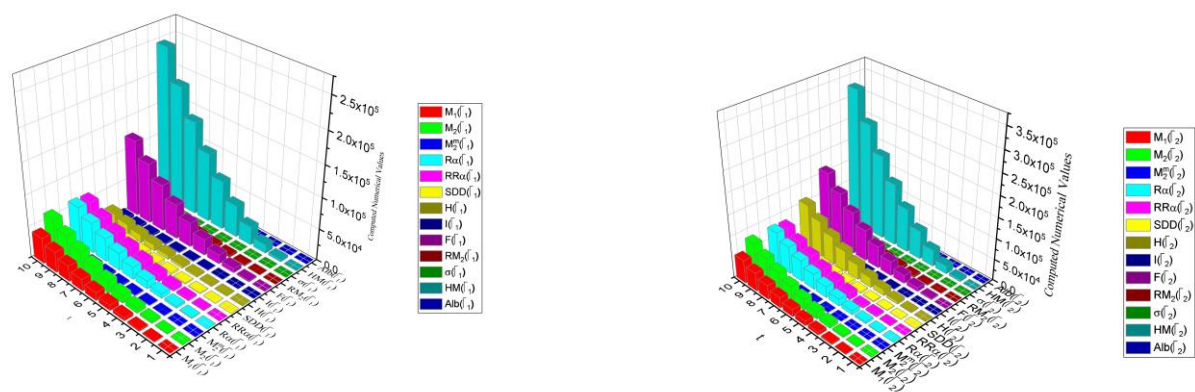


Figure 4: (a) Graphical Representation of different degree-based indices of SP(t);

(b) Graphical Representation of different degree-based indices of STP(t)

6: Conclusion

In this paper, the *M*-polynomial has been employed to calculate fourteen degree-based topological indices. These descriptors provide further insights into the molecular structure and enable chemists to predict various properties of molecular compounds without the need for expensive and time-consuming experiments. The findings of this study have implications for the development of quantitative structure-activity relationship (QSAR) models in pharmaceutical and chemical science. By incorporating these degree-based topological indices into QSAR models, researchers can enhance their predictive capabilities and gain valuable insights into the properties and behaviours of molecular compounds. Furthermore, the paper highlights the potential for future research on computing graph entropies using topological indices specifically for superphenalene and supertriphenylene. Graph entropies provide measures of complexity and information content in molecular structures and can offer further understanding of their properties.

ORCID IDs:

Tony Augustine : <https://orcid.org/0000-0002-5339-2154>

S. Roy : <https://orcid.org/0000-0002-5542-6581>

S. Govardhan : <https://orcid.org/0000-0003-2093-8189>

S. Prabhu : <https://orcid.org/0000-0002-1922-910X>

References

- [1]. Hussein I. Abdel-Shafy, Mona S.M. Mansour, A Review on Polycyclic Aromatic Hydrocarbons: Source, environmental impact, effect on human health and remediation, Egyptian Journal of Petroleum, 25(2016), 107-123
- [2]. M.D. Watson, A. Fechtenkötter, K. Müllen, Big is Beautiful- Revisited from the Viewpoint of Macromolecular and Supramolecular Benzene Chemistry, Chemical Reviews, 101 (2001) 1267–1300.
- [3] M. Randić, X. Guo, Giant Benzenoid Hydrocarbons. Superphenalene Resonance Energy, New Journal of Chemistry 23(2) (1999) 251–260.
- [4] V.S. Iyer, M. Wehmeier, J.D. Brand, From Hexa-peri-hexabenzocoronene to Superacenes, Angewandte Chemie- International Edition in English 36 (1997) 1604–1607.
- [5] I. Gutman, “Degree-based Topological Indices,” Croatica Chemica Acta 86 (2013) 351—361.

- [6] M. Randić and X. Guo, Giant Benzenoid Hydrocarbons. Superphenalene Resonance Energy, *Polycyclic Aromatic Compounds* 18 (1) (2000) 49–69.
- [7] V. Bhalla, H. Singh, H. Arora, M. kumar, Triphenylene to Supertriphenylene: New Chemodosimeter for Fluoride Ions, *Sensors and Actuators B: Chemical* 171 (2012) 1007–1012.
- [8] M. Radhakrishnan, S. Prabhu, M. Arockiaraj, M. Arulperumjothi, Molecular Structural Characterization of Superphenalene and Supertriphenylene, *International Journal of Quantum Chemistry* (2021) <https://doi.org/10.1002/qua.26818>.
- [9] E. Deutsch, S. Klavžar, M-Polynomial and Degree-based Topological Indices, *Iranian Journal of Mathematical Chemistry* 6(2) (2015) 93–102.
- [10] J. Rada, Vertex-Degree Based Topological Indices of Graphene, *Polycyclic Aromatic Compounds* (2020) 1–9.
- [11] K.C. Das, S. Sun, I. Gutman, Normalized Laplacian Eigenvalues and Randić Energy of Graphs, *MATCH Communications in Mathematical and in Computer Chemistry* 77 (2017) 45–59.
- [12] M. Randić, On the History of the Randić Index and Emerging Hostility Toward Chemical Graph Theory, *MATCH Communications in Mathematical and in Computer Chemistry* 59 (2008) 5–124.
- [13] M. Munir, W. Nazeer, S. Rafique, S. Kang, M-polynomial and Related Topological Indices of Nanostar Dendrimers, *Symmetry* 8(9) (2016) 97.
- [14] A. Rajpoot, L. Selvaganesh, Extension of M-Polynomial and Degree Based Topological Indices for Nanotube, *Turkish World Mathematical Society Journal of Applied and Engineering Mathematics* 11 (2021) 268–279.
- [15] K. Julietraja, P. Venugopal, S. Prabhu, J.-B. Liu, M-polynomial and Degree-Based Molecular Descriptors of Certain Classes of Benzenoid Systems, *Polycyclic Aromatic Compounds*, DOI: 10.1080/10406638.2020.1867205.
- [16] S. Prabhu, G. Murugan, Michael Cary, M. Arulperumjothi, Jia-Bao Liu, On Certain Distance and Degree Based Topological Indices of Zeolite LTA Frameworks, *Materials Research Express* 7(5) (2020) 055006.
- [17] Y.-M. Chu, K. Julietraja, P. Venugopal, M.K. Siddiqui, S. Prabhu. Degree-and irregularity-based molecular descriptors for benzenoid systems. *The European Physical Journal Plus* 136(1) (2021) 1–17.
- [18] J.-B. Liu, M. Arockiaraj, M. Arulperumjothi, S. Prabhu, Distance based and bond additive topological indices of certain repurposed antiviral drug compounds tested for treating COVID-19, *International Journal of Quantum Chemistry* 121(10) (2021) e26617.
- [19] V. Gayathri, R. Muthucumaraswamy, S. Prabhu, M.R. Farahani. Omega, Theta, PI, Sadhana polynomials, and subsequent indices of convex benzenoid system, *Computational and Theoretical*

Chemistry 1203 (2021) 113310.

- [20] S. Govardhan, S. Roy, Computation of Neighborhood M-polynomial of Three Classes of Polycyclic Aromatic Hydrocarbons, Polycyclic Aromatic Compounds, (2022)1-17,DOI: 10.1080/10406638.2022.2103576

Radio Labeling of Certain Networks

Tony Augustine and S. Roy

Communicated by V. Loksha

MSC 2010 Classifications: 05C78, 05C15.

Keywords and phrases: Radio labeling, Radio mean labeling, Honeycomb network, Honeycomb torus network.

Abstract For a connected graph G , an injective function $\pi : V(G) \rightarrow N$ such that for every distinct vertices u and v of G , $d(u, v) + |\pi(u) - \pi(v)| \geq 1 + \text{diam}(G)$ is called a radio labeling of G . The radio number of π , $rn(\pi)$ is the highest number allotted to any vertex of G . The radio number of G , $rn(G)$ is the minimum value of $rn(\pi)$ taken over all radio labeling π of G . Let G be a connected graph and $\pi : V(G) \rightarrow N$ is an injective function. Then π is called a radio mean labeling if for every distinct vertex u and v of G , $d(u, v) + \lceil \frac{\pi(u) + \pi(v)}{2} \rceil \geq 1 + \text{diam}(G)$. The highest number allotted to any vertex of G is called radio mean number of π and is denoted by $rmn(\pi)$. The least value of $rmn(\pi)$ taken over all radio mean labeling π of G is called radio mean number of G and is denoted by $rmn(G)$. The upper bound of radio number and radio mean number for honeycomb and honeycomb torus networks are found.

1 Introduction

Radio labeling is inspired by Hale's problem of channel assignment. If we are given a set of radio stations, then the job will be to assign a channel (non-negative integer) to each station (or transmitter) to avoid interference. The interference is intricately linked to the station's geographical position, the closer the stations are uncommon the greater the interference that may occur. Also the packing coloring problem arise from the restrictions concerning the assignment of broadcast frequencies to radio stations, which is similar to radio labeling [1, 2, 3]. The division of channels allocated to the neighbouring stations must be wide enough to prevent interference. To model this problem, the researchers have constructed a graph such that each station is represented by a vertex and two vertices are adjacent when their respective stations are close. The ultimate objective is to find a valid label that reduces the period (range) of the channels used [4, 5]. The radio labeling of different graphs are discussed in [1, 4, 5, 6, 7, 10, 11, 12].

An interconnection network can be modelled by a simple graph whose vertices mean components of network and whose edges mean the connections between them. This idea has been broadly perceived and utilized by computer researchers and engineers. Graph theory is a effective mathematical technique for the design and analysis of topological interconnection network structures. A system's interconnection network logically offers a basic means of linking all device components. For example, hypercubes, butterfly networks, benes networks, honeycomb networks, honeycomb torus networks and grids are some interconnection networks [6, 7, 8, 13].

The definitions of radio number and radio mean number are taken from [5] and [10]. In this paper, the upper bounds of radio numbers and radio mean numbers for honeycomb and honeycomb torus networks are determined.

2 Honeycomb Network

Definition 2.1. An n -dimensional honeycomb network is denoted as HC_n where n is the number of hexagons between central and boundary of hexagon. Honeycomb network HC_n is constructed from HC_{n-1} by adding a layer of hexagons around the boundary of HC_{n-1} . The number of vertices in the honeycomb network HC_n are $6n^2$ and the number of edges is $9n^2 - 3n$. The diameter of the honeycomb network is $4n - 1$ [8, 13].

Theorem 2.2. For, $HC_n, n \geq 2$, $rn(HC_n) \leq 24n^3 - 16n^2 - 2n + 3$.

Proof. The vertices of HC_n are labeled as we see in Figure 1. We know that $diam(HC_n) = 4n - 1$.

Define a mapping $\pi : V(HC_n) \rightarrow N$ as follows

$$\begin{aligned} \pi(v_i) &= 4n(i-1) - 2i + 3, & 1 \leq i \leq 6n^2 - n \\ \pi(u_i) &= 4n(i-1) - 2i + 4, & 1 \leq i \leq n. \end{aligned}$$

Claim: The mapping π is a radio labeling and need to prove that $d(u, v) + |\pi(u) - \pi(v)| \geq 1 + diam(HC_n) = 4n$ holds for all pairs of vertices (u, v) , where $u \neq v$.

Case I: Suppose $u = v_k$ and $v = v_l$, $1 \leq k \neq l \leq 6n^2 - n$, $|k - l| > 1$.

Then,

$$\begin{aligned} \pi(u) &= 4n(k-1) - 2k + 3 \\ \pi(v) &= 4n(l-1) - 2l + 3 \text{ and } d(u, v) \geq 1. \end{aligned}$$

Hence, $d(u, v) + |\pi(u) - \pi(v)| \geq 1 + |(4n-2)(k-l)| \geq 4n$.

Case II: Suppose $u = u_k$ and $v = u_l$, $1 \leq k \neq l \leq n$.

Then,

$$\begin{aligned} \pi(u) &= 4n(k-1) - 2k + 4 \\ \pi(v) &= 4n(l-1) - 2l + 4 \text{ and } d(u, v) \geq 2. \end{aligned}$$

Hence, $d(u, v) + |\pi(u) - \pi(v)| \geq 2 + |(4n-2)(k-l)| \geq 4n$.

Case III: Suppose $u = u_k$ and $v = v_l$, $1 \leq k, l \leq n$.

Then,

$$\begin{aligned} \pi(u) &= 4n(k-1) - 2k + 4 \\ \pi(v) &= 4n(l-1) - 2l + 3 \text{ and } d(u, v) \geq 4n-1. \end{aligned}$$

Hence, $d(u, v) + |\pi(u) - \pi(v)| \geq 4n-1 + |(4n-2)(k-l) + 1| \geq 4n$.

Case IV: Suppose $u = u_k$ and $v = v_l$, $1 \leq k \leq n$, $n+1 \leq l \leq 6n^2 - n$, $|k - l| > 1$.

Then,

$$\begin{aligned} \pi(u) &= 4n(k-1) - 2k + 4 \\ \pi(v) &= 4n(l-1) - 2l + 3 \text{ and } d(u, v) \geq 1. \end{aligned}$$

Hence, $d(u, v) + |\pi(u) - \pi(v)| \geq 1 + |(4n-2)(k-l) + 1| \geq 4n$.

Case V: Suppose $u = v_k$ and $v = v_l$, $1 \leq k \neq l \leq 6n^2 - n$, $|k - l| = 1$.

Then,

$$\begin{aligned} \pi(u) &= 4n(k-1) - 2k + 3 \\ \pi(v) &= 4n(l-1) - 2l + 3 \text{ and } d(u, v) \geq 2. \end{aligned}$$

Hence, $d(u, v) + |\pi(u) - \pi(v)| \geq 2 + |(4n-2)(k-l)| \geq 4n$.

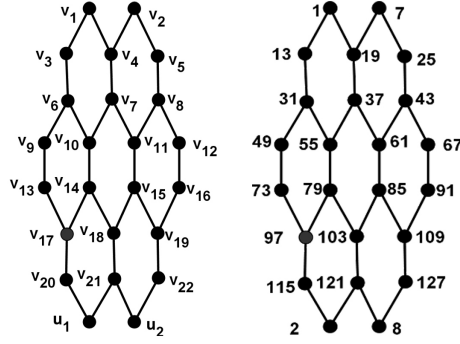
Thus $d(u, v) + |\pi(u) - \pi(v)| \geq 4n$ for all $u, v \in V(HC_n)$, $n \geq 2$. These five cases establish the claim that π is a radio labeling of HC_n . Since the vertex v_{6n^2-n} receives the maximum label, the radio number of honeycomb HC_n satisfies $rn(HC_n) \leq 24n^3 - 16n^2 - 2n + 3$. \square

Theorem 2.3. For, $HC_n, n \geq 2$, $rmn(HC_n) \leq 6n^2 + 4n - 6$.

Proof. The vertices of HC_n are labeled as we see in Figure 2. We know that $diam(HC_n) = 4n - 1$.

Define a mapping $\pi : V(HC_n) \rightarrow N$ as follows

$$\pi(v_i) = \begin{cases} 4(n-1) + i, & 1 \leq i \leq 3n^2 \\ 4, & i = 3n^2 + 1 \\ 4(n-1) + (i-1), & 3n^2 + 2 \leq i \leq 6n^2 - 1 \\ 1, & i = 6n^2. \end{cases}$$

Figure 1. Radio Labeling of HC_2

Claim: The mapping π is a radio labeling and need to prove that $d(u, v) + \lceil \frac{\pi(u) + \pi(v)}{2} \rceil \geq 1 + \text{diam}(HC_n) = 4n$ is true for every pair of vertices (u, v) , where $u \neq v$.

Case I: Suppose $u = v_{6n^2}$ and $v = v_{3n^2+1}$.

Then,

$$\pi(u) = 1$$

$$\pi(v) = 4 \text{ and } d(u, v) = 4n - 3.$$

$$\text{Hence, } d(u, v) + \lceil \frac{\pi(u) + \pi(v)}{2} \rceil \geq 4n - 3 + \lceil \frac{5}{2} \rceil = 4n.$$

Case II: Suppose $u = v_k$ and $v = v_l$, $1 \leq k \neq l \leq 3n^2$, $3n^2 + 2 \leq k \neq l \leq 6n^2 - 1$.

Then,

$$\pi(u) = 4(n - 1) + k$$

$$\pi(v) = 4(n - 1) + (l - 1) \text{ and } d(u, v) \geq 1.$$

$$\text{Hence, } d(u, v) + \lceil \frac{\pi(u) + \pi(v)}{2} \rceil \geq 1 + \lceil \frac{8n - 9 + k + l}{2} \rceil \geq 4n.$$

Case III: Suppose $u = v_k$ and $v = v_l$, $1 \leq k \neq l \leq 3n^2$.

Then,

$$\pi(u) = 4(n - 1) + k$$

$$\pi(v) = 4(n - 1) + l \text{ and } d(u, v) \geq 1.$$

$$\text{Hence, } d(u, v) + \lceil \frac{\pi(u) + \pi(v)}{2} \rceil \geq 1 + \lceil \frac{8n - 8 + k + l}{2} \rceil \geq 4n.$$

Case IV: Suppose $u = v_k$ and $v = v_l$, $3n^2 + 2 \leq k \neq l \leq 6n^2 - 1$.

Then,

$$\pi(u) = 4(n - 1) + (k - 1)$$

$$\pi(v) = 4(n - 1) + (l - 1) \text{ and } d(u, v) \geq 1.$$

$$\text{Hence, } d(u, v) + \lceil \frac{\pi(u) + \pi(v)}{2} \rceil \geq 1 + \lceil \frac{8n - 10 + k + l}{2} \rceil \geq 4n.$$

Case V: Suppose $u = v_{3n^2+1}$ and $v = v_l$, $1 \leq l \leq 3n^2$.

Then,

$$\pi(u) = 4$$

$$\pi(v) = 4(n - 1) + l \text{ and } d(u, v) \geq 1.$$

$$\text{Hence, } d(u, v) + \lceil \frac{\pi(u) + \pi(v)}{2} \rceil \geq 1 + \lceil \frac{4n + l}{2} \rceil \geq 4n.$$

Case VI: Suppose $u = v_{3n^2+1}$ and $v = v_l$, $3n^2 + 2 \leq l \leq 6n^2 - 1$.

Then,

$$\pi(u) = 4$$

$$\pi(v) = 4(n - 1) + (l - 1) \text{ and } d(u, v) \geq 1.$$

$$\text{Hence, } d(u, v) + \lceil \frac{\pi(u) + \pi(v)}{2} \rceil \geq 1 + \lceil \frac{4n + l - 1}{2} \rceil \geq 4n.$$

Therefore, for all $u, v \in V(HC_n)$, $n \geq 2$, $d(u, v) + \lceil \frac{\pi(u) + \pi(v)}{2} \rceil \geq 4n$. Hence these cases verify the claim that π is a radio mean labeling of HC_n . Since the vertex v_{6n^2-1} receives the

maximum label, the radio number of honeycombs HC_n satisfies $rmn(HC_n) \leq 6n^2 + 4n - 6$. \square

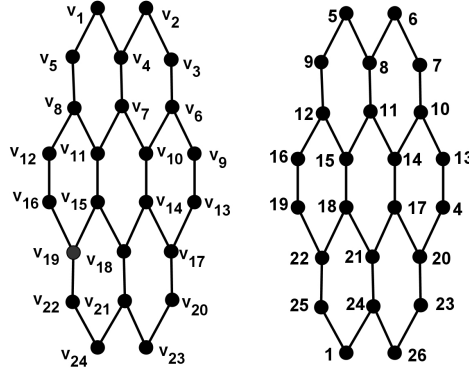


Figure 2. Radio Mean Labeling of HC_2

3 Honeycomb Torus Network

Definition 3.1. The honeycomb torus network is created by linking pairs of honeycomb mesh nodes of degree two. $HCT(r)$ is obtained by adding a layer of hexagons around the boundary of $HC(r-1)$, with wraparound edges. The number of vertices and edges of $HCT(r)$ are $6r^2$ and $9r^2$ respectively [9].

Theorem 3.2. For, $HCT_n, n \geq 2, rn(HCT_n) \leq 12n^3 - 6n^2 - 2n + 2$.

Proof. The vertices of HCT_n are labelled as we see in Figure 3. We know that $diam(HCT_n) = 2n$.

Define a mapping $\pi : V(HCT_n) \rightarrow N$ as follows,

$$\pi(v_i) = 2n(i-1) - i + 2, \quad 1 \leq i \leq 6n^2.$$

Claim: The mapping π is a radio labeling and we need to prove that $d(u, v) + |\pi(u) - \pi(v)| \geq 1 + diam(HCT_n) = 2n + 1$ is true for every pair of vertices (u, v) , where $u \neq v$.

Case I: Suppose $u = v_k$ and $v = v_l, 1 \leq k \neq l \leq 6n^2, |k - l| > 1$.

Then,

$$\pi(u) = 2n(k-1) - k + 2$$

$$\pi(v) = 2n(l-1) - l + 2 \text{ and } d(u, v) \geq 1.$$

Hence, $d(u, v) + |\pi(u) - \pi(v)| \geq 1 + |(2n-1)(k-l)| \geq 2n+1$.

Case II: Suppose $u = v_1$ and $v = v_l, 2 \leq l \leq 6n^2$.

Then,

$$\pi(u) = 2n(1-1) - 1 + 2 = 1$$

$$\pi(v) = 2n(l-1) - l + 2 \text{ and } d(u, v) \geq 1.$$

Hence, $d(u, v) + |\pi(u) - \pi(v)| \geq 1 + |(2n-1)(1-l)| \geq 2n+1$.

Case III: Suppose $u = v_k$ and $v = v_l, 1 \leq k \neq l \leq 6n^2, |k - l| = 1$.

Then,

$$\pi(u) = 2n(k-1) - k + 2$$

$$\pi(v) = 2n(l-1) - l + 2 \text{ and } d(u, v) \geq 2.$$

Hence, $d(u, v) + |\pi(u) - \pi(v)| \geq 2 + |(2n-1)(k-l)| \geq 2n+1$.

Thus for all $(u, v) \in V(HCT_n), n \geq 2, d(u, v) + |\pi(u) - \pi(v)| \geq 2n+1$. Here all the three cases confirm the claim that π is a radio labeling of HCT_n . Since the vertex v_{6n^2} accepts

the maximum label, the radio number of honeycomb torus satisfies $rn(HCT_n) \leq 12n^3 - 6n^2 - 2n + 2$. \square

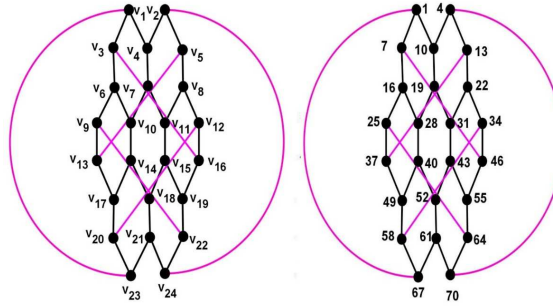


Figure 3. Radio Labeling of HCT_2

Theorem 3.3. For, $HCT_n, n \geq 2$, $rmn(HCT_n) \leq 6n^2 + n - 2$.

Proof. The proof is closely connected to the Theorem 2.3. Radio mean labeling of honeycomb torus HCT_2 is shown in Figure 4. \square

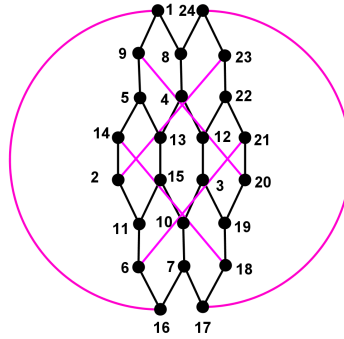


Figure 4. Radio Mean Labeling of HCT_2

Conclusion

We have found the upper bounds of radio numbers and radio mean numbers for honeycomb and honeycomb torus networks. The radio and radio mean number of Benes network is under investigation.

References

- [1] G. Chartrand, D. Erwin, P. Zhang, F. Harary, *Radio labelings of graphs*, Bull. Inst. Combin. Appl., **33**, (2001), 77-85.
- [2] S. Gomathi, P. Venugopal, *Channel Assignment of Triangular and Rhombic Honeycomb Networks Using Radio Labeling Techniques*, Comm. in Math. and Appl., **12(3)**, (2021), 665-676.
- [3] W. Goddard, S. M. Hedetniemi, S.T. Hedetniemi, J.M. Harris, D. F. Rall, *Broadcast Chromatic Numbers of Graphs*, Ars Combin., **86**, (2008), 33-49.
- [4] A. J. Gallian, *A Dynamic Survey of Graph Labeling*, Electron. J. Combin., **24**, (2021), 277-281.
- [5] D. Bantva, S. Vaidya, S. Zhou, *Radio number of trees*, Discrete Appl. Math., **217(2)**, (2017), 110-122.
- [6] M. Ali, M.T. Rahim, G. Ali, M. Farooq, *An upper bound for the radio number of generalized gear graph*, Ars Combin., **107**, (2012), 161-168.

- [7] P. Martinez, J. Ortiz, M. Tomova, C. Wyels, *Radio numbers for generalized prism graphs*, Discuss. Math. Graph Theory., **31(1)**, (2011), 45-62.
- [8] S. Akhter, M. Imran, W. Gao, M. R. Farahani, *On topological indices of honeycomb networks and graphene networks*, Hacet. J. Math. Stat., **47(1)**, (2018), 19-35.
- [9] I. Rajasingh, S. T. Arockiamary, *Total Edge Irregularity Strength of Honeycomb Torus Networks*, Global Jour. of Pure and Appl. Math. **13**, (2017), 1135-1142.
- [10] R. Ponraj, S. S. Narayanan, R. Kala, *Radio mean labeling of a graph*, AKCE Int. J. Graphs Comb. **12(3)**, (2015), 224-228.
- [11] K. Yenoke, P. Selvagopal, K. M. B. Smitha, R. Cranston, *Bounds for the Radio Number of Mesh Derived Architecture*, Int. J. of Innovative Research in Science, Engi. and Tech., **9(6)**, (2020), 4806- 4810.
- [12] M. K. A. Kaabar, K. Yenoke, *Radio and Radial Radio Numbers of Certain Sunflower Extended Graphs*, Int. J. of Math. and Mathe. Sci., **vol. 2022, Article ID 9229409, 9 pages, 2022.**
- [13] B. Rajan, A. William, C. Grigorious, S. Stephen, *On Certain Topological Indices of Silicate, Honeycomb and Hexagonal Networks*, J. Comp. & Math. Sci., **3(5)**, (2012), 530- 535.

Author information

Tony Augustine, School of Advanced Sciences, Department of Mathematics, Vellore Institute of Technology, Vellore, Tamilnadu - 632014., INDIA.

E-mail: pullikkattiltony@gmail.com

S. Roy, School of Advanced Sciences, Department of Mathematics, Vellore Institute of Technology, Vellore, Tamilnadu - 632014., INDIA.

E-mail: roy.santiago@vit.ac.in

Received: July 19, 2021.

Accepted: December 28, 2021.



Molecular Physics

An International Journal at the Interface Between Chemistry and Physics

ISSN: (Print) (Online) Journal homepage: <https://www.tandfonline.com/loi/tmph20>

Topological study on degree based molecular descriptors of fullerene cages

Tony Augustine, S. Roy, J. Sahaya Vijay, Jain Maria Thomas & P. Shanmugam

To cite this article: Tony Augustine, S. Roy, J. Sahaya Vijay, Jain Maria Thomas & P. Shanmugam (2023): Topological study on degree based molecular descriptors of fullerene cages, Molecular Physics, DOI: [10.1080/00268976.2023.2179858](https://doi.org/10.1080/00268976.2023.2179858)

To link to this article: <https://doi.org/10.1080/00268976.2023.2179858>



Published online: 17 Feb 2023.



Submit your article to this journal [↗](#)



View related articles [↗](#)



View Crossmark data [↗](#)

RESEARCH ARTICLE



Topological study on degree based molecular descriptors of fullerene cages

Tony Augustine ^a, S. Roy ^a, J. Sahaya Vijay ^a, Jain Maria Thomas ^b and P. Shanmugam ^c

^aDepartment of Mathematics, Vellore Institute of Technology, Vellore, India; ^bDepartment of Chemistry, St. George's College, Aruvithura, Kerala, India; ^cDepartment of Chemistry, Thammasat University, Pathumthani, Thailand

ABSTRACT

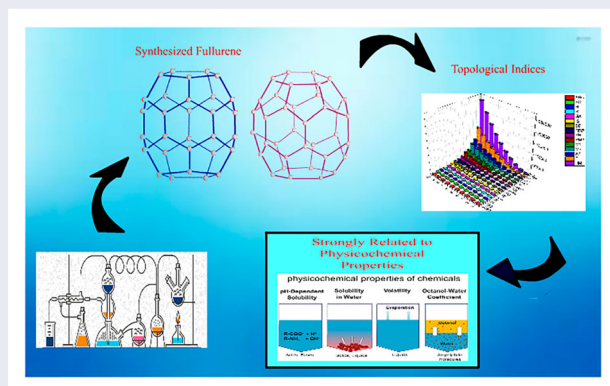
Fullerenes are an allotrope of carbon that create polyhedral cages. Their bond structures match the sole pentagon and hexagonal-faced planar cubic graphs. Several chemical properties of fullerenes can be studied using its graph structure. Any graph that models a particular molecular structure can be given a topological index or molecular descriptor. Based on the molecular descriptor, it is easy to assess mathematical data and conduct further research on a molecule's physicochemical characteristics. It is a beneficial technique to replace time-consuming, expensive, and labour-intensive laboratory experiments. Molecular descriptors play a significant role in molecular structural analysis by investigating quantitative structure-activity relationships (QSARs) and quantitative structure-property relationships (QSPRs). In this study, some novel degree-based topological indices, multiplicative degree-based topological indices, and entropy versions for fullerene cages $C_{36}D_{6h}$ and $C_{30}D_{5h}$ have been computed and derived formula for them. Also, we have obtained the numerical computation and graphical representation of degree-based topological indices and entropy values of $C_{36}D_{6h}$ and $C_{30}D_{5h}$. Understanding the topology of precursor fullerenes is undoubtedly aided by the results of our computations.

ARTICLE HISTORY

Received 17 November 2022
Accepted 8 February 2023

KEYWORDS

Degree based topological indices; entropy; QSPR analysis; fullerene cage



1. Introduction

Chemical graph theory refers to the application of graph theory to chemistry. This multidisciplinary science applies graph theory techniques to address chemistry-related problems (such as isomer enumeration, structure elucidation, etc.) and hence has an impact on chemistry and mathematics. Since the beginning of chemistry, mathematics has been utilised to develop quantitative and qualitative models that aid in understanding the world of chemistry by grasping the constituent parts of molecules. Mathematical models of molecules are developed using graph theory to reveal the physical

characteristics of chemical substances [1]. Some physical features, such as boiling point, are connected to the compound's geometric structure. Chemical graph theory is primarily concerned with the relationship between a compound's molecular graph and its various properties and functions [2].

Only carbon compounds, especially nanoscale materials, are fascinating and draw the attention of scientists from various fields. Carbon atoms have an unusual tendency to link to other carbon atoms through covalent bonds, forming a broad range of large and small molecular structures [3]. Fullerenes are polyhedral cages of

sp^2 hybridised carbon clusters formed by 12 pentagons, and a variable number of hexagons [4]. The number of hexagons in a fullerene with $20 + 2n$ carbon atoms is n [3]. The number of carbon atoms in a fullerene's structure determines its name [5]. The standard formula for fullerene is C_n , where n is an even number and represents the number of carbon atoms in the cage [6].

The chemical and physical properties of different fullerene isomers can vary significantly depending on the geometry and topology. Fullerenes satisfy the EULER's theorem, which states that exactly 12 pentagons must be present in a closed construction made up of hexagons and pentagons [7]. According to this theorem, the most stable, smallest and symmetrical fullerene is C_{60} (Buckyball), which doesn't have any adjacent pentagons and it is spherical in shape [7]. Smaller fullerenes resemble asteroids [7]. The lower fullerenes have mostly attracted theoretical attention because pentagon adjacencies cannot be avoided and are predicted to cause high reactivity and poor stability [8]. Reactivity can be attributed to high strain energy [9]. According to the pentagon adjacency penalty rule (PAPR), for isomers of lower fullerenes, the one with the least pentagon adjacency is energetically most stable [10]. Twelve pentagons and five hexagons make up the elliptical-shaped C_{30} fullerene [11]. The molecular characteristics showed that C_{30} fullerene was more reactive than C_{60} fullerene [11]. Theoretical studies of C_{30} showed that C_{2V} isomer is the most stable one [12]. In the C_{30} fullerene structure, there are two solitary pentagons with opposite faces surrounded by five more pentagons each [13]. According to experimental findings, C_{30} , is the smallest stable fullerene [13]. The first large-scale production of a smaller fullerene, which is more chemically reactive than C_{60} was made by Piskoti and co-workers using the arc-discharge process to create C_{36} crystal [14]. At the beginning of the fullerene study, C_{36} was one of the magic-number tiny fullerenes discovered by mass spectroscopy [15]. A class of intriguing materials with novel structural and electrical features, including covalent bonding, strong reactivity, large steric strain, low gap, high strength, and superconductivity, are thought to be made of this fullerene, and its derivatives [15]. There are 15 conventional fullerene isomers in C_{36} . Among them, the D_{6h} and D_{2d} isomers have minimal neighbouring pentagons and are therefore possibilities for the structure with the greatest stability [8, 16]. Different fullerene isomers can have significantly different chemical and physical properties due to variations in their geometry and topology [17].

Fullerenes have a remarkable three-dimensional structure, a high specific surface area, good electrical conductivity, and high chemical stability [18]. They can undergo

a wide range of reactions, including reduction, oxidation, hydrogenation, halogenation, radical reactions, nucleophilic reactions, reactions involving transition metal complexes, regioselective processes, and so on [19]. Various fullerene/semiconductor nanocomposites are helpful in the wastewater treatment process [20]. Due to their electronegative solid nature, they readily form compounds with atoms that donate electrons, most frequently alkali metals [3]. Numerous researchers are investigating the use of this molecule and its functionalised derivatives in the areas like medicine, photovoltaics, catalysis, adsorption and separation, gas adsorption/storage, and pharmaceuticals due to their distinctive physical and chemical properties [21]. Their binding structures are identical to planar cubic graphs with only a pentagon and hexagonal face and can be used to deduce a number of its chemical characteristics [4].

A fundamental challenge in theoretical chemistry is correctly predicting the physicochemical features of different compounds since chemical graphs can be used to describe chemical compounds. One of the critical techniques in chemical graph theory is the topological index. It is a method of numerically representing a compound's molecular structure [22]. A topological index, therefore, has a close relationship with certain physical and chemical characteristics of substances. Quantitative structure-property and quantitative structure-activity relationships (QSPR/QSAR) are mathematical models that link substances' physical, chemical, and biological properties and activities to their chemical structures [23]. It uses the topological index to convey molecular properties without a wet lab. Topological indices are employed in QSPR/QSAR analysis as a mapping from a set of graphs to a group of real numbers that describe the graph's topology. For isomorphic graphs, it doesn't change. Topological indices can be calculated using their standard definitions, which is time-consuming if one wants to derive numerous indices for a particular category [24].

The research on a degree-based topological index for specific chemical structures is generally limited, even though the molecular structure of several substances has been studied [22]. Therefore, the mathematical study of the topological index of the molecular structure of importance is of great interest to researchers. This paper aims to investigate the fullerene structure's degree-based topological index [23, 24]. These results can guide the application of these substances in the physical and chemical areas. It is generally known that compounds with network structures, biological and chemical characteristics and topological indices have a close relationship [25–27].

Graph entropy was created to describe the complexity of graphs. Entropy was initially used for communication and information by Shannon [28]. It is possible to interpret the entropy of a probability distribution as both a measure of information and uncertainty. In actuality, the quantity of knowledge we gain from observing an experiment's conclusion can be equated mathematically to the degree of ambiguity around the experiment's outcome before its execution [29, 30]. It was created to demonstrate the complexity of information transmission and communication. Still, it now has a wide range of useful applications in a range of scientific areas, including physical dissipative structures, biological systems, engineering domains, and others [31, 32]. The two types of graph entropies are deterministic and probabilistic, respectively. The probabilistic category is the focus of this work since it is widely employed in various domains, such as communication and the description of chemical structures. In addition, statistical methods are separated into intrinsic and extrinsic categories. In intrinsic measures, a probability distribution across the subsets of a graph with similar structural similarities is found [33, 34]. Vertices or edges in the graph are given a probability function for extrinsic measurements. This probability distribution function can be transformed into a numerical number to produce probabilistic measures of graph complexity [35].

2. Fullerene structures

Fullerenes are all carbon molecules discovered in 1985 [36]. They have a hollow cage structure with a spherical or elliptical form. Fullerenes have specified unknown predictions in biomedicine, catalysis, superconduction, and photovoltaic over the past 30 years because of the ongoing advancement of fullerene manufacturing technology [37–40]. Nano molecules play a significant role in the prevention, uncovering, imaging, drug administration, catalysis, and biosensing of cancer [41–50]. Fullerene molecules exhibit distinct nanostructures, exceptional biocompatibility, distinctive electrical properties, and photophysical characteristics. Physicochemical properties of the gage-shape of Fullerene $C_{30}D_{5h}$ and the gage-shape of Fullerene $C_{36}D_{6h}$ are studied in this article. In this study, we consider all the atoms to be called vertices and all the covalent bonds are called edges.

Fullerene structure has a primitive unit cell $C_{36}D_{6h}$ called the β_1 -cage containing 36 vertices and 54 edges in which six hexagons, twelve pentagons are connected and also fullerene structure has a primitive unit cell $C_{30}D_{5h}$, called the β_2 -cage containing 30 vertices and 45 edges in which five hexagons, ten pentagons are connected by sharing a common edge as shown in Figure 1. In this fullerene structure, β_1, β_2 -cages are attached through the

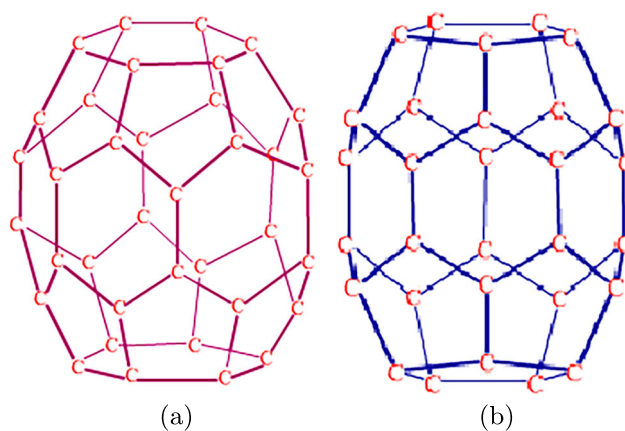


Figure 1. Fullerene structures $C_{36}D_{6h}$ and $C_{30}D_{5h}$. (a) β_1 -cage. (b) β_2 -cage.

double 4-membered ring with each other and grouped in a simple cubic structure and such a method that great cages (α_1, α_2 -cages) are designed among the β_1, β_2 -cages where both α_1, α_2 -cages is an Archimedes polyhedron like a Figure 2 of [51].

The metal atoms incorporation into the fullerene cage results in a variety of unusual characteristics. Fullerenes and their derivatives are highly relevant in terms of technology. Time-consuming purification procedures, unusual solubility, and restricted control over regioselective derivatization remain obstacles to synthetic access and use. By placing the fullerene β_1 -cage in a (p, q, r) -dimensional cuboid known as $C_{36}D_{6h}$ cuboid and it is shown to the readers as front view (See Figure 3(a)), side view (See Figure 3(b)), top view (See Figure 3(c)). The fullerene β_2 -cage in a (p, q) -dimensional lattice sheet is known as $C_{30}D_{5h}$ lattice sheet (See Figure 2). For clarification, we have shown a particular dimension views of $C_{30}D_{5h}(4, 5)$ and $C_{36}D_{6h}(4, 5, 3)$ (See Figure 4).

A graphic framework of the unit cell in the fullerene structure is specified in the same Figure 1 and we represent it as $C_{36}D_{6h}(1, 1, 1)$ (β_1 -cage) and $C_{30}D_{5h}(1, 1, 1)$ (β_2 -cage) due to the amount of β_1, β_2 -cages.

When we array the unit cell of fullerene structure in cuboid form resulting in more generalised fullerene materials and represented by $C_{36}D_{6h}(p, q, r)$ and $C_{30}D_{5h}(p, q, r)$ where $p, q, r \geq 1$. It is certainly realised from the measures of β_1, β_2 -cages that $|V(C_{36}D_{6h}(p, q, r))| = P_1 = 36pqr$, $|V(C_{30}D_{5h}(p, q, r))| = P_2 = 30pq$, $|E(C_{36}D_{6h}(p, q, r))| = Q_1 = 68pqr - 2pq - 6pr - 6qr$ and $|E(C_{30}D_{5h}(p, q, r))| = Q_2 = 52pq - 5q - 2p$. In this section, for the sake of readers comprehension, we have depicted the front view, side view, and top view of the schematic frameworks of $C_{36}D_{6h}$ and lattice sheet of $C_{30}D_{5h}$ (See Figures 2 and 3).

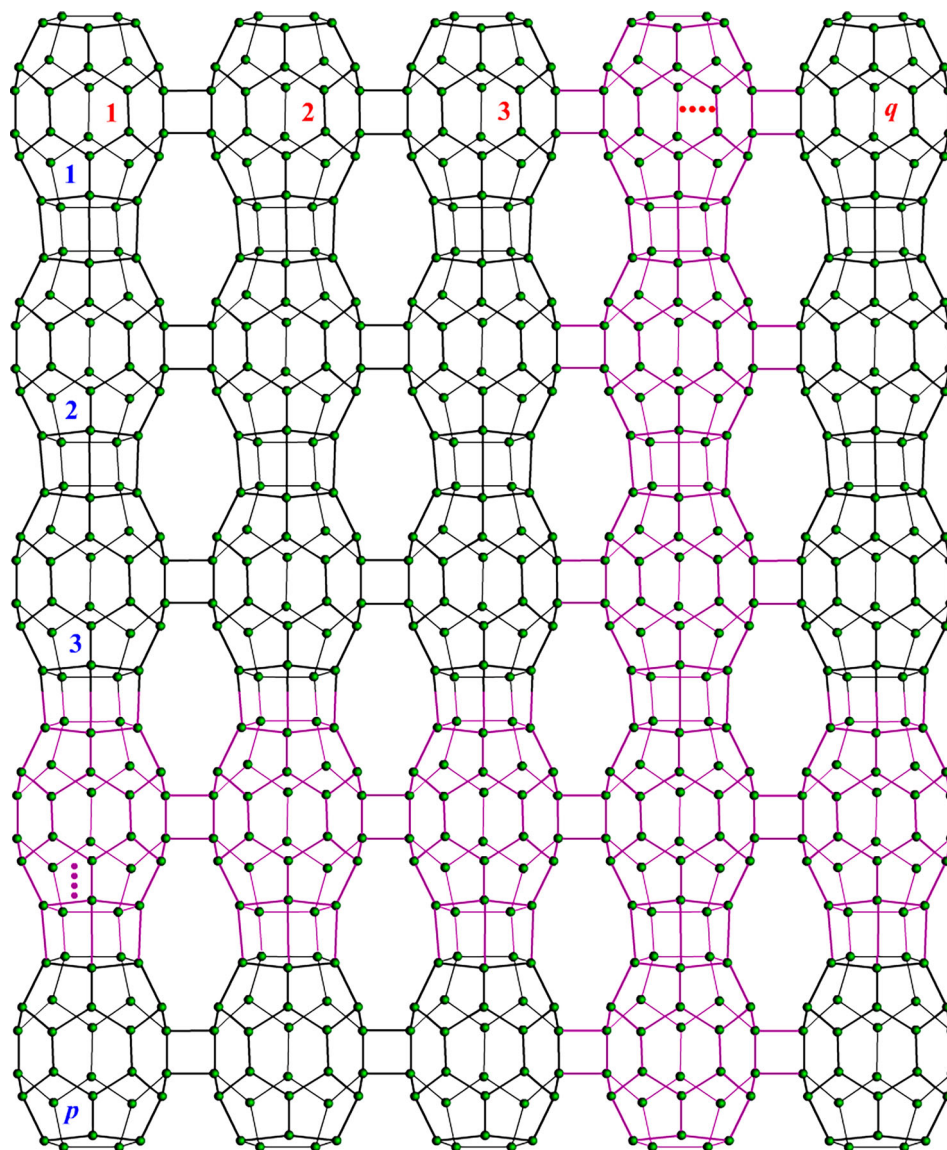


Figure 2. $C_{30}D_{5h}$ structure view.

3. Preliminaries and mathematical terminologies

A number, a polynomial, a series of integers, or a matrix representing the whole graph may be used to identify a graph. Each of these representations aims to be specified explicitly for that graph. A topological index is a numerical value that describes the topology of a graph and is unaffected by graph automorphism. Topological indices may be divided into many broad categories, including degree-based topological indices, distance-based topological indices, polynomials linked to counting [52]. Degree-based topological indices are of tremendous significance and are especially important in chemical graph theory and chemistry.

In this study, γ_1 and γ_2 are considered as connected graphs $C_{36}D_{6h}$ and $C_{30}D_{5h}$ respectively. The letters

$|V(\gamma_1)| = P_1$, $|V(\gamma_2)| = P_2$, $|E(\gamma_1)| = Q_1$ and $|E(\gamma_2)| = Q_2$ respectively, stand for the vertex set and edge set. Let d_u is the degree of the vertex u , where $u \in \gamma$. We employed edge-partitioning approaches to obtain multiplicative topological indices and degree-based entropy measurements for the fullerene structure.

Now, Table 1 [53–60] and Table 2 [61–70] respectively present various degree-based topological descriptors and multiplicative degree-based topological descriptors.

4. Methodology

Among our fundamental discoveries are topological indices, multiplicative indices, and entropy values of $C_{30}D_{5h}$ and $C_{36}D_{6h}$. Flash8 and Chem Draw Ultra are used to illustrate the structures. We converted the $C_{30}D_{5h}$ and $C_{36}D_{6h}$ molecules into a molecular graph. Then, we

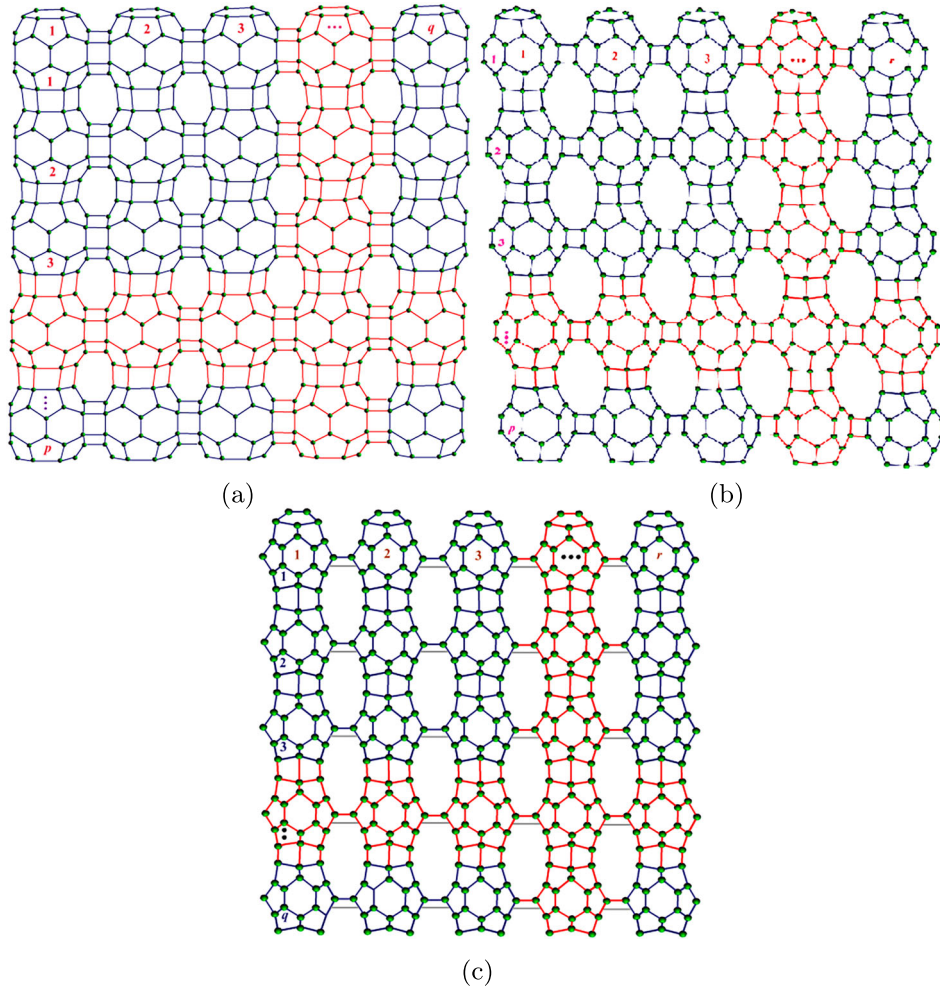


Figure 3. $C_{36}D_{6h}$ structure views. (a) $C_{36}D_{6h}(p, q, 1)$ —front view. (b) $C_{36}D_{6h}(p, 1, r)$ —side view. (c) $C_{36}D_{6h}(1, q, r)$ —top view.

use degree counting, edge partitioning, analytical procedures, graph theoretical tools, and combinatorial computation to get our conclusions. The degree of the terminal vertices of $C_{30}D_{5h}$ and $C_{36}D_{6h}$ was originally discovered using edge partitioning. Next, we use Tables 1 and 2 to compute the topological indices and multiplicative topological indices of $C_{30}D_{5h}$ and $C_{36}D_{6h}$. MATLAB 2019 is used to calculate the entropy, numerical values of entropies, and numerical values of topological indices for $C_{30}D_{5h}$ and $C_{36}D_{6h}$. Maple 2022 is used to create the entropy surface plot. The software Origin 2020 is also used to compare numerical outcomes.

5. Main results

In this section, we have done the results of all topological indices of Tables 1 and 2. Table 3, below illustrates how the structure's edges are divided.

Theorem 5.1: Let γ_1 be $C_{36}D_{6h}$. Then degree based topological descriptors are

- (1) $M_1(\gamma_1) = 520pqr - 28pq - 84pr - 84qr$
- (2) $M_2(\gamma_1) = 992pqr - 70pq - 220pr - 220qr + 4r$
- (3) $RM_2(\gamma_1) = 540pqr - 44pq - 142pr - 142qr + 4r$
- (4) $HM(\gamma_1) = 3992pqr - 288pq - 884pr - 884qr + 8r$
- (5) $AZ(\gamma_1) = \frac{((125943808q - 26424218)p - 26424218q + 1168814)r}{108000} - \frac{7834061pq}{108000}$
- (6) $R(\gamma_1) = \frac{(((24q-4)p-4q-8)r-8pq)\sqrt{3}}{6} + \frac{((66q+7)p+7q+14)r}{6} + \frac{7pq}{3}$
- (7) $RR(\gamma_1) = 14pq - 28pr - 28qr + 28r + 2\sqrt{3}(24pq - 8pq - 4pr - 4qr - 8r) + 176pqr$
- (8) $RRR(\gamma_1) = 8pq - 26pr - 26qr + 20r + \sqrt{6}(24pq - 8pq - 4pr - 4qr - 8r) + 132pqr$
- (9) $H(\gamma_1) = \frac{((750q+1)p+q+2)r}{42} + \frac{pq}{21} + \frac{(((140p+140q+28)r+70pq)\sqrt{3} + ((462q-231)p-231q+42)r - 42pq)\sqrt{2}}{42} + \frac{24\sqrt{7}(((q-\frac{1}{6})p-\frac{q}{6}-\frac{1}{3})r-\frac{pq}{3})}{7}$

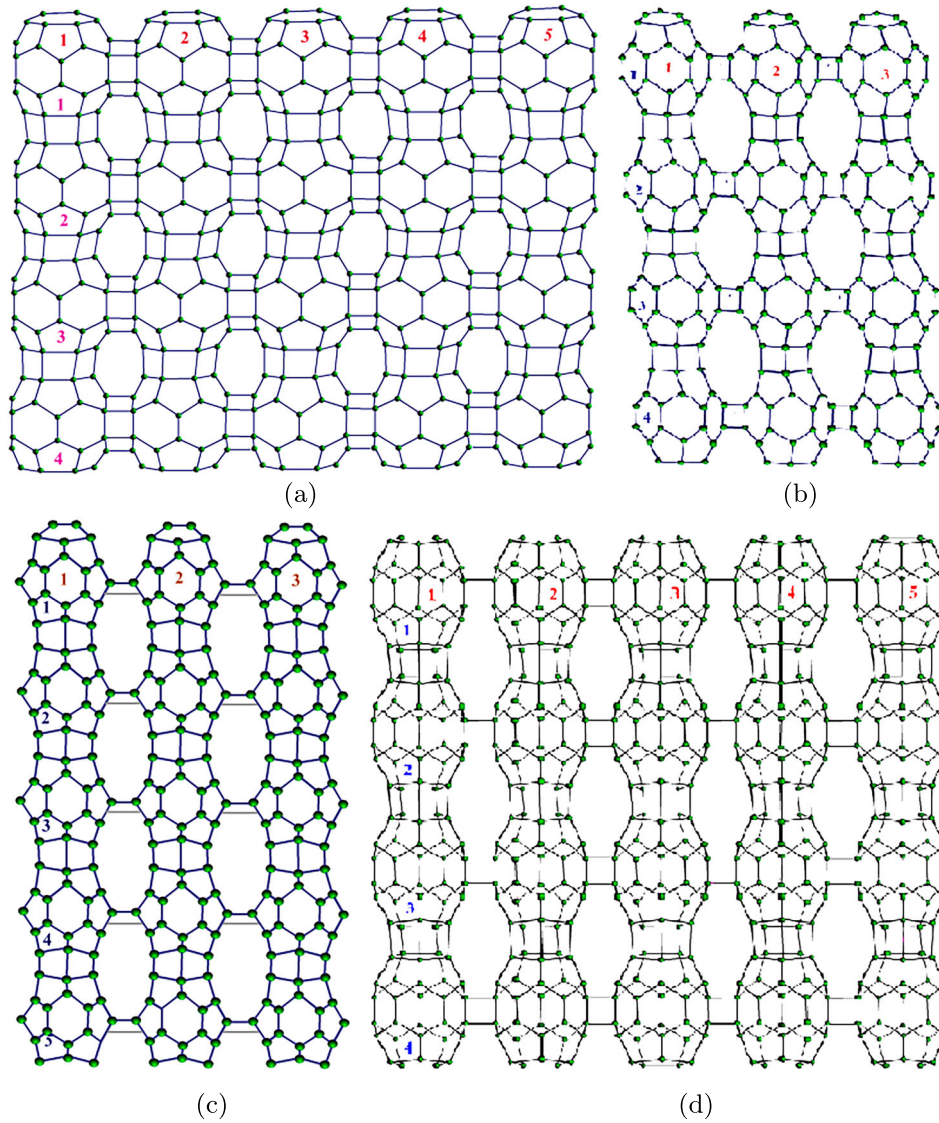


Figure 4. Example for $C_{36}D_{6h}$ and $C_{30}D_{5h}$. (a) $C_{36}D_{6h}(4, 5, 1)$ —front view. (b) $C_{36}D_{6h}(4, 1, 3)$ —side view. (c) $C_{36}D_{6h}(1, 5, 3)$ —top view. (d) $C_{30}D_{5h}(4, 5)$.

$$\begin{aligned}
 (11) \quad GA(\gamma_1) &= \frac{((96q-16)p-16q-32)r-32pq)\sqrt{3}}{7} \\
 &+ \frac{((308q-14)p-14q+56)r}{7} + 6pq \\
 (12) \quad IS(\gamma_1) &= \frac{((904q-146)p-146q+2)r}{7} - \frac{47pq}{7} \\
 (13) \quad SD(\gamma_1) &= \frac{((414q-37)p-37q-2)r}{3} - \frac{14pq}{3} \\
 (14) \quad F(\gamma_1) &= 2008pqr - 148pq - 444pr - 444qrq \\
 (15) \quad ABC(\gamma_1) &= \frac{2\sqrt{(20p+20q+4)r+10pq}}{3} \\
 &+ \frac{\sqrt{((90q-15)p-15q-30)r-30pq}}{3} \\
 &+ \frac{\sqrt{((66q-33)p-33q+6)r-6pq}}{2}
 \end{aligned}$$

Proof: Let γ_1 be a $C_{36}D_{6h}$. The total number of vertices P_1 and edges Q_1 of γ_1 are $36pqr$ and $68pqr-2pq-6pr-6qr$ respectively. Based on the vertex degree, we have

done edge partitions of γ_1 . The following result of $M_1(\gamma_1)$ is obtained by applying the edge partitions (See Table 3) in the definition of the first Zagreb index. And followed by the results of other topological descriptors (See Table 1) are also obtained Theorem 5.1 (2–15).

$$\begin{aligned}
 (1) \quad M_1(\gamma_1) &= (3+3)(10pq+20qr+20pr+4r) + (3+4)(24pqr-8pq-4qr-4pr-8r) \\
 &+ (4+4)(44pqr-4pq-22qr-22pr+4r) = 520pqr - 28pq - 84pr - 84qr. \quad \blacksquare
 \end{aligned}$$

Theorem 5.2: Let γ_1 be $C_{36}D_{6h}$. Then degree based multiplicative topological descriptors are

Table 1. Degree based topological indices.

First Zagreb Index	$M_1(\gamma) = \sum_{uv \in E(\gamma)} [d_u + d_v]$
Second Zagreb Index	$M_2(\gamma) = \sum_{uv \in E(\gamma)} [d_u \times d_v]$
Reduced Second Zagreb Index	$RM_2(\gamma) = \sum_{uv \in E(\gamma)} [(d_u - 1)(d_v - 1)]$
Hyper Zagreb Index	$HM(\gamma) = \sum_{uv \in E(\gamma)} [d_u + d_v]^2$
Augmented Zagreb Index	$AZ(\gamma) = \sum_{uv \in E(\gamma)} \left[\frac{d_u \times d_v}{d_u + d_v - 2} \right]^3$
Randić Index	$R(\gamma) = \sum_{uv \in E(\gamma)} \left[\frac{1}{\sqrt{d_u d_v}} \right]$
Reciprocal Randić Index	$RR(\gamma) = \sum_{uv \in E(\gamma)} [\sqrt{d_u d_v}]$
Reduced Reciprocal Randić Index	$RRR(\gamma) = \sum_{uv \in E(\gamma)} [\sqrt{(d_u - 1)(d_v - 1)}]$
Harmonic Index	$H(\gamma) = \sum_{uv \in E(\gamma)} \left[\frac{2}{d_u + d_v} \right]$
Sum Connectivity Index	$SC(\gamma) = \sum_{uv \in E(\gamma)} \frac{\sqrt{d_u + d_v}}{2\sqrt{d_u d_v}}$
Geometric Arithmetic Index	$GA(\gamma) = \sum_{uv \in E(\gamma)} \frac{d_u + d_v}{d_u d_v}$
Inverse Sum Index	$IS(\gamma) = \sum_{uv \in E(\gamma)} \frac{d_u + d_v}{d_u^2 + d_v^2}$
Symmetric Division Index	$SD(\gamma) = \sum_{uv \in E(\gamma)} \frac{d_u d_v}{d_u^2 + d_v^2}$
Forgotten index	$F(\gamma) = \sum_{uv \in E(\gamma)} d_u^2 + d_v^2$
Atom Bond Connectivity Index	$ABC(\gamma) = \sum_{uv \in E(\gamma)} \sqrt{\frac{d_u + d_v - 2}{d_u d_v}}$

Table 2. Multiplicative degree based topological indices.

Multiplicative First Zagreb Index	$MM_1(\gamma) = \prod_{uv \in E(\gamma)} [d_u + d_v]$
Multiplicative Second Zagreb Index	$MM_2(\gamma) = \prod_{uv \in E(\gamma)} [d_u \times d_v]$
Multiplicative Reduced Second Zagreb Index	$MRM_2(\gamma) = \prod_{uv \in E(\gamma)} [(d_u - 1)(d_v - 1)]$
Multiplicative Hyper Zagreb Index	$MHM(\gamma) = \prod_{uv \in E(\gamma)} [d_u + d_v]^2$
Multiplicative Augmented Zagreb Index	$MAZ(\gamma) = \prod_{uv \in E(\gamma)} \left[\frac{d_u \times d_v}{d_u + d_v - 2} \right]^3$
Multiplicative Randić Index	$MR(\gamma) = \prod_{uv \in E(\gamma)} \left[\frac{1}{\sqrt{d_u d_v}} \right]$
Multiplicative Reciprocal Randić Index	$MRR(\gamma) = \prod_{uv \in E(\gamma)} [\sqrt{d_u d_v}]$
Multiplicative Reduced Reciprocal Randić Index	$MRRR(\gamma) = \prod_{uv \in E(\gamma)} [\sqrt{(d_u - 1)(d_v - 1)}]$
Multiplicative Harmonic Index	$MH(\gamma) = \prod_{uv \in E(\gamma)} \left[\frac{2}{d_u + d_v} \right]$
Multiplicative Sum Connectivity Index	$MSC(\gamma) = \prod_{uv \in E(\gamma)} \frac{\sqrt{d_u + d_v}}{2\sqrt{d_u d_v}}$
Multiplicative Geometric Arithmetic Index	$MGA(\gamma) = \prod_{uv \in E(\gamma)} \frac{d_u + d_v}{d_u d_v}$
Multiplicative Inverse Sum Index	$MIS(\gamma) = \prod_{uv \in E(\gamma)} \frac{d_u + d_v}{d_u^2 + d_v^2}$
Multiplicative Symmetric Division Index	$MSD(\gamma) = \prod_{uv \in E(\gamma)} \frac{d_u d_v}{d_u^2 + d_v^2}$
Multiplicative Forgotten index	$MF(\gamma) = \prod_{uv \in E(\gamma)} d_u^2 + d_v^2$
Multiplicative Atom Bond Connectivity Index	$MABC(\gamma) = \prod_{uv \in E(\gamma)} \sqrt{\frac{d_u + d_v - 2}{d_u d_v}}$

- (1) $MM_1(\gamma_1) = 6^{10pq+20pr+20qr+4r} \times 7^{24pqr-8pq-4pr-4qr-8r} \times 8^{44pqr-4pq-22pr-22qr+4r}$
- (2) $MM_2(\gamma_1) = 2^{224pqr-32pq-96pr-96qr} \times 3^{24pqr+12pq+36pr+36qr}$
- (3) $MRM_2(\gamma_1) = 3^{112pqr-16pq-48pr-48qr} \times 2^{24pqr+12pq+36pr+36qr}$
- (4) $MHM(\gamma_1) = 36^{10pq+20pr+20qr+4r} \times 49^{24pqr-8pq-4pr-4qr-8r} \times 64^{44pqr-4pq-22pr-22qr+4r}$
- (5) $MAZ(\gamma_1) = \left(\frac{729}{64}\right)^{10pq+20pr+20qr+4r} \times \left(\frac{1728}{125}\right)^{24pqr-8pq-4pr-4qr-8r} \times \left(\frac{512}{27}\right)^{44pqr-4pq-22pr-22qr+4r}$
- (6) $MR(\gamma_1) = \frac{1}{3^{10pq+20pr+20qr+4r}} \left(\left(\frac{\sqrt{3}}{6}\right)^{68pqr-12pq-26pr-26qr-4r} \right)$
- (7) $MRR(\gamma_1) = 2^{112pqr-16pq-48pr-48qr} \times 3^{12pqr+6pq+18pr+18qr}$
- (8) $MRRR(\gamma) = 2^{12pqr+6pq+18pr+18qr} \times 3^{56pqr-8pq-24pr-24qr}$
- (9) $MH(\gamma_1) = \frac{\left(\frac{2}{3}\right)^{24pqr-8pq-4pr-4qr-8r} \times 2^{-88pqr+8pq+44pr+44qr-8r}}{3^{10pq+20pr+20qr+4r}} \times \left(\frac{\sqrt{2}}{4}\right)^{44pqr-4pq-22pr-22qr+4r} \times \left(\frac{\sqrt{7}}{7}\right)^{24pqr-8pq-4pr-4qr-8r}$
- (10) $MSC(\gamma_1) = \frac{6^{5pq+10pr+10qr+2r}}{2^{(-44pqr-6pq+2pr+2qr-8r+3)}} \times \left(\frac{2\sqrt{3}}{7}\right)^{24pqr-8pq-4pr-4qr-8r}$
- (11) $MGA(\gamma_1) = 2^{(-44pqr-6pq+2pr+2qr-8r+3)} \times \left(\frac{2\sqrt{3}}{7}\right)^{24pqr-8pq-4pr-4qr-8r}$
- (12) $MIS(\gamma_1) = \left(\frac{3}{2}\right)^{10pq+20pr+20qr+4r} \times \left(\frac{12}{7}\right)^{24pqr-8pq-4pr-4qr-8r} \times 2^{44pqr-4pq-22pr-22qr+4r}$
- (13) $MSD(\gamma_1) = 2^{44pqr+6pq-2pr-2qr+8r} \times \left(\frac{25}{12}\right)^{24pqr-8pq-4pr-4qr-8r}$
- (14) $MF(\gamma_1) = 18^{10pq+20pr+20qr+4r} \times 25^{24pqr-8pq-4pr-4qr-8r} \times 32^{44pqr-4pq-22pr-22qr+4r}$
- (15) $MABC(\gamma_1) = \left(\frac{2}{3}\right)^{10pq+20pr+20qr+4r} \times \left(\frac{\sqrt{15}}{6}\right)^{24pqr-8pq-4pr-4qr-8r} \times \left(\frac{\sqrt{6}}{4}\right)^{44pqr-4pq-22pr-22qr+4r}$

Proof: Let γ_1 be $C_{36}D_{6h}$. The total number of vertices P_1 and edges Q_1 of γ_1 are $36pqr$ and $68pqr-2pq-6pr-6qr$ respectively. Based on the vertex degree, we have done edge partitions of γ_1 . The following result of $MM_1(\gamma_1)$ is obtained by applying the edge partitions (See Table 3) in the definition of the first multiple Zagreb index. And followed by the results of other multiplicative

Table 3. Edge partition of γ_1 and γ_2 .

Fullerene	(3, 3)	(3, 4)	(4, 4)
γ_1	$10pq + 20qr + 20pr + 4r$	$24pqr - 8pq - 4qr - 4pr - 8r$	$44pqr - 4pq - 22qr - 22pr + 4r$
γ_2	$10p + 20q + 15pq$	$18pq - 10q - 8p$	$19pq - 15q - 4p$

topological descriptors (See Table 2) are also obtained Theorem 5.2(2–15)

$$(1) \quad MM_1(\gamma_1) = (3+3)^{(20pr+20qr+4r+10pq)} \\ \times (3+4)^{(-4pr-4qr+24pqr-8pq-8r)} \\ \times (4+4)^{(-22pr-22qr+44pqr-4pq+4r)} \\ = 6^{10pq+20pr+20qr+4r} \times 7^{24pqr-8pq-4pr-4qr-8r} \\ \times 8^{44pqr-4pq-22pr-22qr+4r} \quad \blacksquare$$

Theorem 5.3: Let γ_2 be $C_{30}D_{5h}$. Then degree based topological descriptors are

$$(1) \quad M_1(\gamma_2) = 368pq - 70q - 28p \\ (2) \quad M_2(\gamma_2) = 655pq - 180q - 70p \\ (3) \quad RM_2(\gamma_2) = 339pq - 115q - 44p \\ (4) \quad HM(\gamma_2) = 2638pq - 730q - 288p \\ (5) \quad AZ(\gamma_2) = \frac{1}{216000}(168477337pq - 42092340q \\ - 15668122p) \\ (6) \quad R(\gamma_2) = \frac{1}{12}(pq(36 \times 3^{\frac{1}{2}} + 117) - q(20 \times 3^{\frac{1}{2}} - 35) - \\ p(16 \times 3^{\frac{1}{2}} - 28)) \\ (7) \quad RR(\gamma_2) = 14p + 121pq - 2 \times 3^{\frac{1}{2}}(8p + 10q - 18pq) \\ (8) \quad RRR(\gamma_2) = 8p - 5q + 87pq - 6^{\frac{1}{2}}(8p + 10q - 18pq) \\ (10) \quad SC(\gamma_2) = \frac{(15pq+10p+20q)}{\sqrt{6}} + \frac{(18pq-8p-10q)}{\sqrt{7}} \\ + \frac{(19pq-4p-15q)}{\sqrt{8}} \\ (12) \quad IS(\gamma_2) = \frac{1}{14}(1279pq - 240q - 94p) \\ (13) \quad SD(\gamma_2) = 633pq - 65q - 28p \\ (14) \quad F(\gamma_2) = 1328pq - 370q - 148p \\ (15) \quad ABC(\gamma_2) = (\frac{15pq}{2} - \frac{25q}{6} - \frac{10q}{3})^{\frac{1}{2}} \\ + (\frac{57pq}{8} - \frac{45q}{8} - \frac{3p}{2})^{\frac{1}{2}} + (\frac{40p}{9} + \frac{80q}{9} + \frac{20pq}{3})^{\frac{1}{2}}$$

Proof: Let γ_2 be $C_{30}D_{5h}$. The total number of vertices P_2 and edges Q_2 of γ_2 are $30pq$ and $52pq-5q-2p$ respectively. Based on the vertex degree, we have done edge partitions of γ_2 . The following result of $M_1(\gamma_2)$ is obtained by applying the edge partitions (See Table 3) in the definition of the first Zagreb index. And followed by the results of other topological descriptors (See Table 1) are also obtained Theorem 5.3(2–15)

$$(1) \quad M_1(\gamma_2) = (3+3)(15pq+10p+20q) + (3+4) \\ (18pq-8p-10q) + (4+4)(19pq-4p-15q) \\ = 368pq - 70q - 28p. \quad \blacksquare$$

Theorem 5.4: Let γ_2 be $C_{30}D_{5h}$. Then degree based multiplicative topological descriptors are

$$(1) \quad MM_1(\gamma_2) = 6^{10p+20q+15pq} \times 7^{18pq-10q-8p} \\ \times 8^{19pq-15q-4p} \\ (2) \quad MM_2(\gamma_2) = 9^{10p+20q+15pq} \times 12^{18pq-10q-8p} \\ \times 16^{19pq-15q-4p}$$

$$(3) \quad MRM_2(\gamma_2) = 4^{10p+20q+15pq} \times 6^{18pq-10q-8p} \\ \times 9^{19pq-15q-4p} \\ (4) \quad MHM(\gamma_2) = 36^{10p+20q+15pq} \times 49^{18pq-10q-8p} \\ \times 64^{19pq-15q-4p} \\ (5) \quad MAZ(\gamma_2) = (\frac{729}{64})^{10p+20q+15pq} \times (\frac{1728}{125})^{18pq-10q-8p} \\ \times (\frac{512}{27})^{19pq-15q-4p} \\ (6) \quad MR(\gamma_2) = (\frac{1}{3})^{10p+20q+15pq} \times (\frac{3^{\frac{1}{2}}}{6})^{18pq-10q-8p} \\ \times (\frac{3^{\frac{1}{2}}}{6})^{19pq-15q-4p} \\ (7) \quad MRR(\gamma_2) = 3^{10p+20q+15pq} \times 4^{19pq-15q-4p} \\ \times (2 \times 3^{\frac{1}{2}})^{18pq-10q-8p} \\ (8) \quad MRRR(\gamma_2) = 2^{10p+20q+15pq} \times 3^{19pq-15q-4p} \\ \times (6^{\frac{1}{2}})^{18pq-10q-8p} \\ (9) \quad MH(\gamma_2) = (\frac{1}{4})^{19pq-15q-4p} \times (\frac{2}{7})^{18pq-10q-8p} \\ \times (\frac{1}{3})^{10p+20q+15pq} \\ (10) \quad MSC(\gamma_2) = (2^{\frac{1}{8}})^{19pq-15q-4p} \times (6^{\frac{1}{12}})^{10p+20q+15pq} \\ \times (7^{\frac{1}{14}})^{18pq-10q-8p} \\ (11) \quad MGA(\gamma_2) = 4(\frac{1}{2})^{19pq-15q-4p} \times (\frac{1}{2})^{10p+20q+15pq} \\ \times (2 \times \frac{(3)^{\frac{1}{2}}}{7})^{18pq-10q-8p} \\ (12) \quad MIS(\gamma_2) = (\frac{3}{2})^{10p+20q+15pq} \times (\frac{12}{7})^{18pq-10q-8p} \\ \times 2^{19pq-15q-4p} \\ (13) \quad MSD(\gamma_2) = 2^{19pq-15q-4p} \times 2^{10p+20q+15pq} \\ \times (\frac{25}{12})^{18pq-10q-8p} \\ (14) \quad MF(\gamma_2) = 18^{10p+20q+15pq} \times 25^{18pq-10q-8p} \\ \times 32^{19pq-15q-4p} \\ (15) \quad MABC(\gamma_2) = (\frac{2}{3})^{10p+20q+15pq} \\ \times (\frac{2^{\frac{1}{2}} \times 3^{\frac{1}{2}}}{4})^{19pq-15q-4p} \\ \times (\frac{3^{\frac{1}{2}} \times 5^{\frac{1}{2}}}{6})^{18pq-10q-8p}$$

Proof: Let γ_2 be a $C_{30}D_{5h}$. The total number of vertices P_2 and edges Q_2 of γ_2 are $30pq$ and $52pq-5q-2p$ respectively. Based on the vertex degree, we have done edge partitions of γ_2 . The following result of $MM_1(\gamma_2)$ is obtained by applying the edge partitions (See Table 3) in the definition of the first multiple Zagreb index. And followed by the results of other multiplicative topological descriptors (See Table 2) are also obtained Theorem 5.4(2–15)

$$(1) \quad MM_1(\gamma_2) = (3+3)^{15pq+10p+20q} \\ \times (3+4)^{18pq-8p-10q} \times (4+4)^{19pq-4p-15q} \\ = 6^{10p+20q+15pq} \times 7^{18pq-10q-8p} \times 8^{19pq-15q-4p}. \quad \blacksquare$$

5.1. Degree-based entropy measures

To calculate entropy values using Shannon's method, this section describes constructing the probability function using neighbourhood degree-based topological indices.

Because Shannon's model is the most popular approach, we utilised it to determine probabilistic entropy [60]-[68]. The entropy measured using that topological index TI is given by

$$E_{TI}(\gamma) = \log(TI(\gamma)) - \frac{1}{TI(\gamma)} \left(\sum_{uv \in E(\gamma)} f(e) \log(f(e)) \right)$$

By using the first Zagreb index to calculate the entropy value for the $C_{36}D_{6h}$ and $C_{30}D_{5h}$ structures, the calculation procedure is illustrated below. Also, Figures 5 and 6 are the 3D plots of the entropy of the first Zagreb index.

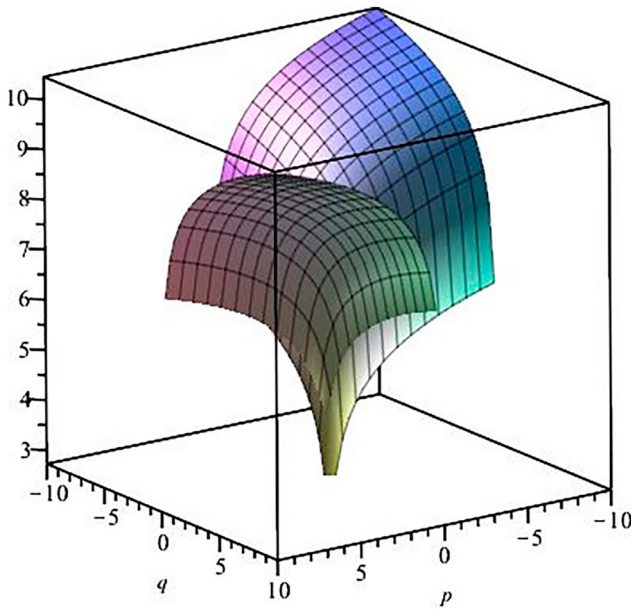


Figure 5. 3D plot of $EM_1(C_{36}D_{6h})$.

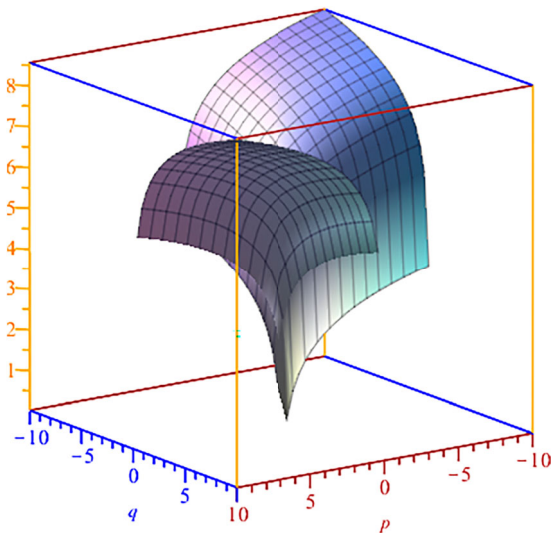


Figure 6. 3D plot of $EM_1(C_{30}D_{5h})$.

First Zagreb entropy for $C_{36}D_{6h}$ molecular graph

$$\begin{aligned} EM_1(\gamma_1) &= \log(520pqr - 84pr - 84qr - 28pq) \\ &\quad - \frac{(10pq + 20qr + 20pr + 4r)(3 + 3)\log(3 + 3)}{520pqr - 84pr - 84qr - 28pq} \\ &\quad - \frac{(24pqr - 8pq - 4qr - 4pr - 8r)(4 + 3)\log(4 + 3)}{520pqr - 84pr - 84qr - 28pq} \\ &\quad + \frac{(44pqr - 4pq - 22qr - 22pr + 4r)(4 + 4)\log(4 + 4)}{520pqr - 84pr - 84qr - 28pq} \\ &= \log(520pqr - 28pq - 84pr - 84qr) \\ &\quad - \frac{6(10pq + 20pr + 20qr + 4r)\log(6) + 7(24pqr - 8pq - 4pr - 4qr - 8r)\log(7) + 24(44pqr - 4pq - 22pr - 22qr + 4r)\log(2)}{520pqr - 28pq - 84pr - 84qr} \end{aligned}$$

After simplifying this, we obtain

$$\begin{aligned} EM_1(\gamma_1) &= \frac{1}{((130q - 21)p - 21q)r - 7pq} \\ &\quad \times (((130q - 21)p - 21q)r - 7pq) \\ &\quad \times \log(((130r - 7)q - 21r)p - 21qr) \\ &\quad + (((-4q + 60)p + 60q - 30)r - 5pq)\log(2) \\ &\quad + (((-42q + 7)p + 7q + 14)r + 14pq)\log(7) \\ &\quad - 15\log(3)((2p + 2q + \frac{2}{5})r + pq). \end{aligned}$$

First Zagreb entropy for $C_{30}D_{5h}$ molecular graph

$$\begin{aligned} EM_1(\gamma_2) &= \log(368pq - 70q - 28p) \\ &\quad - \frac{(15pq + 10p + 20q)(3 + 3)\log(3 + 3) + (18pq - 8p - 10q)(4 + 3)\log(4 + 3)}{368pq - 70q - 28p} \\ &\quad + \frac{(19pq - 4p - 15q)(4 + 4)\log(4 + 4)}{368pq - 70q - 28p} \\ &= \log(368pq - 70q - 28p) \\ &\quad - \frac{\frac{19142417789809141p}{281474976710656} + \frac{384462300234069845q}{2251799813685248}}{\frac{1626966225076201483pq}{2251799813685248}} \\ &\quad - \frac{28p + 70q - 368pq}{2251799813685248} \end{aligned}$$

After simplifying this, we obtain

$$EM_1(\gamma_2) = \log(368pq - 70q - 28p)$$

$$\begin{aligned}
& 153139342318473128p \\
& +384462300234069845q \\
& -1626966225076201483pq \\
& - \frac{4503599627370496(14p + 35q - 184pq)}{1}
\end{aligned}$$

The first Zagreb index of $C_{36}D_{6h}$ and $C_{30}D_{5h}$'s entropy values are graphically shown in Figures 5 and 6, using MATLAB 2020. We first create a horizontal grid using the p and q parameters, then we build a surface on top of that grid. The entropy values show distinct tendencies that correlate to various factors, as seen by this graphic. Depending on the settings, these graphs display different entropy value characteristics. By modulating topological indices and entropy via these factors, we may control a wide range of variables and activities.

Each chemical network's general entropy formulation is too lengthy to be given as a Theorem. Concerning each topological index, the method mentioned above makes generating any degree-based entropies expression easy.

6. Numerical computation

This section displays the numerical outcomes of degree-based topological descriptors and entropy measurements of the structures $C_{36}D_{6h}$ and $C_{30}D_{5h}$. The values of the variables p , q and r range from 1 to 10.

Table 4. Numerical values for degree-based TI for $C_{36}D_{6h}$.

(p, q, r)	(1, 1, 1)	(2, 2, 2)	(3, 3, 3)	(4, 4, 4)	(5, 5, 5)
M_1	324	3376	12276	30144	60100
M_2	486	5904	22206	55344	111270
RM_2	216	3016	11640	29328	59320
HM	1944	23728	89304	222624	447640
AZ	615.0938	7103.3	26462	65687	131780
R	18	143.6649	484.5641	1148.3	2242.3
RR	162	1684	6120.8	15027	29958
RRR	108	1194.3	4403.8	10881	21771
H	18	143.3333	483.1429	1144.6	2234.8
SC	22.0454	186.6446	641.5627	1534.6	3013.4
GA	54	486.8513	1705.1	4115.2	8123.7
IS	81	840	3051.9	7491.4	14934
SD	108	985.3333	3460	8360	16513
F	972	11920	44892	111936	225100
ABC	4.899	24.3834	45.4422	69.6682	96.6671
(p, q, r)	(6, 6, 6)	(7, 7, 7)	(8, 8, 8)	(9, 9, 9)	(10, 10, 10)
M_1	105264	168756	253696	363204	500400
M_2	195936	315294	475296	681894	941040
RM_2	104856	169176	255520	367128	507240
HM	788304	1268568	1912384	2743704	3786480
AZ	231730	372530	561190	804710	1110100
R	3874.4	6151.9	9182.5	13074	17933
RR	52468	84113	126450	181020	249400
RRR	38218	61367	92362	132350	182470
H	3860.9	6130	9149.3	13026	17867
SC	5225.9	8319.7	12443	17743	24367
GA	14137	22562	33805	48273	66371
IS	26153	41925	63024	90225	124300
SD	28748	45892	68773	98220	135060
F	396432	637980	961792	1379916	1904400
ABC	126.1445	157.8795	191.7003	227.4687	265.0705

Table 5. Numerical values for degree-based TI for $C_{30}D_{5h}$.

(p, q)	(1, 1)	(2, 2)	(3, 3)	(4, 4)	(5, 5)
M_1	270	1276	3018	5496	8710
M_2	405	2120	5145	9480	15125
RM_2	180	1038	2574	4788	7680
HM	1620	8516	20688	38136	60860
AZ	512.5781	2585.1	6217.7	11410	18163
R	15	59.8923	134.6769	239.3538	373.923
RR	135	636.7077	1505.1	2740.2	4342.1
RRR	90	442.1816	1056.5	1933.1	3071.8
H	15	59.7857	134.3571	238.7143	372.8571
SC	18.3712	76.0315	172.9811	309.2199	484.7479
GA	45	193.6308	445.8923	801.7846	1261.3
IS	67.5	317.7143	750.6429	1366.3	2164.6
SD	90	391	903	1626	2560
F	810	4276	10398	19176	30610
ABC	4.4721	14.9509	23.2466	31.3826	39.46
(p, q)	(6, 6)	(7, 7)	(8, 8)	(9, 9)	(10, 10)
M_1	12660	17346	22768	28926	35820
M_2	22080	30345	39920	50805	63000
RM_2	11250	15498	20424	26028	32310
HM	88860	122136	160688	204516	253620
AZ	26475	36348	47780	60772	75325
R	538.3846	732.7384	956.9845	1211.1	1495.2
RR	6310.6	8645.9	11348	14416	17852
RRR	4472.7	6135.8	8061.1	10249	12698
H	536.7857	730.5	954	1207.3	1490.4
SC	699.565	953.6714	1247.1	1579.8	1951.7
GA	1824.5	2491.2	3261.7	4135.7	5113.4
IS	3145.7	4309.5	5656	7185.2	8897.1
SD	3705	5061	6628	8406	10395
F	44700	61446	80848	102906	127620
ABC	47.5087	55.541	63.5629	71.5779	79.5879

The generated topological descriptors were plotted using the Origin 2020b programme for a graphical comparison. The results are summarised in Tables 4–7.

This tendency is depicted graphically in three dimensions in Figures 7 and 8. These 3D charts show the differences between each topological index for a specific structure. The two different structures that are the research subject of this article can all have their behaviour for a particular index compared using the 3D graphs. The following tables and pictures analyse various entropies of $C_{30}D_{5h}$ and $C_{36}D_{6h}$ in numerical and graphical ways.

This section will address the γ_1 and γ_2 comparison studies using specific p , q , and r values that can be seen in Tables 4–7 and their associated graphs in Figures 7 and 8. Tables 4 and 5 give the numerical values of different topological indices and Tables 6 and 7 give the numerical computation of entropy values of γ_1 and γ_2 . Figure 7 shows a comparison of the topological indices of γ_1 and γ_2 . From this study, it is observed that the hyper Zagreb index is the highest impact than other indices. However, Entropy comparison (See Figure 8), shows that for ABC index's entropy is significantly affected for γ_1 and γ_2 . The chemists can use these comparisons to analyse the physiochemical characteristics of γ_1 and γ_2 . Chemists can anticipate a range of molecular compound properties using these indices instead of expensive or time-consuming testing.

Table 6. Numerical values for degree-based entropies for $C_{30}D_{5h}$.

(p, q)	(1, 1)	(2, 2)	(3, 3)	(4, 4)	(5, 5)	(6, 6)	(7, 7)	(8, 8)	(9, 9)	(10, 10)
$EM_1(\gamma_2)$	3.8067	5.2607	6.095	6.6821	7.1355	7.5048	7.8165	8.086	8.3235	8.5358
$EM_2(\gamma_2)$	3.8067	5.2383	6.0721	6.6597	7.1134	7.4831	7.7951	8.0649	8.3026	8.515
$ERM_2(\gamma_2)$	3.8067	5.2072	6.0416	6.6303	7.0849	7.4553	7.7677	8.0379	8.2759	8.4886
$EHM(\gamma_2)$	3.8067	5.238	6.072	6.6597	7.1135	7.4833	7.7953	8.0651	8.3028	8.5153
$EAZ(\gamma_2)$	3.8067	5.2454	6.0787	6.6657	7.1191	7.4885	7.8002	8.0699	8.3075	8.5198
$ER(\gamma_2)$	3.8067	5.2618	6.0957	6.6825	7.1357	7.505	7.8166	8.0861	8.3236	8.5358
$ERR(\gamma_2)$	3.8067	5.2608	6.0951	6.6822	7.1355	7.5048	7.8164	8.086	8.3235	8.5358
$ERRR(\gamma_2)$	3.8067	5.2536	6.0876	6.6748	7.1282	7.4976	7.8094	8.079	8.3166	8.5289
$EH(\gamma_2)$	3.8067	5.2616	6.0955	6.6824	7.1356	7.5049	7.8165	8.086	8.3235	8.5358
$ESC(\gamma_2)$	3.8067	5.2662	6.1008	6.6878	7.141	7.5103	7.8218	8.0914	8.3288	8.5411
$EGA(\gamma_2)$	3.8067	5.2679	6.1025	6.6896	7.1428	7.5121	7.8236	8.0931	8.3306	8.5428
$EIS(\gamma_2)$	3.8067	5.2609	6.0951	6.6822	7.1355	7.5048	7.8164	8.086	8.3235	8.5358
$ESD(\gamma_2)$	3.8067	5.2677	6.1024	6.6894	7.1427	7.5119	7.8235	8.093	8.3304	8.5427
$EF(\gamma_2)$	3.8067	5.2376	6.0718	6.6596	7.1136	7.4834	7.7954	8.0653	8.303	8.5155
$EABC(\gamma_2)$	4.2178	6.318	8.5479	10.6737	12.7415	14.7723	16.7772	18.7632	20.7345	22.6942

Table 7. Numerical values for degree-based entropies for $C_{36}D_{6h}$.

(p, q, r)	(1, 1, 1)	(2, 2, 2)	(3, 3, 3)	(4, 4, 4)	(5, 5, 5)	(6, 6, 6)	(7, 7, 7)	(8, 8, 8)	(9, 9, 9)	(10, 10, 10)
$EM_1(\gamma_1)$	3.989	6.1824	7.4375	8.3197	9.0006	9.5552	10.0231	10.4277	10.7842	11.1028
$EM_2(\gamma_1)$	3.989	6.1587	7.4179	8.3029	8.9857	9.5415	10.0103	10.4157	10.7727	11.0918
$ERM_2(\gamma_1)$	3.989	6.1285	7.394	8.2828	8.9679	9.5253	9.9953	10.4015	10.7592	11.0788
$EHM(\gamma_1)$	3.989	6.1589	7.4184	8.3036	8.9865	9.5424	10.0112	10.4166	10.7737	11.0928
$EAZ(\gamma_1)$	3.989	6.1647	7.4216	8.3053	8.9872	9.5425	10.0109	10.416	10.7728	11.0917
$ER(\gamma_1)$	3.989	6.1826	7.437	8.319	8.9999	9.5544	10.0223	10.4269	10.7835	11.1021
$ERR(\gamma_1)$	3.989	6.1824	7.4374	8.3196	9.0004	9.555	10.0228	10.4275	10.784	11.1025
$ERRR(\gamma_1)$	3.989	6.1745	7.4308	8.3139	8.9954	9.5504	10.0186	10.4235	10.7801	11.1989
$EH(\gamma_1)$	3.989	6.1825	7.437	8.3191	9	9.5546	10.0225	10.4272	10.7837	11.1023
$ESC(\gamma_1)$	3.989	6.1883	7.4425	8.324	9.0044	9.5586	10.0262	10.4306	10.787	11.1055
$EGA(\gamma_1)$	3.989	6.1903	7.4442	8.3255	9.0058	9.5599	10.0274	10.4317	10.788	11.1064
$EIS(\gamma_1)$	3.989	6.1823	7.4372	8.3194	9.0002	9.5547	10.0226	10.4272	10.7837	11.1023
$ESD(\gamma_1)$	3.989	6.1902	7.4441	8.3254	9.0056	9.5597	10.0272	10.4316	10.7879	11.1063
$EF(\gamma_1)$	3.989	6.1589	7.4188	8.3043	8.9872	9.5432	10.0121	10.4175	10.7746	11.0937
$EABC(\gamma_1)$	4.5686	8.8668	14.6248	21.3686	29.0264	37.5299	46.8211	56.8513	67.5792	78.9696

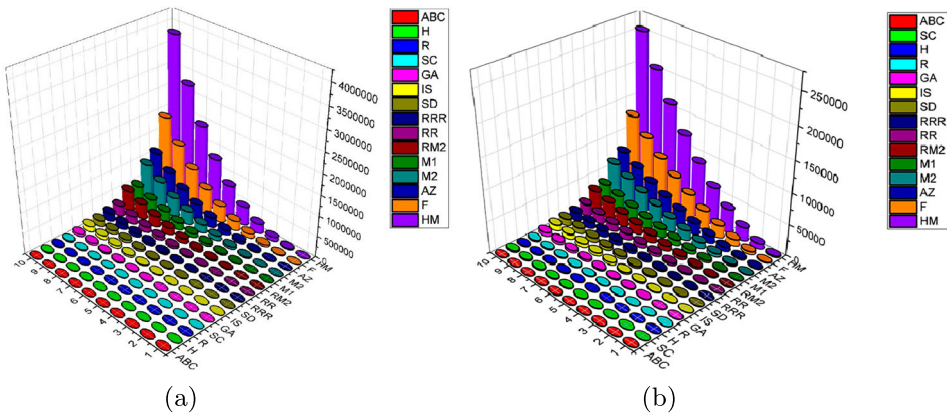


Figure 7. Comparison of degree based indices of $C_{36}D_{6h}$ and $C_{30}D_{5h}$. (a) TI of $C_{36}D_{6h}$. (b) TI of $C_{30}D_{5h}$.

7. Conclusion

We have calculated a few topological indices for $C_{30}D_{5h}$ and $C_{36}D_{6h}$ molecular structures in this study. In addition to that, we also calculated $C_{30}D_{5h}$ and $C_{36}D_{6h}$'s entropy values and neighbourhood topological indices and the graphical analysis which made it easier to comprehend the behaviours of the established models. These

findings represent critical advances in chemical science and provide a foundation for learning the complex topology of these crucial structures. For chemical experts, these finding reveal the best topological features of these structures posses along with how these structures are formed. A few other observations on the results include the following: it is noted that when the parameters p , q and r grow, the topological indices of the considered

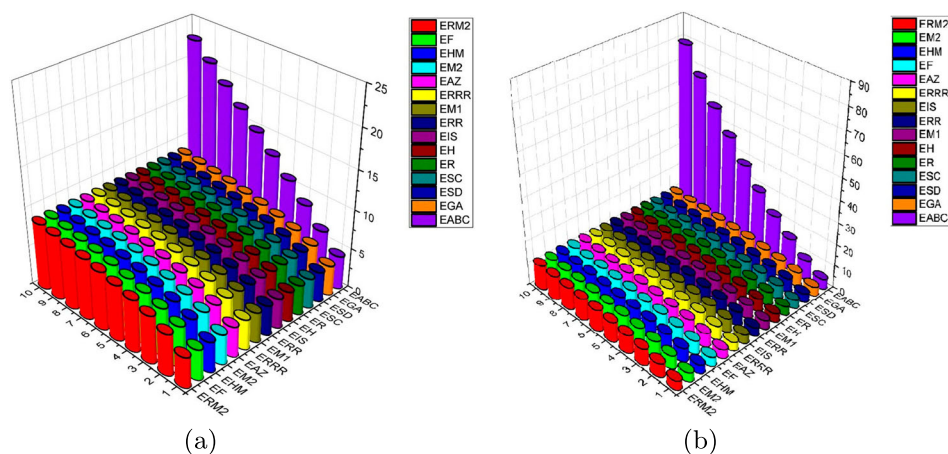


Figure 8. Comparison of entropy measures of $C_{30}D_{5h}$ and $C_{36}D_{6h}$. (a) Entropy of $C_{30}D_{5h}$. (b) Entropy of $C_{36}D_{6h}$.

chemical structures also increase. These results might provide us with a more thorough understanding of the structural properties of $C_{36}D_{6h}$ and $C_{30}D_{5h}$.

Disclosure statement

No potential conflict of interest was reported by the author(s).

ORCID

Tony Augustine <http://orcid.org/0000-0002-5339-2154>

S. Roy <http://orcid.org/0000-0002-5542-6581>

J. Sahaya Vijay <http://orcid.org/0000-0001-6672-0092>

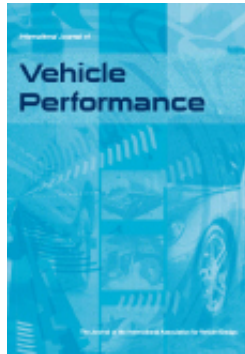
Jain Maria Thomas <http://orcid.org/0000-0003-2597-5237>

P. Shanmugam <http://orcid.org/0000-0002-9535-8771>

References

- [1] W. Gao and M.R. Farahani, *Appl. Math. Nonlinear Sci.* **1**, 99–122 (2016). doi:10.21042/AMNS.2016.1.00009
- [2] W. Gao, H. Wu, M.K. Siddiqui and A.Q. Baig, *Saudi J. Biol. Sci.* **25**, 1212–1219 (2018). doi:10.1016/j.sjbs.2017.11.022
- [3] V. Georgakilas, J.A. Perman, J. Tucek and R. Zboril, *Chem. Rev.* **115**, 4744–4822 (2015). doi:10.1021/cr500304f
- [4] P. Schwerdtfeger, L.N. Wirz and J. Avery, *Wiley Interdiscip. Rev. Comput. Mol. Sci.* **5**, 96–145 (2015). doi:10.1002/wcms.1207
- [5] A. Kausar and R. Taherian, *Electrical Conductivity Behavior of Polymer Nanocomposite with Carbon Nanofillers. Electrical Conductivity in Polymer-Based Composites: Experiments, Modelling, and Applications* (Elsevier Inc., 2018).
- [6] R.C. Haddon, A.F. Hebard, M.J. Rosseinsky, D.W. Murphy, S.J. Duclos, K.B. Lyons, B. Miller, J.M. Rosamilia, R.M. Fleming, A.R. Kortan and S.H. Glarum, *Nature* **350**, 320–322 (1991). doi:10.1038/350320a0
- [7] S. Thakral and R. Mehta, *Indian J. Pharm. Sci.* **68**, 13–19 (2006). doi:10.4103/0250-474X.22957
- [8] P.W. Fowler, T. Heine, K.M. Rogers, J.P.B. Sandall, G. Seifert and F. Zerbetto, *Chem. Phys. Lett.* **300**, 369–378 (1999). doi:10.1016/S0009-2614(98)01385-2
- [9] M. Mohan Gokhale and R. Ravindra Somani, *Mini Rev. Org. Chem.* **12**, 355–366 (2015). doi:10.2174/1570193X12666150930224428
- [10] E. Albertazzi, C. Domene, P.W. Fowler, T. Heine, G. Seifert, C. Van Alsenoy and F. Zerbetto, *Phys. Chem. Chem. Phys.* **1**, 2913–2918 (1999). doi:10.1039/a91600g
- [11] J.H. Lee, B.S. Lee, F.T.K. Au, J. Zhang and Y. Zeng, *Comput. Mater. Sci.* **56**, 131–140 (2012). doi:10.1016/j.commat.2012.01.019
- [12] Y.F. Chang, J.P. Zhang, H. Sun, B. Hong, Z. An and R.S. Wang, *Int. J. Quantum Chem.* **105**, 142–147 (2005). doi:10.1002/(ISSN)1097-461X
- [13] D. Paul, J. Deb and U. Sarkar, *ChemistrySelect* **5**, 6987–6999 (2020). doi:10.1002/slct.v5.23
- [14] C. Piskoti, J. Yarger and A. Zettl, *Nature* **393**, 771–774 (1998). doi:10.1038/31668
- [15] E.A. Hill, H.G. Richey and T.C. Rees, *J. Org. Chem.* **28**, 2161–2164 (1963). doi:10.1021/jo01043a050
- [16] L. Yuan, J. Yang, K. Deng and Q. Zhu, *J. Phys. Chem. A* **104**, 6666–6671 (2000). doi:10.1021/jp0009913
- [17] M. Canales-Lizaola, J.M. Ramirez-De-Arellano, J.S. Arellano and L.F. Magaa, *J. Phys. Conf. Ser.* **1723** (2021). doi:10.1088/1742-6596/1723/1/012054
- [18] Y. Pan, X. Liu, W. Zhang, Z. Liu, G. Zeng, B. Shao, Q. Liang, Q. He, X. Yuan, D. Huang and M. Chen, *Appl. Catal. B Environ.* **265**, 118579 (2020). doi:10.1016/j.apcatb.2019.118579
- [19] R. Taylor, *Fullerene Chemistry A Handbook for Chemists* (Imperial College Press, London U.K., 1999).
- [20] S. Yao, X. Yuan, L. Jiang, T. Xiong and J. Zhang, *Materials (Basel)* **13**, 1–38 (2020). doi:10.3390/ma13132924
- [21] A. Nimibofa, E.A. Newton, A.Y. Cyprain and W. Donbebe, *J. Mater. Sci. Res.* **7**, 22 (2018). doi:10.5539/jmsr.v7n3p22
- [22] M.A. Yirik, K.E. Colpan, S. Schmidt, M. Sorokina and C. Steinbeck, *Chemistry (2021)*. doi:10.20944/preprints202111.0546.v1
- [23] A.L.-A. Hasan and M.N. AL-Baiati, *IOP Conf. Ser. Mater. Sci. Eng.* **571**, 012092 (2019). doi:10.1088/1757-899X/571/1/012092
- [24] T.M. Kotresh, R. Ramani, N. Jana, S. Minu, R.I. Shekar and R. Ramachandran, *ACS Appl. Polym. Mater.* **3**, 3989–4007 (2021). doi:10.1021/acsapm.1c00529

- [25] K.G. Mirajkar, A. Morajkar and H.H. Budihal, AIP. Conf. Proc. **2385** (1), 030002 (2022). doi:10.1063/5.0070746
- [26] J. Devillers and A.T. Balaban, *Topological Indices and Related Descriptors in QSAR and QSPAR* (CRC Press, Boca Raton, FL, USA, 2000).
- [27] A. Mahboob, S. Mahboob, M.M.M. Jaradat, N. Nigar and I. Siddique, J. Math. **2021**, 1–10 (2021). doi:10.1155/2021/4611199
- [28] C.E. Shannon, Bell Syst. Tech. J. **27**, 379–423 (1948). doi:10.1002/bltj.1948.27.issue-3
- [29] C.-P. Li, M.K. Siddiqui, P. Ali, S. Javed, M. Hussain and S. Khalid, J. Quantum Chem. **122** (23), e26996 (2022). doi:10.1002/qua.v122.23
- [30] S.R.J. Kavitha, J. Abraham, M. Arockiaraj, J. Jency and K. Balasubramanian, J. Phys. Chem. A **125**, 8140–8158 (2021). doi:10.1021/acs.jpca.1c06264
- [31] A. Mowshowitz and M. Dehmer, Entropy **14**, 559–570 (2012). doi:10.3390/e14030559
- [32] M. Dehmer, J. Appl. Math. Comput. **201**, 82–94 (2008). doi:10.1016/j.amc.2007.12.010
- [33] M. Dehmer, L. Sivakumar and K. Varmuza, MATCH Commun. Math. Comput. Chem. **67**, 147–72 (2012).
- [34] M. Dehmer and A. Mowshowitz, Inf. Sci. **181**, 57–78 (2011). doi:10.1016/j.ins.2010.08.041
- [35] S. Manzoor, M.K. Siddiqui and S. Ahmad, Arab. J. Chem. **13**, 6285–6298 (2020). doi:10.1016/j.arabjc.2020.05.021
- [36] H.W. Kroto, J.R. Heath, S.C. O'Brien, R.F. Curl and R.E. Smalley, Nature **318**, 162–163 (1985). doi:10.1038/318162a0
- [37] W. Krätschmer, L.D. Lamb, K. Fostiropoulos and D.R. Huffman, Nature **347**, 354–358 (1990). doi:10.1038/347354a0
- [38] J.B. Howard, J.T. McKinnon, Y. Makarovskiy, A.L. Lafleur and M.E. Johnson, Nature **352**, 139–141 (1991). doi:10.1038/352139a0
- [39] H.R. Tian, M.M. Chen, K. Wang, Z.C. Chen, C.Y. Fu, Q. Zhang, S.H. Li, S.L. Deng, Y.R. Yao, S.Y. Xie and R.B. Huang, J. Am. Chem. Soc. **141**, 6651–6657 (2019). doi:10.1021/jacs.9b01638
- [40] H.-G. Zhang, Nanomaterials **11**, 3033 (2021). doi:10.3390/nano11113033
- [41] B. Yang, Y. Chen and J. Shi, Chem. Rev. **119**, 4881–4985 (2019). doi:10.1021/acs.chemrev.8b00626
- [42] N.L. Rosi and C.A. Mirkin, Chem. Rev. **105**, 1547–1562 (2005). doi:10.1021/cr030067f
- [43] K. Ni, T. Luo, G.T. Nash and W. Lin, Acc. Chem. Res. **53**, 1739–1748 (2020). doi:10.1021/acs.accounts.0c00313
- [44] A.R. Kirtane, Nat. Nanotechnol. **16**, 369–384 (2021). doi:10.1038/s41565-021-00866-8
- [45] S. Li, Q. Jiang, S. Liu, Y. Zhang, Y. Tian, C. Song, J. Wang, Y. Zou, G.J. Anderson, J.Y. Han and Y. Chang, Nat. Biotechnol. **36**, 258–264 (2018). doi:10.1038/nbt.4071
- [46] T. Ji, Y. Zhao, Y. Ding, J. Wang, R. Zhao, J. Lang, H. Qin, X. Liu, J. Shi, N. Tao and Z. Qin, Angew. Chem. Int. Ed. **55**, 1050–1055 (2016). doi:10.1002/anie.201506262
- [47] X. Han, Y. Li, Y. Xu, X. Zhao, Y. Zhang, X. Yang, Y. Wang, R. Zhao, G.J. Anderson, Y. Zhao and G. Nie, Nat. Commun. **9**, 3390 (2018). doi:10.1038/s41467-018-05906-x
- [48] F. Lu, L. Gu, M.J. Meziani, X. Wang, P.G. Luo, L.M. Veca, L. Cao and Y.P. Sun, Adv. Mater. **21**, 139–152 (2009). doi:10.1002/adma.v21:2
- [49] L. Feng, S. Zhang and Z. Liu, Nanoscale **3**, 1252–1257 (2011). doi:10.1039/c0nr00680g
- [50] M. Zhu, G. Nie, H. Meng, T. Xia, A. Nel and Y. Zhao, Acc. Chem. Res. **46**, 622–631 (2013). doi:10.1021/ar300031y
- [51] M. Arockiaraj, J. Clement, D. Paul and K. Balasubramanian, Mol. Phys. **119**, e1798529 (2021). doi:10.1080/00268976.2020.1798529
- [52] S. Hayat and M. Imran, Appl. Math. Comput. **240**, 213–228 (2014). doi:10.1016/j.amc.2014.04.091
- [53] K. Balasubramanian, Lett. Drug Des. Discov. **18**, 943–948 (2021). doi:10.2174/1570180818666210719130052
- [54] D.S. Sabirov and I.S. Shepelevich, Inf. Entropy Chem. Overv. Entropy **23**, e23101240 (2021). doi:10.3390/e23101240
- [55] F. Chaudhry, I. Shoukat, D. Afzal, C. Park, M. Cancan and M.R. Farahani, J. Chem. **6679819** (2021 (2021)). doi:10.1155/2021/6679819
- [56] A. Mowshowitz and M. Dehmer, Entropy **14**, 559–570 (2012). doi:10.3390/e14030559
- [57] M. Arockiaraj, D. Paul, S. Klavžar, J. Clement, S. Tigga and K. Balasubramanian, J. Mol. Struct. **1250**, 131798 (2022). doi:10.1016/j.molstruc.2021.131798
- [58] I. Gutman, Croat. Chem. Acta **86**, 351–361 (2013). doi:10.5562/cca2294
- [59] M. Arockiaraj, J. Clement and N. Tratnik, J. Quantum Chem. **119**, e26043 (2019). doi:10.1002/qua.v119.24
- [60] T. Augustine and S. Roy, Symmetry **14**, 1590 (2022). doi:10.3390/sym14081590
- [61] S. Wang and B. Wei, Discrete Appl. Math. **180**, 168–175 (2015). doi:10.1016/j.dam.2014.08.017
- [62] V.R. Kulli, Int. Res. J. Pure Algebra **6**, 342–347 (2016).
- [63] V.R. Kulli, B. Stone, S. Wang and B. Wei, Z. Naturforsch. A **72**, 573–576 (2017). doi:10.1515/zna-2017-0104
- [64] Y.C. Kwun, A.R. Virk, W. Nazeer, M.A. Rehman and S.M. Kang, Symmetry **10**, 320–330 (2018). doi:10.3390/sym10080320
- [65] M. Bhanumathi and K.E.J. Rani, Int. J. Eng. Sci. Adv. Comput. Bio-Technol. **9**, 52–67 (2018). doi:10.26674/ijesacbt/2018/49410
- [66] R. Kulli, J. Math. Comput. Sci. **7**, 599–605 (2016).
- [67] L. Guangyu, S. Hussain, A. Khalid, M. Ishtiaq, M.K. Siddiqui, M. Cancan and M. Imran, Polycycl. Aromat. Compd. **42**, 1–21 (2021). doi:10.1080/10406638.2021.1880450
- [68] Z. Hussain, N. Ijaz, W. Tahir, M.T. Butt and S. Talib, SSRN Electron. J. **2** (2018). doi:10.2139/ssrn.3265836.
- [69] M.P. Rahul, J. Clement, J.S. Junias, M. Arockiaraj and K. Balasubramanian, J. Mol. Struct. **1260**, 132797 (2022). doi:10.1016/j.molstruc.2022.132797
- [70] D.S. Sabirov and I.S. Shepelevich, Inf. Entropy Chem. Overv. Entropy **23**, 1240 (2021). doi:10.3390/e23101240



International Journal of Vehicle Performance

ISSN online: 1745-3208 - ISSN print: 1745-3194

<https://www.inderscience.com/ijvp>

Performance investigation and energy optimisation in hybrid electric vehicle model using reinforcement learning and fuzzy controller

Emmanuel Babu Pukkunnen, Neena M. Joseph, Bos Mathew Jos, Minu C. Joy, K.A. Eldhose

DOI: [10.1504/IJVP.2022.10048782](https://doi.org/10.1504/IJVP.2022.10048782)

Article History:

Received:	22 June 2021
Accepted:	11 January 2022
Published online:	04 January 2023

Performance investigation and energy optimisation in hybrid electric vehicle model using reinforcement learning and fuzzy controller

Emmanuel Babu Pukkunnen*

Department of Electrical and Electronics Engineering,
Mar Athanasius College of Engineering,
Kothamangalam, Kerala, 686 666, India
Email: emmanuel@mace.ac.in

*Corresponding author

Neena M. Joseph

Department of Civil Engineering,
Viswajyothi College of Engineering and Technology,
Muvattupuzha, Kerala, 686 670, India
Email: neenajoseph.m@gmail.com

Bos Mathew Jos

Department of Electrical and Electronics Engineering,
Mar Athanasius College of Engineering,
Kothamangalam, Kerala, 686 666, India
Email: bosmathewjos@mace.ac.in

Minu C. Joy

Department of Civil Engineering,
Viswajyothi College of Engineering and Technology,
Muvattupuzha, Kerala, 686 670, India
Email: minucjoy@gmail.com

K.A. Eldhose

Department of Electrical and Electronics Engineering,
Mar Athanasius College of Engineering,
Kothamangalam, Kerala, 686 666, India
Email: eka@mace.ac.in

Abstract: Hybrid electric vehicles (HEVs) are considered as one of the prominent solutions in reducing vehicular emission. Batteries and internal combustion engines (ICE) are the important components of a HEV, which acts as primary and secondary power source respectively. They simplify the refuelling process by minimising fuel consumption and by reducing virulent emissions. In this research, a series-parallel drivetrain – HEV model is

proposed for investigating the performance and energy optimisation of the HEVs. The model is trained to operate at near optimum efficiency for minimising the energy loss. A deep reinforcement learning and fuzzy logic controller based energy management approach is proposed to optimise the energy consumption in HEVs. Results show that the energy management system (EMS) of the model is controlled effectively by the deep reinforcement learning (DRL) algorithm. Effective speed control is achieved by fine tuning the parameters using a fuzzy based PID controller which can be validated from the simulation results.

Keywords: HEVs; hybrid electric vehicles; series-parallel drivetrain; EMSs; energy management systems; DRL; deep reinforcement learning; fuzzy control logic; PID controllers; speed control.

Reference to this paper should be made as follows: Pukkunnen, E.B., Joseph, N.M., Jos, B.M., Joy, M.C. and Eldhose, K.A. (2023) 'Performance investigation and energy optimisation in hybrid electric vehicle model using reinforcement learning and fuzzy controller', *Int. J. Vehicle Performance*, Vol. 9, No. 1, pp.73–90.

Biographical notes: Emmanuel Babu Pukkunnen completed his BTech (Electrical and Electronics Engineering) in 2003 from the Mahatma Gandhi University, Kerala, India. He has done his MTech (Industrial Power and Automation) from the National Institute of Technology Calicut in 2016. Currently, he is a Research Scholar at the Department of Electrical Engineering at the National Institute of Technology Calicut. He is also a Faculty at the Department of Electrical and Electronics Engineering, Mar Athanasius College of Engineering, Kothamangalam, Kerala, India.

Neena M. Joseph completed her BTech (Civil Engineering) in 2007 from the University of Calicut, Kerala, India. She has done her MTech (Traffic and Transportation Planning) from the National Institute of Technology Calicut in 2011. Currently, she is a Research Scholar at the Centre for Transportation Research at the National Institute of Technology Calicut. She is also a Faculty in the Department of Civil Engineering at Viswajyothi College of Engineering and Technology, Ernakulam, Kerala, India.

Bos Mathew Jos completed his BTech (Electrical and Electronics Engineering) from the Mahatma Gandhi University, Kerala, India. He has done his MTech and PhD from the National Institute of Technology Triruchirapalli. Currently, he is a Faculty in the Department of Electrical and Electronics Engineering at Mar Athanasius College of Engineering, Kothamangalam, Kerala, India.

Minu C. Joy completed her BTech (Civil Engineering) in 2008 from Mahatma Gandhi University, Kerala, India. She has done her MTech from the University of Calicut in 2012. Currently, she is a Faculty in the Department of Civil Engineering at Viswajyothi College of Engineering and Technology, Ernakulam, Kerala, India.

K.A. Eldhose completed his BTech (Electrical and Electronics Engineering) in 2002 from the Mahatma Gandhi University, Kerala, India. He has done his MTech from the University of Calicut, Kerala, India. Currently, he is a Faculty in the Department of Electrical and Electronics Engineering at Mar Athanasius College of Engineering, Kothamangalam, Kerala, India.

1 Introduction

Hybrid electric vehicles (HEVs) are regarded as an optimistic substitute for conventional fuel based vehicles, because of their effectiveness in reducing vehicular pollution and noise. The batteries and internal combustion engine (ICE) in HEV's play an important role in reducing vehicular emission thereby contributing towards a pollution free ecosystem. Battery is one of the significant components in HEV's, whose performance is evaluated with respect to different circuit parameters such as open circuit voltage (OCV), state of charge (SOC), battery resistance and power capacity. These parameters are highly sensitive towards temperature, battery ageing and charging/discharging cycle of the battery (Panday and Bansal, 2015). In HEV's, the battery and ICE act as primary and secondary power sources respectively. They both increase the driving range of the vehicle and ease the mechanism of refuelling with minimised fuel consumption and reduced virulent emissions. HEVs store the electrical power in batteries which significantly reduces the energy demand. In this way, HEVs reduce energy requirement by replacing fossil fuel consumption with electrical energy consumption (Panday et al., 2016). The energy management unit in HEV's uses a rechargeable energy storage system (RESS) which acts as an energy buffer and can be employed for regenerative braking. RESS stores the additional energy which is not required by the system at that particular point of time. For example, in most of the times, the power delivered by ICE is different from the power required by the load and in such cases, RESS provides the flexibility of utilising only the required amount of power while utilising the unused power for charging the battery (Onori et al., 2016). RESS in HEV's offers the feasibility of operating the engine in favourable conditions where there is less emissions. Also, there is a possibility of terminating the engine operation when it is not required (i.e., during low speed conditions) and the engine can be downsized by storing the peak power using RESS (Sun et al., 2015). Though HEV's are efficient in reducing fuel consumption, they suffer from certain drawbacks such as low density and low efficiency. Also the cost of the refuelling infrastructure is quite high, which makes it expensive for small scale applications (Sulaiman et al., 2018). Most of the researchers have focussed on developing an efficient energy management system (EMS) for overcoming the limitations of the conventional HEV's. Advanced EMS models include energy minimisation techniques and application of machine learning and deep learning approaches for increasing the flexibility of the EMS. These approaches are gaining prominence because of their reduced computational complexities and no requirement of pre-defined knowledge (Zhou et al., 2019). There are three main categories for EMS which are rule based EMS, optimisation based EMS and learning based EMS. Rule based EMS are mainly dependent on the outcome of the detailed experimental analysis without having the preliminary knowledge about the conditions of driving. Fuzzy based rules are applied for controlling these EMSs. Optimisation based EMS are used when the control strategies of the HEVs are anticipated on subsequent driving scenarios like dynamic programming (DP) (Ansarey et al., 2014; Vagg et al., 2016), sequential quadratic programming (SQP), genetic algorithms (GA) (Chen et al., 2014), the Pontryagin least guideline (PMP) (Xie et al., 2017). These rules decide the desired power split between the engine and the motor for a specific driving cycle. Learning – based EMS learn from the predefined information or utilise the past driving information for web based learning or application (Tian et al., 2018). Various simulation models have been proposed for HEV's based on the prerequisites of the

systems. Such as series HEVs, parallel HEV's and series parallel HEVs (Meradji et al., 2016).

In this research, the HEV model is developed using a series parallel drivetrain with reinforcement learning and fuzzy logic controllers for investigating the performance and energy optimisation of the HEVs.

The main contributions of this paper can be summarised as follows:

- This paper presents a novel deep reinforcement learning-based framework for energy management in a series parallel drivetrain-HEV model.
- A DRL based deep Q-learning algorithm is employed for achieving energy optimisation in the HEV
- A fuzzy based PI controller is designed for tuning the system parameters.
- The performance of the HEV model in terms of key equations, parameters, and assumptions.

The rest of the paper is structured as follows: Section 2 discusses the review of existing literary works related to energy management in electric vehicles. Section 3 provides a brief description of the proposed methodology for energy management which includes the design of HEV, control of series-parallel drivetrain and implementation of fuzzy logic controllers. Section 4 discusses the simulation results and Section 5 concludes the paper with prominent research observations and future scope.

2 Literature review

Tang et al. (2017) Proposes a novel approach of a simplified torsional vibration dynamic model for analysing the functionalities of the torsional vibration of a compound planetary hybrid propulsion model. The study evaluates the prominent characteristics such as frequency and vibration property. This model can be employed for determining the low-frequency vibrational attributes of the series parallel drivetrain. It also evaluates the controlling mechanism of the hybrid powertrain with respect to engine operation. Wang et al. (2015) analysed a four wheel driven series parallel drivetrain model for heavy duty applications. The model incorporates a rule-based EMS and the performance of the model was evaluated by comparing the model with a rear-wheel-driven hybrid powertrain and the operational parameters are optimised. The proposed model was integrated with a transit bus and the functionalities of the bus were evaluated. Unlike conventional coaxial power-split HEV's, the energy consumption was minimised using the series parallel drivetrain when evaluated for normal road conditions. SPHEV has great potential in minimising energy consumption. However, due to certain uncertainties such as multi power resources and varying driving constraints, it is challenging to develop an optimal EMS. Wang et al. (2018) proposed a novel particle swarm optimisation (PSO) based nonlinear model predictive control (NMPC) technique for EMS with an objective of achieving superior fuel economy. Initially, the framework of NMPC was developed and a transformed PSO was adopted for achieving desired optimisation. The approach uses a two-step optimisation process for achieving fast computation. The performance of the proposed approach was validated by performing simulation analysis based on the aggregated information collected from a driving cycle and a real bus. The efficacy of the

proposed framework was evaluated by determining the rate of fuel consumption by SPHEV. It was observed that the energy consumption was significantly minimised by more than 10%. Wu et al. (2019) proposed application of deep learning algorithms for strengthening the performance of the EMS in electric vehicles. The study adopted a deep reinforcement learning algorithm for a series-parallel electric bus for assigning an appropriate power split of the electric bus. The deep RL based EMS was trained using different samples of driving cycles and the performance of the proposed approach was validated by comparing it with conventional RL methods. From results, it was observed that the deep RL-EMS showed significant enhancement in achieving optimised energy consumption compared to classical RL algorithms. Also, the Deep RL-EMS achieved efficient EMS strategies and explored the adaption of real time traffic data within vehicular EMS through enhanced algorithms. Peng et al. (2017) proposed a rule-based EMS for enhancing the performance of the parallel drivetrain, which is calibrated using dynamic programming (DP). The proposed approach applied DP for locating the optimal extensions for the ICE in parallel HEVs. The study introduces a recalibration technique for strengthening HEVs and the efficacy of the rule-based EMS was validated by evaluating DP algorithm.

3 Research methodology

The preliminary objective of this research is to design and develop a hybrid electric vehicle model using reinforcement learning and fuzzy logic controllers for performance investigation and energy optimisation. The HEV model is developed using a series parallel drive train model which operates at near optimum efficiency to minimise the energy loss. The model is incorporated with the DRL algorithm for control and energy management of the HEV model. This study presents an enhanced EMS procedure based on deep reinforcement learning (DRL) algorithm. The DRL technique integrates Q learning and DRL algorithm to form an effective learning algorithm which can obtain action directly from the states, which is used to improve energy efficiency.

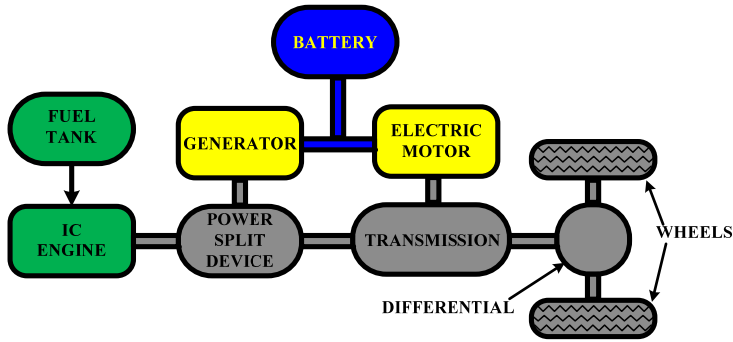
3.1 Design of hybrid electric vehicle model

A series parallel drivetrain based HEV is used for designing a HEV. The model employs a generator, an ICE), a device for storing the energy, coupling components for achieving mechanical coupling, a torque coupler and a traction motor. This model is flexible for operation and is feasible for optimising the torque-speed region. The series parallel drivetrain model is shown in Figure 1.

In the series parallel drive train model, the vehicle is driven by both ICE engine and motor. By combining the series and parallel designs, the engine can drive both the wheels directly (as in the parallel drivetrain), and can be disconnected effectively such that only one electrical device (either electric motor or ICE) is operated per cycle while the other is non-operative and continue to be in discharging state. The operating motor or ICE provides power (as in the series drivetrain) and the non-operative motor or ICE is responsible for charging the battery. However, there is a separate generator that charges the battery during regenerative braking. During braking, the motor behaves like a generator and the lost kinetic energy is restored in the battery. During driving, if the battery needs to be charged, ICE drives the generator to recharge the battery. When the

vehicle stops, the battery can be still charged by the ICE via the generator. ICE supplies the steady state power and the motor is designed to achieve the stability by providing required initial acceleration during low speed conditions. Mechanical coupling is incorporated with torque and speed coupling. In the drivetrain used in this research, an electric generator is connected to the sun gear and ICE is connected to the planet carrier for speed coupling, whereas, the ring gear is connected to the wheels with the help of a fixed gear for torque coupling. The wheels are also connected to a traction motor through fixed gear for establishing coupling between the traction motor and output torque of the ring gear (Borthakur and Subramanian, 2018).

Figure 1 Series parallel drive train model (see online version for colours)



The maximum power generated by the ICE for a constant speed of v_{\max} is presented as:

$$P_{eng(\max)} = \frac{1}{\eta_t} \left(Mgf_r \frac{1}{2} \rho C_d A v_{\max}^2 \right) v_{\max} \quad (1)$$

where $P_{eng(\max)}$ is the maximum energy generated by the ICE, η_t represents transmission efficiency, M states the vehicle mass, f_r defines the coefficient of rolling resistance, C_d states the drag coefficient, v_{\max} is the maximum voltage across ICE, ρ is air density whose value is 1.25 kg/m^3 , and A defines the frontal area. P_m is the power rating of the electric motor, which is given as:

$$P_m = \frac{\gamma M}{2t_a \eta_t} (v_f^2 + v_b^2) \quad (2)$$

Where v_f is defined as the rated speed of the vehicle (km/h) and v_b states the speed of the vehicle with respect to the speed of the motor base and γ is defined as the rotational inertia factor, M is the vehicle mass and t_a is the acceleration time (Nandakumar and Subramanian, 2015). The rotational speed of the ICE (carrier), generator (sun gear) and ring gear is given as:

$$\omega_r = \frac{(1+k)}{k} \omega_{eng} - \frac{\omega_{eng}}{k} \quad (3)$$

where ω_r , ω_{gen} , ω_{eng} are the rotational speeds of ring gear, generator, and engine respectively, k is defined as the planetary gear ratio, stated as the ratio of the radius of the ring, R_r , to the radius of the sun, R_s .

$$v = \omega_w r_e (1-s) = \frac{\omega_r r_e (1-s)}{i_g} \quad (4)$$

where ω_w is defined as the wheel rotational speed, v is defined as the longitudinal speed of the vehicle and s is defined as the slip ratio. The torques which are shifted from the engine (T_{eng}) to the ring gear (T_r) and to the generator (T_{gen}) are defined as shown in the below equations.

$$T_r = \frac{k}{k+1} T_{eng} \quad (5)$$

$$T_{gen} = \frac{1}{k+1} T_{eng} \quad (6)$$

The shaft of the engine and the ring gear are connected through a final reduction gear with a gear ratio, i_g . Now, the overall wheel drive torque is defined using equation (7)

$$T_{wheels} = \frac{1}{i_g \eta_t} (T_m + T_r) = \frac{1}{i_g \eta_t} \left(T_m + \frac{k}{k+1} T_{eng} \right) \quad (7)$$

The specification of the series parallel drivetrain are tabulated in Table 1.

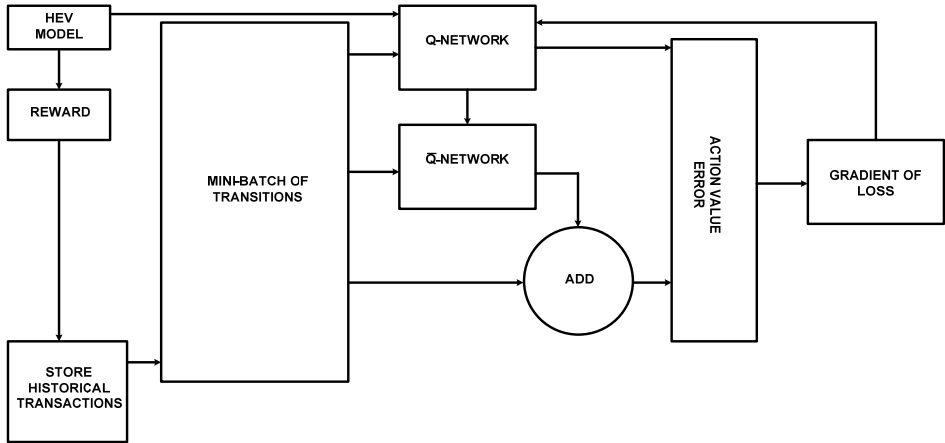
Table 1 Specifications of the series parallel drivetrain

Engine	Max.power (kW)	57
	Max.speed (rpm)	6000
Generator	Torque output (Nm)	80
	Max.speed (rpm)	8000
	Efficiency (%)	87
Traction motor	Torque output (Nm) at speed (rpm)	585 at 2500
	Max.power (kW)	123
	Max.speed (rpm)	12000
	Efficiency (%)	91
Batteries	Battery cells	120
	Initial capacity (Ah)	70
	Power (kW)	125
	Energy output (kWh)	88
Planetary gear ratio (k)		1.3
Final drive ratio		2.16

3.2 Control of series parallel drivetrain

There are different operation modes for controlling the operation of the drivetrain such as hybrid traction mode, regenerative braking etc. This study illustrates the application of a deep reinforcement learning algorithm for controlling the operation of the drivetrain and for effectively handling the EMSs. Figure 2 show the framework of DRL based EMS of an HEV.

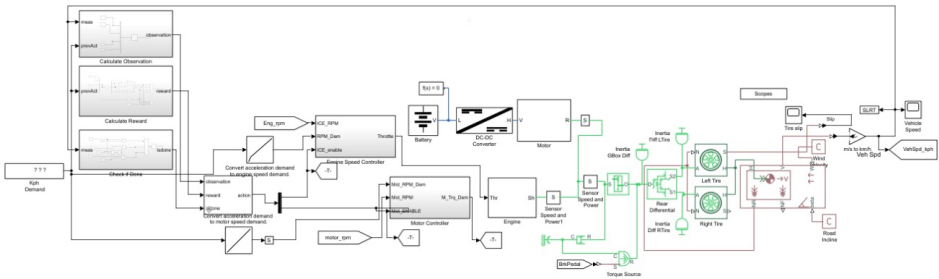
Figure 2 Framework of DRL based EMS of an HEV



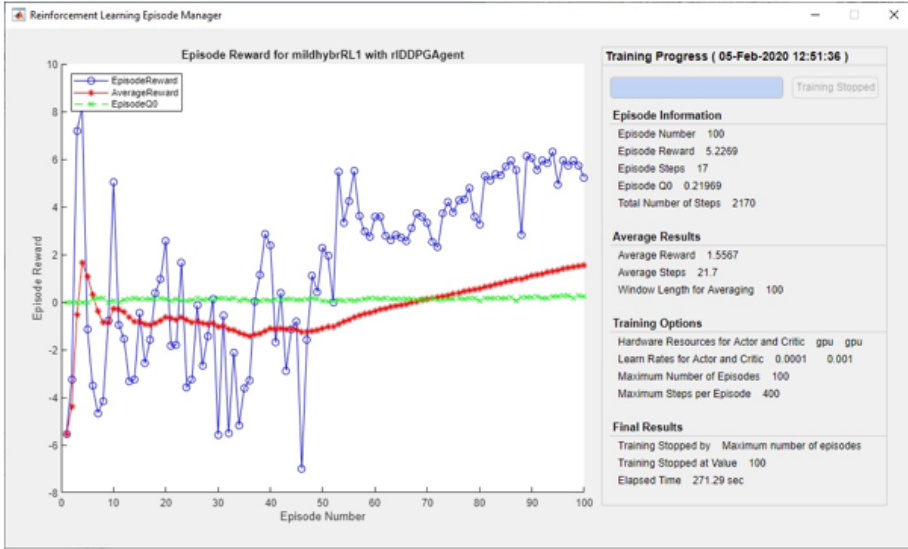
In this study, the DRL-based EMS is proficient with an appropriate arrangement of system components which are dependent on input data with no prediction or predefined rules. The proposed DRL method is integrated with Q learning and DRL to develop an effective learning algorithm for enhancing energy efficiency. Reinforcement learning is used for analysing the system parameters and for generating the enable signal for generator, motor and ICE engine. RL takes input such as SOC of battery, vehicle speed, reference speed and IC engine RPM. In a series parallel drivetrain, the electric motor supplies the power to the vehicle and during high load conditions, the IC engine stabilises the system by supplying motor power to the vehicle. During braking, the IC engine powers the generator and the enable signal from the RL is given as shown in Figure 3. The reinforcement learning manager is used to create and train agents. These agents are generated using neural networks and the system is controlled by Q Learning. The reward observations are analysed from the simulink model.

The simulink model of the HEV is controlled by DRL is presented in Figure 3.

Figure 3 Simulink model of HEV controlled by DRL (see online version for colours)



The reinforcement learning manager is given in Figure 4.

Figure 4 Reinforcement learning manager (see online version for colours)

The DRL-based EMS follows following steps:

- *System state*: The control mechanism of the vehicle is determined by its state. The required torque (T_{dem}) and the battery SOC are used for determining the state of the system which constitute a 2D state space i.e.,

$$s(t) = (T_{dem}(t), SOC(t))^T.$$
- *Control action*: The prominent issue in the HEV-EMS is deciding the required torque-split ratio between battery and ICE. In this study, the ICE's output torque is considered as the control action, defined as $A(t) = T_e(t)$; t is defined as the time step index.
- *Immediate reward*: This is significant to the DRL since it prominently affects the functionalities of the DRL algorithm. The system components of the DRL will try to maximise the reward by considering the optimal action of every step. Hence the immediate reward is constituted based on the optimisation goal. The prominent intent of the HEV-EMS is to enhance the energy efficiency by minimising the fuel consumption without affecting the vehicle stability and state of battery. Based on this objective, the reciprocated value of the power utilisation by ICE at every time step is considered as the immediate reward. Additionally, a penalty value is included for penalising the steps when the SOC crosses the defined threshold value. Immediate reward is determined using the below mentioned equations (Hu et al., 2018):

$$\begin{aligned}
r_{ss}^a &= \frac{1}{C_{ICE}} & C_{ICE} \neq 0 \cap 0.4 \leq SOC \leq 0.85 \\
&\frac{1}{C_{ICE} + C} & C_{ICE} \neq 0 \cap SOC < 0.4 \text{ or } SOC > 0.85 \\
&\frac{2}{Min_{C_{ICE}}} & C_{ICE} = 0 \cap 0.4 \leq SOC \\
&-\frac{1}{C} & C_{ICE} = 0 \cap SOC < 0.4
\end{aligned} \tag{8}$$

where the immediate award is defined by r_{ss}^a , given when the state of the vehicle shifts from s to s' by taking action a . C_{ICE} is defined as the instantaneous value of the fuel consumed by ICE and C is defined as the numerical penalty. $Min_{C_{ICE}}$ is defined as the minimum nonzero value of the fuel consumed by ICE.

- *DRL algorithm:* In this study, the DRL based EMS is defined in the algorithm given below. The two loops (outer loop and inner loop) control the EMS. The number of training states are controlled by the outer loop and the control of EMS within one training state is performed by the inner loop.

Algorithm 1 Deep Q-Learning with experience replay

Initialization:

Step 1: replay memory K to capacity L

Step 2: action value component Q with random weights θ

Step 3: target action value component Q with random weights $\theta^- = \theta$

for episode = 1, N **do**

Environment reset: $s_0 = (SOC_{Initial}, T_0)$

for $t=1, T$, **do**

Selecting a random action a_t for a probability of ϵ

else

Select $a_t = \max Q(s_t, a; \theta)$

Parameter functioning:

Selecting action a_t and observing the reward r_t

Set:

$s_{t+1} = (SOC_{t+1}, T_{t+1})$

storing (s_t, a_t, r_t, s_{t+1}) in memory K

Sample random smaller group of (s_t, a_t, r_t, s_{t+1}) from K

if:

terminal s_{j+1} : set $x_j = r_j$

else

set $x_j = r_j + \gamma \max Q(s_{j+1}, a_{j+1}; \theta^-)$

performing a gradient descent step on $(x_j - Q(s_j, a_j; \theta))^2$

every C steps reset $Q = Q$

end for

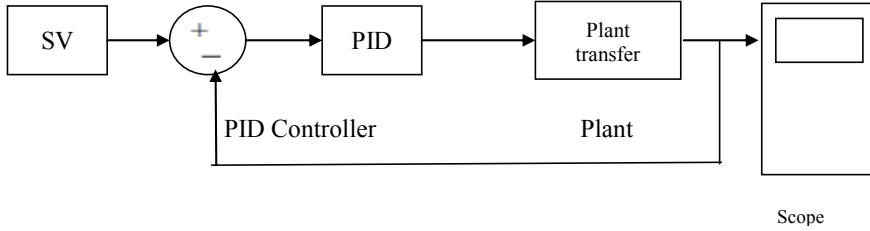
end for

3.3 Fuzzy based PID controller

Fuzzy logic controllers with a self-tuning PID controller are used for parameter tuning of the HEV. Fuzzy-based PID controllers increase stability and provide efficient speed control and smooth torque.

- *PID controller:* The simulink model of the vehicle with PID controller is shown in Figure 5.

Figure 5 Simulink model of the plant with PID controller



The transfer function of the PID controller is defined as:

$$C(s) = K_p + \frac{K_i}{s} + K_d s = K_p \left(1 + \frac{1}{T_i s} + T_d s \right) \quad (9)$$

where K_p , K_i and K_d are defined as the proportional, integral and derivative gain of the controller, and T_i and T_d are the integral time and derivative time respectively.

- *Fuzzy logic control*

FLC is applied for the series parallel drivetrain based HEV, for maintaining constant speed irrespective of uncertainties such as variation in wind resistance and vehicle acceleration. The block diagram of the HEV with FLC and the basic structure of FLC is shown in Figures 6 and 7 respectively.

Figure 6 Block diagram of the HEV with FLC

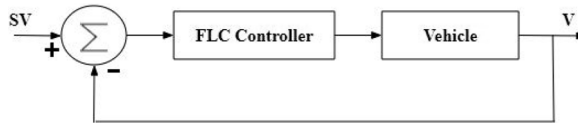
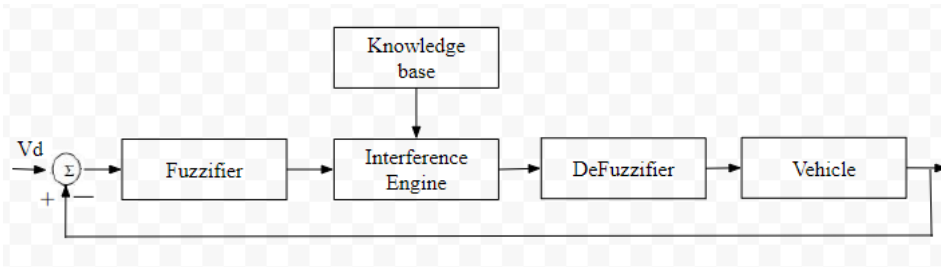


Figure 7 Basic structure of FLC



The design parameters of the fuzzy controller are selected based on the controller's input and output. Four main parameters such as base, inference engine, fuzzification and defuzzification are used for designing FLC.

The error (e) is selected as input to the FLC, given as (Yadav et al., 2011):

$$e(kT) = r - y \quad (10)$$

The change in error (ce) is given as:

$$ce(kT) = (e(kT) - e(kT - T)) / T \quad (11)$$

The output torque of ICE is considered as the output variable.

The basic fuzzy rules for FLC are tabulated in Table 2.

Table 2 Fuzzy rule base

ce	P	Z	N
P	PB	P	Z
Z	P	Z	N
N	Z	N	NB

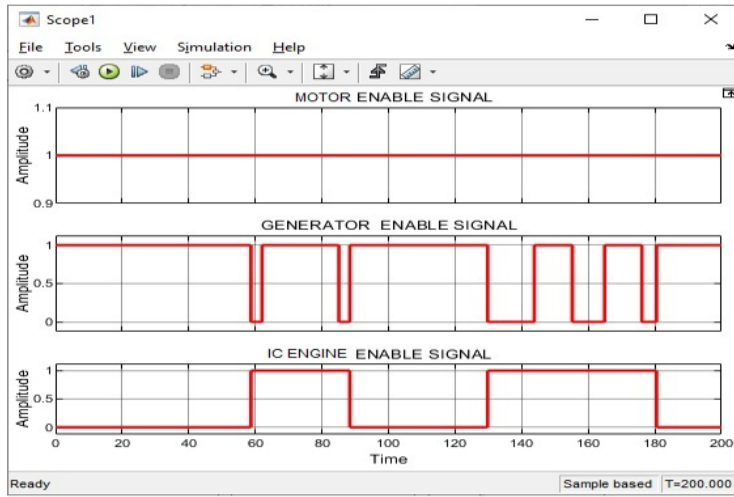
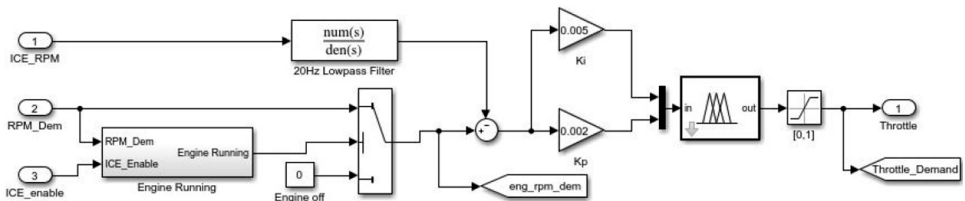
where Z represents 'zero', P represents 'positive' and PB represents 'positive big'. The error difference is the change of error between one instance to another. If the error is positive then the speed of the vehicle is lesser than the set value and the controller should slightly increase the acceleration for increasing the speed. If the present error and error change are positive, then the speed of the vehicle is too slow and it shifts to decelerating mode and in such cases, the controller should increase the acceleration to maintain desired speed. These are known as fuzzy rules. For controlling the ICE using FLC, the RPM of the engine is compared to the IC engine demand which is further compared with IC enable signal from DRL. This generates the IC engine torque demand. Similarly, for controlling the motor, the RPM of the motor is compared with the motor engine demand and it is compared with motor enable signal from DRL. This generates the motor torque demand. The Fuzzy tuned signals for ICE and motor are given in Figures 10 and 12 respectively.

4 Results and discussion

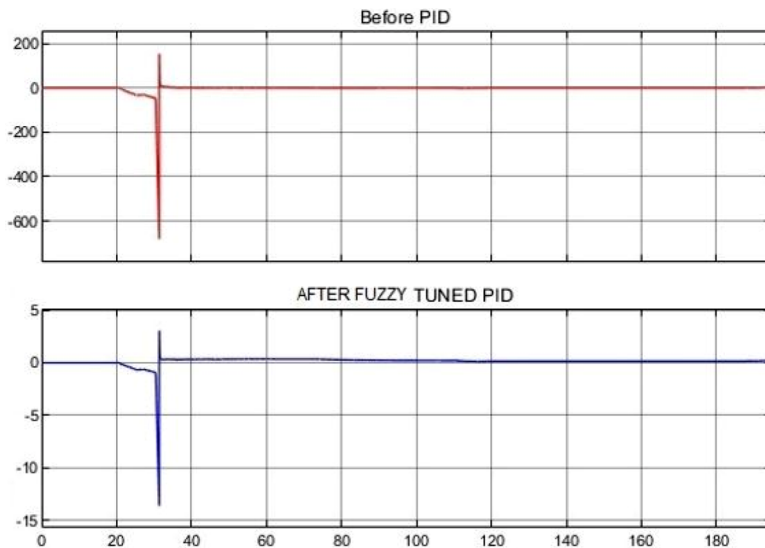
The fuzzy logic controller is used to tune the enable signal from the DRL. The fuzzy tuned signal is given in Figure 8.

The parameter tuning for both, engine and motor unit is performed using a fuzzy based PID controller. The simulink model of the fuzzy-based controller for controlling the speed of ICE and the fuzzy tuned signal for ICE is illustrated in Figures 9 and 10 respectively.

The simulation model of the engine control unit is shown in Figure 9.

Figure 8 Enable signal from DRL algorithm (see online version for colours)**Figure 9** Engine control unit

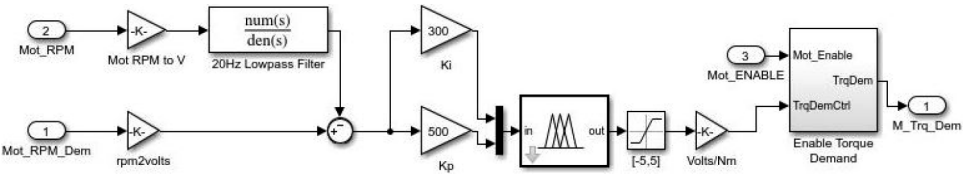
The fuzzy tuned signal generated from engine control unit is given in Figure 10.

Figure 10 Before and after signals of fuzzy based PID controller for engine (see online version for colours)

In practical conditions, real-time systems deviate from the reference path due to driving uncertainties. This unexpected deviation affects the output of the engine and in such cases, the controller must be able to sustain the disturbance created in the engine. As observed from Figure 10, the fuzzy logic PD overshoot occurs and settling time of both FLC tuned PID and before PID are nearly the same. This shows that the response of the system is unaffected due to disturbances.

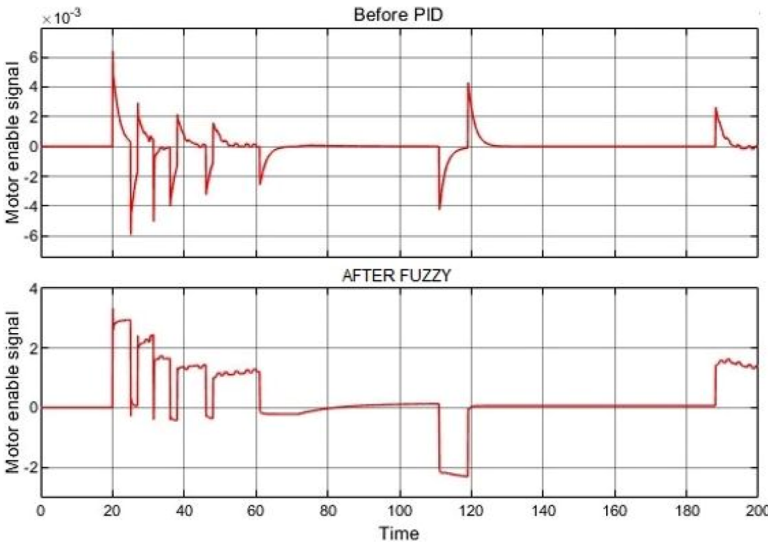
The simulink model of the fuzzy-based controller for controlling the speed of motor and the fuzzy tuned signal for motor is illustrated in Figures 11 and 12 respectively.

Figure 11 Motor control unit



The fuzzy tuned signal generated from engine control unit is given in Figure 12.

Figure 12 Before and after signals of fuzzy based PID controller for motor (see online version for colours)



The fuzzy tuned signal for generator is given in Figure 13.

Figures 12 and 13 show the response of the motor and generator respectively with and without FLC tuned signals. As observed from these figures, the response of the motor and generator improves with the tuning of the PID controller using FLC. The vehicle path is monitored and controlled by using Reinforcement learning methods. It is used for controlling the series parallel drivetrain and for minimising the energy consumption. The reference vehicle path and vehicle speed is shown in Figures 14 and 15 respectively.

Figure 13 Before and after signals of fuzzy based PID controller for generator (see online version for colours)

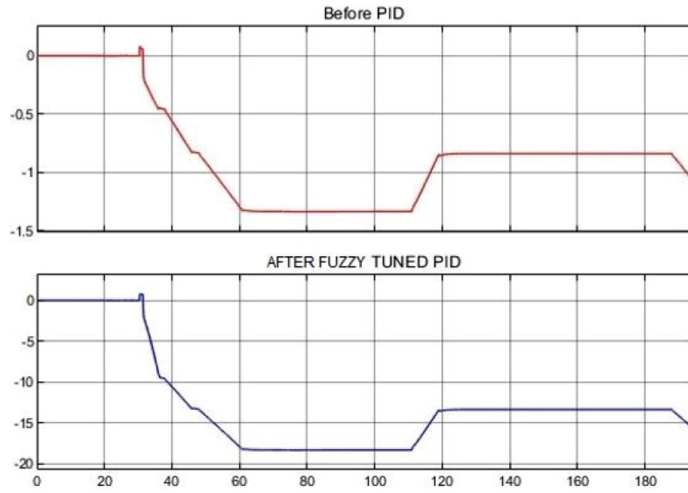


Figure 14 Reference vehicle path (see online version for colours)

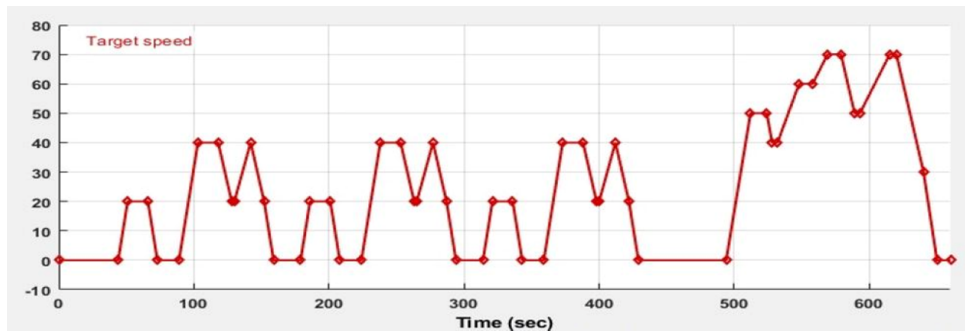
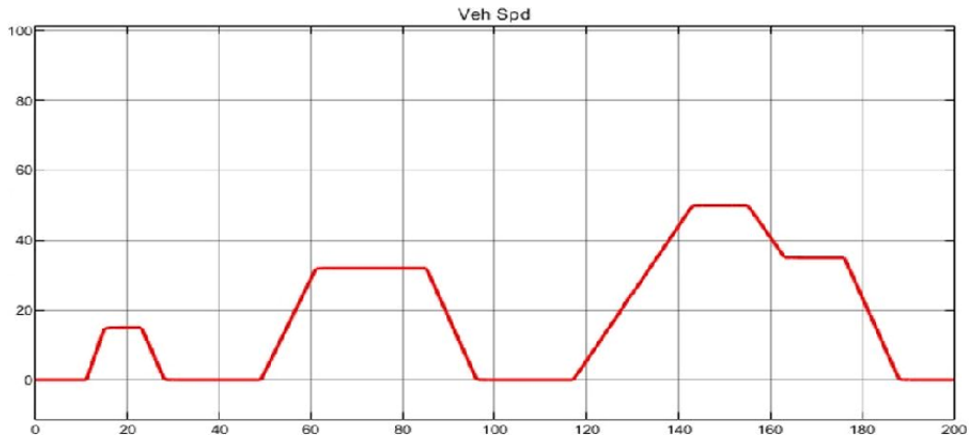


Figure 15 Vehicle speed (see online version for colours)



From the graph shown in Figures 14 and 15, it can be observed that the reinforcement learning method efficiently controls the speed of series parallel drivetrain and reduces the energy consumption of the drivetrain. The fuel economy for the HEV is shown in Figure 16.

Figure 16 Fuel economy

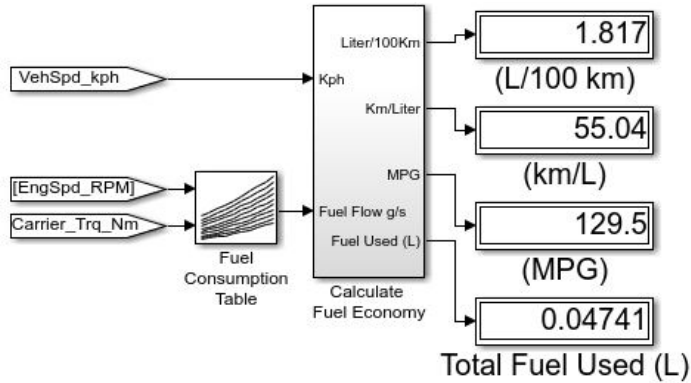


Figure 16 presents the fuel economy of the DRL based HEV model, the total fuel used was 0.04741 (L) for an average of 1.817 l per 100 km with a mileage of 55.04 km/L.

5 Conclusion

The preliminary objective of the research is to investigate the performance of an EMS in HEVs. Considering the influence of EMS in determining vehicle efficiency, an enhanced vehicular transition strategy based on a deep reinforcement learning-based framework was developed and applied for a series parallel drivetrain-HEV model. A DRL based deep Q-learning algorithm was developed for achieving energy optimisation in the HEV whose parameters were fine-tuned using a fuzzy based PID controller. The performance of the HEV model was validated from the simulation results and the prominent observations are as follows:

- The series parallel drivetrain offers the flexibility of selecting the mode of operation for the vehicle i.e., the vehicle can operate either with motor or ICE at once and the energy of the motor or ICE (which is shut down) will be used for charging the batteries. This significantly enhances the energy efficiency in HEVs.
- The vehicle path is monitored and controlled by the DRL algorithm, which effectively controls the series parallel drivetrain and minimises the energy consumption.
- Fuzzy based PID controls provide effective speed control for both motor and engine by fine tuning the motor and engine parameters.

From the simulation results, the effectiveness of the speed control mechanism can be observed. Following the vehicular reference path, the speed consistency was not much deferred as observed from Figure 15.

References

- Ansarey, M., Panahi, M.S., Ziarati, H. and Mahjoob, M. (2014) 'Optimal energy management in a dual-storage fuel-cell hybrid vehicle using multi-dimensional dynamic programming', *Journal of Power Sources*, Vol. 250, pp.359–371.
- Borthakur, S. and Subramanian, S.C. (2018) 'Optimized design and analysis of a series-parallel hybrid electric vehicle powertrain for a heavy duty truck', *IFAC-PapersOnLine*, Vol. 51, No. 1, pp.184–189.
- Chen, Z., Mi, C.C., Xiong, R., Xu, J. and You, C. (2014) 'Energy management of a power-split plug-in hybrid electric vehicle based on genetic algorithm and quadratic programming', *Journal of Power Sources*, Vol. 248, pp.416–426.
- Hu, Y., Li, W., Xu, K., Zahid, T., Qin, F. and Li, C. (2018) 'Energy management strategy for a hybrid electric vehicle based on deep reinforcement learning', *Applied Sciences*, Vol. 8, No. 2, p.187.
- Meradji, M., Cecati, C., Wang, G. and Xu, D. (2016) 'Dynamic modeling and optimal control for hybrid electric vehicle drivetrain', *2016 IEEE International Conference on Industrial Technology (ICIT)*, March, IEEE, Taipei, Taiwan, pp.1424–1429.
- Nandakumar, C.S. and Subramanian, S.C. (2015) 'Design and analysis of a parallel hybrid electric vehicle for Indian conditions', *IEEE International on Transportation Electrification Conference (ITEC)*, Chennai, India, pp.1–12.
- Onori, S., Serrao, L. and Rizzoni, G. (2016) *Hybrid Electric Vehicles: Energy Management Strategies* London: Springer, pp.25–28.
- Panday, A. and Bansal, H.O. (2015) 'Hybrid electric vehicle performance analysis under various temperature conditions', *Energy Procedia*, Vol. 75, pp.1962–1967.
- Panday, A., Bansal, H.O. and Srinivasan, P. (2016) 'Thermoelectric modeling and online SOC estimation of Li-ion battery for plug-in hybrid electric vehicles', *Modelling and Simulation in Engineering*, Rajasthan, India, Vol. 2016, pp.1–12.
- Peng, J., He, H. and Xiong, R. (2017) 'Rule based energy management strategy for a series-parallel plug-in hybrid electric bus optimized by dynamic programming', *Applied Energy*, Vol. 185, pp.1633–1643.
- Sulaiman, N., Hannan, M.A., Mohamed, A., Ker, P.J., Majlan, E.H. and Daud, W.W. (2018) 'Optimization of energy management system for fuel-cell hybrid electric vehicles: issues and recommendations', *Applied Energy*, Vol. 228, pp.2061–2079.
- Sun, C., He, H. and Sun, F. (2015) 'The role of velocity forecasting in adaptive-eCMS for hybrid electric vehicles', *Energy Procedia*, Vol. 75, pp.1907–1912.
- Tang, X., Yang, W., Hu, X. and Zhang, D. (2017) 'A novel simplified model for torsional vibration analysis of a series-parallel hybrid electric vehicle', *Mechanical Systems and Signal Processing*, Vol. 85, pp.329–338.
- Tian, H., Li, S.E., Wang, X., Huang, Y. and Tian, G. (2018) 'Data-driven hierarchical control for online energy management of plug-in hybrid electric city bus', *Energy*, Vol. 142, pp.55–67.
- Vagg, C., Akehurst, S., Brace, C.J. and Ash, L. (2016) 'Stochastic dynamic programming in the real-world control of hybrid electric vehicles', *IEEE Transactions on Control Systems Technology*, Vol. 24, No. 3, pp.853–866.
- Wang, E., Guo, D. and Yang, F. (2015) 'System design and energetic characterization of a four-wheel-driven series-parallel hybrid electric powertrain for heavy-duty applications', *Energy Conversion and Management*, Vol. 106, pp.1264–1275.
- Wang, Y., Wang, X., Sun, Y. and You, S. (2018) 'Model predictive control strategy for energy optimization of series-parallel hybrid electric vehicle', *Journal of Cleaner Production*, Vol. 199, pp.348–358.
- Wu, Y., Tan, H., Peng, J., Zhang, H. and He, H. (2019) 'Deep reinforcement learning of energy management with continuous control strategy and traffic information for a series-parallel plug-in hybrid electric bus', *Applied Energy*, Vol. 247, pp.454–466.

- Xie, S., Li, H., Xin, Z., Liu, T. and Wei, L. (2017) ‘A Pontryagin minimum principle-based adaptive equivalent consumption minimum strategy for a plug-in hybrid electric bus on a fixed route’, *Energies*, Vol. 10, No. 9, p.1379.
- Yadav, A.K., Gaur, P., Jha, S.K., Gupta, J.R.P. and Mittal, A.P. (2011) ‘Optimal speed control of hybrid electric vehicles’, *Journal of Power Electronics*, Vol. 11, No. 4, pp.393–400.
- Zhou, Y., Ravey, A. and Péra, M.C. (2019) ‘A survey on driving prediction techniques for predictive energy management of plug-in hybrid electric vehicles’, *Journal of Power Sources*, Vol. 412, pp.480–495.

Hamiltonian Soft Graphs

Rajesh K. Thumbakara ^a, Jinta Jose ^b and Bobin George ^c

^a Department of Mathematics,
Mar Athanasius College(Autonomous) Kothamangalam,
Kothamangalam 686666 India
rthumbakara@macollege.in

^bDepartment of Science and Humanities,
Viswajyothi College of Engineering and Technology Vazhakulam,
Vazhakulam 686670 India
jinta@vjcet.org

^cDepartment of Mathematics,
Pavanatma College Murickassery,
Murickassery 685601 India
bobingeorge@pavanatmacollege.org

Abstract

In 1999, D. Molodtsov initiated the novel concept of soft set theory. This is an approach for modeling vagueness and uncertainty. It is a classification of elements of the universe with respect to some given set of parameters. The concept of soft graph introduced by Rajesh K. Thumbakara and Bobin George is used to provide a parameterized point of view for graphs. Theory of soft graphs is a fast developing area in graph theory due to its capability to deal with the parameterization tool. In this paper, we introduce the concepts of Hamiltonian soft graph and closure of a soft graph. Also we investigate some properties of them.

Subject Classification:[2020] 05C99.

Keywords: Soft Graph; Soft Hamiltonian Part; Soft Hamiltonian Graph.

1 Introduction

In Mathematics, graph theory is the study of graphs which are mathematical structures used to model pairwise relations between objects. Graphs are one of the principal objects of study in Discrete Mathematics. The basic idea of graphs were first introduced in the 18th century by the Swiss mathematician Leonhard Euler. His work on the famous “Konigsberg bridge problem” is commonly quoted as origin of graph theory. The idea of soft sets was first given by D. Molodtsov [3] in 1999. This is a new mathematical tool to deal with the uncertainties. Many practical problem can be solved easily with the help of soft set theory rather than some well-known theories viz. fuzzy set theory, probability theory etc. since these theories have certain limitations. The problem with the fuzzy set is that it lacks parameterization tools. Many authors like P.K. Maji, A.R. Roy and R. Biswas [4], [5] have further studied the theory of soft sets and used the theory to solve some decision making problems. In 2014, Rajesh K. Thumbakara and Bobin George [6] introduced the concept of soft graph to provide a parameterized point of view for graphs. They also introduced the concepts of soft subgraph, soft tree etc. and some soft graph operations. In 2015, Muhammad Akram and Saira Nawas [7] modified the definition of soft graph. They [8] also defined certain types of soft graphs and also explained the concepts of soft bridge, soft cut vertex, soft cycle etc. J.D. Thenge, B.S. Reddy and R.S. Jain [9] contributed more to connected soft graph. Also they [10] studied about the radius, diameter and center of a soft graph and introduced the concept of degree in soft graph. In 2019, N. Sarala and K. Manju [11] introduced the concept of soft bi-partite graph

and studied some properties. In 2020, J.D. Thenge, B.S. Reddy and R.S. Jain [12] discussed the concepts of adjacency matrix and incidence matrix of a soft graph. Domination over soft graphs is introduced by S. Venkatraman and R. Helen [13]. In this paper we introduce the concepts of Hamiltonian soft graph and closure of a soft graph. Also we investigate some properties of them.

2 Preliminaries

2.1 Graphs

For basic concepts of graph theory we refer [1] and [2]. A graph G consists of two finite sets: V , the vertex set of G which is a nonempty set and E , the edge set which is possibly empty. G can be represented by (V, E) or $(V(G), E(G))$. The degree of a vertex v denoted by $d(v)$ is the number of edges of G incident with v . Let H be a graph with vertex set $V(H)$ and edge set $E(H)$ and G be a graph with vertex set $V(G)$ and edge set $E(G)$. Then we say that H is a subgraph of G if $V(H) \subseteq V(G)$ and $E(H) \subseteq E(G)$. A walk in a graph G is a finite sequence $W = v_0 e_1 v_1 e_2 v_2 \dots v_{k-1} e_k v_k$ whose terms are alternately vertices and edges such that for $1 \leq i \leq k$, the edge e_i has ends v_{i-1} and v_i . We say this walk as a $v_0 - v_k$ walk. Here v_0 is called origin of the walk and v_k is called the terminus of the walk. A $u - v$ walk is called closed or open depending on whether $u = v$ or $u \neq v$. Trivial walk is one containing no edges. The number of edges in the walk is called the length of the walk. If the edges in the walk are distinct then the walk is called a trail. A non-trivial closed trail in a graph G is called a cycle if its origin and internal vertices are distinct. If the vertices of the walk are distinct then that walk W is called a path. A vertex u is said to be connected to a vertex v in a graph G if there is a path in G from u to v . A graph is said to be connected if every two of its vertices are connected. If $C(u)$ denote the set of all vertices in G that are connected to u then the subgraph of G induced by $C(u)$ is called the connected component containing u , or simply the component containing u . A Hamiltonian path in a graph G is a path which contains every vertex of G . A Hamiltonian cycle in a graph G is a cycle which contains every vertex of G . A graph is called Hamiltonian if it has a Hamiltonian cycle.

2.2 Soft Set

In 1999 D. Molodtsov [3] initiated the concept of soft sets. Let U be an initial universe set and let E be a set of parameters. A pair (F, E) is called a Soft Set (over U) if and only F is a mapping of E into the set of all subsets of the set U . That is, $F : E \rightarrow P(U)$.

2.3 Soft Graph

Rajesh K. Thumbakara and Bobin George [6] introduced the concept of soft graph as follows. Let $G = (V, E)$ be a simple graph and A be any nonempty set. Let R be an arbitrary relation between elements of A and elements of V . That is $R \subseteq A \times V$. A mapping $F : A \rightarrow P(V)$ can be defined as $F(x) = \{y \in V : xRy\}$. The pair (F, A) is a soft set over V . Then (F, A) is said to be a Soft Graph of G if the subgraph induced by $F(x)$ in G is a connected subgraph of G for all $x \in A$. Muhammad Akram and Saira Nawas [7] modified the definition of soft graph as follows. Let $G^* = (V, E)$ be a simple graph and A be any nonempty set. Let R be an arbitrary relation between elements of A and elements of V . That is $R \subseteq A \times V$. A mapping $F : A \rightarrow P(V)$ can be defined as $F(x) = \{y \in V : xRy\}$. Also define a mapping $K : A \rightarrow P(E)$ by $K(x) = \{uv \in E : \{u, v\} \subseteq F(x)\}$. The pair (F, A) is a soft set over V and the pair (K, A) is a soft set over E . Then the 4 -tuple $G = (G^*, F, K, A)$ is called a Soft Graph if it satisfies the following conditions:

1. $G^* = (V, E)$ is a simple graph,
2. A is a nonempty set of parameters,
3. (F, A) is a soft set over V ,
4. (K, A) is a soft set over E ,
5. $(F(a), K(a))$ is a subgraph of G^* for all $a \in A$.

If we represent $(F(x), K(x))$ by $H(x)$ then soft graph G is also given by $\{H(x) : x \in A\}$.

3 Hamiltonian Soft Graphs

Definition 3.1. Let $G^* = (V, E)$ be a graph and $G = (G^*, F, K, A)$ be a soft graph of G^* which is also represented by $\{H(x) : x \in A\}$. Then $H(x)$ corresponding to a parameter x in A is called a part of the soft graph G .

Definition 3.2. Let $G = (G^*, F, K, A)$ be a soft graph and v be any vertex of the part $H(x)$ of G for some $x \in A$. Then part degree of the vertex v in $H(x)$ denoted by $d(v)[H(x)]$ is the degree of the vertex v in that part $H(x)$.

Definition 3.3. Let $G = (G^*, F, K, A)$ be a soft graph of G^* represented by $\{H(x) : x \in A\}$. Then any part $H(x)$ of G is called Hamiltonian if there exists a Hamiltonian cycle in that part $H(x)$ of G . That is, $H(x)$ contains a cycle that contains every vertex of $H(x)$.

Definition 3.4. A soft graph $G = (G^*, F, K, A)$ of a graph G^* is called Hamiltonian if all parts $H(x)$ of G are Hamiltonian.

Consider a graph $G^* = (V, E)$ as shown in the following figure 1. Let $A = \{c, m\} \subseteq V$ be a

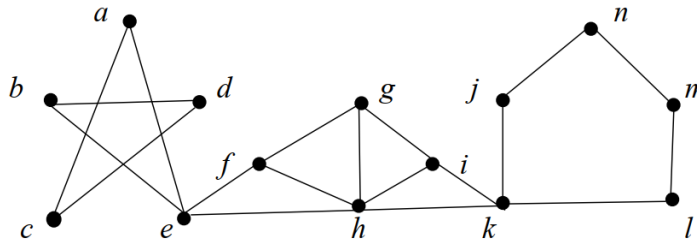


Fig. 1: Graph $G^* = (V, E)$

parameter set and (F, A) be a soft set over V with its approximate function $F : A \rightarrow P(V)$ defined by $F(x) = \{y \in V | xRy \Leftrightarrow d(x, y) \leq 2\}$ for all $x \in A$.

That is, $F(c) = \{a, b, c, d, e\}$ and $F(m) = \{j, k, l, m, n\}$.

Let (K, A) be a soft set over E with its approximate function $K : A \rightarrow P(E)$ defined by $K(x) = \{uv \in E | [u, v] \subseteq F(x)\}$ for all $x \in A$. That is, $K(c) = \{ac, ae, bd, be, cd\}$ and $K(m) = \{mn, nj, jk, kl, ml\}$. Thus $H(c) = (F(c), K(c))$ and $H(m) = (F(m), K(m))$ are subgraphs of G^* as shown in figure 2. Hence $G = \{H(c), H(m)\}$ is a soft graph of G^* . Here G has 2 parts $H(c)$ and

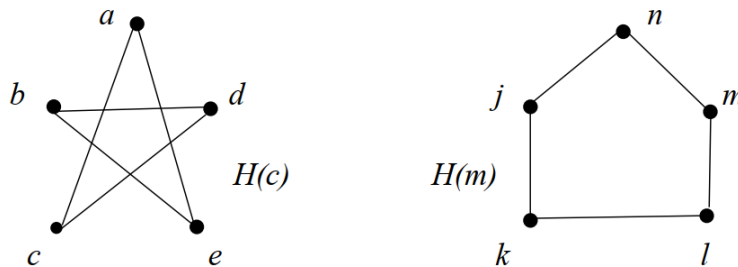


Fig. 2: Soft Graph $G = \{H(c), H(m)\}$

$H(m)$. In $H(c)$, $C_1 = aebdca$ is a Hamiltonian cycle and so $H(c)$ is a Hamiltonian part. Also in $H(m)$, $C_2 = nmlkjn$ is a Hamiltonian cycle and so $H(m)$ is a Hamiltonian part. That is, both the parts of G are Hamiltonian and hence G is a Hamiltonian soft graph.

Consider a graph $G^* = (V, E)$ as shown in the following figure 3. Let $A = \{b, g\} \subseteq V$ be a

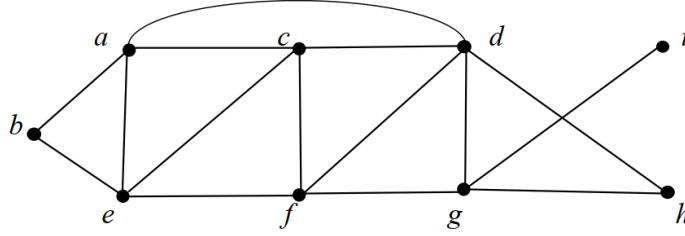


Fig. 3: Graph $G^* = (V, E)$

parameter set and (F, A) be a soft set with its approximate function $F : A \rightarrow P(V)$ defined by $F(x) = \{y \in V | xRy \Leftrightarrow d(x, y) \leq 1\}$ for all $x \in A$.

That is, $F(b) = \{a, b, e\}$ and $F(g) = \{d, f, g, h, i\}$.

Let (K, A) be a soft set over E with its approximate function $K : A \rightarrow P(E)$ defined by $K(x) = \{uv \in E | \{u, v\} \subseteq F(x)\}$ for all $x \in A$.

That is, $K(b) = \{ab, be, ae\}$ and $K(g) = \{df, dg, dh, fg, gh, gi\}$. Thus $H(b) = (F(b), K(b))$ and $H(g) = (F(g), K(g))$ are subgraphs of G^* as shown in figure 4.

Hence $G = \{H(b), H(g)\}$ is a soft graph of G^* . Here G has 2 parts $H(b)$ and $H(g)$. In $H(b)$,

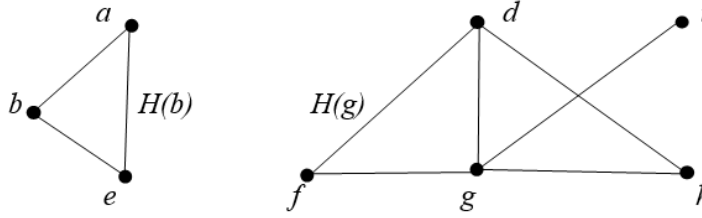


Fig. 4: Soft Graph $G = \{H(b), H(g)\}$

$C_1 = abea$ is a Hamiltonian cycle and so $H(b)$ is a Hamiltonian part. In $H(g)$, there is no Hamiltonian cycle and so $H(g)$ is not a Hamiltonian part. That is, both the parts of G are not Hamiltonian and hence G is not a Hamiltonian soft graph.

Definition 3.5. Let $G = (G^*, F, K, A)$ be a soft graph of G^* represented by $\{H(x) : x \in A\}$. Then a part $H(x)$ of G is called a maximal non-Hamiltonian part if it is not Hamiltonian but the addition of any edge connecting any two non-adjacent vertices in that part $H(x)$ results a Hamiltonian part.

Theorem 3.1. Let $G^* = (V, E)$ be a graph and $G = (G^*, F, K, A)$ be a soft graph of G^* which is also represented by $\{H(x) : x \in A\}$. If $|F(x)| \geq 3$ and $d(v)[H(x)] \geq |F(x)|/2, \forall v \in F(x)$ and $\forall x \in A$ then G is a Hamiltonian soft graph where $|F(x)|$ denotes the number of vertices in the part $H(x)$ of G .

Proof. We assume that the result is false. That is, at least one part $H(x) = (F(x), K(x))$ of the soft graph G is not a Hamiltonian part even if $|F(x)| \geq 3$ and $d(v)[H(x)] \geq |F(x)|/2, \forall v \in F(x)$. Add edges to this part connecting non-adjacent vertices of $H(x)$ until we get a maximal non-Hamiltonian part $J(x)$ having the same vertex set $F(x)$ as in $H(x)$. Here $J(x)$ has $|F(x)|$ vertices and $d(v)[J(x)] \geq |F(x)|/2, \forall v \in F(x)$. We use this maximal non-Hamiltonian part $J(x)$ to prove the result by obtaining a contradiction. $J(x)$ cannot be complete since it is not Hamiltonian. So there

exist two non-adjacent vertices u and v in $J(x)$. Then $J(x) + uv$ will be Hamiltonian since $J(x)$ is maximal non-Hamiltonian. Hence there exist a Hamiltonian cycle C containing the edge uv and every vertex v of $J(x)$. So in $J(x)$ there is a Hamiltonian path $P = v_1 v_2 \cdots v_n$ where $n = |F(x)|$, $v_1 = u$ and $v_n = v$ which is obtained by removing the edge uv from C . If v_1 and v_i are adjacent in $J(x)$, $2 \leq i \leq n$, then v_{i-1} and v_n are not adjacent in $J(x)$. Otherwise $v_1 v_i v_{i+1} \cdots v_n v_{i-1} v_{i-2} \cdots v_1$ is a Hamiltonian cycle in $J(x)$ which is not possible. Hence corresponding to each vertex of $\{v_2, v_3 \cdots v_n\}$ which is adjacent to $v_1 = u$ there corresponds precisely one vertex of $\{v_1, v_2 \cdots v_{n-1}\}$ which is not adjacent to $v_n = v$. Thus $d(u)[J(x)] \leq (|F(x)| - 1) - d(v)[J(x)]$, so that $d(u)[J(x)] + d(v)[J(x)] \leq (|F(x)| - 1)$ which is a contradiction since $d(v)[J(x)] \geq |F(x)|/2, \forall v \in F(x)$. We get this contradiction due to our wrong assumption that the result is false. \square

Theorem 3.2. Let $G = (G^*, F, K, A)$ be a soft graph of G^* represented by $\{H(x) : x \in A\}$. Let u and v be any two non-adjacent vertices of a part $H(x)$ of G for some $x \in A$ satisfying the condition $d(u)[H(x)] + d(v)[H(x)] \geq |F(x)|$, where $|F(x)|$ denotes the number of vertices in the part $H(x)$ of G . Also let $H(x) + uv$ denote the graph obtained from the part $H(x)$ by joining u and v by an edge uv . Then $H(x)$ is Hamiltonian if and only if $H(x) + uv$ is Hamiltonian.

Proof. Assume that $H(x)$ is a Hamiltonian part. Then $H(x) + uv$ must be Hamiltonian since $H(x) + uv$ is a supergraph of $H(x)$.

Conversely assume that $H(x) + uv$ is Hamiltonian. Then if $H(x)$ is not a Hamiltonian, as in the proof of theorem 3.1 we get the inequality $d(u)[H(x)] + d(v)[H(x)] \leq (|F(x)| - 1)$. But it is given that $d(u)[H(x)] + d(v)[H(x)] \geq |F(x)|$. Hence $H(x)$ is Hamiltonian. \square

4 Closure of a Soft Graph

Definition 4.1. Let $G = (G^*, F, K, A)$ be a soft graph of G^* represented by $\{H(x) : x \in A\}$. Let u_1 and v_1 be any two non-adjacent vertices of a part $H(x)$ of G for some $x \in A$ satisfying the condition $d(u_1)[H(x)] + d(v_1)[H(x)] \geq |F(x)|$, where $|F(x)|$ denotes the number of vertices in the part $H(x)$ of G . Then join u_1 and v_1 by an edge to form the supergraph $H_1(x)$. Then if there are two non-adjacent vertices u_2 and v_2 (if any) satisfying the condition $d(u_2)[H_1(x)] + d(v_2)[H_1(x)] \geq |F(x)|$, join u_2 and v_2 by an edge to form the supergraph $H_2(x)$. Continue this procedure until no such pair remains. The final supergraph thus obtained is called part closure and is denoted by $c[H(x)]$.

Definition 4.2. Let $G = (G^*, F, K, A)$ be a soft graph of G^* represented by $\{H(x) : x \in A\}$. Then closure of the soft graph G denoted by $c(G)$ is given by $\{c[H(x)] : x \in A\}$ where $c[H(x)]$ denotes the part closure of $H(x)$.

Consider a graph $G^* = (V, E)$ as shown in the following figure 5. Let $A = \{f, m\} \subseteq V$ be a

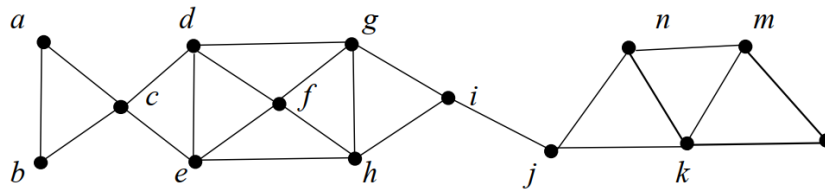


Fig. 5: Graph $G^* = (V, E)$

parameter set and (F, A) be a soft set over V with its approximate function $F : A \rightarrow P(V)$ defined by $F(x) = \{y \in V | xRy \Leftrightarrow d(x, y) \leq 2\}$ for all $x \in A$.

That is, $F(f) = \{c, d, e, f, g, h, i\}$ and $F(m) = \{n, m, j, k, l\}$.

Let (K, A) be a soft set over E with its approximate function $K : A \rightarrow P(E)$ defined by $K(x) = \{uv \in E | \{u, v\} \subseteq F(x)\}$ for all $x \in A$.

That is, $K(f) = \{cd, ce, de, dg, gh, eh, df, gf, ef, hf, gi, hi\}$ and $K(m) = \{mn, nk, nj, kl, jk, lm, km\}$. Thus $H(f) = (F(f), K(f))$ and $H(m) = (F(m), K(m))$ are subgraphs of G^* as shown in figure 6. Hence $G = \{H(f), H(m)\}$ is a soft graph of G^* . Then the closure $c(G) = \{c[H(f)], c[H(m)]\}$

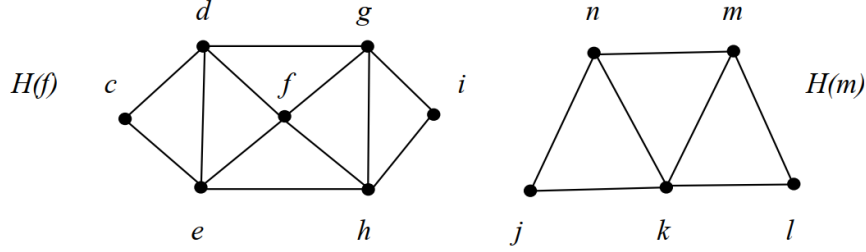


Fig. 6: Soft Graph $G = \{H(f), H(m)\}$

is give in figure 7 below.

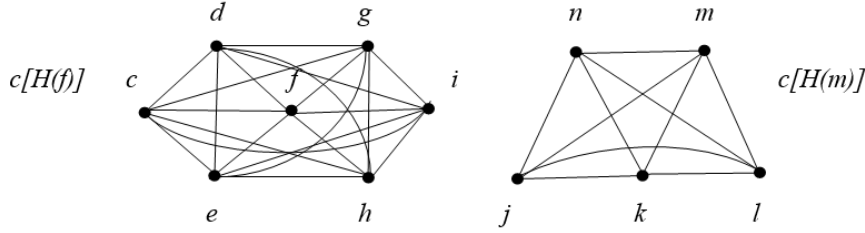


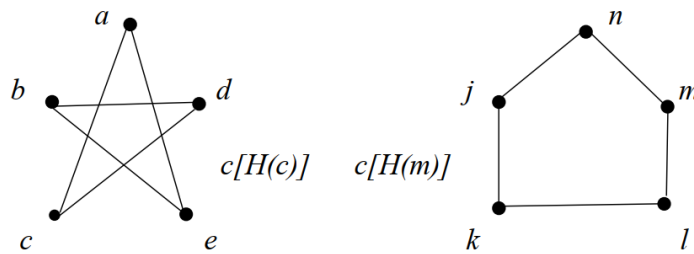
Fig. 7: $c(G) = \{c[H(f)], c[H(m)]\}$

Consider the Soft Graph $G = \{H(c), H(m)\}$ given in figure 2. Its closure $c(G) = \{c[H(c)], c[H(m)]\}$ is given in figure 8 below. This is also an example for a soft graph G having the property $c(G) = G$.

Theorem 4.1. Let $G = (G^*, F, K, A)$ be a soft graph of G^* represented by $\{H(x) : x \in A\}$. Then G is a Hamiltonian soft graph if and only if all of its part closures are Hamiltonian.

Proof. Assume that $G = \{H(x) : x \in A\}$ is a Hamiltonian soft graph. Then $H(x)$ will be a Hamiltonian part, $\forall x \in A$. So the part closure $c[H(x)]$ will be Hamiltonian $\forall x \in A$ since $c[H(x)]$ is a supergraph of $H(x)$.

Conversely suppose that all part closures $c[H(x)]$ of G are Hamiltonian. Consider a part closure $c[H(x)]$ for some $x \in A$. Let $H(x), H_1(x), H_2(x) \cdots H_m(x) = c[H(x)]$ be the sequence of graphs obtained by performing the closure operation on the part $H(x)$. Since the part closure $c[H(x)] = H_m(x)$ is obtained from $H_{m-1}(x)$ by setting $H_m(x) = H_{m-1}(x) + uv$, where u and v are two non-adjacent vertices of $H_{m-1}(x)$ satisfying the condition $d(u)[H_{m-1}(x)] + d(v)[H_{m-1}(x)] \geq |F(x)|$, $H_{m-1}(x)$ is Hamiltonian by theorem 3.2. Similarly $H_{m-2}(x)$, so $H_{m-3}(x) \cdots$ so $H_1(x)$ and so $H(x)$ must be Hamiltonian. Since we selected the part $H(x)$ arbitrarily, we can say that all parts of G are Hamiltonian part. Hence G is a Hamiltonian soft graph. \square

Fig. 8: $c(G) = \{c[H(c)], c[H(m)]\}$

5 Conclusion

Theory of soft graphs is a fast developing research area in graph theory due to its capability to deal with the parameterization tool. Soft graph was introduced by applying the concept of soft set in graph. By means of parameterization, soft graph produces a series of descriptions of a complicated relation described using a graph. In this paper, we introduced Hamiltonian soft graphs and closure of a soft graph and established some important properties of them.

References

- [1] J. Clark, D. A Holton, *A first look at graph theory*, Allied Publishers Ltd., 1995.
- [2] G. Chartrand, L. Lesniak, P. Zhang, *Graphs & Digraphs*, CRC Press, 2016.
- [3] D. Molodtsov, *Soft Set Theory-First Results*, Computers & Mathematics with Applications, 37(1999) 19- 31.
- [4] P.K. Maji, A.R. Roy, R. Biswas, *Fuzzy Soft Sets*, The Journal of Fuzzy Math,9(2001),589-602.
- [5] P.K. Maji, A.R. Roy, R. Biswas, *An Application of Soft Sets in a Decision Making Problem*, Computers and Mathematics with Application, 44 (2002), 1077-1083.
- [6] R. K. Thumbakara, B. George, *Soft Graphs*, Gen. Math. Notes, Vol. 21, No. 2(2014),75-86 .
- [7] M. Akram, S. Nawaz, *Operations on Soft Graphs*, Fuzzy Inf. Eng. (2015) 7, 423-449.
- [8] M. Akram, S. Nawaz, *Certain Types of Soft Graphs*, U.P.B. Sci. Bull., Series A, Vol. 78, iss. 4 (2016), 67- 82.
- [9] J. D. Thenge, B.S. Reddy, R.S. Jain, *Connected Soft Graph*, New Mathematics and Natural Computation, Vol.16, No.2 (2020) 305-318.
- [10] J. D. Thenge, B.S. Reddy, R.S. Jain, *Contribution to Soft Graph and Soft Tree*, New Mathematics and Natural Computation (2020).
- [11] N. Sarala, K. Manju, *On Soft Bi-partite Graph*, International Journal of Basic and Applied Research, Vol. 9 (2019), 249-256.
- [12] J. D. Thenge, B.S. Reddy, R.S. Jain, *Adjacency and Incidence Matrix of a Soft Graph*, Communications in Mathematics and Applications, Vol. 11, No. 1 (2020), 23-30.
- [13] S. Venkatraman, R. Helen, *On domination in soft graph of some special graphs*, Malaya Journal of Matematik, Vol. S, No. 1 (2019), 527-531.